Energetic and Exergetic Approach to a Geothermal Energy Powered Organic Rankine Cycles

Abid Ustaoglu[1], *Mustafa Alptekin*[2,3]

Abstract

Energy is very essential in daily life and industry. Required energy can be supplied from fossil fuels such as coal, oil, natural gas. Since these resources damage the environment and increase greenhouse gas rate, alternative energy resources can be used for different applications such as power generation, refrigeration and air conditioning. Rankine cycle can be commonly used for power generation. However, organic Rankine cycle can be preferred instead of Rankine cycle at low source temperatures. In this study, a thermodynamic analysis of a reheat organic Rankine cycle is performed. The evaporator heat energy is supplied from geothermal energy. R245fa is selected as a working fluid. Energy and exergy balance equations for the thermodynamic model are provided according to the first and second law of thermodynamics. The results such as power output, thermal efficiency, exergy destructions rates and second law efficiency are evaluated as function of condenser pressure and evaporator pressure.

Keywords *: Organic Rankine Cycle, Geotermal energy, thermodynamic analysis, exergy.*

1. INTRODUCTION

Rapid population rise and industrialization in developing and developed countries have been caused substantial demand of energy. About 65% of world energy demand is provided from fossil fuels such as oil and natural gas. However, these resources have disadvantages including eventual depletion and environment hazardous. Therefore, renewable energy is an important alternative to overcome these problems and for a clean energy future. The utilization of renewable energy sources have been increasingly used for both power generation and refrigeration applications in recent years. Geothermal energy is one of alternative resources. The ultimate source of the geothermal energy is the molten core of the earth. This energy is practically inexhaustible compare to the mankind`s energy demand. The natural rate of heat loss per unit area of the earth surface is about 50 kW [1]. The installed capacity of the geothermal power in the world can increase from 10,000 MW to about 58,000 MW between years 2010 and 2050 [1]. This indicates that the geothermal energy has a significant potential of improvement.

Many thermodynamic cycles have been used to utilize the waste heat through the industrial processes, heat of fuel combustion and renewable energy sources by using gas and steam powered energy cycles. Due to low work input requirement of the steam powered cycle, these are commonly used in the power plants. Rankine cycle is a way of power generation and is one of the most general methods. However, it is not an appropriate technology and economic to use low grade heat such as renewable energy sources. On the other hand, Organic Rankine Cycle (ORC) is an appropriate technology in order to generate power by using low grade heat such as solar energy, biomass, low grade waste heat and geothermal energy [2]. Many studies have been carried out about ORC to improve the performance and optimize the operation conditions for different component use in the ORC. Tuo [3] carried out thermo-economic analysis of rankine cycle with reheat enhancement for low grade heat loss. The results showed that optimum high pressures, minimizing the unit heat exchanger area and system cost are much lower than that maximizing the energy performance. Moreover, a reheat cycle is more cost effective than a basic cycle. Chandramouli [4] have done a parametric and optimization studies of reheat and regenerative Braysson cycle. this optimum pressure ratio is a function of turbine inlet temperature. They suggested designing the system for the operating condition of minimum specific fuel consumption rather than for maximum power output. Gogoi and Talukdar [5] made a parametric study in term of exergy analysis method for a combined reheat regenerative thermal power plant and water–LiBr vapor absorption refrigeration system. Among the cycle`s components, exergy destruction rate of the generator is the highest followed by irreversibility contribution of the absorber, condenser and the evaporator. Many high quality studies have been carried about thermodynamic cycle. Although a number of studies have been expressed in this section, there are not much related to reheat ORC cycle. This study is a preliminary work of an advanced exergy analysis of a reheat organic Rankine cycle. The detail of the advanced exergy analysis method can be seen in some studies in the literature [6, 7].

[1] *Corresponding author: University of Bartin, Bartin, 74100, Turkey austaoglu@bartin.edu.tr*

[2]*University of Suleyman Demirel, Isparta, 32260, Turkey, mustafaalptekin@sdu.edu.tr*

[3]*University of Hakkari, Hakkari, 30000, Turkey, mustafaalptekin@hakkari.edu.tr*

2. MATERIAL AND METHOD

2.1 System Description

In order to improve the system performance, usually the evaporator pressure of the system must be increased. However, along with that, the vapor quality of the turbine outlet decreases significantly. In order to solve this problem, the temperature of the working fluid can be increased into very high temperatures. However, this high temperature can damage the turbine due to material resistance. Therefore, this method is not appropriate in applications. Another way is to expand the pressure in two stages and between these turbines a reheat can be applied to the system. Applying reheat to system is a common method in modern steam powered plant. Figure 1 shows the schematic view of a reheat organic Rankine cycle. The working fluid comes to the pump to be saturated liquid and is compressed to the evaporator operation pressure and leaves the evaporator to be superheated fluid. Then, the fluid comes to the high pressure turbine to be expanded. The working fluid after leaving high pressure turbine reenters to the evaporator to increase the temperature of working fluid to the high pressure turbine inlet temperature and then comes to the low pressure turbine where the pressure and temperature decreases by expansion. The working fluid leaves the low pressure turbine to be superheated fluid or saturated liquid vapor mixture at condenser pressure and then comes to the condenser to reject heat to decrease the initial temperature. Thus, the cycle is completed.

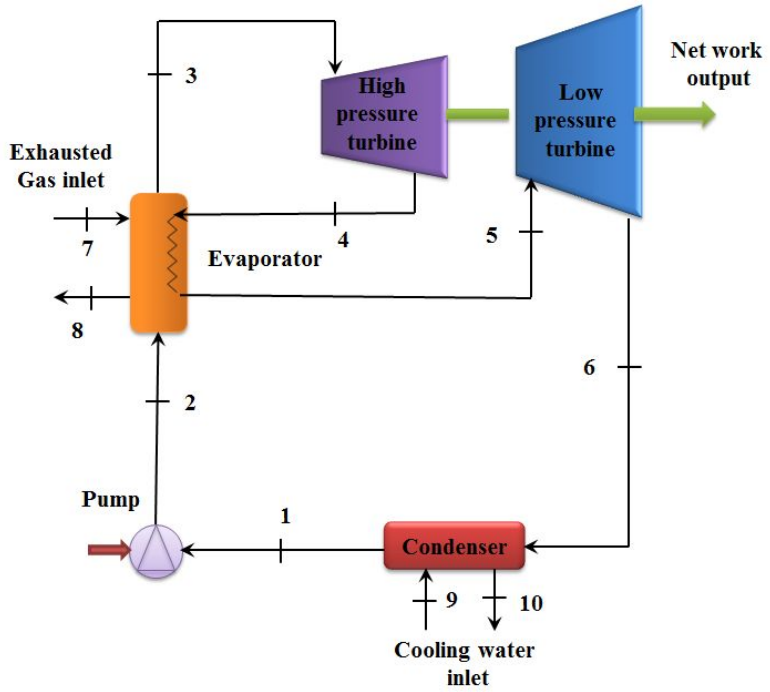

Figure 1. Schmatic view of a Reheat Organic Rankine Cycle

2.2 Thermodynamic analysis

Energy and exergy analysis generally involves applying the first and second laws of thermodynamics and the principles of conservation of mass, while energy analysis usually excludes considerations of the second law of thermodynamics. By neglecting kinetic and potential energies, the conservation of mass for steady-state processes can be expressed as follows [8].

$$\sum \dot{m}_{in} = \sum \dot{m}_{out} \quad (1)$$

The first law of thermodynamics is an express of energy principle. It is expressed for steady state processes as follows [9]-[10];

$$\dot{Q} + \sum(\dot{m}h)_{in} = \dot{W} + \sum(\dot{m}h)_{out} \quad (2)$$

Neglecting chemical, kinetic and potential exergies, exergy balance in a control volume in which a steady state process occurs can be written as [8], [11];

$$\dot{E}x_Q - \dot{E}x_W = \sum(\dot{m}\varepsilon)_{out} - \sum(\dot{m}\varepsilon)_{in} + T_0\dot{S}_{gen} \quad (3)$$

where;

$$\dot{E}x_{dest} = T_0\dot{S}_{gen} \quad (4)$$

where $\dot{E}x_Q$, $\dot{E}x_W$ and ε represent exergy of heat, exergy of work and thermomechanical exergy (flow exergy), respectively. These expressions are shown as follows [2];

$$\dot{E}x_{\dot{Q}_{in}} = \dot{Q}_{in}\left(\frac{T-T_0}{T}\right) \quad (5)$$

$$\dot{E}x_W = \dot{W}_{net,out} \quad (6)$$

$$\varepsilon = (h - h_0) - T_0(s - s_0) \quad (7)$$

$$\dot{S}_{in} + \dot{S}_{gen} = \dot{S}_{out} \quad (8)$$

where 0 subscript expresses reference conditions. The first (thermal) and second law (exergy) efficiencies of the overall system are calculated as follows [12];

$$\eta_I = \frac{\dot{W}_{net,out}}{\dot{Q}_{in}} \quad (9)$$

where

$$\dot{W}_{net,out} = \dot{m}[(h_3 - h_4) + (h_5 - h_6)] - \dot{m}(h_2 - h_1) \quad (10)$$

$$\dot{Q}_{in} = \dot{m}[(h_3 - h_2) + (h_5 - h_4)] \quad (11)$$

$$\eta_{II} = \frac{\dot{E}x_{\dot{W}_{net,out}}}{\dot{E}x_{\dot{Q}_{in}}} \quad (12)$$

The above equations were applied to the geothermal powered reheat ORC system, and were obtained mass, energy and exergy balance equations for each component.

Table 1 shows the input parameters of the system. The ORC system is programmed using Engineering Equation Solver (EES). The some assumptions are made as follows:

(1) All the processes are assumed as steady state.

(2) The pumps and turbines are adiabatic.

(3) The heat transfer to/from ambient and pressure losses in the piping system and in the evaporator and condenser of the reheat ORC system are neglected.

(4) The working fluid at the inlet of the pump is assumed as saturated liquid.

(5) Potential and kinetic energy variations are neglected.

(6) The dead state pressure P_0 and temperature T_0 are considered to be 101.325 kPa and 27 °C, respectively.

Table 1. Input values to the system

Parameters	Values
Pump isentropic efficiency	85%
High Pressure Turbine (HPT) isentropic efficiency	85%
Low Pressure Turbine (LPT) isentropic efficiency	85%
High Pressure Turbine inlet temperature	130 °C
Low Pressure Turbine inlet temperature	130 °C
Condenser pressure	180 kPa
Evaporator pressure	1000 kPa
Reheat pressure	600 kPa
Mass flow rate of working fluid in ORC	100 kg/s
Inlet temperature to condenser of cooling water	20 °C
Outlet temperature from condenser of cooling water	25 °C
Inlet temperature of geothermal water	145 °C
Outlet temperature of geothermal water	75 °C
Inlet and outlet pressure of geothermal water	600 kPa
Ambient pressure	101.325 kPa
Ambient temperature	25 C

3. RESULTS AND DISCUSSION

Figure 2 shows the net work output and exergy destruction as a function of condenser pressure of the reheat organic Rankine cycle. As is known, when the pressure of condenser decreases, the net work output should increase. Thus, the required heat input increases. However, this increase is very small. Therefore, it can increase the performance of the system. The main

objective to decrease the condenser pressure is to reduce the mean low temperature of the system. Thus, the performance increases while the carnot efficiency of system can increase. As seen in the figure, when the condenser pressure increases, the exergy destruction rate increases and net work output decreases. As is well known, the condensers are operated at lower pressure than the atmosphere in the steam power plants in order to improve the performance. However, this pressure should not be lower than the saturation pressure corresponding to the temperature of the cooling water. The highest network output to be 4400 kW and the lowest exergy destruction rate to be 2300 kW was achieved for the condenser pressure of 100 kPa. After the condenser pressure about 160 kPa the total exergy destruction rate of the system is larger than the net work out. Thus, the system must be operated with an condenser pressure lower than 160 kPa. Figure 3 show the thermal efficiency and exergy efficiencies as a function of the condenser pressure. The pressure varies between the 100 kPa and 300kPa. The system shows the best energetic and exergetic performance at 100 kPa. The exergy efficiency of the system is better than the thermal efficiency. By the pressure decrease of 200 kPa at condenser, the thermal efficiency decreases about 6% as the exergy efficiency decreases about 22%. Figure 4 shows the exergy destruction rate as a function of condenser pressure for each component of the cycle. As it seen in the figure, exergy destruction rate of pump and high pressure turbine have no change with variation of condenser pressure. The highest exergy destruction rate occurs in the evaporator and it decreases up to the condenser pressure of about 190 kPa while after this pressure rate the condenser shows the highest exergy destruction rate. The exergy destruction rate of low pressure turbine and evaporator decreases by increasing pressure. Only the destruction rate of condenser increases due the increase in the condenser pressure.

In Figure 5, 6 and 7, the system is analyzed in terms of the evaporator pressure. In that case the condenser pressure is assume to be 180 kPa while the evaporator is considered as a calculation parameter. The main objective to increase the condenser pressure is to achieve a higher mean high-temperature for the system. Figure 5 shows the net work output and total exergy destruction rate of the system. As is known, to increase the mean high temperature of the system has an effect of performance improvement for a basic rankine cycle. However, this also results in a reduction in the vapor quality of the working fluid. This undesirable affect can be eliminated using a reheat ORC. The net work output of the system increases by increasing the evaporator pressure while the exergy destruction rate decreases. These are inversely proportional to each other. The net work output of the system can increase about 2300 kW to 4200 kW by increasing the pressure from 600 kPa to 2000 kPa. On the other hand, until the evaporator pressure of 1000 kPa, the exergy destruction rate is larger than the net work output. Therefore, it is important to operate the system with a higher evaporator pressure of 1000 kPa. The thermal and exergetic efficiencies of the system increase by increasing evaporator pressure. The thermal efficiency increases about only 5% by the pressure increase of 1400 kPa. On the other hand, the exerygetic performance of the system increases from 25% to 40%. In Figure 6, the exergy destruction rate of each component as a function of evaporator pressure is illustrated. The variation of evaporator pressure has no effect on the low pressure turbine, condenser and pump. The pump has almost no destruction rate. The exergy destrucation rate of high pressure turbine increases with increasing pressure while the that of evaporator decreases. The highest exergy destruction rate occurs at the evaporator up to the pressure of about 1100 kPa and its destruction rate reduces under the exergy destruction rate of the condenser.

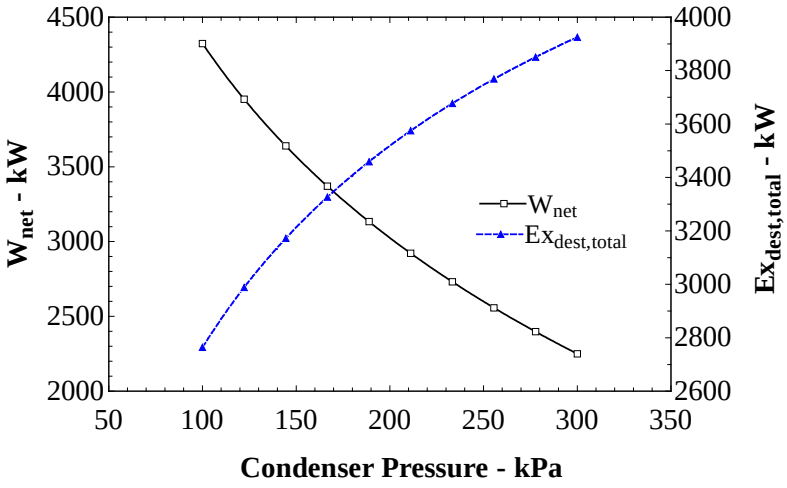

Figure 1. Net work output and total exergy destruction rate as a function of condenser pressure

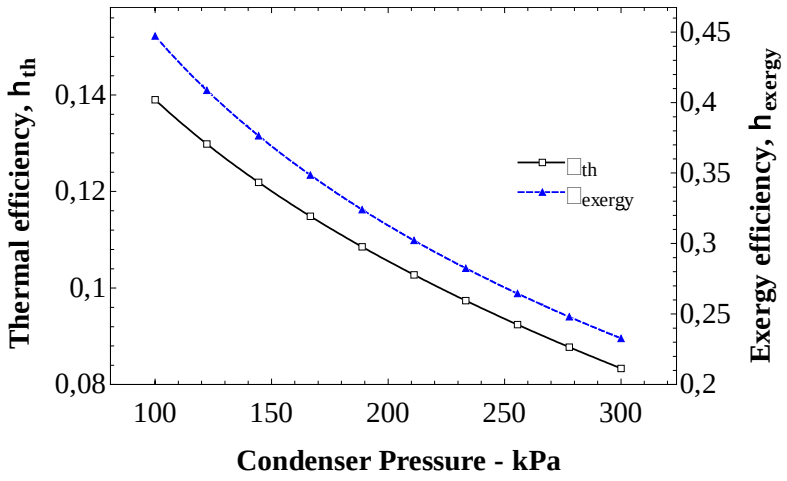

Figure 3. Thermal efficiency and exergy efficiency as a function of condenser pressure

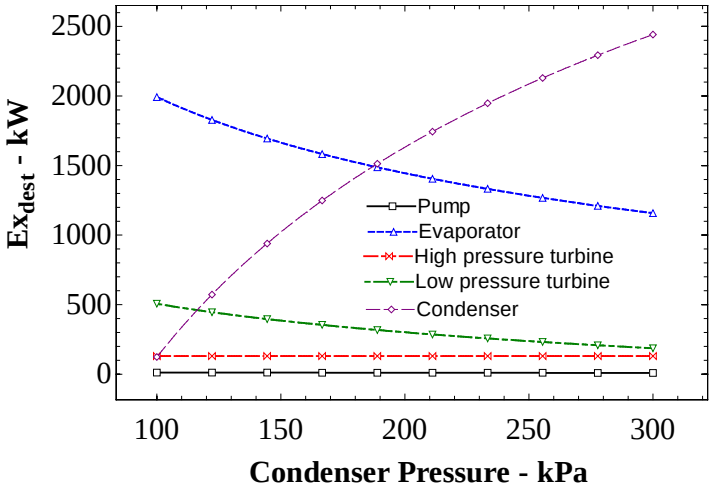

Figure 4. Exergy destruction rate as a function of condenser pressure for each component

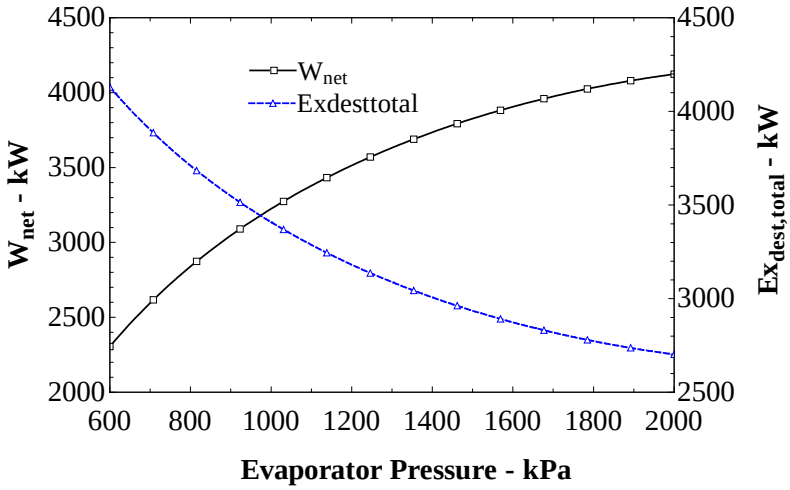

Figure 5. Net work output and total exergy destruction rate as a function of evaporator pressure

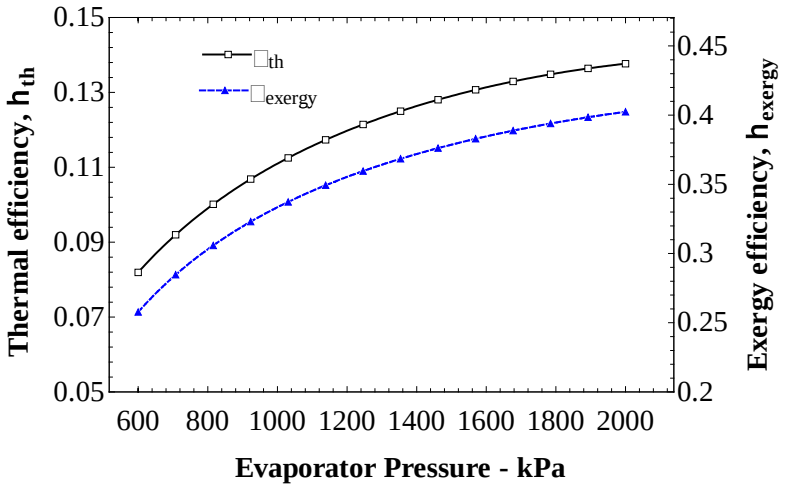

Figure 6. Thermal efficiency and exergy efficiency as a function of evaporator pressure

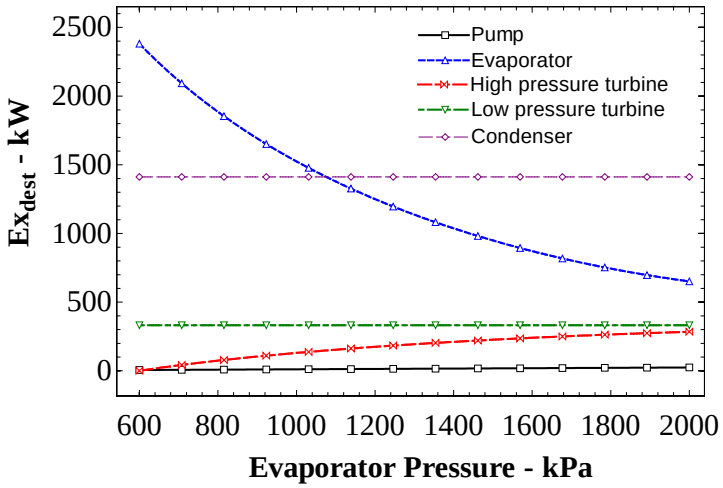

Figure 7. Exergy destruction rate as a function of evaporator pressure for each component

4. CONCLUSIONS

A preliminary study of advanced exergy analysis was carried out by using the conventional exergy analysis method for a reheat organic Rankine cycle. Several calculation parameters including energy efficiency, exergy efficiency, net work output, total exergy destruction rate and the exergy destruction rate of each component were evaluated as a function of condenser and evaporator pressure. The followings points summarize the results.

1. In order to improve the system performance the main idea should be decrease the condenser pressure to reduce the mean low temperature or to increase the condenser pressure to achieve a higher mean high-temperature.
2. The net work output of the system increases by reducing the condenser pressure or increasing the evaporator pressure. The highest network output to be 4400 kW and the lowest exergy destruction rate to be 2300 kW was achieved for the condenser pressure of 100 kPa. After the condenser pressure about 160 kPa the total exergy destruction rate of the system is larger than the net work out. Thus, the system must be operated with an condenser pressure lower than 160 kPa.
3. On the other hand, until the evaporator pressure of 1000 kPa, the exergy destruction rate is larger than the net work output. Therefore, it is important to operate the system with a higher evaporator pressure of 1000 kPa. For a pressure increase from 600 kPa to 2000 kPa, the system can achieve a net work output of 4200 kW.
4. The thermal and exergy efficiency of the cycle decreases accordingly to each other by increasing the condenser pressure. The thermal efficiency of the system is about 14% at the condenser pressure of 100 kPa while the exergy efficiency is about 45% at the condenser pressure of 100 kPa. For the pressure decrease of 200 kPa, the thermal efficiency decrease about 6% as the exergy efficiency decreases about 22%.

5. By increasing the evaporator pressure from 600 kPa to 2000 kPa, the thermal efficiency increase to 14% as the exergy efficiency increase from 25% to 40%.
6. The largest exergy destruction occurs in the case of evaporator, after certain pressure for condenser and evaporator, the component having largest exergy destruction becomes the condenser. Therefore, it is important to concentrate on these components to improve the overall system performance. While the condenser pressure varies, the exergy destruction rate of high pressure turbine and pump remain constant, that of condenser increase and low pressure turbine decreases.
7. Advanced exergy analysis results will be going to show the improvement potential of the system and the interaction of among the component.

REFERENCES

[1]. S.K. Sanyal, "Future of geothermal energy. Proceedings Thirty-Fifth Workshop on Geothermal Reservoir Engineering Stanford University," 2010 SGP-TR-188, Stanford, California, February 1-3.
[2]. O. Kaska, "Energy and exergy analysis of an organic Rankine for power generation from waste heat recovery in steel industry," Energy Conversion and Management, vol. 77, pp. 108–117, 2014.
[3]. H. Tuo, "Thermal-economic analysis of a transcritical Rankine power cycle with reheat enhancement for a low-grade heat source," Int. J. Energy Res., vol.37, pp. 857–867, 2013.
[4]. R. Chandramouli, M.S.S. S. Rao and K. Ramji, "Parametric and optimization studies of reheat and regenerative Braysson cycle," Energy, vol. 93, pp. 2146-2156, 2015
[5]. T.K. Gogoi, K. Talukdar, "Exergy based parametric analysis of a combined reheat regenerative thermal power plant and water–LiBr vapor absorption refrigeration system," Energy Conversion and Management, vol. 83, pp. 119–132, 2014.
[6]. A. Ustaoglu, M. Alptekin, M.E. Akay and R. Selbas, "Advanced exergy analysis of an application of waste heat powered ejector refrigeration system to rotary kiln" Proceedings of the 8th International Exergy, Energy and Environment Symposium, IEEES-8 2016, May 1-4, Antalya, Turkey.
[7]. M. Alptekin, A. Ustaoglu, M.E. Akay and R. Selbas, "Thermodynamic evaluation of absorption-compression cascade refrigeration cycles for advanced exergy analysis" Proceedings of the 8th International Exergy, Energy and Environment Symposium, IEEES-8 2016, May 1-4, Antalya, Turkey.
[8]. L.G.Farshi, A.H. Mosaffa, C.A.I. Ferreira and M.A Rosen., Thermodynamic analysis and comparison of combined ejector–absorption and single effect absorption refrigeration systems, Applied Energy, vol. 133,pp. 335–346, 2014.
[9]. Y.A. Cengel and M.A. Boles, An Engineering Approach Thermodynamics, Fifth Edition,p. 946, 2007.
[10]. A. Bejan, Advanced Engineering Thermodynamics, Wiley, New York, 1997.
[11]. E.K. Akpinar and A.Hepbasli, A comparative study on exergetic assessment of two ground source (geothermal) heat pump systems for residential applications, Building and Environment, vol. 42, pp. 2004–2013 (2007).
[12]. I. Dincer and M.A Rosen., Environment and sustainable development, Elsevier Science, p. 472, 2007.

Design and Multiphase Modelling of a Double Outlet Centrifugal Pump

Muaz Kemerli[1], Zekeriya Parlak[2], Tahsin Engin[3], Halit Yasar[4]

Abstract

The centrifugal pumps are typical pumps which have one inlet and one outlet. In special conditions those pumps can work with double outlet. The most common method is using a valve to direct the flow to the desired outlet. In this study, a double outlet pump has been designed and the flow is directed to desired outlet by changing the rotation of the impeller. A multiphase CFD model have been used for modelling the physics and two outlet pipes have been extended through a specified height to monitor the water levels. The inlet and outlet boundary conditions are set to zero to see the runout condition of the pump. It is assumed that air is entering through the pump body for backflow conditions of the outlets. The gravity effects are considered to calculate the static pressure at the outlets and Volume of Fluid (VOF) multiphase model are used to obtain the results. It is observed that the pump can work with a specific rotation speed and an outlet pipe height to prevent the flow to exit from both outlets. It is explored that the constraints has a critical role for designing such turbomachines.

Keywords**:** *CFD, VOF, Centrifugal Pump,*

1. INTRODUCTION

Centrifugal pumps are the rotodynamic turbomachines which are using a rotating impeller to increase the pressure of a fluid. Design process of a pump needs to an analytical solution and manufacturing different blades and geometries takes a lot of time, effort and costs money. In the last two decades CFD is gaining more and more attention to overcome such difficulties by using a numeric solution instead of making tests and collecting experimental results. Turbomachinery is one of the areas where CFD becomes an important tool in the design process [1]. In this study, design of a double outlet centrifugal pump will be proposed and a proper modelling approach will be presented.

When an engineer has to divide a flow through two different outlets, to overcome such as a specific problem, the first and foremost solution is using a valve. But the valves have to be controlled manually or electronically in order to supply a desired flow through outlets. In most cases the valves are manually controlled but in several applications in process engineering or such cases where a fast response control required, an electronic controller and various sensors will be needed. While using those elements, it is inevitable to use a lot of components inside the flow domain and it is not easy to overcome the problems where the water and humidity involve. That is why an engineer needs to find a solution either direct the flow through different outlets by a control element such as a valve and a sophisticated control system or using a different type of control mechanism which doesn't consist such number of components. In this study it will be investigated if the flow can be directed by changing the rotation of impeller of a centrifugal pump by designing an appropriate hydraulic geometry. To understand the physics, a basic and simple model of a centrifugal pump will be discussed and developed. As it is said before, the physics will be understood by using a CFD software since this specific case is still an unknown phenomenon among the mechanical engineers.

2. DESIGN OF A DOUBLE OUTLET CENTRIFUGAL PUMP

In this study, a double outlet centrifugal pump is designed to pump the fluid through two different outlets. To provide that the impeller is rotating in different directions, when the first outlet needs to be fed, the impeller rotates in clockwise direction and when the other outlet needs to be fed, the impeller starts to rotate in the opposite direction. To achieve that there are two reflectors have been placed in the entrance of the outlet pipes as shown in Figure 1. While the pump starts up, the first reflector prevents the flow to discharge from the first outlet and the second reflector keeps the flow out through second outlet. And when the impeller works in reverse way, the effect of the reflectors has been reversed and the flow is directed to the other outlet. So that, to prevent the flow in one outlet and to keep the flow out in the other outlet can be realized.

[1] *Sakarya University, Department of Mechanical Engineering, 54187, Serdivan/Sakarya, Turkey. mkemerli@sakarya.edu.tr*

[2] *Sakarya University, Department of Mechanical Engineering, 54187, Serdivan/Sakarya, Turkey. zparlak@sakarya.edu.tr*

[3] *Corresponding author: Sakarya University, Department of Mechanical Engineering, 54187, Serdivan/Sakarya, Turkey. engint@sakarya.edu.tr*

[4] *Sakarya University, Department of Mechanical Engineering, 54187, Serdivan/Sakarya, Turkey. hyas@sakarya.edu.tr*

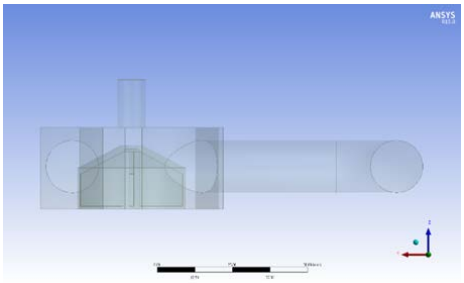

Figure 2. Geometry of the pump modelled in a CAD environment

3. MODELLING OF THE PUMP

The modelling of the designed pump, and the physical model of the operation is realized by using FLUENT software. To achieve this, different models are investigated which can be used to model a turbomachine or a pump in particular [2]. It is a matter of question among the CFD users that which solving approach is better than another [3]. Most of the well-known models which are widely accepted are Moving Reference Frame (MRF) approach, Mixing Plane, Sliding Mesh and Dynamic Mesh approaches [4]. The two latter models are transient models in essence and require a lot of time and computational cost while the two former models are steady-state models and are suitable for more simple solutions.

3.1 Moving Reference Frame (MRF) Method

The MRF method is a method which can simulate the impeller motion by assuming that the whole rotating domain is moving in a specific point of time [5]. The rest of the domain is considered as stationary domain which means there is no external motion is applied but it is effected by the motion of the MRF zone. As the solver iterates, the solution starts to converge to a point where the impeller rotates in a specific point of time and the solution shows an instant from the entire operation in time. Since the impeller position is constant, the method is called as “frozen rotor” method, to emphasize that it is a “frozen” solution which is taken from an instant part of a time. In Figure 2(a) the MRF zone can be seen while in Figure 2(b) the grid structure of the MRF zone is presented.

Figure 3. (a) The MRF zone inside the impeller (b) The grid structure of the MRF zone

3.2 Multiphase Modelling

As a first approach for this specific solution a single phase solution is preferred. But in most cases, the flow can go in reverse way, which is called “backflow”. The backflow condition is well known and it is considered in most of the CFD codes. But when dealing with a pump, and especially in such a double outlet pump, the backflow condition has a greater importance since the backflow fluid is not a liquid or water in particular; rather it is the air which penetrates into the domain. If it is modelled as a single phase solution, it ends up with an unphysical solution because the air wasn’t modelled. So that, a multiphase model is proposed for the model and the air flow is considered as shown in the Figure 3. The gravity effects are also taken in consideration to see the water levels in the outlet pipes.

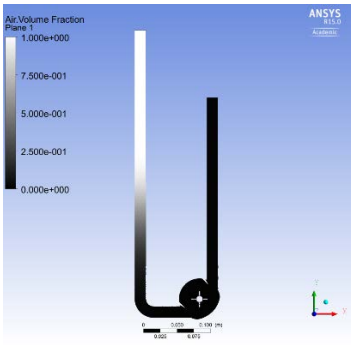

Figure 4. The air volume fraction inside the pump (multiphase VOF model)

To understand the physics of the flow, reverse flow at the outlet boundaries are considered as an air flow inside the pump. This leads an undesired condition which the pump fills with air bubbles or the air penetrates through the vicinity of the impeller and blocks the operation of the pump which can be called as a "vacuum condition". So it is very important to consider this effect since it is a limit for the designer which completely destroys the operation.

After the analysis of multi-phase solution, the values of flow rate around 0-15 l/m, doesn't lead a backflow which might be dangerous for the operation. But for a bigger flow rate, the air can penetrate through the flow domain and this can block the operation. The solution is also can be interpreted as the flow is rising in the one outlet while it flows through the other operating outlet. Figure 3 shows that while the fluid is flowing through the outlet at the right, the water level at the left is smaller than the pipe length. This brings us to another limit which is the overflow of the liquid to the left (undesired) outlet.

3.3 Solution Method

The implicit schemas are used to converge the solution at the desired error. Using a VOF model and MRF model at the same time brings some problems about convergence which has to be controlled by intervening the solution process. It is also an important fact that choosing the right initial condition. In the first iterations the fluid zone starts to propagate inside the domain, which needs to be solved precisely and after a certain convergence value it is a better way to speed up the solution

4. RESULTS AND COMPARISON

The results of the pump is obtained by using different inlet conditions with different velocities. It is also proved that the pump can operate with a proper design and the flow can be directed to the desired outlets. The efficiency of the pump is relatively low since the design is quite simple. But in this study the aim is not optimize the efficiency but it is a work which understands the physics of the pump and develop the structure in a proper way. The plotted data can be seen from the Figure 4(a) and Figure4(b).

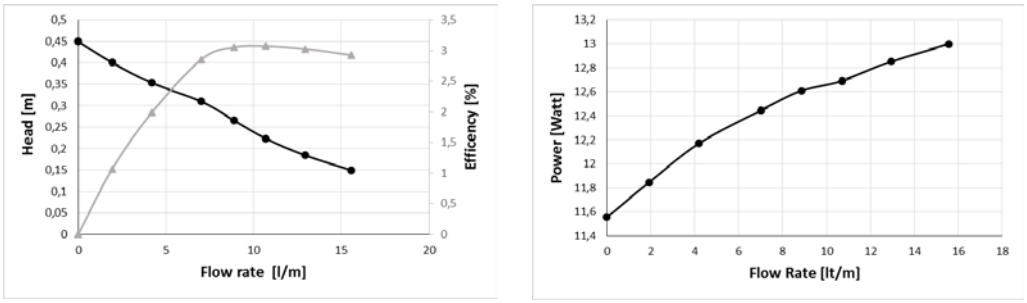

Figure 5 (a) The performance curve of the pump (b) the power consumption of the pump

To plot the pump characteristic curve, the inlet is specified as a velocity inlet and the both outlets is considered as at the atmospheric pressure. The rotation speed is defined at a 3000 rpm rotation speed. The characteristic curve ends at the 15 l/m value since the air starts to enter the flow domain from the other outlet and block the operation for bigger flow rate values.

5. CONCLUSION

The solution method of a double outlet centrifugal pump is offered in this study. The two important conditions are emphasized which are the overflow and vacuum conditions. These two conditions have to be taken in consideration when designing the pump. The study also shows that such double outlet pumps has to be modelled in multiphase physics, else the results will be further away from the actual point. Another key aspect of the solution is the gravity effect which is a profound way to model the water level of the undesired outlet.

On the contrary, it has to be known that the MRF method has some limitations because it is a steady-state model and doesn't able to model the transient effects which occur in the flow domain. Depending on the geometry of the domain, some significant errors might occur but in the other side the transient solution has larger computational cost and the process is time consuming.

ACKNOWLEDGMENT

The authors gratefully acknowledge TUBITAK for making this project possible under Grant No:5130031
The authors acknowledge Sakarya University Scientific Research Projects Commission (SAÜ Bilimsel Araştırma Projeleri) for making this project possible

REFERENCES

[1]. S R Shah, S V Jain, V J Lakhera (2010), CFD Based Flow Analysis of Centrifugal Pump, Proceedings of the 37th National & 4th International Conference on Fluid Mechanics and Fluid Power, December 16-18, 2010, IIT Madras, Chennai, India.
[2]. S. R. Shah, S. V. Jain, R. N. Patel, V. J. Lakhera (2012), CFD for centrifugal pumps: a review of the state-of-the-art, Chemical, Civil and Mechanical Engineering Tracks of 3rd Nirma University International Conference (NUiCONE 2012), Ahmedabad, India.
[3]. TU, J, YEOH, GH, LIU, C, Computational Fluid Dynamics, A Practical Approach, Butterworth Heinemann Massachuset USA, 2012.
[4]. M. Asuaje, F. Bakir, S. Kouidri, F. Kenyery, R. Rey (2004) Numerical Modelization of the Flow in Centrifugal Pump: Volute Influence in Velocity and Pressure Fields, International Journal of Rotating Machinery 2005:3 244-255
[5]. ANSYS FLUENT 15.0 User's Guide, 2013.

Design and Modelling of a Magnetorheological Damper by CFD

Muaz Kemerli[1], Zekeriya Parlak[1], Tahsin Engin[1]*

Abstract

The Magnetorheological (MR) dampers are damping elements which are different from the classic dampers. MR dampers are filled with a magnetic-sensitive fluid and are controlled by a magnetic field. This gives a great advantage and flexibility to control the stiffness of the damper by changing the current which generates the magnetic field by a coil. The required magnetic field is obtained by using very small amount of energy and this makes the use of MR dampers more feasible. In this study, it is intended to model an MR Damper by using a 2D axisymmetric model with a less amount of mesh number and computational cost. Instead of modeling a moving piston, it is preferred to move the boundaries, and keep the piston head stable. A dynamic mesh motion is applied at the boundaries of the domain. A constant magnetic flux is assumed at the edge of the coil through the gap inlet point. The behavior of the MR fluid on different magnetic flux densities is calculated from the datasheet of the producing company. The Non-Newtonian behavior of the fluid around the coil has been modelled with Herschel-Bulkley model. The generated model is compared with the analytic and experimental data. The solution is in a good agreement with both the analytical and experimental data.

***Keywords*:** *MR Damper, Herschel-Bulkley, Non-Newtonian Fluid, CFD*

1. INTRODUCTION

A Magnetorheologic (MR) damper, is a damper which can be semi-actively controlled by an external magnetic field created by a current. To provide that behavior, the damper is filled with a magnetic-sensitive fluid, which is a concentration of iron particles or other type of magnetic particles and oil. The particles inside the oil are magnetic particles and if an external magnetic field is applied they change their positions. The magnetic particles create a chain along the magnetic flux line and causes to block the flow. To understand that behavior the very physical phenomenon is interpreted as a change in the apparent viscosity. In fact, the viscosity of the oil keeps constant but the fluid behaves like a more viscous fluid. Because of the change in the rheological properties of the fluid depending on the applied magnetic flux, this type of fluids are categorized as Magnetoheologic (MR) fluids [1]. As the magnetic field intensity increases the MR fluid gets more viscous and tends to flow slower. A more viscous fluid can generate more viscous force and this provides a stiffer damper. In Figure 1, the behavior of the MR fluid under a magnetic flux is presented.

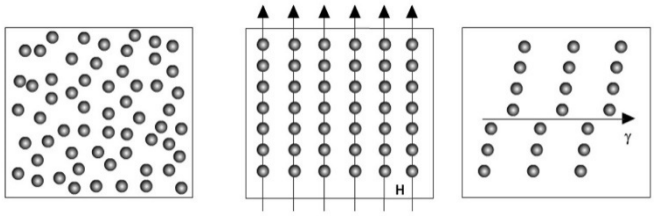

Figure 1. An illustration of the magnetic particles under the magnetic flux

After the exploration of the MR fluid, the practical use of this fluid becomes an important field and various types of designs are proposed. The prominent areas which MR fluid is used are dampers, clutches, prosthesis and such machines which are related upon viscous forces. Biomedical applications, automotive industry, civil engineering and in many other disciplines, the MR fluid gains more attention [3, 4]. One of the most important field which the MR fluid is used, is MR dampers as mentioned before.

[1] *Corresponding Author: Sakarya University, Department of Mechanical Engineering, 54187, Serdivan/Sakarya, Turkey. engint@sakarya.edu.tr*

2. DESIGN OF AN MR DAMPER

A typical mono tube damper works with a viscous fluid and a piston which slides inside the fluid. As the velocity of the piston increases, the fluid generates a reverse friction force proportional to the velocity to stop the motion. An easy way to increase the friction is using a narrow gap for the fluid to pass which provides a bigger friction force since the friction force is inversely proportional to the cross-section of the flow area. It is also important to choose a reasonable position for the coil which provides a magnetic field to change the behavior of the fluid. An accumulator is also needed to keep the pressure above the vapor pressure and prevent the cavitation inside the damper. A fundamental damper design has to be consist of those elements in essence.

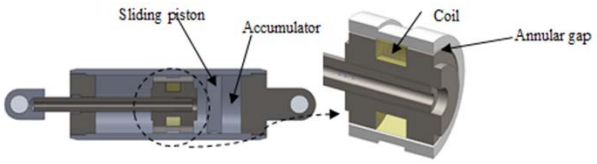

Figure 2. Design of an MR damper

To address the physics of the damper, a simple design is considered. As the study focuses on the coil and piston geometry of the damper and the effects of the geometrical parameters, a single coil model is preferred.

2.1 Modelling the Piston Movement

The model of the MR damper is generated in a 2D domain. The axis is considered as the symmetry edge and the 2D plane is revolved around the axis to create a 360 ° MR damper body. The axisymmetric model enables the usage of smaller mesh elements and the computational cost is decreased tremendously. It also ensures to use quadratic mesh elements which ends up with better results compared to a same mesh number with tetrahedron or tetra meshes.

While considering the motion in the damper, the movement of the piston has to be modelled which necessitate a dynamic mesh approach. Velocity, which is the most important input of a damper, has to be the input for this motion. To create a velocity input, the piston has to be moved or vibrated with a constant frequency and amplitude. As the damper has a limited space it is a reasonable way to apply a sinusoidal movement and velocity to see the behavior of the damper. There are two ways to model the movement. Either the piston head can be moved inside the damper body or the upper and lower boundaries has to be moved. At the first glance, it seems to move the piston head seems to make more sense. But while designing the model if it is looked carefully, it will be find out that a moving boundaries give more advantage to a user rather than the former model. The moving boundaries are shown in the Figure 3 as the A and B boundaries.

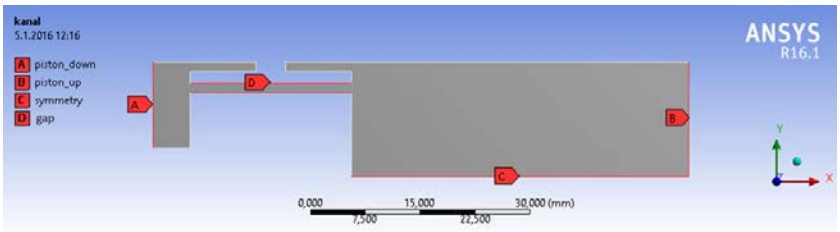

Figure 3. 2D model of the MR Damper

2.2 Modelling the Rheology

To obtain a proper viscosity, the selection of a rheological model has a key role. It is well-known among the researchers that while there is no magnetic flux applied the MR fluid behaves as a Newtonian fluid. But it has a non-Newtonian behavior under certain magnetic fluxes. This makes the model more complicated and sophisticated. Because of the unpredicted structure and unlinearity of the shear force to shear rate, there are lot of different models are proposed. The Papanastasiou model, Power law model or the Herschel Bulkley model are some of the accepted models [5].

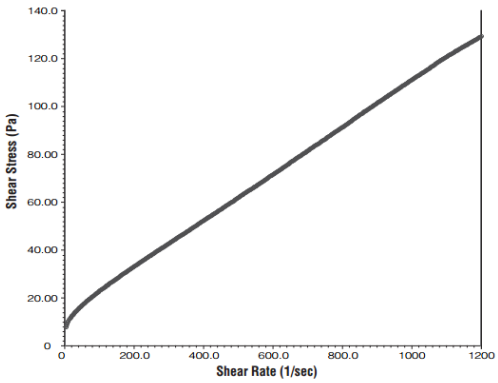

Figure 4. The Behavior of the LORD-MRF-132DG MR Fluid at 40°C Without a Magnetic Field [6]

The MR fluid has Bingham plastic characteristics which behaves as a plastic fluid until the shear stress reaches a certain value. After the shear stress go above the critical shear stress value, the fluid starts to deform but in this case the deformation rate has not a linear correlation with the shear stress. As the shear stress grows the shear rate grows with a slower speed which is called a shear thinning fluid.

In this study the Herschel-Bulkey model is preferred because of its superiority on the other models specifically for the MR fluid. [6]

2.3 Modeling Magnetism and the its effects on Fluid

The effects of the magnetism is discussed above. As mentioned before the area at the vicinity of the coil has a magnetic flux value depending on the current passes through the coil. As the current increases the magnetic flux density grows proportionally. The more flux density means bigger apparent viscosity property are in effect. In the CFD model, the areas which are effected from the magnetic flux are represented with a constant rheological properties which are obtained with a rheometer and the properties are applied to the very location. The magnetized areas are modelled with a different rheological properties while the rest of the geometry is modelled as a Newtonian fluid. At a random instance, the viscosity contour of the fluid is shown in the Figure 5.

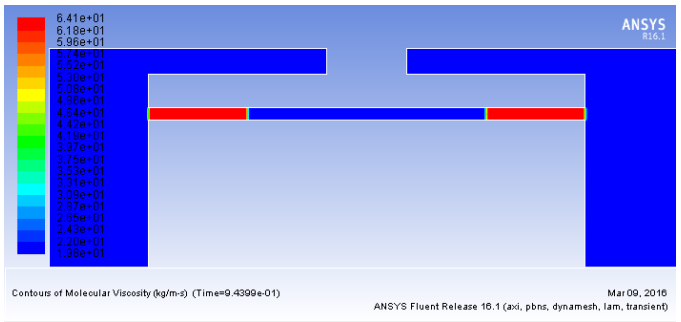

Figure 5. The model of the effects of the magnetic flux on fluid

Rheological properties of the fluid is approximated with an average value since the magnetic flux density doesn't change too much at the magnetically effected area. It is understandable that the viscosity has the same value in the magnetic effected area since the velocity is the same along the gap because of the same cross sectional area.

2.4 Obtaining the Stability and Mesh Convergence

The transient solution is selected and the appropriate time step size achieved by monitoring the convergence. Since the 2D model is preferred the mesh number is quite small and the computational cost is dramatically decreased. By dividing the domain into the small size meshes, the convergence of the solution is obtained. The time step size is evaluated at a stable point and the stable solution is obtained for all points in time since the velocity is varies along a single stroke.

3. RESULTS AND COMPARISON

3.1 Comparison with the Analytic Solution

The analytic solution of the domain is obtained by using the following formula for the calculation of the pressure drop along the gap [2]. ΔP_{μ} represents the uncontrolled viscous pressure drop while the ΔP_{τ} is the controllable pressure drop due to

magnetic effect. Q represents the volumetric flow rate. t_k and τ_y are coil length and the yield stress respectively. R_1 and L represents the average radius of the circular gap and gap length respectively. g is the gap width.

$$\Delta P = \Delta P_\mu + \Delta P_\tau = \frac{6Q\mu L}{\pi R_1 g^3} + c\frac{2t_k}{g}\tau_y \quad (1)$$

by a similar fashion the generated force is obtained for a specific time of the motion with a known displacement and velocity;

$$F_\mu = u_p(A_p - A_k)\frac{6\mu L A_p}{\pi R_1 g^3} \quad (2)$$

$$F_\tau = u_p(A_p - A_k)\frac{6\mu L A_p}{\pi R_1 g^3} \quad (3)$$

$$F = F_\mu + F_\tau + F_s \quad (4)$$

The F_s represents the internal friction forces (or losses), F_τ represents the magnetically controlled forces and F_μ represents the uncontrolled viscous forces. A_p, A_k and u_p are the piston head cross section area, piston rod cross section area and piston velocity respectively.

Table 1. Comparison between the analytic and numeric solution

Value	Analytical Solution	CFD Results	Error (%)
Pressure (Pa)	1.2107e-06	1.26793e-06	4.7
Force (N)	946.8442	933.208	1.4

The analytic solution of the problem is obtained at a random instant of time, where the velocity about to reach its peak value. The results show a good agreement with the analytical solution, especially when calculating the forces as listed in Table 1.

3.2 Comparison with the Test Results

It is also an important way to obtain the test results since the unpredicted effects are influencing the flow domain apart from the gap. To take those effects into consideration, a model with more comprehensive boundaries needs to be created. That is why the numeric solution is needed and the comparison of the numeric solution with the test results proves that necessity. In general, the analytic solution is only can be obtained for the gap geometry since the rest of the domain is not able to be modelled in simple mathematical equations.

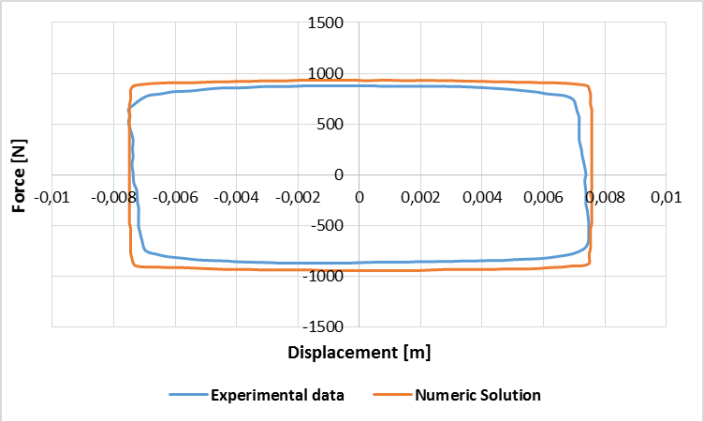

Figure 6. The comparison of the test results with the numerical solution

In Figure 6 the comparison between the test and CFD results are presented. It shows a good agreement with the test results which proves the ability of presentation of the CFD model.

4. DISCUSSION

It is proven that the above CFD model is sufficient and there is no need to create a 3D mesh structure to model an MR damper. It is also not necessary to model the magnetic flux within the flow geometry, in most cases it is enough to use an average value to model the rheological properties of the fluid. It is a great advantage for the software user to have a small amount of mesh and lower computational cost.

CFD is gaining attention in the last decades and its importance still grows as new processors developed with better computational ability. When the question arises for the engineers that if it is more useful to create an analytical model or a numerical model, the study shows that the numerical solution is always at a step further since its ability to understand the flow behavior within the areas where the analytical solution is almost impossible to be obtained.

ACKNOWLEDGMENT

The authors acknowledge Sakarya University Scientific Research Projects Commission (SAÜ Bilimsel Araştırma Projeleri) for making this project possible.

REFERENCES

[1]. Magnetorheological Fluid Technology: Applications in Vehicle Systems, Seung-Bok Choi, Young-Min Han, CRC Press, 2012
[2]. Manyeto-Reolojik Sıvılı Yari-Aktif Bir Sönümleyici Tasarımı Ve Analizi, Zekeriya Parlak, Phd Thesis, Sakarya University, August 2010
[3]. Jolly, Mark R., Jonathan W. Bender, and J. David Carlson. "Properties and applications of commercial magnetorheological fluids." Journal of intelligent material systems and structures 10.1 (1999): 5-13.
[4]. Magnetorheology: Advances and Applications. Norman Wereley (Editor), Royal Society of Chemistry, 2013
[5]. Ghaffari, Ali, Seyed Hassan Hashemabadi, and Mahshid Ashtiani. "A review on the simulation and modeling of magnetorheological fluids." Journal of Intelligent Material Systems and Structures 26.8 (2015): 881-904.
[6]. MRF-132DG Magneto-Rheological Fluid, Lord Corporation Technical Datasheet, 2011 LORD Corporation

Determination of Injection Timing Requirement of A Steam Injected Diesel Engine

Vezir Ayhan[1], Adnan Parlak[2], Idris Cesur[1]*

Abstract

Numerous methods have been used to reduce NOx emission released from diesel engines so far. One of these control methods commonly used in diesel engines is injecting water steam into the engine cylinder. In the present study, a new electronically controlled water steam injection method was used to decrease NOx emissions. This method can be also used to improve the performance and efficiency. The tests were conducted in a single cylinder, naturally aspirated, direct injection (DI), four-stroke diesel engine, different fuel injection timings (32, 35 and 38 ^{o}CA bTDC) and steam injection rates (S0-STD, S10, S20, S30 and S40) under full load conditions. It was determined in full load condition engine tests that NOx emissions reduce up to 33%, power and moment increase up to 3% and specific fuel consumption decrease up to 5% with steam injection. Optimum injection timing and steam ratio were obtained as 35 ^{o}CA and 20% (S20) the performance and the exhaust emissions points of view. Optimal engine speed, injection timing and steam injection rates on the engine performance and exhaust emissions were determined using chi-square's statistic technique.

Keywords: Diesel Engine; Water Steam Injection; Performance; NOx, Chi-square test

1. INTRODUCTION

The emissions from internal combustion engines mainly are; hydrocarbon (HC), carbon monoxide (CO), carbon dioxide (CO2) and nitrogen oxides (NOx). Among them, NOx is the most harmful emissions. It contributes to the formation photochemical smog, acid rain, ozone depletion and greenhouse effect [1].

There are various methods inside and outside of the cylinder to reduce NOx emissions [2]. One of the NOx reduction methods is water injection into the engine cylinder with different methods. These methods can be listed, direct water injection (DWI); water is injected directly combustion chamber through separate injectors, fumigation; water in liquid phase is injected into intake manifold upstream of the intake valve and emulsified fuels (water—fuel mixtures); fuel and water are mixed in different ratios, and injected direct into cylinder by engine fuel system [3-8].

Previous research has shown that water injected into combustion chamber has significant impact on decreasing the peak flame temperatures and thereby reducing the NOx emissions and improving atomization, mixing and combustion efficiency [9]. Ayhan [10], claimed that introducing water into the cylinder seems to have a positive effect on the combustion process through the micro-vaporization of the fuel drops. This vaporization occurs due to the "explosion" of the small water droplets in the fuel during combustion, giving better mix between the fuel and the air. Canfield claimed that improved mixing also helped reduce NOx and carbon emissions forming in the diffusive burning portion of the combustion process [11]. In a study conducted by Selim and Elfeky significant decrease in the particulate matter (PM) and smoke density were obtained by increasing water rate in the mixture [12]. Some of the authors have expressed that introduction into the engine is the most effective method in decreasing NOx, SFC, and results in small increases in carbon monoxide (CO) and hydrocarbon (HC) emissions [13-15]. Yoshimoto et al. state that micro explosions of water content fuels improve brake efficiency and reduce pollutant emissions [16].

However, in addition to the positive aspects described above, these methods have some drawbacks. These drawbacks can be listed above: 1. in the fumigation technique, water is injected into the intake manifold upstream of the intake valve. Corrosive side effects of water on metallic parts of an engine are not yet solved [17]. 2. emulsified fuel blends tend to lower the combustion temperature indiscriminately. Lower temperatures too early in combustion can lead to increased ignition delay and engine noise [18, 19]. DWI has the advantage over fumigation of having the liquid water close to the flame and away from the wall. However, with low speed two stroke engines special difficulties arise in applying this measure due to the large cylinders. The water would have to be injected into the hot reaction zone inside the cylinder. This would require considerable injection distances for the water spray which can hardly be achieved [19].

[1] *Sakarya University, Technology Faculty, Sakarya, TURKEY, vayhan@sakarya.edu.tr*

[2] *Corresponding author: Yildiz Technical University, Naval Architecture and Marine Engineering Faculty, Istanbul, Turkey. aparlak@yildiz.edu.tr*

Nowadays, Steam injection method for NOx control in diesel engines is becoming increasingly popular [1-8].

In this study, apart from methods described above, a new method named “water steam injection” is used to reduce NOx emissions. Main advantages of this method over the fumigation and emulsified fuel techniques, corrosive side effects of water on metallic surface have been eliminated by changing the phase of compressed hot water at 300 kPa and 133 ^{0}C to superheated vapor conditions at 101.325 kPa and inlet temperature. The test results obtained from the full load conditions are given comparatively. Optimal engine speed, injection timing and steam injection rates on the engine performance and exhaust emissions were determined using chi-square’s statistic technique.

2. EXPERİMENTAL SETUP

The engine tests were conducted in single cylinder water cooled, naturally aspirated, four-stroke, water cooled and direct injection diesel engine. The engine specifications are listed in Table 1. The block diagram of the test setup is shown in Fig. 1.

Table 1. Specification of the test engine

Engine Type	Super Star
Bore [mm]	108
Stroke [mm]	100
Cylinder number	1
Stroke volume [dm3]	0.92
Power -1500 rpm, [kW]	14.7
Injection pressure, [bar]	175
Injection advance, [CA bTDC]	35
Maximum speed, [rpm]	2500
Cooling type	Water
Injection type	DI

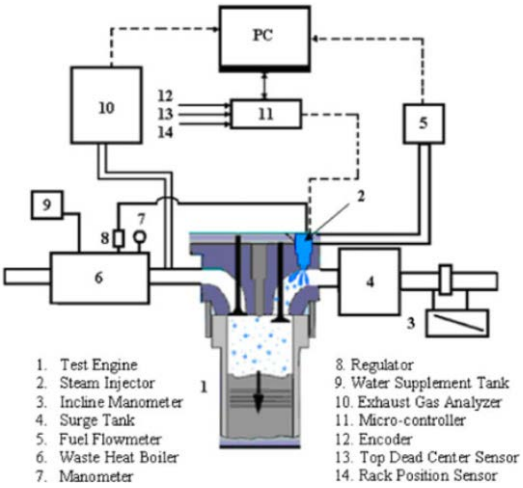

Figure 1. Test set up

In order to measure brake torque, the engine is coupled with a hydraulic type dynamometer using an “S” type load cell with the precision of 0,1 N. Full load tests were conducted at the engine speeds of 1200, 1400, 1600, 1800, 2000, 2200, 2400 rpm and three different fuel injection timing at 320, 350 and 380 crank angle (CA) before top dead center (bTDC). Fuel consumption was measured by an electronically controlled balance with the precision of 0.1 g. So as to injection water steam to engine, an electronically controlled water steam injection system was used. The water steam injection system was introduced previous studies [1-8]. Emitted emission from the engine was measured by MRU Spectra 1600 L type gas analyzer.

3. RESULT AND DISCUSSION

3.1 Determination of optimal operation conditions by chi-square Method

In this study, the effects of water steam injection which is yielded from the exhaust losses heat on the engine performance parameters and exhaust emissions characteristics of a direct injection diesel engine are studied. To evaluate the factors of engine speed, fuel injection timings and steam injection percentage were used chi-square's statistic method. The effects of S10, S20, S30 and S40 steam injections ratio on engine performance and exhaust emissions were comparatively tested with that of standard diesel engine. Three different fuel injection timings and four different steam injection ratios were used during full load tests. Optimal engine speed, injection timing and steam injection rates on the engine performance and exhaust emissions were determined using chi-square's statistic technique.

Experiments were evaluated considering the requirements of the increase in the brake torques and necessitate of lowering the specific fuel consumption (SFC) and exhaust emissions. Table 2 shows analysis of variance (ANOVA) for the parameters considered. According to the results of ANOVA, it is shown that engine speed, steam injection ratio and fuel injection timing affects the engine performance parameters and emissions characteristics.

Table 2. Analysis of variance (ANOVA)

	Source of Variation	Sum of Squares S	Degree of Freedom f	Mean of Squares	Fteorik
TORQUE	[A] Speed	608,16	6	101,36	584,14***
	[B] Injection Timing	50,25	2	25,13	144,81***
	[C] % Steam Ration	8,81	4	2,20	12,69***
	Total	667,22	12,00	55,60	
	e	15,96	92,00	0,17	
SFC	[A] Speed	13299,89	6	2216,65	85,13***
	[B] Injection Timing	411,50	2	205,75	7,90***
	[C] % Steam Ration	604,74	4	151,18	5,81***
	Total	14316,13	12,00	1193,01	
	e	2395,55	92,00	26,04	
NOX	[A] Speed	147474,68	6	24579,11	6,50***
	[B] Injection Timing	1171206,28	2	585603,14	154,83***
	[C] % Steam Ration	326759,76	4	81689,94	21,60***
	Total	1645440,72	12,00	137120,06	
	e	347963,85	92,00	3782,22	
HC	[A] Speed	4824,73	6	804,12	32,05***
	[B] Injection Timing	3073,79	2	1536,89	61,25***
	[C] % Steam Ration	1049,91	4	262,48	10,46***
	Total	8948,43	12,00	745,70	
	e	2308,42	92,00	25,09	
Smoke	[A] Speed	9122,93	6	1520,49	238,25***
	[B] Injection Timing	62,30	2	31,15	4,88**
	[C] % Steam Ration	329,75	4	82,44	12,92***
	Total	9514,99	12,00	792,92	
	e	587,14	92,00	6,38	

*At Least 95 % Confidence
**At Least 99 % Confidence
***At Least 99,9 % Confidence

3.2 Performance Characteristics

In this study, the advance requirement is investigated in case the DI diesel engine was operated with steam injection. The advance timing is determined according to the criteria that not only minimum SFC and maximum torque were obtained but also lower NOx emissions was observed than that of standard diesel engine. Figure 2 shows the effects of steam injection, injection timing and engine speed on NOx and SFC. When steam injection was performed, injection requirement was found 3 ^{0}CA closer to TDC compared to standard diesel engine (38 ^{0}CA bTDC).This is because steam injection contributes to decreased fuel droplet diameters and better atomization and thus improved combustion caharactersitics.

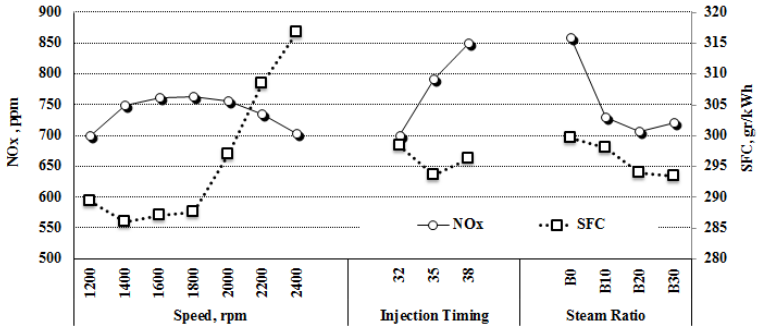

Figure 2. The effect of steam ratio, injection timing and engine speed on NOx and SFC

The comparative results are given in the Figs 3 show how water in the form of steam affects the engine brake torque for various engine speeds at full load conditions and 35^{o} crank angle (CA) injection timing. The brake torque increased with all over the engine speed ranges when water steam is used. Maximum increase rate of torque was found 2.5 % at 1800 rpm in the case of the steam injection.

Maximum torque is 55.5 Nm at 1800 rpm on the condition of engine standard conditions. In case of steam injection, maximum torque is found 56.6 Nm at 1800 rpm with 20% steam. The maximum increase in torque with steam injection is 1.9%, 2.5%, 2.4% and 1.3% for S10, S20, S30 and S40, respectively. To determine the optimum operating conditions using chi-square test method, the effects of factors with 99.9% confidence level on effective is shown in Figure 3. The maximum torque is found at 1600 rpm in 35˚ CA injection timing and S20 with 99% confidence level.

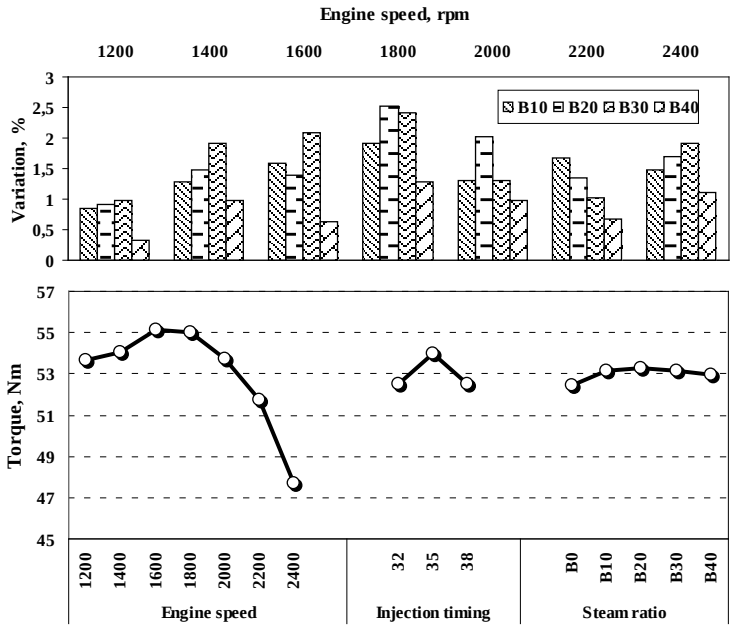

Figure 3. The effect of steam ratio, injection timing and engine speed on torque

Fig.4 shows the specific fuel consumption (SFC) as a function of engine speed at full load conditions. As can be seen from the figure, SFC decreased for all over the engine speeds tested. The decrease rate in SFC is reached to 4.5% at 1200 rpm. The most probable reason to obtain decrease in BSFC with the use of steam injection is the improvement on vaporization and mixing processes leads to a shorter combustion reaction.

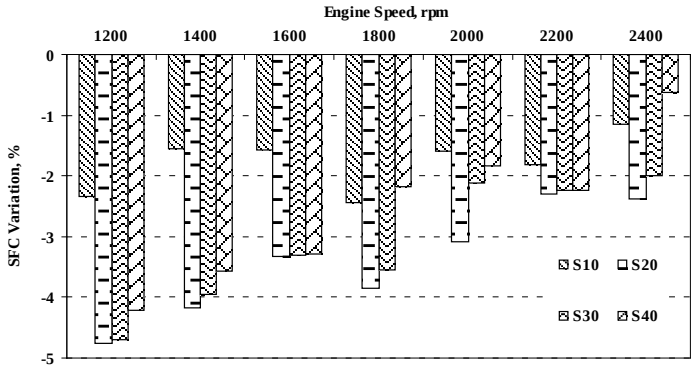

Figure 4. The effect of steam ratio on SFC

In case of steam injection, SFC reduces at all steam ratios. The maximum decrease in SFC is obtained in S20. Whilst the minimum SFC value is 290.5 g/kWh at 1600 rpm, it is 279.4 g/kWh at 1400 rpm with S20. In case of different ratios of steam injection, the maximum reduces in SFC is %2.4, %4.8, %4.7 and %4.2 at B10-1800 rpm, B20-1200 rpm, B30-1200 rpm and B40-1200 rpm, respectively.

Chi-square test considered with engine speed, injection timing and steam ratio, 1400 rpm, 35˚ CA injecting timing and S20 is determined as an optimum value for SFC (figure 2). However, it is not significant change between S20 and S30.

The improvement is based on the internal droplet micro-explosions of water, which produce a secondary atomization, thus improving the mixing process [20-22]. When a water steam and fuel mixing is heated, the water in droplet is vaporized first because water is more volatile than diesel. The vaporization will cause the continuous hydrocarbon phase to “explode”. This occurs at a temperature much above the boiling point of water, around 270 ^{0}C, which is referred to as the superheat limit temperature. It is a general phenomenon that in order to make systems of a lower-boiling liquid immersed as droplets in higher-boiling liquid “explode” one must reach a temperature far above that of lower-boiling component. This phenomenon, known under the name micro explosion, helps in the atomization of the fuel. The violent disintegration is beneficial for mixing of fuel and air because the air-fuel interfacial layer will be larger than the corresponding process without micro explosions. The net result will be that combustion reaction and the burning efficiency will be improved; thus the fuel consumption will be reduced [20]. Reduction of heat losses is another probable reason to obtain improvement in SFC and brake thermal efficiency [12,16].

3.3 Emissions

Figure 5. shows the effect of water steam injection on NOx emissions. NOx emissions considerably decreased with all over the engine speeds in the case of using 20% water steam. The decrease rate in NOx is reached to 33% at 2200 rpm. The figures show that water steam injection method is most useful means in controlling NOx emissions.

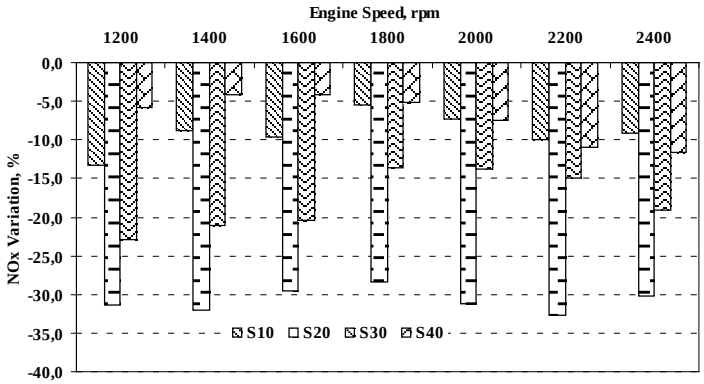

Figure 5. The effect of steam ratio on NOx emissions

In case of steam injection, NOx emissions reduce significantly in regard to standard conditions. The maximum decrease in NOx emissions is 33% at 2200 rpm in S20. Another reduce at 2200 rpm is determined as 10%, 15% and 11% in S10, S30 and S40, respectively. Whilst the maximum NOx emissions of standard conditions are 915 ppm at 2000 rpm, the maximum value of S20 condition is 703 ppm at 1800 rpm.

In case of steam injection in different ratios at intake period, the maximum decrease ratios are 13%, 33%, 23% and 12% in S10-1200rpm, S20-2200 rpm, S30-1200 rpm and S40-2400 rpm, respectively.

Figure 2 illustrates the average values of factors on NOx emissions. The best result is at 1200 and 2400 rpm, 32˚ CA injection timing and S20 conditions with 99.9% confidence level. As can be seen from Figure 7.b, NOx emissions reduce with the decrease of injection timing. However, engine performance parameters are affected contrarily with decrease of injection timing. Therefore, the optimum injection timing is 35˚ CA. The optimum operating conditions for NOx emissions is at 1200 and 2400 rpm and S20 conditions in this injection timing.

Figure 6a and 6b shows how water in the form of steam affects the smoke density for various engine speeds at full load conditions. The improvement on vaporization and mixing processes leads to a shorter combustion reaction. This effect leads to decrease smoke density especially high engine speeds. Under the 1800 rpm, small amount of increase in smoke density have been observed.

In case of steam injection, smoke density does not change significantly. However, smoke density has a little decrease with S10. While the maximum smoke density of standard conditions are 44% at 2000 rpm, 41% at 2000 rpm with S10.

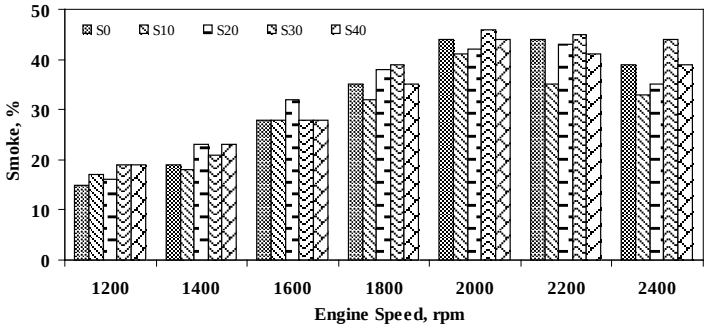

a)

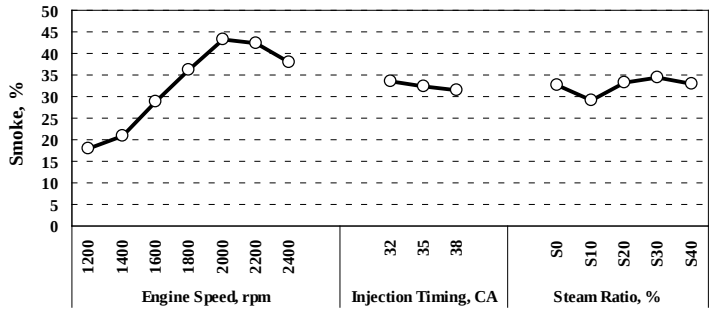

b)

Figure 6. The effect of steam ratio, injection timing and engine speed on smoke density

Figure 6b illustrates the effects of factors on smoke density. The optimum operating conditions is obtained at 1200 rpm, 38˚ CA injection timing and S10 for smoke density.

Comparison of steam injected and standard diesel engines of HC emissions is illustrated in Figure 7ab. There are not significant changes in HC emissions in case of steam injection conditions. The maximum HC emissions are found 28 ppm at 1400 rpm. It is 34 ppm at 1400 rpm and S10 in case of maximum change.

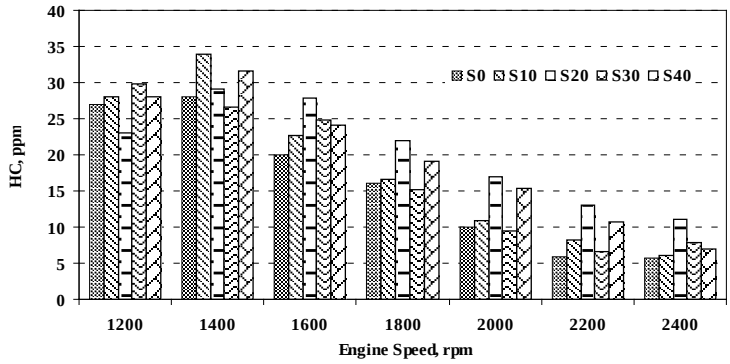

a)

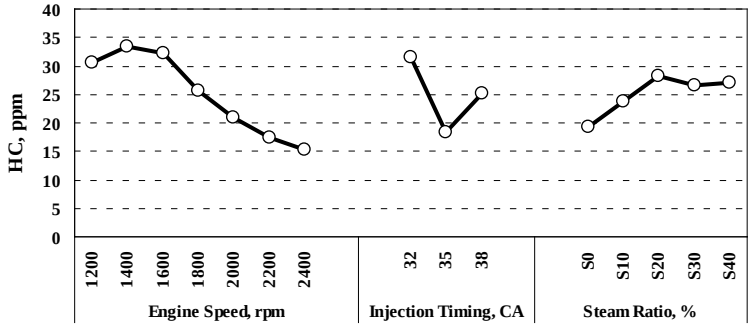

b)

Figure 7. The effect of steam ratio, injection timing and engine speed on HC emissions

Figure 7.b illustrates the effects of factor on HC emissions. As can be seen from figure, the optimum conditions for HC emissions are at 2400 rpm, 35˚ CA injection timing and 30% steam injection ratio.

4. CONCULUSION

In this study, the effects of steam injection into charge air on engine performance and emissions of a DI diesel engine at full load conditions were investigated under various fuel injection timings.

As a result of using steam injection technique improves engine performance parameters and emissions characteristics, especially NOx. Chi-square test was applied to determine the optimum operating conditions in all steam ratios and injection timing angles. 20% steam injection ratio and 35˚ CA (bTDC) injection timing were determined as optimum in regard to engine performance and exhaust emissions parameters at full load conditions. The maximum improvements on the performance parameters and exhaust emission characteristics at these conditions can be concluded as follows:

The maximum torque was founded at 1600 rpm. And the highest change in torque is determined at 1200 rpm as 2.5%. The minimum SFC was obtained at 1400 rpm, the highest change as a standard value of SFC was determined as 4.5%. The minimum NOx emission value was determined at 2400 rpm. The highest change with steam injection was obtained 33 % at 2200 rpm. It is clear that steam injection were not change significantly smoke density and HC emissions.

Consequently, steam injection yields positive effect on performance and NOx emissions at all speeds and full load conditions. After the engine tests, no apparent wear or corrosion was observed. The reason for not observing wear or corrosion can be introducing water into the cylinder as superheated steam. This is the main advantages of this method on the other methods using water for NOx reduction. It can be concluded that the water steam injection has the potential to improve the thermal efficiency, SFC and to suppress the formation of thermal NOx.

ACKNOWLEDGMENT

This study was supported by TUBITAK 1001 Project (project no: 111M065) and Sakarya University (SAU) Scientific Research Project Coordinator (BAPK) (Project no: 2012-05-04-012). Thanks to TUBITAK and SAU BAPK for the financial support.

REFERENCES

[1]. V. Ayhan, Investigation of Steam Injection on Performance and Exhaust Emissions of a DI Diesel Engine, Sakarya University, PhD thesis, 2009 (in Turkish).
[2]. V. Ayhan, I. Cesur, A. Parlak and B. Boru, 10th Int. Combustion Symp., Sakarya, Turkey, September 2008, Sakarya Universty, 446–549.
[3]. A. Parlak, V. Ayhan, I. Cesur, G. Kökkülünk, Investigation of the Effects of Steam Injection on Performance and Emissions of a Diesel Engine Fuelled with Tobacco Seed Oil Methyl Ester, Fuel Processing Technology, Vol. 116, pp. 101 - 109, December, 2013.
[4]. G. Kökkülünk, E. Akdoğan, V. Ayhan, Prediction of emissions and exhaust temperature for direct injection (DI) diesel engine with emulsified fuel using ANN, Turkish Journal of Electrical Engineering & Computer Sciences DOI: doi:10.3906/elk-1202-24.
[5]. I. Cesur, A. Parlak, V. Ayhan, B. Barıs¸ and G. Gonca, The effects of electronic controlled steam injection on spark ignition engine, Applied Thermal Engineering, 2013, DOI:10.1016/j.applthermaleng.
[6]. G. Kokkulunk, A. Parlak, V. Ayhan and G. Gonca, Theoretical and experimental investigation of diesel engine with steam injection system on performance and emission parameters, Appl. Therm. Eng., 2013, 54, 161–170.
[7]. A. Parlak, V. Ayhan, I. Cesur and B. Boru, Proc. 6th Int. Advanced Technologies Symp. (IATS'11), Elazıg, Turkey, May 2011, Firat University, 146–151.
[8]. A. Parlak, V. Ayhan, Y. Ust, B. Sahin, I. Cesur, B. Boru and G. Kokkulunk:, New method to reduce NOx emissions of diesel engines: electronically controlled steam injection system, J. Energy Inst., 2012, 85, (3), 135–139.
[9]. J.P. Mello and A.M. Mellor, NOx emissions from direct injection diesel engines with water/steam dilution, SAE paper, 01-0836, 1999.
[10]. V. Ayhan, The Effects of Emulsified Fuel on the Performance and Emission of Direct Injection Diesel Engine, Journal of Energy Engineering, Vol. 139, pp. 91 – 98, June, 2013.
[11]. C.A. Canfield, Effects of diesel-water emulsion combustion on diesel engine NOx emissions." Master of Science, University of Florida, 1999.
[12]. M.Y.E. Selim and S.M.S. Elfeky, Effects of diesel/water emulsion on heat flow and thermal loading in a precombustion chamber diesel engine, Applied Thermal Engineering, 21, 1565-1582, 2001.
[13]. G. Greeves, I.M. Khan, G. Onion, Effects of water introduction on diesel engine combustion and emissions, Proceedings, 16th Annual Symposium (Int.) on Combustion. Williams & Wilkins Co, 321-336, 1976.
[14]. G.B. O'Neal, J.O. Storment and R.W. Waytulonis, Control of diesel exhaust emissions in underground coal mines, SAE SP-495, Diesel Combustion and Emission Part 3, Int. Off-Highway Meeting &Exposition, Milwaukee, WI, 13-23, 1981.
[15]. R.J. Crookes, M.A.A. Nazha And F. Kiannajad, A Comparison of ignition and emissions characteristics for alternative diesel fuels and emulsions, Mech. E. Seminar, 47-52, 1990.
[16]. Y. Yoshimoto, M. Tsukarhara and T. Muryama, "Studies on the microexplosion of emulsified fuels, Nippon Kikai Gakkai Ronbunshun B Hen, 519, (55), 3538-3543, 1989.
[17]. J.W. Park, Kang Y.Huh and K.H. Park, Experimental Study on the Combustion Characteristics of Emulsified Diesel in a RCEM, Seoul 2000 FISITA World Automotive Congress, June 12-15, 2000, Seoul, Korea.
[18]. C. Trozzi, R.Vaccaro, Methodologies for Estimating Future Air Pollutant emissions from ships, Technical Report, MEET RF98b, 1998.
[19]. F. Bedford, C. Rutland, P. Dittrich, A. Raab and F. Wirbeleit. Effects of Direct Water Injection on DI Diesel Engine Combustion, SAE Paper, (2000) 2000-01-2938.
[20]. Lif, A. and Holmberg, K., Water-in-Diesel emulsions and related sytems, Advanges in Colloid and Interface Science, 231-239, 2006.
[21]. H.Z. Sheng, L.Chen, C.K. Wu. The droplet group micro-explosions in w/o Diesel fuel emulsion sprays. SAE paper 950855, 1995.
[22]. J.M. Ballester, N.Fueyo, C.Dopazo, Combustion characteristics of heavy oil–water emulsions, Fuel 75, 695–705, 1996.

A parametric Study of a Reheat Organic Rankine Cycles (ORC)

Resat Selbas[1], Mustafa Alptekin[2], Abid Ustaoglu[3],

Abstract

Energy is very essential in daily life and industry. Required energy can be supplied from fossil fuels such as coal, oil, natural gas. Since these resources damage the environment and increase greenhouse gas rate, alternative energy resources can be used for different applications such as power generation, refrigeration and air conditioning. Rankine cycle can be commonly used for power generation. However, organic Rankine cycle can be preferred instead of Rankine cycle at low source temperatures. In this study, a thermodynamic analysis of a reheat organic Rankine cycle is performed. The evaporator heat energy is supplied from geothermal energy. R142b and R600a are selected as working fluid. Energy and exergy balance equations for the thermodynamic model are provided according to the first and second law of thermodynamics. The results such as power output, thermal efficiency, exergy destructions rates and second law efficiency are evaluated as function of condenser pressure and evaporator pressure.

Keywords **:** Organic Rankine Cycle, Geotermal energy, thermodynamic analysis, exergy.

1. INTRODUCTION

Because of the increasing energy demand and environmental problems, waste heat utilization in the industrial processes and use of renewable energy sources to generate electricity or meet heat demand of dwellings in vicinity have been attractive and a practical solutions. Low-grade waste heat has been commonly discharged in the industrial process in which thermodynamic cycle is operated or a combustion process is placed, because of the lack of effectiveness. On the other hand, although the abundant amount of source for renewable energy including sun, earth and moon, amount of energy which will be transformed to another or more useful form of energy, per unit area is relatively low for power generation.

Steam power plants operating Rankine cycle is one of the most common ways to generate power. However, using a heat source having a temperature below 613 K is not profitably converted into electricity by a classic Rankine Cycle [1]. Organic Rankine Cycle operates organic fluids instead of water and has significant advantages for low-grade heat source and can generate relatively small scale power since many organic fluids have lower boiling point temperature and can have a higher vapor pressure comparing to water. Therefore, it is one of the preferable methods to utilize low grade heat. Renewable energy sources such as solar energy and geothermal energy usually have low-temperature. Thus, an organic Rankin cycle can be applied to a renewable energy sources such as geothermal energy which is one of the alternative energy sources.

Organic Rankine cycles have very different configurations using different component including generator, heat exchangers and regenerators apart from turbine, pump, boiler and condenser. In order to improve the system efficiency, one way is to increase the evaporator pressure. However, this way causes reduction of the vapor quality at the end of turbine. In order to improve vapor quality, the working fluid in boiler can be overheated. However, this also causes another problem and that is material heat resistance of turbine. This problem can be solved by applying the expansion process in two stages and reheat between two expansions. Many studies have been carried out for different configurations of organic Rankine cycles.

Pedro et al. [2] conducted an analysis of regenerative organic Rankine cycles ‘‘ORC’’ using dry organic fluids, to convert waste energy to power from low-grade heat sources. They selected the dry organic working fluids as working fluid namely, R113, R245ca, R123 and isobutane, and evaluated this system in terms of the first and second law of thermodynamics. They investigated the effects of türbin inlet pressure and temperature on different output parameters. They found out that regenerative ORC produces higher efficiency compared with the basic ORC while also reducing the amount of waste heat required to produce the same power with a lower irreversibility.

Acar [3] performed thermodynamic analysis of the reheat-regenerative rankine cycle. He done energy and exergy analyses for each component in the system and the results tabulated, and graphically investigated the variations of availability difference,

[1]*Corresponding author: University of Suleyman Demirel, Isparta, 32260, Turkey, mustafaalptekin@sdu.edu.tr*

[2]*University of Hakkari, Hakkari, 30000, Turkey, mustafaalptekin@hakkari.edu.tr*

[3]*University of Bartin, Bartin, 74100, Turkey, austaoglu@bartin.edu.tr*

irreversibility and efficiency with several parameters. He determined that the results are a clearer definition of the real losses in the system by using exergy method.

Padilla et al. [4] evaluated thermodynamically of solar receiver driven recompression Brayton supercritical CO2 cycles with and without reheat scenarios. They carried out energy, exergy and mass balances for each component and calculated first law and exergy efficiencies with and without reheating. He conducted optimization by using Sequential Least SQuares Programming (SLSQP) and determined optimum operating conditions based on maximum first law efficiency. As a result of thermodynamic analyses, they found out that the exergy efficiency reaches a maximum value at 600 °C while the first law efficiency increases monotonically with highest temperature of the cycle, and specified that the maximum exergy loss takes place in the solar receiver and cooler, which makes it attractive to implement a bottoming cycle to improve the exergy efficiency.

Khaliq and Kaushik [5] carried out second-law based thermodynamic analysis of Brayton/Rankine combined power cycle with reheat. They investigated the effects of pressure ratio, cycle temperature ratio, number of reheats and cycle pressure-drop on specific power-output, thermal efficiency, exergy destruction in components of the combined cycle, second-law efficiency of each process of the gas-turbine cycle, and second law efficiency of the steam power cycle. They found that the exergy destruction in the combustion chamber represents over 50% of the total exergy destruction in the overall cycle. In addition, they specified that the combined cycle efficiency and its power output were maximized at an intermediate pressure-ratio, and increased sharply up to two reheat-stages and more slowly thereafter.

Although a number of studies have been expressed in this section, there are not much related to reheat ORC cycle. In the previous study, one of the most common working fluid, R245fa is investigated and optimum working parameters were evaluated [6]. In this study, it was performed that thermodynamic analysis of a geothermal powered reheat ORC for two different type working fluids. R142b and R600a are dry and isentropic type fluids, which have approximately same critical temperature, respectively. The effects of condenser and evaporator pressure on net work output, total exergy destruction rate, exergy destruction rate in each component, thermal and exergy efficiencies are investigated.

2. MATERIAL AND METHOD

2.1 System Description

In a previous study the working principle of a reheat organic Rankine cycle is described in detail [6]. For the sake of readers, a brief explanation is given here. Figure 1 illustrates a schematic view of a reheat ORC. The working fluid is coming to the pump as saturated liquid and is compressed to the evaporator pressure and leaves the evaporator to be superheated vapor. Then, the fluid is coming to the high pressure turbine for expansion. After leaving high pressure turbine, the working fluid enters to the evaporator and its temperature increase to the high pressure turbine inlet temperature and then is comeing to the low pressure turbine in which the pressure decreases condenser pressure. The working fluid leaves the low pressure turbine to be superheated fluid or saturated liquid vapor mixture at condenser pressure and then comes to the condenser to reject heat to decrease the initial temperature. Thus, the cycle is completed.

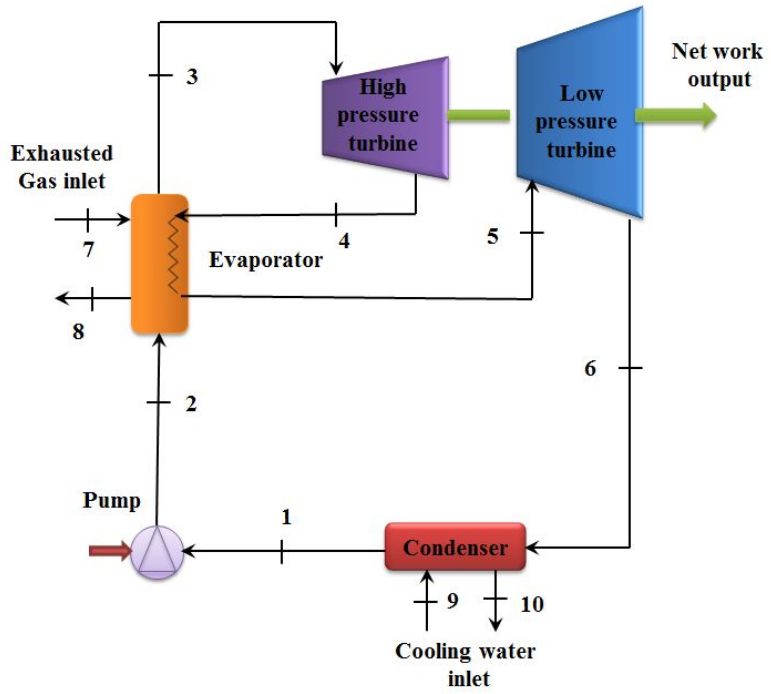

Figure 1. Schmatic view of a Reheat Organic Rankine Cycle[6]

2.2 Thermodynamic analysis

The geothermal energy powered reheat ORC system is modeled based on the first and second laws of thermodynamics, and these laws are applied to each component in the system. General equations of mass, energy and exergy balances by ignoring the kinetic and potential energy variations are expressed, respectively, as in the reference [7]-[8];

$$\sum \dot{m}_{in} = \sum \dot{m}_{out} \quad (1)$$

The first law of thermodynamics is an express of energy principle. It is expressed for steady state processes as follows [9]-[10];

$$\dot{Q} + \sum(\dot{m}h)_{in} = \dot{W} + \sum(\dot{m}h)_{out} \quad (2)$$

Neglecting chemical, kinetic and potential exergies, exergy balance in a control volume in which a steady state process occurs can be written as [8], [11];

$$\dot{E}x_Q - \dot{E}x_W = \sum(\dot{m}\varepsilon)_{out} - \sum(\dot{m}\varepsilon)_{in} + T_0\dot{S}_{gen} \quad (3)$$

where;

$$\dot{E}x_{dest} = T_0\dot{S}_{gen} \quad (4)$$

where $\dot{E}x_Q$, $\dot{E}x_W$ and ε represent exergy of heat, exergy of work and thermomechanical exergy (flow exergy), respectively. These expressions are shown as follows [7];

$$\dot{E}x_{\dot{Q}_{in}} = \dot{Q}_{in}\left(\frac{T-T_0}{T}\right) \quad (5)$$

$$\dot{E}x_W = \dot{W}_{net,out} \quad (6)$$

$$\varepsilon = (h - h_0) - T_0(s - s_0) \quad (7)$$

$$\dot{S}_{in} + \dot{S}_{gen} = \dot{S}_{out} \quad (8)$$

where 0 subscript expresses reference conditions. The first (thermal) and second law (exergy) efficiencies of the overall system are calculated as follows [12];

$$\eta_I = \frac{\dot{W}_{net,out}}{\dot{Q}_{in}} \quad (9)$$

where

$$\dot{W}_{net,out} = \dot{m}[(h_3 - h_4) + (h_5 - h_6)] - \dot{m}(h_2 - h_1) \quad (10)$$

$$\dot{Q}_{in} = \dot{m}[(h_3 - h_2) + (h_5 - h_4)] \quad (11)$$

$$\eta_{II} = \frac{\dot{E}x_{\dot{W}_{net,out}}}{\dot{E}x_{\dot{Q}_{in}}} \quad (12)$$

The above equations were applied to the geothermal powered reheat ORC system, and were obtained mass, energy and exergy balance equations for each component.

Table 1 shows the input parameters of the system. The ORC system is programmed using Engineering Equation Solver (EES). The some assumptions are made as follows:

(1) All the processes are assumed as steady state.

(2) The pumps and turbines are adiabatic.

(3) The heat transfer to/from ambient and pressure losses in the piping system and in the evaporator and condenser of the reheat ORC system are neglected.

(4) The working fluid at the inlet of the pump is assumed as saturated liquid.

(5) Potential and kinetic energy variations are neglected.

(6) The dead state pressure P_0 and temperature T_0 are considered to be 101.325 kPa and 27 °C, respectively.

Table 1. Input values to the system

Parameters	Values
Pump isentropic efficiency	85%
High Pressure Turbine (HPT) isentropic efficiency	85%
Low Pressure Turbine (LPT) isentropic efficiency	85%
High Pressure Turbine inlet temperature	130 °C
Low Pressure Turbine inlet temperature	130 °C
Condenser pressure	300 kPa
Evaporator pressure	1000 kPa
Reheat pressure	600 kPa
Mass flow rate of working fluid in ORC	100 kg/s
Inlet temperature to condenser of cooling water	20 °C
Outlet temperature from condenser of cooling water	25 °C
Inlet temperature of geothermal water	145 °C
Outlet temperature of geothermal water	75 °C
Inlet and outlet pressure of geothermal water	600 kPa
Ambient pressure	101.325 kPa
Ambient temperature	25 C

3. RESULTS AND DISCUSSION

Figures 2, 3 and 4 illustrate the effect of condenser pressure on system performance for two different working fluids. The variation of net work output and total exergy destruction rate is shown as a function of condenser pressure in Figure 2. The net work output decreases with increase of condenser pressure while the total exergy destruction rate increases for both two fluids. R600a has higher than R142 the net work output. However, total exergy destruction rate in case of R600a is lowest. The highest network output to be 5639 kW and the lowest exergy destruction rate to be 3581 kW was achieved for the condenser pressure of 275 kPa. Figure 3 shows the thermal efficiency and exergy efficiencies of the overall system as a function of the condenser pressure. Both the thermal and exergy efficiencies decreases when the condenser pressure increases from 275 kPa to 500 kPa. Trend in the thermal efficiency of both R600a and R142b is very similar and closer each other. However, R600a has higher than R142b the exergy efficiency. The thermal and exergy efficiencies decrease from 9.8% to 5.7% and from 33.1% to 17.5%, respectively, in case of R600a with rise of condenser pressure of 225 kPa. Figure 4 illustrates the exergy destruction rate in each component of the system as a function of condenser pressure. While exergy destruction rate in the low pressure turbine and evaporator decreases with increasing of condenser pressure, exergy destruction rate in the condenser is directly proportional with condenser pressure. Irreversibilities in the pump and high pressure turbine are very small and constant with rise of condenser pressure. This figure is plotted for R600a, which is the highest fluid. Increment exergy destruction rate in the condenser is higher than decrement exergy destruction rate in the low pressure turbine and evaporator. Therefore, total exergy destruction rate in the system increases when the condenser pressure increases from 275 kPa to 500 kPa.

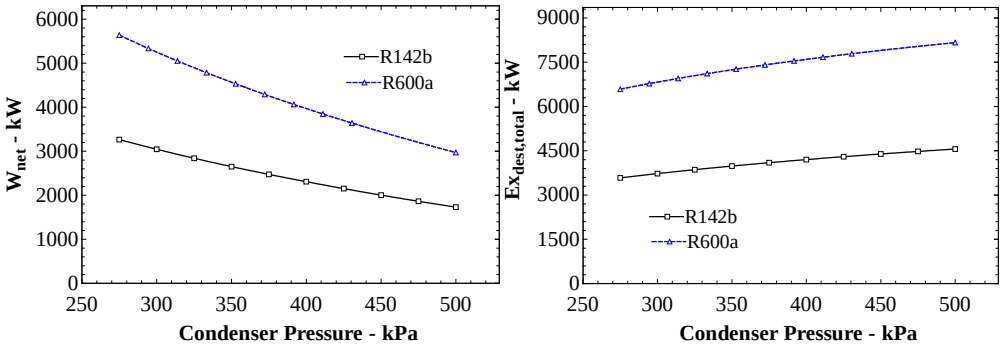

Figure 2. Net work output and total exergy destruction rate as a function of condenser pressure

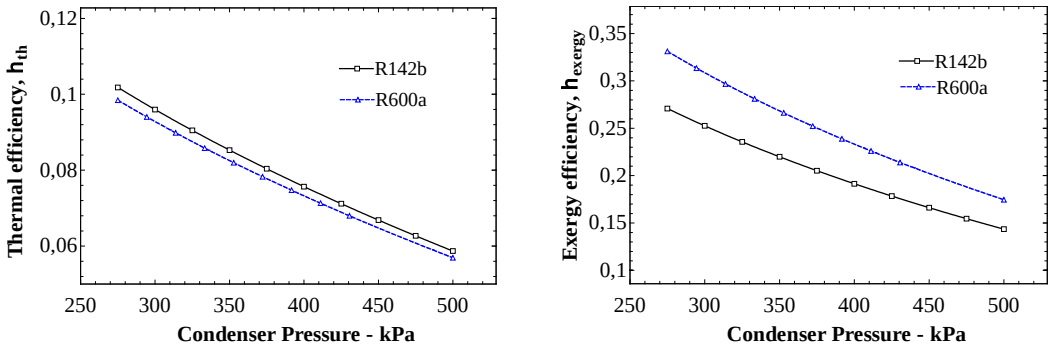

Figure 3. Thermal efficiency and exergy efficiency as a function of condenser pressure

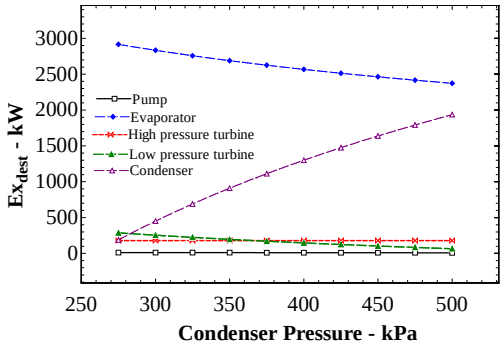

Figure 4. Exergy destruction rate as a function of condenser pressure for each component

The effect of evaporator pressure is shown in Figure 5, 6 and 7. High and low pressure turbine inlet temperature and condenser pressure are fixed at 130 °C and 300 kPa. Figure 5 presents the variation of the net work output and total exergy destruction rate with evaporator pressure. The total exergy destruction rate decreases for both two fluids while the net work output increases with increase of evaporator pressure. Decrements in the exergy destruction rate of both two fluids are very similar. It is noticed that R142b have the highest exergy destruction rate. Both R600a and R142b have same work output at low evaporator pressures. However, the net work output of R600a increases rapidly and reaches largest values at high pressures. Figure 6 shows the effect of evaporator pressure on the thermal and exergy efficiencies of the overall system for two working fluids. The thermal and exergy efficiencies increase as the evaporator pressure increases from 600 kPa to 2300 kPa. R142b has the highest efficiencies. Increment in the net work output for two fluids is very similar. The exergy efficiency of R142b is higher than R600a at low evaporator pressures. However, the exergy efficiencies of these fluids are very closer each other at high pressures. The thermal and exergy efficiencies of R142b increase from 5.9% to 13.2% and from 33.2% to 16.3%, respectively.

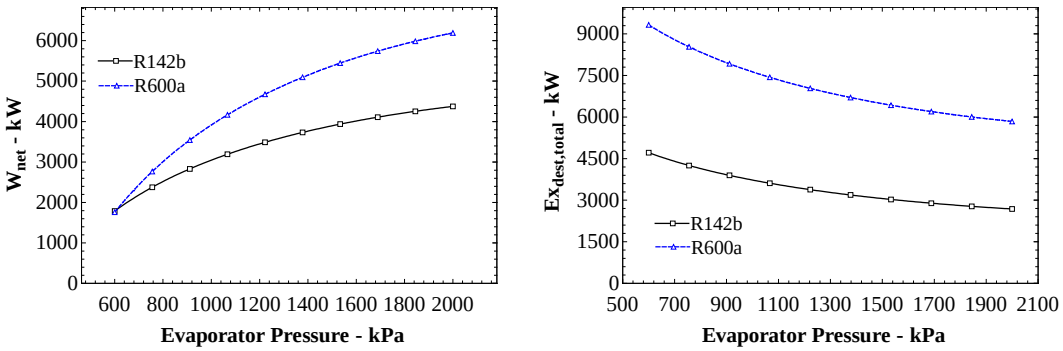

Figure 5. Net work output and total exergy destruction rate as a function of evaporator pressure

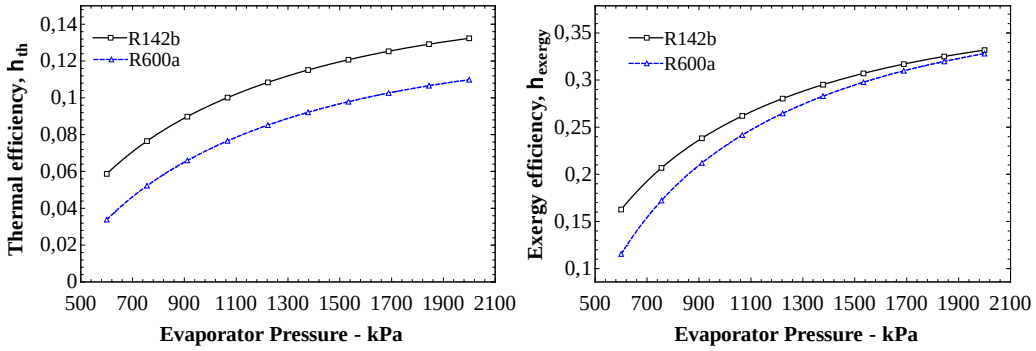

Figure 6. Thermal efficiency and exergy efficiency as a function of evaporator pressure

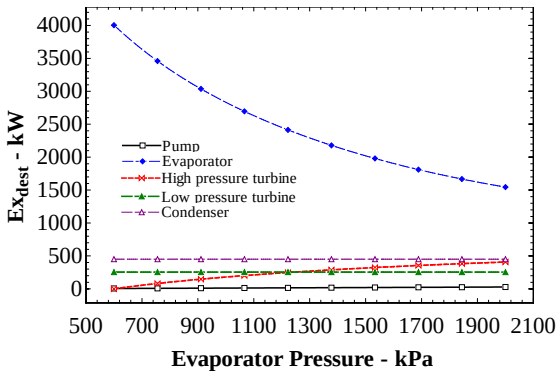

Figure 7. Exergy destruction rate as a function of evaporator pressure for each component

Figure 7 shows the exergy destruction rate of each component as a function of the evaporator pressure. The exergy destruction rate of the evaporator decreases by increasing evaporator pressure and the largest exergy destruction rate occurs in the eva. On the other hand, the exergy destruction rate of high pressure turbine increases slightly. The other components` exergy destruction rate does not change with the variation of evaporator pressure.

4. CONCLUSIONS

In this study, a dry and an isentropic working fluids, R600a, R142b, respectively, are investigated. Several calculation parameters including energy efficiency, exergy efficiency, net work output, total exergy destruction rate and the exergy destruction rate of each component were evaluated as a function of condenser and evaporator pressure. The followings points summarize the results.

1. Condenser pressure must be decreased or evaporator pressure must increased in order to improve the system performance.

2. The net work output of the system increases by reducing the condenser pressure or increasing the evaporator pressure. The highest network output to be 5639 kW and the lowest exergy destruction rate to be 3581 kW was achieved for the condenser pressure of 275 kPa.
3. Trend in the thermal efficiency of both R600a and R142b is very similar and closer each other. However, R600a has higher than R142b the exergy efficiency. The thermal and exergy efficiencies decrease from 9.8% to 5.7% and from 33.1% to 17.5%, respectively, in case of R600a with rise of condenser pressure of 225 kPa.
4. Increment exergy destruction rate in the condenser is higher than decrement exergy destruction rate in the low pressure turbine and evaporator. Therefore, total exergy destruction rate in the system increases when the condenser pressure increases from 275 kPa to 500 kPa. In addition, the evaporator has the highest irreversibility since there is heat input to the evaporator.
5. Both R600a and R142b have same work output at low evaporator pressures. However, the net work output of R600a increases rapidly and reaches largest values at high pressures.
6. R600a has the best performance with increase of condenser pressure while R124b is best working fluid with increase of evaporator pressure. In addition, the thermal and exergy efficiencies of R142b increases from 5.9% to 13.2% and from 33.2% to 16.3%, respectively, when the evaporator pressure increases from 600 kPa to 2000 kPa.
7. Advanced exergy analysis results will be going to show the improvement potential of the system and the interaction of among the component.

REFERENCES

[1]. S.K. Sanyal, “Future of geothermal energy. Proceedings Thirty-Fifth Workshop on Geothermal Reservoir Engineering Stanford University,” 2010 SGP-TR-188, Stanford, California, February 1-3.
[2]. P.J. Mago, L.M. Chamra, K. Srinivasan and C. Somayaji, “An examination of regenerative organic Rankine cycles using dry fluids,” Applied Thermal Engineering, vol. 28, pp. 998–1007, 2008.
[3]. H.I. Acar, “Second law analysis of the reheat-regenerative rankine cycle,” Energy Conversion and Management, vol. 38, pp. 647-657, 1997.
[4]. R.V. Padilla, R.G. Benito and W. Stein, “An exergy analysis of recompression supercritical CO2 cycles with and without reheating,” Energy Procedia, vol. 69, pp. 1181–1191, 2015.
[5]. A. Khaliqa and S.C. Kaushik, “Second-law based thermodynamic analysis of Brayton/Rankine combined power cycle with reheat,” Applied Energy, vol. 78, pp. 179–197, 2004.
[6]. A. Ustaoglu, M. Alptekin, Energetic and Exergetic Approach to a Geothermal Energy Powered Organic Rankine Cycles. Proceedings of the 2th International Conference on Engineering and Natural Science. ICENS-2 2016. (2016), May 24-28, Sarajevo, Bosnia
[7]. O. Kaska, “Energy and exergy analysis of an organic Rankine for power generation from waste heat recovery in steel industry,” Energy Conversion and Management, vol. 77, pp. 108–117, 2014
[8]. L.G.Farshi, A.H. Mosaffa, C.A.I. Ferreira and M.A Rosen., Thermodynamic analysis and comparison of combined ejector–absorption and single effect absorption refrigeration systems, Applied Energy, vol. 133,pp. 335–346, 2014.
[9]. Y.A. Cengel and M.A. Boles, An Engineering Approach Thermodynamics, Fifth Edition,p. 946, 2007.
[10]. A. Bejan, Advanced Engineering Thermodynamics, Wiley, New York, 1997.
[11]. E.K. Akpinar and A.Hepbasli, A comparative study on exergetic assessment of two ground source (geothermal) heat pump systems for residential applications, Building and Environment, vol. 42, pp. 2004–2013 (2007).
[12]. I. Dincer and M.A Rosen., Environment and sustainable development, Elsevier Science, p. 472, 2007.

Influence of ZnS Thickness on Electrical and Photoelectrical Properties of ZnS/p-Si Heterojunction

Yusuf Selim Ocak[1]

Abstract

In recent years, zinc sulphide (ZnS) has a great interest because of its potential application in the optoelectronic industry. ZnS has a wide and direct band gap. It is an n-type II-VI semiconductor. Similar to other sulphide semiconductors it is a photoconductor and used in the fabrication of many devices such as solar cells and thin film transistors.

Many methods including sol-gel methods, thermal evaporation and sputtering have been used to deposit ZnS thin films on various substrates. Sputtering method is one of the most preferred methods. Homogenious and large area coating is possible using sputtering method.

The study contains the deposition of ZnS thin films by RF sputtering technique. Three ZnS films with different thickness were formed on p-Si semiconductors to obtain ZnS/p-Si heterojunctions. Key electrical parameters such as barrier height, ideality factor and series resistance values were calculated by the help of current-voltage measurements in dark. Furthermore, the photoelectrical characterizations of heterojunctions were examined using a solar simulator with AM1.5 global filter.

***Keywords*:** ZnS; Heterojunction, Electrical properties

1. INTRODUCTION

Because of outstanding behaviours of II–VI nanomaterials, they have been sensitized and used in the fabrication of many kinds of devices including solar cells, heterojunctions, photodiodes and field effect transistors [1-3]. There is a great interest for the usage of ZnS in optoelectronic applications because it is a wide band semiconductor with high refractive index and high transmittance in visible range of solar spectrum.

Many methods including spin coating, chemical bath method, spray prolysis and sputtering have been used for the formation of ZnS thin films on various substrates. Sputtering process is one of the most suitable method to obtain uniform and homogeneous thin films on large areas. It is preferred for ceramics and refractory materials.

As it is known that formation conditions of thin films influence the structural, optical and electrical properties of films. Thin film thickness also can affect the performance of the junctions especially in metal-insulator-semiconductors (MISs) and heterojunctions.

In this study, it is aimed to examine the effect of ZnS thin film thickness on electrical and photoelectrical properties of ZnS/p-Si heterojunctions. Three ZnS thin films were deposited on p-Si substrates by RF sputtering technique and electrical and photoelectrical properties of ZnS/p-Si heterojunctions were studied using their current-voltage measurements in dark and various illumincation conditions.

2. MATERIALS AND METHODS

A P-Si wafer with (100) orientation and 1-10 □cm resistivity w
trichloroethylene and cleaned by ultrasonically vibrating in acetone and methanol for 5 min. After each step, the wafer was washed with deinozed water. After cleaning procedures, the wafer is dried under nitrogen ambient. The p-Si semiconductor was put into the vacuum chamber. Al metal was evaporated at 10^{-6} Torr and p-Si/Al structure was annealed under nitrogen ambient for 3 min at 570 °C to make high quality ohmic contact. ZnS thin films were deposited on p-Si semiconductors by RF sputtering technique. Thin films deposition processes continued for 5, 15 and 30 min. High purity ZnS target used for sputtering process. During sputtering process 40 W power were applied to substrates and pressure was fixed for 20 mTorr. The substrate temperatures were kept at 40 °C during sputtering processes. Al metal was evaporated to obtain front contact. The circular diameters of the Al contacts were about 1.5 mm. To make circular front contacts a shadow mask is used. The

[1] *Corresponding author: Dicle University, Faculty of Education, Department of Science, 21280, Diyarbakır, Turkey, yusufselim@gmail.com*

schematic diagram of Al/ZnS/p-Si device is given in Fig. 1. Electrical characteristics of Al/ZnS/p-Si structures were analyzed using its current-voltage (*I-V*) in dark and under a solar simulator by the help of Keitley 2400 sourcemeter.

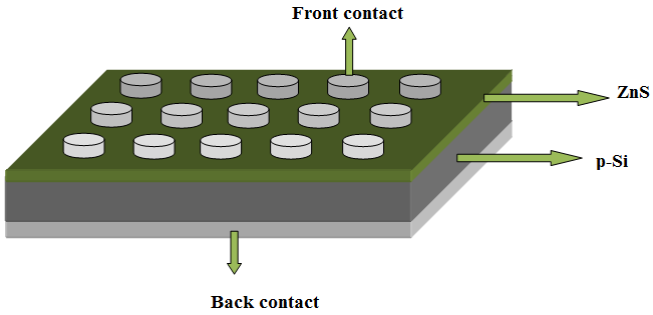

Figure 1. The schematic diagram of Al/ZnS/p-Si devices

3. RESULTS AND DISCUSSION

Current-voltage measurements of ZnS/p-Si heterojunctions obtained using various ZnS thicknesses are presented in Figure 2. As it is seen all structures have excellent rectification. When the series resistance of a heterojunction is taken into account, the current-voltage relationship can be written as [4]

$$I = I_0 \exp\left(\frac{q(V - IR_s)}{nkT}\right) \qquad 2$$

Where I_0 is the saturation current which can be written

$$I_0 = AA^*T^2 \exp\left(-\frac{q\Phi_b}{kT}\right) \qquad 3$$

where, q is the electron charge, V is the applied voltage, R_S is the series resistance, n is dimensionless ideality factor, k is the Boltzmann constant, T is the absolute temperature, A^* is Richardson constant and Φ_b is the barrier height. The ideality factor of a diode can be calculated from the slope of the linear region of the In*I-V* plot of the diode using the equation

$$n = \frac{q}{kT}\frac{dV}{d\ln(I)} \qquad 4$$

The barrier height values of the heterojunctions are given in Table 1. As seen from the table, the ideality factor values of all structures are greater than unity. For an ideal diode, ideality factor should be very close to 1. The ideality factor values show the deviation from ideal structure. Furthermore, the ideality factor values increase with the increase of the ZnS thickness. These deviations may be attributed to the effects of R_S of the structure, the interface state density at the interface, and fabrication-induced defects.

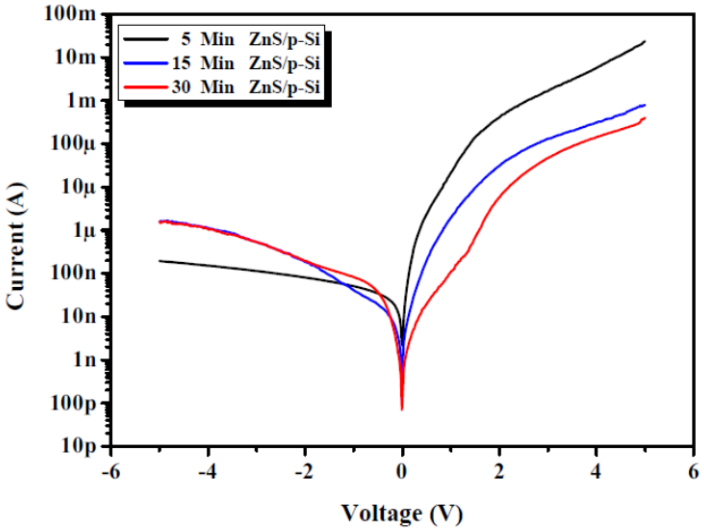

Figure 2. Current-voltage plots of ZnS/p-Si heterojunction obtained using various ZnS thickness

Table 1. Some electrical parameters of Al/ZnS/p-Si heterojunctions

ZnS deposition time	ln*I-V*		Norde			
	n	Φ_b (eV)	*F(V)* (V)	V_0 (V)	Φ_b (eV)	R_S (Ω
5 min	2.463	0.759	0.7408	0.1912	0.779	63
15 min	3.541	0.795	0.7872	0.2112	0.814	495
30 min	4.223	0.829	0.8199	0.1513	0.824	7076

The barrier height of the junction can be calculated using I_0 value obtained from interception of In*I-V* plot to *I* axis by the help of the equation

$$\phi_b = \frac{kT}{q}\ln\left(\frac{AA^*T^2}{I_0}\right) \qquad 5$$

The barrier heights of the devices were calculated using saturation current values by the help of the equation 5. Barrier height value of Al/ZnS/p-Si devices determined as 0.759, 0.795 and 0.829 eV for the devices obtained by sputtering ZnS for 5, 15 and 30 min. The barrier height of heterojunctions increase with the increase in the thickness of ZnS thicknesses. This situation implies the metal-interlayer-semiconductor (MIS) device properties of the junctions.

The current-voltage measurement plots of the Al/ZnS/p-Si devices shown in Figure 2 have deviation from linearity at high voltages because the effect of series resistances of the structures results from the contact wires or bulk resistance of the ZnS and p-Si semiconductors. The series resistances of the Al/ZnS/p-Si structures were calculated by means of Norde functions given below as [5]

$$F(V) = \frac{V}{\gamma} - \frac{kT}{q}\left(\frac{I(V)}{AA^*T^2}\right) \qquad 6$$

where γ is the first integer greater than ideality factor and *I(V)* is the current obtained from *I–V* measurements. The barrier height of device can be calculated using the minimum value of *F* vs. *V* plot using the equation

$$\phi_b = F(V_0) + \frac{V_0}{\gamma} - \frac{kT}{q} \qquad 7$$

where $F(V_0)$ is the minimum *F(V)* value and V_0 is the corresponding voltage value. F*(V)–V* curves of Al/ZnS/p-Si heterojunction structures are shown in Figure 3. The series resistances of the devices can be determined through the relation

$$R_S = \frac{kT(\gamma - n)}{qI_{min}} \qquad 8$$

where I_{min} the corresponding current value at V_0. The barrier height and series resistance values of the Al/ZnS/p-Si heterojunction structures are also shown in Table 1. The barrier height values of the devices are greater than the ones obtained from ln*I-V* plots. This situation can be attributed the calculation methods. While only the linear part is used for the calculation of barrier height from lnI-V plots, all part of forward bias current-voltage data is used for Norde method. The series resistance of the devices strongly depends on the thickness of ZnS. This situation implies for the MIS characteristics of the devices.

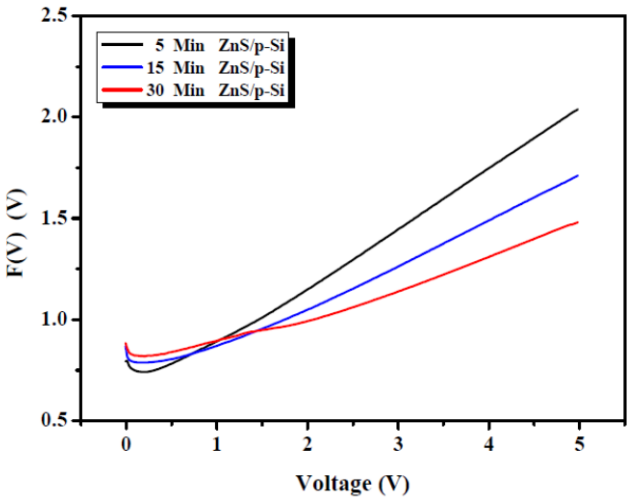

Figure 3. Norde plots of ZnS/p-Si heterojunction obtained using various ZnS thickness

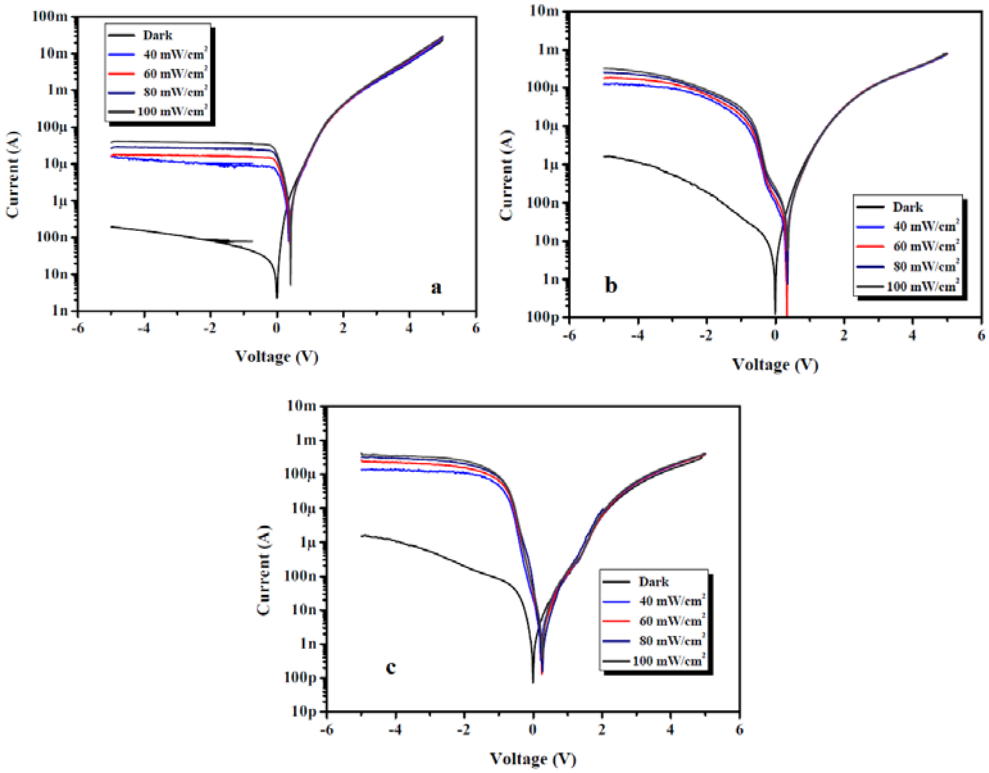

*Figure 4. lnI-V plots of ZnS/p-Si heterojunctions obtained sputtering of ZnS thin film for **a)** 5 **b)** 15 and **c)** 30 min in dark and under various illumination conditions.*

The influence of light intensity on photoelectrical characteristics of all ZnS/p-Si heterojunctions is presented in Figure 3. As seen from the figure all devices have photoresponse. Light generates photocurrent by forming electron hole pairs at the ZnS/p-Si interfaces. When the light intensity increases, the photocurrent increases for all junctions. It shows the relationship between the photon number and electron hole pairs. Some photoelectrical parameters of all devices obtained under a sun (100 mW/cm^2) are presented in Table 2. As seen in the table while sensitivity to light of all devices at -5 V increases, the open circuit voltage (V_{OC}) and short circuit current (I_{SC}) decreases. The decrease of V_{OC} and I_{SC} can be attributed the increase of series resistance values with the increase of ZnS layer.

Table 2. Some photoelectrical parameters of Al/ZnS/p-Si heterojunctions

ZnS deposition time	Sensitivity to light (times)	V_{OC} (mV)	I_{SC} (□A)
5 min	192	410 mV	19.3
15 min	201	351 mV	0.246
30 min	272	271 mV	0.04

4. CONCLUSIONS

Current-voltage measurements of ZnS/p-Si heterojunction fabricated by sputtering of ZnS for 5, 15 and 30 min on p-Si substrates showed that the devices had excellent rectification. The electrical properties of the junctions were characterized by means of thermionic emission theory. It was seen that thickness of ZnS thin films had very strong effects on both electrical and photoelectrical parameters of ZnS/p-Si junctions. It was reported that the ideality factor, barrier height and series resistance values of junctions increased with the increase in ZnS thickness. Furthermore, the photovoltaic parameters such as VOC and ISC decreased with the increase in ZnS thickness.

REFERENCES

[1] T. Nakada, M. Mizutani, Japanese Journal of Applied Physics, 41 (2002) L165.
[2] Y.-Q. Yu, L.-B. Luo, Z.-F. Zhu, B. Nie, Y.-G. Zhang, L.-H. Zeng, Y. Zhang, C.-Y. Wu, L. Wang, Y. Jiang, CrystEngComm, 15 (2013) 1635-1642.
[3] M. Lingalugari, K. Baskar, P.-Y. Chan, P. Dufilie, E. Suarez, J. Chandy, E. Heller, F. Jain, Journal of electronic materials, 42 (2013) 3156-3163.
[4] E.H. Rhoderick, Metal–Semiconductor Contacts, Oxford University Press, Oxford, 1978.
[5] H. Norde, Journal of Applied Physics, 50 (1979) 5052-5053.

Biography: Dr. Yusuf Selim OCAK graduated from METU in 2002, Ankara, Turkey. He took his master and Phd. Degrees in Dicle University. He works on formation and characterization of thin films for various applications including solar cells, gas sensors and antibacterial surfaces. He have over 40 in SCI indexed journals. He is the head of renewable energy application and research center in Dicle University.

The Effect of Lead Mine Waste used as concrete Aggregate on Some Physical and Mechanical Properties of Concrete

Mustafa Cullu[1], Hakan Bolat[1], Fatih Sultan Semiz[1]*

Abstract

The aim of this study is to determine the physical and mechanical of concretes produced from lead mine waste which cannot be processed economically as the lead content is low in the mines they are extracted. Lead mine waste were exchanged at ratios of 25%, 50% and 75% respectively with barite and limestone aggregates and samples were prepared at C16/20, C25/30 and C35/45 classes. The density, water absorption and Permeable pore space volume ratio of prepared samples were determined. Besides, the compressive strength of prepared samples were determined via destructive and non-destructive methods. For this purpose, the samples were prepared in 10x20 cm dimensions. It was seen from the experimental measurements that the aggregates produced by lead mine waste had positive effect on physical and mechanical properties of concretes. As a result, depending on the increasing ratio of lead mine waste in aggregates added into the concrete mixture, a better physical and mechanical properties were obtained as compared with limestone aggregate.

***Keywords*:** *Lead mine waste, aggregate, physical and mechanical properties*

1. INTRODUCTION

The most significant one of the environmental studies conducted in order to protect the wildlife is the recycling of the waste that provides to be reduced of the use of natural sources. In particular to be used of the wastes as aggregate in the production of concrete, besides the reduction of the environmental damages, it reduces the consumption of natural aggregate and their environmental effects [1].

In the mining quarries where the industrial products are produced the wastes are in the form of dust, slurry or schist. These wastes are generally thrown to agricultural land, forest land or filled into the mines again. There is no systematic method of disposal of such wastes in the mines [2].

Today, the construction and demolition waste, marble waste, tire waste, brick waste and industrial waste "fly ash, blast furnace slag and silica fume" rates that varies according to the country and city, holds a large share of solid waste. The reusing and recycling of these wastes are of great importance environmentally and economically. There are many studies conducted on this subject [3-10].

The aggregate comprises the 55% to 80% of the concrete. If no alternative aggregate sources are found, the worldwide concrete industry consumes 8-12 billion tons of natural aggregate each year [1]. Thus, the decrease in raw materials, the increasing costs of transportation and environmental effects, has become a requirement of the use of the recycling aggregates [11].

In this study, the use of schist that is stored as a waste in the lead mines and some physical and mechanical features of concrete were examined.

2. MATERIAL AND METHODS

2.1 Material

In order to prepare concrete sample, CEM I 42.5R Portland cement was used in the study. The chemical, physical and mechanical properties of the cement are presented in Table 1.

[1] *Corresponding author: Gumushane University, Faculty of Engineering and Natural Sciences, 29100, Gumushane, Turkey.*
mustafacullu@hotmail.com

Table 1. Chemical, physical and mechanical properties of CEM I 42.5 R

Chemical properties (%)		**Physical properties**	
SiO_2	18.59	Setting time, Initial (min)	02:33
Al_2O_3	4.69	Setting time, final (min)	03:18
Fe_2O_3	3.04	Volume stability (mm)	0.7
CaO	60.34	Specific surface (blaine), (cm^2/g)	4145
MgO	1.92	Specific gravity (g/cm^3)	3.08
SO_3	2.89		
Na_2O	0.11	**Mechanical properties**	**Comp. Strength (MPa)**
K_2O	0.64	2. days	23.9
Loss on ignition	7.19	7. days	51.1
Insoluble residue	0.57	28.days	57.8
S.CaO	0.38		

The lead mine waste and limestone aggregates used in the study were crushed by jaw crusher so as to be suitable for concrete aggregate in terms of dimension. Aggregates were grouped in (0-4 mm, 4-11.2 mm, 11.2-22.4 mm) classes. (Figure 1).

Figure 1. Crushed aggregate in jaw broken and separated in classes

Table 2 shows the physical properties of aggregate classes

Table 2. Physical properties of aggregate

		Physical properties			
Aggregate type	Aggregate class	Density (Oven-dry) (g/cm^3)	Density (SSD) saturated-surface-dry (g/cm^3)	Absorption (%)	Apparent porosity (%)
Lead mine waste	0-4 (Fine)	2.67	2.78	4.02	10.71
	4-32 (Coarse)	2.78	2.81	1.10	3.06
Limestone	0-4 (Fine)	2.52	2.63	4.21	10.62
	4-32 (Coarse)	2.54	2.59	1.93	4.89

Table 3 shows the chemical analysis of aggregate classes.

Table 3. Chemical properties of aggregate

Chemical properties (%)	Lead mine waste	Lime stone
SiO_2		2.95
Al_2O_3		0.43
Fe_2O*	4.65	0.46
MgO		-
Ca**		
CaO	34.6	73.93
$MgCo_3$		22.24
Ba		
S**		
Zn	1.11	
Pb	0.98	
Cu	<0.01	
H_2O	7.96	
Other volatiles weighted (CO_2, etc.)	50.74	
O***		
Total	100.04	100.01

* Total Fe

** Ca and Ba analyzed by MP-AES and ICP-Ms and given in table without calculation to oxide.

*** O and S values were calculated using Barite formula, because other impurities are under detection limonite and/or are negligible, they weren't given

2.2 Methods

2.2.1 Preparation of Concrete Samples

The concrete samples on which physical and mechanical tests was applied were designed in three groups as: lead mine waste aggregates, limestone- lead mine waste aggregates and limestone. The aggregates were exchanged among each other at ratios of 25%, 50% and 75% respectively and samples with dimensions of 10x20 cm were prepared at C16/20, C25/30 and C35/45 concrete density, absorption, permeable pore space volume and compressive strength with destructive and nondestructive methods were determined on these produced composite materials. The coding of concrete series and their proportional changes can be observed in Table 4.

Table 4. The coding of concrete series and their proportional changes

Concrete type	Aggregate ratio (%)
100MW	100% Lead mine waste
100LS	100% Limestone
25MW75LS	25% Lead mine waste- 75% Limestone
50MW50LS	50% Lead mine waste- 50% Limestone
75MW25LS	75% Lead mine waste- 25% Limestone

Mixture proportions are given in Table 5.

Table 5. Mixture proportions for concrete (kg/m^3)

Concrete class	Concrete type	Water (w)	Cement (c)	w/c	Fine aggregate		Course aggregate	
					Lead mine waste	Limestone	Lead mine waste	Limestone
C16/20	100MW	218	315	0.69	898	-	947	-
	100LS	218	315	0.69	-	849	-	873
	25MW75LS	218	315	0.69	224	637	237	655
	50MW50LS	218	315	0.69	449	425	473	436
	75MW25LS	218	315	0.69	673	212	710	218
C25/30	100MW	218	411	0.53	856	-	902	-
	100LS	218	411	0.53	-	810	-	831
	25MW75LS	218	411	0.53	214	608	226	624
	50MW50LS	218	411	0.53	428	405	451	416
	75MW25LS	218	411	0.53	642	203	677	208
C35/45	100MW	218	558	0.39	792	-	832	-
	100LS	218	558	0.39	-	750	-	767
	25MW75LS	218	558	0.39	198	562	208	575
	50MW50LS	218	558	0.39	396	375	416	383
	75MW25LS	218	558	0.39	594	187	624	192

2.2.2 Identification of density

Density (*D*) was calculated on five 100x200 mm cylindrical concrete samples according to EN 12390-7 principles. Equation 1 was used to calculate *D* [12].

$$D = m/V \quad (1)$$

Where; *D*= density of concrete sample, g/cm^3, *m*= mass of the concrete sample depending on its condition during the experiment, g, *V*= volume of the concrete sample which is identified by a special method, cm^3 [12].

2.2.3 Identification of water absorption

Water absorption ratio (*m*) was calculated on five 100x200 mm cylindrical concrete samples according to ASTM C642 principles. Equation 2 was used to calculate *m* [13].

$$m = ((B-A)/A)x100 \quad (2)$$

Where; *m*= water absorption ratio by weight, (%), *A*= mass of oven-dried sample in air, g, *B*= mass of surface-dry sample in air after immersion, g [13].

2.2.4 Identification of permeable pore space volume

Permeable pore space volume (B_0) was calculated on five 100x200 mm cylindrical concrete samples according to ASTM C642 principles. Equation 3 was used to calculate B_0 [13].

$$B_o = ((C-A)/(C-D))x100 \quad (3)$$

Where; B_o= Permeable pore space volume, (%), *A*= mass of oven-dried sample in air, g, *C*= mass of surface-dry sample in air after immersion and boiling, g, *D*=apparent mass of sample in water after immersion and boiling, g [13].

2.2.5 Identification of compressive strength

Compressive strength (f_c) was calculated on five 100x200 mm cylindrical concrete samples according to EN 12390-3 principles. Equation 4 was used to calculate f_c [14].

$$fc = F/Ac \quad (4)$$

where: *fc* = Compressive strength, MPa, *F*= total maximum load, N, *Ac*= area of loaded surface, mm^2 [14].

2.2.6 The Assignation of Non Destructive Testing Methods and Concrete Compressive Strength

In determining the compressive strength with non-destructive method, the Surface Hardness (Schmidt Hammer) according to the principles specified in ASTM C805 and Ultrasound pulse velocity tests according to the principles specified in ASTM C597 were carried out. In the calculation of the compressive strength;

In the Surface Hardness Method;

$$f_c = 0.0092N^{2.27} \quad (5)$$

N= Rebound number

In the Ultrasound Pulse Velocity Method;

$$V = {}^{L}/_{t} \quad (6)$$

fc= 6(V-1.8)1.8

V= Ultrasonic Pulse Velocity (km/sec), L= Gage Length (km), t= Sound Pulse Velocity (sec)

The devices used in the study are shown in Figure 2.

Figure 2. Schmidt Hammer and Ultrasonic Pulse Velocity Device

3. RESULTS AND DISCUSSION

3.1 Concrete Density

In the prepared concrete samples, the substitution of limestone aggregates with lead mine waste aggregates in varying proportions have led to the increase in density of concrete samples. With the increase of the compressive strength the densities of the concrete samples were increased. There is no linear change in the density increase of the concrete samples with the increase of the lead mine waste aggregates. This situation is considered to be resulted from the varying amounts of lead within the aggregate. The density values of the concrete types in C16/20, C25/30 and C35/45 strength classes are shown in Figure 3.

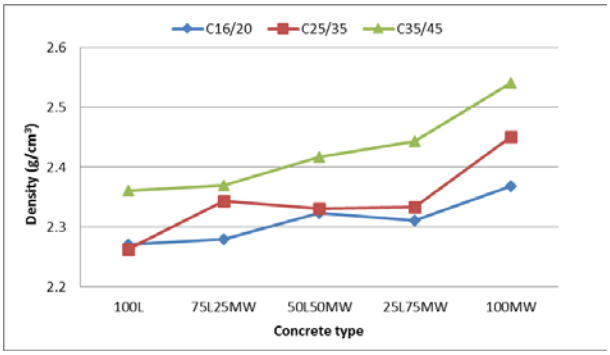

Figure 3. The density values of the concrete types and classes

In the density assessment of the concrete samples when the density value of 100L concrete type is 2.27g/cm^3 in the C16/20 strength class, it is 2.37g/cm^3 in 100MW concrete type. In C25/30 strength class, the density value of 100L concrete type is

2.26 g/cm^3 and it is 2.45 g/cm^3 in 100MW concrete type. In C35/45 strength class, the density value of 100L concrete type is 2.36 g/cm^3 and it is 2.54 g/cm^3 in 100MW concrete type.

3.2 Concrete Absorption

In the water suction values of the concrete samples, a decrease is observed by the increment of the lead mine waste aggregates. In addition, also the increase of the strength class causes a decrease in the water suction values by reducing the amount of voids in the concrete. With the increasing amount of lead mine waste aggregates within the concrete samples, an improvement is observed in the water suction values. The water absorption values of the concrete types are shown in Figure 4.

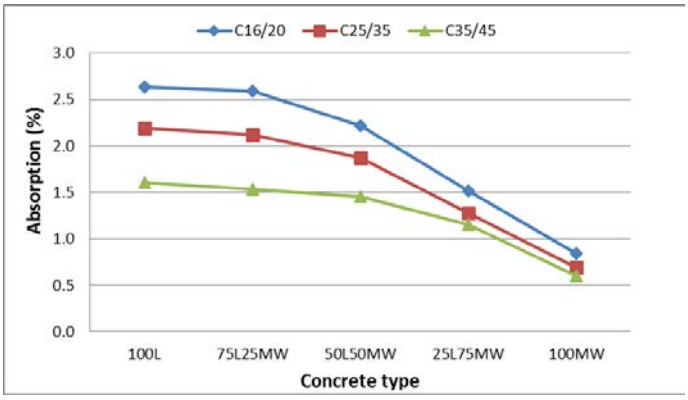

Figure 4. The water absorption values of the concrete types and classes

In the absorption assessment of the concrete samples when the absorption value of 100L concrete type is 2.64% in the C16/20 strength class, it is 0.84% in 100MW concrete type. In C25/30 strength class, the absorption value of 100L concrete type is 2.19% and it is 0.69% in 100MW concrete type. In C35/45 strength class, the absorption value of 100L concrete type is 1.6% and it is 0.6% in 100MW concrete type.

3.3 Concrete permeable pore space volume

In the permeable pore space volume values, a decrease is observed by the increment of the lead mine waste aggregates. Also, the increase of the strength class causes a decrease in the permeable pore space volume values by reducing the amount of voids in the concrete. The decrease in the permeable pore space volume values of the concrete samples shows similarity with the water suction values. The permeable pore space volume values of the concrete types are shown in Figure 5.

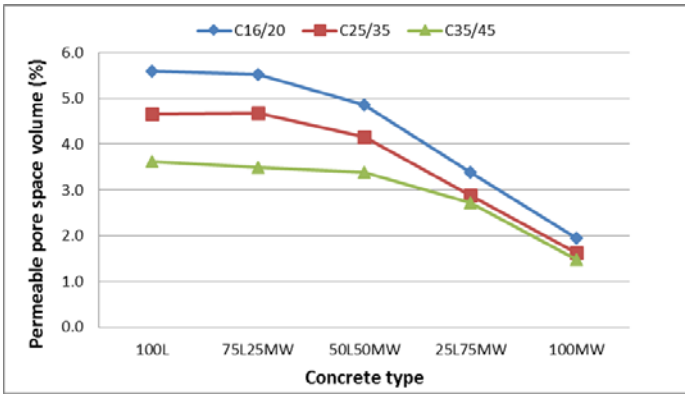

Figure 5. The permeable pore space volume values of the concrete types and classes

In the permeable pore space volume assessment of the concrete samples when the permeable pore space volume value of 100L concrete type is 5.59% in the C16/20 strength class, it is 1.95% in 100MW concrete type. In C25/30 strength class, the permeable pore space volume value of 100L concrete type is 4.67% and it is 1.63% in 100MW concrete type. In C35/45 strength class, the permeable pore space volume value of 100L concrete type is 3.62% and it is 1.47% in 100MW concrete type.

3.4 The Compressive Strength Relations According to the Destructive and Nondestructive Test Methods

A relationship is established between the destructive and nondestructive test methods on concrete samples with the compressive strength values. Large differences aren't seen between the destructive and non-destructive testing methods in C16/20 strength class with the results obtained. With the increment amount of lead mine waste aggregates within the concrete and in the strength significant increases are being observed. The relationship between the compressive strength values obtained with the destructive and non-destructive testing methods of the concrete samples is shown in Figure 6.

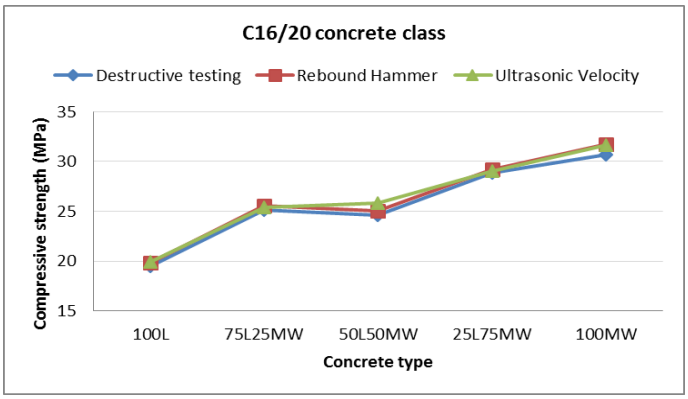

Figure 6. The compressive strength values obtained in the C16/20 strength classes with destructive and non-destructive methods

In the C16/20 strength class with the Schmidt hammer values and between the values obtained by the destructive method, in the 100MW, 75MW25L, 50MW50L, 25MW75L and 100L concretes, respectively a greater compressive strength of 3.5%, 1.2%, 1.7%, 1.8% and 1.6% was obtained. Between the ultrasonic pulse velocity values and the values obtained by the destructive method, in the 100MW, 75MW25L, 50MW50L, 25MW75L and 100L concretes, respectively a greater compressive strength of 3.2%, 0.4%, 4.9%, 1.2% and 2.4% was obtained.

The relationship between the compressive strength values obtained with the destructive and non-destructive testing methods of the concrete samples in C25/30 is shown in Figure 7.

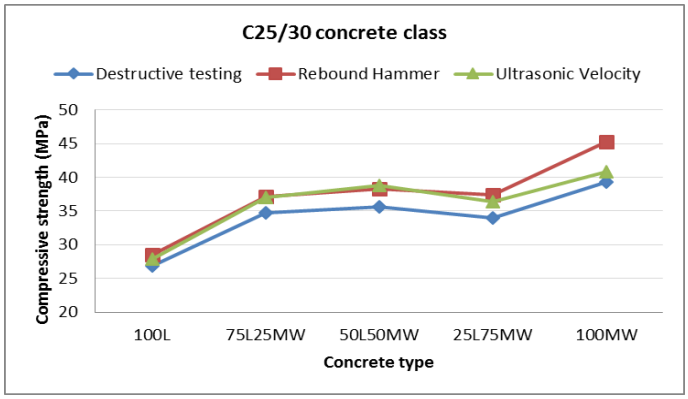

Figure 7. The compressive strength values obtained in the C25/30 strength classes with destructive and non-destructive methods

In the C25/30 strength class with the Schmidt hammer values and between the values obtained by the destructive method, in the 100MW, 75MW25L, 50MW50L, 25MW75L and 100L concretes, respectively a greater compressive strength of 15%, 10.2%, 7.5%, 7.2% and 5.9% was obtained. Between the ultrasonic pulse velocity values and the values obtained by the destructive method, in the 100MW, 75MW25L, 50MW50L, 25MW75L and 100L concretes, respectively a greater compressive strength of 3.7%, 7%, 8.9%, 6.8% and 3.8% was obtained.

The relationship between the compressive strength values obtained with the destructive and non-destructive testing methods of the concrete samples in C35/45 is shown in Figure 8.

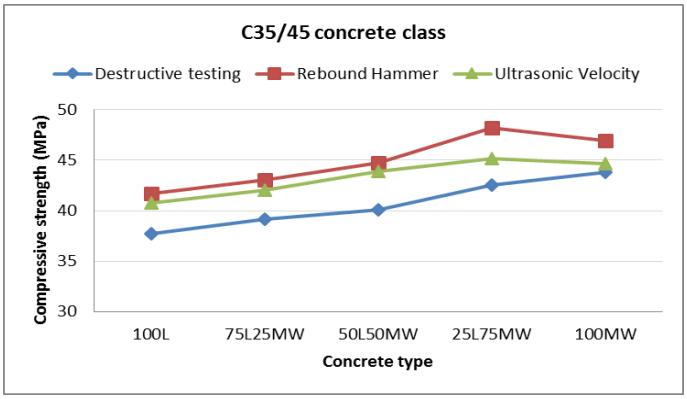

Figure 8. The compressive strength values obtained in the C35/45 strength classes with destructive and non-destructive methods

In the C35/45 strength class with the Schmidt hammer values and between the values obtained by the destructive method, in the 100MW, 75MW25L, 50MW50L, 25MW75L and 100L concretes, respectively a greater compressive strength of 7.1%, 13.4%, 11.8%, 10.1% and 10.6% was obtained. Between the ultrasonic pulse velocity values and the values obtained by the destructive method, in the 100MW, 75MW25L, 50MW50L, 25MW75L and 100L concretes, respectively a greater compressive strength of 1.9%, 6.3%, 9.5%, 7.5% and 8.2% was obtained.

4. CONCLUSION

In the use of lead mine wastes as aggregate within the concrete, the effect on the physical and mechanical properties of the concrete is observed. With the increment of the amount of lead mine wastes within the concrete, it was determined that the density of the concrete increases when compared to limestone and water suction and permeable pore space volume values decrease. In the increment of the density of the concrete, the lead within the lead mine wastes affects the amount.

Between the non-destructive methods used for the determination of compressive strength of the concrete samples and the compressive strength values obtained by destructive methods in C25/30 and C35/45 strength classes, differences were observed.

The materials that are stored in the storage areas by mining with the use of lead mine wastes within the concrete and which could lead to pollution of the environment with the environmental impacts will be brought into the economy. Furthermore, also the investigation of the effects that can be harmful to human health originating from the use of lead-containing aggregates in the concrete is recommended.

ACKNOWLEDGMENT

The authors wish to thank the TUBITAK (The Scientific and Technological Research Council of Turkey) for supporting this work under the project number of 113M317.

REFERENCES

[1]. Tu Y T, Chen Y Y, Hwang L C, Properties of HPC with Recycled Aggregates, Cement and Concrete Research36: 943–950, 2006.
[2]. Kore, S.D., Vyas, A.K., Impact of marble waste as coarse aggregate on properties of lean cement concrete, Case Studies in Construction Materials. 4:85–92, 2016.
[3]. Binici, H., Shah, T., Aksogan ,O., Kaplan, H., Durability of concrete made with granite and marble as recycle aggregates. Journal of Materials Processing Technology, 208:1-3, 299-308, 2008.
[4]. Uygunoğlu, T., Topçu, İ.B., Çelik, A.G., Use of waste marble and recycled aggregates in self-compacting concrete for environmental sustainability, Journal of Cleaner Production, 84:1, 691-700, 2014.
[5]. Vegas, I., Cano, M., Arribas, I., Frías, M., Rodríguez, O., Physical–mechanical behavior of binary cements blended with thermally activated coal mining waste, Construction and Building Materials, 99, 169-174, 2015.
[6]. González-Corrochano, B., Alonso-Azcárate, J., Rodas, M., Barrenechea, J.F., Luque, F.J., Microstructure and mineralogy of lightweight aggregates manufactured from mining and industrial wastes, Construction and Building Materials, 25, 3591-3602, 2011.
[7]. Gomes, P.C.C., Ulsen, C, Pereira, F.A., Quattrone, M., Angulo, S.C., Comminution and sizing processes of concrete block waste as recycled aggregates, Waste Management, 45, 171-179, 2015.
[8]. Hansen, T., Narud, H., Strength of recycled concrete made from crushed concrete coarse aggregate, Concrete International, 5:1, 79-83, 1983.
[9]. Padmini, A., Ramamurthy, K., Mathews, M., Influence of parent concrete on the properties of recycled aggregate concrete, Construction and Building Materials, 23: 2, 829-836, 2009.
[10]. Zega, C., Villagrán-Zaccardi, Y., Di Maio, A., Effect of natural coarse aggregate type on the physical and mechanical properties of recycled coarse aggregates, Materials and Structures, 43:1-2, 195-202, 2010.
[11]. Rakshvir M, Barai V S, Studies on Recycled Aggregates-based Concrete, Waste Management & Research Res., 24: 225–233, 2006.

[12]. ASTM C642 Standard Test Method for Density, Absorption, and Voids in Hardened Concrete. Annual Book of ASTM Standards. Philadelphia, USA. 2004. Pp. 1-3.
[13]. EN 12390-7 Testing hardened concrete - Part 7: Density of hardened concrete. Turkish Standards Institute. Ankara. pp. 1-11. 2010.
[14]. EN 12390-3 Testing hardened concrete – Part 3: Compressive strength of test specimens. Turkish Standards Institute. Ankara. pp. 1-19, 2010.

BIOGRAPHY

Mustafa ÇULLU was born in 1975 in Adana-Turkey. Received his BA (2001), MA (2004) and PhD (2010) education in Gazi University Institute of Natural Sciences Department of Construction Education in Ankara-Turkey. His MA Thesis is about Alkali-silica reaction and PhD Thesis is about antifreeze for concrete.

He gave undergraduate and graduate lessons such as Construction Drawing, Material Science, Concrete Technology and construction management in Hacettepe University and Gumushane University. Currently he has been worked as an Assistant Professor at Gumushane University in Turkey since 2010. He continue to researches of about heavy aggregate and radiation shielding. He is married and has two children.

The Effects of Aggregate Types on Abrasion Resistance of Heavy Weight Concretes

Mustafa Cullu[1], *Hakan Bolat*[1], *Oguz Burnaz*[1]

Abstract

The aim of this study is to determine the effects of abrasion resistance of heavy weight aggregates on abrasion resistant of concretes. In this study, the heavy weight aggregates that are magnetite, barite and limonite were used. Abrasions were determined according to ASTM C131 and ASTM C535. Selected concrete classes are C16/20, C25/30 and C35/45; in addition, these are subjected to abrasion according to ASTM C944. Consequently, it is seen that aggregate types affects the abrasion resistance of all type of concrete.

***Keywords*:** *Heavy weight aggregates, abrasion, magnetite, barite, limonite*

1. INTRODUCTION

The concrete which is a composite material consists of two phases including coarse aggregate phase and dough phase that is formed by the concrete together with the fine aggregate. The abrasion resistance of the concrete is being evolved in accordance with the more resistant than one among those two. The abrasion resistance of the concrete is being high, that is produced with natural aggregates such as basalt with high abrasion resistance, granite and produced with hard aggregate such as blast furnace slag. On the other hand, although the hard aggregates have better abrasion resistance, as they cause more abrasion and tear on the mechanical parts in crusher plants, they also increase the operating expenses. However, still it is necessary to take advantage of this resistant form of hard aggregates in concrete road pavements [1].

The incoming forces to the concrete surfaces as friction or impact lead to the destruction of the concrete surfaces and the surface abrasion. The abrasion mechanism as a physical and mechanical event occurs in a slow tempo in course of time and generally it is seen on the pavements and concrete roads comprising human and traffic loads and also in the water structures which are exposed to corrosive effects of the sweepings materials carried by the rivers. In such places, using high abrasion resistance material is essential, in terms of being able to minimize the damages that will be generated by the abrasion. In the surveys conducted on the abrasion resistance of the concrete [2]-[9] it is expressed that the abrasion resistance is depending on the implemented test methods, the surface finishing methods, the structural characteristics of the concrete surface that will be exposed to abrasion forces, the curing conditions, to the use of the mineral additives and strength characteristics. The factors that are important criteria of strength such as, water / cement ratio, aggregate-paste interface, aggregate and binder paste quality are also said to be effective on abrasion resistance [10].

2. MATERIAL AND METHODS

2.1 Material

In order to prepare concrete sample, CEM I 42.5R Portland cement was used in the study. The chemical, physical and mechanical properties of the cement are presented in Table 1.

[1] *Corresponding author: Gumushane University, Faculty of Engineering and Natural Sciences, 29100, Gumushane, Turkey.*
mustafacullu@hotmail.com

Table 1. Chemical, physical and mechanical properties of CEM I 42.5 R

Chemical properties (%)		**Physical properties**	
SiO_2	18.59	Setting time, Initial (min)	02:33
Al_2O_3	4.69	Setting time, final (min)	03:18
Fe_2O_3	3.04	Volume stability (mm)	0.7
CaO	60.34	Specific surface (blaine), (cm^2/g)	4145
MgO	1.92	Specific gravity (g/cm^3)	3.08
SO_3	2.89		
Na_2O	0.11	**Mechanical properties**	**Comp. Strength (MPa)**
K_2O	0.64	2. days	23.9
Loss on ignition	7.19	7. days	51.1
Insoluble residue	0.57	28.days	57.8
S.CaO	0.38		

The magnetite, barite and limonite aggregates used in the study were crushed by jaw crusher so as to be suitable for concrete aggregate in terms of dimension. Aggregates were grouped in (0-4 mm, 4-11.2 mm, 11.2-22.4 mm) classes. Figure 1.

Figure 1. Crushed aggregate in jaw broken and separated in classes

Table 2 shows the physical properties of aggregate classes

Table 2. Physical properties of aggregate

		Physical properties			
Aggregate type	Aggregate class	Density (Oven-dry) (g/cm^3)	Density (SSD) saturated-surface-dry (g/cm^3)	Absorption (%)	Apparent porosity (%)
Magnetite	0-4 (Fine)	3.44	3.63	5.64	19.42
	4-32 (Coarse)	4.11	4.13	0.67	2.75
Limonite	0-4 (Fine)	3.48	3.62	4.17	14.49
	4-32 (Coarse)	3.32	3.43	4.02	13.36
Barite	0-4 (Fine)	3.76	3.95	5.13	19.25
	4-32 (Coarse)	3.84	3.87	0.66	2.54

Table 3 shows the chemical analysis of aggregate classes.

Table 3. Chemical properties of aggregate

Chemical properties (%)	Magnetit	Limonite	Barite
SiO_2		0.001	
Al_2O_3		1.89	
Fe_2O*	57,79	49.93	
MgO	4,02	2.07	
Ca**	2.05	4.72	
$MgCo_3$			
Ba			46.04
S**			13.4
H_2O	4.6	21.8	
Other volatiles weighted (CO_2, etc.)	31.55	19.59	
O***			40.6
Total	100.01	100.001	100.04

* Total Fe
** Ca and Ba analyzed by MP-AES and ICP-Ms and given in table without calculation to oxide.
*** O and S values were calculated using Barite formula, because other impurities are under detection limonite and/or are negligible, they weren't given

2.2 Methods

2.2.1 Preparation of Concrete Samples

The concrete samples on which abrasion resistance tests was applied were designed. The samples with dimensions of 10x20 cm were prepared at C16/25, C25/35 and C35/45 concrete classes. The image of concrete samples is shown Figure 2.

Figure 2. The produced test specimens for experimental studies to be conducted

2.2.2 The Determination of the Amount of Aggregate Abrasion (Los Angeles Test)

Within the scope of the study in determining the abrasion characteristics of permanent way aggregates the most commonly used Los Angeles Abrasion Test was conducted. The abrasion amounts of the aggregates that were used in the study, was made according to the principles specified in ASTM C131 for "9.5 – 19 mm" aggregates and specified in ASTM C535 for "19 – 37.5 mm" aggregates [11, 12]. For aggregates smaller than 38 mm (for 500 cyclic test);

Abrasion Rate (%); $AR = \frac{G_0 - G_{500}}{G_0} x100$

Here, AL: Abrasion rate (%), G_0: The amount of the initial material (g), G_{500}: 1.7 mm sieve material amount after 500 cycles (g). Los Angeles Abrasion Test Device is shown in Figure 3.

Figure 3. Los Angeles Abrasion Test Device

2.2.3 The Determination of Abrasion Resistance

The Abrasion Resistance was conducted in accordance with the principles stated in ASTM C944 test standard, on 10 x 20 cm cylinder concrete samples [13]. In the calculation of the abrasion rate:

$$AR = \frac{W_0 - W_1}{W_0} \times 100$$

Equation was used. Here, the followings are represented as AR: Abrasion Rate (%), W_0: The initial weight (g), W_1: The weight after abrasion (g). The abrasion device used in the study is shown in Figure 4.

Figure 4. The abrasion device and etched concrete sample

3 RESULTS AND DISCUSSION

3.1 Aggregate Abrasion Rates

Magnetite aggregates have demonstrated minimal abrasion due to its robust construction. Barite aggregates are an aggregate type with the highest abrasion rate, despite its massive appearance. In the 9.5 -19 mm group aggregates specified in the ASTM C131 standard, the lowest aggregate abrasion rate is in magnetite aggregates with 17.65 % and the largest aggregate abrasion rate is in barite aggregate with 69.5 %. In the 19-37.5 mm group aggregates specified in the ASTM C535 standard, the lowest aggregate abrasion rate is in magnetite aggregates with 11.2 % and the largest aggregate abrasion rate is in barite aggregate with 55.26 %. The abrasion rates of the aggregate types according to ASTTM C131 and ASTM C535 standards are shown in Figure 5.

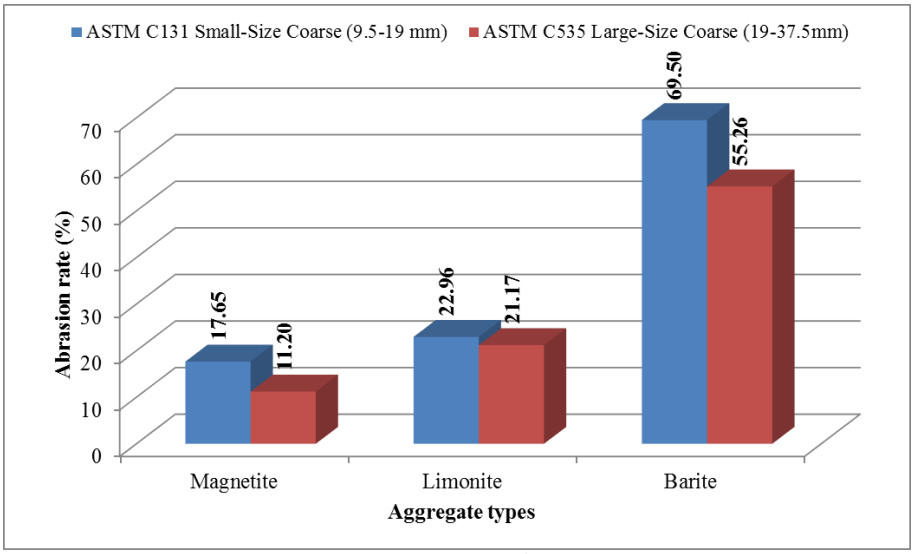

Figure 5. The abrasion rates of the aggregates

3.2 The Abrasion Rates of the Heavyweight Concrete

The Abrasion rates of the concrete samples according to all Strength classes and aggregate types are shown in Figure 6. In C16/20 strength class, the largest aggregate abrasion is in Limonite aggregates with 2.69 % and the lowest abrasion is in barite aggregate with 0.81 %. In C25/30 strength class, the largest abrasion is in Limonite aggregates with 1.92% and the lowest abrasion is in Magnetite aggregates with 0.73%. In C35/45 strength class, the largest abrasion is in Limonite aggregates with 1.76% and the lowest abrasion is in Magnetite aggregates with 0.40%. The abrasion rate decreases with the increase of strength class. The abrasion rates of the Magnetite containing concrete samples shows similarity to the abrasion rates of the magnetite aggregates. Although the Limonite aggregates abrasion values are being low when compared to barite aggregates, exactly an opposite situation is observed in the concretes prepared with limonite and barite. This situation is thought to be caused not demonstrating enough adherences to the concrete due to the alteration of limonite aggregates.

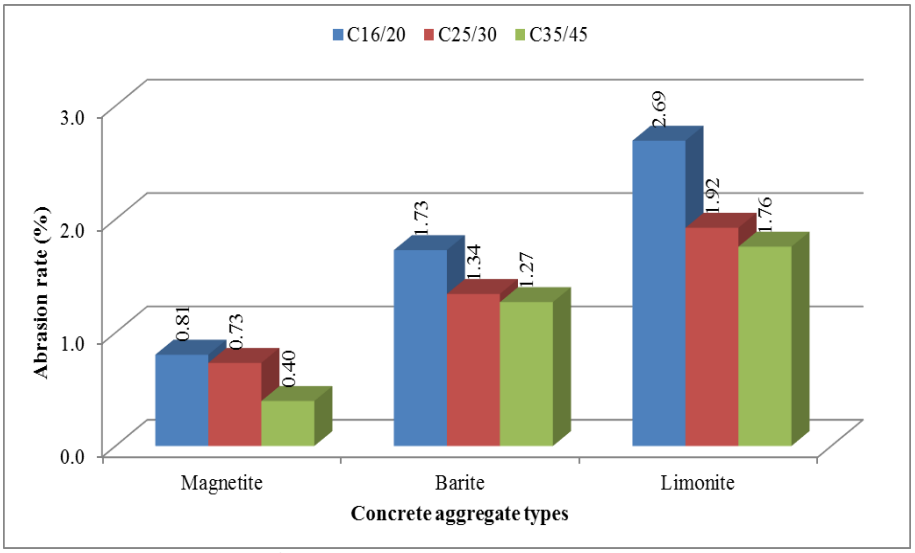

Figure 6. The abrasion rates of the concrete samples according to the strength class and aggregate type

4. CONCLUSIONS

Heavy aggregates are used in the production of heavyweight concrete. In general, the purpose of the production of heavyweight concrete is radiation absorbing. In fact, it is also preferred in the production of dam concrete. In cases where abrasion strength is important, the determination of the abrasion resistances of aggregates are required. Magnetite, Limonite and Barite aggregates are widely used in heavyweight concrete production in terms of their density values. Limonite aggregate schist is difficult to be found as a massive state in nature. Just as the limonite aggregates used in this study, it is generally in altered manner. Due to the altered surface characteristics of Limonite, its adherence with the cement phase was weak. Therefore, the largest abrasions in the concrete samples were in Limonite aggregates. When considering the aggregate and concrete abrasion rates, the most appropriate aggregate type is determined as magnetite.

ACKNOWLEDGMENT

The authors wish to thank the TUBITAK (The Scientific and Technological Research Council of Turkey) for supporting this work under the project number of 113M317.

REFERENCES

[1]. S. M. Metev and V. P. Veiko, *Laser Assisted Microtechnology*, 2nd ed., R. M. Osgood, Jr., Ed. Berlin, Germany: Springer-Verlag, 1998.
[2]. Karpuz, O., Akpınar, M.V., The Effect of Fine Aggregate Type on Wear Resistance of Pavement Concrete, Electronic Journal of Construction Technologies, Vol:5, No:2, Pp:1-8, 2009.
[3]. Sadegzadeh, M., Page, C. L., Kettle, R. J., Surface microstructure and abrasion resistance of concrete," Cement Concrete Research, Vol:17, Pp: 581-590, 1987.
[4]. Sadegzadeh, M., Page, C. L., Kettle, R. J., Surface microstructure and abrasion resistance of concrete," Cement Concrete Research, Vol:17, Pp: 581-590, 1987.
[5]. Horszczaruk, E., Abrasion resistance of high-strength concrete in hydraulic structures, Wear, Vol:259, Pp:62-69, 2005.
[6]. Ramezanianpour, A.A., Haghollahi, A., Investigation and modelling of abrasion in industrial concrete floors, Amirkabir Journal of Science Technology, Vol:115, Pp:55–61, 2004.
[7]. Atiş, C.D., Karahan, O., Arı, K., Çelik, Ö., Bilim, C., Relation between strength properties (flexural and compressive) and abrasion resistance of fiber (steel and polypropylene) reinforced fly ash concrete, Journal of Materials in Civil Engineering, Vol: 21, Pp: 402-408, 2009.
[8]. Gesoğlu, M., Guneyisi, E., Khoshnaw, G., Ipek, S., Abrasion and freezing–thawing resistance of pervious concretes containing waste rubbers, Construction and Building Materials, 73:19–24, 2014.
[9]. Yoshitake, I., Ueno, S., Ushio, Y., Arano, H., Fukumoto, S., Abrasion and skid resistance of recyclable fly ash concrete pavement made with limestone aggregate, Construction and Building Materials, 112:440–446, 2016.
[10]. Ramesh Kumar G.B., Sharma U.K., Abrasion resistance of concrete containing marginal aggregates, Construction and Building Materials, 66:712-722, 2014.
[11]. Gaedicke, C., Marines, A., Miankodila, F., Assessing the abrasion resistance of cores in virgin and recycled aggregate pervious concrete, Construction and Building Materials, 68:701-708, 2014.
[12]. Oymael, S., Yeğinobalı, A., Additive Effects of Oil Shale Ash Concrete Abrasion Resistance, Proceedings of The Fourth National Concrete Conference, Pp. 359-367, Istanbul, Turkey, 1996.
[13]. ASTM C131, Standard Test Method for Resistance to Degradation of Small-Size Coarse Aggregate by Abrasion and Impact in the Los Angeles Machine, Annual Book of ASTM Standards. Philadelphia, USA. pp. 1-5, 2004.
[14]. ASTM C535, Standard Test Method for Resistance to Degradation of Large-Size Coarse Aggregate by Abrasion and Impact in the Los Angeles Machine, Annual Book of ASTM Standards. Philadelphia, USA. pp. 1-3, 2004.
[15]. ASTM C944, Standard Test Method for Abrasion Resistance of Concrete or Mortar Surfaces by the Rotating-Cutter Method, Annual Book of ASTM Standards. Philadelphia, USA. pp. 1-5, 2004.

BIOGRAPHY

Mustafa ÇULLU was born in 1975 in Adana-Turkey. Received his BA (2001), MA (2004) and PhD (2010) education in Gazi University Institute Of Natural Sciences Department of Construction Education in Ankara-Turkey. His MA Thesis is about Alkali-silica reaction and PhD Thesis is about antifreeze for concrete.

He gave undergraduate and graduate lessons such as Construction Drawing, Material Science, Concrete Technology and construction management in in Hacettepe University and Gumushane University. Currently he has been worked as an Assistant Professor at Gumushane University in Turkey since 2010. He continue to researches of about heavy aggregate and radiation shielding. He is married and has two children.

Performance Measurement Issue in Clothing Retailing: Turkish Case

Turan Atilgan[1], *Seher Kanat*[2]

Abstract

The clothing sector possesses a market structure which is significantly and rapidly affected by economical and socio-cultural developments and alterations. Too many enterprises with different sizes operate in clothing retailing area because clothes are one of the basic consumption expenditures of people. These enterprises basically operate in three different market segments which are intended for low-income group, middle income group and luxury consumption. The clothing retailers, which operate in clothing market that shows too much variability and property, differ from each other in terms of enterprise properties and standards.

Clothing retailers, whose numbers and properties are rapidly increased and altered, confront with store performance measurement problem as a serious issue. Retailing, which constitutes the ultimate ring of added value chain for clothing enterprises, strengthens brand value and power as well as increasing profitability by providing brand awareness and customer loyalty. In this context, store performance measurement is as important as store location selection and store atmosphere design and management because retailing is a prestigious activity with high costs. Poor store performance damages enterprises financially. Besides, it negatively affects enterprise goodwill by damaging brand image.

This study, analyzes the retail performance measurement methods and their effects in clothing sector. The research is based on field research which involves significant clothing enterprises that operate in Turkish clothing sector.

Keywords: Retailing, clothing retailing, performance measurement, Turkish clothing sector

1. PERFORMANCE CONCEPT IN RETAILING AND PERFORMANCE MEASUREMENT METHODS

The performance of modern organizations that operate in competitive market places is based on multiple interrelated dimensions, which are both endogenous (controllable by the organizations) and exogenous (either non-controllable or partially controllable by the organizations) [1]. Performance measurement plays a critical role in understanding how a business is operating, it helps to identify where improvements might be made and ultimately informs the strategic planning process [2].

In the business context, performance is defined as the efficiency of actions, which is how organizational resources are consumed to produce value [3]. Performance analysis can help retailers to enhance their operational performance and thus establish a competitive advantage. For this reason, the measurement of performance (in terms of operational efficiency) has become increasingly important to retailers. A better measurement tool can provide more accurate information to improve the performance of a system [4].

Financial performance of retailers is influenced by many factors such as; gross profit percentage, inventory turnover, number of employees, store size and number of competitors [5]. Earlier researches have predominantly explained market based store performance (sales, market share) by using variables including distance, size of the store and trade area demographics. Another study has focused on the effect of a store's internal and external environment on sales and sales per square foot [6].

On the other hand, retail productivity is one of the most significant and widely used methods of retail performance measurement. Conceptually productivity can be defined as the ration of output to input and in retail context too, productivity index is a key performance indicator [7]. Also, data envelopment analysis is reported to be appropriate for the assessment of the efficiency levels of the intra chain retail stores where with data envelopment analysis integration of a variety of performance metrics and obtaining a structured methodology to appraise retail store performance are possible. In the literature; number of full time employees, number of part time employees, labor costs, store sizes, store locations, number of sale points, age of stores, rent costs, inventory amounts and/or values, general costs of the stores, sales amounts and/or values, promotion amounts and/or values, profits, customer satisfaction are used as inputs and outputs while evaluating retail store performance [8].

[1]*Corresponding author: Ege University, Department of Textile Engineering, 35100, Bornova/İzmir, Turkey, turan.atilgan@ege.edu.tr*

[2]*Ege University, Department of Textile Engineering, 35100, Bornova/İzmir, Turkey, seher.kanat@ege.edu.tr*

The evaluation and improvement of the efficiency of the clothing industry business also require the use of analytical techniques that provide more precise and objective information than the one obtained when analyzing financial indicators or profitability indicators. In most of the firms of the clothing industry, the performance is evaluated based on financial and operational ratios, quite often using profits as the main key performance indicator, complemented with the comparison between defined goals and what effectively was accomplished [9].

2. RETAILING PERFORMANCES OF TURKISH CLOTHING ENTERPRISES

Turkish retailing sector passes through a huge transformation process. On the one hand; square meters of stores, number of customers and employees are increased. However, on the other hand number of store closures is increased too. Retailers' toleration towards inefficient stores are decreased according to past. Therefore, they rapidly close unprofitable stores. The basic rule of closure decision is the share of store rent within turnover. If the store rent exceeds 15% of turnover, closure decision is taken. Number of store closures is also increased due to the mergence and acquisitions between enterprises and the trend of opening large stores instead of small ones [10].

This study analyzes the retail performance measurement methods of successful Turkish clothing enterprises, which possess their own brands and retail chains, and effects of these methods. For this purpose, interviews have been made with marketing managers and store managers and a questionnaire form consisting of 14 questions has been used. The obtained results are given below.

2.1 Mavi

Mavi, which is established in 1991, produces denim wear and non-denim sportswear for women and men. Mavi has been the leading jeans brand in Turkey since the last 18 years with 11 % market share. The enterprise aims to create a Mediterranean brand around blue jean culture and perfect fitting jeans.

Mavi possesses 305 stores (235 domestic, 70 foreign) in total. The enterprise has opened 38 domestic stores and 16 foreign stores within 2015. On the other hand, it has closed 7 domestic stores and 5 foreign stores in the same year. The enterprise plans to open 45 new domestic stores and 30 new foreign stores in 2016. 218 of its stores operate in shopping centers whereas 87 of them operate in main streets. The stores, which are located in shopping centers, constitute 71% of all domestic and foreign stores. Enterprise's average store sizes alter between 400 and 800 square meters.

The enterprise tolerates its inefficient stores for one year. In other words, it tolerates for two main seasons. The enterprise indicates its store closure reason as store inefficiency. The enterprise uses; sales value per invoice, sales amount (quantity) per invoice and shares of each customer's sales value within total sales value; in order to measure store performance.

2.2 DeFacto

DeFacto, which is established in 2003, produces women, men, children and teenager clothes. The enterprise aims to become a world brand in 10 countries within 10 years.

DeFacto possesses 354 stores (297 domestic, 57 foreign) in total. The enterprise has opened 59 domestic stores and 26 foreign stores within 2015. On the other hand, it has closed 10 domestic stores in the same year. However it has not closed any foreign stores. The enterprise plans to open 43 new domestic stores and 49 new foreign stores in 2016. 317 of its stores operate in shopping centers whereas 37 of them operate in main streets. The stores, which are located in shopping centers, constitute 90% of all domestic and foreign stores. Enterprise's average store size is 1033 square meters.

The enterprise tolerates its inefficient stores for two years. The enterprise indicates its store closure reasons as store inefficiency, location alterations and increase in rent expenses. The enterprise uses; inventory turnover, investment return of the store, store efficiency per square meter, costs of products, sales value per invoice, sales amount (quantity) per invoice, daily or monthly customer numbers of store, actualization ratio of determined store targets, costs of employees, share of store rent within turnover which does not involve value-added tax; in order to measure store performance.

2.3 Adil Işık Grup

Adil Işık Group, which is established in 1992, produces women clothes. The group possesses adL and Love my body brands. Besides, famous Turkish designer Cengiz Abazoğlu designs a special collection for adL brand in every year. Also, there are codentry and night zoom lines (collections) within adL brand. The philosophy of the enterprise consists of right place, right product, right price and right time.

Adil Işık possesses 160 stores (115 domestic, 45 foreign) in total. The enterprise has opened 17 domestic stores and 15 foreign stores within 2015. On the other hand, it has closed 9 domestic stores and 11 foreign stores in the same year. The enterprise plans to open 15 new domestic stores and 19 new foreign stores in 2016. 126 of its stores operate in shopping centers whereas 34 of them operate in main streets. The stores, which are located in shopping centers, constitute 79% of all domestic and foreign stores. Enterprise's average store sizes alter between 240 and 1000 square meters.

The enterprise tolerates its inefficient stores for one year. The enterprise indicates its store closure reason as store inefficiency. The enterprise uses; profitability (expenses-turnover balance), daily, weekly and monthly sales values on average, daily,

weekly and monthly sales value per invoice and daily, weekly and monthly sales amount (quantity) per invoice; in order to measure store performance.

2.4 Kiğılı

Kiğılı, which is established in 1938, produces suits, shirts, trousers, jackets and casual wear for men. The enterprise owns two brands which are named as Kiğılı and Abdullah Kiğılı Exclusive Cut. The enterprise aims to become one of the ten leading global male brands.

Kiğılı possesses 264 stores (225 domestic, 39 foreign) in total. The enterprise has opened 20 domestic stores and 4 foreign stores within 2015. On the other hand, it has closed 4 domestic stores and 5 foreign stores in the same year. The enterprise plans to open 25 new domestic stores and 6 new foreign stores in 2016. 200 of its stores operate in shopping centers whereas 64 of them operate in main streets. The stores, which are located in shopping centers, constitute 76% of all domestic and foreign stores. Enterprise's average store sizes alter between 150 and 300 square meters.

The enterprise tolerates its inefficient stores for six months. The enterprise indicates its store closure reasons as store inefficiency, issues related with shopping centers, stores which are located too close to each other and increase in rent expenses. The enterprise uses; profitability, daily or monthly turnover of the store and daily or monthly sales amount (quantity) of the store; in order to measure store performance. Besides, if the store rent exceeds 15% of turnover, closure decision is taken.

2.5 Sarar

Sarar, which is established in 1944, produces men and women clothes. The enterprise possesses Sarar, Sarar Women, Interview Sarar, C.C.S, Sarar Scarf, Sarev and Sartoria brands. Sarar still maintains the unique workmanship and elegant quality of its peerless collections, as it has since its very first day.

Sarar possesses 340 stores (250 domestic, 90 foreign) in total. The enterprise has opened 20 domestic stores and 11 foreign stores within 2015. On the other hand, it has closed 8 domestic stores and 9 foreign stores in the same year. The enterprise plans to open 20 new domestic stores and 15 new foreign stores in 2016. 203 of its stores operate in shopping centers whereas 137 of them operate in main streets. The stores, which are located in shopping centers, constitute 60% of all domestic and foreign stores. Enterprise's average store sizes alter between 120 and 1000 square meters.

The enterprise tolerates its inefficient stores for one year. The enterprise indicates its store closure reasons as store inefficiency, location alterations, stores which are located too close to each other and increase in rent expenses. The enterprise uses; turnover per square meter and sales amount (quantity) per square meter; in order to measure store performance.

3. RESULTS AND GENERAL EVALUATION

Nowadays, enterprises must preserve their profitability and efficiency under intensive rivalry conditions in order to survive in clothing sector which is a dynamic, variable and rapid sector. In this context, efficiency of their retail chains, which are established in order to increase customer satisfaction and profitability and efficiency of their supply chains, gains great importance. Therefore, clothing enterprises measure performances of their stores, which are a part of their retail chains, with different methods. They rehabilitate stores after determining their inefficiency and if this rehabilitation process fails, they take closure decision. In the past, enterprises accept store closures as failure. However, nowadays, if they do not close their inefficient stores, it is accepted as failure.

According to our research results, our clothing enterprises possess 160-354 domestic and foreign stores in total. 60-90% of these enterprises operate in shopping centers whereas 10-40% operates in main streets. As it can be seen, enterprises prefer to open both of their domestic and foreign stores in shopping centers. Today's intensive and hard working conditions both shorten the lifetimes for rest and decrease their quality. Therefore, shopping centers are preferred in which plenty of needs can be fulfilled shortly in the same place. People both socialize and fulfill their needs in their limited resting periods.

According to another research result, enterprises' new domestic store opening ratios are between 8% and 20% whereas their new foreign store opening ratios are between 10% and 45%. Besides our clothing enterprises' new domestic store opening targets for 2016 alter between 8% and 19%. On the other hand, their new foreign store opening targets for 2016 alter between 15% and 85%. As it can be seen, enterprises give great importance to enlarging their foreign retail chains. The participating enterprises are very successful both in domestic market and in their internationalization processes. In this context, enterprises aim to focus on international markets instead of domestic market.

The domestic store closure ratios of participating enterprises are between 2% and 8% whereas their foreign store closure ratios are between 7% and 24%. The foreign store closure ratios are higher than domestic store closure ratios. This situation can be explained with domestic market dominance of enterprises, high domestic store ratios, fluctuations, shrinkages and uncertainties in international markets, faults in foreign store location choices and market researches.

As it can be seen from obtained results, enterprises' average store sizes alter between 120 and 1033 square meters. The enterprises tolerate their inefficient stores for six months at least and for two years at maximum. In other words, they approximately tolerate their inefficient stores for one year. Approximately 15-20 years ago store closures are accepted as

failure. When this situation is taken into consideration, it can be clearly seen that the toleration period is substantially shortened.

The participating enterprises indicate that their store closure reasons as store inefficiency, increase in rent expenses, issues related with shopping centers, location alterations and stores which are located too close to each other. Store management becomes difficult due to the reasons such as; astronomic rent values of stores which are located in domestic shopping centers, shopping centers which are opened too close to each other and increment at the number of shopping centers. The stores, which are located too close to each other, are named as cannibal stores. These stores decrease each other's efficiency. On the other hand, managerial issues of shopping centers, which are rapidly opened without accurate planning, negatively affect store management and cause efficiency decreases in stores.

According to another research result; enterprises use different methods in order to measure their store performances. These methods are; profitability, daily or monthly turnover of the store, daily or monthly sales amount (quantity) of the store, share of store rent within turnover, turnover per square meter, sales amount (quantity) per square meter, daily, weekly and monthly sales values on average, daily, weekly and monthly sales value per invoice and daily, weekly and monthly sales amount (quantity) per invoice. Store efficiencies are determined according to the evaluation of these data. If the obtained data are lower than expected, primarily rehabilitation process is fulfilled. If this rehabilitation process fails, store closure decision is taken.

To sum up, nowadays clothing enterprises establish and enlarge their own retail chains in order to survive and to be successful. In this context, they give great importance to new store openings and store performance measurements of existing stores. The inefficient stores are closed according to the results which are obtained from multi-criteria performance measurements. In recent rivalry conditions, store closure is seen as a necessary condition in order to eliminate failure.

REFERENCES

[1] Zervopoulos P.D., Brisimi T.S., Emrouznejad A., Cheng G., 2016, Performance measurement with multiple interrelated variables and threshold target levels: evidence from retail firms in the US, European Journal of Operational Research, No.250, p:262-272

[2] Gunawan G., Ellis-Chadwick F., King M., 2008, An empirical study of the uptake of performance measurement by internet retailers, Internet Research, Vol. 18, No.4, p:361-381

[3] Abdolvand N., Albadvi A., Aghdasi M., 2015, Performance management using a value-based customer-centered model, International Journal of Production Research, Vol.53, No.18, p:5472-5483

[4] Fu H.P., Chang T. H., Shieh L.F., Lin A., Lin S.W., 2015, Applying DEA-BPN to enhance the explanatory power of performance measurement, Systems Research and Behavioral Science, Vol.32, p:707-720

[5] Chu H.L., Liu S.Z., 2008, The impact of manager promotion programs on store performance: evidence from 3C chain stores in Taiwan, The Service Industries Journal, Vol.28, No.9, p:1215-1224

[6] Kumar V., Karande K., 2000, The effect of retail store environment on retailer performance, Journal of Business Research, Vol.49, p:167-181

[7] Mishra A., Ansari J., 2013, A conceptual model for retail productivity, International Journal of Retail&Distribution Management, Vol.41, No.5, p:348-379

[8] Yumurtacı I.Ö., 2011, Retail Store Performance Assessment Through Supply Chain Perspective, İzmir University of Economics, Graduate School of Social Sciences, Department of Business Administration, PhD Thesis, 271 p.

[9] Xavier J.M., Moutinho V.M., Moreira A.C., 2015, Efficiency and convergence analysis in a women's clothing retail store chain: evidence from Portugal, International Journal of Retail&Distribution Management, Vol.43, No.9, p:796-814

[10] Tarcan Aksakal A., 2015, Time is shortened – Closures are increased, Capital, Vol.23, No.9, p:114-120 (in Turkish)

Predictive Modelling of Surface Roughness in the Electro-Discharge Machining of Die Steels

Ali Unuvar[1], Murat Kiyak[2], Orhan Cakir[3]

Abstract

Electric discharge machining (EDM) is the one of the important non-traditional machining processes and it is widely as a standard machining process in manufacture of forming tools to produce moulds and dies. The method is based on removing material from a work piece by means of a series of repeated electrical discharges, produced by electric pulse generators at short intervals, between an electrode and a part being machined in dielectric fluid medium. In this work, it is considered to examine the effects of machining parameters on shaped mold surface roughness. Selected machining parameters are pulsed current, pulse time and pulse pause time. Mathematical models have been developed for surface roughness prediction using Response Surface Methodology.

Keywords: *EDM, RSM, Pulse time, Pulse current, Pulse pause time, Surface roughness*

1. INTRODUCTION

Electrical Discharge Machining (EDM) is commonly employed in manufacturing of die cavities. Especially it is a preferred method in machining high alloy or high strength metals. The electrically conductive tool electrode is prepared to machine the die cavity. In EDM, a power supply delivers high frequency electric pulses to the tool and the workpiece. The gap between the tool and workpiece is flushed with a stream of dielectric liquid. When an electric pulse is delivered from the power supply, the insulating property of the dielectric liquid is momentarily broken down. This allows a small spark to jump the shortest distance between the electrode and workpiece. In this method, materials break out from workpiece surface and create small craters on the workpiece surface and remove from medium by dielectric liquid [1]. Crater sizes directly relate with pulse time, pause time and energy of a pulse. Ramarao et al. [2], stated that surface roughness depend on two important parameters as pulse time and pause time and also they created surface topology depending on two parameters by assisting regression analysis. Wang et al. [3], made experiments thereby using different currents and discharge durations and determined removal rate, electrode wear rate and surface roughness values. They experimentally determined the change of surface roughness with the applied current and the pulse duration and found out its relations as semi- empirical expression. Lee et al. [4, 6] researched effects on machining performance of machining parameters in machining tungsten carbide workpieces. They stated that surface roughness increases as discharge current, discharge voltage and pulse duration increase, however they declared that their optimum values can be obtained for a defined dielectric liquid pressure and pause time. Halkaci et al. [5], investigated that effects on surface roughness of different machining parameters as power, pulse time and pause time using copper electrode and pure carbon steel. They identified a power function from obtained data and compared with an empirical formula. Guu et al. [7] investigated in machining of AISI D2 tool steel by EDM and defined resolidified layer of material using SEM microscope and also measured the surface roughness of the workpiece. They determined that resolidified layer thickness and surface roughness values depend on discharge current from experiment results. Cogun et al. [8] experimentally and theoretically investigated surface profiles of workpieces machined under varying machining parameters in electric discharge machining. They also investigated effects of machining parameters, namely, discharge current, pulse duration and dielectric flushing pressure on surface roughness. It is found that surface roughness increases with increasing discharge current, pulse duration and dielectric flushing pressure. Keskin et al. [9] researched effects of machining parameters on workpiece surface roughness in electric discharge machining. They explained effects of current, pause time and pulse time on workpiece surface roughness by using a previously defined empirical equation. Ozgedik et al. [10] investigated effects of various machining parameters on electrode wear characteristics, material removal rate and workpiece surface roughness in electric discharge machining and found out that dielectric liquid pressure creates the most effect on electrode wear.

Surface roughness of the dies and moulds is one of the most performance measures in electric discharge machining. Moreover surface finish of the components has greater influence on the quality of the product. Surface finish in EDM has been found to be influenced in varying amounts by a number of factors such as pulse time, discharge current, discharge voltage and pause time. Since surface roughness has been important factor to predict machining performances of any machining operation,

[1] *Corresponding author: Department of Mechanicl Engineering, Selcuk University, 42075 Konya, Turkey.* aunuvar@selcuk.edu.tr
[2] *Department of Mechanical Engineering, Yildiz Technical University, 34349 Istanbul, Turkey*

surface roughness prediction model is necessary. The number of surface roughness prediction model available in literature is very limited. Taraman [11] used Response Surface Methodology (RSM) for predicting surface roughness in turning. Hasegawa et al. [12] conducted 34 factorial design to conduct experiments for the surface roughness prediction model.

2. METHODOLOGY

RMS is a collection of mathematical and statistical techniques that are useful for the modeling and analysis of problems in which a response of interest is influenced by several variables and the objective is to optimize this response [13, 14].

In this work, experimental results were used for modeling using RSM. RSM is practical, economical and relatively easy for use and it was used by lot of researchers for modeling machining processes. It was also used for application in tool life testing, surface analysis, and friction damping characteristics. The experimental data was utilized to build mathematical model (first and second model) by regression method.

2.1 RSM mathematical formulation

The data collected from the experiments was used to build a mathematical surface model using RSM. The RSM is a collection of mathematical and statistical techniques that are useful for modeling and analyzing problems in which response of interest is influenced by several variables and the objective is to obtain the response.

The following linear relationship could be considered for achieving this.

$$Y = f(ia,ta)+\varepsilon \quad (1)$$

Where ia,ta are pulsed current, pulse time respectively of the machining processes, and ε is error which is normally distributed with mean observed response Y.

$$\text{Let } f(ia,ta) = \eta \quad (2)$$

The surface represented by 'η'is called response surface. The relationship between surface roughness and other independent variables is modeled as follows

$$Ra = C\, ia^{\alpha 1}\, ta^{\alpha 2} \quad (3)$$

Where 'C' is a constant and α1, α2, are parameters. The above function can be represented in linear mathematical form as follows

$$LnRa = lnC + \alpha 1 \ln ia + \alpha 2 \ln ta \quad (4)$$

The first-order linear model of the above equation can be represented as follows:

$$Y1' = y - \varepsilon = b0x0 + b1x1 + b2x2 \quad (5)$$

Where Y1′ is the estimated response based on first-order equation and y is the measured surface roughness on a logarithmic scale. x1, x2 are logarithmic transformations of pulsed current and pulse time respectively,' ε' is the experimental error and b values are estimates of corresponding parameters.

The second-order model is as follows

$$Y2' = y - \varepsilon = b0x0 + b1x1 + b2x2 + b12\, x1x2 + b11x1^2 + b22x2^2 \quad (6)$$

Where the parameters i.e. b0, b1, b2 etc are to be estimated. Y2′is the estimated response based on second-order equation.

3. EXPERIMENTAL DETAILS

A detailed survey has been carried out to find out how machining parameters affect surface roughness. Based on this, the two parameters, namely pulsed current and pulse time were selected for experimentation [11]. A simple three level (32) factorial design of experiments was adopted for experimentation. A Taylor Hobson Surtonic 3+ instrument was used to measure surface roughness (Ra) of the machined components. A AJAN EDM982 model machine was used for experimentation. The work-piece material used for experimentation was 40CrMnNiMo864 die steel. Dimension of work- piece used is 20x70x315 mm. The properties of work-piece material are given in Table 2.The electrode used for experimentation were a copper rod with diameter of 22 mm, and its working surface was machined precisely by turning. The Picture of work piece and electrode is shown in Fig.1. Two times x nine (32) experiments for two and three seconds waiting time were conducted by varying all the parameters identified, to study the influence of these parameters on surface roughness. Every machined surface was taken to measure surface roughness. The surface roughness was measured with the instrument at 0.8 mm cut-off value.

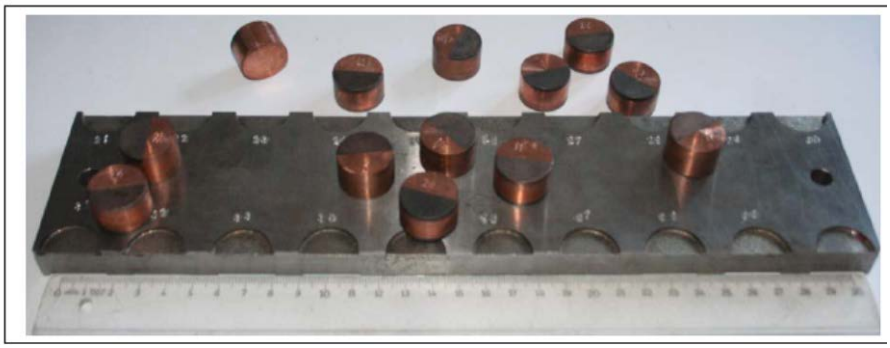

Figure 1. Workpieces and electrodes used in experiments

In this work, it was taken as machining parameters of pause time, pulsed current, and pulse time, other parameters were constantly taken. At the experiments, pulsed currents as 8, 16 and 24 A., pulse time as 2, 3, 4, 6, 12, 24, 48, and 100 µs, pause time as 2 and 3 µs were taken. The depth of machining were allowed as 5 mm. Pulse time shows the voltage generation time. Pause time shows voltage reduction time. The gap between electrode and machining surface of work-piece are provided by servo-control mechanism, and protected a distance of 0.02 mm as continuously. Electrodes should be at the perpendicular position to work-piece during the experimental studies. Therefore the tool holder which was attached to electrode was adjusted by controlling its perpendicular in respect to the machine using comparator.

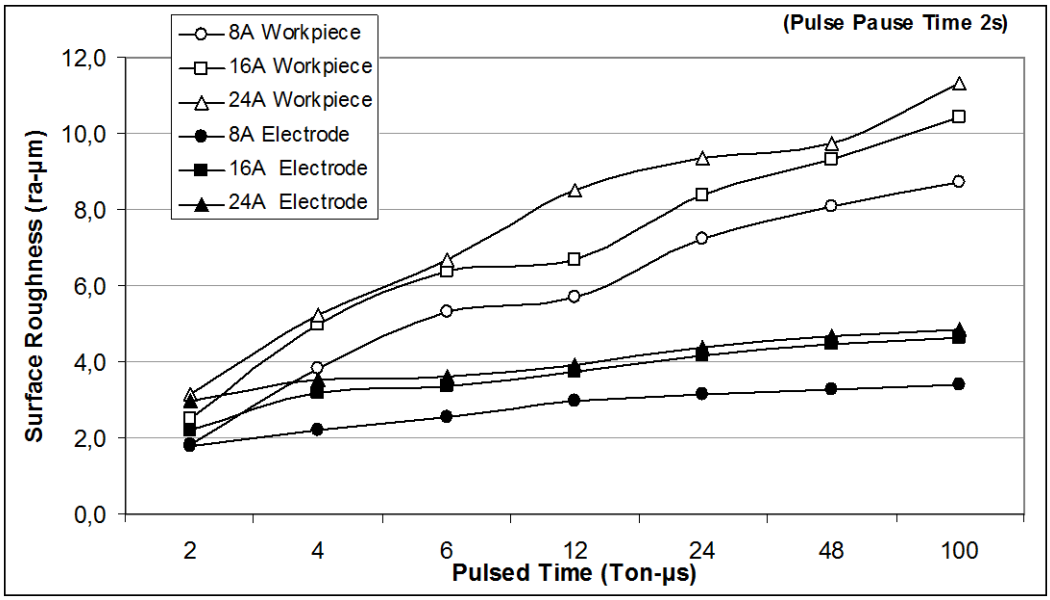

Figure 2. Workpiece surface roughness changing with respect to pulse time at different current values

(for pause time of 2 µs)

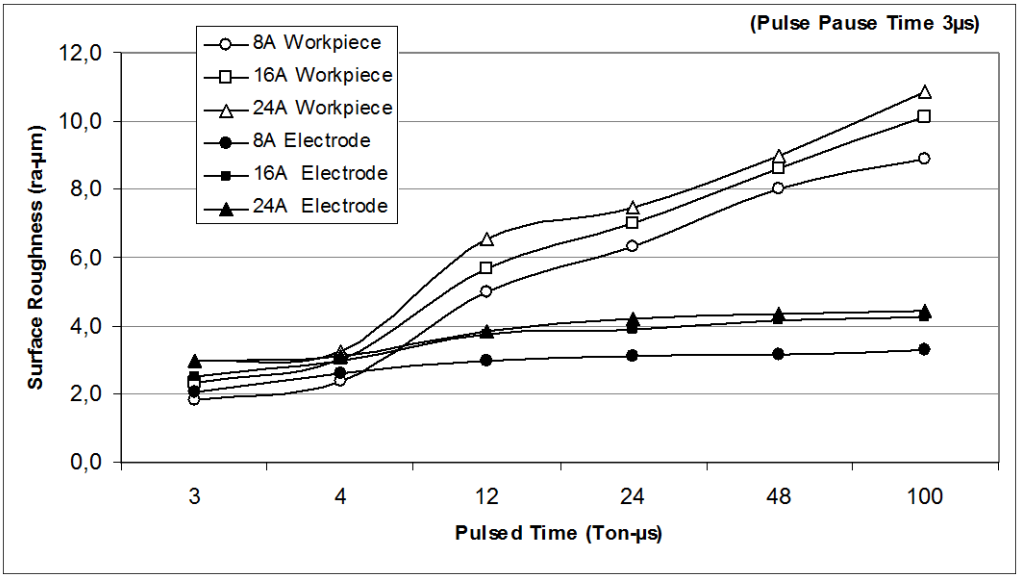

Figure 3. Workpiece surface roughness changing with respect to pulse time at different current values (for pause time of 3 µs)

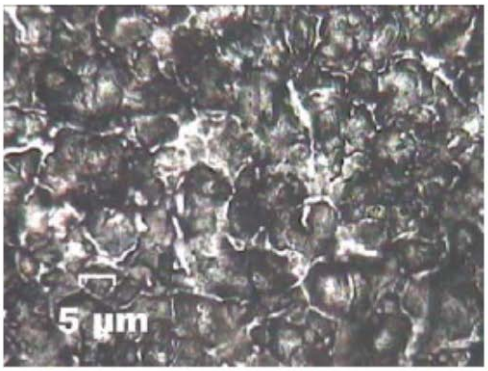

Current 8A, Pulse time 2 µs; pause time 2 µs

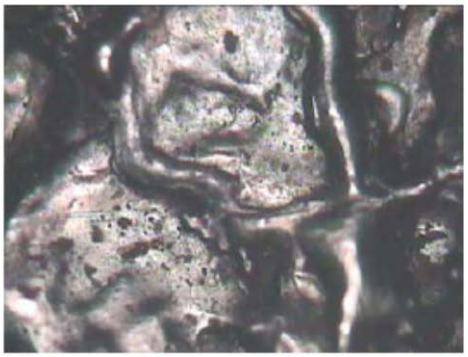

Current 24A, Pulse time 100 µs; pause time 2 µs

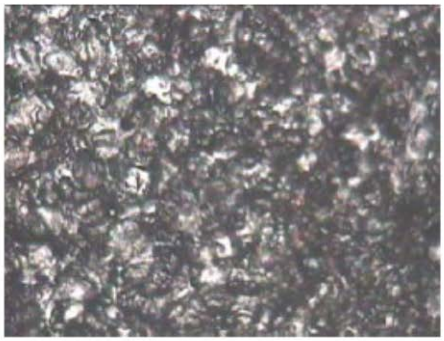

Current 8A, Pulse time 2 µs; pause time 2 µs

Current 24A, Pulse time 100 µs; pause time 2 µs

Figure 4. Work piece surface photographs

4. EXPERIMENTAL DESIGN

Modeling provides reliable equations obtained from the data of properly designed experiments. Therefore it is essential to have a well-designed set of experiments. The range of values of each factor was set at 3 different levels, namely low, medium, and high as shown in Table 1 and Table 2, selected on the basis of present day manufacturing requirements. A full factorial design was employed so that all the interactions between the independent variables could be investigated. Based on this, a total number of 10 experiments for pause of 2 µs and 10 experiments for pause of 3 µs, each having a combination of different levels of factors was carried out. These experiments are employed to establish first and second-order model. The variables were coded by taking into account the capacity and limiting cutting conditions of the machine.

Table 4. Process variables and their levels for pause time 2 µs

Parameter	Symbol, Unit	Level-I(low)	Level-II (Medium)	Level-III(High)
Pulsed current	i_a, A	8	16	24
Pulse time	t_a, µs	6	24	100

Table 2. Process variables and their levels for pause time 3µs

Parameter	Symbol, Unit	Level-I(low)	Level-II (Medium)	Level-III(High)
Pulsed current	i_a, A	8	16	24
Pulse time	t_a, µs	4	20	100

The coded values are calculated by using the following transformation equation.

$$x = \frac{\ln p \; - \ln p_{high}}{\ln p_{high} - \ln p_{low}} + 1 \qquad (7)$$

where x is the coded value of any factor corresponding to its natural value, is the natural value of the factor at any level, is the natural value of the factor at medium level, and the natural value of the factor corresponding to the low level.

5. RESULTS AND DISCUSSION

Influence of pulse time, pause time and pulsed current has been assessed by conducting experiments. Firstly, profiles of machined surface have been investigated with varying several parameters in electric discharge machining. The variation surface roughness with respect to process variables selected in this study is shown in the Figure 2 and Figure 3. Pause time has been taken 2 µs in the Figure 2 and 3 µs in the Figure 3. Some of micro photographs of the workpiece surface obtained in this study have been given in the Figure 4. It was found from Figure 2 and 3 that the workpiece surface roughness increases with increase in pulsed current and pulse time. Discharge energy increases with increase in current, so more material from workpiece removes, and the greater large craters create on the surface of workpiece. More than ones cause increase in the surface roughness values.

In the second section of the experiment study, the change of electrode surface roughness created by wear of front face with machining parameters has been investigated. Pause time has been constantly taken 2 µs the experimental studies shown in the Figure 2 and 3 µs the experimental studies shown in the Figure 3.

5.1 Roughness Model

The surface finish of any manufacturing process has become critical because of increased quality demands. There are various factors which govern the surface finish in EDM process and hence, development model help to understand the machining process better. In the present work the mathematical models (first-order and second-order) were developed on the basis of experimental results of EDM machining and the validity of the models was tested using statistical techniques.

Analysis of variance (ANOVA) has been performed to find the effect of factors and their interaction on the responses. Though the experiments are conducted using full factorial design, replications of experiments with each combination could not be carried out as it involves laborious experimentation.

Accordingly it has been assumed that the two factor interaction is not present and the corresponding sums of squares and degrees of freedom have been taken as residual/error to conduct the ANOVA.

5.2 Development of First-Order Model

Using the machining experimental results, empirical equations have been obtained to estimate surface roughness with the significant parameters i.e., pulsed current and pulse time. The first-order model obtained from the above functional relationship using RSM method for pause time of 2 μs is as follows:

$$Y1' = 2.0725 + 0.12725x1 + 0.254x2 \quad (8)$$

The transformed equation of surface roughness prediction is as follows:

$$Ra = 2.49\ ia^{0.22154}\ ta^{0.18} \quad (9)$$

Equation (9) is derived from equation (8) by substituting the coded values of x1 and x2 in term of ln ia and ln ta. Analysis of the variance (ANOVA) and F-ratio test have been performed to justify the goodness of fit for the mathematical model

Confidential ranges for 95% confidential and 5% sensitivity of the first order model found as follows: The variance of the mathematical model

S2= (Y´- y)2/3= 0.01166/3=0.0038867

Confidential range for vertex points

Y´±t3,0.025 .0.0509= Y' +- 0.11976

Confidential range for central point

Y´± 0.0598

Table 3. Analysis of variance for first order model for pause time of 2 μs

	Sum of squares	Degree of freedom	Mean squares	F-ratio
Regression	26.0893000	3	8.6964000	
Due to zero order model	25.7719520	1	25.7719520	
Due to first order model	0.3173573	2	0.1586786	
b_1	0.0592670	1	0.0592670	
b_2	0.2580890	1	0.2580890	
Residual	0.01166	3	0.003866667	
Lack of fitness	0.01159	2	0.005795	83.66
Error	0.000069267	1	0.000069267	
Sum Σy_i^2	26.09319597	6		

Since $F_{tabulated}$ (2,1)= 200>$F_{calculated}$ (2,1)=83.66 , then the lack of is not significant, the model is adequate

$R^2 = 0.9645$

Multiple regression coefficient of the first order model was found to be 0.9645. This result shows that the first-order model can explain the variation in surface roughness to the extent 96.45%. The first-order model has high predictability.

The first-order model obtained from the above functional relationship using RSM method for pause time of 3 μs is as follows:

$$Y1' = 1.727 + 0.02625x1 + 0.26325x2 \quad (10)$$

The transformed equation of surface roughness prediction is as follows:

$$Ra = 1.5273\ ia^{0.04777}\ ta^{0.3926} \quad (11)$$

Equation (11) is derived from equation (10) by substituting the coded values of x1 and x2 in term of ln ia and ln ta. Analysis of the variance (ANOVA) and F-ratio test have been performed yo justify the goodness of fit for the mathematical model.

Confidential ranges for %95 confidential and %5 sensitivity of the first order model found as follows:

The variance of the mathematical model

S2= (Y´- y)2/3= 0.01149585/3=0.00383195

Confidential range for vertex points

Y´± t3,0.025 .0.0509= Y' +- 0.37648

Confidential range for central point

Y' ± 0.188

Table 4. Variance analysis of first order model for pause time of 3 μs

	Sum of squares	Degree of freedom	Mean squares	F-ratio
Regression	19.5036	3	6.5012	
Because of zero order model	17.8969	1	17.8969	
Because of first order model	1.60677	2	0,803385	
b_1	0.02756	1	0.02756	
b_2	1.60402	1	1.60402	
Residual	0.1149585	3	0.003866667	
Lack of fitness	0.1144465	2	0.00572232	111.764
Error	0.000512	1	0.000512	
Sum Σy_i^2	26.09319597	6		

Since $F_{tabulated}$ (2,1)= 200>$F_{calculated}$ (2,1)=111.764 , the model is adequate

R^2 = 0.935

Multiple regression coefficient of the first order model was found to be 0.935. This shows that the first-order model can explain the variation in surface roughness to the extent 93.5 %. The first-order model has high predictability.

5.3 Development of Second-Order Model

The second-order model was developed utilizing the full factorial design and the model parameters of the equation were estimated using the method of least squares. The second-order surface roughness model thus developed for pause time of 2 μs is given as follows:

$Y2' = 2.153 + 0.12455x1 + 0.245766x2 + 0,00745\ x1x2 - 0.06265x1^2 - 0.04063x2^2$

Table 5. Variance analysis of second order model for pause time of 2 μs

Source	Sum of Squares	Degree of Freedom	Mean Squares	Calculated F-Ratio
Regression	44.20059	6	0.227741379	3163
Due to zero order	43.73159264	1		
Due to first order	0.455482758	2	0.00022201	
Due to second order	0.013514602	3	0.016416	
Interaction effect	0.00022201	1		3.08347
Quadratic effect	0.03283292	2		228
Residual	0.004037946	4	0.001	
Due to lack of fit	0.003965946	3	0.001321982	18.36
Due to Pure Error	0.000072	1	0.000072	
Total	44.204629	10		

where Y_2' is the estimated response of surface roughness, $x_1$and x_2; are the coded values of pulsed current, and pulse time.

F-Ratio can be calculated as follows:

F-ratio of the model =$F_{calculated}$ =18.36 < $F_{tabulated}$ (3,1, 5%)= 216

Since 18.36< 216, then the lack of fit is not significant, the postulated model is adequate.

F-ratio of the interaction terms =$F_{calculated}$ =3.083 < $F_{tabulated}$ (1,1, 5%)= 161

Since 3.083<161, second order interactive terms are not significant

F-ratio of the quadratic terms =$F_{calculated}$ =195 < $F_{tabulated}$ (2,1, 5%)= 200

Since 195<200 , second order quadratic terms are not significant

F-ratio of the first order terms =$F_{calculated}$ =363 > $F_{tabulated}$ (1,1, 5%)=161

Since 363> 161 , first order terms are significant

Since the regression sum of squares can be expressed as $B'X'y$, the calculation of sum of squares of an individual first order term is as follows:

Sum of square of X_1 = 0.12455*0.7473=0.09307

Sum of square of X_2 = 0.245766*1.4746=0.3624

These values are the mean squares of each variable since they have all 1 degree of freedom.

F-ratio of X_1 = 0.09307/0.000072= 1292

$F_{tabulate}$ (1,4,5%)=7.71

$F_{calculate}$ > $F_{tabulate}$, the variable X_1 is significant.

F-ratio of X_1 = 0.3624/0.000072= 5033

$F_{tabulate}$ (1,4,5%)= 7.71

$F_{calculate}$ > $F_{tabulate}$, the variable X_2 is also significant.

Table 6. Significance testing of individual variables

Source	Sum of Squares	Degree of freedom	Mean Squares	Calculated F-ratio
X_1	0.09307	1	0.09307	1292
X_2	0.3624	1	0.3624	5033

The second-order surface roughness model thus developed for pause time of 3 μs is given as follows:

$Y2' = 2.1943 + 0.11885x1 + 0.6228x2 - 0,02625\ x1x2 - 0.02563x1^2 - 0.2x2^2$

where Y2′ is the estimated response of surface roughness, x1and x2; are the coded values of pulsed current, and pulse time. Similarly, confidential of the second order model and significance test were obtained and it was found that x1, x2 is significant.

On the basis of multiple regression coefficients (R2), it can be concluded that the second-order model was adequate to represent this process. Hence the second-order model was selected as the objective function for optimization using GA (Generic Algorithms). Using the second order model, the surface roughness of the components produced by EDM can be estimated with reasonable accuracy. Hence, this model would be used in optimization using GA.

6. CONCLUSIONS

A useful technique for surface roughness modeling is provided by Response Surface Methodology in this study. By using a statistically selected set of combinations for two variables, a first order and a second polynomial function is established for surface roughness modeling of EDM. Adequacy of model is tested in the variance analysis by calculating the F-ratio of lack of fit to pure error.

The established equations clearly show that pulse time was main factor on the surface roughness. It increased with increasing the pulse time and pulsed current.

The variance analysis for the second-order model that the interaction terms and the square terms are insignificant. Moreover, it is seen that the first order effect of pulse time and pulsed current is significant.

The predicted values and measured values are fairly close which indicates that the developed surface roughness prediction model can be effectively used to predict the surface roughness from the EDM process, with 95 % confident intervals for both case.

Obtaining a surface roughness model by RSM has resulted in a fairly useful method of obtaining process parameters in order to attain the required surface quality.

Surface roughness decreases with increasing pause time in the developed first and second order models.

Fig 5 shows surface roughness values taken from both on the electrode surface and machined workpiece surface when 2μs pulse pause time applied during EDM operation as well as RSM approach results. In the present work the mathematical models (first-order and second-order) were developed on the basis of experimental results of EDM machining and the validity

of the models was tested using statistical techniques. Under the selected experimental conditions, the prediction is 93.5%. For similar experimental study, surface roughness can be calculated using Equation 8.

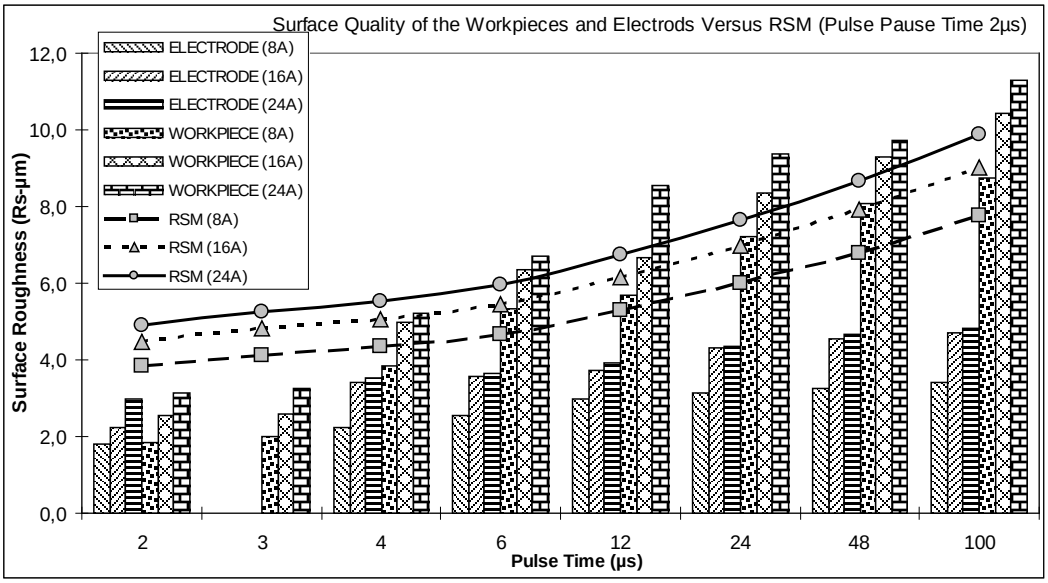

Figure 5. Surface roughness changes on electrode and machined workpiece surfaces with RSM approach for 2µs pulse pause time

Fig 6 gives surface roughness results for electrode and workpiece surfaces in case of 3µs pulse pause time EDM operation. Again the figure provides RSM values. The prediction level is 96.45% and this result is better than 2µs pulse pause time EDM operation. Equation 10 can be used for similar experimental studies providing possible surface roughness.

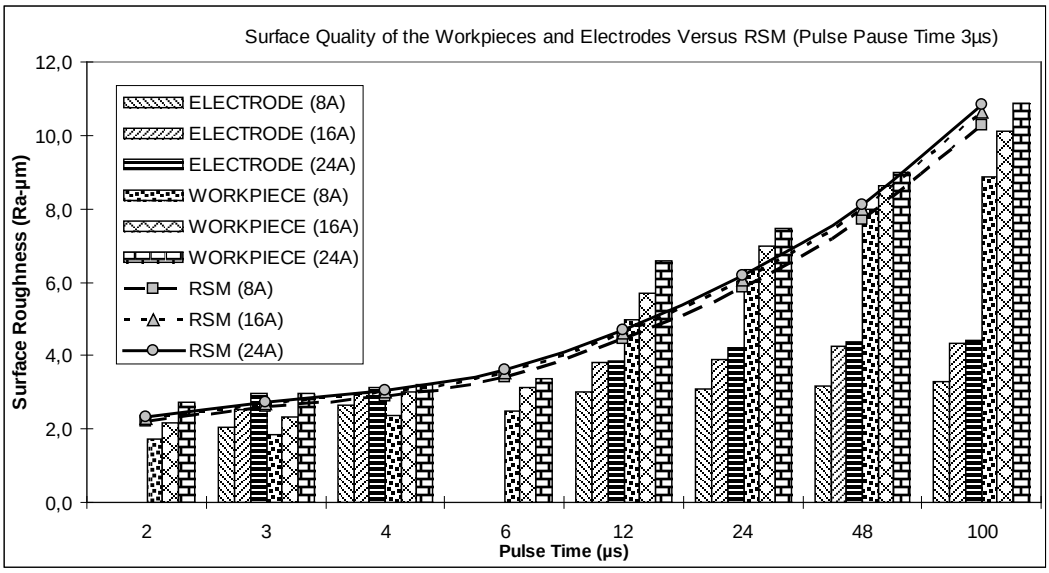

Figure 6. Surface roughness changes on electrode and machined workpiece surfaces with RSM approach for 3µs pulse pause time

REFERENCES

[1]. K.H. Ho, S.T. Newman, State of electrical discharge machining(EDM), International Journal of Machine Tools and Manufacturing, 43(13), (2003) 1287-1300

[2]. P.V. Ramarao, M.A. Faruqi, Characteristics of the surface obtained in electro-discharge machining, Precision Engineering, 4(2), 1982, 11-113

[3]. Cung W.C., Hwa Y.B., Ming C.H., Yasua S., Cutting austempered ductile iron using an EDM sinker, Journal of Material Processing Technology, 88(1), (1999), 83-89

[4]. S.H. Lee, X.P. Li, Study of the effect of machining parameters on the machining characteristics in electrical discharge machining of tungsten carbide, Journal of Material Processing Technology, 115(3), (2000), 344-358

[5]. H.S. Halkaci, A. Erden, Experimental investigation of surface roughness in electrical discharge machining, Proceeding of ESDA2000: 6th Biennial Conference on Engineering System Design and Analysis, 2000
[6]. L.S. Hiong and L. Xiaoping, Study of the surface integrity of the machined workpiece in the EDM of tungsten carbide, Journal of Material Processing Technology, 139(1-3), (2003), 315-321
[7]. Y.H. Guu, H. Hocheng, C.Y. Chou, C.S. Deng, Effect of electrical discharge machining on surface characteristics and machining damage of AISI D2 tool steel, Material Science and Engineering A., 358(1-2), (2003), 97-106
[8]. C. Çogun, B. Kocabaş, A. Özgedik, Elektro erozyon ile işlemede iş parçası yüzey pürüzlülük profilinin deneysel ve teorik incelenmesi, Journal of the Faculty of Engineering and Architecture of Gazi University. 19(1), (2004), 97-106
[9]. Y. Keskin, H.S. Halkaci, M. Kızıl, An experimental study for determination of the effects of machining parameters on surface roughness in electrical discharge machining, The International Journal of Advanced Manufacturing Technology, 29, (2006), 1119-1121
[10]. A. Özgedik, C. Çogun, An experimental investigation of tool wear in electrical discharge machining, The International Journal of Advanced Manufacturing Technology, 27(5-6), (2006), 488-500
[12]. K. Taraman, Multi-machining output-multi independent variable turning research by response surface methodology, International Journal of Production Research, 12, (1974), 233-245
[13]. M. Hasegawa, A. Seireg, R.A. Linberg, Surface roughness model for turning, Tribology International, December 1976, 285-289
[14]. D.C. Montgomery, Design and analysis of experiments, 4th ed., Wiley, New York, 1997
[15]. A. Mital, M. Mehta, Surface roughness prediction models for fine turning, International Journal of Production Research 16, (1988), 1861-1876

An Expert System Application in the Education

Hasan Kuzu[1], Ersin Ozdemir[2]

Abstract

Today, traditional methods are insufficient to meet the increasing need for knowledge and learning. Lived in Ephesus (535-475 BC) the philosopher Heraclitus said, "The only thing constant is change". Various methods and techniques are improved, the use of intelligent teaching systems in education, with progress in knowledge technology. Each student's level of competence and learning is different. Intelligent tutoring systems, student-focused and allows students to be assessed individually.

In this study; new smart learning model has been introduced. One of the methods of artificial intelligence, expert systems have been used with method of backward reasoning. Each student is evaluated on an individual basis. According to the result, video sequence is determined by the expert system using a database has been created that is contains lessons and videos and assessment exams.. In this system, there are two main modules which are teachers and students modüle. By using this method, a special education can be given to the students from different places as per their understanding levels. While the time allocated for each student increases, costs for education and training decrease. In this system, the teacher is moved to a course manager position directing the class according to the knowledge needs of the students rather than being a course repeater.

Keywords: *Education, Expert system, Artifical intelligence, rules-based systems*

1. INTRODUCTION

Education is our future. Each individual's life needs education that one of the most important element for the civilization. Nowadays the learning process is not only specific to school age. It has turned into a lifelong learning process.[1].

Today, classical education methods is inadequate to meet countries and the growing educational needs of society. This situation has led seeking to enter the different educational methods out of educators of traditional training methods. Rapid developments in technology and science has put into alternative solutions for countries in meeting the needs of education [2] [3]. The opportunities provided by the technology must be used in the most efficient manner in educational activities [4].

Student-centered education in the 21st century, time and place independent, the results are considered to be focused [5]. To provide this training come to mind first is undoubtedly the computer and the Internet. Initially, the use of technology in education "educational tools" were composed. This notion has undergone many changes over time. Education in many disciplines hosting people, communication, technology, software and artificial intelligence has become a new concept. These changes have opened a new era in the field of education, has led to the emergence of new methods and techniques [6].

1.2 The importance of the study

In parallel with the world population, the need for education is increasing. Educators are aiming to apply the same teaching methods for many students with different levels of knowledge, the interest and ability. This method remains incomplete in terms of individual pupils. individual personal weaknesses and strengths of the students can not be assessed. As a solution to this situation students can work interactively with computers, demonstrated several methods [3]. The role of teaching, training was carried out by computer models began to gain importance. Individual learning situation of students have been evaluated by the developed teaching software. Higher achievements in education has attempted to obtain, taking into account individual learning difficulties with this software [7]. Thus in education Computer Aided Education (CAE) has emerged the concept.

1.2.1. Computer Aided Education (CAE)

Computer Aided Education is defined as the content and activities of Education to transfer students using computer technology[8]. Computer technology is used for education and training purposes for teachers or students the independent spaces (home or school) and independent of time (synchronous or asynchronous) [9]. Today, CAE are used in almost all educational field and has become an indispensable element of education. The importance of the issue, is reflected in the state of education policy. It is known to increase the level of success in education in equipped grades with computer and multimedia facilities in japan. The application of CAE in classrooms with prepared software 42% success rate in math class has risen to 99% in Israel [10].Currently in our country, there is a project called "Fatih Project" is a CAE project of Ministry

[1] *İskenderun Technical University, Dörtyol Vocational School, 31600,Dörtyol/Hatay, Turkey.* hasan.kuzu@iste.edu.tr

[2]*Corresponding author: İskenderun Technical University, Faculty of Electronics , 31200,İskenderun/Hatay, Turkey.* ersin.ozdemir@iste.edu.tr

of Education of Turkey. To use CAE draws attention to the stages such as equipment selection, design class, such as the preparation of teacher training and course software [11]. Researchers have made many scientific studies on the use of technology in education. In general, these studies have been conducted under the following headings; Interactive training CD, audio-visual technology use in education, computer assisted instruction, distance learning, e-learning, online learning translation, integrated learning, constructivist learning, situated learning, collaborative learning, teaching allies [6]. Coming together of different disciplines, computer-assisted training systems are undergoing changes. The new generation of computer-assisted teaching systems, in holding various decision-makers, students followed, according to the student's understanding of the situation, are intelligent teaching system that can set the course level. [12], [13]. Şimşek, A. et al, have found that not much research done on individual differences and learning strategies [6].

1.2.2. Intelligent Tutoring Systems

Intelligent teaching system is a computer system that decides who, what and how to teach by utilizing artificial intelligence techniques. The quality of teaching intelligent learning system which has been found to accelerate the learning time and increases of 43% [14].

Intelligent tutoring system model was introduced in 1973 by Hartley and Sleeman. Intelligent tutoring system model consists of four components, expert knowledge module, student module, teaching modules and a user interface.

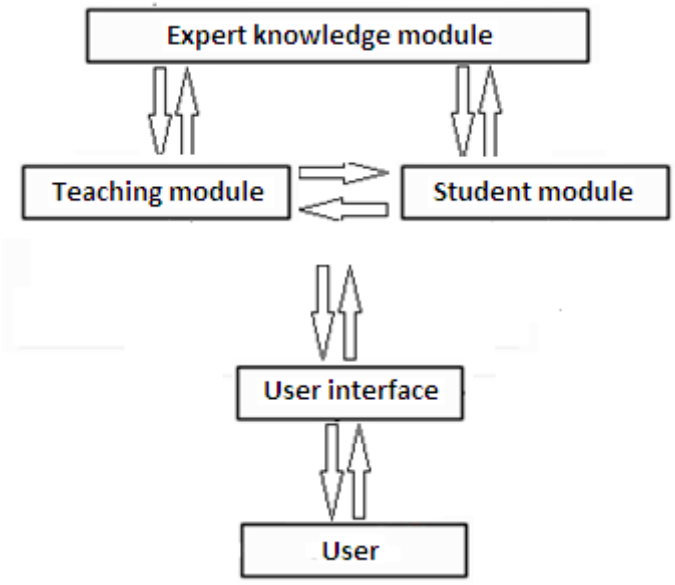

Figure 1. Components of the Intelligent Tutoring Systems

The system assists the best presentation of training materials for the students[12].

1.2.3. Artificial Intelligence

The term artificial intelligence was proposed by John McCarthy at first. Artificial intelligence is intellectual and behavioral artificial system that specific to human intelligence covering topics such as perception, learning, thinking, decision making, reasoning, problem solving. In short, human behavior is considered to be intelligence, is intended to be done by machine. [15].

History of Artificial Intelligence concept has emerged in parallel to computer science. Alan Mathison Turing asked, "Can machines think?" and Machine Intelligence unveiled in the debate [17]. Artificial Intelligence techniques used under the following headings

Expert systems: expert knowledge is transferred to the computer program.

Neural networks: improved inspired by neurons in the human brain.

Genetic algorithms: it aims to produce an optimal solution.

Fuzzy logic: It aims to result from uncertainty.

1.2.4. Expert Systems

Expert system is a system that uses human knowledge to solve problems that require expertise, stored on the computer. ES can solve many problems can be considered in the difficult level in different areas. In a specific area of expertise, using information gathered from the people and are able to develop software in time [15].

While artificial intelligence software aims to solve the problem can not be resolved by a human. Expert system software aims to solve problems like a person expert who has knowledge on the subject. Well developed an ES software do operations such as design, planning, diagnostics, interpret, summarize, generalize, checking and making recommendations [23].

Expert systems have widespread applications such as manufacturing, education, medicine, chemistry, agriculture, industry, design and planning.

The units constituting the structure of the expert system are;

• Knowledge base: a database that stores data containing special experience.

• Inference mechanism: Performs comparison between rules and functions.

• Description unit: explains how to do the comparison.

• User Interface: enables communication between the user and the system [25] (Figure 2.)

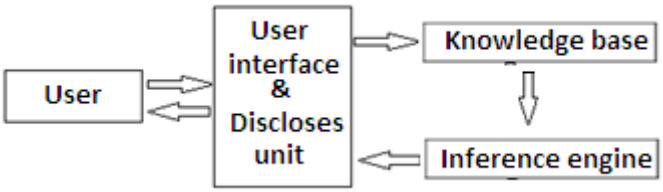

Figure 2. The general structure of an expert system

The methods used for expert systems;

• Forward chaining (Forward chaining)

• Backward chaining (backward chaining)

• Inductive

• hypothetic reasoning

• Dynamic rule change, as can be listed [24].
Within the methods listed above, forward and backward chaining techniques are used in general [26].]

1.2.5. Rule-based systems

Rules-based contains a set of rules and conditions is created from a human expert's knowledge and experience. Forward chaining or backward chaining approach is used to manipulate the rules in the knowledge base and get a result.

Forward chaining method

The system starts from the first rule. The rules are applied, respectively to information received from the user for searching the results.

Backward chaining method

The system goes to the cause from the outcome. Defined rules are applied until the result can be found. [29],[30].

In this study; a smart new teaching model was introduced using the Backward Chaining technique in ES. The presented model is aiming to reach each student with different levels of learning and competence.

2. MATERIALS AND METHODS

2.1 System Architecture

The system is consists of a teacher room, a computer for the teacher, a computer lab, student computers, local network and internet connection, a projection device, at least two IP cameras for teacher and students for video calls and developed expert system software.(Figure 3)

In the developed expert system software has two modules for teacher and students. A database has been created in the system. This database includes students, lessons, subjects of the course, the videos and assessment tests that measured the level of student understanding. Each student's learning process individually evaluated than the order of lecture videos is determined by the system.

Teacher is connected to the system with the interface teacher module. Students, lessons and topics of each lesson ar described by teachers. The system is loaded the related videos and assessment exams for each subject. Teachers can monitor the situation in the course of the students in the classroom through the IP camera. Students can also follow the teacher in the IP camera. Thus, teachers and students are in partially interaction.

Each student is connected to the system with the student module software. Students are identified for each course separately and can watch videos of lectures on the subject of these courses. An evaluation test in the system that the teacher has installed is performed for students at the end of each video lesson. The exam results are reported to the students at the same time are kept in the database system. Teachers can follow the results of the exam. It can be seen as a graph of the examination results. Exam results of students can be determined individually by the system.

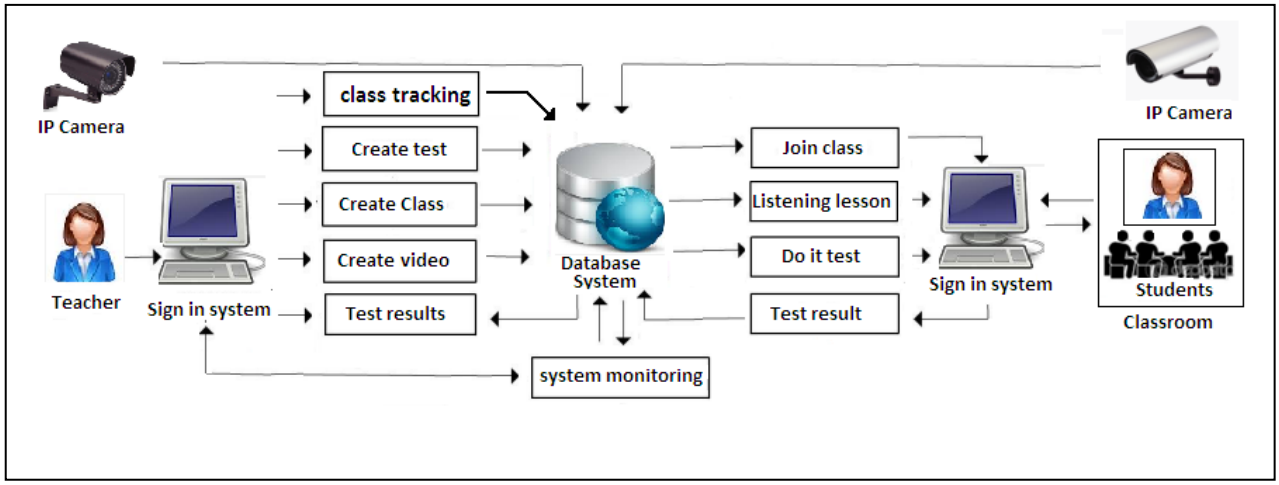

Figure 3. System architecture

2.2. Expert Ssystems Software

Developed expert system software is composed of teachers and students module. Each module makes process according to user roles.

The following operations can be carried out in the teacher module

2.2.1. In the Video menu;

It can be added a new tutorial videos for any course.

2.2.2. Exam Menu Inside;

- can be created a exam for the course
- students can be defined for the exam
- the duration for the exam, number of questions, answer key can be created
- examinations can be evaluated
- students can see the results of the exam.

2.2.3. Inside the Course Menu;

- Student enrollment is done.
- Video can be watched separately
- According to the results of the examinations are determined to continue the new course for each student's videos.

2.2.4. Statistics Menu Inside;

- student achievement statistics can be seen by the graph.
- statistics of the average achievement can be seen with graphics

2.2.5. Inside the Student Menu;

- new student registration can be done.
- students can be listed using automation.
- the students entered the exam and not can be listed.

2.2.6. Exit menu;

- are used to close the program.
- The following operations can be performed in the student module.

2.2.7. The Menu in My Info;

- Students can see credentials and change the login password.

2.2.8. in The Course Menu;

- student can see responsible for that course and videos of lessons

2.2.9. The Menu in The Exam;

- Active exams can be seen, the test can be started and the test scores can seen.

2.2.10. Exit menu;

- It is used to close the program

3. DISCUSSION

Using this method, students can be found in different places to be given special training according to the student's personal level. In this system, the time devoted to each student is increased and education costs are reduced.

The teacher is not the person making the course again that task has been changed. He/She is a course manager, giving direction to the course, according to the information needs of students,

$$\text{The average achievement of students in the subjects} = \frac{\sum_{k=1}^{n} Subject_k}{n} \quad \textbf{(1)}$$

$$\text{The average achievement of students} = \frac{\sum_{k=1}^{n} Student_k}{n} \quad \textbf{(2)}$$

Improved expert system is applied to a test group consisting of a total of 10 students. Lecture videos in 5 different topics were shown to students. Examination was conducted at the end of each topic. Personal success of each student and class success was measured. Examination results are evaluated over 100. (Table 1)

As can also be seen in the table 1, our expert system evaluate results for each topic and interpret them according to each student's course results separately. The grade point average is weak that support videos are chosen by the system.

Table 1. performance table of course of algorithms and programming 1

ALGORITHMS AND PROGRAMMING I	Subject1	Subject2	Subject3	Subject4	Subject5	The average achievement of students (2)
Student1	80	70	70	60	70	70
Student2	50	60	60	50	60	56
Student3	40	50	30	40	40	40
Student4	50	60	60	80	70	64
Student5	50	60	60	70	50	58
Student6	60	70	70	60	70	66
Student7	60	70	70	60	50	62
Student8	50	60	60	70	70	62
Student9	80	70	80	80	70	76
Student10	70	80	80	70	70	74
The average achievement of students in the subjects (1)	59	65	64	64	62	62,8

Expert systems, has found overall success of the students No. 3 is insufficient. For this student, if grade remains below 50 the topic about that support video was wachted and the student will be applied again evaluation exams. The student 3's achievement is improved as can be seen in the table 2 below.

The student's achievement has increased from 40% to 52%. According to the entire issue, has increased an average of 12 points on a student's success

Tablo 2. Success of Student_3

	Subject1	Subject2	Subject3	Subject4	Subject5	Avarege Topics
Student 3's	60	50	50	60	40	52

The exam results for each topic will be seen in our expert system which can evaluate tables and each student's results separately.

4. RESULTS

Each student will be evaluated on an individual basis and the order of the video course determined by the system. with expert system software that we developed it has been shown to increase student achievement.

Computers, is the indispensable tools of the information society. Computer technology has been the greatest impact in the field of education all over the world in the 21st century. According to surveys, intelligent teaching system that maintains the advantages to students more successful. Therefore, technological equipment in schools should be increased and should be strengthened with intelligent teaching system applications.

REFERENCES

[1]. A. Karataş, *Yaygın Eğitimde Bilgisayar Eğitimine devam eden kursiyerlerin eğitim sürecini değerlendirilmesi , yüksek lisans tezi*, Marmara Üniversitesi Fen Bilimleri Enstitüsü, İstanbul, Türkiye, 2013.
[2]. A.A. Carr, *DistingurshingSystemicFromSystematicTeach Trend forLeadership in Educationand Training*, London, England, 1996
[3]. C. Alkan, *Eğitim teknolojisi (5. baskı), Anı yayınları*, Ankara, Turkey, 1997.
[4]. Edmunds, R.,Thorpe, M., &Conole, G. *Student attitudestowardsand use of ICT in course study, work and social activity: A technology acceptance model approach. British Journal of EducationalTechnology, 43(1), 71–84. doi:10.1111/j.1467- 8535.2010.01142.x.* ,England , 2012
[5]. Aggarwal, *Web-Based Learning andTeaching Technologies: Opportunities and Challenges.*, Hershey-USA: Idea Group Publishing, 2000.
[6]. A. Şimşek, N. Özdamar, G. Becit,K. Kılıçer,Y. Akbulut, Y. Yıldırım, *Türkiye'deki eğitim teknolojisi araştırmalarında güncel eğilimler, Çanakkale Onsekiz Mart Üniversitesi Eğitim FakültesiI. Uluslararası Bilgisayar ve Öğretim TeknolojileriSempozyumu, Sayfa 440-450*, Çanakkale, Türkiye, 2007
[7]. F. Bahçeci, M. Gürol, *Eğitimde akıllı öğretim sistemleri uygulamalarına yönelik bir model önerisi,e-Journal of New World Sciences Academy Volume: 5, Number: 2, Sayfa 122-128*, Elazığ, Türkiye, 2010
[8]. TDK ,*www.tdk.gov.tr* , (Erişim tarihi:19/04/2016).
[9]. M. Yenitepe ,Z. Karadağ, *Application of Computer Aided Mathematics Teaching in a SecondarySchool,TOJET, Volume:2,Issue:1,Article 1*, İstanbul, Türkiye ,2003
[10]. İ. Ediz, *Bilgisayar Destekli Eğitimin İlköğretim Matematik Dersinde Kullanımının Tarihsel Gelişimi Yüksek lisans tezi, Abant İzzet Baysal Üniversitesi Sosyal Bilimler Enstitüsü* , Bolu, Türkiye, 2008.
[11].S. Uşun , *Bilgisayar Destekli Öğretimin Temelleri, Nobel Yayın Dağıtım* , Ankara, Türkiye, 2004
[12]. F. Bahçeci, *Kişiye Özgü Öğretim Portalının Öğrenenlerin Akademik Başarısı ve Tutumları Üzerindeki Etkisi, Fırat Üniversitesi Eğitim Bilimleri Enstitüsü*, Elazığ, Türkiye, 2011
[13]. Patricia A. Jaques , Henrique Seffrin , Geiseane Rubi, Felipe de Morais, Cassio Ghilardi , Ig Ibert Bittencourt, Seiji Isotani , *Rule-based expert systems to support step-by-step guidance in algebraic problem solving: The case of the tutor PAT2Math , Expert Systems with Applications 40 5456–5465, 2013*
[14]. F. Dağ, K. Erkan, *Prolog tabanlı zeki öğretim sistemi, Pamukkale Üniversitesi Mühendislik Bilimleri Dergisi, Sayı:10 Sayfa:47-55*, Denizli, Türkiye, 2004
[15] A. Taharov, *Bilgisayar Destekli Bilgi Sistemleri , Journal of QafqazUniversity, sayı:27, sayfa:123-133*, Azerbaycan, 2009
[16]. H. Pirim, *Yapay Zeka, Journal of Yasar University, sayı: 1(1), sayfa: 81-93*, İzmir, Türkiye, 2006
[17]. Wikipedia, *https://tr.wikipedia.org/wiki/Yapay_zek%C3%A2*, (Erişim tarihi:19/04/2016).
[18]. H. Schildt, *Advanced Turbo PROLOG*, McGrow-Hill, Berkeley, California , 1987
[19]. Ç. Elmas, Yapay Sinir *Ağları (Kuram, Mimari, Eğitim, Uygulama, Seçkin Yayıncılık*, Ankara, Türkiye, 2003
[20]. E. Öztemel, *Yapay sinir ağları kitabı, Papatya yayıncılık*, Türkiye, 2003
[21]. E. Turban, *Artificialintelligence*, California StateUniversity, 1992
[22]. G. Engin, B. Aksoyer, M. Avdagic, D. Bozanlı, U. Hanay, D. Maden, G. Ertek, *Rule-based expert systems for supporting university students, 2nd International Conference on Information Technology and Quantitative Management, ITQM 2014, Procedia Computer Science 31 (2014) 22 – 31*, 2014
[23]. VV. Nabiyev, *Yapay Zeka. Seçkin Yayınları*, Ankara, Tükiye, 2003

[24]. İ.C. Kırmanlı, *Açık işletmelerde optimum ekipman seçimi Doktora tezi, İstanbul Teknik Üniversitesi, Fen Bilimleri Enstitüsü*, İstanbul, Türkiye, 2004
[25.]G. Winstanley , *ArtificialIntelligence in Engineering*, New York, 1991
[26]. A.T. Hotomaroğlu, *Bilgisayar destekli öğretim için uzman sistem tabanlı bir kabuk programın geliştirilmesi ve etkinliğinin değerlendirilmesi, Doktora tezi, Gazi Üniversitesi*, Ankara, Türkiye, 2002
[27]. A.S. Anagün, Selecting *Inventory Models Using an Expert System, Computers and Industrial Engineering*, 33 (1-2), 299-302, 1997
[28]. A.S. Anagün**,** *Örnekleme Dağılımının Belirlenmesinde Uzman Sistem Yaklaşımı, IV. Ulusal Ekonometri ve İstatistik Sempozyumu, 955-961, 1999*
[29]. M.D. Salim, A. Villavicencio, M.Timmerman A. A, *Method for Evaluating Expert System Shells for Classroom Instruction, Journal of IndustrialTechnology, Volume 19*, 2002
[30]. Bareen Haval Sadiq Mzori , *Forward and Backward Chaining Techniques of Reasoning in Rule-Based Systems, Institute of Graduate Studies and Research, Master's Thesis, Eastern Mediterranean University*, Cyprus, 2015

ICENS
INTERNATIONAL CONFERENCE ON ENGINEERING AND NATURAL SCIENCES
24-28 May 2016 /Sarajevo

Analytical Modeling of Solid Particle Erosion of Polymer Matrix Composites

Emine Feyza Sukur* [1], ***Mehmet Bagci*** [1], ***Huseyin Imrek*** [1]

Abstract

Solid particle erosion (SPE) is one of the most important failure modes of composite materials in various applications such as piping of hydraulic or pneumatic transportation, blades of water or wind turbines, turbine blades of aircraft engines and helicopter blades and so on. The studies on analytical modeling have gained importance due to the limited changes in the level of experimental parameters. In the present work, an analytical model for predicting the SPE of pure glass fibre reinforced epoxy composites (GF/EP) , which captures the effects of impingement angle, velocity, properties of target materials and abrasive particles, has been developed by using dimensional analysis technique. The erosion rates of GF/EP are investigated experimentally at three particle impact velocities, (23, 34 and 53 ms^{-1}), three impingement angles (30^{o}, 60^{o} and 90^{o}) and at two different fiber directions (0^{o} and 45^{o}) by using alumina abrasive particles. The experiments have been performed at room temperatures on a special test device designed based on ASTM G76–95 standard test method where the composite specimens were subjected to erodent bombardments from dry and pressurized air. From the results of solid particle erosion testing, the erosion rate increases with increase in particle impact velocity, decrease in impact angle and non-angular changes in the fibre directions. This situation denote the ductile erosion wear in the literature. Furthermore, the predicted results are in a reasonable agreement with the experimental measurements.

***Keywords*:** *Analytical modeling, erosion rate, polymer matrix composites, SPE*

1. INTRODUCTION

Erosion is defined as material loss at surface caused by continuous impact of particles having various shape, dimension, structure and a certain velocity carried by liquid or gas ambient. In studies in literature the parameters affecting erosion and erosion process are examined under two headlines as theoretical and experimental. Apart from these in some of the studies theoretically developed mathematical models were compared with experimental results and the consistency of the model was researched. As in other tribological systems, erosion is related with operation parameters (particle velocity, particle flow rate, impact angle to target material, temperature) abrasive particle properties (shape, dimension, hardness, density), target material properties and environmental test conditions. As it is not possible to express a lot of parameters and their effects to process on a mathematical model, different mathematical models were derived in researches aiming at modeling erosion.

In studies made in this field models were generally developed for ductile and brittle materials and in case single abrasive particle or multiple abrasive particles track the surface. Studies started with Finnie's development of an erosion model on ductile materials at low and high impact angles and for a single abrasive particle, including basic concepts and assumptions for future studies [1]. After that he modified this model and listed the parameters affecting ductile erosion (impact angle, particle velocity, dimension, shape and resistance, surface properties, liquid density on liquid flow) and gave details for the effects of some of them [2]. In similar studies conducted for single particle, parameters such as particle hardness characteristics [3] and particle shape belonging to leaving trace situation on the surface were taken into consideration [4]. On the other hand material loss occurring by multiple tracking mechanism were expressed as sum of losses occurring due to plastic deformation and cutting [5, 6] and accordingly the mathematical model formed by this approach was used after being simplified within time or combined with Finnie erosion model [7, 8]. In another study belonging to ductile erosion the erosion on surface was defined and modeled as primary and secondary erosion [9]. Hutchings [10], in his model he developed for predicting erosion rates of metals affected from circular particles at normal impact angles, he assumed that abrasive particles do not deform and ignored elastic effects and used energy balance equations. In other studies made for ductile materials, effects of especially parameters such as particle impact angle, velocity, shape, dimensions and target material hardness [11-14] and also hardening, load slack ratio and critical strain were taken into consideration and the formed models were compared with experimental results [15-17]. Besides it was also experimentally determined that erosion of target surface has an important place in ductile erosion and as a result of dimensional analysis it was used as an effective parameter in mathematical models [15, 18]. For materials such as brass, aluminum and soft steel in order to evaluate the effects of particle concentration, particle size and impact velocity, experiments were generally made in pot erosion test device and correlation based models predicting erosion rate [19-21].

[1] *Corresponding author: Selcuk University, Department of Mechanical Engineering, 42003, Selcuklu/Konya, Turkey.*
efeyzasukur@selcuk.edu.tr

When mathematical models developed for predicting erosion rate of brittle materials were examined it was observed that there are limited number of studies about this subject. In the beginning of studies impact damage of brittle materials in elastic-plastic impact regime was evaluated and radial cracks (penetration) and breaking threshold was analyzed. By using breaking mechanics relation was established between radial crack formation on the material and fracture toughness of the material and an erosion model which can be assumed to be basic for brittle materials was developed [22]. In a similar study erosion rate of brittle materials with single crystal was expressed by a statistical model after two different mechanism were defined [23].

When studies made in the literature were examined it can be observed that there are no developed models for glass fiber reinforced composite materials. In this study an analytical model was developed by using dimension analysis technique for the purpose of predicting the solid particle erosion of glass fiber reinforced composite materials. In this developed model impact angle, impact velocity, abrasive particle properties and target material properties were taken into consideration. Erosion rates found experimentally were compared with erosion rates calculated with the model and the accuracy of the model was evaluated.

2. MATERIAL AND METHOD

2.1 Material

The glass fiber reinforced epoxy composite materials which were used in experiments and properties of which were given on table 1 are obtained by the reaction of polyphenol and epichlorohydrin under basic conditions. Apart from having very high resistance in room temperature it demonstrates good dielectric loss and electrical resistance under dry and moist conditions. They have high chemical resistance and can harden in low and high temperatures.

Table 5. Properties of test specimens

Property	GF/EP
Fibre diameter (µm)	17
Fibre aerial weight (g/m^2)	200
Fibre density (g/cm^3)	2.6
Density (g/cm^3)	1.683
Tensile strength (MPa)	533
Modulus of elasticity (MPa)	144.3
Hardness (HB)	87
Fibre volume ratio	0.50

Test samples were produced as plates by hand lay-up technique (110 Bar pressure, 120 °C temperature and a time of 3 top of the hour) with a thickness of 3 mm and dimensions of 1m x 1m. After that, test sample sizes were reduced to final size of 30x30 mm^2 so as to fit samples to sample holder in test set. Diamond saw was used in order to bring samples to suitable size for experiments.

2.2 Solid Particle Erosion Testing

In the study in order to find the solid particle erosion rates of glass fiber reinforced composite materials a test method in which abrasive particles are inflicted to surface of test sample with the help of dry and pressurized air (Fig. 1). The fact that the sample geometry used in this test method allows easy examination of dimensional change and weight reduction in erosion measurements (ASTM G76–95 2000).

In the experiments erosion rates were found for pure glass fiber reinforced epoxy composite materials and for three different impact angles (30^0, 60^0 and 90^0), three different impact velocity (≈23, 34 and 53 m/s) and two different fiber direction (0^0 and 45^0). Erosion test conditions were given in table 2.

Table 2. Erosion test conditions

Test parameters	GF/EP
Erodent	Aluminium (Al^2O^3)
Erodent size (µm)	~200
Erodent shape	Angular
Erodent mass flow rate (g/s)	182.5
Impingement angle, α (^{0})	30-60-90
Impact velocity (m/s)	~23-34-53
Fibre orientation (^{0})	(0/90)–(45/45)
Test temperature (^{0}C)	Room temperature
Nozzle to sample distance (mm)	10
Nozzle diameter (mm)	6
Nozzle length (mm)	86

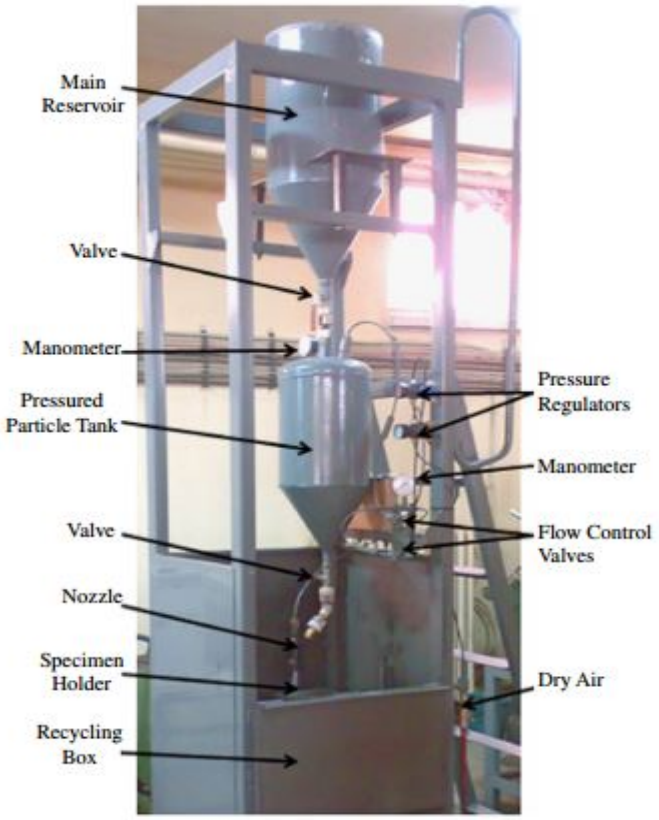

Figure 1. Test apparatus for erosion wear [24]

In the experiments alumina abrasives with angular geometric structure and an average diameter of ≈200 µm and the SEM view of the particles were given in figure 2 and their chemical compositions were given in table 3.

Table 3. Properties of erodent

Test parameters	GF/EP
Density (gcm^3)	3.94
Hardness (Mohs)	9
Melting temperature (^{0}C)	1950

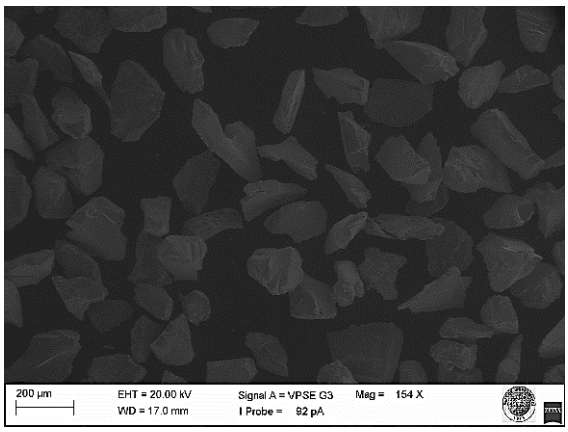

Figure 2. SEM view of Al^2O^3 erodent

3. PREDICTING MODEL FOR SOLID PARTICLE EROSION

Researches about erosion modeling and accordingly pre-estimation of possible erosion of machine element have been made for years. In literature there are many researches made about this subject. However majority of these models are correlation based and are strictly dependent to the system on which trial is made. Namely each model gives results that are unique to the system on which they were established. According to the established model it is not possible to make a generalization. Due to these characters of erosion models many changes occurred in erosion parameters and constants. In models to be created for solid particle erosion that are under the effect of more than one parameter dimension analysis is used to create a rule in times when a functional bond can not be formed between equation variables and found equations. While making dimension analysis quantity of physical magnitude is more important than quality. For this reason only dimensions are taken into consideration in the analysis. Dimension of each physical magnitude is expressed by dimension and symbol of basic magnitudes: for length 'L', for mass 'M' and for time 'T'.

3.1 Dimensional Analysis Technique

A single equation obtained as a result of dimension analysis made on a physical problem shows the relation between all parameters affecting the problem. However the power of each parameter in this equation is different and as a result of a suitable analysis to be made in order to determine the power correct steps about experimental measurements can be taken through the occurring non-dimensional number groups. Although there are other methods used for dimension analysis, Buckingham π theorems are among most prevalent methods. Two theorems suggested by Buckingham are named as first π theorem and second π theorem.

3.1.1. 1st π Theorem

In a system where number of physical magnitudes is 'm', if number of basic dimensions forming these physical magnitudes (M,L,T) is 'n', there are 'm-n' non-dimensional numbers (π group).

In other words when the physical magnitudes forming the system

$$\square(Q_1, Q_2, Q_3, \ldots\ldots\ldots, Q_m)=0 \quad (1)$$

is represented by equation (1), π groups showing the relation between these variables

$$\square(\pi_1, \pi_2, \pi_3, \ldots\ \ldots\ \ldots, \pi_{m-n})=0 \quad (2)$$

can be shown by equation (2).

3.1.2. 2st π Theorem

Each π group, should be determined so as to be the function of n repeated variables and at least one different variable affecting the physical problem directly.

Compliant to second π theorem, it is necessary to take below factors onto consideration on selection of n variables that will be repeated in all π groups:

1. When the dimensions of the variable to be repeated are evaluated together a selection should be made so as to give 3 basic dimensions (M, L,T).

2. When the variables to be repeated are gathered together non-dimensional groups by themselves should not be formed.

3. The variables to be repeated should preferably be magnitudes that can be measured by experiments.

3.2 Formulation of Erosion Model

In the model to be formed for solid particle erosion by using Buckingham pi theorem the parameters affecting target material mass loss (mt) are density of target material (ρt), velocity of abrasive particle (Vp), abrasive particle flow (Q), abrasive particle mass (mp), abrasive particle hardness (Hp), density of abrasive particle (ρp), target material hardness (Ht) and impact angle (α). Symbolic unit and dimensions representing these parameters were given in table 4.

Table 4. Dimensions of the erosion variables

Parameters	Symbols	SI Units	Dimensions
Target material mass loss	m_t	kg	M
Density of target material	ρ_t	kgm^{-3}	ML^{-3}
Velocity of abrasive particle	V_p	ms^{-1}	LT^{-1}
Abrasive particle flow	Q	kgs^{-1}	MT^{-1}
Abrasive particle mass	m_p	kg	M
Abrasive particle hardness	H_p	$kgm^{-1}s^{-2}$	$ML^{-1}T^{-2}$
Density of abrasive particle	ρ_p	kgm^{-3}	ML^{-3}
Target material hardness	H_t	$kgm^{-1}s^{-2}$	$ML^{-1}T^{-2}$

These parameters can be written as,

$$m_t = \phi(\rho_t, V_p, Q, m_p, H_p, \rho_p, H_t, \alpha) \text{ veya} \quad (3)$$

$$0 = \phi(m_t, \rho_t, V_p, Q, m_p, H_p, \rho_p, H_t, \alpha) \quad (4)$$

single equation. When dimension analysis was applied equation can be written by placing the dimensions

$$[M]^m [ML^{-3}]^p [LT^{-2}]^q [MT^{-1}]^r [M]^s [ML^{-1}T^{-2}]^t [ML^{-3}]^v [ML^{-1}T^{-2}]^z = [M^0L^0T^0] \quad (5)$$

in their places. In this final equation, 'm, p, q, r, s, t, v, z' values represent the unknown powers. (Table 5).

Table 5. Matrix of the variables dimensions

	(m)	(p)	(q)	(r)	(s)	(t)	(v)	(z)
	m_t	ρ_t	V_p	Q	m_p	H_p	ρ_p	H_t
M	1	1	0	1	1	1	1	1
L	0	-3	1	0	0	-1	-3	-1
T	0	0	-1	-1	0	-2	0	-2

As a result of dimension analysis the non-dimensional number groups appear depending on powers of parameters. As impact angle is dimensionless they will be incorporated to the system after mathematical model is formed. After removing these parameters the number of physical magnitudes in the model to be m=8 and number of repeating variables to be n=3, m-n=5 π group will be formed. As variables to be repeated m_p, ρ_p and H_t each of which can be measured experientially were selected. Basic condition for the formed π groups to be dimensionless is $M^0L^0T^0$. In both sides of the equation powers of same basic dimension should be same. When equations are solved by making powers equal to 0, results given in table 6 are reached.

Table 6. Results of dimensional analysis

Parameters/ π	π_1	π_2	π_3	π_4	π_5
(m)	1	0	0	0	0
(p)	0	1	0	0	0
(q)	0	0	1	0	0
(r)	0	0	0	1	0
(s)	-1	0	0	-2/3	0
(t)	0	0	0	0	1
(v)	0	-1	1/2	1/6	0
(z)	0	0	-1/2	-1/2	-1

When the powers given in the table are written in their places in the final equation the dimensionless number groups π_1, π_2, π_3, π_4 and π_5 can be found respectively as below.

$$\pi_1 = \frac{m_E}{m_p} \quad (6)$$

$$\pi_2 = \frac{\rho_E}{\rho_p} \quad (7)$$

$$\pi_3 = \frac{V_p\sqrt{\rho_E}}{\sqrt{H_E}} \quad (8)$$

$$\pi_4 = \frac{Q\sqrt[6]{\rho_p}}{2\sqrt{m_p}^2\sqrt{H_E}} \quad (9)$$

$$\pi_5 = \frac{H_p}{H_E} \quad (10)$$

Accordingly the analyzed solid particle erosion problem can be expressed as the function of dimensionless five π group.

$$f(\pi_1, \pi_2, \pi_3, \pi_4, \pi_5)=0 \quad (11)$$

$$\pi_1 = f(\pi_2, \pi_3, \pi_4, \pi_5)=0 \quad (12)$$

If π groups are arranged according to equation 12;

$$\frac{m_E}{m_p} = f\left(\frac{\rho_E}{\rho_p}\right).\left(\frac{V_p\sqrt{\rho_E}}{\sqrt{H_E}}\right).\left(\frac{Q\sqrt[6]{\rho_p}}{2\sqrt{m_p}^2\sqrt{H_E}}\right).\left(\frac{H_p}{H_E}\right) \quad (13)$$

equation is obtained. When power law approach is applied k_1,k_2,k_3 and k_4 indexes are added to equation as power. And therefore,

$$\frac{m_E}{m_p} = C.\left(\frac{\rho_E}{\rho_p}\right)^{k_1}.\left(\frac{V_p\sqrt{\rho_E}}{\sqrt{H_E}}\right)^{k_2}.\left(\frac{Q\sqrt[6]{\rho_p}}{2\sqrt{m_p}^2\sqrt{H_E}}\right)^{k_3}.\left(\frac{H_p}{H_E}\right)^{k_4} \quad (14)$$

general equation is obtained.

In wear problems erosion rate is ratio of target material loss to abrasive particle mass in its simplest form.

$$\textit{Erosion rate}\ (E_R) = \frac{m_E}{m_p} \quad (15)$$

when the expression in equation no 15 is placed in equation 14,

$$E_R = C.\left(\frac{\rho_t}{\rho_p}\right)^{k_1}.\left(\frac{V_p^{a}\rho_t^{0.5}}{H_t^{0.5}}\right)^{k_2}.\left(\frac{Q.\rho_p^{1/2}}{m_p^{1/2}.H_t^{0.5}}\right)^{k_3}.\left(\frac{H_p}{H_t}\right)^{k_4} \quad (16)$$

the analytical model predicting solid particle erosion rate is found. . Impact angle is incorporated to the model as multiplier in sine function as in other studies. As a result erosion model is arranged as below.

$$E_R = C.\left(\frac{\rho_t}{\rho_p}\right)^{k_1}.\left(\frac{V_p^{a}\rho_t^{0.5}}{H_t^{0.5}}\right)^{k_2}.\left(\frac{Q.\rho_p^{1/2}}{m_p^{1/2}.H_t^{0.5}}\right)^{k_3}.\left(\frac{H_p}{H_t}\right)^{k_4}.(\sin\alpha)^{k_5} \quad (17)$$

Here the proportion constant (C) and power indices (k_1, k_2, k_3, k_4, k_5), experiment parameters and erosion rates obtained from experiments are written in their places in equation and found with the help of MATLAB software. (Tabloe7).

Table 7. Erosion model constants

Material	Log C	k_1	k_2	k_3	k_4	k_5
GF/EP	$-1.08x10^2$	-10.21	-4.41	158.35	-4.99	1.38

4. RESULTS AND DISCUSSION

4.1 Experimental Results

Erosion behaviors of glass fiber reinforced epoxy composite materials were examined by changing impact velocity, impact angle, abrasive particle size and fiber direction. It was observed that changing impact angle caused erosion rate change in all experiment samples and most negative effect on erosion rate was observed in 30° impact angle. Namely a tendency which is similar to the situation faced in ductile materials was faced and the increase in impact angle (from 30° to 90°) brought decrease in erosion rate together. As a result of the increases occurred in impact velocity (≈23, 34, 53 m/s) ≈ by 1,5 times erosion rates increased in all experiment samples. It was concluded that fiber direction effect of erosion rate was more limited compared to other variables and this effect was supported by statistical data. Apart from this in case the fiber direction is 45° the impact angle of abrasive particles are changed so resistance of experiment sample surfaces were increased even a little.

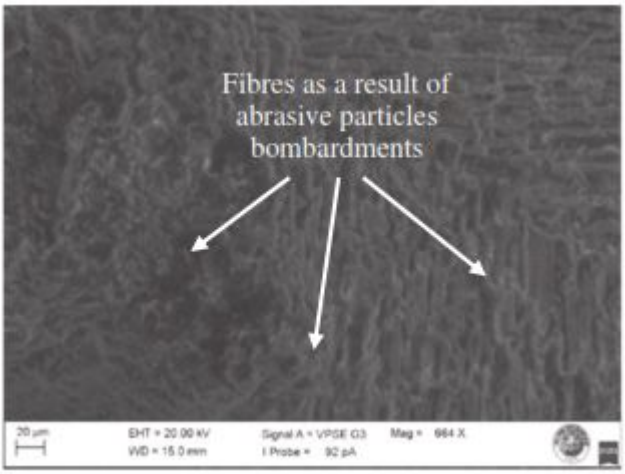

Figure 3. SEM view of pure GF/EP test specimens at velocity, angle and fibre directions of 34 m/s, 90 ^{0} and 0/90, respectively

In figure 3, the SEM view of glass fiber reinforced epoxy composite experiment samples were given at an impact velocity of 34 m/s, impact angle of 90°, fiber direction of 0° and abrasive particle size of 200µm. In case particle size is considered to be singular the particle size affecting on sample surface increases so accordingly it was observed that deformation of sample surfaces were increased. In SEM views, broken abrasive particles remaining after erosion were also observed.

4.2 Comparison Of The Model Prediction With Experiment

The constant (C) and power indices (k_1, k_2, k_3, k_4 and k_5) have been estimated by MATLAB software after putting values of known parameters in equation (17) for pure glass fibre reinforced epoxy composite.

The error has been determined from the solid particle erosion predictive model following equation,

$$Error\ (\%) = \left(\frac{E_E - E_P}{E_E}\right) * 100 \quad (18)$$

where, EE and EP are the experimental and predictive erosion rate results, respectively.

Table 8 presents comparisons of the predictive erosion rate results with the experiments, the predicted results are in a reasonable agreement with the experimental measurements, where the error range remained ~13% - ~21%.

Table 8. Erosion rate comparison between experiment and predictive model

	Experiment	Predictive model	Error (%)
Erosion rate (mg/kg)	1.93	1.61	16
	1.87	1.57	15
	3.32	2.91	20.5
	3.06	2.80	13
	4.51	4.17	17
	3.88	3.55	16.5
		Average error	16.3

The predicted results of the erosion rates gives a reasonable level of accuracy in the range of ~83% while dealing with the effect of impact velocity.

5. CONSLUSIONS

In the present work, an analytical model for predicting the SPE of pure glass fibre reinforced epoxy composites has been developed by using dimensional analysis technique and the erosion rates of GF/EP are investigated experimentally.

According to the experimental results,

• Test specimens exhibit maximum erosion rates at 30^0 impact angle and thus exhibiting similar behaviour as that observed for ductile materials.

• Test specimens with 45/-45 fibre directions are more wear resistant than their counterparts with 0/90 fibre direction.

• The increase in impact velocity cause substantial changes in wear rates.

The predicted results of the erosion rates gives a reasonable level of accuracy in the range of ~83% while dealing with the effect of impact velocity. If the constant (C) and power indices (k_1, k_2, k_3, k_4 and k_5) have been estimated experimentally, the predictive model could be able to give a reliable prediction.

ACKNOWLEDGEMENT

This work is supported by the Academic Staff Training Program (ÖYP) of Selçuk University with the project number of 2015-ÖYP-139.

REFERENCES

[1] I. Finnie, “Erosion of surfaces by solid particles,” Wear, vol. 3, no. 2, pp. 87-103, 1960/03/01, 1960.
[2] I. Finnie, “Some observations on the erosion of ductile metals,” Wear, vol. 19, no. 1, pp. 81-90, 1972/01/01, 1972.
[3] G. L. Sheldon, and A. Kanhere, “An investigation of impingement erosion using single particles,” Wear, vol. 21, no. 1, pp. 195-209, 1972/08/01, 1972.
[4] M. Hashish, “Modified model for erosion,” Seventh International Conference on Erosion by Liquid and Solid Impact, pp. 461-480, 1987.
[5] J. G. A. Bitter, “A study of erosion phenomena part I,” Wear, vol. 6, no. 1, pp. 5-21, 1//, 1963.
[6] J. G. A. Bitter, “A study of erosion phenomena: Part II,” Wear, vol. 6, no. 3, pp. 169-190, 5//, 1963.
[7] J. H. Neilson, and A. Gilchrist, “Erosion by a stream of solid particles,” Wear, vol. 11, no. 2, pp. 111-122, 2//, 1968.
[8] A. Forder, M. Thew, and D. Harrison, “A numerical investigation of solid particle erosion experienced within oilfield control valves,” Wear, vol. 216, no. 2, pp. 184-193, 4/1/, 1998.
[9] G. P. Tilly, “A two stage mechanism of ductile erosion,” Wear, vol. 23, no. 1, pp. 87-96, 1973/01/01, 1973.
[10] I. M. Hutchings, “A model for the erosion of metals by spherical particles at normal incidence,” Wear, vol. 70, no. 3, pp. 269-281, 1981/08/15, 1981.

[11] W. Tabakoff, R. Kotwal, and A. Hamed, “Erosion study of different materials affected by coal ash particles,” Wear, vol. 52, no. 1, pp. 161-173, 1979/01/01, 1979.
[12] A. V. Reddy, and G. Sundararajan, “Erosion behaviour of ductile materials with a spherical non-friable erodent,” Wear, vol. 111, no. 3, pp. 313-323, 1986/09/15, 1986.
[13] Y. I. Oka, K. Okamura, and T. Yoshida, “Practical estimation of erosion damage caused by solid particle impact: Part 1: Effects of impact parameters on a predictive equation,” Wear, vol. 259, no. 1–6, pp. 95-101, 7//, 2005.
[14] C. Huang, S. Chiovelli, P. Minev, J. Luo, and K. Nandakumar, “A comprehensive phenomenological model for erosion of materials in jet flow,” Powder Technology, vol. 187, no. 3, pp. 273-279, 11/20/, 2008.
[15] G. Sundararajan, and P. G. Shewmon, “A new model for the erosion of metals at normal incidence,” Wear, vol. 84, no. 2, pp. 237-258, 1983/01/15, 1983.
[16] G. Sundararajan, “A comprehensive model for the solid particle erosion of ductile materials,” Wear, vol. 149, no. 1, pp. 111-127, 1991/09/30, 1991.
[17] Y. I. Oka, and T. Yoshida, “Practical estimation of erosion damage caused by solid particle impact: Part 2: Mechanical properties of materials directly associated with erosion damage,” Wear, vol. 259, no. 1–6, pp. 102-109, 7//, 2005.
[18] W. H. Jennings, W. J. Head, and C. R. Manning, “A mechanistic model for the prediction of ductile erosion,” Wear, vol. 40, no. 1, pp. 93-112, 1976/10/01, 1976.
[19] R. Gupta, S. N. Singh, and V. Sehadri, “Prediction of uneven wear in a slurry pipeline on the basis of measurements in a pot tester,” Wear, vol. 184, no. 2, pp. 169-178, 5//, 1995.
[20] B. K. Gandhi, S. N. Singh, and V. Seshadri, “Study of the parametric dependence of erosion wear for the parallel flow of solid–liquid mixtures,” Tribology International, vol. 32, no. 5, pp. 275-282, 4//, 1999.
[21] M. S. Patil, E. R. Deore, R. S. Jahagirdar, and S. V. Patil, "Study of the parameters affecting erosion wear of ductile material in solid-liquid mixture." pp. 6-8.
[22] A. Evans, M. Gulden, and M. Rosenblatt, "Impact damage in brittle materials in the elastic-plastic response regime." pp. 343-365.
[23] S. Johansson, F. Ericson, and J.-Å. Schweitz, “Solid particle erosion — a statistical method for evaluation of strength properties of semiconducting materials,” Wear, vol. 115, no. 1, pp. 107-120, 1987/03/01, 1987.
[24] M. Bagci, “Investigation of erosion wear behaviour of glass fibre reinforced composite materials.” PhD thesis. The Graduate School of Natural and Applied Science of Selcuk University; 2010 [in Turkish].
[25] E. Buckhingham, “On physcially similar systems; illustrations of the use of dimensional equations.” Phys Rev 4, 345-76, 1914

Investigation of Optimum Asphamin Content for Warm Mix Asphalt

M.Ali Colak[1], Sinan Hinislioglu,[2] H.Ferit Bayata[1],Fatih Hattatoglu[1], O.Unsal Bayrak [1]

Abstract

Warm mix asphalt (WMA) technology has become increasingly popular in pavement construction because of its environmental benefits and its ability to improve the engineering properties of asphalt binders and mixtures. Several new processes have been developed to reduce the mixing and compaction temperatures of hot mix asphalt without sacrificing the quality of the resulting pavement. Asphamin which is the most used additive materials for WMA plays a significant role on decreasing the temperatures. Asphamin contains approximately 21 percent water by mass and is released in the temperature range of 85-182°C. When Asphamin is added to the mix at the same time as the binder, water is released. This water release creates a volume expansion of the binder that results in asphalt foam and allows increased workability and aggregate coating at lower temperatures.

In this study, 5% of optimum asphalt content is determined for chosen gradation by the Marshall Design method. The optimum asphamin content is tried to determine at temperatures of 110, 120, 130, 140 and 150oC by adding the asphamin to the asphalt of 4, 5, 6, 7 and 8% by weight of asphalt for each temperature using optimum asphalt content. The appropriate rate for optimum asphamin content for mixing temperature at 110oC, 120oC, 130oC, 140oC and 150oC can be suggested as 8%, 7%, 6%, 6% and 4%, respectively, according to Marshall Quotient.

Keywords: *WMA, Marshall Design, Asphamin*

1. INTRODUCTION

Hot mix asphalt (HMA) is a complex composite made up of heated aggregate, asphalt and has been using in many countries as a paving material. One of the disadvantages of HMA is the emissions occurred when asphalt heated. The main cause of emissions in an asphalt plant is dust, fume, exhaust steam and other gases [1]. Emissions occurred from HMA and WMA are shown in figure 1. A number of new processes and products have become available that have the capability of reducing the temperature at which HMA is mixed and compacted without compromising the performance of the pavement [2]. In order to ensure environmental benefits and energy saving, many studies were made about HMA and WMA mixtures. However, WMA could not take the place of HMA up to now. Compaction and mixing temperatures are between 100-140oC for WMA design and 150-180oC for HMA design [3]. Thus, decreasing in the temperature and emissions increased WMA's importance in recent years.

WMA can be used in all asphalt concrete mixtures such as dense graded asphalt, stone mastic asphalt, porous asphalt and mastic asphalt mixtures. Since this mixture can be applied in various thickness, it can be used in the roads with various traffic volumes [4]. The leading factors for improving WMA in Europe are below.

Environmental awareness and the concept of sustainable development especially the reduction of energy consumption and hence decreasing CO2 emissions,

The improvement of conditions in compacting mixtures,

Provide a clean environment to the workers

[1] *Corresponding author: Erzincan University, Department of Civil Engineering, 24120, Erzincan, Turkey. macolak@erzincan.edu.tr*

[2] *Selahaddin Eyyubi University, Faculty of Engineering and Architecture,21070, Diyarbakır, Turkey sinan.hinislioglu@seu.edu.tr*

Figure 1. Emissions of HMA and WMA

The main advantages of WMA are below:

Reduction in the emissions (reduction in the amount of emissions are given in Table 1)

Table 1. Reduction of Emissions in WMA Technology comparing to a Typically HMA Production

Emissions	Emission decrement ratio in a typical production (%)
CO_2 and SO_2	30-40
Volatile organic compounds	50
CO	Oct-30
Nitrogen oxides (NOx)	60-70
Dust	20-25

Reduction in fuel consumption: The provided fuel saving by WMA technology is varied between 11 – 35%. The fuel saving in the production of asphalt and asphalt concrete with low energy is more than 50%. In the production, aggregates are not need to heat the boiling point of water.

Workability advantages during production: The mixture with adequate workability can be transported to long distances. In addition, higher rates at low temperatures enables to reuse of the old asphalt.

Reduction in the emissions exposed to the workers; it was justify that the usage of WMA instead of HMA decrease the steam and polyaromatic hydrocarbons (PAH) between 20-50% [5].

Asphamin is one of the several additives used in the production of WMA. Generally Asphamin is added into the bitumen at a rate of 0.3% by weight of mixture. Asphamin is added to the bitumen after the mixture is heated to the mixing temperature. The mixture of Asphamin and bitumen are mixing with aggregate and the samples are prepared according to the Marshall design.

The objective of this study is to determine optimum Asphamin ratio in different mixing temperatures for an aggregate gradation within the specification limits. Asphamin was added to the mixtures at levels of %4, 5, 6, 7 by weight of mixture at the temperature of 110oC, 120oC, 130oC, 140oC, 150oC by Marshall Design.

2. MATERIALS AND METHOD

The base asphalt cement used in this study was obtained from TUPRAS Bitumen Company, Batman, Turkey. The characteristics of the asphalt used in this study was shown in Table 1. It conforms to the Turkish Standard requirement for an asphalt binder of 70/100 penetration grade.

Table 2. Asphalt binder properties

Characteristics	Method	Result
Penetration at 25 °C, 100 g 5 s, 0.1 mm	ASTMD5	85
Softening Point, °C	ASTM D36	47
Flash Point, °C	ASTMD92	205
Specific Gravity	ASTMD7	1.041

Crushed calcareous based aggregate from Akbaba Hill Quarry was used. The properties of aggregate were seen in Table 2. Aggregate grading curves for asphalt mixtures were obtained from the Turkish Highway Construction Specifications. Sieve analyses were carried out and the aggregate grading curve was selected as Type 2 wearing course as shown in Fig 2.

Table 3. The physical properties of aggregates

Properties		Coarse Aggregate	Fine Aggregate	Filler
Specific Gravity (25oC, gr/cm3)	ASTM C127	2,678	2,686	2,738
Water Absorption (%)	ASTM C128	0,4	0,52	-
Los Angeles Wearing (%)	ASTM DC 131	27,6	-	-
Freezing and Thawing (%)	ASTM c88	2	-	-

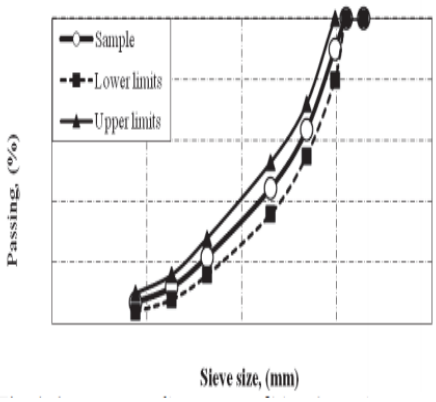

Figure. 2. Aggregate grading curves (generally 0,3% weight of bitumen asphamin added)

Many additives are used in the production of warm mix asphalt. One of them is asphamin. Asphamin with 0.3% by total weight of mixture is generally used by adding to asphalt. When the asphalt is reached to mixing temperature, It is added to asphalt and, then, mixtured to spread. The mixing of asphalt and asphamin are added to aggregate blend. Then samples are prepared to Marshall Test Method. In this study, asphamin was obtained aspha-min GmbH Company. The physical and chemical properties of asphamin were shown in Table 4.

Table 4. The physical and chemical properties of asphamin

Consistence	**Granular powder or powde**
Color	White
Smell	Odourless.
Specific Gravity g/cm^3	2
Chemical Proportieses	Hydrothermally crystallized aluminum nitrate silica. Crystal water content is 21% by weight.
Shape	Average particul diameter 3,5µm
Compaction density	500 g/l
pH (in saturated solution)	11,6
Solubility (in water)	Insoluble
Storage	Storage temperature -15+70^{o}C

The Marshall Test Method was used for determining the optimum bitumen content (OBC). Marshall Specimens were fabricated in accordance with ASTM D 1559. 75 blows were applied on each side of the specimen. A total of 21 specimens were fabricated to determine optimum asphalt content (OBC) from 4% to 7% asphalt by weight of aggregate. A total of 126 specimens were prepared and the Specifications of the General Directorate of Turkish Highway for Wearing Coarse Subjected to High Volume of Traffic was used (Table5).

Table 5. Specification for wearing course (Anonymous 2006).

Properties of Marshall specimen	**Specification limits**
Stability (MS) (kg)	Min 900
Air voids (%)(75;50 blows)	3-5; 4-6
Flow (mm)	2-4
Voids of mineral aggregate (VMA)(%)	Min 14
Voids of filled with asphalt cement (VFA)(%)	65-70

3. RESULTS AND DISCUSSION

In this study, impacts of the asphamin used in asphalt production at diffrenet temperatures and contents on the performance of asphalt concrete were investigated.

Performance of the samples produced with asphamin was compared with HMA and optimum bitumen content (OBC) was found. Additive content of asphamin and mixing temperature were taken respectively as 0% and 150 ° C. OBC was found as %5 for this design. Bitumen ratio was taken as 5% for the samples produced by asphamin. Different asphamin usage rates were calculated as percentage by weight of bitumen.

Asphamin usage ratios were taken as %4-5-6-7-8 at 110^{o}C mixing temperature. When all results are considered together; the highest stability value was obtained on the samples produced at 150^{o}C and the lowest stability value was obtained on the samples produced at 110^{o}C. Lowest void percentages were observed on the samples produced at 130^{o}C and highest void percentages were observed on the samples produced at 120 ^{o}C. In the terms of Dp and VFA , highest values were observed at 130 ^{o}C and lowest values were observed at 120 ^{o}C.

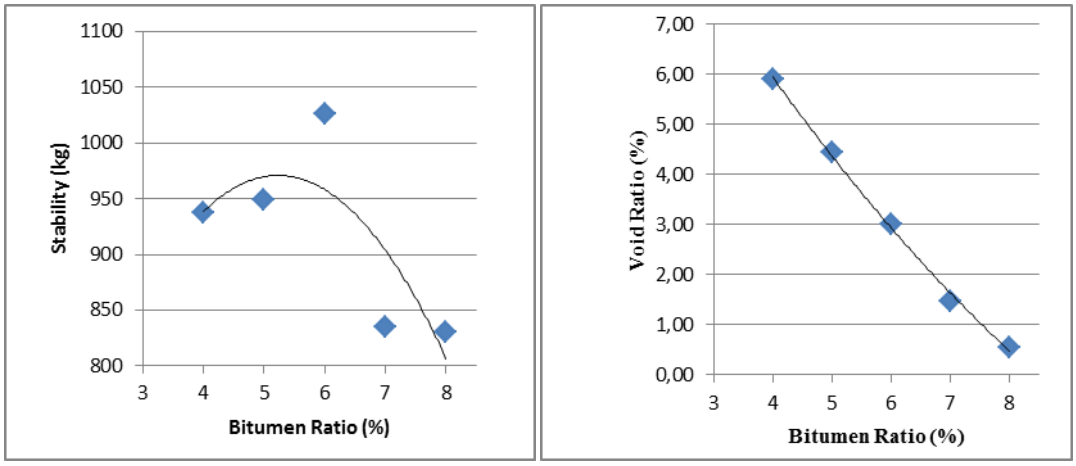

Figure 3 130°C Stability–void ratio bitumen ratio relationship.

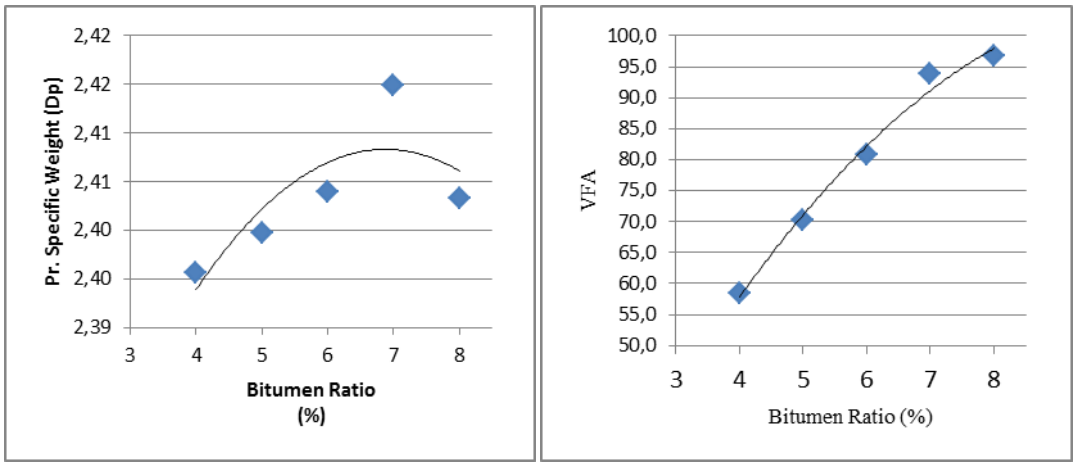

Figure 4 130°C Pr. Specific weight -VFA bitumen ratio relationship.

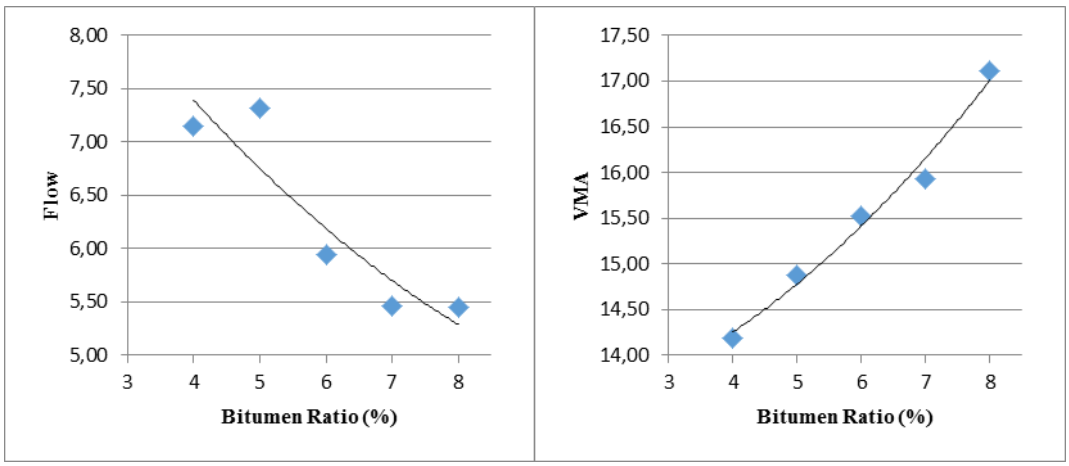

Figure 5 130°C VMA-flow bitumen ratio relationship (Fig 3 , fig 4 , and Fig 5 shows 130°C samples)

Asphamin performance can be researchs in different gradations and different type of aggregate. In this study we determined the aspamin ratio by the weight of bitumen but Asphamin ratio can be determined by total weight of mixtures.

REFERENCES

[1]. R. E. Sorace, V. S. Reinhardt, and S. A. Vaughn, “High-speed digital-to-RF converter,” U.S. Patent 5 668 842, Sep. 16, 1997.
[2]. Khan Z, Al-Abdul Wahab H., Asi I., Ramadhan R., 1998. Comparative study of asphalt concrete laboratory compaction methods to simulate field compaction, Constructionand Building Materials, Vol 12, pp.373-384
[3]. Karnik, “Performance of TCP congestion control with rate feedback: TCP/ABR and rate adaptive TCP/IP,” M. Eng. thesis, Indian Institute of Science, Bangalore, India, Jan. 1999.
[4]. J. Padhye, V. Firoiu, and D. Towsley, “A stochastic model of TCP Reno congestion avoidance and control,” Univ. of Massachusetts, Amherst, MA, CMPSCI Tech. Rep. 99-02, 1999.
[5]. Goetz W. H., 1989. "The evaluation of Asphalt Concrete Mix design: Development of more rational approaches ASTM STP 1041, Philadelphia, pp. 5-14.
[6]. Hınıslıoğlu S., ve Hattatoğlu F., Marshall Tasarımında Optimum Asfalt Oranı Yerine Optimum Bitüm Aralığının Belirlenmesi, 5.Ulusal asfalt sempozyumu, 2009.

Risk Assessment of Hazardous Waste

Mehmet Emin Argun[1], Havva Ates[2]

Abstract

Hazardous substances are estimated to be generated about 1.5 million tons in Turkey. Some amount of these wastes recycled and about 35 percent of wastes eliminated in disposal facilities. Recovering, recycling or suitable disposing of hazardous wastes are generally insufficient in a lot of countries. Insufficient waste transportation, handling and disposing methods lead to the important public and environmental risks, threatening hazardous waste management.

Transport of hazardous waste must abide by international rules and standards for packaging, labeling and transport of waste. However some accidents during transportation of hazardous materials could cause a lot of serious health and environmental problems. Therefore estimating of accidents and release rates is essential for risk assessments in highway transportation of hazardous materials. Although there is a lot of analytical modeling for transportation of hazardous materials, the models in terms of providing environmental data are inadequate.

This study aimed to investigate some risks related with scenario of truck accident carrying solvent waste and interpretation of hazards. By using hazard assessment model some outputs are obtained such as distribution of the hazardous waste, reaching time to receiver, affected people and environment. With the model work possible harmful effects on humans and the environment will be prevented. In addition to, the impact on people and the environment which is irreversible will be prevented or reduced.

***Keywords**: Hazardous wastes, accidents, solvent, risk assessment*

1. INTRODUCTION

Waste diversity is increasing because of population growth, change of production and consumption habits, advancing technology and differentiation of products and competition environment. There are many various classification criteria in the literatüre regarding the waste classification. The most common classification wastes are grouped under 3 main headings: 1- hazardous and harmless wastes, 2- solid, liquid and gas wastes, 3- domestic, industrial, agricultural and special wastes.

In our country hazardous wastes for the first time describes in Solid Waste Control Regulation at 1991: "explosive, sparkler, spontaneous combustion, generating flammable gas when it in contact with water, oxidizing agent, containing organic peroxides, toxic, corrosive, releasing toxic gas when it in contact with water and air, and other wastes considering as hazardous wastes by Undersecretariat are hazardous wastes [1]. In recent years evaluating, handling, storing and disposal of hazardous wastes came to the forefront. In industrial sector was applied wastewater treatment and solid waste plants, however still has been done anything about disposal of hazardous wastes. Hazardous substances has been used in a wide range of fields so in many countries national or international laws implement due to potential danger of hazardous wastes. This laws, including directly hazardous waste producers and the industry which use the hazardous materials in industrial and manufacturing processes [2].

Determination of characterization of hazardous wastes is important with regard to precautions and urgent action plans in case of possible exposing and the dangers which people and environment can be affected. Hazardous wastes which has wide range of usage are classified into nine types: explosives, gases, inflammable liquid and solids, oxidizing agents and organic peroxides, toxics and etiological materials, radioactive effluents, corrosive and others. In environmental risk assessment, it is approved four fundamental hazard criterias for that much substances (toxicity, corrosivity, reactivity and sparklers), and the substance is characterised by that criterion. [3].

Physical and chemical characteristics of wastes (flammability, corrosion, toxicity and reactiveness) inform about whether or not hazardous. A potential danger of one chemical compound can determine easily with the exist methods but in case of waste is mixture, potential danger is determined according to component which have most dangerous chemical characteristic. Characterization of waste should be known for handling, storing and disposal of waste, structural characteristics of load-bearing elements, recycling (if possiple) and immediate action plan. [4], [5].

[2]*Corresponding author: SelcukUniversity, Department of Environmental Engineering, 42075, Konya/ Turkey. havvaates@selcuk.edu.tr*

[1] *SelcukUniversity, Department of Environmental Engineering, 42075, Konya/ Turkey. argun@selcuk.edu.tr*

After chemical accidents the proper intervention provide velocity for minimize accident's negative effects on environment. There are a lot of models applied to the effects of possible accident in future. However this is a complicated task because of the number of processes affecting the environmental effects. Moreover, assessing a future effect of a hypothetical accident, as a step in a planning process, is even more difficult.

In such studies risk assessment made by considering in the aggregate region characteristics with chemical characteristic. Studies of risk assessment, be constituted method and guidebook for immediate action plans and management of risks. [6]. Such studies includes multimedia transport and transformation models of hazardous waste, exposure scenario models, and determine quantify and reduce uncertainty in multimedia (such as soil, air, water) [7], [8], [9]. Determination of potential level of pollution by storage yard and around of radioactive effluents, considering to have similiar characteristics [10].

In present work after hypotetical accident, environmental impacts of a tanker which carrying thinner as hazardous waste are discussed and evaluated by using related model.

2. MATERIAL

Scenario: Tanker accident on the road

Hazardous waste: Thinner

Volume of trailer: 15 m^3

District: Bus terminal of Konya

Maximum population density of the area: 17462 kişi/km^2

Dominant wind direction: North-Northeast

Wind speed: 2 m/s

Spill area of hazardous material: 100 m^2

The diffusion area of thinner determined from Gaussian Puff Dispersion Model [11]. Because thinner have volatile structure.

2.1 Properties of Thinner

Thinner is using as degreasing and cleaning etc. in nearly all manufacturing sectors of industry. This solvents investigated as halogenated and halogen-free compounds. Thinners considering as hazardous substance and hazardous wastes because of their chemical properties. Cellulosic thinners has powerful solvers in their structure. They are colorless and clear. In cellulosic dyes thinner provide that properly diffuse all over the surface and it has specific scent. It is a sparkler and quite simple flammable liquid. Thinners used all kind of cellulosic dyes, primer, thinning of lacquer and cleaning of application accessories. For production of cellulosic thinner using above 90 percent toluene as a primary commodity and at the rate of 5 percent varied solvents. Production of cellulosic thinner is simple mixture but we should be careful because thinner has excessive burnable and sparkler. In the other hand thinner has so many affect healthwise.

Table1: Physicochemical Properties of Thinner [12]

Physical phase	Achromic Liquid	
Odour	Original	
Density (20°C)	0,895 g/ml	
Boiling Range (°C)	138 - 195	
Flash Point (°C)	> 35	
Melting Point (°C)	< -25	
Autoignition Temperature (°C)	> 240 °C	
Blasting limit	lover limit 1,1 v/v	upper limit 7,0 v/v

Waste amount in vehicle=density of thinner*volume of vehicle

waste amount=0.895 g/ml*15 m^3=13425 kg=13425*106 mg

stability classes for 200 m

$\sigma y = \sigma x = 32$ m

σz=20 m

Notation of point source dispersion

$$C(x,y,0,t) = \frac{Q}{(2\pi^{\wedge}(1.5)x\sigma x\ \sigma y\ \sigma z)^{\wedge}(0.5)} \exp\left(-\frac{1}{2}\right)\frac{((x-ut)^2}{((\sigma x)^2} + \frac{(y)^2)}{(\sigma y)^2)}$$

As specified in Table 3 establishments results show that; after approximate 150 m concentration is decreasing that's why the dispersion distance is chosen 150 m.

Table 3. Determination of distance of x and y which threshold concentration reached

x (m)	y (m)	Time(s)	mg/m^3
0	0	0	28121409,48
10	10	5	26781413,67
20	20	10	23132508,91
30	30	15	18121944,89
40	40	20	12875962,4
50	50	25	8297503,051
…	…	…	…
140	140	105	179,5388261
140	140	105	179,5388261
142,5	**142,5**	**105**	**150,4164658**
144,5	144,5	105	129,4161076
150	150	140	0,124401033
160	160	105	30,9620185

Horizontal spreading distance: 0.15km
Vertical spreading distance : 0.15 km
Diffusion area diameter: 35 m
Evacuation area: 0.014 km^2
Maxsimum disaster potential:

DP=0,5*S*Dmax
DP = 0,5*0,014*17462=123 person

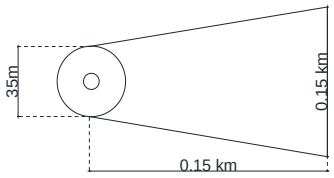

Figure 1 Influence area in instant of accident

3. METHOD

Rating system is constituted for determination of hazardous waste. This system has 2 principal heading. These principals; risk assesment of hazardous materials, hazardous material character(HM_C), Ecosystem character (E_C). HM_C is function of physical and chemical characteristics, assessment of exposure, modes of transport and accidents of hazardous material. E_C is function of county line, enviromental resources, purpose of hazardous materials. This 2 parameters consist of a lot of constituents. Rating for constituents a lot of proporties of waste given in Table 4. Rate of risk assesment establishing as the following:

RAR = (HM_C + E_C) x Q

Table 2. The components and various properties of the thinner

Hazardous material component	Percentage by weight (% w/w)	Solublity (S), mg/L	exposure limits				Toxicological specifications	Ecologic data	Hazardous Proporties	Risk (R)	Application properties
			TLV –TWA (8 h)*		TLV-STEL(short-term)**						
			mg/m^3	ppm	mg/m^3	ppm	Acute toxicity	Ecotoxicity			
Xylene (CAS no: 1330-20-7, EINECsno: 215-535-7)	50-75	150-300	221	50	442	100	LC50 (rat, breathing, 4 h) : 20 mg/l LD50 (rabbit, dermal) : > 2000 mg/kg LD50 (rat, mouth) : > 2000 mg/kg	LC50 (fish, 96 h) : 3,77 - 13,5 mg/l EC50 (water flea, 48 h) : 7,4 mg/l	Xn (harmful)	R10: flammable R20/21: for inhalation and contact with skin it is harmful. R36/38: it is irritating for eyes and skin.	
2-Butanol(CAS no: 1330-20-7, EINECsno: 215-535-7)	20-30	169000		25		50	LC50 (rat, inhalation, 4 h) : > 2,7 mg/l LD50 (rabbit, dermal) : 1500 mg/kg LD50 (rat, mouth) : 560 mg/kg	LC50 (fish, 96h) : > 100 mg/l EC50 (water flea, 24 h) : > 100 mg/l	Xn (harmful)		
2-Butanol acetate (CAS no: 111-76-2, EINECsno: 203-905-0)	30-50	6170	133	20	333	50	LC50 (rat, inhalation, 4 h) : 2 - 20 mg/l LD50 (rabbit, dermal) : 400 - 2000 mg/kg LD50 (rat, mouth) : 200 - 2000 mg/kg				immisciblewith water.

(*)permissible exposure limit for that compound 8 h in a day 40 h in a week

(**)permissible exposure limit for that compound is 15min

Waste amount in vehicle=density of thinner*volume of vehicle

waste amount=0.895 g/ml*15 m^3=13425 kg=13425*106 mg

stability classes for 200 m

σy= σx= 32 m

σz=20 m

Notation of point source dispersion

$$C(x,y,0,t) = \frac{Q}{(2\pi^{\wedge}(1.5)x\sigma x\ \sigma y\ \sigma z)^{\wedge}(0.5)} \exp\left(-\frac{1}{2}\right)\frac{((x-ut)^2}{((\sigma x)^2} + \frac{(y)^2)}{(\sigma y)^2)}$$

As specified in Table 3 establishments results show that; after approximate 150 m concentration is decreasing that's why the dispersion distance is chosen 150 m.

Table 3. Determination of distance of x and y which threshold concentration reached

x (m)	y (m)	Time(s)	mg/m^3
0	0	0	28121409,48
10	10	5	26781413,67
20	20	10	23132508,91
30	30	15	18121944,89
40	40	20	12875962,4
50	50	25	8297503,051
…	…	…	…
140	140	105	179,5388261
140	140	105	179,5388261
142,5	**142,5**	**105**	**150,4164658**
144,5	144,5	105	129,4161076
150	150	140	0,124401033
160	160	105	30,9620185

Horizontal spreading distance: 0.15km
Vertical spreading distance : 0.15 km
Diffusion area diameter: 35 m
Evacuation area: 0.014 km^2
Maxsimum disaster potential:

DP=0,5*S*Dmax
DP = 0,5*0,014*17462=123 person

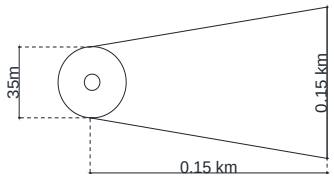

Figure1. Influence area in instant of accident

4. RISK ASSESSMENT RATE FOR HYPOTHETICAL ACCIDENT

4.1 Hazardous Material Characteristics

The thinner has scored in view of the fact that the range of the values of the specified properties (according to Table 4)for each componenet. In the following table presents the maximum points and the rating of thinner properties such as the physical, chemical and ecological.

Table 5. Rating values for components of hazardous material character(HM_c)

Properties	Value	Score	Max Score
Solubility(S)	0,058>0,05	3	4
Density (D)	0,895 g/ml<1g/ml	2	2
Flmmability(F)	35^0C<60 ^{0}C	2.8	2.8
Corrosiveness (C)		-	4
Peroxide and Reaktivite (PR)	Instable –highly reactive	4	4
Ecot	2 (54,32 mg/l(10-100))		
Ht	3	5	10
Toxicity (Tox)	2+3 = 5		
Exposure Mode (EM)	Exposing by breathing	3	3
Transportation Mode (TM)	Highway	3	4
Accident: A (transportation)x(industrial use)	3x2	6	9

$HM_C = S+D+F+C+RP+Tox+EM+TM+A = 28.8$

4.2 Assesment of Ecosystem Characteristic (E_c)

Table 6. Rating values for Regional Boundaries(RB)

Properties	**Value**	**Score**	**Max Score**
Spill / diffusion area	0.0001km^2<1 km^2	2	10
Area of the region	0.583 km^2<10 km^2	2	10
Transport lines	-	-	-
Residential Mode (RM)	Organized industrial zones city	8	10
Transportation (TR)	Highway	2	10
Touristic and Recreation areas (TR)	Recration	5	10
Population Density (PD)	17462 (1000-2000)	8	10

$E_C = RB + RM + IC + Ag + TR + MU + CA + FR + FF + PD = 27$

4.3 Quantity

Table 7. Rating values for quantity (Q)

Properties	**Value**	**Score**	**Max Score**
Q	13.425ton (100-1ton)	2.5	4

RAR = $[(HM_C + E_c) \times Qi / (HM_c + E_c)_{max} \times Q_{max}] \times 100$

RAR =$[((27 + 28.8) \times 2.5) / ((42.8+60) \times 4)] \times 100 =$ 34%

5. CONCLUSION

Because of risk assessment rate is 34% (20% to 39%) its belong to low risk group. According to this risk assessment ratio;

***** Our area can be considered as rich or poor in terms of environment resources but also have a higher tolerance.

***** Besides, its assummed as controlled industrial areas in terms of exposure time to hazardous waste

A, B, C plans should be ready

Plan A: If it is determined that human life is under direct and acute danger, emergency action plan's first priority should be preventing this threat. This determination must be ensured directly implementing of the plan A. Even though short-time exposure to direct and acute danger it may be mortal human life.

Plan B, Even if it is not dangerous directly for human life It should be considered acute and cronical effects resulting in killing. In this situation, implementations from plan A to plan C can applied by consulting managerical decision.

Plan C, Although it is not usually influence human health directly, it may affect people by food chain affecting adversely other ecosystem lives.

Plan D, Plan D includes remediation and recovery methods by determining acute and chronic effects on environment.

ACKNOWLEDGMENT

Presentation of this research has been supported by Selcuk University Scientific Research Project Fund (BAP-16701223).

REFERECENCES

[1]. Official newspaper, 14.03.1991, 20814
[2]. Tenikler, "Hazardous Waste Management in Turkey and A Comparative Analysis with European Union Countries," Doctoral thesis, Dokuz Eylül University Institute of Social Sciences, Izmir, Turkey, 2007.
[3]. Kahraman, "Hazardous Substances and Environmental Risks Evaluation Approach, Case Study" M. Eng. thesis, İstanbul Technical University Institute of Science, İstanbul, Turkey, July 2002.
[4]. S.L. Stafford, "Hazardous Substances",Reference Module in Earth Systems and Environmental Sciences,Encyclopedia of Energy, Natural Resource, and Environmental Economics, vol. 3, pp. 98–102, 2013
[5]. S. Stafford, The effect of punishment on firm compliance with hazardous waste regulations, *J. Environ. Econ. Manage*, vol. 44, pp. 290–308, 2002.
[6]. A. S. Andersson, M. Tysklind, I. Fangmark, " Amethod to relate chemical accident properties and expert judgements in order to derive useful information for the development of Environment-Accident Index," *Journal of Hazardous Materials*, vol. 147, pp. 524–533, Jan. 2007.
[7]. J.P. Gupta, B.S. Babu, "A new hazardous waste index," *J. Hazard. Mater.* Vol. 67, pp. 1–7, 1999.
[8]. I. Talınlı, R. Yamanturk, E. Aydın, S. Basakcılardan-Kabakcı, "A rating system for determination of hazardous wastes," *J Hazard Mater*., vol. 126(1-3), pp. 23-30, July 2005.
[9]. T.E. McKone, "CalTOX, A Multimedia Total-Exposure Model for Hazardous-Wastes Sites," Part 1. Executive summary. A report written for The Office of Scientific Affairs Department of Toxic Substances Control California Environmental Protection Agency Sacramento, Clifornia by The Lawrence Livermore National Laboratory.
[10]. A.S.M. Alves, P.F. Frutuoso Melo, E.M. Passos, G.S. Fontes, "Stochastic and deterministic models to evaluate the critical distanceof a near surface repository for the disposal of intermediate and lowlevel radioactive wastes," Nuclear Engineering and Design, vol. 287, pp. 57–67, Jan. 2015.
[11]. A User's Guide For the CALPUFF Dispersion Model, Earth Tec. Inc., 2000.
[12]. The dyo website, Available: http://www.dyo.com.tr/dyo/pdf/MT-9900t02012006rev00.pdf

The Prediction of Tool Life by Using Changes in Cutting Forces During Turning Process

Osman Ozturk[1], *Ali Unuvar*[2]

Abstract

The present study concentrates on the relationship between cutting force and tool wear for different parameters in cylindrical turning of AISI 4140 steel under conditions where cutting fluid is used. The set of experiments consist of three different levels of three different parameters. Three of these parameters are feed rate (0.05, 0.1, 0.2mm/rev), three of them are cutting speeds(150, 190, 250 m/min) and the rest of them are depths of cut(0.5, 0.87, 1.5mm). Cutting forces were measured in each experiment of different combination of parameters. The aim of these experiments is to predict tool wear by using cutting forces. For these reason progression of tool wear A mathematical model of tool life is obtained by using experimental results. Relationship between cutting force and cutting parameters are investigated according to design of experiment. Results indicated that increase in cutting speed slightly increases cutting force while increase in feed rate and depth of cut significantly increases cutting force. The changes in the magnitude of machining forces and the alterations in tool wear progression were investigated. Correlation between time-dependent cutting forces and tool wear was analyzed. By using changes in cutting forces, tool life is obtained in a shorter time period, while it takes a lot of time to determine tool life obtained by measuring wear. In addition, predicted tool life and experimental results of tool life is compared.

Keywords: *Cutting force, tool life, tool wear, turning process.*

1. INTRODUCTION

Tool wear is a complex phenomenon occurring in different ways. Generally, worn tools adversely affect surface finish of the work piece and tool life; therefore it is necessary to develop tool-monitoring systems. One of the most commonly used techniques for tool wear detection and breakage involves the measurement of cutting forces. In turning operations, it is convenient to consider the forces as a three-component system. These are the tangential component, the axial component and the radial component. The components of the cutting forces in metal cutting operations provide an abundance of information on the metal removal process. Changes in these forces indicate changes in machining parameters, such as depth of cut, feed rate, cutting speed and condition of tool. Thus the accuracy of machining operations could be improved through the cutting force feedback. Many attempts have been made to use cutting forces for tool wear monitoring. Turning process is widely used in machining process which is accepted by any manufacturing industry. In the turning process, a single point cutting tool removes the material from the surface of a rotating work piece. In order to investigate the influence of machining conditions on response factor, i.e., tool wear—three cutting parameters cutting speed, feed rate and depth of cut were selected as the input parameters.

Flank wear is an important criterion for machinability assessment of a material. Flank wear is usually seen in the flank face of a cutting insert. Among the different forms of tool wear, flank wear is the significant measure of tool life as it affects the surface quality of the work piece. The nature and the rate of growth of flank wear with machining time are the most important criteria for judging the life of the tool. Abrasion and adhesion are the two wear mechanisms for flank wear. The flank wear is usually caused due to crack development and intersection by hard asperities or wear particles acting as small indenters on the cutting face. Tool life is generally measured based on the flank wear of the tool when it is machined to steel. The current study is therefore restricted to wear on the flank of the cutting tool.

Davim et al. presented a study of the relationship between cutting forces and tool wear of polycrystalline diamond (PCD), measured when machining the composite A356/20/SiCp-T6 [1]. The nature of tool wear in metal cutting, unfortunately, is not yet clear enough in spite of numerous investigations carried out over the last 50 years. Tool wear has a large influence on the

[1]*Corresponding author: Selçuk University, Department of Mechanical Engineering, 42003, Selçuklu/Konya, Turkey. osmanozturk@selcuk.edu.tr*

[2]*Selçuk University, Department of Mechanical Engineering, 42003, Selçuklu/Konya, Turkey. aunuvar@selcuk.edu.tr*

economics of the machining operations. Prediction of tool wear is a complex process because of the complexity of machining systems. Tool wear in cutting process is produced by the contact and relative sliding between the cutting tool and the workpiece, as well as between the cutting tool and the chip under the extreme conditions of cutting area. Bin Li focused on the new development in predicting the tool wear evolution and tool life in orthogonal cutting with FEM simulations[2].

Li et al. presented an experimental study of the tool wear propagation and cutting force variations in the end milling of Inconel 718 with coated carbide inserts. Their experimental results showed that significant flank wear was the predominant failure factor that affects the tool life[3]. In order to find out suitable way to slow down the wear process, many works are carried out to analyze the wear mechanism in metal cutting. It is found that tool wear is not formed by a unique tool wear mechanism but a combination of several tool wear mechanisms. Tool wear mechanisms in metal cutting include abrasive wear, adhesive wear, solution wear, diffusion wear, oxidation wear [4, 5].

Scheffer described an in-depth study on the development of a system for monitoring tool wear in hard turning. In their study, various aspects associated with hard turning were investigated with the aim of designing an accurate tool wear monitoring system for hard turning. They stated that the suggested wear-monitoring system is simple and flexible enough for online implementation, which will allow more reliable hard turning process in industry[6]. Wong et al. investigated flank and crater wear of coated carbide tools during the machining of carbon steels. They stated that two-body and three-body wear models are used in describing flank wear of cutting tools in machining pearlitic and spherodized steels[7]. Sikdar et al. described the relationship between flank wear area and cutting forces for turning operations. A set of experiments were performed on a CNC lathe without coolant. They also presented mathematical modeling for better understanding of the relationship between flank wear area and cutting forces[8].

The present study is an attempt to evaluate the influence of factors such as cutting speed, feed rate and depth of cut on flank wear and cutting force during turning of AISI 4140 steel with tungsten inserts. This paper presents a study of the relationship between cutting forces and tool wear of tungsten carbide, measured when machining the AISI 4140 steel.

2. MATERİALS AND METHODS

The experimental set up developed in this research consists of a dynamometer fitted with a CNC lathe. machine. During the course of experimentation, the flank wear of worn inserts was measured using a Tool Makers Microscope. Experimental setup and microscope is given in Figure 1. The experimental work was developed considering the turning operations, through the continuous measurement of the cutting forces with appropriate piezoelectric dynamometers. The wear type was identified and its evolution with cutting time was measured. In turning, correlations were obtained between the progression of flank wear of the insert and the cutting forces which are the main cutting force, feed force and radial forces.

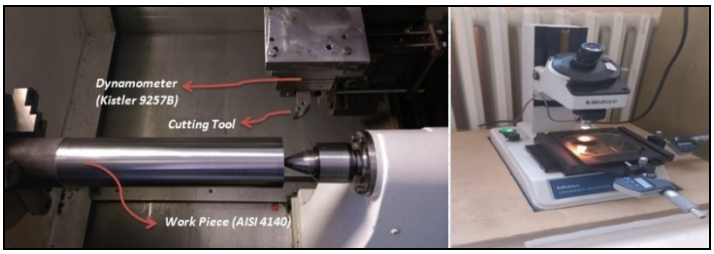

Figure 1. On the left, experimental setup. On the right, Tool Makers Microscope.

The turning tests performed allowed evaluation of the wear resistance of the inserts in machining the AISI 4140 steel and the influence of the wear on the cutting forces. It is an abrasive form of flank wear in the turning cutting insert, which can be measured as VB (according to ISO 3685). Example of this wear type in a turning insert has been shown in Figure 2. It was taken VB=0.3 mm as wear criterion. The cutting experiments were carried out on a CNC lathe. Machining was carried on AISI 4140 steel using coated carbide tool. The tool holder was PCLNR 2525 M12. Cutting fluid was used during the turning operations. Experiments were carried out under different cutting speeds in the ranges of 150–250 m/min. Feed rates employed were 0.05–0.2 mm/rev and depth of cut were 0.5-1.5 mm. Flank wear of the carbide insert was measured using a toolmaker microscope. The flank wears were measured in the interval of predetermined cutting time. The carbide insert was then taken out of the measuring microscope. After that the turning operation was resumed. This procedure was continued until the tool failed.

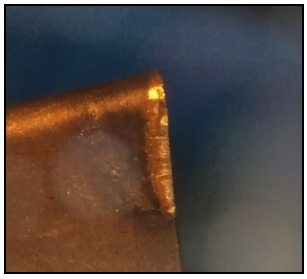

Figure 2. Example of a flank wear of one of the performed experiments.

The tool shank was attached to a three-component piezo-electric dynamometer (Kistler type 9257B) mounted on the cross slide of the lathe. The dynamometer was used to determine the cutting forces exerted during the cutting operation. The three components of the cutting force, axial, radial and tangential forces were amplified with the charge amplifier (Kistler type 5019) and then displayed in the screen using Dynoware software. Experimental equipment and ranges of cutting parameters are given in Table 1.

Table 1. Experimental equipment and materials and the ranges of cutting parameters.

Equipment			
Workpiece Material	AISI 4140		
Cutting Insert	WNMG 080404PP		
Machine Tool	Mori Seiki NL2500 (11 kW Lathe)		
Environment	Cutting Fluid		
Cutting Parameter	**Level 1**	**Level 2**	**Level 3**
Cutting Speed (m/min)	150	190	250
Feed Rate (mm/rev)	0.05	0.1	0.2
Depth of Cut (mm)	0.5	0.87	1.5

3. RESULTS AND DISCUSSION

In this section, the experimental results were evaluated and then the variations of wear and cutting forces as depending cutting time at the various cutting conditions to express the relationship between the cutting forces and the flank wear were discussed. The flank wear is caused by the abrasive and adhesive actions between the cutting tool and the machined surface. It starts at the cutting tip and then widens as the contact area increases, thus forming the wear land. The width, shape and growth rate of the wear land depend on the tool material, workpiece material and cutting parameters. Different cutting parameters that are used in experiments are given in Table 2. The first three set of experiments include various cutting speeds. The second three set of experiments include various cutting depths. The third three set of experiments include various feed rates.

Table 2. Cutting parameters used in experiments.

Experiment No.	Cutting Speed, *v* (m/min)	Feed Rate, *f* (mm/rev)	Depth of Cut, *d* (mm)
1	150	0.1	0.87
2	190	0.1	0.87
3	250	0.1	0.87
4	190	0.1	0.5
5	190	0.1	0.87
6	190	0.1	1.5
7	190	0.05	0.87
8	190	0.1	0.87
9	190	0.2	0.87

Figure 3(a) indicates the progression of tool flank wear and main cutting force for v=150 m/min, f=0.1 mm/rev and d=0.87 mm. It is clear that main cutting force increases when tool wear reaches 0.3 mm criteria. Figure 3(b) indicates the progression of tool flank wear and main cutting force for v=250 m/min, f=0.1 mm/rev and d=0.87 mm. Compared to Figure 3(a), same relationship is found but with a substantially shorter tool life. It can be seen that the increase of main cutting force with respect to cutting time is less than flank wear.

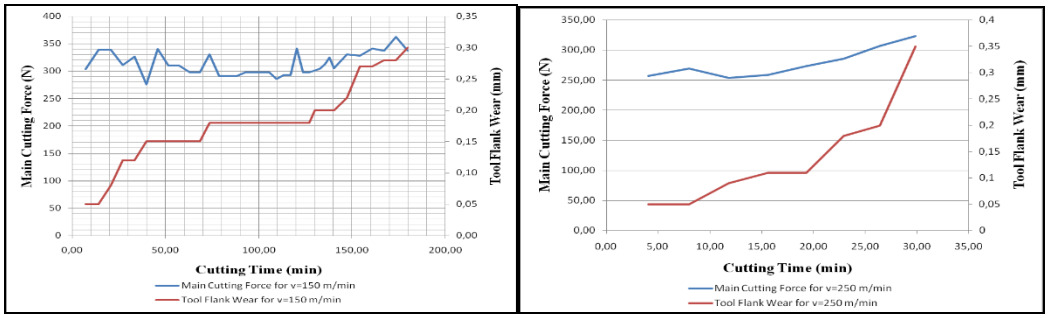

Figure 3. (a) Results for v=150 m/min. *(b) Results for v=250 m/min.*

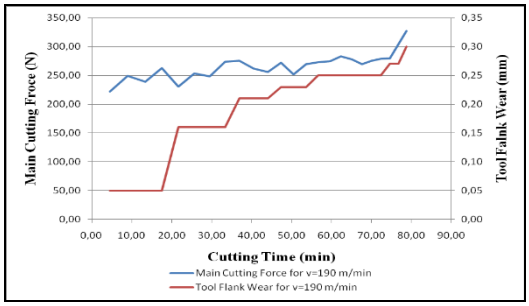

Figure 3. (c) Results for v=190 m/min.

Figure 4(a) indicates the progression of tool flank wear and main cutting force for f=0.05 mm/rev, v=190 m/min and d=0.87 mm. It is clear that main cutting force increased when tool wear reached 0.3 mm criteria. Figure 4(c) indicates the progression of tool flank wear and main cutting force for f=0.2 mm/rev, v=190 m/min and d=0.87 mm. Compared to Figure 4(a), same relationship is found but with a substantially shorter tool life.

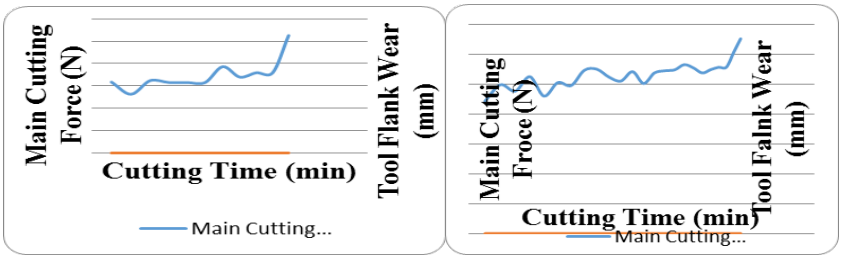

Figure 4. (a) Results for f=0.05 mm/rev. (b) Results for f=0.1 mm/rev.

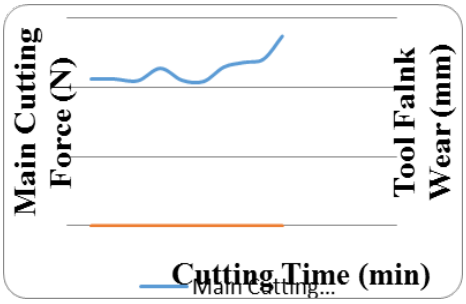

Figure 4. (c) Results for f=0.2 mm/rev.

Effect of parameters are analyzed in Figure 5(a), (b) and (c). In Figure 5(a), It is clear that the main cutting force reaches nearly same value for tool wear criteria (VB=0.3 mm), but in a shorter time when cutting speed is increased. Tool life where *v*=150 m/min cutting speed is used is dramatically better than the two remaining parameters(190m/min and 250 m/min).

In Figure 5(b), It can be seen that the main cutting force reaches different values for tool wear criteria, but in a shorter time for higher cutting depths. Tool life where 0.5 mm cutting depth parameter is used is better than the two remaining parameters(0.87 mm and 1.5 mm).

In Figure 5(c), It can be seen that the main cutting force reaches different values for tool wear criteria, but in a shorter time for higher feed rates. Tool life where 0.2 mm/rev feed rate parameter is used is extremely shorter than the two remaining parameters(0.05 mm/rev and 0.1 mm/rev).

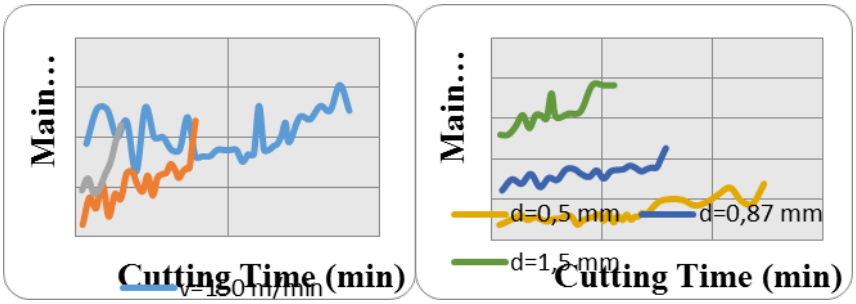

Figure 5. (a) Results for variable cutting speed, v. (b) Results for variable cutting depth, d.

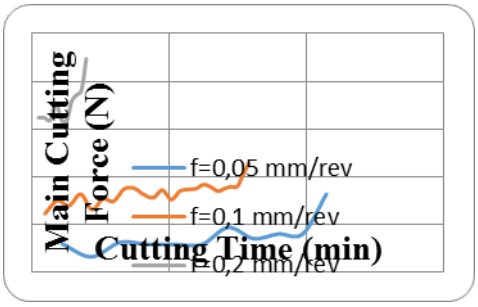

Figure 5. (c) Results for variable feed rate, f.

4. CONCLUSION

In conclusion, the relationship between tool flank wear and tangential cutting force is investigated for turning operation of AISI 4140 workpiece material with a WNMG cutting insert. Effect of the cutting parameters to both tool life and cutting forces is also investigated and results are given below.

- Total increase rate of tool flank wear is substantially higher than increase in tangential cutting force.
- When cutting depth and feed rate is constant, choosing higher cutting speed results in a shorter tool life. When cutting depth and cutting speed is constant, choosing higher feed rate results in a shorter tool life. When cutting speed and feed rate is constant, choosing higher cutting depth also results in a shorter tool life.
- The most convenient tool life is found for the parameters of *v*=150 m/min, *f*=0.1 mm/rev and *d*=0.87 mm.
- For constant cutting depth and feed rate, different cutting speeds results in nearly same cutting force.

- For constant cutting speed and feed rate, different cutting depths results in completely different cutting forces.
- For constant cutting speed and cutting depth, different feed rates results in completely different cutting forces.

REFERENCES

[1]. J. P. Davim, A. M. Baptista, "Relationship between cutting force and PCD cutting tool wear in machining silicon carbide reinforced aluminium", *Journal of Materials Processing Technology*, vol. 103, pp. 417-423, Jan. 2000.
[2]. B. Li, "A review of tool wear estimation using theoretical analysis and numerical simulation Technologies", *Int. Journal of Refractory Metals and Hard Materials*, vol. 35, pp. 143–151, May. 2012.
[3]. H.Z. Li, H. Zeng, X.Q. Chen, "An experimental study of tool wear and cutting force variation in the end milling of Inconel 718 with coated carbide inserts", *Journal of Materials Processing Technology*, vol. 180, pp. 296–304, Jul. 2006.
[4]. LJ Xie, J. Schmidt, C. Schmidt, F. Biesinger, "2D FEM estimate of tool wear in turning operation", *Wear*, vol. 258(10), pp. 1479–1490, Nov. 2005.
[5]. J. Hu, Y.K. Chou. "Characterizations of cutting tool flank wear-land contact", *Wear*, vol. 263(7–12), pp. 1454–1458, Jan. 2007.
[6]. C. Scheffer, H. Kratz, P.S. Heyns,, F. Klocke, "Development of a tool wear-monitoring system for hard turning" *International Journal of Machine Tools & Manufacture*, vol. 43, pp. 973–985, Apr. 2003.
[7]. T. Wong, W. Kim, P. Kwon "Experimental support for a model-based prediction of tool wear", *Wear*, vol. 257, pp. 790–798, Mar. 2004.
[8]. S.K. Sikdar, M. Chen, "Relationship between tool flank wear area and component forces in single point turning" *Journal of Materials Processing Technology*, vol. 128, pp. 210–215, Jun. 2002.

ICENS
INTERNATIONAL CONFERENCE ON ENGINEERING AND NATURAL SCIENCES
24-28 May 2016 /Sarajevo

The Effects of Weathering State on the Shear Strength of Discontinuity: A Case Study on the Weathered Granitic Rock Joints, NE Turkey

Sener Ceryan[1],Samet Berber[2], Nurcihan Ceryan[1]

Abstract

The aim of the study is that effects of the weathering state on shear strength of discontinuities are investigated. In order to determine the shear strength of discontinuities which have various weathering degrees and roughness, pull tests, tilt test, and direct shear test were carried out and empirical approach was applied on the samples from Kurtun Granatoid NE Turkey. Before these testing, weathering conditions, weathering depth, roughness and strength and filling of the discontinuities surface were defined. And weathering state of discontinuity surface was determined by macroscopic observation, simple mechanical tests and thin section taking from discontinuity wall. The persistence of these discontinuity surfaces is 100%. The statically meaningful relationships between friction angles and the properties including joint roughness coefficient and weathering degree of the joint wall were found. According to the results of the study, the peak friction angle of discontinuities surfaces found by the pull tests depend mainly on surface roughness, wall strength and the filling material type while the basic friction angle depend on surface mineralogy.

Keywords*: shear strength, discontinuity, weathering, direct shear test, pull test, granitic rock, NE Turkey,*

1. INTRODUCTION

In mining, civil, and petroleum engineering, engineers often face problems associated with jointed rock mass. The mechanical behavior of rock masses and the stability conditions of natural or excavated slopes are mostly controlled by the discontinuity network and the mechanical behavior of the discontinuities. And, it is important to study a single joint for comprehensively evaluating the mechanical behavior of jointed rock mass [1]. The shear mechanism of discontinuity is strongly affected by loading conditions and discontinuity surface conditions including roughness, filling material, discontinuity wall compressive strength It is known that discontinuity surface conditions mainly depends on the weathering state. A natural rock joint surface may degrade progressively by means of chemical or mechanical weathering processes. These weathering processes may reduce the shear strength of a rock joint by modifying the joint surface geometry, by chemical decomposition, by reduction uniaxial compressive strength of the joint wall, by widening joint openings, or by filling the joint opening with fine particles [2]. It can be said that the Joint Roughness Coefficient representing the roughness of joint wall and the uniaxial compressive strength of the joint wall are decreasing with increasing of the weathering. In decomposition progresses, the amount of the softer minerals is increasing in the joint wall. Therefore, it is expected to reduce the shear strength of the discontinuities with increasing of weathering. In this study, the changes of basic and peak friction angles of the natural joint wall due to weathering were investigated. Basic friction angle (ϕ_b) represent minimum shear resistance of the joint wall. Conceptually, ϕ_b refers to smooth, planar surface in joint wall and can be considered as a material constant. In the literature, peak friction angle was defined as the sum of the basic friction angle and dilation angle (i). The dilation angle is the angle of inclination to the shear stress direction due to surface irregularities and visible roughness. The different shear strength models were suggested by the researches. In the study, Mohr-Coulomb criterion was taking into consideration and also Barton's criterion was applied to obtain the shear strength of the natural individual joint from the granitic rocks exposed in Kurtun (Gumushane) NE turkey. In order to evaluate the effects of the weathering state on shear strength of discontinuities, the pull tests in the field and direct shear test were performed on the natural joint samples. And then, the basic and peak friction angles obtained by the said test were associated with the weathering degree of the joint wall.

[3] *Corresponding author :Department of Geological Engineering, Balikesir University, Balikesir, Turkey, sceryan@balikesir.edu.tr*

[2]*Department of Geological Engineering, Balikesir University, Balikesir, Turkey*

[3] *Mining and Mineral Extraction Department, Balıkesir University, Balikesir, Turkey*

2. METARIAL AND METHODS

2.1 Geological Setting

In this study, rock joints of Kurtun granitoids exposed on the area between Kurtun (Gumushane) NE Turkey (Fig.1) were tested. The Kurtun granodiorite is a Late Cretaceous batholith, intruding Late Cretaceous volcanoclastic rocks [3]. The intrusion comprises hornblende-biotite-granodiorite, crosscut abundantly by dykes of quartz porphyry, dacite and dolerite. The granodiorite is holocrystalline with an equigranular texture and some porphyritic mega crystals of plagioclase. The constituent minerals are plagioclase, quartz, alkali feldspar, biotite, and hornblende and, locally, clinopyroxene Accessory phases are ilmenite, magnetite and titanite. Hydrothermally formed minerals include chlorite, calcite, quartz and epidote. The granitdiorite joint samples were taken directly from rock blocks in cut slopes along a highway on the study area [3].

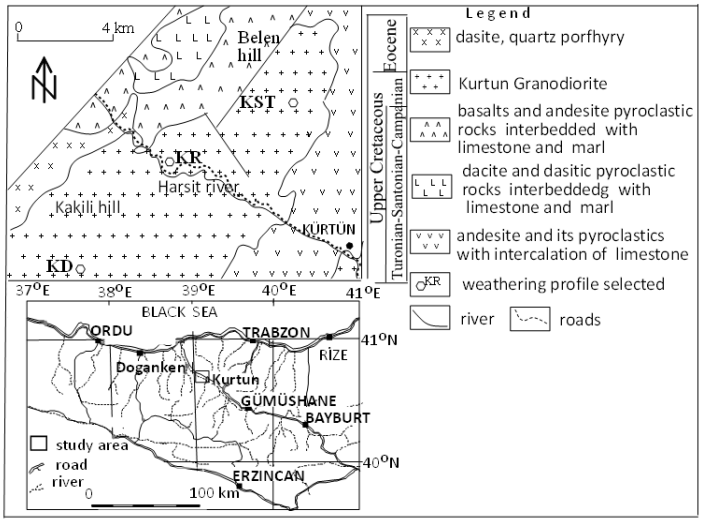

Figure 1. The geology of the study area [3]

2.2 The measuring of the joint wall properties

The pull test in the field and the laboratory direct shear test were performed on the joint samples investigated (Fig. 2). Before these tests, the properties of discontinuities surface including weathering state, roughness, filling material, joint wall strength, weathering to depth, was investigated. In order to the weathering state of the joint wall, the mineralogical and petrographic analysis in thin-section and macroscopic investigation with naked eyes and magnifier were performed. And the definition weathering degree was obtained with Schmidt hammer rebound test (Eq. 1, Table 1)

$$Wc=(R_f/R_w) \quad (1)$$

Where R_f: Schmidt hammer rebound value for unweathered rock materials, R_w: Schmidt hammer rebound value for discontinuity surface Wc <1.1in fresh surface, 1.1<Wc<1.5 in slightly weathered surface, 1.5<Wc<2.0 in moderately weathered, Wc>2.0 in highly weathered surface ([4]

Schmidt hammer rebound test on the joint walls constitutes an appropriate method of evaluating the JCS index. The relative weathering of joint walls can also be characterized by the ratio between the uniaxial compressive strength of the rock material (UCS) and the JCS value estimated by the Schmidt hammer rebound test. In this study, the following statically relationships suggested by Ceryan [5] was used to estimate UCS of joint wall (UCSjw) and the Schmidt hammer rebound value (R)

$$UCSjw=0.00276R^{2.86} \quad (2)$$

(a) (b)

Figure 2. The joint samples for pull test (a) and direct shear test (b)

Barton and Choubey [6] proposed 10 standard rough-ness profiles corresponding to JRC (Joint Roughness Coefficient) values ranging from 0 to 20. Most of the joint surface roughness values can be determined from a visual comparison of these 10 standard profiles (Fig. 3a). The appearance of the discontinuity surface is compared visually with the profiles shown and the JRC value corresponding to the profile which most closely matches that of the discontinuity surface is chosen. In the case of small scale laboratory specimens, the scale of the surface roughness will be approximately the same as that of the profiles illustrated [7]. However, in the field the length of the surface of interest may be several meters or even tens of metros and the JRC value must be estimated for the full scale surface. An alternative method for estimating JRC is presented in Figure 3b [7]. In this study, Figure 3a was used to define roughness of the laboratory specimens, while Figure 3b was used to define roughness of the pull test specimens

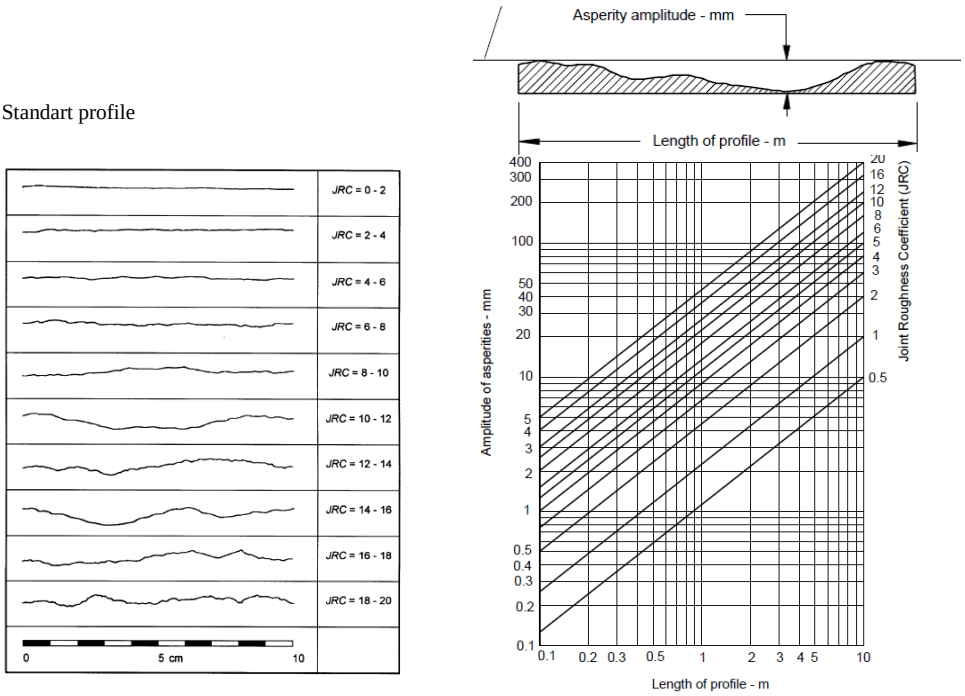

Figure 3. Roughness profiles and corresponding Joint Roughness Coefficient values [6] (a) and Figure 6: Alternative method for estimating JRC from measurements of surface roughness amplitude from a straight edge [7] (b).

2.3 Pull test in-situ and direct shear tests in laboratory

The construction of this experiment are given in the following figures (Figure 4a-b. This experiment was repeated at least 4 times for the same surface discontinuities. At results of the pull test, the peak friction angle of the joint walls investigated were obtained. Direct shear tests were conducted on 8 joints samples groups so as to determine the basic friction angle. The joint samples investigated were taken directly from the granitic rocks exposures in the study area. Direct shear test carried out according to the ISRM suggested methods [8].

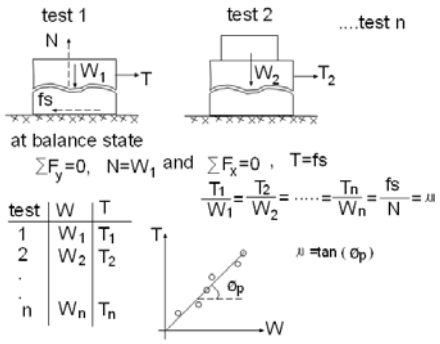

(W: weight of block,
T: pull force,
fs: friction force,
N: normal force,
Fx: the forces in the direction *x* ,
Fy: the forces in the direction *y*,
μ: the confident of the friction the joint wall,
ϕp; peak friction angle of the joint wall)

Figure 4. The pull tests procedure

The samples were fixed into the mold and were hardened with concrete. Shear rates were selected 0.2-0.3 mm/min. Total shear displacement ranged between 5.0 and 16.0 mm. In order to obtain the basic friction angle for the same joint group, at least five normal stresses related to the in-situ stress were imposed on the joint specimens. In the individual test, shear stress, shear displacements ($\Delta\delta$) and dilation (Δv) were measured. Shear stress-shear displacements curves under different normal stress level changed 0.2 to 1.6 MPa were plotted. And, the correction was made for dilation using following equations [1]. Then normal stress- shear stress graph was plotted (Fig. 5-6).

$i=\tan^{-1}(\Delta h/\Delta \delta)$, $\sigma_i=(\sigma \cos i+ \tau \sin i)\cos i$ and $\tau_i=(\tau \cos i- \sigma \sin i)\cos i$ (3)

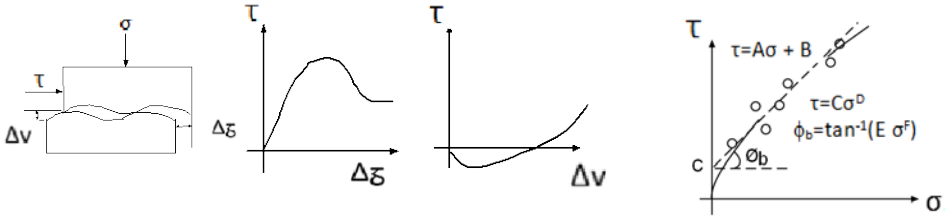

Figure 5. The Direct shear tests procedure

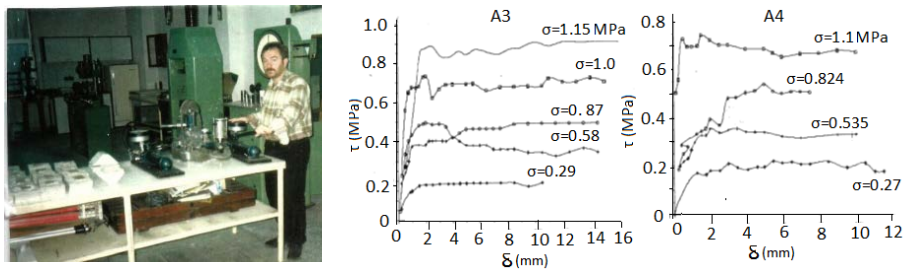

Figure 6. The Direct shear tests apertures and the shear stress- shear displacements curves obtained in the test.

The relationships between σ and τ were obtained as linear and non-linear. In the Figure 5 A, B, C, D, E and F are the coefficients of these relationships. With this way, basic friction angle of the joint wall, was obtained. Cohesion values obtained in the laboratory should be treated with caution and may not be representative of cohesion in the field.

2.4 Barton's criterion

Barton's criterion is based on the choice of the correct value for the roughness parameter, the joint roughness coefficient (JRC). After recognizing the inadequacy of the linear Coulomb model, Barton [9] proposed an empirical criterion for the shear strength of the unfilled joint (that is, there is rock-to-rock contact across the plane), as follows:

$$\tau_p = \sigma_n \tan\left[\mathrm{JRC}\log_{10}\left(\frac{\mathrm{JCS}}{\sigma_n}\right) + \phi_b\right] \quad (4)$$

Where σ_n is the effective normal stress acting on the joint, JRC is the joint roughness, JCS is the unconfined compressive strength of the rock immediately surrounding the joint (joint wall) and ϕ_b is the basic friction angle. There are some constraints on the use of the criterion, as follows [10];

-Barton and Choubey [6] recommended that the peak shear strength curves should be truncated for design purposes at a maximum allowable shear strength given by arctan $(\tau/s\ \sigma_n)=70^o$

-For unfilled joints the roughness and compressive strength of the walls are important, whereas in the case of filled joints the physical properties of the material separating the joint walls are of primary concern. Barton's criterion is only valid where joint walls are in rock-to-rock contact [6].

-Due to the relatively low normal stress levels involved in the determination of the criterion, Hoek and Bray [11] reported that the criterion is valid for the normal stress range $0.01< \sigma_n /JCS<0.3$

3. RESULT AND DISCUSSION

The results of the pull test in the field performed on the joint samples with different weathering state, roughness, filling material, joint wall strength, weathering to depth were given at Table 1).

Table 1. The surface characteristics of the joint wall investigated and peak friction angles from the pull test

No	JRC	R	JCS	W_c	Surface condition	ϕ_p
1a	11	46	153.77	1.09	Unaltered joint walls, surface staining only	49.9
1b	11	46	153.77	1.09	Clayey sandy-silt coatings, slightly weathered, weathering to depth<roughness	42.8
1c	11	46	153.77	1.09	Clay coating, weathering to depth<roughness	39.8
2a	7	37	82.49	1.35	surface staining, slightly weathered, weathering to depth<roughness	49.5
2b	7	37	82.49	1.35	clayey sandy-silt coatings, slightly weathered, weathering to depth<roughness	40.2
2c	7	37	82.49	1.35	Clay coating, slightly weathered, weathering to depth<roughness	37.1
3a	8	34	64.77	1.47	surface staining, moderately weathered, weathering to depth<roughness, wet surface	37.7
3b	8	34	64.77	1.47	clayey sandy-silt coatings, moderately weathered, weathering to depth<roughness	30.9
3c	8	34	64.77	1.47	Clay, moderately weathered, thickness of infilling materials equal to roughness	26
4a	11	37	82.49	1.35	surface staining, moderately weathered, weathering to depth<roughness	42.4
4b	11	37	82.49	1.35	Sandy clayey silt, moderately weathered, weathering to depth<roughness	36.8
4c	11	37	82.49	1.35	Clay coating, moderately weathered, thickness of infilling materials < roughness	31
5a	7	14	5.12	3.57	surface staining, highly weathered, weathering to depth>roughness	35.5
5b	7	14	5.12	3.57	Sandy clayey silt, highly weathered, weathering to depth>roughness	29.7
5c	7	14	5.12	3.57	Clay coating, highly weathered, weathering to depth>roughness	24.2
6a	10	48	173.7	1.04	Unaltered joint walls, surface staining only	45.8
6b	10	48	173.7	1.04	surface staining, slightly weathered, weathering to depth<roughness	40.1
7a	8	39	95.9	1.28	surface staining, slightly weathered, weathering to depth<roughness	36.0
7b	8	39	95.9	1.28	Sandy clayey silt, slightly weathered, weathering to depth<roughness	31.2
8a	12	43	126.79	1.16	surface staining, slightly weathered, weathering to depth<roughness	48.3
8b	12	43	126.79	1.16	Sandy clayey silt, slightly weathered, weathering to depth<roughness	42.8
8c	12	43	126.79	1.16	Clay coating, slightly weathered, weathering to depth>roughness	32

In the Table 1, JR is joint roughness coefficient, R is Schmidt hammer rebound , JCS is joint wall strength (MPa), ϕ_p is peak friction angle (degree) and W_c is weathering degree of joint wall

JRC concerns the surface geometry of the discontinuity walls; this has an important influence on the mechanical properties, especially under low normal stress. In this study, the pull test were carried out under low normal stress. Although JRC values of joint surfaces that are more weathered (moderately and highly weathered) are equal to or greater compared to those of fresh or slightly weathered joint wall instigated, the peak friction angles of the fresh surfaces are generally higher (Table 1). This is

due to the weathering effects, which greatly reduce the peak friction angle of weathered joint wall. In contrast, the roughness of the joint wall has the greatest effect for fresh joints wall. The statically meaningful relationships between peak frictional angel (ϕp) and the joint wall characteristics including joint roughness coefficient (JRC) and weathering degree (W_c) was obtained for the granitic joint wall investigated.

$$\phi_p = \tan^{-1}(0.992\ (JRC/20) - 0.103\ W_c + C) \quad (R^2=0.732) \qquad (5)$$

where ϕ_p is peak frictional angel JRC is joint roughness coefficient, W_c is weathering degree C is 0.558, -0.1227 and -0.19443 for clean, clayey sandy-silt coatings and clay coating, respectively

The weathering degree of the surface of discontinues (joint wall) was described according to petrographical analysis in thin section (Table 2). The second minerals ratio, SM is <6% in the fresh surfaces, 6-25% slightly weathered surface, 25-35 in the moderately weathered surface and >35% in the highly weathered surface. In decomposition progresses, the amount of the softer minerals is increasing in the joint wall. According to the result of the direct shear tests, the basic friction angles is decreasing with weathering (Table2 and Fig. 7). And, the following relationships between the weathering degrees obtained by Schmidt hammer rebound value and the basic friction angles of the joint wall.

$$\phi_b = \tan^{-1}(0.6537 Wc^{-0.2123}) \quad (R^2=0.741) \qquad (5)$$

Table 2. The surface characteristics of the joint sample for the direct shear test

No	R	JCS	Wc	Condition
G	50	195.6	1.0	Fresh, no visible signs of weathering are seen, but hydrothermal alteration caused some changes on minerals. SM second minerals ratio, SM= 6%
F1	48	173.7	1.04	Discoloration, slightly weathered, weathering to depth<roughness, Sericite and epidote have developed on 18 % of the plagioclases, 15 % of ortachlase shows dissolution, 27% of biotite and 28% of horblende have altered to epidote, chlorite and oxide minerals. SM=23%
F2	46	1538	1.09	Discoloration, slightly weathered, weathering to depth<roughness, Sericite and epidote have developed on 24% of the plagioclases, 11% of ortachlase shows dissolution, 23% of biotite and 27% horblende have altered to epidote, chlorite and oxide minerals. SM=21%
E	33	59.47	1.53	Discoloration, moderately weathered, weathering to depth > roughness 34% of the plagioclase has decomposed to sericite. epidote and clay minerals.25% of the orthoclase has decomposed to sericite and clay minerals. Chlorite, epidote. Fe-oxides and clay minerals growths make 43 % of biotite and hornblende. SM= 33%
D	37	82.49	1.35	Discoloration, Fe oxide stained, Slightly weathered Weathering to depth equal to roughness, 30% of the plagioclase has decomposed to sericite. epidote and clay minerals. 21% of the orthoclase has decomposed to sericite and clay minerals. Chlorite, epidote. Fe-oxides and clay minerals growths make 35 % of biotite and hornblende. SM= 31%
C	31	49.73	1.62	Discoloration, moderately weathered, weathering to depth> roughness 37% of the plagioclase has decomposed to sericite. epidote and clay minerals.27% of the orthoclase has decomposed to sericite and clay minerals. Chlorite, epidote. Fe-oxides and clay minerals growths make 28 % of biotite and hornblende. SM= 34%
B	18	10.56	2.78	Highly weathered, weathering to depth> roughness 45% of plagioclase turns to epidote and clay minerals. 52 % of orthociase show dissolution effects and on their surfaces clay minerals develop. 58 % of biotite and hornblende turns to chlorite, clay and opaque minerals SM= 43%
A	14	5.61	3.57	Highly weathered, weathering to depth> roughness 48% of plagioclase turns to epidote and clay minerals. 59 % of orthociase show dissolution effects and on their surfaces clay minerals develop. 68 % of biotite and hornblende turns to chlorite, clay and opaque minerals SM= 58%

According Barton's criterion, shear strength of the joint wall is depended on normal stress, joint roughness (JRC), basic friction angles and the uniaxial compressive strength (UCS) of the joint wall. In the granitic rock masses with different weathered degree investigated in the study, JRC is decreasing with weathering. This is also valid for the joint samples investigated (Fig. 8). In the same, the UCS of the joint wall investigated is decreasing with weathering (Table 2). Therefore, shear strength of the joint wall is decreasing with weathering. The difference between the shear strength of fresh and weathered surfaces is not very clear. Other hand, the decreasing of the shear strength of the joint wall due to weathering is accelerated from the moderately weathered degree. (Fig. 8)

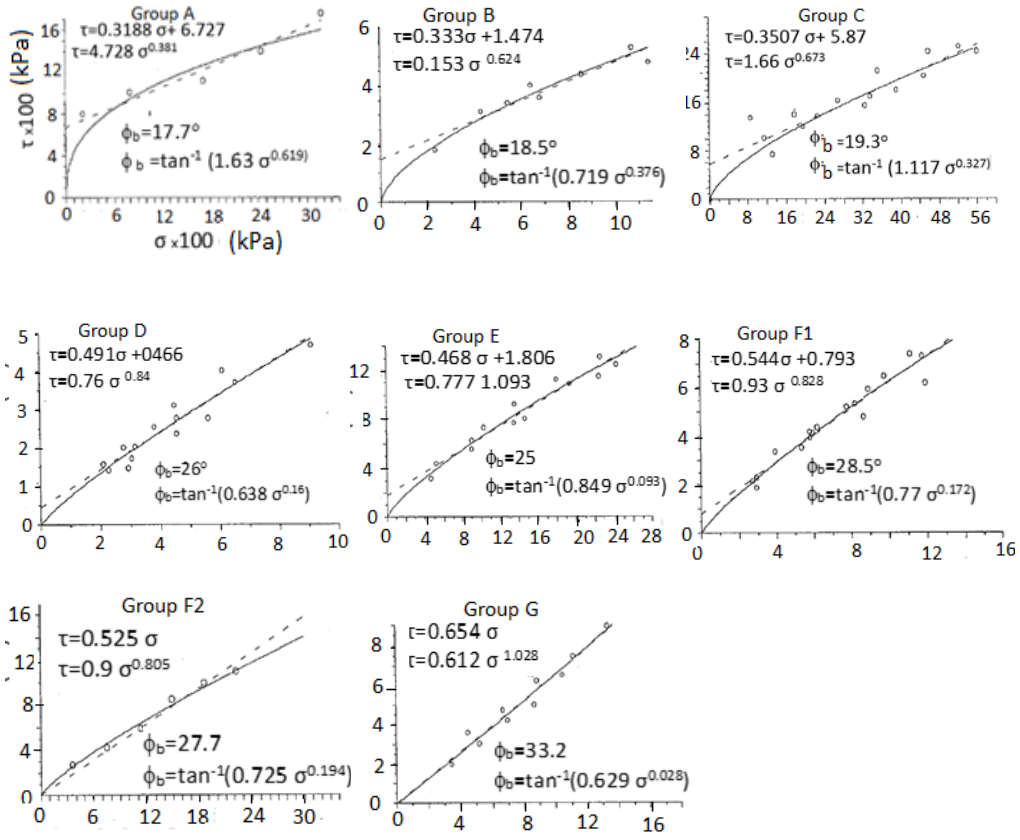

Figure 7. The measured the basic friction angles and curves obtained the direct shear test carried on the joint samples group

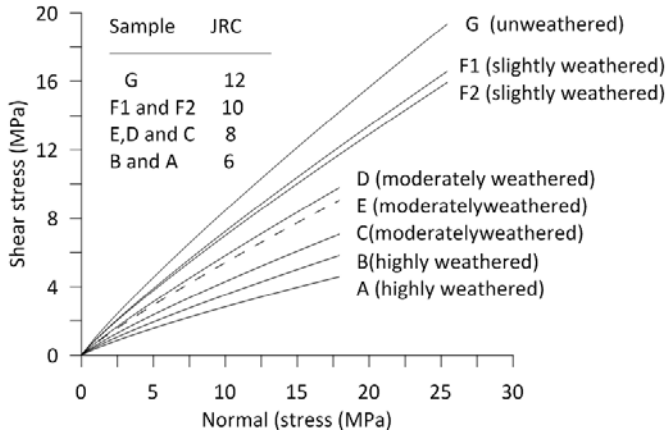

Figure 8. The measured peak shear strength and curves calculated by Barton's criterion for the joint samples group

4. CONCLUSION

In the study, effects of the weathering state on shear strength of discontinuities from the granitic rocks, NE turkey are investigated. These granitic joint wall samples have various weathering degrees and roughness. On these samples, pull tests, and laboratory direct shear test were carried out and the Barton's criterion was applied. The relationships between peak and basic friction angles of the joint wall and weathering degree were found. In addition, the shear strength of the joint wall with different weathered degree were obtained from the Barton's criterion. This study shows, however, some limits: the influences of mineral size of granite joint surface on the shear strength were not considered. The results of the test performed in the study and relationships are valid for the granitic joint wall investigated .And, Similar studies for different rock may be useful.

REFERENCES

[1] Hencer, S.R. "The Implications of Joints and Structure for Slope Stability", Slope Stability (Editors: M.G. Anderson and K.S. Richards), John Wiley& Sons Ltd., 1987, p: 145-185.
[2] Woo, I., Fleurisson, J.A. and Park, H.Y. " Influence of weathering on shear strength of joints in a porphyritic granite rock mass in Jechon area, South Korea" Geosciences Journal Vol. 14, No. 3, p. 289 − 299, 2010
[3] Ceryan, S. "New Chemical Weathering Indices for Estimating the Mechanical Properties of Rocks: A Case Study from the Kurtun Granodiorite, NE Turkey" Turkish Journal of Earth Sciences, 2008, 17, 187–207
[4] Gokceoglu, C. and Aksoy, H. "New approaches for the characterization of clay-bearing, densely jointed and weak rock masses", Engineering Geology, 2000. 58 (1), 1-23.
[5] Ceryan S. "Weathering of Harsit Granitoids, Classification and Effects of Weathering on Engineering of the Granitoids", PhD. Thesis, Karadeniz Technical University, Trabzon, Turkey, 1999, (in Turkish)
[6] Barton, N. and Choubey. V. "The shear strength of rock joints in theory and practice",Rock Mech., 1977,10:1–54
[7] Barton, N.R. and Bandis, S.C." Effects of block size on the the shear behaviour of jointed rock". 23rd U.S. Symp. on Rock Mechanics, Berkeley, ş-760.
[8] International Society for Rock Mechanics, ISRM 2007. The Complete ISRM Suggested Methods for Rock Characterization, Testing and Monitoring; 1974-2006, suggested Methods prepared by the Commission on testing Methods. ISRM. R. Ulusay and J.A. Hudson (eds). Kozan Ofset. Ankara
[9] Barton N. "Review of a new shear strength criterion for rock joints". Engineering Geology, 1973,7, 287–332.
[10]Wines, D.R. and Lilly, P.A. "Estimates of rock joint shear strength in part of the Fimiston open pit operation in Western Australia", International Journal of Rock Mechanics & Mining Sciences, 2003, 40,929–937
[11] Hoek, E. and Bray, J.W. "Rock slope engineering, 3rd ed. London:Institute of Mining and Metallurgy, 1981.

Temperature Dependent Electrical Parameters of NiO/n-Si Heterojunction

Omer Celik[1],Yusuf Selim Ocak[1], Savin H. Omar[1], Sezai Asubay[1]

Abstract

In this study, it was aimed to obtain NiO/n-Si heterojunction and determine its temperature dependent electrical properties. For this aim, NiO thin films were growth on an n-Si semiconductor and a glass by radio frequency (RF) reactive sputtering technique. High purity Ni was used as target and oxygen was used as reactive gas. Al metal was evaporated to obtain front contact. Temperature dependent electrical parameters of Al/NiO/n-Si heterojunction were executed its current-voltage (I-V) measurements between 305 and 480 K in dark. It was seen that electrical parameters such as ideality factor, barrier height and series resistance were strongly sensitive to temperature. Furthermore, optical properties of thin film on a glass were analyzed by means of uv-vis data.

Keywords: *NiO; Heterojunction, Electrical properties*

1. INTRODUCTION

Nowadays, metal oxides are popular in the formation many a number of devices because of their electrical and optical properties. Most of the oxide semiconductors such as zinc oxide (ZnO) and indium doped tin oxide (ITO) have n-type semiconducting property. To find a suitable p-type metal-oxide-semiconductor has a great interest. Nickel oxide with NiO chemical formula is p-type conductivity with high band gap. There is a great interest on NiO thin films owing to their excellent electrical, optical and magnetic properties as well as good chemical stability. They have been used p-type transparent conducting films for solar cells, active layer in the fabrication of chemical sensors, ultra violet light emitting diodes, photodedectors and in electrochromic devices [1-4]

NiO thin films have been grown on different substrates using various methods including spin coating, spray pyrolysis, chemical vapor deposition and sputtering. Among all methods, magnetron sputtering technique is a unique method to obtain uniform thin films of ceramics refractory metals or ceramics.

In this study, it was aimed to obtain NiO/n-Si heterojunction and determine its temperature dependent electrical properties. For this aim, NiO thin films were growth on an n-Si semiconductor and a glass by radio frequency (RF) reactive sputtering technique. High purity Ni was used as target and oxygen was used as reactive gas. Al metal was evaporated to obtain front contact. Temperature dependent electrical parameters of Au/NiO/n-Si heterojunction were executed its current-voltage (*I-V*) measurements between 305 and 480 K in dark. It was seen that electrical parameters such as ideality factor, barrier height and series resistance were strongly sensitive to temperature. Furthermore, optical properties of thin film on a glass were analyzed by means of uv-vis data.

2. MATERIALS AND METHODS

An n-Si wafer with (100) orientation and 1-10 □cm resistivity i
trichloroethylene and cleaned by ultrasonically vibrating in acetone and methanol for 5 min. After each step, the wafer was washed with deinozed water. After cleaning procedures, the wafer is dried under nitrogen ambient. The n-Si semiconductor was put into the vacuum chamber. Au metal was evaporated at 10^{-6} Torr and n-Si/Au structure was annealed under nitrogen ambient for 3 min at 420 °C to make high quality ohmic contact. NiO thin films were growth on n-Si semiconductor and glasses by reactive sputtering technique using Nanovak NVTS 400 vacuum system. Ni metal was used as target and O_2 was used as reactive gas. Pressure of the vaccum system was decreased at 10^{-6} Torr. Argon gas was send to system and the pressure was increased to 20 mTorr. The flow of the Argon gas was about 4 ccm. 80 W power was applied to high purity Ni target and 0,4 ccm oxygen was send to vacuum system to make reactive sputtering process. This process continued 10 minutes. The substrate temperatures were kept at 40 °C during sputtering process. To increase crystallianity, NiO thin films were annealed at 500 °C for 30 minutes in air ambient. Au metal was evaporated to obtain front contact. The circular diameters of the Au contacts were about 1.5 mm. To make circular front contacts a shadow mask is used. The schematic

[1] *Corresponding author: Dicle University, Faculty of Education, Department of Physics, 21280, Diyarbakır, Turkey, celiko21@yahoo.com*

diagram of Au/NiO/n-Si device is given in Fig. 1. Temperature dependent electrical characteristics of Au/NiO/n-Si structure were analyzed using its current-voltage (*I-V*) measurements between 305 and 480 K by the help of Keitley 2400 sourcemeter. Optical properties of the thin film on a glass were analyzed using Shimadzu 3600 Uv-vis-nir spectrophometer.

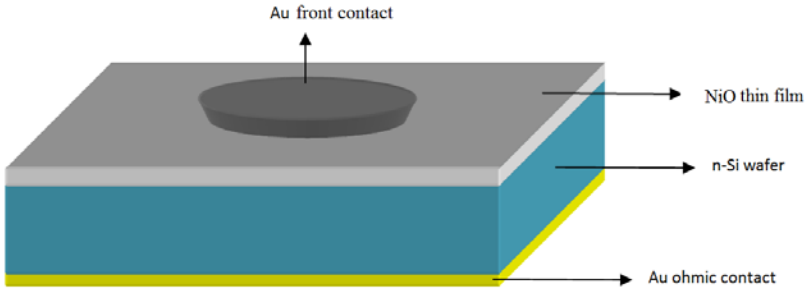

Figure 1. The schematic diagram of Au/NiO/n-Si devices

3. RESULTS AND DISCUSSION

UV-Vis spectra were used to determine the optical properties of the reactively sputtered NiO thin film. The film was deposited on a glass and its absorbance and transmittance properties were determined. Figure 2 shows the both absorbance vs. wavelength and transmittance vs. wavelength plots. As seen from the figure, the transmittance value of the NiO thin film has a sharp increase between 300 and 500 nm. The transmittance value is NiO thin film at 300 nm is 59 % and this value reaches 88 % at 530 nm. The increase continues till 1000 nm. At 1000 nm the transmission value of the film is 98 %. After 1000 nm the transmittance of the film is nearly constant. It means that the NiO thin film is very transparent visible region and nearly full transparent in infrared region.

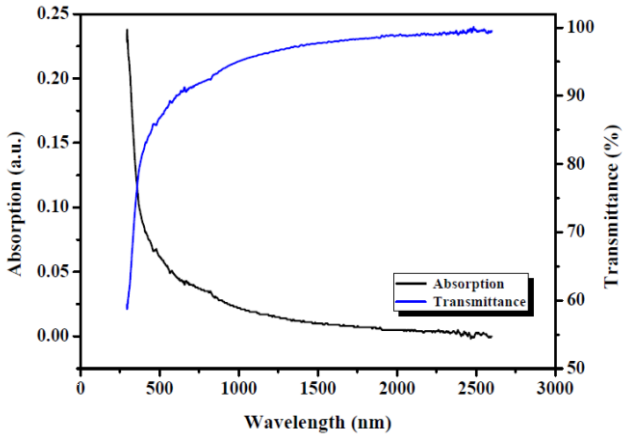

Figure 2. Absorbance vs. wavelength and transmittance vs. wavelength plots of NiO thin film on a glass

Furthermore, the absorbance of the film decreases sharply between 300 and 500 nm. The decrease continues till 1000 nm. After 1000 nm, the film has nearly no absorbance.

The optical band gaps (E_g) of the NiO can be calculated through the equation

$$\alpha h\nu = B(h\nu - E_g)^m \qquad 1$$

where α is the absorption coefficient, B is a constant, h is the Plank constant, m is ½ for direct band gap and 2 for indirect band gap. NiO has direct band gap. Therefore, the direct band gap of reactive sputtered NiO thin film was determined by using absorption vs. wavelength data with the help of equation 1 using $(Ahv)^2$–hv plot. Figure 3 shows the $(Ahv)^2$–hv thin film. The E_g of the NiO thin film was determined as 3.02 eV by extrapolating the straight line of the graph to intercept the photon energy.

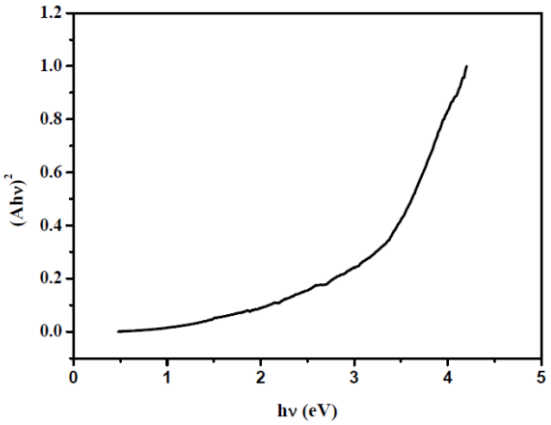

Figure 3. (Ah ²-H) plot of NiO thin film on a glass

Current-voltage measurements of NiO/n-Si heterojunction showed that the device had an excellent rectification. When the series résistance of a diode is taken into account, the relationship between current and voltage is given as [5]

$$I = I_0 \exp\left(\frac{q(V - IR_s)}{nkT}\right) \qquad 2$$

where, q is the electron charge, V is the applied voltage, R_S is the series resistance, n is dimensionless ideality factor, k is the Boltzmann constant, T is the absolute temperature and I_0 is the saturation current which can be written

$$I_0 = AA^*T^2 \exp\left(-\frac{q\Phi_b}{kT}\right) \qquad 3$$

Where A is the diode area, A^* Richardson constant, Φ_b is the barrier height. The ideality factor of a diode can be calculated from the slope of the linear region of the InI-V plot of the diode using the equation

$$n = \frac{q}{kT}\frac{dV}{d\ln(I)} \qquad 4$$

The ln$I$-V plots of Au/NiO/n-Si structure measured between 305 and 480 K are given in Figure 4. The ideality factor at 305 K calculated as 2.472. The idality factor of for an ideal diode is should be unity. The deviation from 1 shows non-ideal diode behavour. This deviation can be because of the effects of native insulator layer on n-Si surface, interface states and the effect of series resistance. The electrical parameters of the Au/NiO/n-Si diode are given in table 1. As seen from the table, the idality factor of the structure decreases by increasing temperature. The ideality factor decresed from 2.472 (305 K) to 1.704 (480 K). Similar results have been reported for vaious heterojunctions. Tombak et al [6] formed Coumarin 30/p-Si heterojucntion device and determined its basic electrical parameters in the range from 300 and 380 K. They reported that the ideality factor decreased from 2.2 to 1.77.

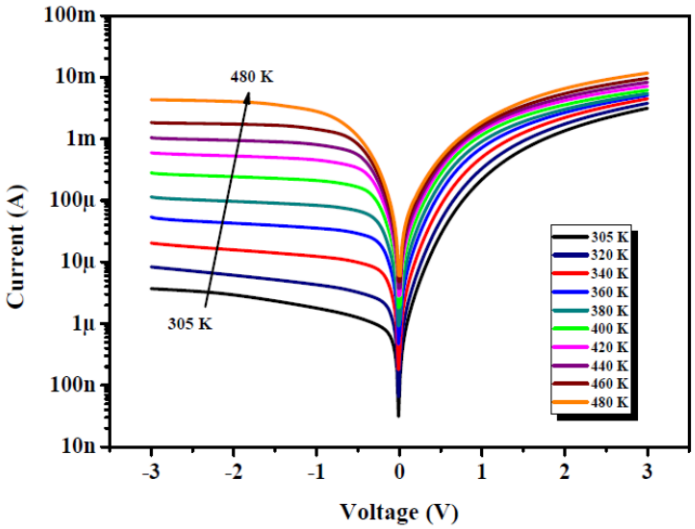

Figure 4. lnI-V plots of Au/NiO/n-Si structure between 305 and 480 K

Table1. Some electrical parameters of NiO/p-Si heterojunction

	lnI-V			Norde		
Temperature (K)	*n*	□ (eV)	*F* (*V*$_0$) (V)	*V*$_0$ (V)	□ (eV)	*R*$_S$ (□)
305	2.472	0.725	0.7126	0.1114	0.723	9279
320	2.372	0.747	0.7321	0.1115	0.742	7136
340	2.245	0.777	0.7593	0.1116	0.767	4863
360	2.121	0.807	0.7860	0.1117	0.792	3222
380	2.013	0.841	0.8163	0.1314	0.827	1951
400	1.946	0.871	0.8598	0.0711	0.861	499
420	1.887	0.905	0.8911	0.0713	0.890	481
440	1.828	0.941	0.9280	0.0516	0.916	369
460	1.784	0.978	0.9602	0.0711	0.956	275
480	1.704	1.014	0.9942	0.0916	0.999	243

The barrier height of the junction can be calculated using I_0 value obtained from interception of In*I-V* plot to *I* axis by the help of the equation

$$\phi_b = \frac{kT}{q}\ln\left(\frac{AA^*T^2}{I_0}\right) \qquad 5$$

The barrier heights of the device were calculated using saturation current values by the help of the equation 5. Barrier height value of Au/NiO/n-Si device determined as 0.725 eV at 305 K. Table 1 and Figure 5 also show the increases of barrier height from 0.725 to 1.014 eV with increasing the temperature i*n the range* between 305 and 480 K. As seen from both table and figure, the increase in barrier height linearly depend on temperature.

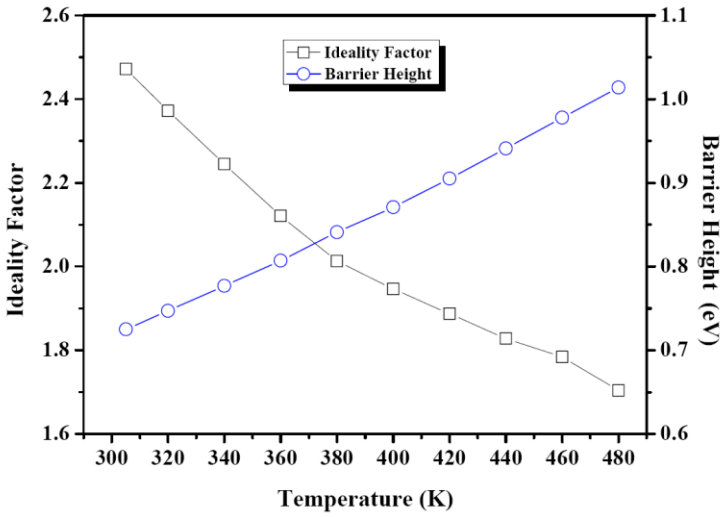

Figure 5. Temperature dependence of ideality factor and barrier height values obtained from lnI-V plot

Current-voltage measurement plots presented in Figure 4 have deviation from linearity at high voltages. This deviation implies the effect of series resistance. The series resistance results from the contact wires or bulk resistance of the NiO and n-Si semiconductors. The series resistances of the Au/NiO/n-Si structure were calculated by means of Norde functions given below as [7]

$$F(V)=\frac{V}{\gamma}-\frac{kT}{q}\left(\frac{I(V)}{AA^{*}T^{2}}\right) \qquad 6$$

where γ is the first integer greater than ideality factor and $I(V)$ is the current obtained from I–V measurements. The barrier height of device can be calculated using the minimum value of F vs. V plot using the equation

$$\phi_b = F(V_0)+\frac{V_0}{\gamma}-\frac{kT}{q} \qquad 7$$

where $F(V_0)$ is the minimum $F(V)$ value and V_0 is the corresponding voltage value.

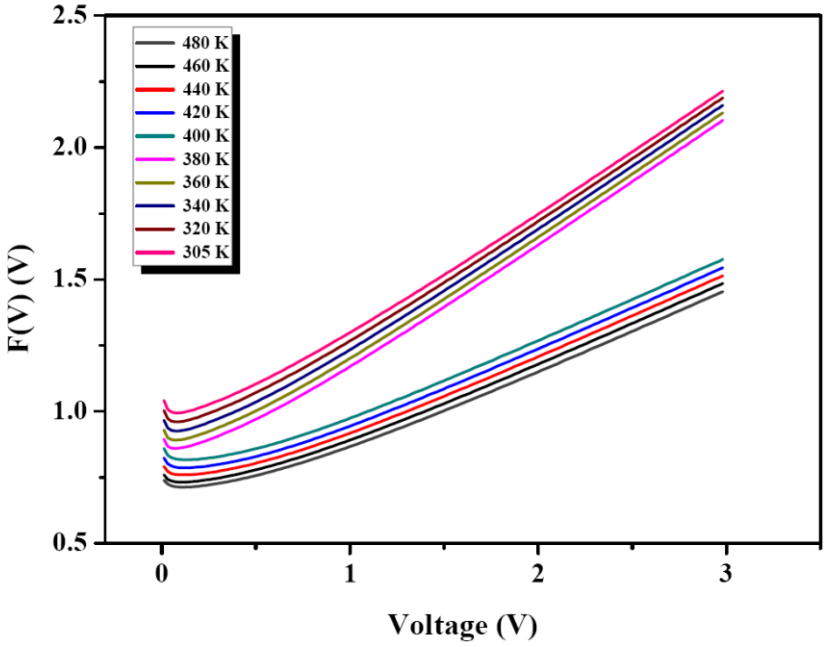

Figure 6. Norde plots of NiO/n-Si heterojunction between 305-480 K

F(V)–V curves of Au/NiO/n-Si heterojunction structure with respect to temperature is shown in Figure 6. The series resisnstance of the device is executed through the relation

$$R_S = \frac{kT(\gamma - n)}{qI_{min}} \qquad (8)$$

where I_{min} the corresponding current value at V_0.

The barrier height and the series resistance values of the heterojunction are also depicted in table 1 and Figure 7. As it is seen from the table and figure, the series resistance of the diode calculated as 9279 □□ at 305 K. Thi with the increase in temperature. The series resistance value of the device calculated as 243 □□□ at 480 K. T the strong effect of the temperature on series resistance of the diode.

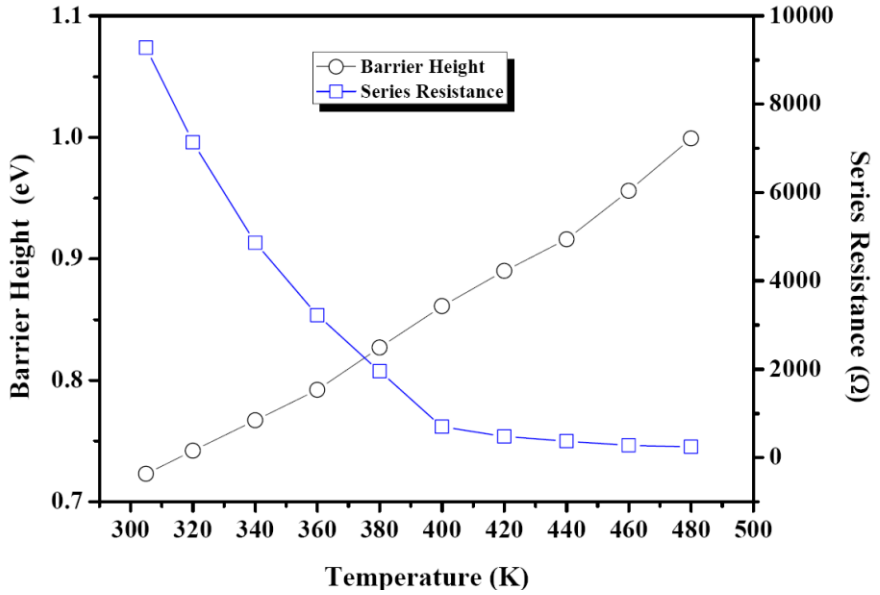

Figure 7. Temperature dependence of barrier height and series resistance values obtained from Norde plots

Furthermore, the barrier height values of the heterojunction increased from 0.723 (at 305 K) to 0.999 eV (at 400 K) with the increase in temperature. These results proved that the thermionic emission theory has a strong dependence to the temperature as seen in equation 2. At lower temperatures, electrons are able to pass over the lower barriers and the current transport will be dominated by current flow through the patches of lower Schottky barrier height and a larger ideality factor. When the temperature increases, more electrons can get sufficient energy to pass over the higher barrier. Tecimer et al fabricated Au/(Zn-doped)PVA/n-GaAs Schottky barrier diodes by electrospinning technique [8]. They reported the the barrier height of diode as 0.145 eV at 80 K and 0.606 eV at 350 K. Deniz et al formed Au/Fe_3O_4/p-Si Schottky diodes using Fe_3O_4 nanoparticles [9]. They made current-voltage measurements in a wide temperature range. They showed that series resistance of Schottky diode increased with the fall in temperature and it was because of the factors responsible for the increase of ideality factor or lack of free carrier concentration at low temperature.

4. CONCLUSIONS

Current-voltage measurements of NiO/n-Si heterojunction showed that the device had an excellent rectification. The electrical properties of the junction were characterized by means of thermionic emission theory. The electrical parameters of the Au/NiO/n-Si diode are given in table 1. As seen from the table, the ideality factor of the structure decreases by increasing temperature. The ideality factor decreased from 2.472 (305 K) to 1.704 (480 K). The barrier height of the junction calculated using I_0 value obtained from interception of In*I*-*V* plot to *I* axis by the help of the equation 5. Barrier height value of Au/NiO/n-Si device was determined as 0.725 eV at 305 K. Table 1 and Figure 5 also show the increases of barrier height from 0.725 to 1.014 eV with increasing the temperature i***n the range*** between 305 and 480 K. As seen from both table and figure, the increase in barrier height linearly depend on temperature.

REFERENCES

[1] H. Tian, B. Xu, H. Chen, E.M. Johansson, G. Boschloo, ChemSusChem, 7 (2014) 2150-2153.
[2] M.R. Shahmiri, A. Bahari, H. Karimi-Maleh, R. Hosseinzadeh, N. Mirnia, Sensors and Actuators B: Chemical, 177 (2013) 70-77.
[3] Y. Shen, X. Yan, Z. Bai, X. Zheng, Y. Sun, Y. Liu, P. Lin, X. Chen, Y. Zhang, RSC Advances, 5 (2015) 5976-5981.
[4] B.O. Jung, Y.H. Kwon, D.J. Seo, D.S. Lee, H.K. Cho, Journal of Crystal Growth, 370 (2013) 314-318.
[5] E.H. Rhoderick, Metal–Semiconductor Contacts, Oxford University Press, Oxford, 1978.
[6] A. Tombak, Y.S. Ocak, S. Asubay, T. Kilicoglu, F. Ozkahraman, Materials Science in Semiconductor Processing, 24 (2014) 187-192.
[7] H. Norde, Journal of Applied Physics, 50 (1979) 5052-5053.

[8] H. Tecimer, A. Türüt, H. Uslu, Ş. Altındal, İ. Uslu, Sensors and Actuators A: Physical, 199 (2013) 194-201.
[9] A.R. Deniz, Z. Çaldıran, Y. Şahin, M. Şinoforoğlu, Ö. Metin, K. Meral, Ş. Aydoğan, Metallurgical and Materials Transactions A, 44 (2013) 3809-3814.

Performance of Environmental Impact Assessment (EIA) on Hyroelectric Power Projects in Turkey

Ozum Aydinol [1], Nuriye Say[2]

Abstract

Since 1980's, demand for energy and electricity generation are on the rise in paralel with the increase in population and the growth in economy in Turkey. Based on these developments, the policies that Turkey preferred resulted in two conditions. First, extreme usage of fossil fuel caused the oscillation of CO2. The second important result is that all of the natural gas used in termal power plants is imported product. Based on these two reasons Turkey, in the last decade, had to increase the usage of local sources in energy consumption, espically in electricity, and to determine its energy policies in this way. In this direction, hydroelectric potential becomes prominent as the richest local renewable source which the country has.

Hydroelectric power plants are mandatory activities for EIA regulations. Sectoral and local distribution of EIA decisions proved general information about the industrial investments, priorities, local priorities, development tendecies and policies of a country. A large amount of EIA reports in Turkey is prepared for petrol with the ratio of 26% and for energy investments with the ratio of 24%. Taking into account the energy situation of Turkey and the policies for the last 20 years, it is possible to say that HPP projects will gradually continue in the upcoming years.

Depending upon the increasing HPP projects in the recent years, discussions and concerns started about the efficiency of EIA process. In this study, HPP development in Turkey is researched and EIA process implemented to these projects is examined.

***Keywords**: Environmental Impact Assessment, Energy, HPP*

1. INTRODUCTION

EIA, until today, is described by evaulation in almost the same context as a concept in many literatures [1]-[5]. Consensus in these studies is that; EIA process and consequently EIA reports are legal decision making tools for administrative mechanisms in a country. Decision making bodies, which will give investment authorisation for any project, make decisions by accepting the validity of the declacrations of EIA reports for the related project. For this reason, quality of the report and inclusion of reliable information are in the same importance for the sustainable development as the transparency and objectivity of the process.

Since EIA was legally taken into practice in 1993, 3992 of EIA reports were prepared. 3858 of them were positive, 32 of them were negative. Sectoral distribution of these reports is presented in Figure 1 [6]. Energy investments have a very important share as it is clear in the figure. About 80% of these investments are consist of HPP projects.

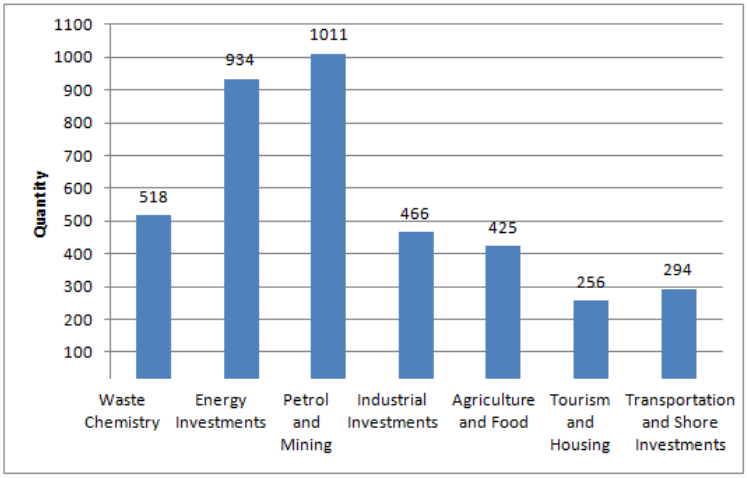

[1] Corresponding author: *Cukurova University, Department of Landscape Architecture, 01380, Sarıçam/Adana, Turkey.* ozumaydinol@gmail.com

[2] *Cukurova University, Department of Landscape Architecture, 01380, Sarıçam/Adana, Turkey., nursay@cu.edu.tr*

Figure 1. The Quantity of EIA Reports Settled on the Sectoral Basis Between the Years 1993 and 2015 in Turkey [6].

Since 1980's, demand for energy and electricity generation are on the rise in paralel with the increase in population and the growth in economy in Turkey. Based on these developments, the policies that Turkey preferred resulted in two conditions.

First, extreme usage of fossil fuel caused the CO_2 emission and cycle stations that generate electricity have a great share in total oscillation. CO_2 emission that regularly shows increase every year, was 5,85 ton in 2014. According to the forecasts made due to IPPC (Intergovernmental Panelon Climate Change) method, it is estimated that 38% of the CO_2 emission are belong to thermal power stations which use fossil fuel. The second important result is that all of the natural gas used in termal power plants is imported product. This situation is one the most basic elements that make Turkey externally dependent. Although our country has significant coal reserves, almost all of the petrol and natural gas are imported. Based on these two reasons Turkey, in the last decade, had to increase the usage of local sources in energy consumption, espically in electricity, and to determine its energy policies in this way. In this direction, hydroelectric potential becomes prominent as the richest local renewable source which the country has. In recent years, country policies have given great importance to renewable energy sources and made extensive studies over this matter. Local renewable energy potential in our country is presented in Table 1.

Table 1. Potential of Renewable Energy in Turkey [7].

Hydroelectric	80-100 Billion kWh
Wind	90-100 Billion kWh
Geothermal	5-16Billion kWh
Sun	380 Billion kWh
Biogas	35 Billion kWh

In recent years Turkey speed up HPP projects for the reasons summarized above. Turkey has 1,5% of hydroelectric potential in the world, and 17,6% of the total potential of Europe .

However, Turkey uses 60% of the potential of its 25 stream basins today. [8]- [15].

The number of HPP projects in our country is showed in Table 2. While there are 496 numbers of HPP projects in 2015, totally 989 numbers of HPP projects, which are at construction, planning and licencing stage, are under construction.

Table 2. HPP Projects in Turkey [16].

Stage of the Projects		Quantity	Installed Capacity (MW)	Yearly Production (GWh/yıl)	Production Rate (%)	
OPERATION	DSİ	65	12 369	43 357	26,5	50,6
	Private Sector	355	8 917	30 976	18,9	
	Other	76	2 331	8 463	5,2	
	Total	496	23 616	82 796		
CONSTRUCTION	DSİ	4	1 940	6 161	3,8	15,3
	Private Sector	145	6 253	18 788	11,5	
PLANNING-PROJECT-LICENCE	DSİ	81	1 491	5 153	3,1	34,1
	Private Sector	759	14 478	50 761	31,0	
DEVELOPED POTENTIAL	DSİ (total)	150	15 800	54 671	33,4	100
	Private Sector (total)	1259	29 648	100 525	61,4	
	Other (total)	76	2 331	8 463	5,2	
	GRANDTOTAL	1485	47 599	163 659	100	

Depending upon the increasing HPP projects in the recent years, discussions and concerns about the efficiency of EIA process show increase. It is very common in recent days to see news about the subjects such as HPP projects of which EIA reports are cancelled, protests of local people and non-governmental organizations, meetings that cannot be set up due to these protests. These developments opened the reliance of the EIA reports in HPP projects up for discussion. Although it has been practiced in Turkey for 23 years, the studies that determine the efficiency and reliance of EIA are restricted.

In this study, the efficiency of the EIA process practiced to HPP projects in our country is analysed and suggestions are aimed to be developed for enhancing the efficiency of EIA in accordance with its conceptual basic criterias.

2. EIA PROCESS IN TURKEY AND PERFORMANCE REVIEW

Since the year when EIA was taken into practice, the regulations undergo a change seven times; 1993, 1197, 2002, 2003, 2008, 2013 and 2014.

Process of EIA consists of 9 main topics. Firstly the evaulations of whether the planned activity is in the context of EIA Regulations; application of Selection Elimination Criterias for the projects in the contexts of Appendix 2 of Regulations; starting the EIA process; and the organization of the Board of Inspection And Survey. As 4th stage there are; civil participation, defining content and special format, preparing EIA report and defining its suitability, inspection and survey of the report and decision stages.

Performance of EIA system in Turkey against evaluation criteria categorized are presented in Table 3 [17].

Table 3. Performance of EIA system in Turkey against evaluation criteria by used Ahmed and Woods (2002) [17].

Systemic measures	
(1) EIA legislation	
1.1 Legal provisions for EIA	Enabling legislation: EIA Regulation 25.11.2014/ 29186
1.2 Provisions for appeal by the developer or the public against decisions	None
1.3 Legal or procedural specification of time limits	The decision made within 10 days of submission of final report
1.4 Formal provisions for SEA	None
(2) EIA administration	
2.1 Competent authority for EIA and determination of environmental acceptability	MoEU by
2.2 Review body for EIA	Commission established by MoEU
2.3 Specification of sectoral authorities'responsibilities in the EIA procss	Not specified
2.4 Level of coordination with other planning and pollution control bodies	None
(3) EIA process	
3.1 Specified screening categories	Not specified
3.2 Systematic screening approach	List for EIA mandatory plus application through special screening forms on case by case basis and the MoEU will determine EIA requirement
3.3 Systematic scoping approach	EIA formats is prepared by the MoEU
3.4 Requirement to consider alternatives	If the alternative offered by the project owner.
3.5 Specified EIA report content	General guidelines for comprehensive EIA
3.6 Systematic EIA report review approach	No defined systematic approach to review EIA report
3.7 Public participation in EIA process	2 times
3.8 Systematic decision-making approach	Projects don't start its activity without obtaining EIA report permit from MoEU
3.9 Requirement for environmental management plans	None
3.10 Requirement for mitigation of impacts	Article 12 of EIA Regulation
3.11 Requirement for impact monitoring	Article 18 of EIA Regulation
3.12 Experience of SEA	None
Foundation measures	
(4) Existence of general and/or specific guidelines including any sectoral authority procedures	None
(5) EIA system implementation monitoring	None
(6) Expertise in conducting EIA (national universities, institutes, consultancies with EIA technical expertise)	Approved consultancies by MoEU
(7) Training and capacity-building	No information available

3. CONCLUSION

According to the lastly published EIA Regulations in 25.11.2014, EIA should be practised to the places in "Appendix 1 List";

- Dam and ponds with more than 10 million m^3 reservoir volume
- HPP projects which have the installed power about 10 MWm and above.

In "Appendix 2 List;

- Dam and ponds with more than 15 million m^3 reservoir volume
- HPP projects which have the installed power about 1-10 MWm

According to data gathered from Ministry of Environment And Urbanization, since EIA was legally taken into practice in 1993, EIA was implemented to 488 numbers of HPP prjects and dams. 466 of these reports were positive and 22 of the reports were negative and cancelled.

9 numbers of EIA reports prepared in different basins were analysed within the scope of this study. In the evaluation of these reports, the effects of the dams and HPP projects and the precautions for these effects that are developed by Environmental Impact Assesment Sourcebook (1991) were taken into consideration. Accordingly, the evaulations about reports were made in the topics such as Procedure, Effects and Precautions and they are summerized below.

Processual (Procedure)

Depending upon the EIA Regulations in Turkey, the process has some strong sides:

- All stages of guidelines (legal process) are completed

- Process is completed in timewise

- Certainity of the authorized institutions

- Mandatory application of civil participation

The most riveting lacking sides of the legal process may be sorted as below:

-Stage of inspection and evaluation are procedured more transparently in addition to present application.

-Differentation of authorisation between institutions and parts in EIA process is more explicit.

Effects

It is stated in the evaluated reports that the main problems in determining and estimating the effects are mainly caused by lack of methodological applications. According to evaluations;

-Specifying the effects that will be faced at the stage of construction and operation may seem positive for an objective evaluation.

-There are some shortcomings in specifying the effects in a quantitative way. As a result, it is very difficult to compare the effects with the legal limitations.

-Projections of the effects are not made in reliable methods.

-There are some shortcomings in defining the social effects.

-There is not any study which is enough for the ecologic effects that will be caused by the change of the river flow system.

-The subjects such as; land cover as a result of HPP projects and indirectly the change in quality of the landscape are not studied enough.

-Present biological variety and change after project are inadequate.

-Giving importance to literature data rather than the field work especially in vegetation analyse is a significant shortcoming.

-Evaluation about visual effects are not procedured in almost any reports.

Precautions

-According to the deficiencies in the subjects about specifying, comparing and defining the effects, it may be stated that the precautions are inadequate.

-There is not legal and institutional cleanness in practising the precautions.

REFERENCES

[1] B. Noble,2006. Introduction to Environmental Impact Assessment: A Guide to Principles and Practice. Oxford University Press.
[2] N. Peker, 1996. Checklists can be used for EIA Reports Some Types of Activity and Creating Evaluation Matrix. Master's Thesis. Çukurova University, Adana.
[3] M. Yücel, 1996. Environmental Impact Assessment. Textbook Ed. no :11, Adana.
[4] C. Wood, 1995. Environmental Impact Assessment: A Comparative Review. Longman Scientific & Technical. Michigan University, UK.
[5] J. Glasson , R. Therivel, A. Chadwick, 1994. Introduction To Environmental Impact Assessment., Routledge, UK.
[6] (2015) MoEU website. https://www.csb.gov.tr/turkce/index.php
[7] S. Polat, H. Şekerci. Energy Efficiency of Turkey's and Renewable Future Goals. Yaşar University, İzmir.
[8] C. Ilkilic, H. Aydin, 2015. Wind Power Potential And Usage İn The Coastal Regions Of Turkey. Renewable And Sustainable Energy Reviews 44 (2015) 78–86.
[9] As of January 2015 Energy Outlook Report of Turkey: Energy Policy is increased dependency on Deadlock. Chamber of Mechanical Engineers, Ankara. http://www.mmo.org.tr/resimler/dosya_ekler/0c34e931f9884e5_ek.doc?tipi=2&turu=X&sube=0
[10] (2014) MoEaNR website. http://www.enerji.gov.tr

[11] E. Kentel, E. Alp, 2013. Hydropower in Turkey: Economical, Social And Environmental Aspects And Legal Challenges. Environmental Science & Policy. Volume 31, 2013, Pages 34–43.
[12] C. Koç, 2014. A Study On The Development Of Hydropower Potential İn Turkey. Renewable And Sustainable Energy Reviews 39 (2014) 498–508.
[13] M. Melikoğlu, 2013. Vision 2023: Feasibility Analysis Of Turkey's Renewable Energy Projection. Renewable Energy Volume 50, 2013, Pages 570–575.
[14] N. Say, M. Yücel, 2006. Energy Consumption and CO_2 Emissions in Turkey: Empirical Analysis and Future Projection Based on An Economic Growth. Energy Policy Volume 34, Issue 18, December 2006, Pages 3870-3876.
[15] O. Yukseka, M. I. Kömürcü, I. Yuksel, K. Kaygusuz, 2006. The Role Of Hydropower İn Meeting Turkey's Electric Energy Demand. Energy Policy 34 (2006) 3093–3103.
[16] (2016) MoFaWM website. http://www.ormansu.gov.tr/osb/AnaSayfa.aspx?sflang=tr
[17] C. Wood, 1999. Comparative Evaluation of Environmental Impact Assessment Systems. Handbook of EIA. Ed. J. Petts, Vol 2, Oxford.

Effect of Mn Element on the Corrosion Behavior of Mg5Al1Ti Alloy in NaCl+HCl Solution

H. Ahlatci,[1] H Cug,[1] Y. Turen [1], Y. Sun [1], E. Cevik[1]

Abstract

One of the major causes of magnesium alloys is low corrosion reistance. In this study, the effects of Mn addition on the microstructure, and corrosion resistance of the Mg5Al1Ti alloy produced by casting method were investigated. The percentage of Mn added to the master alloy are 4%. Optical microscope (LOM), X-ray diffraction analysis (XRD) and SEM were used for microcharacterization. As a result of the microstructural characterization, $Mg_{17}Al_{12}$ grain boundary intermetallic was formed in α–Mg matrix whereas the microstructures having higher Mn additions showed differences. Al_6Mn phase was formed by 4% Mn addition. The corrosion rate of the Mg5Al1Ti alloy correlates with Mn ratio in the solid solutions and intermetallics. Mn addition of Mg5Al1Ti master alloy improved the corrosion resistance.

Keywords**:** *Magnesium alloys, Casting, Microstructure, Corrosion.*

1. INTRODUCTION

Magnesium alloys have received an increasing interest in the past 12 years for potential applications in the automotive, aircraft, aerospace, and electronic industries [1-3].

Aluminum (Al) and manganese (Mn) are the main alloying elements adding to magnesium (Mg) base alloys. Also Al and Mn are used to increase the strength of the Mg alloy sufficiently [4]. Reports about Ti element is limited in the literature on the effects of properties of Mg alloy [5]. Ti element have excellent properties such as high corrosion resistance, good mechanical properties. The literature showed that Ti element with low density and high strength could refine the as-cast microstructure. As metals, Ti elements resistant almost up to platinum are capable resist of the exposure acids, chlorine gases and common sult solution [6,7]

Despite the positive attributes listed about Mg, place in engineering applications is limited due to low corrosion resistance. The development of mechanical and corrosion characteristics of the Mg alloys is possible by adding appropriate alloying elements and casting procedure [3].

The main objective of this study includes investigation of effect of Mn addition on microstructure, mechanical and corrosion properties of Mg alloy containing 5 % Al and as well as 1 % Ti elements (coded as Mg5Al1Ti).

2. MATERIALS AND METHODS

The investigated alloys in this study were produced in an atmospheric controlled 1200 ºC capacity electric resistance furnace. Commercially pure (99,8%) Mg and Al10Ti were used as starting materials to prepare the Mg5Al1Ti code alloys. After that 4% Mn was added to the master alloy remelting at 800ºC.

In accordance with the standard metallographic procedure, including a grinding process up to 1200 mesh and a following polishing process with a diamond solution and then etching with 2% nitric acid, conducted on the specimens. Microstructural analysis on the prepared specimens was conducted using light optical microscopy (LOM) and a scanning electron microscope (SEM). XRD analyses were carried out by Rıgaku Ultra IV model X-ray diffractometer using Cu Kα radiation. Diffraction patterns were obtained over range of Bragg angle from 20º to 90º. The LOM (Nikon Epiphot 200 Model) and SEM (Carl Zeıss Ultra Plus Gemini Fesem) images were taken. Energy Dispersive Spectroscopy (EDS) analyses were carried out on the light and grey coloured spots in the microstructural images captured.

[1]*Corresponding author: Karabük University, Department of Metallurgical and Materials Engineering, 78150, Karabük, Turkey.*
hahlatci@karabuk.edu.tr

Corrosion experiments were carried out in solutions (30 g/l NaCl+10 ml/l HCl) according to the weight loss measurement methods in determination of the corrosion attitudes.

3. RESULT AND DISCUSSION

3.1. Microstructural analysis

Microstructural and XRD analysis results of the alloy produced by casting are given in the Figure 1. The microstructures showed that the intermetallic phases generally seem to occur mainly along grain boundaries in α-Mg matrix.

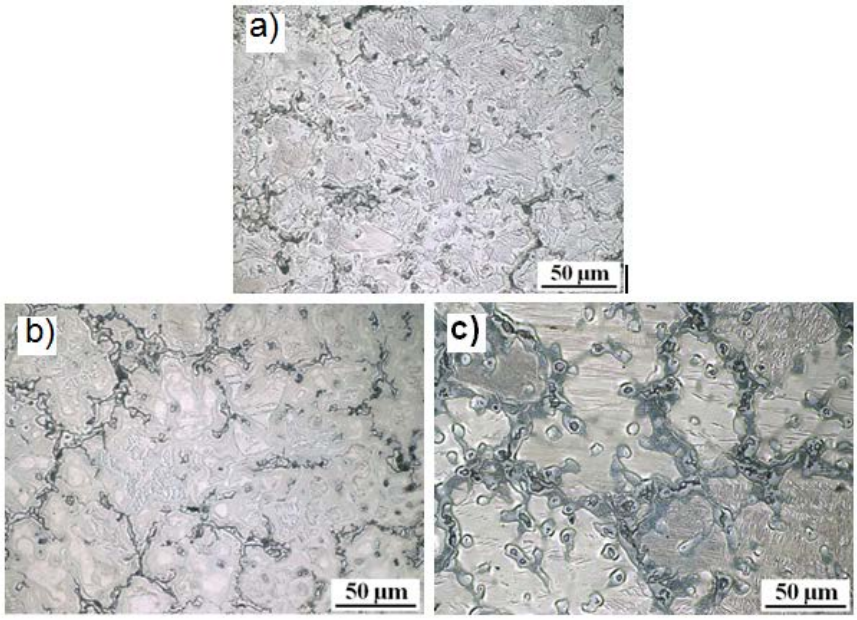

Figure 1. Microstructure of; a) Mg5Al1Ti, b) Mg5Al1Ti-0,5Mn ve c) Mg5Al1Ti-4Mn

Considering to the XRD analysis (Figure 2), in the α-Mg matrix structure of Mg5Al1Ti master alloy added Ti element any phase containing Ti element was not observed. Up to 4% Mn element addition of Mg5Al1Ti has emerged Al_6Mn and $Mg_{17}Al_{12}$ phases with respect to literature [8-10].

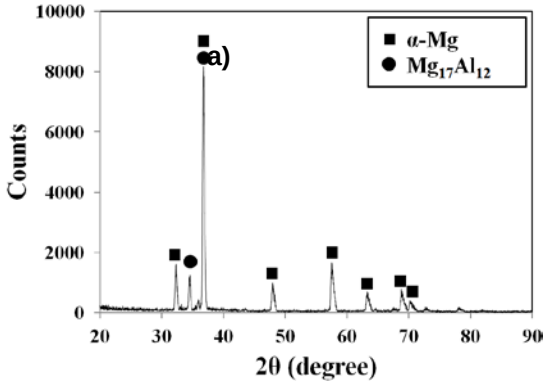

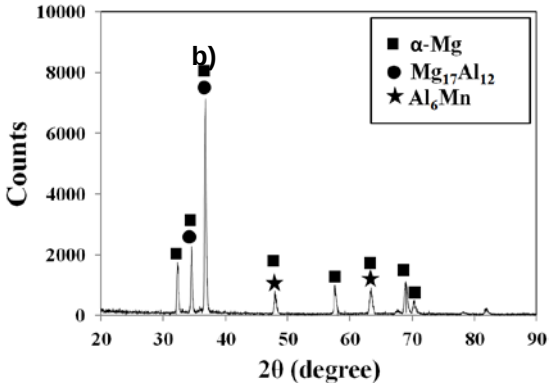

Figure 2. XRD patterns of a) Mg5Al1Ti ve b) Mg5Al1Ti-4 % Mn alloys.

Results of grain size and hardness measurements of the investigated alloys are given in Figure 3. As shown in Figure 3 while the coarse grain size decreases the hardness fine grain size increases the hardness. This case is in accordance with Hall Petch relationship.

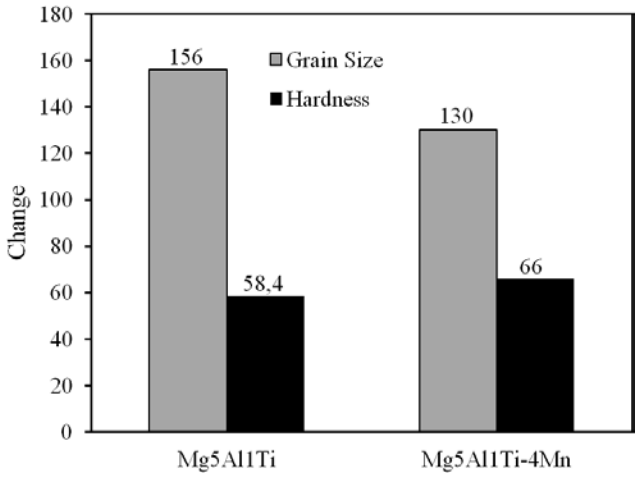

Figure 3. Change of grain size and the hardness of the investigated alloys.

3.2. Mechanical Properties

The mechanical properties of the investigated alloys was determined by tensile tests and hardness measurement. The results of yield strength (MPa), maximum tensile strength (MPa), and % elongation values obtained in the tensile tests are given in Figure 4. Yield and tensile strength increases with increasing alloy content in accordance with hardness measurements, as shown Figure 3. An increase in ductility has been observed with the increase in strength. Increase in ductility is attributable to the refining of the grain size.

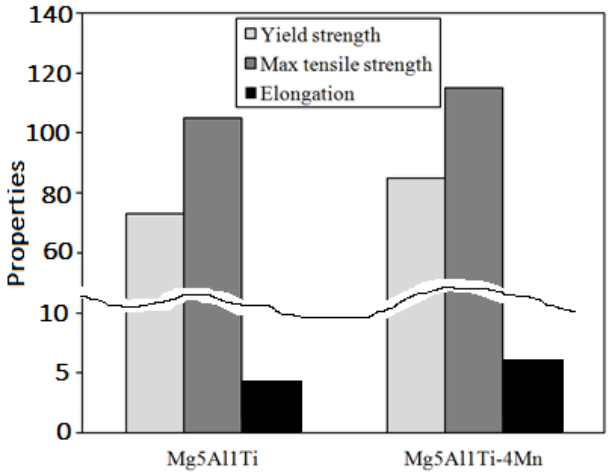

Figure 4. Tensile test results of the investigated alloys.

An increase in the mechanical properties of Mg5Al1Ti master alloy results from Al_6Mn phase and $Mg_{17}Al_{12}$ intermetalics observed with the addition of the Mn element detected by XRD analysis. This positive effect on mechanical properties of the phases which are reported in the literature [10-12], in accordance with this study.

3.3. Corrosion Behaviour

The effect of Mn addition on corrosion resistance of the investigated alloys is plotted as the change of mass loss according to time in Figure 5.

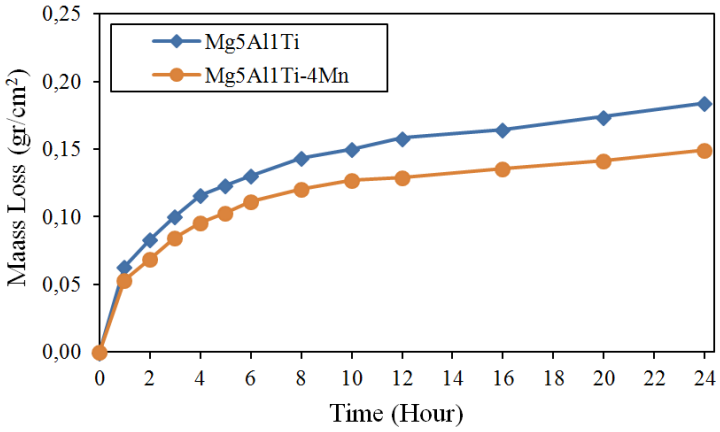

Figure 5. Immersion corrosion test results of the investigated alloys in 30gr/l NaCl+10ml/l HCl solution.

Consider the weight loss of the studied alloys in the 30 g/l NaCl + 10 ml/l HCI solution after 24-hour time (Figure 5), the Mg5Al1Ti master alloy with no Mn addition exhibits maximum weight loss (0.184 g/cm2) while the weight loss of the Mg5Al1Ti alloy with 4% Mn addition was measured as 0.149 g / cm2. When the change of the weight loss with respect to time given in Figure 9 soared within the first 5 hours, after that the weight loss increased steadily with increasing the time [12].

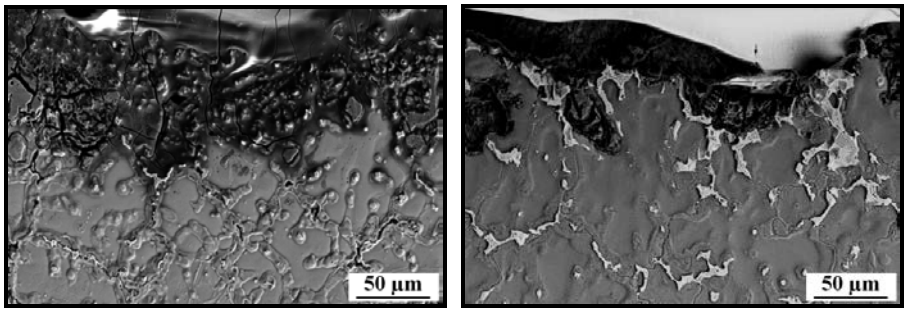

a) b)

Figure 6. SEM micrographs showing cross section of a) Mg5Al1Ti and b) Mg5Al1Ti-4 % Mn alloys in 30gr/l NaCl+10ml/l HCl solution.

The sample subsurfaces after the corrosion tests were examined under SEM and the progress mechanism of corrosion is shown in Figure 6. As seen in Figure 6, corrosion damage in Mg5Al1Ti master alloy is advanced towards the interior of the material. The progress of corrosion demage into the Mg5Al1Ti master alloy containing 4% Mn addition was stopped by the mixed intermetallic layer of eutectic phase, $Mg_{17}Al_{12}$ and Al_6Mn [12,13].

4. CONCLUSIONS

The microstructural investigations, mechanical and corrosion experiments of Mg5Al1Ti master alloy and Mg5Al1Ti containing 4 % Mn alloy gives us the following results.

1. In the investigated misrostructure $Mg_{17}Al_{12}$ structure and Al_6Mn phases are formed with Mn addition.
2. Compared to the Mg5Al1Ti mater alloy the alloys containing 4% Mn addition have fine grain sizes, high mechanical properties (hardness, yield strength and tensile strength) and improved ductility.
3. While the progress of corrosion demage was stopped by the mixed intermetallic layer and eutectic phase in the matrix with addition 4% Mn, the corrosion resistance of the alloys was improved.

ACKNOWLEDGMENT

This study is a part of project which has been supported by Karabük University. (Project code: 13/2 - DR006)

REFERENCES

[1]. Kulekci, M. K., “Magnesium and its alloys applications in automotive industry”, International Journal Advanced Manufacturing Technologies, 39: 851–865 (2008).
[2]. Chen, H., and Alpas, A. T., “Sliding wear map for the magnesium alloy Mg–9Al–0.9 Zn (AZ91),” Wear, 246: 106–116 (2000).
[3]. Blawert, C., Hort, N., and Ku, K., “Automotive applications of magnesium and its alloys”, Transactions of The Indian Institute of Metals, 57: 397–408 (2004).
[4]. Guangyin, Y., Manping, L., Wenjiang, D., and Inoue, A., “Mechanical properties and microstructure of Mg–Al–Zn–Si–base alloy”, Materials Transactions, 44: 458–462 (2003).
[5]. Sudholz, A. D., Birbilis, N., Bettles, C. J., and Gibson, M. A., "Corrosion behaviour of Mg-alloy AZ91E with atypical alloying additions", Journal of Alloys and Compounds, 471 (1–2): 109–115 (2009).
[6]. Matthew, J., Donachie, J., and Tıtanıum, A., "Technical Guide", Metals Park, OH: ASM International, ISBN 0-87170-309-2, 11, (1998).
[7]. Yu, Z., Zhao, H. Y., Hu, X. D., and Ju, D. Y., “Effect of elements Zn, Sn and In on microstructures and performances of AZ91 alloy”, Transactions of Nonferrous Metals Society of China, 20: 318–323 (2010).
[8]. Candan, Ş., Kusdemir, H., Türkmen, M., Koç, E., Ünal, M. and Candan, E., Effect of Ti additions on corrosion behaviour of AZ91 magnesium alloys, 5. Uluslararası İleri Teknolojiler Sempozyumu (IATS’09), Karabük, 60-65, 2009.
[9]. Ai, X., and Quan, G., Effect of Ti on the Mechanical Properties and Corrosion of Cast AZ91 Magnesium Alloy, The Open Materials Science Journal, vol. 6, 6-13, 2012.
[10]. Choi, J. Y. and Kim, W. J., Significant effects of adding trace amounts of Ti on the microstructure and corrosion properties of Mg–6Al–1Zn magnesium alloy”, Journal of Alloys and Compounds, vol. 614, 49-55 2014.
[11]. Yu, Z., Zhao, H. Y., Hu, X. D. and Ju, D. Y., Effect of elements Zn, Sn and In on microstructures and performances of AZ91 alloy, Transactions of Nonferrous Metals Society of China, vol. 20, 318-323 2010.
[12]. H.Çuğ "Mg5Al1Si ve Mg5Al1Ti alaşımlarının korozyon ve mekanik özelliklerine Zn ve Mn ilavesinin etkisi" Phd Thesis, Karabük University Science and Technology Institude, Karabük, 2015.
[13]. Dasa, S., Morales, A. T. and Alpas A. T., Microstructural evolution during high temperature sliding wear of Mg–3% Al–1% Zn (AZ31) alloy, Wear, vol. 268, 94-103, 2010.

Regression Model for the Prediction of the Minimum Cost of Reinforced Concrete Retaining Walls

Ugur Dagdeviren[1], *Burak Kaymak*[2]

Abstract

Analysis and design of the reinforced concrete retaining walls (RCRWs) are one of the important problems encountered in geotechnical and structural engineering. In the design procedure of RCRWs, firstly, design variables such as cross-sectional dimensions and material properties are selected based on previous design experiences. Then, the static and dynamic analyses for the wall are applied and checked in terms of external and internal design criteria. In order to minimize the cost of the wall, the design variables are redefined by trial and error process, and these procedures are repeated several times. Since it is extremely difficult and time consuming to obtain optimal design satisfying all the stability requirements, it is beneficial to consider the problem as an optimization problem. In this study, the effects of the surcharge load, height of retaining wall and the angle of internal friction of the backfill on optimum wall design resting on soil with high bearing capacity were investigated by using the ABC algorithm. A total of 125 analyses were carried out for different surcharge loads, the heights of wall and angles of internal friction of the backfill. Based on the analysis results, a multiple regression analysis was made between these parameters and minimum cost (C_{min}), and a regression equation was proposed. The proposed equation gives a high coefficient of determination (R^2 = 0.9983), a low root mean square error (RMSE = 5.08 $/m), and a low mean absolute relative error (MARE = %1.68). It is very simple and practical to determine the minimum cost of the RCRW resting on soil with high bearing capacity.

Keywords**:** *Artificial bee colony (ABC), Minimum cost, Optimization, Regression analysis, Retaining wall.*

1. INTRODUCTION

Retaining structures are most widely used to support earth in civil engineering practice. One of the most common types of retaining structures is the reinforced concrete retaining wall (RCRW). The overall stability assessment of RCRWs needs to consider many different failure modes. The stability of RCRWs must be controlled versus overturning, sliding, no tension condition and bearing capacity of the soil under the foundation of the wall. In addition to these controls, bending and shear controls must be performed for the critical sections of the stem, toe and heel of the retaining wall. In the classical design procedure of RCRWs, design variables such as cross-section dimensions and material properties are firstly selected based on previous design experiences, then, they checked in terms of design criteria. In order to economize the cost of the wall under the design constraints, these procedures are repeated several times. Since it is extremely difficult and time consuming to obtain optimal design satisfying all the stability requirements, it is beneficial to consider the problem as an optimization problem.

The optimization problems can be solved by mathematical and meta-heuristic methods. Nowadays, meta-heuristic methods have been widely applied in many civil engineering optimization problems. The artificial bee colony (ABC) algorithm, which is an optimization algorithm based on a particular intelligent behavior of honey bee swarms, is one of the recently developed meta-heuristic optimization techniques [1-3]. In literature, the optimization studies using ABC algorithm is reported by some researchers [4-6].

In this study, the effects of the surcharge load, height of retaining wall and the angle of internal friction of the backfill on optimum wall design resting on soil with high bearing capacity were investigated by using the ABC algorithm. The active and passive earth pressures were computed by the Rankine Theory. Structural design was performed based on TS 500/2000, which is the Turkish Code for the requirements for design and construction of reinforced concrete structures [7]. A total of 125 analyses were carried out for different surcharge loads, the heights of wall and angles of internal friction of the backfill. Based on the analysis results, a multiple regression analysis was made between these parameters and minimum cost (C_{min}), and a regression equation was proposed.

2. ARTIFICIAL BEE COLONY ALGORITHM

The artificial bee colony algorithm is a meta-heuristic method based on the foraging behavior of honey bee colonies proposed by Karaboga [1]. Unconstrained and constrained optimization problems can be solved using this algorithm [2-5]. The ABC algorithm has fewer control parameters compared with other meta-heuristic methods. The simplicity, flexibility and robustness

[1] *Corresponding author: Dumlupinar University, Department of Civil Engineering, 43100, Kutahya, Turkey.* ugur.dagdeviren@dpu.edu.tr

[2] *Dumlupinar University, Department of Civil Engineering, 43100, Kutahya, Turkey,* burak.kaymak@dpu.edu.tr

are other advantages of artificial bee colony method. Basic mathematical and logical operators are easily used in this algorithm. These specifications make the method attractive [8]. It has been successfully applied for many engineering problems. The details of the ABC algorithm could be found in several papers [1-3].

3. DEFINITION OF THE OPTIMIZATION PROBLEM

3.1 Design of the RCRW

The typical vertical forces acting on the retaining walls shown in Fig. 1, are the weight of the stem and foundation of the wall (W_w) and the weight of the backfill soil (W_s) acting on the heel. The horizontal forces acting on the retaining walls are active (P_a) and passive (P_p) earth forces resulting from the weight of backfill and natural soil and lateral force induced by surcharge (P_q). When the ground surface on the front and back of the wall is horizontal and there is no friction between the wall and soil, Rankine's earth pressure theory can be used to calculate the active and passive earth pressure.

The design of RCRW must satisfy two requirements: The wall must have adequate 1) external stability (the geotechnical design), 2) internal stability (the structural design). In the external stability, the wall as a whole has to be safe against overturning, sliding, bearing capacity and eccentricity. Then internal stability of the stem and foundation of the wall must be checked against shear and moment failure. The wall section and reinforcement must be able to carry applied loads without rupturing. If the requirements are not satisfied, the wall dimensions are modified and the stability analyses are repeated. This trial-error process is repeated until the minimum cost of the wall is obtained. In general, the weight of soil on the toe, surcharge load above the heel and passive earth pressure are neglected in external stability analyses.

A RCRW must have adequate resistance against overturning. The factor of safety against overturning around the toe can be expressed as in Eq. 1. The minimum desirable value for the factor of safety with respect to overturning ($FS_{(o,min)}$) is 1.5 for granular soils.

$$FS_{(overturning)} = \frac{\Sigma M_R}{\Sigma M_O} \geq FS_{(o,min)} \quad (1)$$

where;

ΣM_R is sum of the moments of forces tending to resist overturning around point O shown in Fig. 1a.

ΣM_O is sum of the moments of forces tending to overturn around point O.

The factor of safety against sliding failure can be calculated by Eq. 2. The minimum acceptable factor of safety for sliding ($FS_{(s,min)}$) is 1.5 for backfill such as sand, gravel and rock.

$$FS_{(sliding)} = \frac{\Sigma F_R}{\Sigma F_S} \geq FS_{(s,min)} \quad (2)$$

ΣF_S is sum of the horizontal sliding forces.

ΣF_R is sum of the horizontal resisting forces and can be calculated from;

$$\Sigma F_R = P_p + \Sigma V . tan(k_1 . \phi_2) + B . (k_2 . c_2) \quad (3)$$

ΣV is total vertical load transferred to the soil,

B is width of the foundation,

P_p is passive earth force. The passive earth force is generally neglected.

ϕ_2 and c_2 are shear strength parameters of the foundation soil,

k_1 and k_2 are reduction coefficients in the range of 1/2 to 2/3.

The vertical pressure transmitted to the soil by the foundation of the retaining wall must be checked against the ultimate bearing capacity of the soil. The base stress under the foundation varies linearly as shown in Fig. 1a. The maximum and minimum base stresses are at the end of the toe and heel sections, respectively. The bearing capacity of the foundation must be great enough to resist the maximum base stress. The minimum factor of safety against bearing capacity failure ($FS_{(b,min)}$) is generally 3. Furthermore, the minimum base stress below the foundation of the retaining wall must be greater than zero.

$$FS_{(\text{bearing})} = \frac{q_{ult}}{q_{max}} \geq FS_{(b,min)} \quad (4)$$

$$FS_{(\text{no tension})} = \frac{B/6}{e} \geq 1 \quad (5)$$

where,

e is eccentricity. e can be determined as;

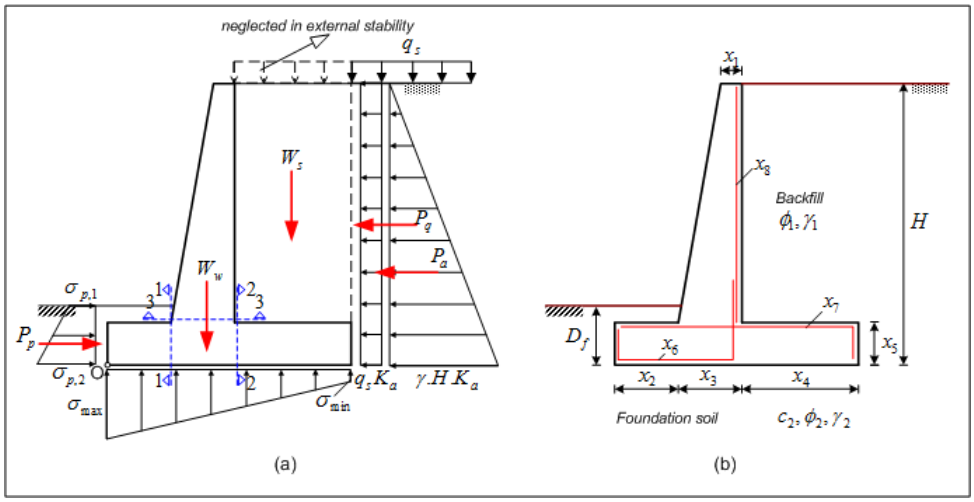

Figure 1. a) The forces acting on the RCRW, b) Design variables and parameters for RCRW

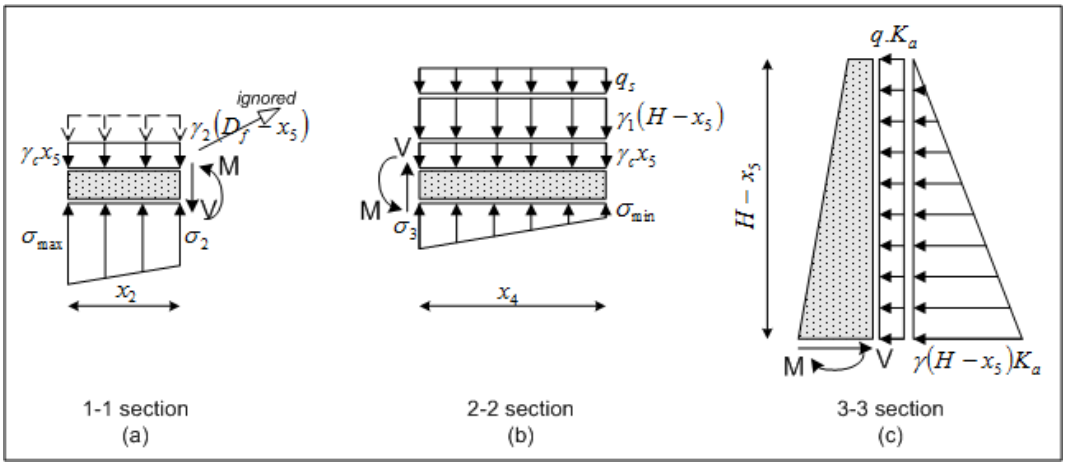

Figure 2. The stress distributions acting on the critical sections

$$e = \frac{B}{2} - \frac{\Sigma M_R - \Sigma M_O}{\Sigma V} \quad (6)$$

The internal stability analyses for RCRWs are generally applied to three critical wall sections, which are stem of the wall, toe and heel of the foundation. The stress distributions acting on these critical sections (1-1, 2-2 and 3-3) are shown in Fig. 2. The stem, toe and heel are analyzed as a beam, satisfying both flexure and shear requirements [9]. The moment and shear capacity of these sections must be greater than the design moment (M_d) and design shear force (V_d). In TS 500/2000, the moment capacity (M_r) and shear capacity (V_r) for the reinforced concrete members are given

$$M_r = A_s . f_{yd} . \left(d - \frac{a}{2}\right) \geq M_d \quad (7)$$

$$V_r = 0.65 f_{ctd} . b_w . d \geq V_d \quad (8)$$

The reinforcement ratio in each section of the retaining wall must be between the minimum and maximum reinforcement ratios. The minimum (ρ_{min}) and maximum (ρ_{max}) reinforcement ratio are defined by Turkish Code as;

$$\rho_{min} = 0.8\frac{f_{ctd}}{f_{yd}} \tag{9}$$

$$\rho_{max} = 0.85\left(0.85k_1.\frac{f_{cd}}{f_{yd}}.\left(\frac{600}{600+f_{yd}}\right)\right) \tag{10}$$

3.2 Design Variables and Parameters

In this study, the design variables are divided into two categories; 1) geometric dimensions of the cross-section of wall and, 2) reinforcement ratios. There are five geometric design variables and three reinforcement ratio design variables in this optimum design model. The design variables are shown in Fig. 1b and described in Table 1.

The design parameters such as backfill and base soil properties, external loads, geometric properties of the wall, safety factors, concrete and steel specifications are considered as the input parameters. These parameters given in Table 2 are kept constant during optimization process.

Table 6. Description of the design variables

Design variable	Description	Unit (SI)
X_1	Stem thickness at the top	m
X_2	Width of the toe	m
X_3	Stem thickness at the bottom	m
X_4	Width of the heel	m
X_5	Thickness of the foundation	m
X_6	Main reinforcement ratio of the toe	1/m
X_7	Main reinforcement ratio of the heel	1/m
X_8	Main reinforcement ratio of the stem	1/m

Table 2. Design parameters

Design parameter	Symbol	Unit (SI)	Used values in analyses
Height of wall	H	m	4 ~ 8
Depth of soil in front of wall	D	m	1.0
Surcharge load	q_s	kPa	0 ~ 40
Internal friction angle of backfill	ϕ_1	degree	28° ~ 36°
Internal friction angle of base soil	ϕ_2	degree	30°
Cohesion of base soil	c_2	kPa	200
Unit weight of backfill	γ_1	kN/m^3	17
Unit weight of base soil	γ_2	kN/m^3	18
Unit weight of concrete	γ_c	kN/m^3	23.5
Compression strength of concrete	C	MPa	25
Yield strength of steel	S	MPa	420

3.3 Design Constraints

In this optimization problem, the design requirements are classified into three categories of design constraints; 1) failure modes for external stability, 2) failure modes for internal stability, and 3) additional geometric constraints. The normalized design constraints for the optimization problem are given in Table 3.

Table 3. Normalized design constraints

Design constraints	Description	Design constraints	Description
$g_1(X) = \frac{FS_{(x,min)}}{FS_{(overturning)}} - 1 \leq 0$	Overturning failure mode	$g_7(X) = \frac{M_{d,toe}}{M_{r,toe}} - 1 \leq 0$	Toe moment failure mode
$g_2(X) = \frac{FS_{(x,min)}}{FS_{(sliding)}} - 1 \leq 0$	Sliding failure mode	$g_8(X) = \frac{V_{d,toe}}{V_{r,toe}} - 1 \leq 0$	Toe shear failure mode
$g_3(X) = \frac{FS_{(z,min)}}{FS_{(crushing)}} - 1 \leq 0$	Bearing failure mode	$g_9(X) = \frac{M_{d,heel}}{M_{r,heel}} - 1 \leq 0$	Heel moment failure mode
$g_4(X) = \frac{1}{FS_{(tension)}} - 1 \leq 0$	No tension condition mode	$g_{10}(X) = \frac{V_{d,heel}}{V_{r,heel}} - 1 \leq 0$	Heel shear failure mode
$g_5(X) = \frac{M_{d,stem}}{M_{r,stem}} - 1 \leq 0$	Stem moment failure mode	$g_{11}(X) = 1 - \frac{50(x_2 - x_1)}{H - x_s} \leq 0$	Geometric constraint
$g_6(X) = \frac{V_{d,stem}}{V_{r,stem}} - 1 \leq 0$	Stem shear failure mode	$g_{12}(X) = \frac{x_s}{H} - 1 \leq 0$	Geometric constraint

3.4 Objective Function

The objective function for the optimum design of RCRW is to minimize the cost of the retaining wall. When the cost of excavation, formwork and backfill is neglected, the objective function is formulated as;

$$f(x) = C_s W_s + C_c V_{c,net} \quad (11)$$

C_s is unit cost of steel and selected as \$0.40/kg [10],

W_s is the weight of steel per unit length of the wall,

C_c is unit cost of concrete and selected as \$40/m^3 [10],

$V_{c,net}$ is the net volume of concrete per unit length of the wall.

4. RESULTS AND DISCUSSIONS

4.1 The Results of the Analyses

In this study, the effects of the surcharge load (q), height of retaining wall (H) and the angle of internal friction of the backfill (ϕ_1) on minimum cost design of RCRWs resting on soil with high bearing capacity were investigated by using the ABC algorithm. In the ABC algorithm used, the following parameters were selected: colony size, CS = 100, modification rate, MR = 0.8, limit = 400 and maximum number cycles, MNC = 10000. The analyses were repeated 30 times for each starting from random population with different seeds. In this study, a total of 125 analyses were carried out for different surcharge loads (0 - 40 kPa), the heights of wall (4 m – 8 m) and the angles of internal friction of the backfill (28° - 36°). In all cases, the unit weight of backfill was taken as 17 kN/m^3. The knowledge obtained from previous experiences shows that the cost of the wall are not affected from the properties of base soil with high bearing capacity. Therefore, all of the analyses were made for strong

base soil conditions. In order to reflect the strong soil conditions, the shear strength parameters of the base soil were selected as c_2 = 200 kPa and ϕ_2 = 30°. The input parameters used in the analyses are given in Table 2.

Fig. 3 shows the effects of surcharge load on the cost of the wall having different angle of internal friction of the backfill. As the surcharge load increases, the cost of the wall nearly linearly increases for the walls of which their heights are both 4 m and 7 m. When the surcharge load increases from 0 to 40 kPa, it is seen that an increase in the cost of the wall between 59% and 79% occurs, depending on the angle of internal friction of backfill. This change remains between 54% and 59% for the wall of which its height is 7 m.

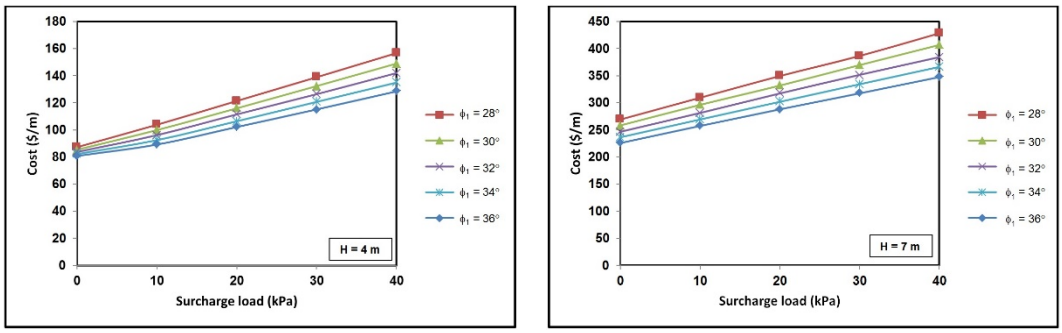

(a) (b)

Figure 3. The effects of surcharge load on wall cost

Fig. 4 illustrates the cost variation with the angle of internal friction of backfill (ϕ_1) for different values of the surcharge load. When the height of wall and surcharge load are constant, the cost of the wall decreases with increasing internal friction angle of backfill. This decrease trend is in linear form. As the angle of internal friction of backfill increases from 28° to 36°, the cost of the wall decreases 17% in average for all wall heights.

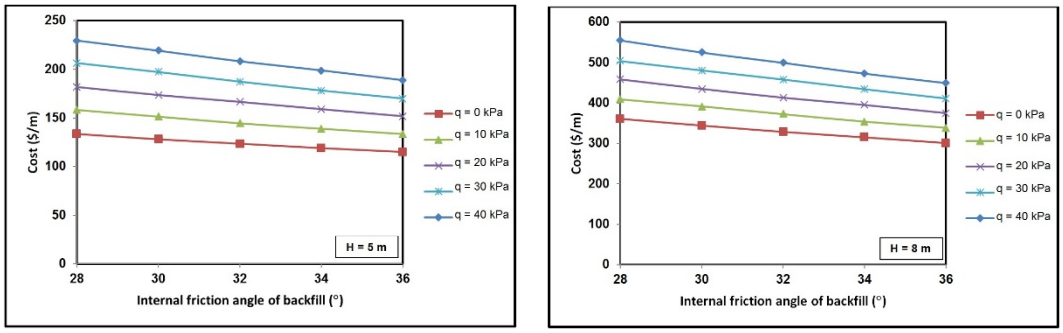

(a) (b)

Figure 4. The effects of internal friction angle of backfill on wall cost

Fig. 5 shows the cost variation with the height of wall. The height of wall is the main factor influencing the economy of the design. The cost increases exponentially as the height of wall increases. As H changes from 4 to 8 m, the optimum cost increases between 250% and 277%.

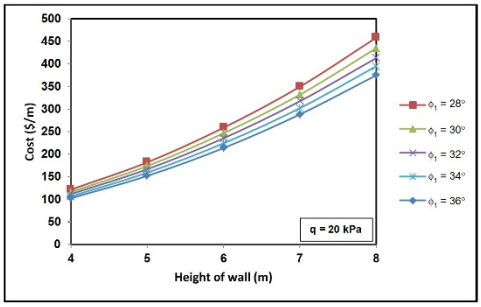

Figure 5. The effects of height of wall on wall cost

4.2 Regression Analysis

In this work, the three variables, which are q, ϕ_1 and H, were utilized to establish the regression equations for the determination of optimum cost of the wall. As is clear from Fig. 3 and 4, there is a nearly linear relationship between q or ϕ_1 and the cost of the RCRW. Therefore, q and ϕ_1 was taken into account as linear form in the regression model. The cost of the RCRW is exponentially affected by H. In order to evaluate the performance of the proposed regression model, the correlation

coefficient (R), the root mean squared error (RMSE) and the mean absolute relative error (MARE), that are given in Eqs. (12)-(14) respectively, were used as statistical measures.

$$R = \frac{\sum_{i=1}^{n}\left(C_{i,m} - \overline{C_{i,m}}\right)\left(C_{i,p} - \overline{C_{i,p}}\right)}{\sqrt{\sum_{i=1}^{n}\left(C_{i,m} - \overline{C_{i,m}}\right)^2 \times \sum_{i=1}^{n}\left(C_{i,p} - \overline{C_{i,p}}\right)^2}} \quad (12)$$

$$RMSE = \sqrt{\frac{\sum_{i=1}^{n}\left(C_{i,m} - C_{i,p}\right)^2}{n}} \quad (13)$$

$$MARE = \frac{\sum_{i=1}^{n}\left|\frac{C_{i,m} - C_{i,p}}{C_{i,m}}\right|}{n} \quad (14)$$

where $C_{i,m}$ and $C_{i,p}$ are the measured and predicted output values; $\overline{C_{i,m}}$ and $\overline{C_{i,p}}$ are the averages of the measured and predicted output values, respectively. n is the number of analyses. The RMSE and MARE values approaching zero and R values approaching 1 indicates that the regression model provides accurate predictions.

The regression model equation for calculation of the minimum cost of the wall (C_{min}) is as follows:

$$C_{min} = a_0 + a_1\phi_1 + a_2 q \quad (14)$$

where;

$$a_0 = 8.7439 \times H^{2.0726}$$

$$a_1 = -0.1173 \times H^{2.1499} \quad (15)$$

$$a_2 = 0.1812 \times H^{1.5195}$$

The comparison between the minimum cost between calculated by ABC algorithm and the minimum cost predicted by the regression analysis has been presented in Fig. 6. The predicted values are in good agreement with calculated values. Statistical performance evaluation criteria for regression analysis are presented in Table 4. This table shows a strong and significant correlation. The regression model gives R value of 0.9991. The RMSE and MARE values have great significance for the statistics in addition to the R value, and RMSE and MARE are 5.08 $/m and 1.68%, respectively. This determination shows that the minimum cost of the RCRW resting on strong base soil can be estimated using the proposed equation.

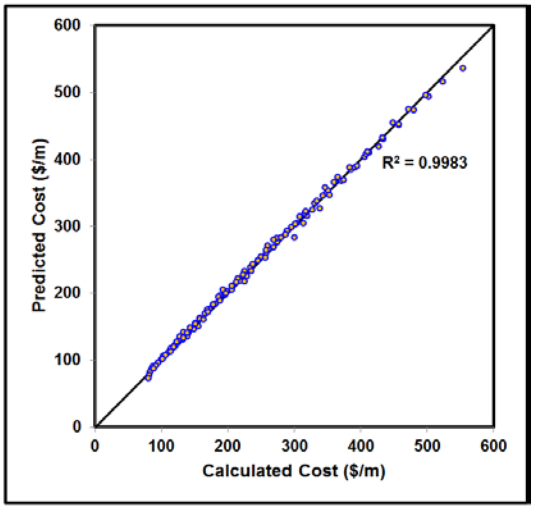

Figure 6. Comparison of calculated cost by ABC and predicted cost by regression model

Table 4. Statistical evaluation of regression analysis

Equation form	R	RMSE	MARE
$C_{min} = a_0 + a_1\phi_1 + a_2 q$	0.9991	5.08 $/m	1.68%

5. CONCLUSIONS

In this study, a multiple regression model for prediction of the cost of the RCRWs resting on strong base soil was proposed. The optimum cost of the wall has been obtained by ABC algorithm. The correlation coefficient (R), root mean squared error (RMSE) and mean absolute relative error (MARE) were used for the performance evaluation of the multiple regression model. The results of the model found that 0.9991; 5.08$/m and 1.68% for R, RMSE and MARE, respectively. The regression model gave a high correlation coefficient and low RMSE and MARE values. The results indicated that the regression model can be successfully predicted the cost of the walls. Consequently, proposed regression model can be used to predict the minimum cost of the RCRW resting on strong base soil.

REFERENCES

[1]. D. Karaboga, *"An idea based on honey bee swarm form numerical optimization,"* Technical Report TR06, Erciyes University, Turkey, 2005.
[2]. D. Karaboga and B. Basturk, *"Artificial bee colony (ABC) optimization algorithm for solving constrained optimization problems,"* LNCS: Advances in Soft Computing: Foundations of Fuzzy Logic and Soft Computing, Vol: 4529/2007, pp: 789-798, Springer- Verlag, 2007, IFSA 2007.
[3]. D. Karaboga and B. Akay, *"A modified artificial bee colony (ABC) algorithm for constrained optimization problems," Applied Soft Computing* **11**(3): 3021-3031, 2011.
[4]. M. Sonmez, *"Discrete optimum design of truss structures using artificial bee colony algorithm,"* Structural and Multidisciplinary Optimization **43**(1): 85-97, 2011.
[5]. M. Sonmez, *"Artificial bee colony algorithm for optimization of truss structures,"* Applied Soft Computing **11**(2): 2406-2418, 2011.
[6]. H. Garg, *"Solving structural engineering design optimization problems using an artificial bee colony algorithm,"* Journal of Industrial and Management Optimization **10**(3): 777-794, 2014.
[7]. TS 500-2000. *Requirements for design and construction of reinforced concrete structures.* Turkish Standards Institution.
[8]. A.L. Bolaji, A.T. Khader, M.A. Al-Betar, M.A. Awadallah, *"Artificial bee colony algorithm, its variants and applications: a survey,"* Journal of Theoretical and Applied Information Technology **47**(2): 434-459, 2013.
[9]. J.N. Cernica, *Geotechnical Engineering: Foundation Design*. John Wiley and Sons, Inc. New York, 1994.
[10]. A. Saribas and F. Erbatur, *"Optimization and sensitivity of retaining structures,"* Journal of Geotechnical Engineering **122**(8): 649-656, 1996.

ICENS
INTERNATIONAL CONFERENCE ON ENGINEERING AND NATURAL SCIENCES
24-28 May 2016 /Sarajevo

Geochemical and Mineralogical Properties of Zeolites from Gördes (Manisa) and Its Near Vicinity

Alaaddin Vural[1], Mustafa Albayrak[2]

Abstract

The study area which are rich in zeolite occurrences in volcanic rocks is located at Gordes and its near vicinity (Manisa, Turkey). In the area, Menderes Massif metamorphic rocks which consist of gneiss, migmatites, mica-schist and quartzite are basement rocks. These rocks are unconformably overlain by Kürtköy formation which consists of tufa, conglomerate and sandstone, and is overlain by Yeniköy formation which consists of conglomerate, sandstone, limestone and sandstone containing lignite and lignite. Çıtak formation consisting limestone, shale, mudstone, sandstone, tuff and bituminous shale is situated on Yeniköy formation and rhyolitic Gökyar tuff and Azimdağ volcanics pass upward respectively. Azimdağı volcanics are characteristics with dacite, rhyodacites, and rhyolitic lava domes. On the Azimdağ volcanic, Tekkedere formation consisting carbonaceous shale at the bottom and limestone in upper is situated. lacustrine limestone is situated to on Tekkedere formation. The youngest units are alluviums.

42 rock samples were collected from the area and investigated for geochemical and mineralogical propersties of zeolite minerals using XRF (such as major element oxides, minor and trace elements) and XRD (for minerals) . According to chemical analiysis: the ranges of major oxides, lost of ignition (LOI) vaules are 0.1 to 1.6% for Na2O, 0.2 to 12.4% for Mg, 1.5 to 15.5% for Al2O3, 32.2 to 73.7% for SiO2, 0.3 to 4.4% for K2O and 0.9 to 17.0% for CaO and 6.55 to 30.30% for LOI. According to XRD analysis, zeolite minerals were mainly clinoptilolite and rarely is heulandite type. In the some part of area, both of zeolite minerals, eg. clinoptilolite and heulandite were found together. SEM-EDX analysis is carried out on some samples, and the both results obtained from XRD analysis are confirmed by SEM. On the basis of geological, geochemical, and mineralogical studies, general properties of the area were brought out.

Keywords: *Zeolites, Geochemistry, Mineralogy, Gördes, Turkey*

1. INTRODUCTION

The term zeolite was originally called in 1756 by Swedish mineralogist Axel Fredrik Cronstedt. He observed that upon rapidly heating the material stilbite, it produced large amounts of steam from water that had been adsorbed by the material. The word “zeolite” means “boiling rock”, derives from Greek zeo, meaning “boil” and lithos, meaning “stone” [1]. Because zeolite group minerals bearing rocks explode and decompose when heated. Zeolites are a group of basic, hydrous aluminosilicate minerals. They possess an open aluminosilicate framework structure containing channels filled with water molecules and cations which are usually exchangable at temperatures below 100 ^{o}C. Zeolite minerals include empty spaces and channels in their structures. They can lose the water in these empty spaces and channels without changing their structures under high temperatures, due to their loose skeletal structures, they have replaceable cations. For this reason, they are commonly used in adsorbtion, ion exchange and dehydration industry [2]. About 42 species of natural zeolites are known and they show a wide compositional variation. These variations reflect various factors such as P-T conditions, chemistry of original material and pore water etc. [2-3].

Natural zeolites are composed of various processes and lithology: a) saline-alkaline lacustrine deposits formed through essentially closed-system alteration of volcanic ash; b) vertical sedimentary sequences formed through open-system alteration and/or burial diagenesis of volcanic ash; c) hydrothermally altered volcanic or sedimentary rocks; and d) deep-sea sediments [4].

The distribution of zeolitic rocks is usually very closely related to the site of volcanism. Zeolites of hydrothermal, contact metamorphism, burial diagenesis and percolating groundwater origins are commonly widespread in the younger orogenic belts and hot spots where thick deposition and contemporaneous volcanism occurred (Iijima, 1980). Most of the zeolite deposits are derived from tuffs, and the hydration of volcanic glass is often considered to be the preliminary stage of zeolitization.

The study area which are rich in zeolite occurrences in volcanic rocks is located at Gordes and its near vicinity on the Aegean region of western Turkey (Manisa, Turkey) (Fig. 1). Zeolites in the area are found in acidic tuffs. Two levels of acidic tuffs, of

[1] *Corresponding author: Gümüşhane University, Department of Geological Engineering, 29000, Bağlarbaşı/Gümüşhane, Turkey.* alaaddinvural@hotmail.com

[2] *General Directorate of Mineral Researh and Exploration,Çankaya, Ankara, Turkey,* mustafa_albayrak@hotmail.com

about 60 m thickness each, are observed in a volcano-sedimentary sequence of Miocene age about 1000 m thick [5]. Zeolite-bearing tuffs are white color and stratified and were formed in a lacustrine environment in Neogene age, while fedding by volcanic activity in the form of ash flow [6].

There are some papers related to zeolite occurences in the region [5, 7-10]. Some of them are mostly concerned with diagenetic, mineralogical, technological properties of zeolites. The purpose of this paper is to explicate the geological, mineralogical and geochemical properties of zeolites of Gördes and its near vicinity (Gördes Basin).

1.1 Geological Setting

The basement of the Western Anatolian region is made up of several tectono-stratigraphic units; including the Menderes Massif, belonging to the Anatolide block, and the rocks of Sakarya Continent. These units were amalgamated along the İzmir-Ankara Suture Zone. The Menderes Massif is composed of poly-metamorphic middle crustal units, such as gneisses, schist and schist–marble alternations. The basement rocks are covered by late Cenozoic volcano-sedimentary units that were mainly deposited in lacustrine environments [12-15].

The Gördes Basin, trend at approximately right angles to the more topographically expressed, E–W-trending Alaşehir (Gediz) Graben and is located at an elevated plateau area bordered by rolling hills, c. 600 m above sea level. It is bounded by metamorphic rocks of the Menderes Massif on its eastern, southern, and southwestern sides. The northwestern margin of the basin includes extensive exposures of ophiolitic melange [16], an allochthonous unit that was initially emplaced southwards in latest Cretaceous–early Tertiary time from the northern Neotethys, rooted within the İzmir-Ankara suture zone [17]. The volcanic rocks and related Neogene sediments of the basin rest on continental blocks and suture zone rocks. The Neogene volcanic activity in the basin is post-orogenic extensional [18]. As a result of Neogene volcanic activity and sedimentary process in the region, Lower Miocene Kürtköyü, Yeniköy and Çıtak formations unconformably overlie the Menderes massif. Kürtköyü formation is commonly composed of large chunks of rock, coarse conglomerate, conglomerate and sandstones. It is overlain by the Yeniköy formation with the lateral and vertical transition relationship, which is comprised dominantly of conglomerate, sandstone and mudstones including lignite levels. There are algal limestone interbeds at the upper levels of this formation. Çıtak formation (Küçükderbent formation) conformably and transitively overlies the Yeniköy formation. It is dominantly comprised of clayey limestone, shale, mudstone, sandstone, tuff and less bituminous shales which reflect a lacustrine environment. This unit is unconformably overlain by Gökyar formation which is made up of rhyolitic tuffs (Fig 1).

The volcano-sedimentary formations known as Gördes zeolites were formed by flowing and deposition of rhyolitic, rhyo-dacitic eruptions of Gökyar formation (Kobaklar Volcanism, [11]) located in the north of Gördes into the Lake Gördes which was a sedimentation basin in that period.

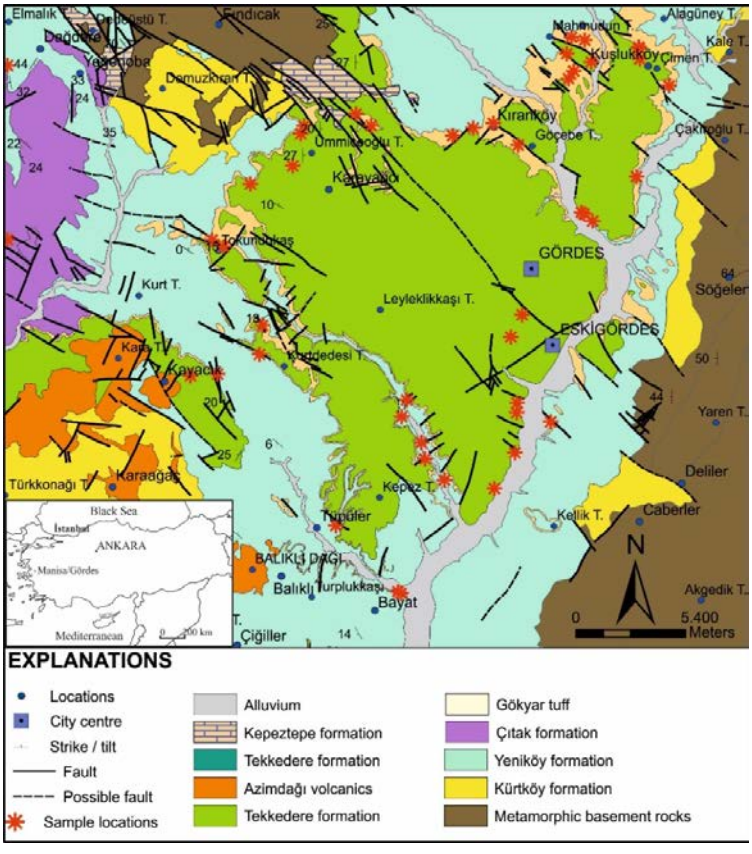

Figure 1. Geology of study area (modified after Göktaş et al., [11]*) and sample locations*

2. MATERIAL AND METHODS

In this study, field studies for geological purposes were carried out and the zeolite bearing samples collected from area were investigated for their mineralogical and geochemical properties. For this reason, thin sections of the samples were prepared for their mineralogical and petrographic determinations. X-ray Diffraction (XRD), X-Ray Fluorescence (XRF) and Scanning Electron Microscopy coupled with Energy Dispersive X-ray (SEM-EDX) Spectroscopy analyses were also performed for geological and geochemical properties. The types of zeolite minerals were determined by petrographic studies, XRD and SEM-EDX analyses. As for the geochemical characteristics and geological setting of the zeolites and related rocks, different geochemical diagrams, such as spider, TAS; AFM were drawn using GCDKit 4.1. Mineralogical-petrographic studies, XRD and geochemical analysis by X-Ray Flurecence were mainly conducted in the laboratories of the Department of Mineral Analysis and Technology of The Directorate of Mineral Research and Exploration (MTA). SEM-EDX analyses were conducted in Laboratories of Turkish Cement Manufacturers' Association (LOTCMA).

Zeolite samples from the study area were analyzed by means of Powder X-ray diffraction (XRD) using a Rigaku-Geigerflex model diffractometer with monochromatic Cu Kα radiation operated at 40 kV and 30 mA, scanning from 2 to 70° 2 theta with a step size of 0.02° and a counting time of 1 s/step and mineralogical determinations were carried out using MDI/JADE6 software. Samples are collected from all the potentially zeolite bearing units were prepared for XRD analysis by crushing and then grinding in an agate ball mill.

Types and characterizations of the zeolite minerals such as morphology, type, chemistry etc. were investigated using SEM-EDX in LOTCMA. Before analysis by SEM-EDX, the samples were coated with gold (350 ^{o}A) to enhance conductivity. During the analysis, it was taken SEM images and obtained EDX spectrum.

X-ray fluorescence spectrometry (XRF) was used to determine the major and trace element concentration samples from the area. element abundances were measured on fused discs and pressed powder pellets, respectively, using an automated Rigaku X-ray fluorescence spectrometer at LOTCMA. Loss on ignition (LOI) was determined by heating a separate aliquot of rock powder at 900 ^{o}C for 2 h.

3. RESULTS AND DISCUSSION

In the region, of zeolite minerals, mostly clinoptilolite and less hoylandite and analcime bearing levels are observed [8]. Calcalkaline volcanism comprised of lava and tuffs of dacitic, rhyodacitic composition which activated in Early Upper Miocene ends the Çıtak lacustrine deposition. These volcanics in Gökyar formation were defined as Karaboldere volcanics (Ercan, 1983). All these units were unconformably overlain by Upper Miocene-Pliocene sedimentary sequence (Fig. 1). To investigate of geological, mineralogical and geochemical properties of zeolite from the region were collected the samples from the area and analyzed using XRD to determine zeolite minerals. According to XRD measurements, mostly clinoptilolite and less heulandite, lesser extent analcime as zeolite minerals were determined in the area. With these minerals, smectite group clay minerals, mica, quartz, feldspar and the amorphous material was also detected (Table 1).

Figure 2. Zeolitization at lower part of Dedetepe hill. a) Upper level of Gökyar formation's tuff which contains zeolite, b) same place from different view

SEM-EDX analysis were performed on 2 of the samples to determine the morphology, type, chemistry etc. of the zeolite minerals Micromorphological images of clinoptilolite and smectite minerals as well as amorphous substance were obtained. SEM analysis on zeolites samples confirmed the XRD results and reveal that clinoptilolite minerals well-developed as plate in gaps and crack (Fig. 3). Conducting EDX analysis, peaks of K, Na, Ca, Al, O and Si were observed, that refers to the mineral clinoptilolite (Fig 3). In some back-scattered electron images of zeolite samples, platy clinoptilolite minerals, smectite minerals and the presence of globular amorphous material was also observed (Fig. 3).

When EDX analysis performed at different the points, in addition to K, Na, Ca, Al, O and Si peaks, increasing Mg peaks were observed that refers to smectite minerals.

Table 1. XRD Results of the sample

Samples	Minerals	Samples	Minerals
Gör.1	Clinoptilolite, amorphous materials	Kay.3	Heulandite, amorphous materials.
Oğul.1	Zeolite group mineral (heulandite-clinoptilolite), mica, quartz, smectite group clay minerals	Kay.4	Heulandite, amorphous materials.
Oğul.2	Zeolite group mineral (heulandite-clinoptilolite), amorphous materials	Kay.5	Clinoptilolite, amorphous materials.
Oğul.3	Heulandite, mica, smectite group clay, amorphous materials	Kay.6	Quartz, Zeolite group mineral (?Mordenite), mica.
Oğul.4	Clinoptilolite, mica, smectite group clay, amorphous materials	Kay.7	Clinoptilolite, amorphous materials.
Oğul.5	Clinoptilolite, mica, amorphous materials	Kay.8.	Clinoptilolite, Opal-CT, smectite group clay, mica, amorphous materials.
Oğul.6	Clinoptilolite, amorphous materials	Kay.9	Clinoptilolite, amorphous materials.
Enli Ocak	Zeolite group mineral (heulandite-clinoptilolite), amorphous materials	Kay.10	Quartz, amorphous materials.
SA.1	Feldspar, Zeolite group mineral (heulandite-clinoptilolite), mica	Kay.11	Quartz, amorphous materials.
SA.2	Zeolite group mineral (heulandite-clinoptilolite), mica, smectite group clay, amorphous materials	Kay.12.	Dolomite.
AR.1	Zeolite group mineral (heulandite-clinoptilolite), mica, smectite group clay, amorphous materials	Kay.13.	Clinoptilolite, smectite group clay, amorphous materials.
AR.2	Zeolite group mineral (heulandite-clinoptilolite), mica, amorphous materials	Kay.14.	Clinoptilolite, amorphous materials.
AR.3	Zeolite group mineral (heulandite-clinoptilolite)	Kay.15	Zeolite group mineral (heulandite-clinoptilolite), smectite group clay, amorphous materials.
AR.4	Zeolite group mineral (heulandite-clinoptilolite), amorphous materials	Kır.1.	Clinoptilolite, mica, quartz, amorphous materials.
KAL.1	Zeolite group mineral (heulandite-clinoptilolite), Opal-CT, smectite group clay, mica, amorphous materials	Kır.2	Clinoptilolite, amorphous materials.
KAL.2	Zeolite group mineral (heulandite-clinoptilolite), amorphous materials	Kır.3	Clinoptilolite, amorphous materials.
KAL?3	Zeolite group mineral (heulandite-clinoptilolite), amorphous materials.	Kır.4	Clinoptilolite, amorphous materials.
KAL.4	Zeolite group mineral (heulandite-clinoptilolite), mica, amorphous materials.	Kır.5	Clinoptilolite, amorphous materials.
KAL.5	Zeolite group mineral (heulandite-clinoptilolite), mica	Kır.6	Clinoptilolite, amorphous materials.
Kay.1	Heulandite, feldspar, mica, smectite group clay, amorphous materials.	Kır.7	Clinoptilolite, amorphous materials.
Kay.2	Heulandite, mica, smectite group clay, amorphous materials.	Kır.8	Zeolite group mineral (heulandite-clinoptilolite), quartz, feldspar, mica, amorphous materials.

3.1 Geochemical Evaluation

29 of the samples analyzed for major (Na_2O, MgO, Al_2O_3, SiO_2, K_2O, CaO, TiO_2 and total FeO) and some trace element (V, Zn, Sr, Y, Zr, etc.) using XRF. The descriptive statistics (minimum, maximum, mean and standart deviation) of the 29 elements determined in samples are collectively listed in Table 2. pH of the samples are in the range 6,97 to 9,91 which refers neutral to slightly basic. Loss of ignitions (LOI) values of the samples range between 6,55 and 30,30% with an average of 9,50. These values show that rocks in the area were exposed to intensely alteration. As to major oxides, SiO_2 values range 68-73.9% omitting one basaltic rock, mean all rocks show acidic characters except one.

Major element distributions are illustrated on Harker variation diagrams (Fig. 4) where Al2O3, MgO, CaO and FeOt decrease with increasing SiO2 and display negative trends (Fig. 4) compatible with the magmatic differentiation. Contrary to expectation related zeolitization, Na_2O decrease with increasing SiO_2 and display poor negative correlation with increasing SiO_2 but this negativity is not seen clearly. K_2O increase with increasing SiO2 and display positive trends compatible with the alteration process and zeolitization.

On the Zr/TiO2 versus SiO2 diagram of Winchester and Floyd [19] the zeolite bearing volcanic rocks are mainly rhyolitic, rhyodacitic and less commonly trachytic composition and plot in the subalkaline field (Fig. 5a). On the Nb/Y versus Zr/Ti diagram of Pearce [20] limited samples (due to Nb and Y absence) are commonly trachytic composition and less commonly rhyolitic, dacitic composition (Fig. 5b).

According to molar Na_2O-K_2O-Al_2O_3 triangular diagram, all samples display metaluminous/peraluminous and potassic trend compatible with alteration and zeolitization process (Fig. 5c).

Considering the spider patterns normalized lower continental crust [21], volcanic rocks are clearly enriched in LREE/incompatible elements and unfractionated HREE patterns, which are similar with the upper continental crust rather than the lower crust (Fig 5d).

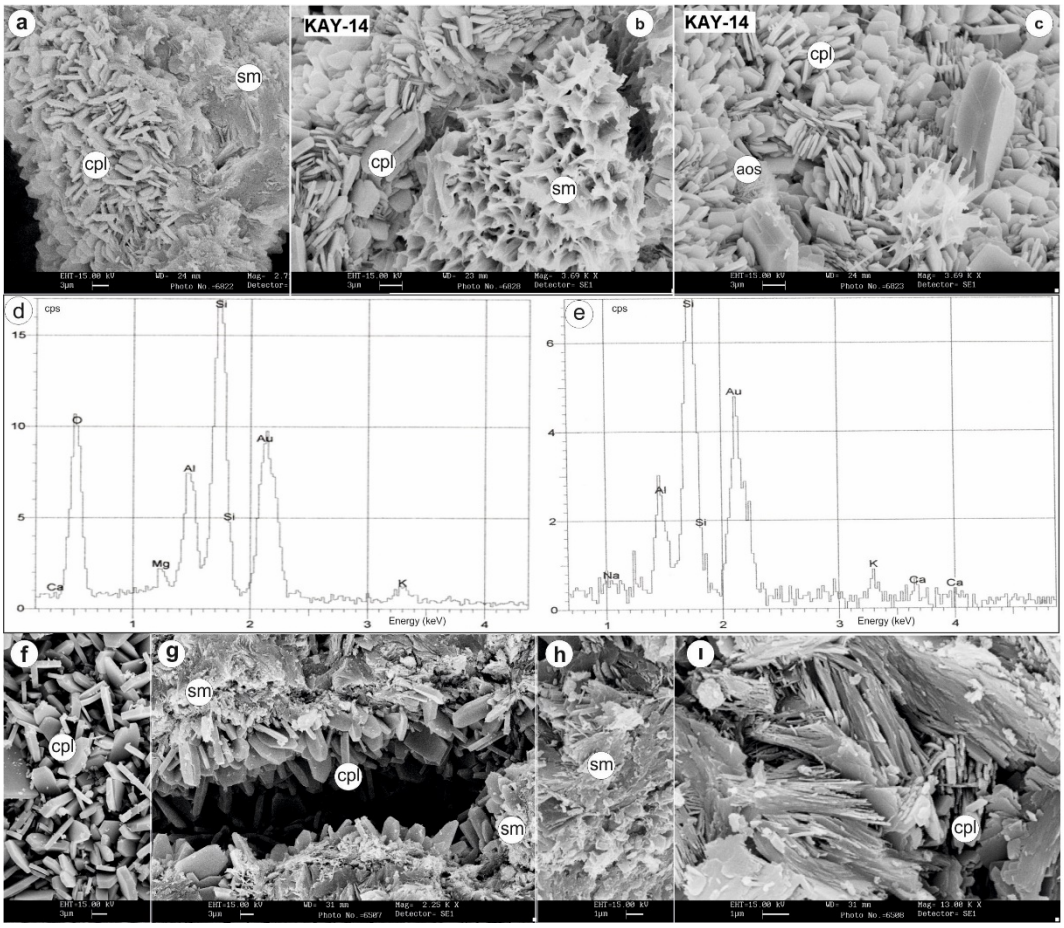

Figure 3. Back-scattered electron images showing aspects of zeolite group minerals, and its EDX graphs from some location a) clinoptilolite and smectite togetter, b) well-developed smectite and platy clinoptilolite minerals c) clinoptilolite platy minerals, smectite minerals and globular amorphous substance d) EDX graph showing smectite, e) EDX graph showing clinoptilolite, f) platy clinoptilolite different locality from the study area, g) well developed platy clinoptilolite minerals in gaps and cracks of tuff, h) entirely smectite containing samples ı) ongoing development of the clinoptilolite

Table 2 Descriptive statistics of major oxides and some trace elements (major oxides percent, trace elements in ppm)

	N	Minimum	Maximum	Mean	Std. Deviation
pH	29	6,97	9,91	8,67	0,66
LOI	29	6,55	30,30	9,52	4,16
Na2O	29	0,10	1,60	0,43	0,40
MgO	29	0,20	12,40	1,21	2,19
Al2O3	29	1,50	15,50	11,68	2,26
SiO2	29	32,20	74,10	69,59	7,52
K2O	29	0,30	4,40	2,58	1,02
CaO	29	0,90	17,00	3,40	2,73
TiO2	29	0,10	0,20	0,10	0,02
FeOt	29	0,20	2,20	1,03	0,50
V	18	12,00	34,00	17,61	6,03
Cr	5	91,00	6322,00	1413,60	2744,97
Zn	28	14,00	80,00	35,86	15,48
Rb	29	33,00	290,00	134,38	69,40
Sr	29	39,00	2336,00	591,69	396,37
Y	27	10,00	57,00	28,30	11,40
Zr	29	59,00	139,00	99,10	18,62
Nb	7	22,00	36,00	29,57	4,89
Ba	28	132,00	1289,00	565,86	335,22
Pb	25	24,00	147,00	57,44	31,38
Nd	11	20,00	37,00	28,55	6,23
Th	26	13,00	34,00	23,65	5,48
U	5	10,00	20,00	13,20	4,09

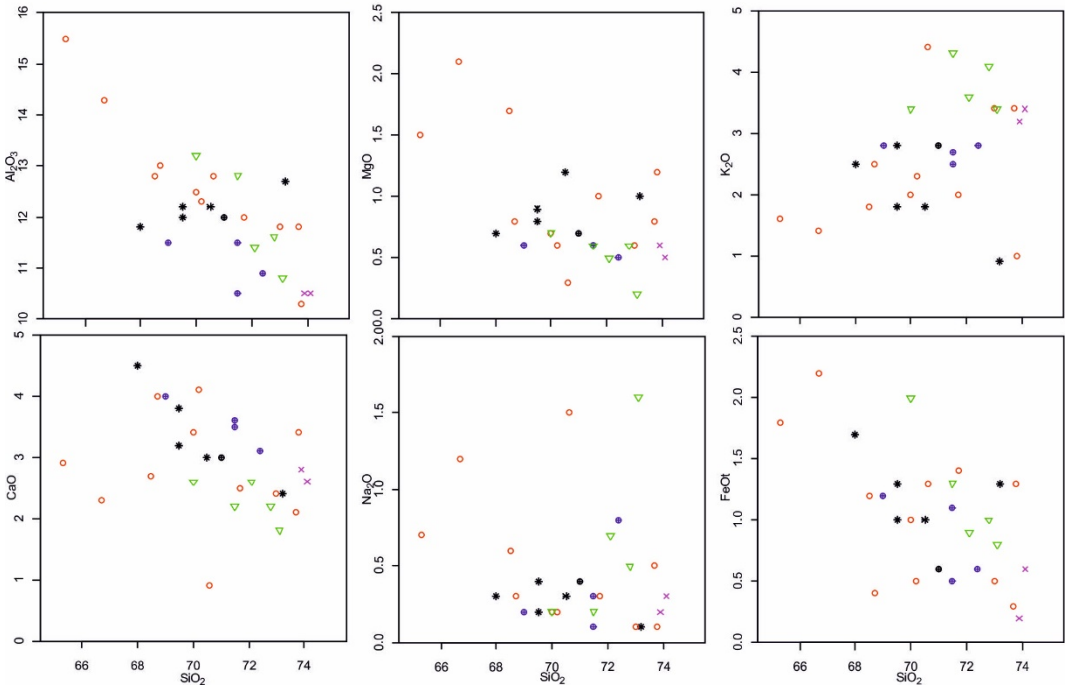

Figure 4. Diagrams of SiO_2 vs other major oxides

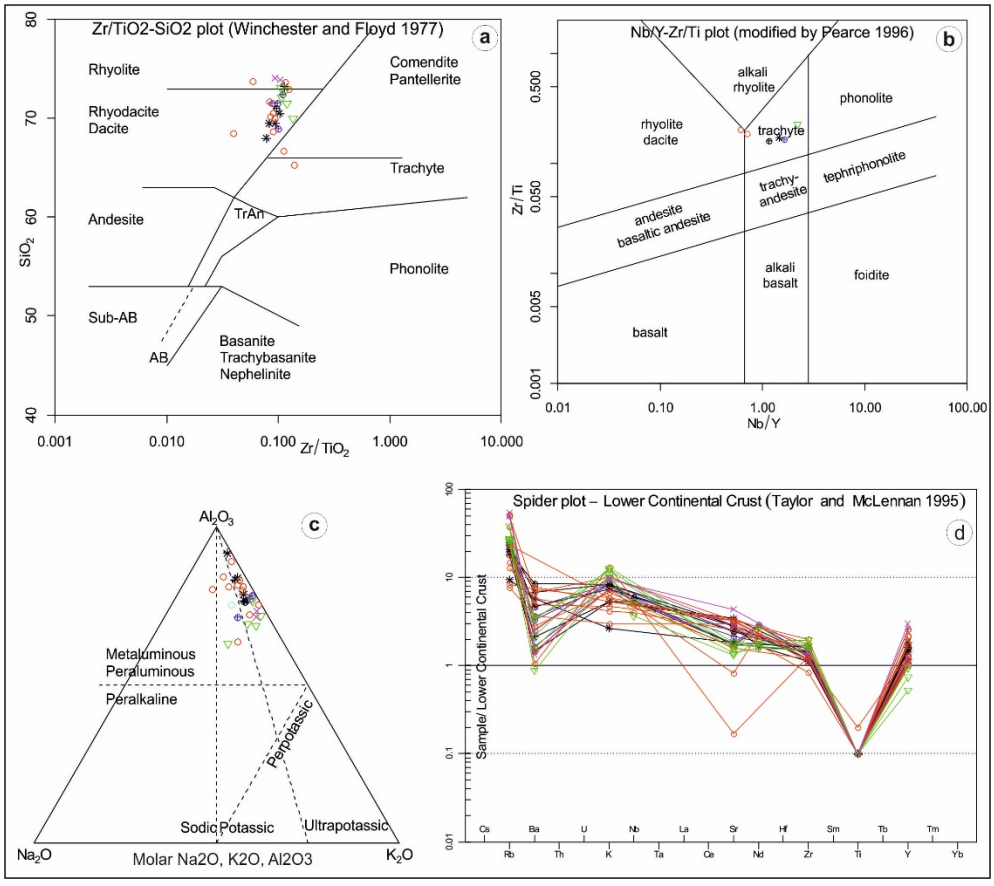

Figure 5. Diagrams of geological setting related (all samples are zeolite bearing samples, so not be given sample marks)

4. CONLCUSION

Rock samples were collected from the study area and investigated for geochemical and mineralogical propersties of zeolite group minerals using XRF (for geochemical purposes) and XRD and SEM-EDX (for minerals). According to XRD analysis, zeolite minerals were mainly clinoptilolite and rarely is heulandite type. In the some part of area, both of zeolite minerals, eg. clinoptilolite and heulandite were found together. SEM-EDX analysis is carried out on some samples, and the both results obtained from XRD analysis are confirmed by SEM. According to chemical analysis: the ranges of major oxides, lost of ignition (LOI) vaules are 0.1 to 1.6% for Na2O, 0.2 to 12.4% for Mg, 1.5 to 15.5% for Al2O3, 32.2 to 73.7% for SiO2, 0.3 to 4.4% for K2O and 0.9 to 17.0% for CaO and 6.55 to 30.30% for LOI. These values show that rocks in the area were exposed to intensely alteration. pH of the samples are in the range 6,97 to 9,91 which refers neutral to slightly basic. :

Major element distributions illustrating on Harker variation diagrams show that K_2O increase with increasing SiO2 and display positive trends compatible with the alteration process and zeolitization.

On the Zr/TiO2 versus SiO2 diagram of [19] and the Nb/Y versus Zr/Ti diagram of [20], the zeolite bearing volcanic rocks are mainly rhyolitic, rhyodacitic and less commonly trachytic composition and plot in the subalkaline field. As to molar Na_2O-K_2O-Al_2O_3 triangular diagram, all samples display metaluminous/peraluminous and potassic trend compatible with alteration and zeolitization process too.

Considering the spider patterns, zeolite bearing volcanic rocks are clearly enriched in LREE/incompatible elements and unfractionated HREE patterns, which are similar with the upper continental crust rather than the lower crust.

ACKNOWLEDGMENT

This study is supported by General Directorate of Mineral Research and Exploration (MTA, Ankara-Turkey). Authors thank to all MTA's officials. Presentation of the study were also supported Gümüşhane University.

REFERENCES

[1] H. Yücel, "Zeolitler ve Uygulama Alanları," 1987, pp. 391–402.
[2] K. Kayabalı, "Engineering aspects of a novel landfill material: Bentonite amended natural," *Eng. Geol.*, vol. 46, no. 105–114, 1997.
[3] A. Iijima, "Geology of natural zeolites and zeolitic rocks," in *Proceedings of the Filth International Conference on Zeo- IRes*, pp. 103–108.
[4] F. Bish and G. Guthrie, "Clays and zeolites," in *Health Effects of Mineral Dusts. Rev. Mineral*, G.D. Guthrie and B.T. Mossmann, Ed. 1994, pp. 28:168–184.
[5] F. Esenli and I. Özperek, "Zeolitic diagenesis of the Neogene basin in the vicinity of Gördes and mineralogy of heulandite-clinoptinolite.," *Bull. Geol. Congr. Turkey*, vol. 8, pp. 1–18, 1993.
[6] F. Esenli, "Geological, mineralogical, and geochemical investigation of Neogene series and zeolitization in the vicinity of Gördes.," Istanbul, Turkey, 1992.
[7] H. Türkbileği, "İzmir (Cumaovası-Urla-Çeşme-Karaburun) ve Manisa (Gördes Akhisar) zeolit yatakları maden jeolojisi raporu," Ankara, 1988.
[8] A. Vural and M. Albayrak, "Gördes ve Civarı Zeolitlerinin Mineralojisi," in *58th Geological Congress of Turkey*, 2005, pp. 140–141.
[9] M. Albayrak, "Albayrak, M., 2008. Batı Anadolu,Trakya,Kapadokya Yöresi Zeolitleri Mineralojik Veri Kitabı," Ankara, 2008.
[10] M. Albayrak, "Manisa (Gördes) bölgesi zeolitlerinin mineralojik, kimyasal ve teknolojik incelenmesi," *Kibited*, vol. 1, no. 4, pp. 273–285, 2010.
[11] F. Göktaşı, "Gördes Neojen Havzasının Jeolojisi," Ankara, 1996.
[12] G. SEYİTOĞLU, "Late Cenozoic tectono-sedimentary development of the Selendi and Uşak-Güre basins: a contribution to the discussion on the development of east–west and north trending basins in western Turkey," *Geol. Mag.*, vol. 134, no. 2, pp. 163–175, 1997.
[13] Y. Yılmaz, Ş. C. Genç, F. Gürer, M. Bozcu, K. Yılmaz, Z. Karacık, Ş. Altunkaynak, and A. Elmas, "When did the Western Anatolian grabens begin to develop? In: Bozkurt, E. Winchester, J.A., Piper J.A.D. (Eds.), Tectonics and Magmatism in Turkey and the Surrounding Area.," *J. Geol. Soc. London*, vol. 173, pp. 131–162, 2000.
[14] Y. Ersoy, C. Helvaci, H. Sözbilir, F. Erkül, and E. Bozkurt, "A geochemical approach to Neogene-Quaternary volcanic activity of western Anatolia: An example of episodic bimodal volcanism within the Selendi Basin, Turkey," *Chem. Geol.*, vol. 255, no. 1–2, pp. 265–282, 2008.
[15] E. Y. Ersoy, C. Helvac, and M. R. Palmer, "Mantle source characteristics and melting models for the early-middle Miocene mafic volcanism in Western Anatolia: Implications for enrichment processes of mantle lithosphere and origin of K-rich volcanism in post-collisional settings," *J. Volcanol. Geotherm. Res.*, vol. 198, no. 1–2, pp. 112–128, 2010.
[16] M. Purvis, "The Late Tertiary–Recent tectonic-sedimentary evolution of extensional sedimentary basins of the Northern Menderes Massif," 1998.
[17] A. Şengör and Y. Yılmaz, "Tethyan evolution of Turkey: a plate tectonic approach," *Tectonophysics*, vol. 75, pp. 181–241, 1981.
[18] Ö. Karaoğlu, C. Helvaci, and Y. Ersoy, "Petrogenesis and 40Ar/39Ar geochronology of the volcanic rocks of the Uşak-Güre basin, western Türkiye," *Lithos*, vol. 119, no. 3–4, pp. 193–210, 2010.
[19] J. A. Winchester and P. A. Floyd, "Geochemical discrimination of different magma series and their differentiation products using immobile elements," *Chem. Geol.*, vol. 20, no. C, pp. 325–343, 1977.
[20] J. A. Pearce, "A user's guide to basalt discrimination diagrams," *Geol. ical Assoc. Canada Short Course Notes*, vol. 2, no. 79–113, 1996.
[21] S. R. Taylor and S. M. McLennan, "The geochemical evolution of the continental crust," *Rev. Geophys.*, vol. 33, pp. 241–265, 1995.

Study on Surface Roughness of Carbon and Glass Fiber Filled Polytetrafluoroethylene in Turning Process

Muhammet Emre Sanci[1], Serdar Halis[2], Yavuz Kaplan[1]

Abstract

Although polytetrafluoroethylene (PTFE) has been used in many industrial applications such as sliding bearings, wiring in aerospace and computer applications, research about the machinability of this engineering plastic is inadequate. This paper focuses on investigation into turning of %25 carbon and %25 glass fiber filled PTFE in order to analyze the effect of machining parameters on surface roughness. The dry turning was carried out to examine average surface roughness by using a MAHR mobile roughness measuring instrument. Selected machining parameters are cutting speed (100 m/min), three different feed rate (0.1, 0.2, and 0.3 mm/rev) and three different depth of cut (1, 2, 3 mm).

Keywords*: Polytetrafluoroethylene, Surface Roughness, Turning, Machinability*

1. INTRODUCTION

Polytetrafluoroethylene (PTFE) is a thermoplastic polymer which exhibits good chemical resistance, high thermal stability, dielectric properties. The excellent mechanical properties and low friction coefficient of PTFE, makes it the preferred engineering plastic for many applications and processing techniques. It has been used such as seals, O-rings, V-rings, bearings, valve body, electrical insulators, laboratory instruments requiring chemical resistance or it is used in applications of non-stick surfaces, engine parts, biotechnology and medical applications. In addition, PTFE is used for coating automotive parts such as clutch, valves [1,3,4,5].

Mechanical properties of PTFE can be enhanced with glass fiber and carbon fillers. However, fillers may increase the machining difficulties. Polymer composites behaviors under machining processes differ from metals due to the time–temperature dependence of polymers and the addition of structural fillers. Surface roughness, cutting speed, feed rate and depth of cut play a significant role while determining the quality of the machined surface. To obtain good machinability and superior product quality, it is desired to have minimum surface roughness values [2,6].

The effect of cutting parameters such as cutting speed, feed rate and depth of cut on the surface roughness of PTFE composites were investigated during the dry turning operations. This study presents determination of cutting parameters (cutting speed, feed rate, and depth of cut) considering surface roughness into turning of %25 carbon and %25 glass fiber filled PTFE.

2. MATERIALS AND METHODS

Researchers conducted experiments using MAHR MARSURF PS 1 mobile roughness measuring instrument. The cutting tool was preferred as TiN coated carbide insert Korloy WNMG-NC5330. The machining parameters considered a cutting speed (100 m/min), three different feed rate (0.1, 0.2, and 0.3 mm/rev) and three different depth of cut (1, 2, 3 mm) and response considered was average surface roughness (Ra). The experiments was carried out on commercial pure, %25 carbon and %25 glass fiber filled PTFE with cylindrical specimens with a diameter of 50 mm. The values reported in study are the average of three readings taken at different lines around the workpiece.

3. RESULTS AND DISCUSSION

The surface roughness tests were conducted on CNC turning machine in dry conditions. Effect of feed rate and depth of cut on surface roughness in turning of PTFE is shown in Fig. 1.

[1] *Pamukkale University, Department of Mechatronics Engineering, Denizli, Turkey* ***msanci@pau.edu.tr***

[2] *Gazi University, Department of Automotive Engineering, Ankara, Turkey* **shalis@pau.edu.tr**

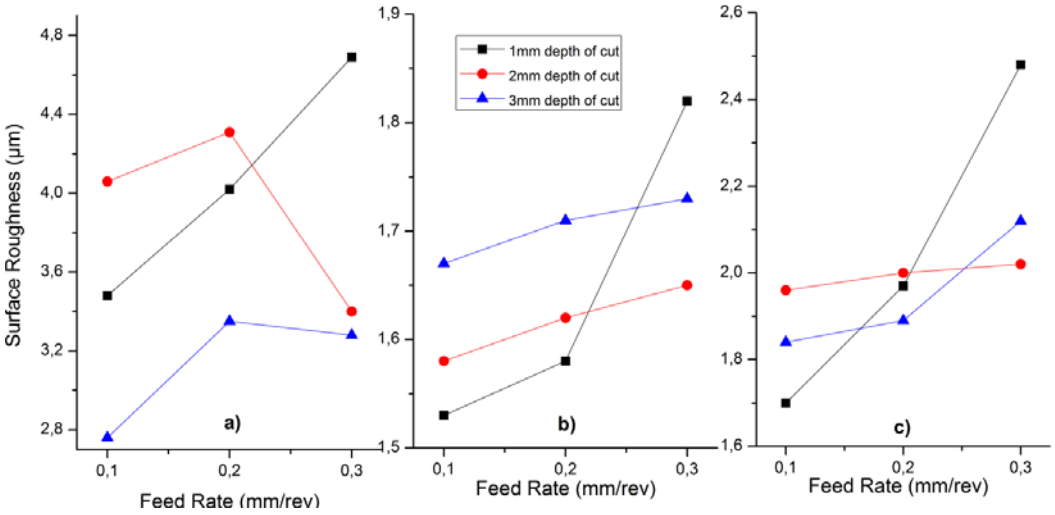

Figure 1. Effect of feed rate and depth of cut on surface roughness in turning of PTFE

a) Pure b) %25 carbon filled c) %25 glass fiber filled

It has seen that surface roughness of pure, %25 carbon filled and %25 glass fiber filled PTFE generally increases with increase of feed rate in all depth of cut parameters. Therefore, increasing feed rate is resulted in higher surface roughness and low feed rate is believed to produce a better surface finish. In addition, the highest Ra value was observed on pure PTFE in turning of 0.3mm/rev feed rate and 1mm depth of cut as 4.69µm. However, in these conditions, the effect of depth cut on the surface roughness is very complex and it does not show a regular behavior.

Fig. 2 displays a comparison of the surface roughness between pure, %25 carbon and %25 glass fiber filled PTFE.

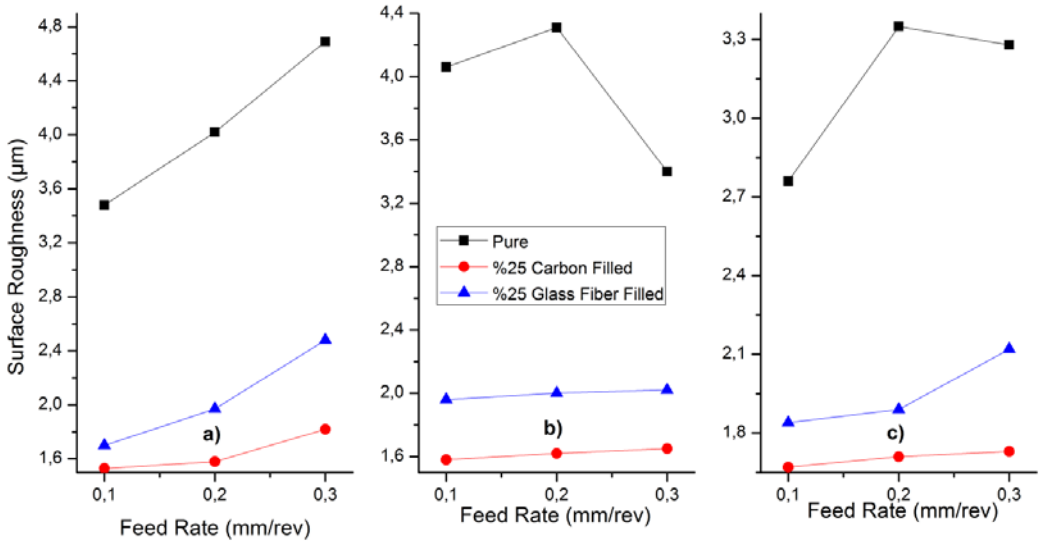

Figure 2. Effect of feed rate and filled materials on surface roughness in turning of PTFE

a) 1mm depth of cut b) 2mm depth of cut c) 3mm depth of cut

Figure 2 reveals that the highest Ra values were obtained on pure PTFE in turning for all machining parameters. The lower surface roughness values were observed on carbon and glass fiber filled PTFE. This indicates that carbon and glass fiber fillers lead to better surface finish in preferred experimental parameters. Specially, carbon fillers provide to obtain good machinability and superior product quality by minimum surface roughness values.

4. CONCLUSION

Differences between average surface roughness values are observed after applying manufacturing parameters on pure, %25 carbon filled and %25 glass fiber filled PTFE samples. Generally it is obtained that feed rate is an important factor in the turning process of PTFE materials. Besides, the effect of depth cut on the surface roughness does not show a regular behavior. The lowest surface roughness value was obtained on carbon filled PTFE in turning 0.1 mm/rev feed rate and 1mm deep of cut parameters as 1.53µm and the highest Ra value was observed on pure PTFE in turning of 0.3mm/rev feed rate and 1mm depth of cut as 4.69µm. Consequently, fillers materials that used in experiments provide to obtain better surface finish than unfilled PTFE.

REFERENCES

[1] A. Akıncı, H. Akbulut, F. Yılmaz, "Floropolimer (Teflon) kaplamaların yapı ve özellikleri" ,vol.133,pp. 53-59, 2003.
[2] C. Fetecau and F. Stan, Study of cutting force and surface roughness in the turning of polytetrafluoroethylene composites with a polycrystalline diamond tool, Measurement, vol. 45, pp. 1367-1379, 2012.
[3]. L. J. V. Royen, H. Bissett, M. C. Khoathane, J. K. Kocsis, "Preparation of PTFE/graphene nanocomposites by compression moulding and free sintering: A guideline", vol. 133, 2016.
[4]. F. Li, K. Hu, J. Li, B. Zhao, "The friction and wear characteristics of nanometer ZnO filled Polytetrafluoroethylene", vol. 249, pp. 877-882, 2001.
[5]. DuPont-Fluoroproducts, Teflon, PTFE, properties handbook, Tech. Rep. H-37051-3, DuPont; 1996.
[6]. D. Karayel, "Prediction and control of surface roughness in CNC lathe using artificial neural network", vol. 209, pp. 3125-3137, 2009.

The Investigation of the Response Against to ECF and TCF Bleaching of Wheat Straw Alkaline Sulfite-Anthraquinone (AS-AQ) Pulp

Evren Ersoy Kalyoncu[1], Huseyin Kirci[1], Emrah Pesman[2]

Abstract

ECF and TCF methods were used to investigate optimum alkaline sulfite-anthraquinone (AS-AQ) pulping conditions for wheat straw and bleaching of resulting pulp. In AS-AQ pulping experiments active alkali charge, maximum cooking temperature, heating time to maximum cooking temperature, alkali ratio, AQ dosage and liquor to straw ratio were kept constant at 17.5%, 170 °C, 70 min, 80/20, 0,2% and 5/1 respectively. Cooking time at maximum temperature was varied from 60 to 150 min. Optimum cooking time at maximum temperature was determined to be 90 min. The wheat straw pulps which produced under optimum cooking conditions were bleached with conventional DEDED and AOPaQPPa sequences as ECF and TCF methods respectively. In TCF bleaching, the usage of A stage ensured significantly lower HexA and metal ion content in the pulp. Eventually, considerable decrease in the consumption of bleaching chemicals was taken place. Although the pulp bleached by TCF method resulted in milder delignification, brightness of the pulp reached 83.5 %ISO. On the other hand, except for the tearing index, breaking length and bursting index of TCF bleached pulp were somewhat lower than for ECF bleached pulp.

Keywords: *AS-AQ pulping, ECF bleaching, TCF bleaching, wheat straw*

1. INTRODUCTION

Annual plant pulping is gaining more and more importance, particularly in countries with deficient wood resources. As a pulping raw material wheat straw has advantages such as: lower cost compared to wood, higher growing potential (over 10 tons/hectare), lower lignin content and more open structure for penetration of pulping liquor [1]. For non-wood plant pulping, mostly soda and soda-AQ pulping have been employed and nearly all bleaching investigations have considered CEH, HH or similar simple sequence based on these bleaching agents. Soda pulping is a well-understood process which is able to process a large variety of annual plant species, but this process has particular disadvantages as well. Strongly alkaline cooking liquors decompose carbohydrates by peeling-off reactions and alkaline hydrolysis. Sodium hydroxide easily dissolves phenolic lignin structure. In non-phenolic lignin moieties only β-ether linkages are cleaved. Under strongly alkaline conditions lignin fragments undergo condensation reactions which reduce the reactivity of residual lignin [2]. This has also a negative impact on bleaching. On the other hand, non-wood plants have fairly high silica content and strongly alkaline pulping liquors dissolve them to a high extent. The dissolved silica creates mainly precipitation problems in evaporators, recovery boilers and in the causticising plant [3].

Pulping at lower pH level can enable some advantages in the yield, strength and brightness properties of the pulp. The AS-AQ pulping method was developed by Ingruber et al. to produce a bleachable grade pulp from softwood species with kraft-like strength properties [4]. Patt and Kordsachia conducted some pulping experiments by adding methanol to AS-AQ liquor to obtain a pulp with high yield and brightness, low residual lignin content and good strength properties [5]. Similar results were had with the ASAE method by using ethanol as solvent for softwood species [6], [7].

Non-wood plants have low lignin content and more permeable structure for penetration of pulping liquor compared to woody structure and delignifying them only AS-AQ pulping liquor can be possible. Khristova et al. studied pulping of depithed Sudanese bagasse with soda-AQ and AS-AQ processes and bleaching environmentally friendly (TCF) techniques [8]. The results showed that the AS-AQ process gave superior yield, viscosity brightness, strength properties and delignification, capacity when compared to soda and soda-AQ pulps. The TCF bleaching of AS-AQ pulp with QO(OP)QP sequence gave pulp of good brightness and strength properties [8]. In another study bagasse AS-AQ pulps were bleached with OQ(OP) sequences with the resulting brightness of the pulps at 80% ISO. Short beating in a Jokro mill was sufficient to attain good

[1] *Corresponding author: Karadeniz Technical University, Arsin Vocational School of Higher Education, 61900 Arsin-Trabzon, Turkey.* *eersoy@ktu.edu.tr*

[2] *Artvin Coruh University, Department of Forest Product Engineering, 08000 Artvin, Turkey.* *emrahpesman@artvin.edu.tr*

pulp strength [9]. Hedjazi et al. studied AS-AQ pulping of wheat straw and totally chlorine free (TCF) bleaching of its resulting pulp [10]. According to the results of this study AS-AQ pulps were produced with a lower kappa number (10-14) and higher viscosity (1000-1100 ml/g) with using only 16% active alkali than those of soda and soda-AQ wheat straw pulps. Also the resulted pulp brightness was over the 80% ISO level after OQ(OP)P bleaching sequence.

In this study, AS-AQ cooking was applied to wheat straw using with high active alkali- (17.5%, as NaOH) and low alkali buffer (alkali to sodium sulfite ratio is 20/80) containing pulping liquor in order to obtain more selective delignification and silica stabilization. For TCF bleaching, wheat straw AS-AQ pulps were bleached with AOPaQPPa sequence then properties of the bleached pulp were compared with conventional ECF bleached pulp.

2. EXPERIMENTAL

2.1. Raw Material

Wheat straw (*Triticum aestivum L.*) was collected from the field in Kastamonu province in Turkey and delivered to Pulping and Papermaking Laboratory at the Forest Products Department of Karadeniz Technical University. The stalks were cleaned, dried at the ambient temperature and then chopped to approximately 3-5 cm in length, prior to pulping experiments. For maceration, wheat straw sample was treated with a mixture of 30% hydrogen peroxide and acetic acid (1:1) for 48 hours, at 60°C on a stove. Permanent micro-slides were prepared and digital photos were taken at 56x magnification for fiber length and 90x magnification for fiber and lumen width measurements. The following international TAPPI standard methods were used for the determination chemical composition and solubility of wheat straw: T-222 for lignin, T-211 for total ash, T-244 for silica, T-207 for cold and hot water solubility, T-204 for alcohol-benzene solubility and T-212 for NaOH 1% solubility [11].

2.2. Pulping

All cooks performed in a 15 L. stainless steel rotating digester having digital temperature controller and pressure measurement. All cooking experiments were performed with 500 g o.d. straw. Four chemical treatment times (60, 90, 120 and 150 minutes after reaching the pulping temperature) were studied. The other cooking parameters were kept constant as following: 17.5 % active alkali (calculated as NaOH, based on oven dry weight of straw), 170 ^{o}C as maximum cooking temperature, 80/20 as Na_2SO_3/NaOH, 0.2% AQ charge (on o.d. pulp), 5/1 liquor to straw ratio. At the end of the each cooking, pulped mixtures were discharged in a 200 mesh washing screen, disintegrated in a standard laboratory pulper and then screened on a laboratory screen having 0.15 mm slot to determine screened pulp yield, reject ratio and total yield. Screened pulp was dewatered and stored in polyethylene bags at 4 ^{o}C until further processing.

2.3. Bleaching

For the Totally Chlorine Free (TCF) bleaching, an AOPaQPPa sequence was applied to wheat straw AS-AQ pulp, produced at the optimum cooking conditions. Distilled peracetic acid solution was produced from the hydrogen peroxide-acetic acid mixture. The power of this solution was determined by iodine-thiosulfate titration [12]. For the Elemental Chlorine Free (ECF) bleaching, a DEDED bleaching sequence was also applied to wheat straw AS-AQ pulp, as a reference. Chlorine dioxide (ClO_2) used in D stages was made from sodium chlorate using the Solvay method at laboratory scale. Active chlorine content of the chlorine dioxide solution was calculated by iodimetric titration. The kappa factor was taken as 0.20 for calculating of active chlorine dioxide charge at the first D stage. Needed chlorine dioxide and alkali amounts of the other stages were calculated according to formulas of Gullichsen and Fogelholm [12]. Only O stage of TCF bleaching sequence performed in a 15 L. stainless steel rotating digester, other stages of both TCF and ECF bleaching sequences were conducted in polyethylene bags and hot water bath. During the bleaching periods in hot water bath, the sample was hand kneaded. At the end of each bleaching trial, the pulp was thoroughly washed with tap water, dewatered and finally hand sheets were prepared for further testing. TCF and ECF Bleaching conditions were showed in Table 1.

Table 1. ECF and TCF bleaching conditions of AS-AQ pulps

Bleaching sequences	Bleaching stages	Bleaching conditions
ECF Bleaching (DEDED)	D_0	*ClO_2 charge to the pulp*: 2.74% as active chlorine, *Temperature*: 70 °C, *Time*: 60 min., *Pulp consistency:* 7%, *pH*: 3.6
	E_1	NaOH charge to the pulp: 1.15%, *Temperature*: 70 °C, *Time*: 60 min., *Pulp consistency*: 110%, *pH*: 12.17
	D_1	*ClO_2 charge to the pulp*: 0.91% as active chlorine, *Temperature*: 70 °C, *Time*: 90 min., *Pulp consistency:* 10%, *pH*: 3.8
	E_2	NaOH charge to the pulp: 0.73%, *Temperature*: 70 °C, *Time*: 60 min., *Pulp consistency*: 110%, *pH*: 12.17
	D_2	*ClO_2 charge to the pulp*: 0.46% as active chlorine, *Temperature*: 70 °C, *Time*: 120 min., *Pulp consistency:* 10%, *pH*: 4.6
TCF Bleaching (AOPaQPPa)	A	*pH*: 3.0±0.1 (adjusted by 0.1 N H_2SO_4), *Temperature*: 100 °C, *Time*: 70 min, *Pulp consistency*: 3%
	O	*NaOH charge to the pulp*: 1,5%, *$MgSO_4.7H_2O$ charge to the pulp*: 0.5%, *Oxygen pressure*: 7 kg/cm^2, *Temperature*: 100 °C, *Time*: 60 min., *Pulp consistency*: 12%, *pH*: 13.0
	Pa_1	*Peracetic acid charge to pulp*: 1.0%, *$MgSO_4.7H_2O$ charge to the pulp:*0.2%, *$CaSO_4$ charge to the pulp*: 0.2%, *DTPA charge to the pulp*: 0.2%, *pH*: 5.5±0.1 (adjusted 0.1 N NaOH), *Pulp consistency*: 10%, *Temperature*: 80 °C, *Time*: 60 min.
	Q-P	Q Stage: *Charge of chelating agent*: 0.76 mMol DTPA per 100 g pulp, *Pulp consistency:* 3%, *Temperature*: 70 °C, *Time*: 60 min., *pH*: 5±0.1 (adjusted by 0.1 N H_2SO_4) P Stage: *H_2O_2 charge to the pulp*: 2%, *NaOH charge to the pulp*: 1,4%, *$MgSO_4.7H_2O$ charge to the pulp*: 0.5%, *$Na_2S_2O_7$ charge to the pulp*: 0.1%, *DTPA charge to the pulp*: 0.2%, *Pulp consistency*: 12%, *Temperature*: 70 °C, *Time*: 120 min., *pH*: 11.7
	Pa_2	*Peracetic acid charge to pulp*: 0.7%, *$MgSO_4.7H_2O$ charge to the pulp:*0.2%, *DTPA charge to the pulp*: 0.2%, *pH*: 5.5±0.1 (adjusted 0.1 N NaOH), *Pulp consistency*: 10%, *Temperature*: 80 °C, *Time*: 60 min.

2.4. Methods of Pulp Characterizations

The following international TAPPI standard methods were used for pulp analysis: kappa number T 236; Hexenuronic acid content: T282 (Using Shimadzu UV-1208 model UV-VIS spectrophotometer); ash content: T211; silica content T244, Metal ion content (Mn, Cu and Fe): T266 (using ATI UNICAM AA-929 model spectrometer). Hand sheets produced from bleached and unbleached pulps were conditioned under TAPPI T 402 standard condition, and their strength properties were determined according to TAPPI T 220 standard [11]. The viscosity of the pulp was determined by Scan Test Methods, SCAN-CM 15:88 standards. Also the brightness of the pulp was determined according to ISO 2470 standard using Minolta CM-2600d model spectrophotometer [13], [14].

3. RESULTS AND DISCUSSION

3.1. Fiber Dimensions and Chemical Composition

Fiber dimensions and chemical composition of wheat straw were given in Table 2 with comparing hardwood and softwood species. According to the Table 2, fiber length of wheat straw was similar with those of hardwood species. Thinner fiber could give good strength and surface smoothness during papermaking. Wheat straw had higher polysaccharide, lower lignin content and more porous structure compared to woody materials, so it was easy to delignify wheat straw using a lower alkali ratio. High ash and silica content of agricultural crops was confirmed at this study as 6.3% and 4.4% respectively. Higher 1% NaOH solubility (44.4%) of the straw originated from its higher hemicellulosic constituents with lower DP and liphophilic extractives, and the results were conformed to literature findings [15].

Other possible variations on the fiber dimensions and chemical composition could be based on some factors related growing and harvesting conditions of wheat straw samples such as location, soil composition, climate and harvesting time [16].

Table 2. Fibre dimensions and chemical composition of wheat straw

	Wheat straw Determined	Hardwood species	Softwood species	Wheat straw (Eroğlu et al 1983)
Fiber length (mm)	1.34	0.7-1.8	3-7	1.39
Fiber width (µm)	16.6	20-35	32-43	13.5
Lumen width (µm)	3.98	5-15	22-30	7.0
Holocellulose (%)	76.0	78-80	70-74	73.9
Cellulose (%)	47.7	45-55	45-55	48.0
Lignin (%)	17.1	17-24	25-30	15.7
Total ash (%)	6.3	0.2-1.0	0.2-1.0	4.4
Silica (%)	4.4	nd	nd	2.6
Solubility in alcohol-benzene (%)	7.8	2-6	2-8	5.3
Solubility in 1% NaOH (%)	44.4	14-20	9-16	40.1
Solubility in Hot water (%)	10.0	2-5	3-6	10.5
Solubility in cold water (%)	8.6	2-4	2-5	7.6

3.2. Pulping

In order to obtain a pulp with higher yield and lower residual lignin content, Ingruber's original AS-AQ cooking method was applied and NaOH to Na_2SO_3 ratio was held constant at 1/4 [4]. Thus, pulping was finished at a lower pH level of approximately 10 without serious carbohydrate degradation. Consequently, high screened yield (47-50%), pulp viscosity (976-1130 ml/g) and ISO brightness (50.8-54.7%) were achieved at low kappa number (6.5-8.3) level (Table 3).

Table 3. Cooking variables and pulp properties of AS-AQ pulps

Cooking time at max. temp. (min)	Screened yield (%)	Reject Ratio (%)	Total Yield (%)	Kappa no	Viscosity of pulp (ml/g)	Brightness (% ISO)	End pH
60	50.6	0.45	51.1	8.3	1130	50.8	10.3
90	49.1	0.32	49.4	6.6	1123	55.6	10.1
120	48.3	0.27	48.6	6.6	1120	55.0	10.0
150	46.9	0.18	47.1	6.5	976	54.7	10.0

Constant cooking variables pulps: 17.5% active alkali (as NaOH), 20/80 alkali ratio, 0.2% AQ dosage, 5/1 liquor to straw ratio, 70 min heating time to maximum temperature and 170 ^{o}C maximum cooking temperature.

As it seen in Table 3, delignification slows somewhat above 90 minute cooking time at maximum temperature. The best results were obtained at 90 minute cooking time: 49.1% screened yield, 6.6 kappa number, 1123 ml/g pulp viscosity and 55.6% ISO brightness. Usta et al. cooked the wheat straw with the ASAE method using 0.1% anthraquinone and 50% ethanol at the similar pulping condition. The most striking result of this study was higher pulp yield (54.8%) arising from carbohydrate stabilization by the alcoholic pulping medium [17]. The results showed that wheat straw AS-AQ pulp produced at the optimal conditions had the potential for easy bleaching with TCF bleaching.

3.3. Bleaching

Bleaching is a process of discoloration of the pulp to produce adequate contrast on printing paper. Bleaching of the paper can be carried out in case of multistage sequences using with chlorine containing agents (conventional or ECF bleaching) or only

with oxygen based bleaching agents (TCF bleaching). Some properties of unbleached, ECF and TCF bleached wheat straw AS-AQ pulps were given in Table 4.

Table 4. Pulp properties of unbleached and bleached AS-AQ pulp produced at optimum cooking condition.

	Screened yields (%)	Kappa no	SCAN viscosity (ml/g)	ISO brightness (%)	HexA Content (µmol/g)	Ash content (%)	Silica content (%)
Unbleached pulp	49.1	6.6	1023	55.6	3.05	6.4	5.4
TCF-bleached pulp	44.7	1.5	860	83.4	0.9	2.6	1.8
ECF-bleached pulp	45.7	0.2	957	85.6	2.6	4.7	4.2

In the beginning of the TCF bleaching sequence, an acid washing stage (A) was applied in order to remove hexenuronic acids (HexA) and transition metal ions to reduce decomposition of bleaching solution. As shown in Figure 1, after A stage, kappa number of the pulp decreased to 4.1 with the 38.4% reduction, due to removing of HexA and acid insoluble lignin. *According to some researchers***,** one-third of the permanganate consumption in kappa analysis is caused by HexA [18], [19].

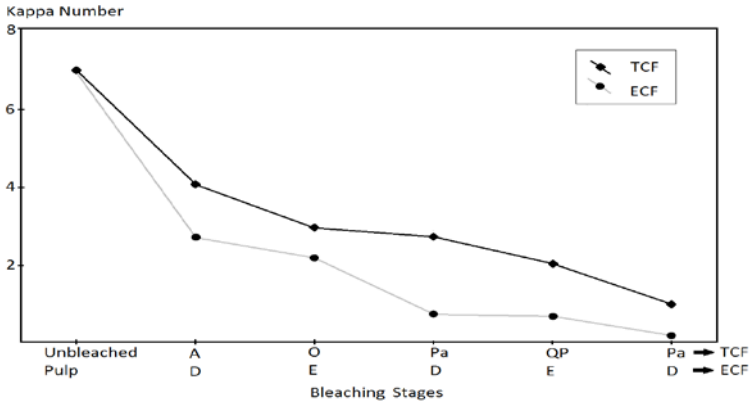

Figure 1. Changes in kappa number during the TCF- and ECF-bleaching sequences

In the following stage, oxygen delignification (O), the kappa number was reduced to 3.0 using only 1.5% sodium hydroxide. Peracetic acid (Pa) stage was applied to the pulp for breakdown of residual lignin and to convert it soluble form in alkali medium. Hereby, the kappa number of the pulp decreased to 2.1 following the chelation (Q) and peroxide bleaching (P) stage. After the second Pa stage, the kappa number the pulp diminished to 1.5 (Figure 1). The course of kappa number throughout the ECF bleaching sequence (DEDED) followed similar trend, but lower kappa numbers were obtained after the final stage.

Figure 2 showed a downward trend of pulp viscosity during ECF and TCF bleaching sequences. However decrement in the pulp viscosity was quite slower at for ECF bleaching than for TCF bleaching. In comparison with unbleached pulp, total viscosity losses were found 6.5% and 15.3% for ECF and TCF bleaching respectively.

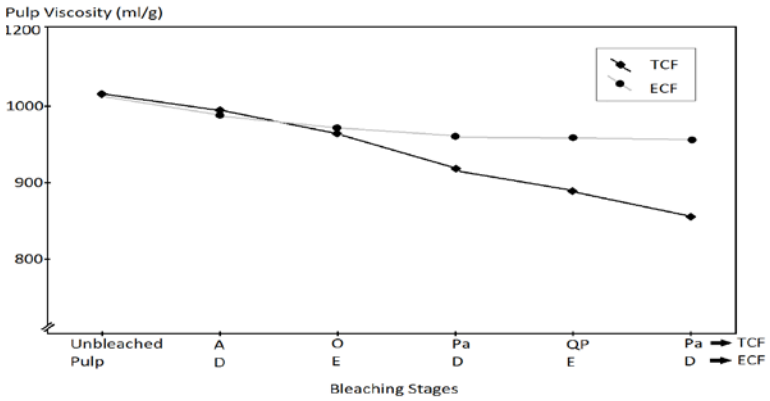

Figure 2. Changes in pulp viscosity during the TCF and ECF bleaching sequences

Augmentations in pulp brightness throughout the bleaching sequences were illustrated in Figure 3. In the TCF bleaching sequence, a regular brightness enhancement was observed during bleaching sequence excluding the first stage (A stage) of the sequence. Brightness of the pulp reached 83.4 in the TCF bleaching stage using only 1.7% peracetic acid and 2% hydrogen peroxide. However after ECF bleaching, the ISO brightness reached 86.4% by using 4.1% active chlorine consumption.

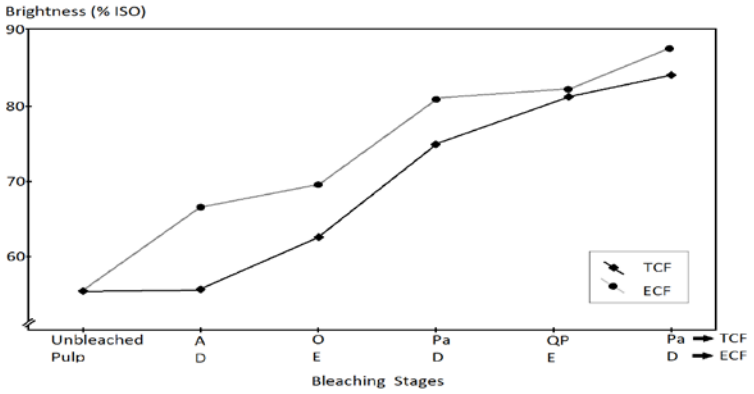

Figure 3. Development of brightness during the TCF- and ECF-bleaching sequences

According to Figure 4, HexA content of the pulp decreased with acidic stages such as A, Pa and D, but increased with alkaline stages such as O, E and P. These findings verify the HexA formation released from 4-O-Me-glucuronoxylan in the alkali containing pulping and bleaching media [20]. Petit-Breuilh et al. was found that peracids effectively remove HexA from hardwood kraft pulp even under mild condition [21]. This can explain lower HexA content of TCF-bleached wheat straw AS-AQ pulp.

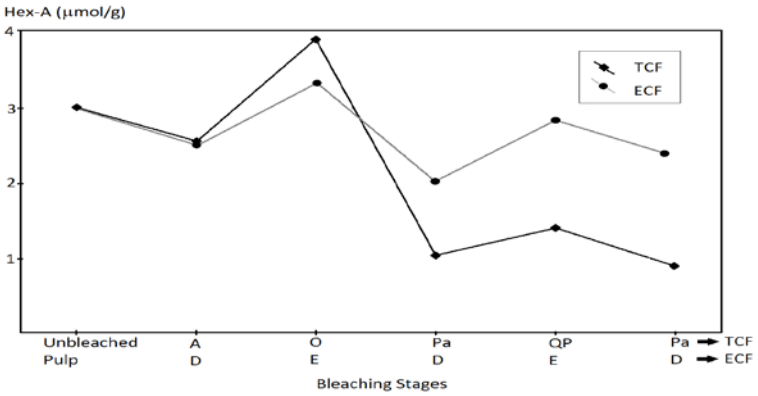

Figure 4. Changes in Hex-A content of the pulp during TCF- and ECF-bleaching sequences

The effects of different agents used in the chelating (Q) stage on residual metal ion concentration of the pulp were shown in Table 5.

Table 5. Effects of chelating agents on residual metal ion content in wheat straw AS-AQ pulps

	Mn (mg.kg^{-1})	Fe (mg.kg^{-1})	Cu (mg.kg^{-1})
Unbleached AS-AQ Pulp	7.56	20.92	4.77
AOPa	1.12	18.91	2.47
AOPaQ$_{DTPA*}$	0.34	4.58	1.32
AOPaQ$_{EDTA*}$	0.42	3.40	1.76
AOPaQ$_{DTMPA*}$	0.70	18.74	2.34
* Dosage of chelating agents: 0.2 mmol/g pulp			

Harmful metal ions removed from the pulp prior to Q stages were comprised of 85%, 48% and 10% for Mn, Cu and Fe ions respectively in comparison with unbleached pulp. In the chelation (Q) stage three chelating agents such as DTPA, EDTA and DTPMA were used and these chemicals were added to the pulp at 0.2 mmol/g. The best ion removal happened with DTPA for Mn and Cu ions as 70% and 76% respectively. The efficiency of Fe ion removal was obtained with EDTA and DTMPA as 82% and 76% respectively. As a chelating agent, DTPMA was found ineffective for Fe ion removal.

Some strength properties at the 50 SR^{o} freeness level of unbleached, TCF and ECF bleached wheat straw AS-AQ pulp were shown in Table 6.

Table 6. Strength properties at the 50 ^{o}SR freeness level of unbleached and bleached AS-AQ pulp produced at optimum cooking condition.

		Unbleached pulp	TCF-bleached pulp	ECF-bleached pulp
Tensile index (Nm/g)	Mean	52.5	55.7	59.3
	Stnd. Dev.	3.0	4.9	3.7
Burst index (kPa.m^2/g)	Mean	3.9	3.5	4.2
	Stnd. Dev.	0.08	0.17	0.21
Tear index (mN.m^2/g)	Mean	3.2	3.9	3.7
	Stnd. Dev.	0.18	0.59	0.39

As it was shown in the Table 6, tensile and tear indexes of the ECF and TCF bleached pulp were significantly higher than unbleached pulp due to increased fiber bonding characteristic of lignin removal from the bleached pulps. In general, the strength properties of TCF-bleached pulp were lower than ECF-bleached pulp excluding the burst index.

4. CONCLUSIONS

Wheat straw can be an important raw material for the pulp and paper industry due to higher polysaccharide, lower lignin content and more porous structure compared to woody materials. The fiber characteristics of wheat straw are similar to most of hardwood species growing in temperate zone of the world, utilized widely as a short fiber resource in the paper industry.

It was concluded that, pulping of wheat straw using 17.5% active alkali containing a 1/4 alkali ratio had higher yield and brightness, and a lower kappa number. As a result, it was possible to produce a pulp easily bleachable and suitable to totally chlorine free bleaching applications.

AOPaQPPa sequence was carried out as a TCF-bleaching technique for AS-AQ pulp produced from wheat straw and findings were compared the properties of the pulp bleached with elemental chlorine free (ECF) DEDED sequence. The most interesting result was the small amount of chemical usage in the bleaching process due to the removal of HexA and harmful metal ions by acid washing (A) and peracetic acid (Pa) stages. Eventually 83.4% ISO pulp brightness was provided with expending only 1.7% peracetic acid and 2% hydrogen peroxide. However totals active chlorine consumption must be hold 4.1% in order to achieve 86.4% ISO brightness for DEDED bleaching sequence.

The application of AOPaQPPa sequence as TCF-bleaching process gave the pulp high brightness and strength properties as much as ECF-bleached pulp. As a result, TCF bleaching of wheat straw AS-AQ pulp fulfills the requirement of the quality of writing and printing grade paper.

REFERENCES

[1]. H. Eroğlu, M. Usta and H. Kırcı, " A review of oxygen pulping conditions of some nonewood plants growing in Turkey" in *TAPPI Nonwood Plant Fiber Pulping*, 1994, Progress Report, No.21, pp33-40.
[2]. H. Sixta, *Handbook of Pulp*, edited by H. Sixta (Ed.), Weinheim, Wiley-VCH, 2006, pp 608.
[3]. S. Hedjazi, O. Kordsachia, R. Patt, A.J. Latibari, U. Tschimer, "Alkaline Sulfite-Antraquinone (AS/AQ) Pulping of Wheat Straw and Totally Chlorine Free (TCF) Bleaching of Pulps" , *Industrial Crops and Products*, vol.29, pp. 27-36, 2009.
[4]. O.V. Ingruber, M. Stradal, J.A. Histed, "Alkaline Sulphite-AQ Pulping of Eastern Canadian Woods", *Pulp and Pap. Mag. Canada*, vol. 83(12), pp. 342-348, 1982.
[5]. R.Patt and O. Kordsachia, " Herstellung von Zellstoffen unter verwendung von alkalischen Sulfitlosungen mit Zusatz von Anthrachinon und Methanol", *Papier*, vol. 40(10A), pp. 1-8, 1986.
[6]. H. Kırcı, Ş. Bostancı, M.K. Yalınkılıç, "A New Modified Pulping Process Alternative to Sulphate Method "Alkali-Sulfite-Antraquinone-Ethanol" (ASAE)", *Wood Science Technology*, vol.28, pp 89-99, 1994
[7]. E. Gümüşkaya, E. Erişir, H. Kırcı, N. Mısır, "The Effect of Sodium Borohydride on Alkaline Sulfite-Anthraquinone Pulping of Pine (Pinus pine) Wood", *Ind. Eng. Chem. Res*, vol. 50(3), pp. 8340-8343, 2011
[8]. P. Khritova, O. Kordsachia, R. Patt, I. Karar, T. Khider, "Environmentally Friendly Pulping and Bleaching of Bagasse", *Industrial Crops and Products*, 23, pp. 131-139, 2006.
[9]. S. Hedjazi, O. Kordsachia, R. Patt, A.J. Latibari, U. Tschirner, "Bagasse alkaline sulfite-anthraquinone (AS/AQ) pulping and totally chlorine free (TCF) bleaching", *Holzforschung*, vol. 62, pp.142-148, 2008.
[10]. S. Hedjazi, O. Kordsachia, R. Patt, A.J. Latibari, U. Tschimer "Alkaline Sulfite- Antraquinone (AS/AQ) Pulping of Wheat Straw and Totally Chlorine Free (TCF) Bleaching of Pulps", *Industrial Crops and Products*. vol. 29, pp. 27-36, 2009.
[11]. *TAPPI Test Methods*, Technology Park Atlanta: Tappi Press, 2002.
[12]. J. Gullichsen, C.J. Fogelholm, *Chemical Pulping*, *Papermaking Science and Technology Series* 6A, USA: Tappi Press, 1999.
[13]. *SCAN Test Methods*, Stockholm Sweden: Scandinavian Pulp, Paper and Board Committee, 1999.
[14]. *Paper, Board and Pulps-Measurement of Diffuse Blue Reflectance Factor (ISO Brightness)*, ISO Standards, ISO/DIS 2470, 1999.
[15]. H. Eroğlu, "Soda-Oxygen Pulping of Wheat Straw" in *Nonwood Plant Fiber Pulping Conference*, 1983, Tappi Press Progress Report No: 14, p. 99-106.
[16]. R.M. Rowell, R. A. Young, J.K. Rowell, *Paper and Composites from Agro-Based Resources*, Boca Raton, FL:CRC Lewis Publishers, 1997,446p.
[17]. M. Usta, H. Eroğlu, C. Karaoğlu, "ASAE Pulping of Wheat Straw *(Triticum aestivum L.)*", *The Journal of Cellulose Chemistry and Technology*, vol. 33, pp. 91- 102, 1999.
[18]. J. Li and G. Gellerstedt, "The contribution to kappa number from hexenuronic acid groups in pulp xylan", *Carbohydrate Res.*, vol.302, pp.213-218.
[19]. H.U. Suess, C. Leporini, K. Schmidt and B. Hopf, "Lower kappa with activated acidic hydrogen peroxide - a removal of lignin or hexenuronic acids?" in 59th Appita Annual Conference and Exhibition: Incorporating the 13th ISWFPC (International Symposium on Wood, Fibre and Pulping Chemistry), 2005, proceedings. p. 375-377.
[20]. P. Bajpai, *Environmentally Benign Approaches for Pulp Bleaching*, 1st ed., Amsterdam: Elsevier, 2005.
[21]. X. Petit-Breuilh, C. Zaror and R. Melo, "Hexenuronic acid removal from unbleached kraft eucalyptus pulp by peroxymonosulfuric acid", *Journal of Chilean Chemical Society*, vol.49(4), pp. 355-360, 2004.

Characterization of Enriched Leucite From Afyon Region/Turkey

Sevgi Karaca[1], Ali Ucar[1], Veli Uz[1], Nihal Derin Coskun [1], Ali Issi[1], Yasar Kibici[1]*

Abstract

Leucite is used today in advanced technology materials as a syntetic product. However, the use of naturel leucite with outstanding properties such as high strength and wide thermal expansions coefficient has not been studied upon any work. Therefore, the pre-research has been performed on the use of advanced technology fields by enrichment of Afyon region naturel leucite. To use leucite mineral which is taken from nature is not possible in advanced materials. It has been attempted to obtain pure leucite as possible, so high intensity magnetic seperations were performed, respectively, in order to remove to Fe_2O_3 which is at a rate of 7.51% in leucite. Phase analysis (XRD), chemical analysis (XRF), thin section optical microscopy analysing and thermal behavior (DTA/TGA) were determined for enriched leucite. As a result of studies, the leucite was obtained with 20% K_2O, 22% Al_2O_3, 54.03% SiO_2 and 0,57% Fe_2O_3 content.

Keywords: *Leucite, enrichment, characterization*

1. INTRODUCTION

Pseudoleucite are potash-rich igneous rocks found in nature in the $K[AlSi_2O_6]$ formula [1]. It is a mineral that is formed of basic lava made up of K_2O, Al_2O_3 and SiO_2 [2]. Leucite is generally found in phonolite rock in the form of leucite crystals as pheno crystals; scattered inside the matrix made up of feldspar, amphibole and pyroxene micro-crystals. There is not much deviation in the chemistry of its natural form [3]. The phase transformations of the crystal system of leucite were discovered in the 19th century and the optical properties in 1890 by Charles and Georges, whereas the first X-Rays were discovered in 1976 by Mazzi et.al. [4]. Leucite mineral is made up of orthorhombic or monoclinic individuals.

Leucite is an important material used in dental ceramics in addition to its use in the ceramic and glass industries. The alumina and alkaline feldspars in its structure are used as fluxing agents in glass structure and affect the strength, toughness and durability of ceramic products [5]. Leucite has also been used in ceramic applications in recent years [6].

Even though there is a large number of studies on leucite enrichment and the use of synthetic leucite, there is no study on the use of leucite in advanced technological equipment following its enrichment. Hence, the objective of this study was to provide a pre-study to the use of leucite in different areas by putting forth the characteristics of natural leucite.

2. EXPERIMENTAL

Afyon region leucitophire was used in this study. The samples obtained from this region were cut via diamond cutter and polished for analysis Nikon Eclipse LV100POL optical microscopy and NIS-Elements D 4.00.00 programme was used for thin section images of natural leucite. Some of the samples obtained from the mine field were passed initially through a jaw crusher in the laboratory thus reducing their size to below 0,5 mm. The samples with dimensions of below 0,5mm were enriched in high intensity roller dry magnetic separator after which 3 samples were taken as feeding, concentrate and tailing on which characterization studies were carried out.

Fine powders were prepared in an agate mortar in order to be analyzed by X-ray fluorescence (XRF) and X-ray diffraction (XRD) techniques. In chemical analysis Panalytical Axiosmax XRF device was used. Phase analyses of the samples performed by a Rigaku X Ray Diffractometer model Rint 2000 with a monochromatic filter. XRD spectra were obtained operating at 30 KV and 15mA (Cu-Kα, λ=1,541 A0, 2θ 5-70º, 2º/minute at a step size of 0,020). Sintering behaviours of enriched leucite was evaluated by Netzsch STA 449 f3 Jupiter instrument with thermal gravimetric-differential thermal analysis (TG-DTA) techniques in order to estimate the sintering behaviours. The microstructure images of concentrate, tailing, feeding and natural leucite were obtained using Nova nano SEM 650 model and FEI brand scanning electron microscopy.

2.1. Binocular microscope images

Leucite minerals are found as phenocrystals scattered inside the matrix made up of feldspar, amphibole and pyroxene microcrystals inside the leucitophre rock. The images obtained using a binocular microscope of matrix and leucite were given

[1]*Corresponding author: Dumlupınar University, Materials Science and Engineering, Kütahya/Turkey, sevgi.karaca@dpu.edu.tr*

in Figure 1. Matrix and the leucite scattered in the matrix were determined in the polarized microscope images. The leucites in the cross-sections taken from the matrix were scattered as transparent and white colored particles of different sizes. Leucite has a microcrystal texture and microscopically it is observed as unique crystals.

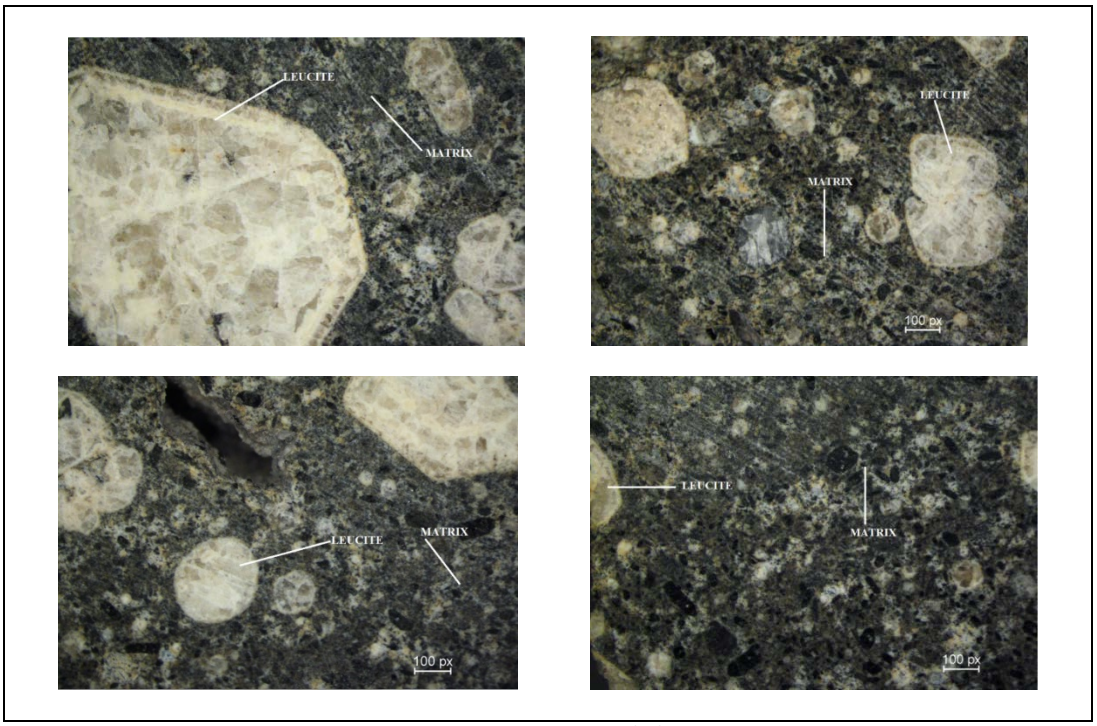

Figure 1. Binocular microscope images of Afyon Region Leucite

3. RESULTS

3.1. Chemical analysis

The chemical analysis results of feeding, concentrate and tailing have been given in Table 1. Whereas K_2O ratio is ~ %8-9 in the feeding and tailing, they were determined as 20% K_2O in the concentrate obtained after enrichment. It was observed in the direction of these data that K_2O ratio increases with enrichment. Whereas, when Fe_2O_3 ratio was examined, it was observed that it decreased from ~%7-8 to ~%0,5 in the concentrate obtained after enrichment.

Table 1. The chemical analysis of feeding,concentrate and tailing

Component	Feeding	Concentrate	Tailing
SiO_2	52.76	54.03	52.91
Al_2O_3	16.36	22.00	16.37
K_2O	9.16	20.00	8.91
CaO	7.99	1.20	7.70
Fe_2O_3	7.51	0.57	7.41
Na_2O	0.72	0.28	0.82
MgO	1.95	0.06	2.97
TiO_2	1.14	0.22	1.11
SO_3	0.21	0.09	0.12
A.Z.	2.00	1.55	2.20

3.2. Phase analysis of feeding, tailing and concentrate leucite

X-Ray diffraction patterns of feeding, tailing and concentrate were given in Figure 2. When the phase analyses of the leucite prepared as feeding are examined, it can be observed that the highest peaks are of leucite, sanidine and pyroxene phases. Product that obtained after enrichment consist of sanidine structures together with pyroxene phases. Hence we can clearly observe leucite phase after enrichment. Enrichment of the concentrate with a K_2O ratio of 20% determined via chemical analyses and it supported via mineralogical analysis as well. Phase analysis showed that concentrate, tailing and feeding consist of leucite, pyroxene and sanidine, pyroxene, sanidine and leucite phases together with, respectively.

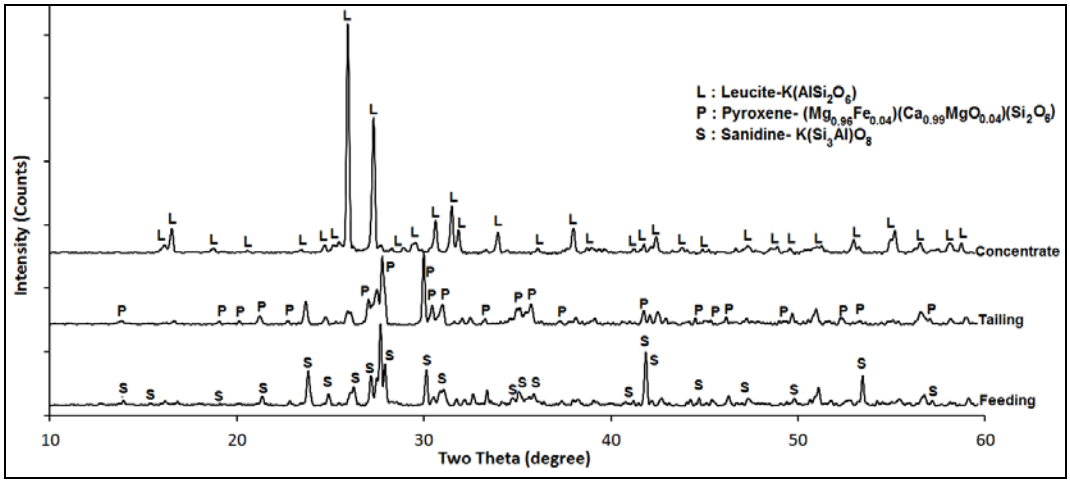

Figure 2. X-ray diffraction patterns of feeding, concentrate and tailing leucite

3.3 Thermal analysis (DTA/TGA)

The determination of which behavior the material will display at which temperature during sintering depending on mineralogy so, it can be obtained without deformation production and its faster firing at the sintering stage. The (DTA/TGA) curve of the enriched leucite has been given in Figure 3. The values at the critical temperature points were taken into account in determining the critical sintering stage.

When the (DTA/TGA) curve given in Figure 3 is examined, it can be observed that the downwards slope of the endothermic peak at and after 737ºC enables the glass transition temperature as well as the existence of a glassy phase mixture. The thermal analyses yield a melting point interval rather than a melting point since the leucite crystals are not pure [7].

The endothermic peak at about 100ºC shows us the characteristic absorbed water loss at the surface of the mineral. When analyzed with regard to crystallization as a result of thermal analysis, it can be observed that there is an endothermic peak between 750-780ºC which has a tendency to form with slow heat regime. The K_2O glass modifying oxides may result in the decrease of the viscosity of the glassy structure at low temperatures thus leading us to think that the concentrate obtained can be used in low temperature applications [8].

When the TGA curve values were examined, it was observed that there was a weight loss of about ~1.70% up to 800ºC, whereas this value was around ~0.17% after 800ºC. This shows that the particles will bind to each other during sintering after 800 ºC. The fact that melting takes place after 800ºC puts forth that the melting temperature of the material is low. This creates a potential for use in low temperature products by working on concentrated leucite.

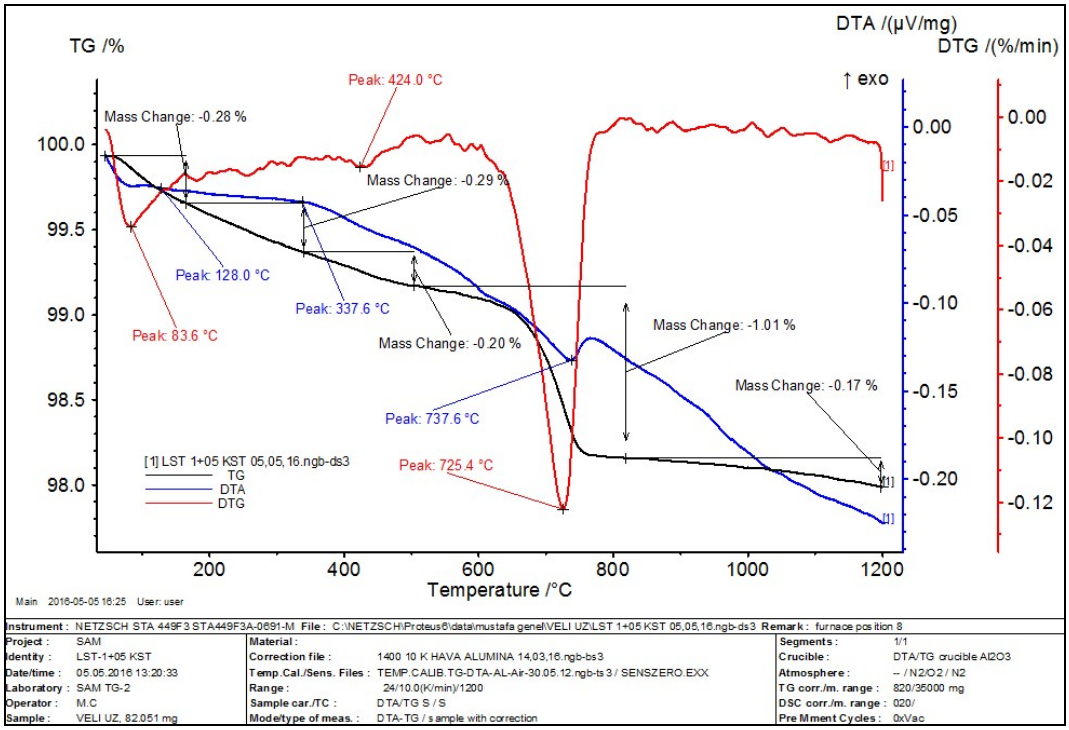

Figure 3. Thermal analysis (DTA/TGA) of concentrate leucite

3.4. Microstructure of feeding, tailing and concentrate leucite

The microstructure analyses of raw, feeding, tailing and concentrate samples have been given in Figure 4. When the microstructure analysis of natural leucite in Figure 4 is examined, it can be observed that it has a unique intensive vesicular structure and that it includes the leucite comprised of crystals scattered homogeneously. Figure 4.b shows the leucite crystals in the back scattered images obtained from the leucite structure used as feeding in under 0,5 mm enrichment subject to grinding in the light colored crystal forms inside the matrix. Whereas it is observed in Figure 4.c that tetragonal structures decrease in the tailing with high Fe_2O_3 ratio and low K_2O ratio, it is possible to observe the light colored and more intensive tetragonal structures of the tetragonal leucite minerals in Figure 4. The leucite structure that is stated to transform to a cubical structure with increasing temperature after 605ºC affects properties such as strength and toughness in ceramics thus ensuring that higher quality products are obtained [9]. When the thermal analysis curve given in Figure 3 of the tetragonal structure which is observed in the microstructure analyses of Figure 4 is examined, it can be observed that it starts to melt after 737ºC. It is thought that this temperature value which is different than that stated in literature is due to the chemical difference between the concentrated product obtained as a result of enrichment and the matrix-leucite. However, the exothermic tendency peak that forms around 750-780ºC puts forth that the structure has undergone a crystallographic change.

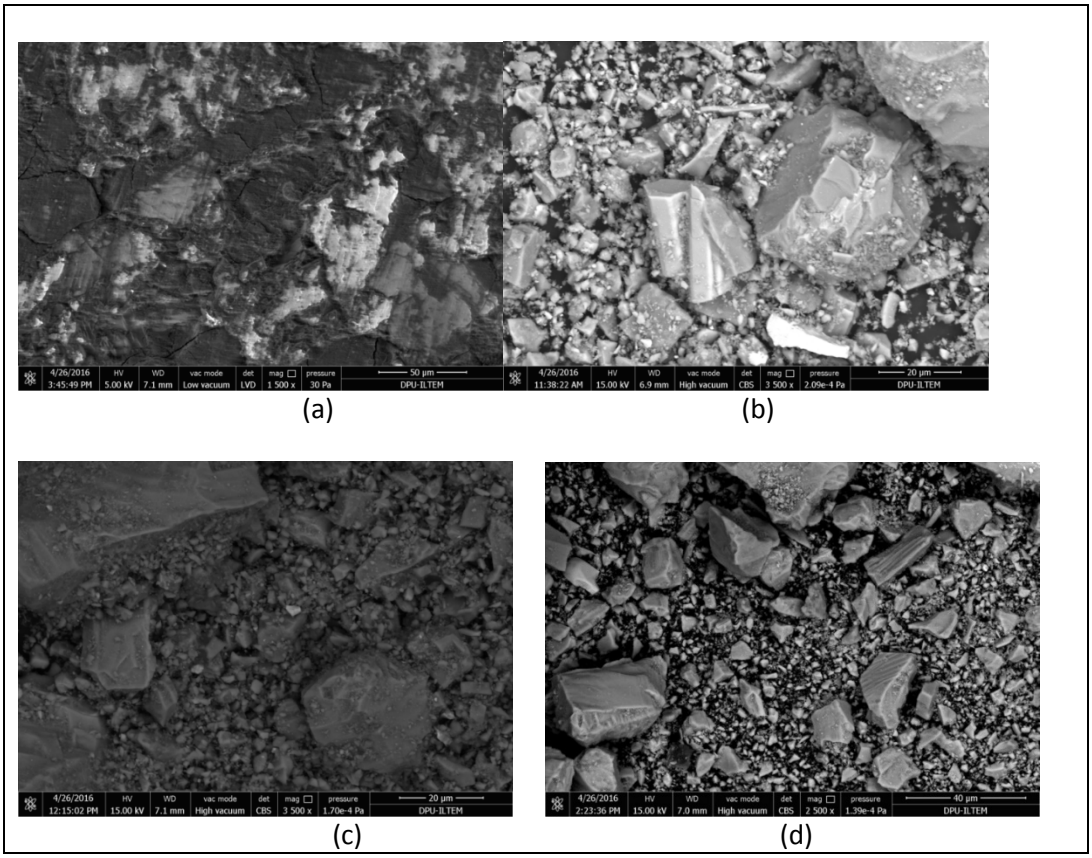

Figure 4. Microstructure of raw (a,) feeding (b), tailing (c) and concentrate (d)

4. CONCLUSIONS

It was determined via mineralogical and chemical analyses carried out as part of this study that the K_2O content of the leucite obtained from the Afyon Region can be increased by 7-8% and that it can be enriched. It is thought that better results can be obtained by carrying out detailed and different enrichment methods.

The melting of the acquired concentrate product at low temperature provides a significant potential for use in ceramic applications. It was determined as a result of low temperature firing trials carried out on ceramic products that its contributions to product properties and product cost can be examined. It has a commercial potential for use in glass, ceramic and advanced technology materials due to its high potassium and low iron content.

It was observed as a result of microstructure images that the ore and gang minerals form separately. This formation mechanism will be examined and its applicability on synthetic leucites will be studied. In regard to removing the gangue minerals accompany raw leucite by using the mineral processing methods, there would be a wide range of utilization areas for pure leucite crystals.

After enrichment K_2O rate has increased over 100% and Fe_2O_3 rate reduced from 7% to 0.5%. Also it was defined that leucite intensified in concentrate but other minerals were collected in tailing . Sanidine, pyroxene and leucite minerals were determined in feeding.

Analysis showed; leucite can be separated from other gangue minerals by magnetic seperation. It was determined that particle size is greater on feeding and tailing than concentrate. So ıt has been found that leucite can be seperated at smaller particle sizes because gangue minerals and leucite have different milling behaviours. Thermal behavior of leucite showed an endothermic reaction at 730°C and DTA curve due to the tendency of endo has been determined a glassy phase formation above this temperature value. Because Fe_2O_3 ratio is decreased below 0.5% after magnetic enrichment Afyon Region leucite accured using potential in many advanced ceramic products. However, it will be possible to use leucite in high value added ceramics by lowering the rate of Fe_2O_3 with using different enrichment methods.

Acknowledgement

We would like to express our gratitude to İltem (Dumlupınar University Advanced Technology Center, Kütahya/Turkey) and SAM (Ceramic Research Center, Eskişehir/Turkey) for the contribution to microstructures analysis, thermal analysis and chemical analysis and Departments of Material Science and Engineering and Mining Engineering in Dumlupınar University.

And also we would like to thank to the administration of Dumlupınar University due to the support provided for this study under the scientific research projects (BAP) with the project number of 2016-11.

REFERENCES

[1]. Y. Seki and G.C. Kennedy, An experimental study on the leucitepseudoleucite problem, The American Mineralogist, VOL. 49, September-October, 1964.
[2]. C. S. Hurlbut, Mineralogy, Vol. 2., 227-299, 1982.
[3]. M. Çelik, N.Karakaya, Sistemetik Mineraloji, 201-203, 1998.
[4]. T.L. Stokes, Annals of surgery, Second Edition, 1955.
[5]. V. Bozkurt, Y. Uçbaş, H. Özdağ, Turkey Recovery of Leucite from Phonolite, Proceedıngs of the 11th Internatıonal mineral processing symposium, 21-23 October, Belek-Antalya, 2008.
[6]. S. Değer, M.B. Caniklioğlu, E. Demirkesen, B. Akkayan, Metal-Seramik Çalışmalarda Kullanılan Seramik Materyallerinin Lösit İçeriklerinin ve Tekrarlanan Fırınlamaların Lösit İçeriğine Etkisinin Araştırılması, Türkiye Klinikleri, J. Dental Sci., 3(3):173-8, 1997.
[7]. N. L. Bownn and R. B. Ennsrao, Leucıte and pseudoleucıte Journal miner., Logıcal socıety of America.
[8]. M.B. Volf, Chemical Approach to Glass. Glass Science and Technology, vol. 7, Elsevier, 1984.
[9]. R. A. Lange, I. S. E. Carmichael, J. F. Stebbins, Phase transitions in leucite ($KAlSi_2O_6$), orthorhombic $KAlSiO_4$, and their iron analogues ($KFeSi_2O_6$, $KFeSiO_4$), American Mineralogist, Volume 71, pages 937-945, 1986.

Effect of Magnetic Field Intensity on The Recovery of Leucite Minerals by Magnetic Seperation

Ali Ucar[1], Veli Uz[1] Nihal Derin Coskun[1], Sevgi Karaca[1], Mustafa Akar[1], Yasar Kibici[1]

Abstract

Leucite which occurs with alkaline lava in nature, is a potassium aluminium silicate ($K[AlSi_2O_6]$) mineral. According to the results of chemical analysis for the ore taken from the Afyon region, it was determined that there was a content of 5.4% Fe_2O_3 in ore. It was aimed to remove the gangue minerals having magnetic properties as they are not desired in advanced technology materials by means of high intensity dry magnetic roll seperator. The influence of different field intensities (4000, 6000 and 10000 Gauss) and blade angles (100, 105, 110 and 120°) on the seperation was performed. During the experimental works, Fe_2O_3 content was reduced to 1.02% by a field intensity of 10000 Gauss together with a blade angle of 100°. As the content of Fe_2O_3 should be under 0.5% for the advanced technology materials, the result obtained was found to be insufficient and for the future works, it is planned to use high intensity wet magnetic seperator.

Keywords: Blade angle, magnetic field intensity, leucite, magnetic seperation

1. INTRODUCTION

Leucite is a feldispathoid mineral in the form of potassium alumino-silicate ($K[AlSi_2O_6]$). It is found as scattered phenocrystals inside the matrix made up of feldspar, amphibole and pyroxene micro crystals that form impurities in the phonolite rock structure formed by K_2O rich silica poor basic lava. In addition, it is also found inside the rock in the opaque minerals formed by metals such as Fe, Ti. It has a cubical form above temperatures of 605 ^oC and a tetragonal form below this temperature value. There is a 1.2% volume expansion as a result of this temperature change (e.g. [1], [2], [3], [4], [5], [6], [7], [8]).

Today, leucite is used in many advanced technological materials. It is used especially in external ceramic applications as a result of its thermal properties in addition to the strength it provides to the structure (e.g. [8], [9], [10]). In addition, it has been started to be used more frequently due to the superior features of leucite and the following reasons in areas such as glass, ceramic, welding electrode, paint, plastics, construction, porcelain, ornaments, electro-porcelain, ceramic glaze (e.g. [2], [3], [4], [8], [11]).

- It has higher potassium content.
- It enables operation at lower melting temperatures since it can react easily with quartz.
- More homogeneous, stronger products with greater quality are obtained in more stable working conditions.
- Production is increased due to shorter firing time.
- It has better cutting properties.
- It has a greater thermal expansion coefficient (20 to 25 × 10^{-6}/°K) and
- Leucite increases the flexural strength of porcelain by 10 to 30% more in comparison with feldspar.

In addition, leucite has also been used to obtain Al in Italy, Norway and Canada ([12]). Since the use of leucite mineral in advanced technological equipment in its natural form is not possible, it has to go through many processes. Iron is among the undesired impurities. Hence, the iron content of leucite has to be decreased below a certain value before it can be used. The enrichment methods used for this purpose are classified according to the characteristic of the iron mineral as low and high intensity magnetic separation or in some cases flotation method can also be used [(13)]. Whereas the number of studies on the enrichment of leucite via magnetic separation is very low in [12] and [14], there is no study on flotation or other enrichment methods.

Sodium feldspar ores are quite a lot in our country, whereas potassium feldspar ores are quite low. The required potassium feldspar is generally imported. This results in high costs. Hence, there is a need for high quality potas sources. This demand can be met via obtaining feldspar from rocks such as granite, syenite, pegmatite in [13], [15], [16], [17] and [18]. However, these feldspars do not have the required quality for use in advanced technological equipment.

[1] *Corresponding author: Dumlupınar University, Department of Mining Engineering, 43100, Kütahya, Turkey, ali.ucar@dpu.edu.tr*

That is why, the objective of the study is to examine the means of enriching leucite rocks (leucitophyre) with no silica content and high K_20 content in Afyon region and to shed light on the evaluation of a raw material source for use in various areas.

2. MATERIALS AND METHODS

The samples acquired from the Afyon region (Turkey) were passed through jaw crusher in the laboratory after which they were passed through a roll crusher that works as close circuit with a 0.5 mm sieve hence decreasing their size. They were then passed through a 0.25 mm sieve and the samples classified within the size interval of -0.5+0.25 mm were stored as about 500 g. parts via reducing methods. The chemical analysis of the sample (XRF) was carried out first and the results have been given in Table 1.

Table 1. Chemical Analysis of the sample

Component	Content, %
SiO_2	49.49
Al_2O_3	19.02
K_2O	10.54
Fe_2O_3	5.40
CaO	5.43
MgO	1.37
TiO_2	0.74
Na_2O	1.58

High intensity dry magnetic roll seperator which has gained recent popularity for the enrichment of various industrial raw materials such as feldspars was used in this study. The experiments were carried out at intensities of 4000, 6000 and 10000 Gauss and knife angles of 100, 105, 110 and 120° in order to examine the effects of magnetic field intensity and knife angle on separation. In addition, the belt speed was kept constant at 40 rev/min.

3. RESULTS AND DISCUSSION

According to the chemical analysis (XRF) carried out on the samples, it is observed that there is 5.4% Fe_2O_3 in the leucitophire (Table 1). However, the Fe_2O_3 ratio of leucite to be used in advanced technological equipment should be below 0.5% and the firing color is desired to be white. Hence, high intensity dry magnetic roll seperator was used to remove the minerals with iron content in the sample since it is simpler and more economical.

According to the experiments carried out using a magnetic separator, the effects of magnetic field intensity and knife angle on grade has been given in Figure 1 whereas their effects on recovery have been given in Figure 2. Alkali feldspars are used as fluxing agents in ceramic and glass industries due to their alkali and alumina contents. They help to lower the temperature at which the liquid phase is formed and improve the strength, toughness, and durability of the ceramic body. K-feldspar has some advantages over Na-feldspar when used in ceramic bodies. When K-feldspar is used instead of Na-feldspar, viscosity of the liquid phase formed during firing is higher and a decrease in viscosity with an increasing temperature is slower as a result of these, deformations in products are much less ([14]). In addition, the Fe_2O_3 content of the leucite that will be used in advanced technological equipment is desired to be <0.5%. According to the experiment results given in Figure 1, it is observed that the Fe_2O_3 value decreases whereas K_2O value increases with decreasing knife angle and increasing magnetic field intensity.

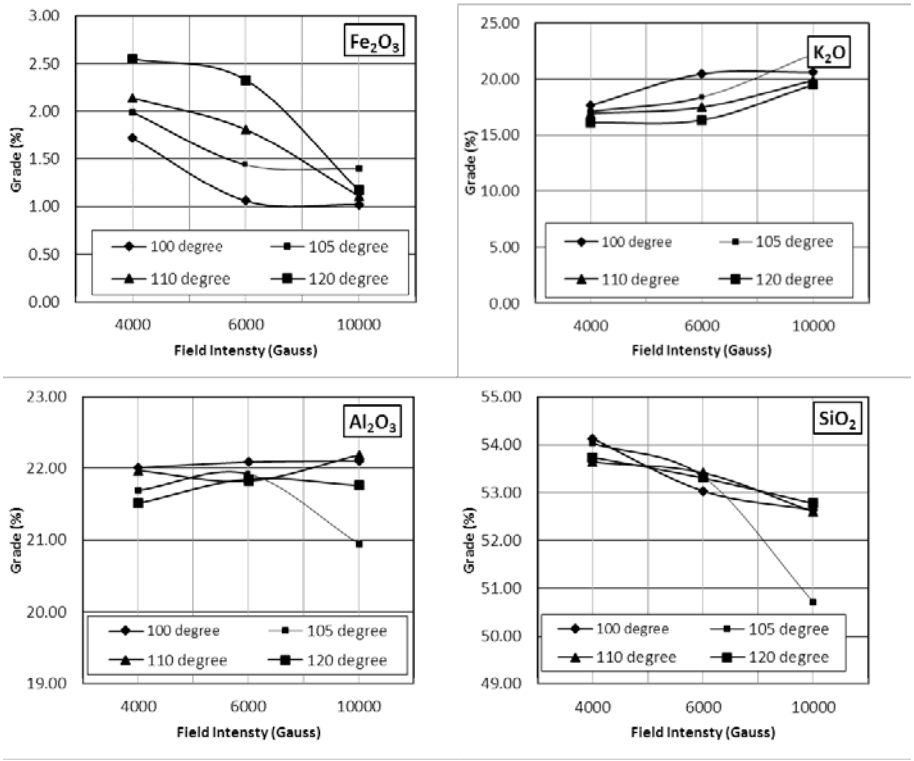

Figure 1. The effects of magnetic field intensity and knife angle on grade

In comparison with the experiments carried out at 4000 Gauss field intensity and 120° knife angle, the experiments carried out at 10000 Gauss field intensity and 100° knife angle put forth a 60% decrease in Fe_2O_3 ratio and a 27.87% increase in the K_2O ratio. According to the results of the experiment carried out at the maximum field intensity and the minimum knife angle, the acquired grades were 1.02% Fe_2O_3, 20.60% K_2O, 22.11% Al_2O_3 and 52.63% SiO_2. Whereas the recoveries at the same conditions were 1.62% Fe_2O_3, 17.36% K_2O, 11.88% Al_2O_3 and 10.60% SiO_2 (Figure 2).

Fe_2O_3 and SiO_2 grade decreased, K_2O grade increased and Al_2O_3 grade did not change significantly with increasing magnetic field intensity. The reason why Fe_2O_3 ratio did not decrease to the desired levels might be due to the fact that there are Fe_2O_3 particles inside the leucite at these particle sizes. Whereas the decrease of SiO_2 grade is due to the fact that SiO_2 content decreases with increasing leucite concentration impurity acquired dependant on magnetic intensity since there is no free SiO_2 in the leucitophyre and the concentration of the other silicate minerals in the tailing. Hence, it is normal for the K_2O ratio to increase. The leucite recovery by weight was determined as 9.67%.

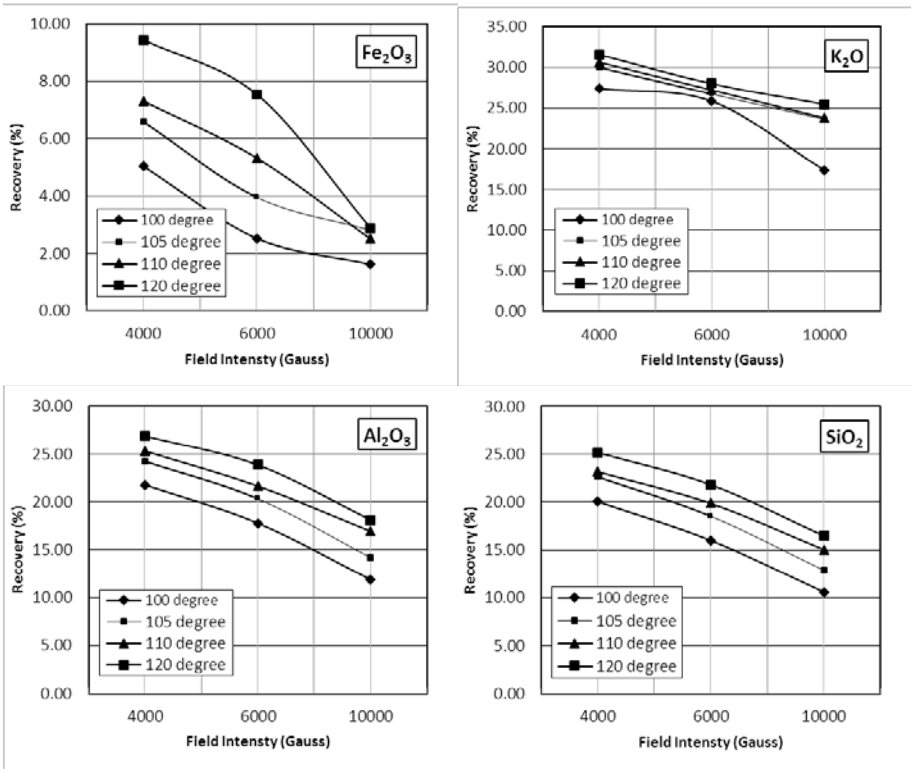

Figure 2. The effects of magnetic field intensity and knife angle on recovery

4. CONCLUSIONS

The magnetic impurities in the leucitophyre samples acquired from the Afyon Region were tried to be removed via high intensity dry magnetic roll seperator. Under the following experiment conditions, leucite concentrate;

Magnetic field intensity, Gauss	:	10000
Knife angle, degree	:	100
Roller speed, r/min	:	40
Particle size, mm	:	-0,5+0,25

- With 1.02% Fe_2O_3 grade and 1.62% removal rate,
- With 20.60% K_2O, 22.11% Al_2O_3 and 52.63% SiO_2 grades at recoveries of 17.36%, 11.88% and 10.60% respectively.
- Thus, the product obtained does not have the desired Fe_2O_3 content for use in advanced technological equipment despite the 81.11% Fe_2O_3 removal and 95.45% K_2O enrichment in comparison with the feed sample.
- However, product with high K_2O content was obtained which has limited production in Turkey.
- This product obtained can be used in traditional ceramics. However, the Fe_2O_3 content should be decreased in order to increase the area of use of this material.
- The recovery by weight is 9.67%.

ACKNOWLEDGMENT

We would like to express our gratitude to İltem (Dumlupınar University Advanced Technology Center, Kütahya/Turkey) and SAM (Ceramic Research Center, Eskişehir/Turkey) for the contribution to microstructures analysis, thermal analysis and chemical analysis and Departments of Material Science and Engineering and Mining Engineering in Dumlupınar University. And also we would like to thank to the administration of Dumlupınar University due to the support provided for this study under the Scientific research projects (BAP) with the project number of 2016-11.

REFERENCES

[1]. M. Çelik, N. Karakaya, Sistemetik Mineraloji, 201-203, 1998.
[2]. R.N. Raghavan, Ceramics in Dentistry, Sintering of Ceramics – New Emerging Techniques, Dr. Arunachalam Lakshmanan (Ed.), ISBN: 978-953-51-0017-1, InTech, Available from:http://www.intechopen.com/books/sintering-of-ceramics-new-emerging techniques/ceramics-in-dentistry, pp. 203-225, 2012.
[3]. E.M. Erbe (Stillwater), R.S. Sapieszko (Woodbury), "Chemically derived leucite", United States Patent, 5 622 551, April 22, 1997.
[4]. J.L. Ong, D.W. Farley, B.K. Norling, "Quantification of leucite concentration using X-ray diffraction", *Dental Materials*, vol. 16, pp. 20–25, 2000.
[5]. C. Akal, "Mineralogy and Geochemistry of Melilite Leucitites, Balçıkhisar, Afyon (Turkey)", *Turkish Journal of Earth Sciences (Turkish J. Earth Sci.)*, vol. 12, pp. 215-239, 2003.
[6]. R.A. Lange, I.S.E. Carmıchael, J.F. Stebbins, "Phase transitions in leucite (KAlSi2O6), orthorhombic KAlSiO4, and their iron analogues (KFeSi2O6, KFeSiO4)", *American Mineralogist*, vol. 71, pp. 937-945, 1986.
[7]. T.I. Kakhia, "Aluminium minerals (Ore)", *Chemical Books and Articles*, pp. 368, http://tarek.kakhia.org/books_eng/Alumminium_Ore.Tarek_Kakhia.pdf.
[8]. S.T. Rasmussen, C.I. McLaren, W.J. O'Brien, "The Effect of Cesium-Containing Leucite Additions on the Thermal and Mechanical Properties of Two Leucite-Based Porcelains", *Journal of Biomedical Materials Research, Part B, Applied Biomaterials*, vol. 69, pp. 195–204, 2004.
[9]. M.J. Cattell, T.C. Chadwick, J.C. Knowles, R.L. Clarke, D.Y.D. Samarawickrama, "The Nucleation and Crystallization of Fine Grained Leucite Glass-Ceramics for Dental Applications", *Dental Materials*, vol. 22, pp. 925–33 2006.
[10]. J.R. Mackert, C.M. Russell, "Leucite crystallization during processing of a heat-pressed dental ceramic" *Second Edition, The International Journal of Prosthodontics*, vol. 9 (3), pp. 261–265, 1996.
[11]. I. Denry, J.A. Holloway, "Ceramics for Dental Applications: A Review", *Materials*, vol. 3, pp. 351-368, 2010.
[12]. M.L. Dolan, D.H. Hains, D.R. Ash, "High-Alumina Rocks in Ontario: Resources and Process Technology, Ontario Ministry of Northern Development and Mines", *Industrial Minerals Background Paper*, vol. 10, pp. 130, 1991.
[13]. H. Bayhan, İ. Girgin, "Bayındır - Akpınar (Kaman) Nefelin Siyenitlerinin Zenginleştirilmesi", *Madencilik*, vol. 32(2), pp.19-26, 1993.
[14]. V. Bozkurt, Y. Uçbaş, H. Özdağ, "Recovery of Leucite from Phonolite", *Proceedıngs of The 11th Internatıonal Mıneral Processıng Symposıum*, 21-23 October 2008, Belek-Antalya, Turkey.
[15]. Ö.Y. Gülsoy, İ. Bayraktar, N.M. Can, "Altere Granitlerden Yüksek Potasyumlu Feldispat Üretimi", *Madencilik*, vol. 42(3), pp. 3-9, 2003.
[16]. Ö.Y. Gülsoy, E.C. Orhan, N.M. Can, "Bursa-Orhaneli Siyenitlerinden Feldispat Üretimi", *Madencilik*, vol. 43(4), pp. 17-28, 2004.
[17]. D.A.C. Manning, "Where in the world is the potash that we need?", *19th World Congress of Soil Science, Soil Solutions for a Changing World*, 1 – 6 August 2010, Brisbane, Australia. Published on DVD, pp. 298-301.
[18]. İ. Bayraktar, S. Ersayın, Ö.Y. Gülsoy, Z. Ekmekçi, M. Can, "Temel Seramik ve Cam Hammaddelerimizdeki (Feldispat, Kuvars ve Kaolin) Kalite Sorunlan ve Çözüm Önerileri", *3. Endüstriyel Hammaddeler Sempozyumu*, 14-15 Ekim 1999, pp. 22-33, İzmir, Türkiye.

The Prediction of Butterworth Type Active Filter Parameters in Low-Pass Sallen-Key Topology by Backtracking Search Algorithm

Bahadir Hicdurmaz*[1], Burhanettin Durmus[1], Hasan Temurtas[1], Serdar Ozyon[1]

Abstract

Filters are electronic circuits which let the desired frequency components of electrical signals that are applied to the inputs and besides purify these signals from harmonics and parasites. Filters are divided into two as active and passive filters. Filters done with transistors or op-amps are called active filters. The active filters are more advantageous in terms of its cost compared with the passive filters. Especially at low frequencies these filters are preferred due to their low costs. Active filters that can be set to a wide frequency region are very practical in terms of size and weight and easy to design. These filters can be easily cascaded without affecting each other. In this study, parameter values for a low-pass Sallen-Key topology Butterworth type active filter with wide-range of use have been defined by Backtracking Search Algorithm (BSA). The obtained results have been compared with ideal Butterworth filter's frequency scaling factor (FSF) and quality factor (Q) values.

Keywords: *Active filters, Low-pass Sallen-Key topology, Backtracking search algorithm*

1. INTRODUCTION

Active filters find use in a wide variety of applications such as tone signaling, instrumentation, audio and signal sources. Commonly used active filter circuit uses op-amps in combination with RC feedback networks to provide countless filter functions with a wide range of frequency-selective properties [1].

There are many ways of setting up active filters. Sallen-Key filter introduced by R. P. Sallen and E. L. Key is one of the widely used general-purpose circuits. This topology presents good stability, needs a few elements, and has low impedance, which is important for cascading filters with four or more poles [2].

One of four classic active filter types is Butterworth filter [1]. It exposes an almost flat passband with no ripple. That is, it is a maximally flat filter. The roll off is sleek and monotonic with roll off rate of 20 dB/decade for every pole. Thence, 10^{th}-order Butterworth low-pass filter (LPF) would have an attenuation rate of 200 dB for every decade beyond the cut-off frequency. Butterworth filters have quite good phase response. Because of these properties, generally it is focused on designing Butterworth active filters.

The work of optimal active filter design by hand is very difficult owing to manufacturing limitations. Generally, the components values are chosen to be equal each other [3]. This case limits the flexibility of the design [4].

Recently, the application of metaheuristic algorithms in filter design and optimization is a promising area. The popular ones of these applications are tabu search (TS), differential evolution (DE), genetic algorithm (GA), particle swarm optimization (PSO) and artificial bee colony (ABC). A parallel TS algorithm was described for component value selection analog filter and less design error was obtained when compared with results of conventional methods [5]. Another study of filter design is given in [6] for selection of optimal circuit elements using DE algorithm. In [7], GA was used for component value optimization of analog filter. ABC and PSO have been utilized for the optimal circuit design in [8] and [9], respectively. In [10], Butterworth and Chebyshev low-pass filter designs were realized by using ABC, DE and PSO. Among these algorithms, it was shown that the most design results were obtained by PSO.

[1] *Corresponding author: Dumlupınar University, Department of Electrical and Electronics Engineering, 43100, Kütahya, Turkey.* bahadir.hicdurmaz@dpu.edu.tr

[2,4] *Dumlupınar University, Department of Electrical and Electronics Engineering,43100, Kütahya, Turkey.* burhanettin.durmus@dpu.edu.tr , serdar.ozyon@dpu.edu.tr

[3] *Dumlupınar University, Department of Computer Engineering, 43100, Kütahya, Turkey.* hasan.temurtas@dpu.edu.tr

In this study, a 10th-order LPF is designed. BSA is used for selection of filter circuit's component values. FSF, Q and error values are calculated according to optimized values components. Obtained results are compared with ideal Butterworth FSF and Q values.

Rest of this paper is organized as follows. Section 2 provides LPF design. In Section 3, the basic aspects of BSA are described. Simulation results are presented in Section 4 and finally in Section 5 conclusions are interpreted.

2. SALLEN-KEY TOPOLOGY BUTTERWORTH LPF

An active LPF, which is one of the main active filters, is an electronic device that allows all frequency components below its cut-off frequency and rejects or attenuates all frequency components above. In Figure 1, a 2nd-order unity-gain Sallen-Key LPF architecture is given [1].

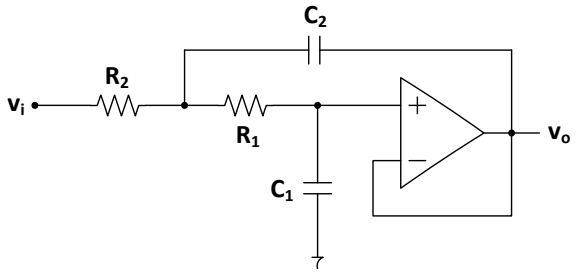

Figure 1. 2nd order unity-gain Sallen-Key LPF architecture

From circuit analysis, transfer function, $H_{LPF}(s)$ is obtained as

$$H_{LPF}(s)=\frac{V_o(s)}{V_i(s)}=\frac{1}{1+s(R_1+R_2)C_1+s^2R_1R_2C_1C_2} \quad (1)$$

In equation (1), substituting s = j2πf gives

$$H_{LPF}(f)=\frac{1}{1-(2\pi f)^2R_1R_2C_1C_2+j2\pi f(R_1+R_2)C_1} \quad (2)$$

The standard form of $H_{LPF}(f)$ is expressed as [10]

$$H_{LPF}(f)=\frac{1}{1-\left(\frac{f}{FSF\cdot f_c}\right)^2+j\frac{f}{Q\cdot FSF\cdot f_c}} \quad (3)$$

where f_c is the cut-off frequency, $FSF=1/(2\pi f_c\sqrt{R_1R_2C_1C_2})$ is frequency scaling factor, and $Q=(\sqrt{R_1R_2C_1C_2})/((R_1+R_2)C_1)$ is the quality factor.

Then, the amplitude response of the filter is found as

$$\left|H_{LPF}(f)\right|=\frac{1}{\sqrt{\left(1-(2\pi f)^2R_1R_2C_1C_2\right)^2+\left(2\pi f(R_1+R_2)C_1\right)^2}} \quad (4)$$

A 10th order LPF are constructed by cascading five 2nd order stages. To realize 10th order Butterworth LPF, FSF and Q values of each stage are given in Table 1 [11]. Designed filter circuit has cut-off frequency of 10 kHz.

Table 1. FSF and Q values of 10th order Butterworth Filter

Filter Order	Stage 1	Stage 2	Stage 3	Stage 4	Stage 5	Stage 6	Stage 7	Stage 8	Stage9	Stage 10
	FSF	***Q***	***FSF***	***Q***	***FSF***	***Q***	***FSF***	***Q***	***FSF***	***Q***

10	1.000	0.5062	1.000	0.5612	1.000	0.7071	1.000	1.1013	1.000	3.1969

3. BACKTRACKING SEARCH ALGORITHM

BSA is a population-based iterative method designed to be a global minimizer [12]. The flow chart of BSA is shown in Figure 2, which consists of 5 steps: initialization, selection-I, mutation, crossover and selection-II.

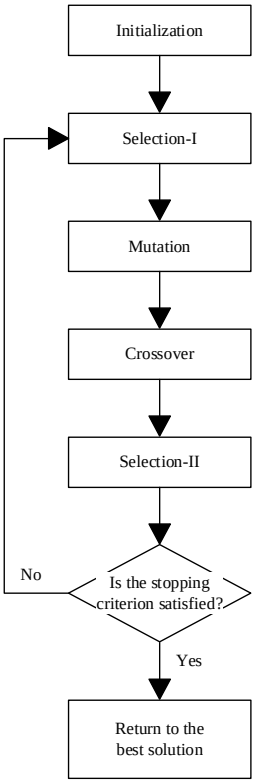

Figure 2. Flow chart of BSA

BSA initializes the population P as following:

$$P_{i,j} \sim U(\min_j, \max_j) \quad i = 1,...N \quad and \quad j = 1,...D \tag{5}$$

where N is the population size, D is the problem dimension, P_i is a target individual in the population P, and U is uniform distribution [1].

Then, selection-I determines the historical population $oldP$ to be used for calculating the search direction. At the beginning of each iteration, $oldP$ is redefined through the following rules:

$$if \quad a < b \quad then \quad oldP := P \mid a, b \sim U(0,1) \tag{6}$$

$$oldP := permuting(oldP) \tag{7}$$

where $:=$ is the update operation, a and b are random values uniformed in (0,1).

In the BSA's mutation stage, the initial form of the trial population Mutant is obtained by Eq. (4).

$$\mathrm{Mutant} = P + F(oldP - P) \tag{8}$$

where F controls the amplitude of the search-direction matrix $(oldP - P)$.

BSA's crossover process generates the final form of the trial population T. Trial individuals with better fitness values are used to evolve the target population individuals. A binary integer-valued matrix (*map*) of size N is calculated. D that indicates

individuals of T to be manipulated by using the relevant individuals of P. If $map_{n,m} = 1$, T is updated with $T_{n,m} := P_{n,m}$, $n \in \{1,2,3...N\}$ and $m \in \{1,2,3...D\}$.

In selection-II, the $T_i s$ that have better fitness values than the corresponding $P_i s$ are used to update the $P_i s$ based on a greedy selection. If the best individual of $P(P_{best})$ has a better fitness value than the global minimum value obtained so far by BSA, the global minimum is updated to be P_{best}.

4. SIMULATION AND RESULTS

In application of BSA, each passive component of filter belonging to each stage was encoded in the string form as shown in Table 2. In this case, the components values of the filter are successively adjusted by BSA until the error is minimized. The design error of the filter is summation of cost function errors of *FSF* and *Q*, and given as [10]

$$Error_1 = \sum_{i=1}^{5} \frac{\left|FSF_{t,i} - FSF_i\right|}{FSF_{t,i}}$$

$$Error_2 = \sum_{i=1}^{5} \frac{\left|Q_{t,i} - Q_i\right|}{Q_{t,i}} \qquad (9)$$

$$Error_{Total} = \alpha \times Error_1 + (1-\alpha) \times Error_2$$

where $FSF_{t,i}$ is target FSF, $Q_{t,i}$ target quality factor, and α is the constant $(\alpha = 0.5)$. The aim is to keep the total error as low as possible.

Table 2. Representing the component values in the string form

Stage 1				**…**	**Stage 5**			
R_{11}	C_{11}	R_{21}	C_{21}	**…**	R_{15}	C_{15}	R_{25}	C_{25}

In simulation studies, the population size *NP* is 25 and iteration number is set to 1000 for BSA. Experiments are performed over 25 independent runs. Obtained results are presented in Table 3-5.

Table 3. Statistical results of design for independent 25 runs

Best Error	**Mean Error**	**Worst Error**	**Standard Deviation**	**Elapsed Time (sec)**
1.227221e-03	3.211799e-03	1.110271e-02	1.888565e-03	25*1.21558

Table 4. Design parameter of filter

Method	**Stage1**		**Stage 2**		**Stage 3**		**Stage 4**		**Stage 5**	
	FSF	***Q***	***FSF***	***Q***	***FSF***	***Q***	***FSF***	***Q***	***FSF***	***Q***
Target	1.0000	0.5062	1.0000	0.5612	1.0000	0.7071	1.0000	1.1013	1.0000	3.1969
Ideal values	1.0003	0.5060	0.9998	0.5609	0.9999	0.7068	1.0003	1.1013	1.0001	3.1972

Table 5. Component values of best solution for filter design

Component	Stage 1	Stage 2	Stage 3	Stage 4	Stage 5
$R_1(k\Omega)$	2.71177	3.17965	2.76532	2.51472	1.81156
$R_2(k\Omega)$	2.94517	2.38655	2.7725	3.41985	2.34398
$C_1(nF)$	5.55832	5.09852	4.06644	2.43457	1.19773
$C_2(nF)$	5.70233	6.55024	8.12594	12.0916	49.7915

According to obtained results, by using BSA algorithm, it is possible to realize circuit designs close to the ideal cases. A total design error of 1.227221e-03 is obtained in 25*1.21558 second. The gain curves of each stage and total gain curves for target and computed solutions are plotted in Figure 3 and Figure 4, respectively.

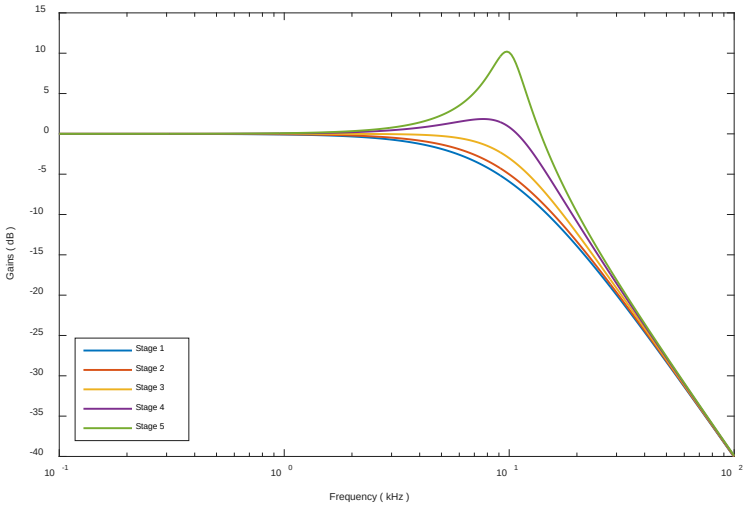

Figure 3. Gain curves of each filter stage

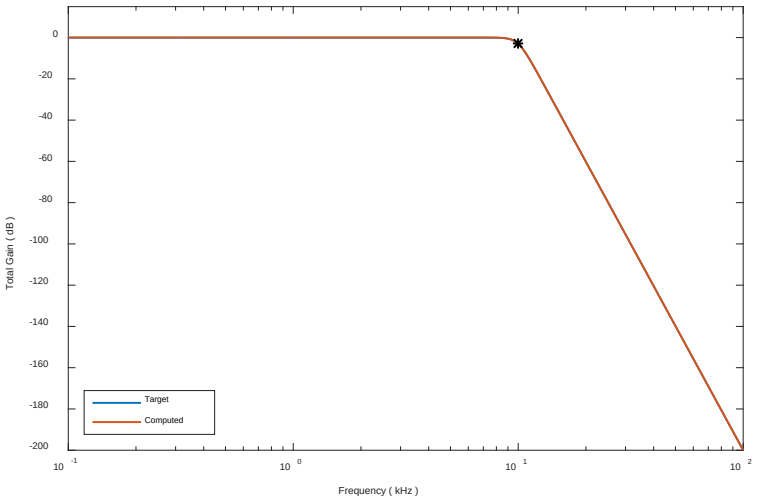

Figure 4. Total gain curves for target and computed solutions

Figure 5 shows the cost function versus iteration number. In this figure, it can be seen that BSA designs an acceptable filter at around 600 iterations. It has a fast convergence rate.

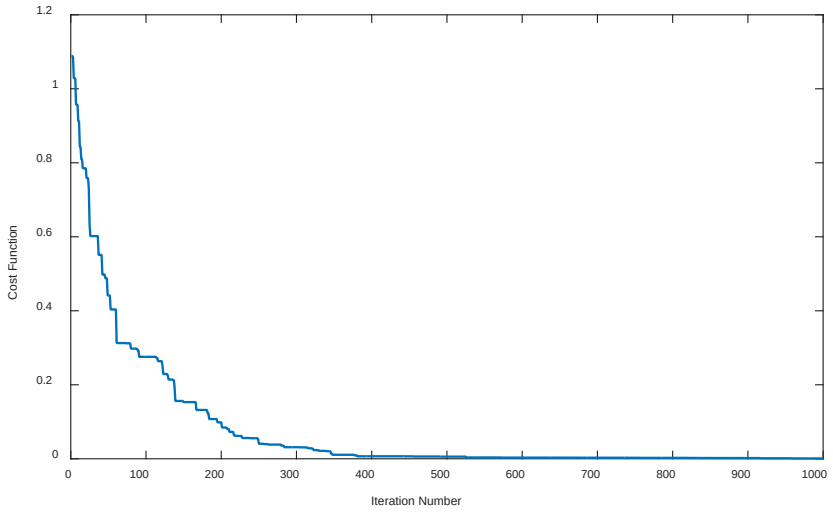

Figure 5. The cost function versus iteration number

5. CONCLUSIONS

In this study, an application of BSA is carried out for analog active filter design. The 10th-order Butterworth low pass filter design was investigated for prediction of component values. It is apparently seen that BSA successfully minimized the design error in a short computation time. From obtained results, BSA is considered to be able to used efficiently for more complex circuit design in future works.

REFERENCES

[1]. S. A. Pactitis, "Active Filters Theory and Design" CRC Press, Taylor & Francis Group, 2007.
[2]. R. P. Sallen, E. L. Key, "A practical method of designing RC active filters" IRE Transactions-Circuit Theory, 1955.
[3]. D. H. Horrocks, Y. M. A. Khalifa,"Genetically derived filters circuits using preferred value components," *in Proc. IEE colloquium on analogue signal processing*, 1994, p. 4/1-4/5.
[4]. E Sanchez-Sinencio, J. Silva-Martinez,"CMOS transconductance amplifiers, architectures and active filters: a tutorial," *IEEE Proc. Circuits Devices Syst.*, vol. 147, pp. 3-12, 2000.
[5]. A. Kalinli, "Component value selection for active filters using parallel tabu search algorithm," *Int, J. Electron. Commun.*, vol. 60, pp. 85-92, Jan. 2006.
[6]. A. F. Sheta, "Analogue filter design using differential evolution," *Int. J. Bio-Inspired Comput.*, vol. 2 (3), pp. 233-241, 2010.
[7]. C. Goh, Y. Li, "GA automated design and synthesis of analog circuits with practical constraints," in *Proc. CEC2001*, 2001, vol. 2, p. 170-177.
[8]. R. A. Vural, T. Yıldırım, T. Kadioğlu, A. Basargan, "Performance evaluation of evolutionary algorithms for optimal filter design," *IEEE Trans. Evolut. Comput.*, vol. 16, pp. 135-147, Feb. 2012.
[9]. R. A. Vural, T. Yıldırım. "Component value selection for analog active filter using particle swarm optimization," in *Proc. ICCAE*, 2010, vol. 1, p. 25-28.
[10]. D. Ustun, M. Akkus, M. B. Bicer, H. Temurtas, A. Akdagli, "Sezgisel algoritmalar ile Butterworth ve Chebyshev alçak geçiren filre tasarımı", SIU-2015 Sinyal İşleme ve İletişim Uygulamaları Kurultayı, 16-19 Mayıs 2015, p. 108-111.
[11]. J. Karki, "Active low-pass filter design." Texas Instruments, Dallas-Texas, Application Rep. SLOA049B, 2002.
[12]. P. Civicioglu, "Backtracking search optimization algorithm for numerical optimization problems," *Appl. Math. Comput.*, vol. 219 (15), pp. 8121–8144, Apr. 2013.

BIBLIOGRAPHIES

Bahadır Hiçdurmaz was born in Kütahya, Turkey, in 1978. He received B.Sc. degree from the Electrical&Electronics Engineering Department, Eskişehir Osmangazi University, Eskişehir, Turkey, in 2001, M.Sc. degree from the Electrical&Electronics Engineering Department, Dumlupınar University, Kütahya, Turkey, in 2006, and Ph.D. degree from the Electronic Engineering Department of Uludağ University, Bursa Turkey. He is currently working as Assistance Professor in Department of Electrical&Electronics Engineering, Dumlupınar University. His research interests include optical fiber

communication systems, nonlinear fiber optics, applications of nonlinear optics, effects of nonlinear phenomena on WDM systems, and system optimization.

Burhanettin Durmuş was born in Pazaryeri, Turkey, in 1978. He received B.Sc. and M.Sc. degrees in 2000 and 2003 from the Department of Electrical&Electronics Engineering, Dumlupınar University, Kütahya, Turkey respectively. He received Ph.D. degree from Sakarya University. He is currently working as Assistance Professor in Department of Electrical&Electronics Engineering, Dumlupınar University. His areas of research include optimization techniques and computational intelligence.

Hasan Temurtaş was born in Mersin, Turkey, in 1967. He received B.Sc. degree in Electrical&Electronics Engineering from Middle East Technical University, Ankara, Turkey in 1993 and M.Sc. degree from the Department of Electrical&Electronics Engineering, Dumlupınar University, Kütahya, Turkey in 1996, Ph.D. degree in Electrical&Electronics Engineering from Sakarya University, Sakarya, Turkey in 2004. He is currently working as Assistance Professor in Department of Computer Engineering, Dumlupınar University. His areas of research include programming languages, control algorithms and optimization techniques.

Serdar Özyön was born in Ayaş, Turkey, in 1981. He received B.Sc. degree in Electrical Electronics Engineering from Dumlupınar University, Kütahya, Turkey, in 2005 and M.Sc. degree from the Department of Electrical&Electronics Engineering, Dumlupınar University, Kütahya, Turkey in 2009. He is working as research assistant in Department of Electrical&Electronics Engineering, Dumlupınar University. His areas of research include analysis of power systems, economic operation of power systems, power distribution systems, renewable energy systems and optimization techniques.

ICENS
INTERNATIONAL CONFERENCE ON ENGINEERING AND NATURAL SCIENCES
24-28 May 2016 /Sarajevo

Defining the Parameters of the High-Pass Active Filter by Using Backtracking Search Algorithm

Burhanettin Durmus*[1], Bahadir Hicdurmaz[1], Hasan Temurtas[1], Serdar Ozyon[1]

Abstract

Filter circuits are used widely in electronic systems in order to pass electric signals at certain frequencies or frequency ranges but to prevent the passage of others. Filters are designed in two basic types as active and passive. While passive circuit elements such as resistor, capacitor, and inductor are used in the design of passive filters, in active filters, together with resistors and capacitors, active circuit elements such as transistor or op-amp are used. Active filters are more advantageous compared with the passive filters in terms of their costs. The output impedance of the active filter is very low however the input impedance is very high. Therefore, it is out of the question that the circuit and the circuit elements that will be connected to the inputs or outputs of the active filters are affected. Hence, active filters can be connected in a row easily. In this study, the parameter values for 10th-order Butterworth type active high-pass filter (HPF) have been defined by Backtracking Search Algorithm (BSA), which is a meta-heuristic algorithm. In traditional approaches, circuit elements are accepted as ideal and unlimited. In the practice, the use of these values rather increases the cost of the design. This study has used standard series values known as E24 in order to decrease the costs of design. The ideal values defined by BSA have been rounded to the nearest values obtained from the E24 series. The frequency scaling factor (FSF) and quality factor (Q) of the designed filter have been calculated separately by both of these obtained parameter values. The calculated values have been compared with ideal Butterworth FSF and Q values.

Keywords: *Active filters, HPF, E24 series, Backtracking search algorithm*

1. INTRODUCTION

Filters are often utilized in electronic systems to allow signals in certain frequency ranges and to stop signals in other frequency ranges. An analog active filter is a type of electronic filter which uses active elements such as op-amps or transistors in addition to resistors and capacitors without using inductors. Active filters have several applications in high precision large scale integrated circuits [1].

Lately, metaheuristic algorithms such as differential evolution (DE), genetic algorithm (GA), particle swarm optimization (PSO) [2] and artificial bee colony (ABC), have attracted attention by researchers in the field of circuit design. An application of filter design based on DE is given in [3] for selection of optimal circuit elements using DE algorithm. In [4], GA was used for component value optimization of analog filter. ABC and PSO have been utilized for the optimal circuit design in [5] and [6], respectively.

In recent years, BSA [7] has attracted attention in solving optimization problems. In this work, a 10th-order Sallen-Key configuration Butterworth type HPF is designed by using BSA. This algorithm is used for selection of filter parameters according to FSF and Q values of 10th order Butterworth filter type. Then, component values defined for infinite value range are rounded to values produced from E24 series for resistors and capacitors. Finally, obtained results are compared with ideal results.

2. SALLEN-KEY BUTTERWORTH TYPE HPF

In HPF, above its cut-off frequency f_c inputs are transmitted to output with no attenuation whereas below f_c inputs are infinitely attenuated. A 2nd-order unity-gain Sallen-Key HPF architecture is given as [1]

[2] *Corresponding author: Dumlupınar University, Department of Electrical and Electronics Engineering, 43100, Kütahya, Turkey.* bahadir.hicdurmaz@dpu.edu.tr

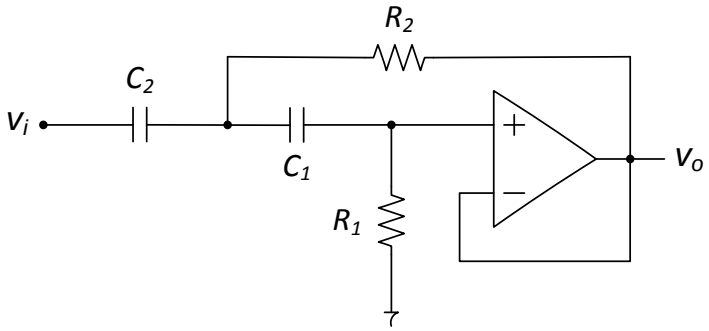

Figure 1. 2nd order unity-gain Sallen-Key HPF architecture

From circuit analysis, transfer function, $H_{HPF}(s)$ is obtained as

$$H_{HPF}(s)=\frac{V_o(s)}{V_i(s)}=\frac{1}{1+\frac{C_1+C_2}{sR_1C_1C_2}+\frac{1}{s^2R_1R_2C_1C_2}} \tag{1}$$

In equation (1), substituting s = j2πf gives

$$H_{HPF}(f)=\frac{1}{1-\left(\frac{1}{2\pi f\sqrt{R_1R_2C_1C_2}}\right)^2-j\frac{C_1+C_2}{2\pi fR_1C_1C_2}} \tag{2}$$

The standard form of $H_{HPF}(f)$ is expressed as [8]

$$H_{HPF}(f)=\frac{1}{1-\left(\frac{f_c}{FSF\cdot f}\right)^2-j\frac{f_c}{Q\cdot FSF\cdot f}} \tag{3}$$

where f_c is the cut-off frequency, $FSF=2\pi f_c\sqrt{R_1R_2C_1C_2}$ and $Q=(\sqrt{R_1R_2C_1C_2})/(R_2(C_1+C_2))$.

Then, the amplitude response of the filter is found as

$$\left|H_{HPF}(f)\right|=\frac{1}{\sqrt{\left(1-\left(\frac{f_c}{FSF\times f}\right)^2\right)^2+\left(\frac{f_c}{Q\times FSF\times f}\right)^2}} \tag{4}$$

A 10th order HPF are constructed by cascading five 2nd order stages. Then, resultant transfer function is multiplication of each stages transfer function. To realize 10th order Butterworth HPF, FSF and Q values of each stages are given in Table 1 [8]. Cut-off frequency of designed filter is 10 kHz.

Table 1. FSF and Q values of 10th order Butterworth Filter

Filter Order	**Stage 1**		**Stage 2**		**Stage 3**		**Stage 4**		**Stage 5**	
	FSF	***Q***	***FSF***	***Q***	***FSF***	***Q***	***FSF***	***Q***	***FSF***	***Q***
10	1.000	0.5062	1.000	0.5612	1.000	0.7071	1.000	1.1013	1.000	3.1969

3. BACKTRACKING SEARCH ALGORITHM

BSA is a population-based iterative method including five processes [7]. These processes are initialization, selection-I, mutation, crossover and selection-II. BSA initials current population as,

$$P_{i,j} \sim U(\min_j, \max_j) \quad i = 1,...N \quad and \quad j = 1,...D \tag{5}$$

where N is the population size, D is the problem dimension, P_i is a target individual in the population P, and U is uniform distribution [7].

Then, selection-I determines the historical population $oldP$ to be used for calculating the search direction. At the beginning of each iteration, $oldP$ is redefined through the following rules:

$$if \quad a < b \quad then \quad oldP := P \mid a, b \sim U(0,1) \tag{6}$$

$$oldP := permuting(oldP) \tag{7}$$

Where $:=$ is the update operation, a and b are random values uniformed in (0,1).

In mutation stage of BSA, the initial form of the trial population *Mutant* is provided by Eq. (8).

$$\text{Mutant} = P + F(oldP - P) \tag{8}$$

where F controls the amplitude of the search-direction matrix ($oldP - P$).

The crossover process of BSA generates the final form of the trial population T. Trial individuals with better fitness values are used to evolve the target population individuals. A binary integer-valued matrix (*map*) of size N is calculated. D that indicates individuals of T to be manipulated by using the relevant individuals of P. If $map_{n,m} = 1$, T is updated with $T_{n,m} := P_{n,m}$, $n \in \{1,2,3...N\}$ and $m \in \{1,2,3...D\}$. In selection-II, the T_is that have better fitness values than the corresponding P_is are used to update the P_is based on a greedy selection. If the best individual of $P(P_{best})$ has a better fitness value than the global minimum value obtained so far by BSA, the global minimum is updated to be P_{best}.

4. SIMULATION AND RESULTS

In application of filter design based on BSA, each passive component of high pass filter belong to each stage was encoded in the string form as shown in Table 2. The aim is to estimate the preferred values of resistors and capacitors produced from E24 series. In this case, the components values of the filter are successively adjusted by BSA until the error is minimized. The design error of the filter, $Error_{Total}$ is given as [2]

$$Error_1 = \sum_{i=1}^{5} \frac{\left|FSF_{t,i} - FSF_i\right|}{FSF_{t,i}}$$

$$Error_2 = \sum_{i=1}^{5} \frac{\left|Q_{t,i} - Q_i\right|}{Q_{t,i}} \tag{9}$$

$$Error_{Total} = \alpha \times Error_1 + (1-\alpha) \times Error_2$$

where $FSF_{t,i}$ is target FSF, $Q_{t,i}$ target quality factor, and α is the constant ($\alpha = 0.5$). The aim is to keep the total error as low as possible.

Table 2. Representing the component values in the string form

Stage 1				**…**	**Stage 5**			
R_{11}	C_{11}	R_{21}	C_{21}	**…**	R_{15}	C_{15}	R_{25}	C_{25}

In simulation studies, the population size *NP* is 25 and iteration number is set to 1000. Experiments are performed over 25 independent runs. Obtained results are presented in Table 3-6.

Table 3. Ideal component values of best solution

Componenet	**Stage 1**	**Stage 2**	**Stage 3**	**Stage 4**	**Stage 5**
$R_1(k\Omega)$	3.96872	3.66355	3.59545	8.56386	44.345
$R_2(k\Omega)$	3.77231	2.90656	1.72949	1.76232	1.07201
$C_1(nF)$	4.88353	4.97122	7.77892	4.27496	2.57844
$C_2(nF)$	3.46296	4.78751	5.23608	3.92686	2.06725

Table 4. Nearest preferred E24 series component values of best solution

Componenet	**Stage 1**	**Stage 2**	**Stage 3**	**Stage 4**	**Stage 5**
$R_1(k\Omega)$	3.9	3.6	3.6	8.2	43
$R_2(k\Omega)$	3.9	3	1.8	1.8	1.1
$C_1(nF)$	4.7	5.1	7.5	4.3	2.7
$C_2(nF)$	3.6	4.7	5.1	3.9	2

Table 5. Performance evaluation of designed filter

Method	**Stage1**		**Stage 2**		**Stage 3**		**Stage 4**		**Stage 5**	
	FSF	***Q***	***FSF***	***Q***	***FSF***	***Q***	***FSF***	***Q***	***FSF***	***Q***
Target	1	0.5062	1	0.5612	1	0.7071	1	1.1013	1	3.1969
Ideal values	0.9998	0.5054	1.0003	0.5612	0.9999	0.7070	1.0001	1.1012	1.0002	3.1963
E24 series	1.0080	0.4956	1.0109	0.5473	0.9892	0.6942	0.9885	1.0659	1.0042	3.0913

In Table 3 and 4, the best solution results of the filter optimization are presented for ideal values and nearest preferred E24 series component values, respectively. In order to find the optimum set of components that are within the E24 series of components, the ideal component values found are simply rounded to the nearest component values of the E24 series. Performance evaluation of designed 10^{th}-order Sallen-Key configuration Butterworth type HPF is shown in Table 5. Obtained error values with ideal and nearest preferred E24 series component values are expressed in Table 6.

Table 6. Obtained error values with ideal and nearest preferred E24 series component values

Component Values	$Error_1$	$Error_2$	$Error_{Total}$
Ideal	8.086645e-04	2.096787e-03	1.452726e-03
Nearest E24 series	4.534716e-02	1.292585e-01	8.730284e-02

In Figure 2 and Figure 3, total gain curves are plotted for HPF. As seen in these figures, total gain curves of designed filter are closely following the target gain curve.

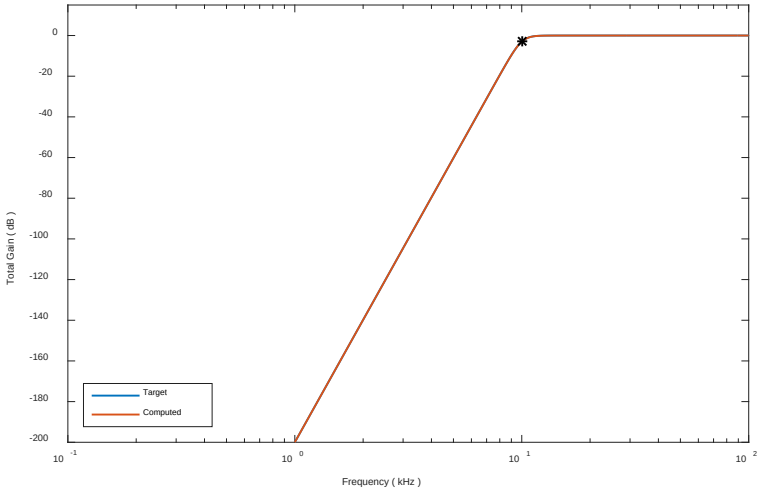

Figure 2. Total gain curves for ideal values

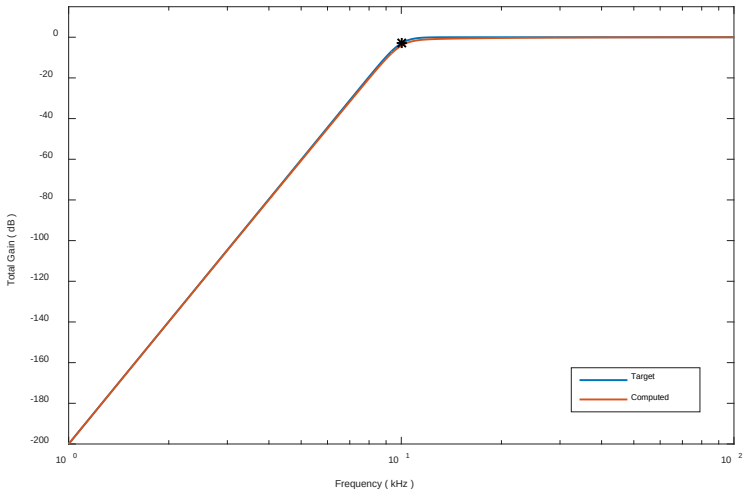

Figure 3. Total gain curves for rounded E24 series component values

Figure 4 shows the cost function versus iteration number. In this figure, it can be seen that BSA designs an acceptable filter at around 700 iterations.

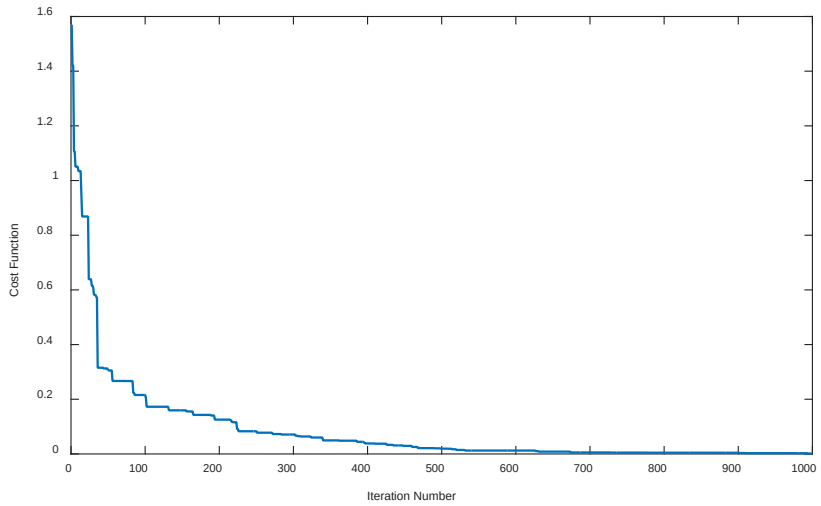

Figure 4. The cost function versus iteration number

5. CONCLUSIONS

In this paper, BSA based component value selection of active filter has been applied to 10th-order Sallen-Key configuration Butterworth type HPF. Ideal component values were obtained by BSA algorithm and these values were rounded to nearest E24 series values. The performance of application based on BSA was interpreted by comparing FSF and Q values founded by both ideal component values and E24 series values with ideal Butterworth FSF and Q values. It was shown that BSA algorithm provided a successful solution of the analog active filter component selection problem.

REFERENCES

[1]. S. A. Pactitis, "Active Filters Theory and Design" CRC Press, Taylor & Francis Group, 2007.
[2]. D. Ustun, M. Akkus, M. B. Bicer, H. Temurtas, A. Akdagli, "Sezgisel algoritmalar ile Butterworth ve Chebyshev alçak geçiren filre tasarımı", SIU-2015 Sinyal İşleme ve İletişim Uygulamaları Kurultayı, 16-19 Mayıs 2015, p. 108-111.
[3]. A. F. Sheta, "Analogue filter design using differential evolution," *Int. J. Bio-Inspired Comput.*, vol. 2 (3), pp. 233-241, 2010.
[4]. C. Goh, Y. Li, "GA automated design and synthesis of analog circuits with practical constraints," in *Proc. CEC2001*, 2001, vol. 2, p. 170-177.
[5]. R. A. Vural, T. Yıldırım, T. Kadioğlu, A. Basargan, "Performance evaluation of evolutionary algorithms for optimal filter design," *IEEE Trans. Evolut. Comput.*, vol. 16, pp. 135-147, Feb. 2012.
[6]. R. A. Vural, T. Yıldırım. "Component value selection for analog active filter using particle swarm optimization," in *Proc. ICCAE*, 2010, vol. 1, p. 25-28.
[7]. P. Civicioglu, "Backtracking search optimization algorithm for numerical optimization problems," *Appl. Math. Comput.*, vol. 219 (15), pp. 8121–8144, Apr. 2013.
[8]. J. Karki, "Active low-pass filter design." Texas Instruments, Dallas-Texas, Application Rep. SLOA049B, 2002.

BIBLIOGRAPHIES

Burhanettin Durmuş was born in Pazaryeri, Turkey, in 1978. He received B.Sc. and M.Sc. degrees in 2000 and 2003 from the Department of Electrical&Electronics Engineering, Dumlupınar University, Kütahya, Turkey respectively. He received Ph.D. degree from Sakarya University. He is currently working as Assistance Professor in Department of Electrical&Electronics Engineering, Dumlupınar University. His areas of research include optimization techniques and computational intelligence.

Bahadır Hiçdurmaz was born in Kütahya, Turkey, in 1978. He received B.Sc. degree from the Electrical&Electronics Engineering Department, Eskişehir Osmangazi University, Eskişehir, Turkey, in 2001, M.Sc. degree from the Electrical&Electronics Engineering Department, Dumlupınar University, Kütahya, Turkey, in 2006, and Ph.D. degree from the Electronic Engineering Department of Uludağ University, Bursa Turkey. He is currently working as Assistance Professor in Department of Electrical&Electronics Engineering, Dumlupınar University. His research interests include optical fiber communication systems, nonlinear fiber optics, applications of nonlinear optics, effects of nonlinear phenomena on WDM systems, and system optimization.

Hasan Temurtaş was born in Mersin, Turkey, in 1967. He received B.Sc. degree in Electrical&Electronics Engineering from Middle East Technical University, Ankara, Turkey in 1993 and M.Sc. degree from the Department of Electrical&Electronics Engineering, Dumlupınar University, Kütahya, Turkey in 1996, Ph.D. degree in Electrical&Electronic Engineering from Sakarya University, Sakarya, Turkey in 2004. He is currently working as Assistance Professor in Department of Computer Engineering, Dumlupınar University. His areas of research include programming languages, control algorithms and optimization techniques.

Serdar Özyön was born in Ayaş, Turkey, in 1981. He received B.Sc. degree in Electrical&Electronics Engineering from Dumlupınar University, Kütahya, Turkey, in 2005 and M.Sc. degree from the Department of Electrical&Electronics Engineering, Dumlupınar University, Kütahya, Turkey in 2009. He is currently working as research assistant in Department of Electrical&Electronics Engineering, Dumlupınar University. His areas of research include analysis of power systems, economic operation of power systems, power distribution systems, renewable energy systems and optimization techniques.

A Wide Band Metasurface Polarization Converter Designed by Three Nested Rectangular Resonator

Olcay Altintas[1], Emin Unal[1], Oguzhan Akgol[1], Muharrem Karaaslan[1]*

Abstract

In this study, we design a wide band polarization converter metasurface (MS) structure to convert linearly polarized signal into circularly polarized signal. We calculate the results at C band microwave regime both numerically and experimentally. The proposed MS structure is periodically designed by using planar technology. The unit cell of MS consists of three nested rectangular resonator which has two metallic patches at its crossed corners. Numerical results are achieved by full wave commercial electromagnetic solver simulation software. And this results are confirmed by experimental results by using a vector network analyzer and two microwave antennas. S-parameters are obtained by co-polar and cross-polar responses and the axial ratio (AR) calculated by division of these two responses. AR is kept in below 3 dB to obtain effective polarization conversion activity. Proposed MS has two dip points which occur perfect polarization activities at about frequencies of 4.7 and 4.8 GHz. Axial ratio bandwidth (ARBW) is about 800 MHz between frequencies of 4.60 GHz and 5.40 GHz. Since circularly polarized signals are not affected by weather conditions or ionosphere effects abnormally, the proposed structure can be used by some weather radars and satellite communication applications. In addition, The MS can be fabricated easily, configurable for desired frequency range and integrated antennas which is compatible its surface.

Keywords: *Axial ratio, axial ratio bandwidth, metasurface, polarization conversion*

1. INTRODUCTION

MTMs are artificial materials having many unusual electromagnetic properties such as reverse Cherenkov Effect, negative refraction and double negative media. The first theoretical study on MTMs was realized by Veselago in 1968 [1]. This study was about simultaneously negative values of permittivity and permeability. In 2000, Smith et al. actualized the theory with a split ring and wires [2]. Today, MTMs have numerous potential application areas such as absorbers, sensors and super lenses [3]-[6].

Metasurface (MS) is a two dimensional form of metamaterial (MTM) [7]-[8]. MSs are less lossy structures and take less physical space than three dimensional MTMs. They also have many potential application areas such as controllable smart surfaces [9], polarization converters [10] and wave guide structures [11].

In this paper, we offer a wide band MS polarization converter to transform linearly polarized signal into circularly polarized one at microwave frequencies. The study is numerically and experimentally achieved at C band and results are in good agreement. The key parameter is axial ratio (AR) in polarization conversion study. The axial ratio is obtained by division of co-polar and cross-polar responses of horn antennas and it is kept in below 3 dB. The proposed model offers a polarization conversion activity approximately 800 MHz between frequencies of 4.60 GHz and 5.40 GHz. There are two dip points in which occur perfect polarization conversion at 4.70 GHz and 4.80 GHz. Because circularly polarized signals are less affected by weather conditions than linearly polarized one, proposed MS polarization converter can be used in some radar applications which operate at C band.

2. DESIGNING OF METASURFACE

The unit cell of proposed model consists of three nested rectangular resonator. The construction of model is periodically arranged by 16 unit cell in a 4 X 4 layout. Roger RT5870 is used as a dielectric substrate having a thickness, loss tangent and relative permittivity of 1.575 mm, 0.012 and 2.33, respectively. The MS converter is called as left handed polarization converter (LHPC) to transform linearly polarized signal into left handed circularly polarized one as shown in Figure 1(a). Similarly, it is called as RHPC to convert linearly polarized signal into right handed circularly polarized one as shown in Figure 1(b). The unit cell dimensions of structure are 68.096 mm, 70.640 mm, 15.824 mm, 16.460 mm, 0.960 mm and 1.523 mm which represent Lx, Ly, x, y, w and gp, respectively.

[1]*Iskenderun Technical University, Department of Electrical and Electronics Engineering, 31200 Iskenderun/Hatay, Turkey,* olcay.altintas@iste.edu.tr

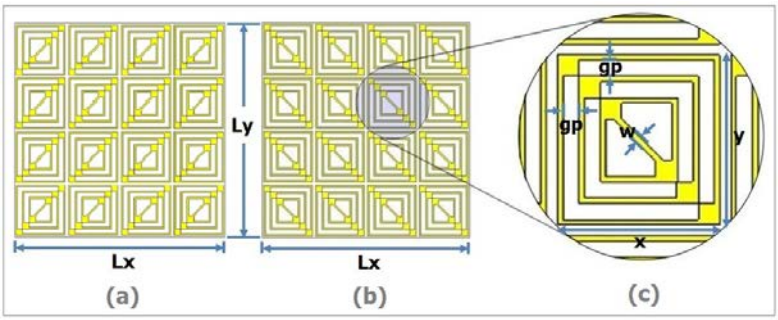

Figure 6. (a) LHPC (b) RHPC (c) unit cell dimensions of MS polarization converter

3. NUMERICAL AND EXPERIMENTAL STUDY

Numerical study of the MS converter is realized by using commercial full wave solver simulation program with floquet port mode. About 1 GHz of axial ratio bandwidth (ARBW) is obtained in the simulation between 4.60 GHz and 5.60 GHz. Proposed MS structure is produced by LPKF ProtoMat E33 prototyping machine in the form of 8X8 layout as shown in Figure 2(a).

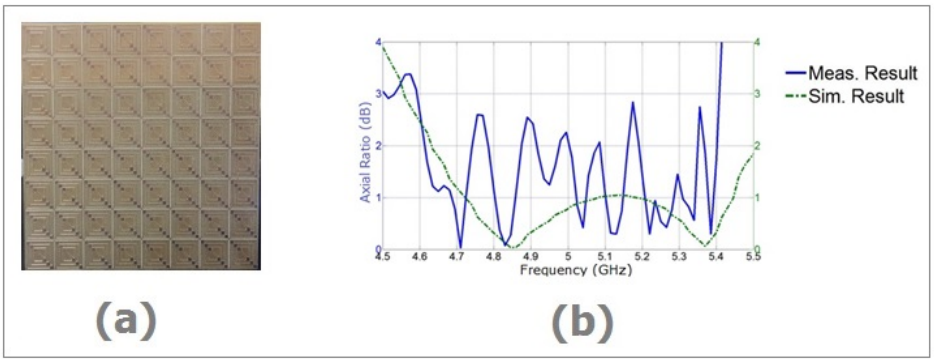

Figure 2. (a) Fabricated MS polarization converter (b) measured and simulated AR results

Experimental study is realized by using a vector network analyzer and two horn antennas. Antennas are at the same direction to obtain co-polar response however one of the antennas is rotated by 90° to obtain cross-polar response. Axial ratio is then calculated by division of these responses. About 800 MHz of axial ratio bandwidth is observed in measurement result between 4.60 GHz and 5.40 GHz. Perfect polarization activities are occurred at 4.70 GHz and 4.80 GHz. Comparison of measured and simulated AR results is kept in below 3 dB as shown in Figure 2(b). The ARBWs of two results are almost at the same level. Although, there is a minor difference originated from manufacturing defects between the results, experimental and numerical studies are in a good agreement.

4. CONCLUSION

A wide band metasurface polarization converter based on three nested rectangular resonator is designed to convert linearly polarized signal into circularly polarized signal at microwave frequency regime. Numerical and experimental studies are compared to each other and results are in a good agreement. Perfect polarization conversion activities are obtained at 4.70 GHz and 4.80 GHz. Operating frequency range of MS converter is 800 MHz from 4.60 GHz to 5.40 GHz. Since the circularly polarized signals are almost not affected by bad weather conditions, the proposed polarization converter can be efficiently used in some radar applications at C band. In addition proposed model can be easily fabricated and configurable for any desired frequency range.

ACKNOWLEDGMENT

We would like to thank the Scientific and Technological Research Council of Turkey (TUBITAK 114E295 and 113E290) for its financial support.

REFERENCES

[1]. V. G. Veselago, "The electrodynamics of substances with simultaneously negative values of Ɛ and μ," Sov. Phys. Usp., Vol. 10, No. 4, p. 509–514, 1968.
[2]. D. R. Smith and N. Kroll, "Negative Refractive Index in Left-Handed Materials", Physical Review Letters, vol. 85, no. 14, p. 2933-2936, 2000.
[3]. F. Dincer, M. Karaaslan, E. Unal, K. Delihacioglu, C. Sabah, "Design of polarization and incident angle insensitive dual-band metamaterial absorber based on isotropic resonators," Progress In Electromagnetics Research, Vol. 144, p.123-132, 2014.
[4]. F. Dincer, M. Karaaslan, S. Colak, E. Tetik, O. Akgol, O. Altintas, C. Sabah, "Multi-band polarization independent cylindrical metamaterial absorber and sensor application", Modern Physics Letter B, vol. 30, p. 1650095, 2016.
[5]. M. Karaaslan and M. Bakir, "Chiral metamaterial based multifunctional sensor applications," Progress In Electromagnetics Research, Vol. 149, p. 55-67, 2014.
[6]. Y. Zhang, M. A. Fiddy, "Covered image of super lens," Progress In Electromagnetics Research. Vol. 136, p. 225-238, 2013.
[7]. C. L. Holloway, E. F. Kuester, J. A. Gordon, J. F. O'hara, J. Booth, D. R. Smith, "An overview of the theory and applications of metasurfaces:The two-dimensional equivalents of metamaterials, " IEEE Antennas Propag. Mag., Vol. 54, No. 2, p. 10-35, 2012.
[8]. C. L. Holloway, D. Love, E. F. Kuester, J. A. Gordon, D. A. Hill, "Use of generalized sheet transition conditions to model guided waves on metasurfaces/metafilms, " IEEE Trans. Antennas Propag., Vol. 80, No. 11, p. 5173-s5186, 2012.
[9]. C. L. Holloway, M. A. Mohamed, E. F. Kuester and A. Dienstfrey, "Reflection and transmission properties of a metafilm: with an application to a controllable surface composed of resonant particles," IEEE Trans. Electromag. Compat., vol. 47, no. 4, p. 853-865, 2005.
[10]. H. L. Zhu, S. W. Cheung, K. L. Chung, T. I. Yuk, "Linear-to-circular polarization conversion using metasurface," IEEE Transactions on Antennas and Propagation, Vol. 61, No. 9, p. 4615-4623, 2013.
[11]. S. Sajuyigbe, M. Ross, P. Geren, S. A. Cummer, M. H. Tanielian and D.R. Smith, "Wide angle impedance matching metamaterials for waveguide-fed phased-array antenna," IET Microwaves, Antennas, and Propagation, vol. 4, no. 8, p. 1063-1072, 2010.

Metasurface Polarization Converter Designed by Horizontal and Cross lines in C Band

Olcay Altintas[1], Emin Unal[1], Oguzhan Akgol[1], Muharrem Karaaslan[1]*

Abstract

We present a metasurface (MS) polarization converter to transform linearly polarized signal to circularly polarized signal at a certain frequency range both numerically and experimentally. The unit cell consists of horizontal and cross lines placed in a rectangular loop. Simulated results are performed by a commercial full wave electromagnetic (EM) solver simulation software and these results are in a good agreement with experimental results which are achieved by a PNA-L vector network analyzer and two microwave horn antennas. The axial ratio (AR) is main parameter to determine polarization conversion quality in reference to AR < 3dB. AR is calculated by division of transmission ratios which are co-polar and cross-polar responses. Frequency range of effective polarization conversion activity is about at 600 MHz (i.e. axial ratio bandwidth (ARBW) is 600 MHz) from 3.8 GHz to 4.4 GHz and within this frequency band AR is below 3 dB. Also, at about frequencies of 4.10 GHz and 4.22 GHz, perfect polarization conversion is obtained. It is more reliable to use a circular polarization than a linear polarization because linear polarized signals are affected negatively from Faraday rotation force in the ionosphere, but circularly polarized signals are not affected from these anomalies directly. Thus, the suggested MS polarization converter can be used for some weather and airport surveillance radar and satellite applications. In addition, the proposed structure is reconfigurable for any desirable frequency bands.

Keywords: *Axial ratio, axial ratio bandwidth, metasurface, polarization conversion*

1. INTRODUCTION

Metamaterials (MTMs) represent double negative (DNG) media which does not exist in nature. They have many extraordinary electromagnetic features such as negative refraction. This phenomenon was theoretically studied by Veselago in 1968 [1]. In the later 20th century, Pendry et al. and Smith et al. achieved to produce materials which have the feature of simultaneously negative permittivity and negative permeability by using wires and split ring [2]-[4]. In recent years, MTMs attract great attention due to many potential application areas such as optic, absorber and sensor [5]-[8].

Metasurfaces (MSs) are that two dimensional equivalent form of MTMs [9]. These types of MTMs which is sometimes called as metafilms have some advantages on three dimensional MTMs such as taking a small space and low loss. MSs also have some application areas such as polarization converters [10], wave guide structures [11] and absorbers [12].

In this paper, we study a MS polarization converter based on horizontal and cross lines to convert linearly polarized signal into circularly polarized signal at C band, numerically and experimentally. Since circularly polarized signals are not easily degenerated by bad weather conditions, they are commonly used in radar and satellite systems. Proposed MS polarization converter has about 600 MHz of axial ratio bandwidth (ARBW) between 3.80 GHz and 4.40 GHz below 3 dB in experiment result. It provides perfect polarization activity at 4.10 GHz and 4.22 GHz.

2. DESIGNING OF METASURFACE

The unit cell of proposed MS structure consists of horizontal and cross lines. Construction of converter is arranged by placing 16 unit cells periodically in a 4x4 layout. The dielectric substrate layer is Rogers RT5870 type material which has a thickness, loss tangent and relative permittivity of 1.575 mm, 0.012 and 2.33, respectively. Since the MS polarization converter transforms linearly polarized signal into left handed circularly polarized signal, it is called as left handed polarization converter (LHPC) in Figure 1 (a). Likewise, it is called as right handed polarization converter (RHPC) because the MS converts linearly polarized signal into right handed circularly polarized one in Figure 1 (b). Dimensions of the unit cell are 56.80, mm 9.58 mm, 14.20 mm, 17.396 mm, 1.528 mm, 9.752 mm, 8.46 mm and 14.526 which represent Lx , Ly, x, y, a, tx, ty and tz, respectively.

[1]*Iskenderun Technical University, Department of Electrical and Electronics Engineering, 31200 Iskenderun/Hatay, Turkey, olcay.altintas@iste.edu.tr*

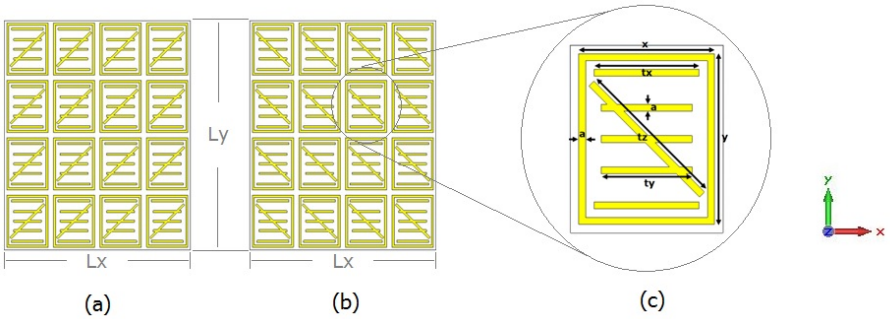

Figure 7. (a) LHPC (b) RHPC (c) unit cell dimensions of MS polarization converter

3. NUMERICAL AND EXPERIMENTAL STUDY

Simulation study of the proposed structure has been realized by commercial full wave electromagnetic solver with periodic boundary conditions. The key parameter to determine the circularity is axial ratio (AR). AR is kept in below 3 dB due to polarization conversion quality. Numerically obtained operating bandwidth called as axial ratio bandwidth (ARBW) of the proposed MS is about 800 MHz between 3.80 GHz and 4.60 GHz as shown in Figure 2 (b). Perfect polarization activities have been realized at 3.90 GHz and 4.42 GHz. Proposed MS polarization converter is fabricated by LPKF E33 ProtoMat prototyping machine in 8X8 layout as shown in Figure 2(a).

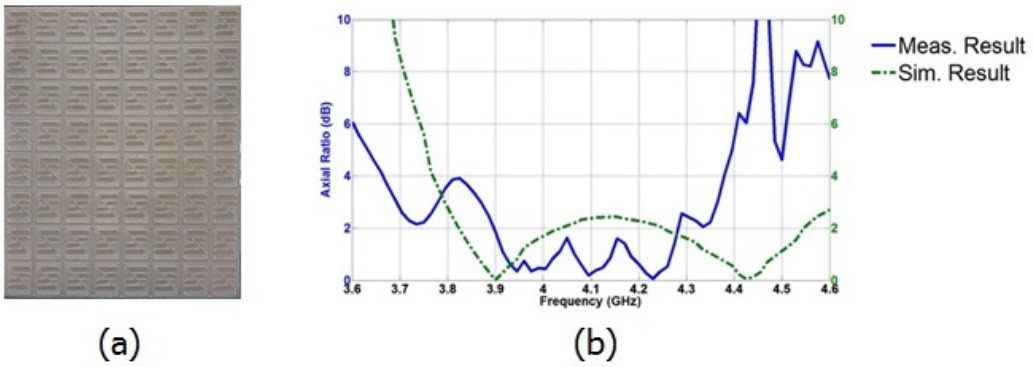

Figure 2. (a) Fabricated MS polarization converter (b) measured and simulated AR results

Measurement result is obtained by using a vector network analyzer and two microwave horn antennas in free space. AR is calculated by division of the co-polar and cross-polar transmission values of antennas. About 600 MHz of ARBW is obtained in experimental study between 3.80 GHz and 4.40 GHz as shown in Figure 2(b). At 4.10 GHz and 4.22 GHz, AR is at zero point which realizes perfect conversion activity. ARBW of the measured result is narrower than simulated result due to manufacturing defects; still results are in good agreement.

4. CONCLUSION

In this study, we offer a metasurface polarization converter to transform linearly polarized signal into circularly polarized signal at microwave frequency, numerically and experimentally. While the axial ratio is below 3 dB for polarization quality, axial ratio bandwidth is about 600 MHz between 3.80 GHz and 4.40 GHz in measured result. Simulated and measured results are in good agreement. Since circularly polarized signals can keep the signal stable at bad weather conditions, it has a vital role in some radar and satellite applications. The proposed MS polarization converter can be efficiently used some C-band applications such as weather radar, airport surveillance radar, and satellite communications.

ACKNOWLEDGMENT

We would like to thank the Scientific and Technological Research Council of Turkey (TUBITAK 114E295 and 113E290) for its financial support.

REFERENCES

[1]. V. G. Veselago, “The electrodynamics of substances with simultaneously negative values of Ɛ and μ,” Sov. Phys. Usp., Vol. 10, No. 4, p. 509–514, 1968.
[2]. D. R. Smith and N. Kroll, “Negative Refractive Index in Left-Handed Materials”, Physical Review Letters, vol. 85, no. 14, p. 2933-2936, 2000.
[3]. J. B. Pendry, A. J. Holden, W. J. Stewart, I. Youngs, “Extremely low frequency plasmons in metallic mesostructures,” Physical Review Letters, Vol. 76, p. 4773–4776, 1996.
[4]. J. B. Pendry, A. J. Holden, D. J. Robbins, W. J. Stewart, “Magnetism from conductors and enhanced nonlinear phenomena,” IEEE Transactions on Microwave Theory and Techniques, Vol. 47, p. 2075–2084, 1999.,
[5]. C. Monzon, D. W. Forester, “Negative refraction and focusing of circularly polarized waves in optically active media,” Phys. Rev. Lett. Vol. 95, p. 123904, 2005.
[6]. F. Dincer, M. Karaaslan, E. Unal, K. Delihacioglu, C. Sabah, “Design of polarization and incident angle insensitive dual-band metamaterial absorber based on isotropic resonators,” Progress In Electromagnetics Research, Vol. 144, p. 123-132, 2014.
[7]. F. Dincer, M. Karaaslan, S. Colak, E. Tetik, O. Akgol, O. Altintas, C. Sabah, “Multi-band polarization independent cylindrical metamaterial absorber and sensor application”, Modern Physics Letter B, vol. 30, p. 1650095, 2016.
[8]. M. Karaaslan and M. Bakir, "Chiral metamaterial based multifunctional sensor applications," Progress In Electromagnetics Research, Vol. 149, p. 55-67, 2014.
[9]. C. L. Holloway, E. F. Kuester, J. A. Gordon, J. F. O'hara, J. Booth, D. R. Smith, “An overview of the theory and applications of metasurfaces:The two-dimensional equivalents of metamaterials, ” IEEE Antennas Propag. Mag., Vol. 54, No. 2, p. 10-35, 2012.
[10]. H. L. Zhu, S. W. Cheung, K. L. Chung, T. I. Yuk, “Linear-to-circular polarization conversion using metasurface,” IEEE Transactions on Antennas and Propagation, Vol. 61, No. 9, p. 4615-4623, 2013.
[11]. S. Sajuyigbe, M. Ross, P. Geren, S. A. Cummer, M. H. Tanielian and D.R. Smith, “Wide angle impedance matching metamaterials for waveguide-fed phased-array antenna,” IET Microwaves, Antennas, and Propagation, vol. 4, no. 8, p. 1063-1072, 2010.
[12]. Y. Kotsuka, K. Murano, M. Amano and S. Sugiyama, “Novel right-handed metamaterial based on the concept of ‘autonomous control system of living cells,’ and its absorber applications,” IEEE Trans. Electromag. Compat., vol. 52, no. 3, p. 556-565, 2010.

Examination of the Effect of Terminal Layout Plan on the Container Terminal Performance

Olgay Oksas[1], Gokhan Kara[1], E.Gul Emecen Kara[1]*

Abstract

Container transportation has an increasing share in maritime transport. Container ports are essential component of this transportation process. Container terminals where many operations are carried out at the same time have a complex and dynamic structure. Therefore, in order to evaluate operational efficiency of container terminals, different performance indicators are used from the arrival of vessel, till gating out of the container. In this study, the performance indicators which are related to container terminal layout plan is examined and the effect of layout plan on the terminal efficiency is analyzed

***Keywords**: Container transportation, container port layout, port efficiency.*

1. INTRODUCTION

Container transportation is a liner service in maritime transport which offers a scheduled plan to customers. Speed and on time delivery are important components of this kind of liner services. During a voyage of liner vessel, it is foreknown when the vessel will arrive further ports and how long will stay at these ports. Except for force major situations transit time of a vessel can be calculated and predicted before arrival. However, actual staying time at port is dependent on many variables which are connected to each other. Any disruptions during loading/unloading operations of a vessel may extend the staying time of the vessel at the port. This causes to reschedule the rest of voyage and possible economic losses.

Container ports are complex systems with lots of equipment that working together or independently. A significant amount of investment is needed in order to develop and maintain both their infrastructure and super structure. Also, they must have suitable management strategies in the allocation of scarce resources to meet demand, increase throughputs and success a fast transshipments process combined with reduced costs. Therefore, terminal productivity and performance measurements are very important issues for the container terminal system. There are many factors affecting port performance. Factors related to terminal layout are ones of the most important factors. In this study, performance indicators of container terminal and importance of terminal layout plan on terminal performance are investigated.

2. CONTAINER PORT LAYOUT

Layout plan of a container terminal is decided before construction of the port according to main functions of the port, expected container traffic, geographical location and inter-relations. With a well prepared master layout plan, detailed planning on various different levels are foreseen, such as berth allocation planning, yard planning, traffic planning within the port area, planning of intermodal operations, lock operation planning and planning related to tidal conditions in estuary ports. All these elements should be aligned in order to realize smooth port operations [1].

[1] *Corresponding author: Istanbul University, Department of Maritime Transportation Management Engineering, 34320, Avcilar/İstanbul, Turkey. olgay.oksas@istanbl.edu.tr*

Figure 8. Configuration of a container terminal [2]

Standard layout plan of a container terminal is shown in Figure 1. Main elements are described shortly as below according to [2]:

- *Docking area*, represents a berth where a containership can dock and have technical specifications such as length and draft.
- *Loading / unloading area*, is very close to the piers and under the gantry cranes. This zone is between the cranes and the storage areas where containers are either brought in to be lifted on the containership or unloaded to be immediately picked up and brought to storage areas by straddle carriers.
- *Container storage*, is a temporary zone where containers stay until loading on the vessel or picking up for inland transport. Container storage can be arranged by export, import, special and empty containers.
- *Gate*, is the terminal's entry and exit point. For export containers, truck drivers gives necessary information at the gate to unload full container to the correct storage area. For import containers, delivery documents should be presented at the gate.
- *Administration*, is the management facility of the terminal where controls terminal area and necessary paperwork is done.
- *On-dock rail terminal*, is the intermodal connection of containers through railway which reduces long haul distance transport costs.

Operations on the storage area are much more complicated than other part of a terminal. Because all containers (import, export, empty) are handled in this area simultaneously [3]. Due to this reason, terminal layout plan becomes more important for an efficient terminal management.

3. OPERATIONS AT CONTAINER TERMINAL

Operations at container terminals can be separated as quayside where the loading/unloading operations of the ships are done and landside where containers are stored and loaded or unloaded on/off trucks.

Container terminals have different sizes, functions and layouts but basically operations materialize with the same systems. There are quay cranes at the berthing area for loading/unloading vessels. Behind the berthing area usually there is a yard where containers are stacked. And these containers are transported either to quayside or to gate for outside transportation systems. When a container arrives terminal it is directed to storage area according to its booking data such as vessel name, destination, commodity type and shipping line. It’s stacked at yard area by specific cranes. When the designated vessel arrives

port, the container is transported from yard area to the berth by internal trucks and loaded on vessel by quay cranes. The opposite of these operations is carried out for import containers [4]. A schematic view of container terminal system is shown in Figure 2. The voyage of the containers in a container terminal is summarized in Figure 2 from ship where arrive port, to trucks/train where link to outside transportation systems and vice versa.

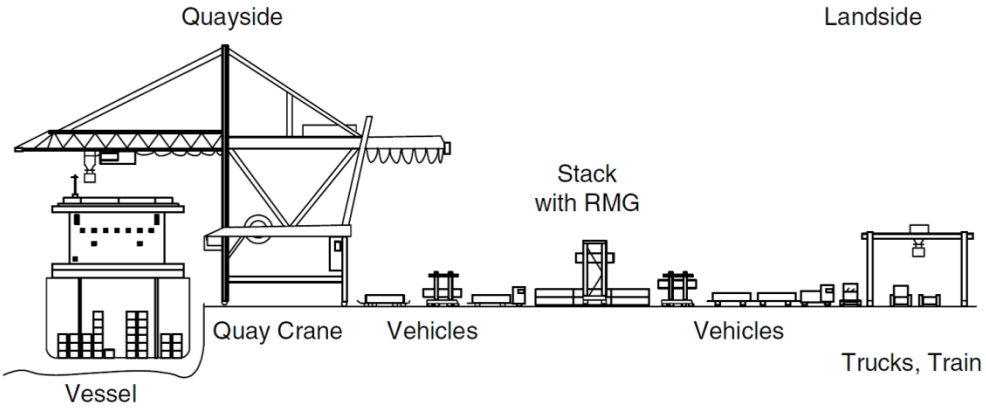

Figure 9. Schematic view of container terminal systems [5]

3.1. Quayside Operations

It consists mostly operations about ship. Loading containers to a ship and unloading them by quay cranes is the main part of these operations. The containers are transported between quay and storage area by internal equipment, mostly trucks [2].

3.2. Landside Operations

Storage yard operations is one of the landside operations. Generally there are different stacks at storage yards which are differentiated into rows, bays and tiers. These stacks are mostly separated into areas for export, import, special and empty containers. In the storage yard, yard cranes or straddle carriers are used to stack containers. Optimum stacking is very important in container terminals. Stacking requires close attention to be paid to the location of the container within the storage block to prevent multiple reshuffles or misplaced containers [5,6].

Internal truck operations are also considered as a landside operation. Quay cranes unload containers from ships and place them on internal trucks to move containers to the storage locations in the yard. Containers, which are stored in the storage yard, leave the terminal by trucks to reach their final destinations. In most European container terminals, there is also a railway link to transport containers from/to the terminal up to final destinations [6]. Gate operations which are mainly gate in/out of full/empty containers by trucks or trains are a kind of landside operations.

4. PERFORMANCE MEASUREMENT OF CONTAINER TERMINAL

Performance indicators are used in many areas to evaluate performance. Ports are one of the complex systems where performance indicators are used effectively. Basically, financial and operational indicators are found in the literature but to find appropriate indicators depends on which aspects of the port are being measured.

The United Nations Conference on Trade and Development (UNCTAD) suggested two main indicators in 1976 which are shown in Table 1. It was aimed to improve port operations and to plan future port development, therefore financial and operational indicators were defined and listed [7].

Table 7. Financial and operational indicators [7]

Financial indicators	Operational indicators
Total tonnage worked	Arrival rate
Berth occupancy revenue per ton of cargo	Waiting time
Cargo handling revenue per ton of cargo	Service time
Labor expenditure per ton of cargo	Turn-round time
Capital equipment expenditure per ton of cargo	Tonnage per ship
Contribution per ton of cargo	Fraction of time berthed ships worked
Total contribution	Number of gangs employed per ship per shift
	Tons per ship-hour in port
	Tons per ship hour at berth
	Tons per gang hour
	Fraction of time gangs idle

Most of the studies focus on operational efficiency. Tongzon [8] suggested a model to measure port performance and efficiency with the determinants of throughput which are location, frequency of ship calls, port charges, economic activity and terminal efficiency. And terminal efficiency was also calculated with the indicators of container mix, work practices, crane efficiency, vessel size and cargo exchange.

The most widely used performance indicator is throughput volume. Ports are ranked according to the volume of cargo that is handled but there are some limitations to take throughput as a performance indicator such as volumes of different commodities to one aggregated throughput figure limits the value of a comparison between ports. A second performance indicator that is used in a number of ports is the value added generated in seaports. This indicator is relevant for assessing the economic importance of the port but not enough to give any idea about port efficiency. Due to these reasons new indicators are proposed. These indicators are summarized under three main titles which are cargo transfer product, logistics product and port manufacturing product. Performance indicators, related to these titles are listed as throughput volume and ship waiting time for cargo transfer product, value added in logistics and m² logistics space for logistics products and value added and investment level in port related manufacturing for port manufacturing product [9].

There are various performance indicators for port operations, that all provide part of the picture of port performance. Main performance metrics exist on the level of cranes, berths, yards, gates and gangs, both in terms of utilization rates (such as TEUs/year per crane, vessels/year per berth, TEUs/per year per hectare, and containers/hour per lane) and productivity (moves per crane-hour, vessel service time, truck time in terminal and number of gang moves per man-hour) [1]. Merk [1] discussed that effective port operations are dependent on the quality of inputs and the quality of organization and institutions as it is shown in Table 2.

Table 8. Building blocks for effective port operations [1]

Quality of inputs	Quality of organization and institutions
Labor	Port planning
Equipment	Port information systems
Land	Competition
	Coordination between ports

Except for performance indicators there is another formation which is named CTQI (container terminal quality indicator). It is a conventional benchmarking system to adjudicate the efficiency and quality of global port terminal operations. This “Container Terminal Quality Indicator Standard”, defines clearly 80 container terminal performance measures. Some

examples are: average peak berth occupancy in the week, terminal productivity, number of ship calls/day, traffic import-traffic export, dwell time, berth working index, ship productivity. The authors broadly divide all these container terminal performance measures into four groups: Traffic(Production), Productivity, Utilization and Service [10].El et al. [11] made assessment of container terminal efficiency through these four groups with mentioned indicators in Table 3.

Table 9. Performance measures in container terminals [11]

Production measurements	Number of vessels
	Berth throughput (TEUs)
Productivity measurements	Average moves per hours in port
	Average moves per hours in berth
	Average moves per working hour
	Quay productivity TEUs per meter of quay
	Average TEUs per ship
Utilization measures	Berth occupancy ratio
Service measures	Average vessels turnaround time
	Average pre-work waiting time
	Average working time
	Average after work waiting time
	Average anchorage waiting time

The layout of a container terminal is an influential factor in the productivity of the container handling operations and proposes ways to define which layout type and what sized blocks should be used for a given size of a yard. These decisions about the layout will affect the throughput rate of the ship operation and the delivery and receiving operation as well as the storage capacity of the container yard [12]. Some of these indicators related to layout are the travel time of internal trucks, the area allocated for the container yard, the width of a container block, the average number of containers stacked in the yard, the available ground space for stacking containers, the expected round-trip travel distance of road trucks between the gate and a random position in the yard and berth [12].

5. OPTIMAL CONTAINER LAYOUT PLAN AND TERMINAL PERFORMANCE

Container layout plan is developed in a way that will provide the least transportation of container in the terminal and will not affect other operations. That is, it is aimed to minimize transport of containers in the terminal area.

Containers are located at the storage yard according to their types. Transshipment containers and export containers are stacked close to the quays where ships are berthed. Thus, fuel loss and waste of time would not be happened and containers reach vessels faster and in a short haul. Contrary to this, import containers are stored close to the terminal gates and away from quayside in order not to affect ship traffic. This makes faster gate out process possible. Except for full containers, empty containers are also stored at the terminals as well. Empty containers mostly stay more than full containers at the ports. Generally, they are stacked at the behind or sides of the container yard and away from general storage and active operation areas. In addition to this, empty containers are close to CFS areas where cargoes are stuffed into.

There are different types of yard cranes used in container terminals. Types and specifications of yard cranes have an important influence on the efficiency of storage yard usage and layout. Different yard cranes need different space requirements for an efficient operations. Thus, storage yard layout is developed according to yard cranes' specifications.

Another important factor effecting terminal efficiency is traffic scheme in the port. Outside transportation systems which bring export containers to the terminal and deliver import containers from the terminal affect landside and quayside operations in a negative way. Different operation processes, such as buffer zone, might be designed in busy ports in order to avoid congestion of outside trucks at the storage yard. Buffer zones are places where containers are waited to deliver importers or receive from exporters. However, this might increase the operational costs.

Factors related to terminal layout are among the most important factors affecting terminal performance. Some of the important operational indicators which are directly related to container terminal layout are listed below:

- Round trip time of internal trucks
- Round trip travel distance between the gate and the yard
- Round trip travel distance between the yard and berth

- Shifting time of a container in the yard
- Travel time of outside trucks in the port
- The area of the container yard
- Dimensions of the container block
- Dimensions of the container yard
- Length and width of roads in the terminal
- Number of containers stacked in the yard
- Number of ground slots in a container yard
- Specifications of yard crane
- Number of rows, bays, tiers in the container block

6. CONCLUSIONS

Container terminals are dynamic systems where many operations are carried out simultaneously. Besides, each terminal has different handling equipment and its own characteristics. Therefore, factors affecting efficiency at terminals are different from each other. Although there are many performance indicators in order to measure efficiency in the literature, there is not a standard performance measurement method for a terminal.

Performance indicators which are used to measure terminal efficiency are mostly related to terminal layout. Therefore, terminal layout plan must be developed by taking account of terminal efficiency. The aim of the layout planning is to design a terminal which minimizes the circle and transport of containers in the terminal area.

REFERENCES

[1]. Merk, O., *The competitiveness of global port-cities: synthesis report.* 2013.
[2]. Rodrigue, J.-P., C. Comtois, and B. Slack. *The geography of transport systems*. 2013; Available from: http://people.hofstra.edu/geotrans/eng/ch4en/ch4menu.html.
[3]. Chen, C., W.-J. Hsu, and S.-Y. Huang. *Simulation and optimization of container yard operations: A survey*. in *Proceedings of International Conference on Port and Maritime R and D and Technology*. 2003.
[4]. Günther, H.-O. and K.-H. Kim, *Container terminals and terminal operations.* OR Spectrum, 2006. 28(4): p. 437-445.
[5]. Steenken, D., S. Voss, and R. Stahlbock, *Container terminal operation and operations research - a classification and literature review*. OR Spectrum, 2004. 26(1): p. 3-49.
[6]. Kulak, O., O. Polat, and H. Guenther, *Performance evaluation of container terminal operations.* IT Based Planning and Control of Seaport Container Terminals and Transport Systems, 2008.
[7]. UNCTAD, *Port Performance Indicators*. 1976, Geneva: United Nations Publication.
[8]. Tongzon, J.L., *Determinants of port performance and efficiency.* Transportation Research Part A: Policy and Practice, 1995. 29(3): p. 245-252.
[9]. de Langen, P., M. Nidjam, and M. van der Horst, *New indicators to measure port performance.* Journal of Maritime Research, 2007. 4(1): p. 23-36.
[10]. Iñigo, L.-A., et al., *Berth Management in Container Terminals: Quality of Service.* Journal of Shipping and Ocean Engineering, 2012. 2(6): p. 340.
[11]. El, M.M.A. and R.F.H. El, *Assessment of Alexandria Container Terminal Efficiency by Applying Performance Indicators.* Journal of Shipping and Ocean Engineering, 2012. 2(5).
[12]. Kim, K.H., Y.-M. Park, and M.-J. Jin, *An optimal layout of container yards.* OR Spectrum, 2007. 30(4): p. 675-695.

Port State Control Inspections in the Black Sea Region and its Effect on Maritime Safety

E.Gul Emecen Kara[1], Olgay Oksas[2]

Abstract

Port State Control is one of the most important ways to ensure maritime safety at the world seas. There are Regional Agreements on Port State Control which cover most of the world seas. The Black Sea MOU that is one of these regional agreements includes the Black Sea region and it aims to enhance maritime safety in the Black Sea region. In this study, the effectiveness of Black Sea MOU port state control inspections is investigated.

Keywords: *Maritime transport, port state control, regional MOU, Black Sea MOU, safety.*

1. INTRODUCTION

Maritime shipping has high risk on the environment and human health. Owing to its global character, environmental disasters resulting from shipping accidents affect the whole world nations. Therefore, international regulations have been introduced to reduce the risks in the maritime transport, provide safety of ships and the protection of the marine environment. In addition to Flag state control, Port State Control mechanism has been established to ensure maritime safety. Port State Control (PSC) is defined as "It is the inspection of foreign ships in national ports for the purpose of confirming that condition of the ship and its equipment comply with the requirements of international conventions and that the ship is manned and operated in compliance with applicable international laws" by IMO [1]. Regional agreements on PSC (Memorandum of Understanding on Port State Control- MOU) have been created in order to ensure effectiveness of inspections, effective monitoring and uniformity of inspections. At present there are nine regional PSC agreements in operations. Although these PSC regimes are same, there are differences in the applications such as target inspections rate of ships, assessment of performance of flag states and selecting priority flags and ships for inspection [2].

The Black Sea MOU that is one of these regional agreements includes the Black Sea region and it aims to enhance maritime safety in the Black Sea region. This study aims to investigate effectiveness of Black Sea MOU port state control inspections and discuss importance of port state control inspections on maritime safety in the Black Sea region.

2. THE BLACK SEA MOU

The Black sea MOU was signed in 2000. Member Authorities are Bulgaria, Georgia, Romania, Russian Federation, Turkey and Ukraine. It aims to eliminate substandard ships and to decrease risks posed from maritime shipping in the Black Sea region. A Foreign- flagged ship visiting a seaport of Black sea is inspected with respect to the instruments relevant for the purposes of this Memorandum. These "relevant instruments", "which are together with the protocols and amendments to these instruments and related codes of mandatory status in force", are [3].

- The International Convention on Load Lines, 1966 (Load Lines 66);
- The International Convention for the Safety of Life at Sea, 1974 (SOLAS 74);
- The International Convention for the Prevention of Pollution from Ships,1973,as modified by the Protocol of 1978, (MARPOL 73/78);
- The International Convention on Standards of Training Certification and Watch keeping for Seafarers, 1978 (STCW 78);
- The Convention on the International Regulations for Preventing Collisions at Sea, 1972 (COLREG 72);
- The International Convention on Tonnage Measurement of Ships,1969(TONNAGE 69);
- The Merchant Shipping (Minimum Standards) Convention, 1976 (No. 147);
- The Maritime Labour Convention, 2006 (MLC, 2006);
- International Convention on the Control of Harmful Anti-fouling Systems on Ships, 2001;

[1] *Corresponding author: Istanbul University, Department of Maritime Transportation Management Engineering, 34320, Avcilar/İstanbul, Turkey.* emeceng@istanbul.edu.tr

[2] *Istanbul University, Department of Maritime Transportation Management Engineering, 34320, Avcilar/İstanbul, Turkey.* olgay.oksas@istanbul.edu.tr

- The International Convention on Civil Liability for Bunker Oil Pollution Damage, 2001 (BUNKERS 2001)

- Black Sea Mou Port State Control Inspections

Annual number of inspection is about 5000 in the Black Sea MOU. Table 1 shows number of inspection, percentage of detentions and percentage of inspection with deficiencies in the Black Sea MOU between 2005 and 2014. Number of detention is the highest value with 367 in 2007. It is seen that there is a decreasing in detention rates from 2005 to 2014. Average deficiencies percentage is 66% for this period. Deficiencies percentage is below 60% only in 2014.

Table 10. Number of inspections, percent of deficiencies and detention (2005-2014) [4]

Years	2005	2006	2007	2008	2009	2010	2011	2012	2013	2014
Number of Inspections	5069	4658	4499	5161	4805	4929	4657	4607	5080	5092
Number of Detentions	316	259	367	329	278	286	249	215	184	151
Deficiencies Percentage (%)	62,93	69,39	72,42	67,89	66,93	64,74	67,77	65,16	65,08	59,92
Detention Rate (%)	6,23	5,56	8,16	6,37	5,79	5,80	5,35	4,67	3,62	2,97

Table 2 shows inspection rates of member Authorities and regional inspection rate for the periods 2005-2014. These data are obtained from the annual reports which are found in the Black Sea MOU website [5]. Inspections rate is the ratio of the number of individual ships inspected to number of individual ship visits. Regional inspection rate in the Black Sea MOU has increased significantly since 2007. Average Regional inspection rate is approximately 65 % in the period 2008-2014. Number of inspections per country in the region has different values. Ukraine, Russia, Romania have the highest number of individual ship visits in 2014. Also, Russia and Ukraine have higher inspection rate than other member states of Black Sea MOUs. As the target, the Black Sea MOU Committee intends a regional annual inspection rate of 75% of the total number of individual ship visits in the region [3].

Table 2. Inspection rates of member Authorities and regional inspection rates (2005-2014).

Years	2005	2006	2007	2008	2009	2010	2011	2012	2013	2014
Bulgaria	27,67	31,23	39,53	62,03	32,67	31,30	35,20	39,42	33,64	31,76
Georgia	93,46	87,39	58,86	68,21	64,10	61,08	58,26	56,06	39,95	42,74
Romania	35,63	27,99	45,05	48,67	49,62	49,78	38,20	38,40	36,14	36,69
Russia	57,86	53,14	62,28	62,69	61,94	59,05	58,26	62,22	59,49	59,44
Turkey	23,39	23,34	32,97	26,92	29,18	25,48	26,40	43,25	34,36	38,36
Ukraine	31,64	27,49	26,25	45,39	19,54	29,51	43,21	28,85	54,65	56,58
Regional	36,16	38,11	41,37	68,45	58,60	62,74	69,88	61,92	63,62	69,41

Figure 1 shows average detention rates of flag states for the period 2012-2014. Tanzania, Moldova, Togo, Comoros and Cambodia are flags which have the five highest detention rate. In this figure, some flags are not shown, because their total number of inspection was less than thirty in this period. Ukraine has the highest detention rate in among the Black sea MOU members.

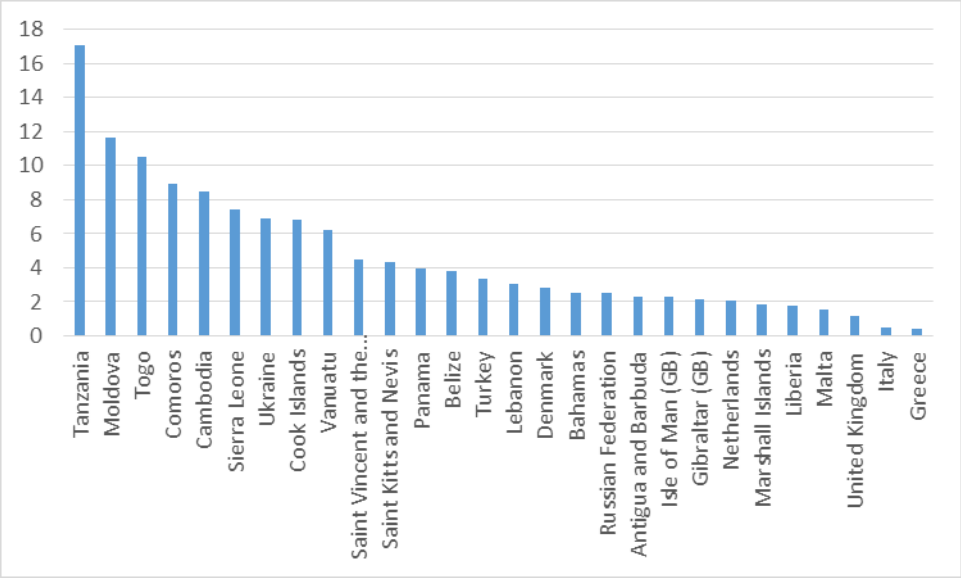

Figure 1. Average detention rates of flags for the period 2012-2014 (%).

Table 3 shows average detention rate and average % of inspections with deficiencies by ship type for the period 2012-2014. While Special Purpose Ship, Ro-Ro Passenger Ship, Livestock Carrier and General Cargo/Multi-Purpose Ship have high detention rate, Chemical Tanker and Oil tanker have low detention rates for this period.

Table 3. Average detention rate and average %of inspections with deficiencies by ship type (2012-2014) [4].

Ship Type	Average Detention %	Average %of Inspections with Deficiencies
Bulk Carrier	2	51,7
Chemical Tanker	0,9	51
Container Ship	3,50	62,5
Gas Carrier	1,4	63,2
General Cargo/Multi-Purpose Ship	6,3	77,9
Heavy Load Carrier	4,4	72,6
Livestock Carrier	8,8	95,6
MODU and FPSO	2,6	94,7
Oil Tanker	0,7	43,4
Passenger Ship	3	59,6
Refrigerated Cargo Carrier	2,8	58,9
Ro-Ro Cargo Ship	8,1	84,4
Ro-Ro Passenger Ship	8,8	76,1
Special Purpose Ship	10,2	72,9

Detected deficiencies per category for the period 2012-2014 are given in Table 4. These deficiency categories are determined using inspections data of 2012-2014. The categories with the greatest percentage of deficiency are Safety of navigation and Lifesaving appliances, Living and working conditions and Certificate and Documentation and Fire safety in Black Sea MOU. Living and Working conditions that comprise subgroups of Living Conditions and Working Conditions have 13,61 % deficiency percentage. About 11 % of these deficiencies belong to Working Conditions. Certificate and Documentation comprises subgroups of ship certificate, crew certificate and documents. Pollution Prevention- MARPOL which includes 6 Annexes has about 3% deficiency percentage. Annex I is regulations for the prevention pollution by oil, Annex II is about control of pollution by noxious liquid substance in bulk, Annex III is about pollution by harmful substances carried by sea in packaged form, Annex IV is about pollution by sewage from ship, Annex V is for pollution by garbage from ship and Annex VI is about air pollutant from ships [6]. Annex I and Annex V have the highest deficiency values among MARPOL Annexes.

Table 4. Categories of deficiency (2012-2014).

Categories of Deficiency	%	%
• Safety of Navigation		17,28
• Life Saving Appliances		13,64
• Living and Working Conditions		
- Living Conditions	2,30	
- Working Conditions	11,31	13,61
• Certificate and Documentation		
- Ship Certificates	5,27	
- Crew Certificates	1,55	13,58
- Documents	6,76	
• Fire Safety		9,08
• Radio Communications		5,28
• Propulsion and Auxiliary Machinery		4,78
• Labour Conditions		4,48
• Emergency Systems		4,34
• Water/Weathertight Conditions		4,07
• Structural Conditions		3,71
• Pollution Prevention - MARPOL		
- Annex I	1,45	
- Annex II	0,06	
- Annex III	0,03	
- Annex IV	0,37	3,26
- Annex V	1,08	
- Annex VI	0,28	
• ISM		2,60
• Alarms		0,41
• Cargo Operations Including Equipment		0,34
• Dangerous Goods		0,22
• Pollution Prevention - Anti Fouling		0,02
• Other		0,74

5. CONCLUSIONS

Annual number of inspection is about 5000 in the Black Sea MOU and average deficiencies percentage is 66% for the period 2005-2014. A decreasing in detention rates is shown from 2005 to 2014. This indicates that Black Sea PSC inspections have been successful in raising standard of ships visiting the Black sea Region. Inspection rates of member Authorities are different from each other. They are varied between 30 % and 60% for this periods. Russia and Ukraine have higher inspection rate. Average Regional inspection rate has increased since 2008 and it reached about 70 % in 2014.

Safety of navigation, Lifesaving appliances and Fire safety are the deficiency categories with the greatest percentage for the period 2012-2014. Tanzania, Moldova, Togo, Comoros and Cambodia are flags which have the five highest detention rate. Special Purpose Ship, Ro-Ro Passenger Ship, Livestock Carrier and General Cargo/Multi-Purpose Ship are ship types which have high detention rate.

Black sea MOU PSC inspections are very important for maritime safety of Black Sea region. These inspections help to provide that substandard ships visiting the Black Sea ports are eliminated, thus a pollution risk decrease and a healthy and safe environment is provided. Black Sea PSC inspections may be evaluated as successful in reducing the risk arising from maritime shipping. The effectiveness of Black Sea MOU port state control inspections has increased over time. If the effectiveness of port state control inspections improves more, the marine environment of Black sea would be safer.

REFERENCES

[1]. International Maritime Organization (IMO), Available online: http://www.imo.org/ (accessed on 12 September 2015).
[2]. Emecen Kara, E.G.; Okşaş, O., Evaluation of Maritime Safety in Istanbul Strait using Port State Control Inspections. International Conference on Engineering and Natural Sciences (ICENS), Skopje, Macedonia, 15 May - 19 June 2015.
[3]. Black Sea MOU, Available online: http://www.bsmou.org/about/ (accessed on 7 March 2016).
[4]. Black Sea MOU, 2014 Annual Report. Available online: http://www.bsmou.org/ (accessed on 11 February 2016).
[5]. Black Sea MOU, Annual Reports. Available online: http://www.bsmou.org/ (accessed on 8 February 2016).
[6]. International Maritime Organization (IMO), International Convention for the prevention of Pollution from ships (MARPOL) Available online: http://www.imo.org/en/About/Conventions(accessed on 1 February 2016).

Modbus Industrial Protocol Based Diesel Generator Set Controller Design and Evaluations on Power Generation Performances

Metin Varan[1], *Motuma Abafogi*[2]

Abstract

Diesel generators are prominent for their high reliability and low use of fuel which makes them largely applicable to industries. They are also used as standby power supplies in case of sudden interruption thus aiding in the continuation of manufacturing operations. A generator set (genset) controller allows the user to monitor and control the proper functioning of these generators. Some of the existing genset controllers provide functionalities such as remote starting and stopping of the engine, reading the generator's power measurements, modifying adjustable parameters and many more. Nowadays, MODBUS/TCP has become one of the most widely used network protocol in industrial applications for establishing connections amongst products such as PLCs, I/O devices etc. Its ability to run over nearly all communication media makes the establishment of MODBUS/TCP connection on an existing or new industrial floor quite easy. In this paper, a generator set controller has been designed for monitoring and controlling of diesel generators. Different generator parameters of two diesel generators have been acquired in real time and proper control measures is taken accordingly. Qt C++ software is employed in the design of an interactive user interface that works efficiently with the established MODBUS/TCP protocol connection. By using a data acquisition system, evaluations on electricity power generation performances have been discussed in respect of principles of designed genset controller.

Keywords: *Diesel generator, Real-time control, Generator Set Controller, Modbus, Qt*

1. INTRODUCTION

Diesel generators mainly constitute a diesel engine combined with electric generators while as a set they comprise additional auxiliary devices such as control systems and circuit breakers and usually referred to as generating sets or gensets. Various industries utilize diesel generators as main or backup sources of power [1]. Currently, the need for a proper power system management has gotten more attention thus leading to the development of different kinds of control and monitory systems. Generator set controllers providing numerous functionalities have been developed and hence the user is able to remotely control the operations of these generators.

2. MODBUS TCP PROTOCOL

A modbus protocol is a widely used industrial protocol that controllers use to communicate with one another regardless of the communication networks over which they communicate. It has its own message sending and receiving frame format including error detection mechanisms. All modbus protocol enabled devices use a similar format for their message fields. The four types of data utilized in a modbus protocol are Coil, Input Status, Input Register and Holding Register.[2][3]

In the Modbus protocol, a Protocol Data Unit (PDU) which constitutes the function type and the main data is explicitly defined regardless of the underlying communication layer. However, some buses or networks can include extra fields on the Application Data Unit (ADU).

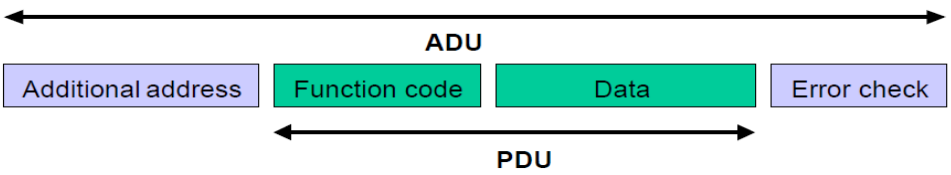

Figure 1: A general Modbus Frame [2]

[1] *Corresponding author: Asst. Prof. Dr., Sakarya Univ. Faculty of Technology - Department of Electrical and Electronics Engineering., mvaran@sakarya.edu.tr*

[2] *Sakarya Univ. Institute of Science - Department of Electrical and Electronics Engineering, motuma@gmail.com*

During the delivery of the message over MODBUS TCP/IP network the representation looks like the following figure 2. A dedicated MBAP (MODBUS Application Protocol) header is used on TCP/IP to identify the MODBUS Application Data Unit.

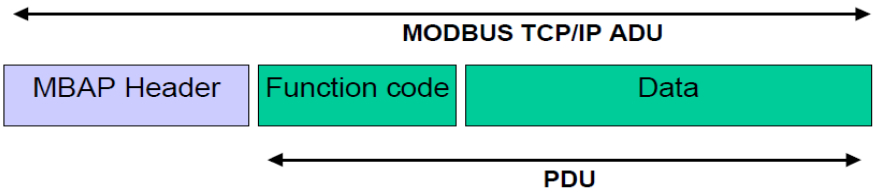

Figure 2: MODBUS request/response over TCP/IP [2]

3. PARALLEL SYNCHRONIZATION OF DIESEL GENERATORS

Diesel generator set control systems use an intelligent control system resulting in a great improvement in the operation of diesel generators. Parallel operation of generators is greatly applicable in a situation where the standard generators available are unable to meet the demands of a company. Generators having the same output rating and alternator pitch could be used to establish a parallel operation of generators. Generators of variable output could also be connected in parallel with paralleling switchgear to achieve the requirements at all times. [4][5]

Nowadays, it has become much simpler to operate generators in parallel by using generator set (genset) controllers to monitor and control the overall settings of a generator. It is very critical to synchronize the phase of each generator to that of the overall system. The figure 3 below illustrates the connection between diesel generators and control panels.

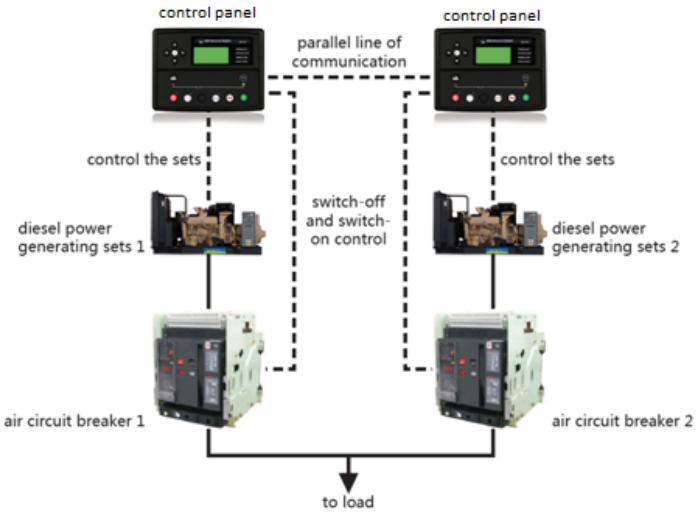

Figure 3: Composition of parallel connection control system [4]

4. MULTIPLE DIESEL GENERATOR CONTROL VIA MODBUS

Modbus TCP/IP is a robust protocol for creating a communication between electronic devices. Our first step in the design of the diesel generator controller is to create a virtual slave/server program employing the modbus TCP protocol that emulates actual control panels and implement all operations such as read/write registers by connecting our Master/Client program to it as shown in figure 4.

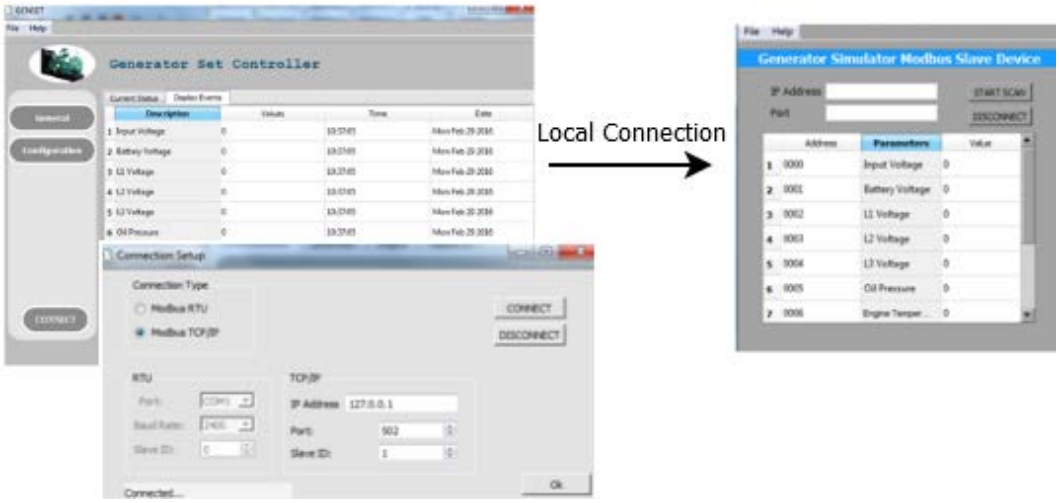

Figure 4: Modbus TCP/IP connection emulation of client and server

The figure 5 below describes the Ethernet connection between two generator control panels and our Modbus TCP/IP generator panel control and synchronization program designed using Qt C++. We have obtained real-time status of the operating generators such as engine speed, fuel level, oil temperature, L-N voltages etc from the generators via the modbus TCP connection between our program and the control panel and are able to maintain control of the generators remotely.

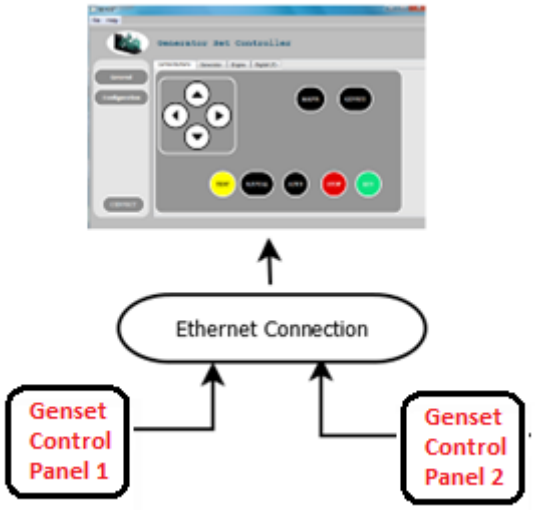

Figure 5: Modbus connection over Ethernet between our controller program and generator control panels

5. MODBUS/TCP CLIENT AND SERVER IMPLEMENTATION

Using MQX™ RTOS application development for real-time systems a MODBUS/TCP client/server is implemented on the Freescale Kinetis K-Series Processor (K-60). MQX contains core system components such as RTCS network stack, MFS files system and USB host/device drivers which could be integrated to any project as software libraries.

The MQX software libraries include [6][7][8][9]:

- RTCS network stack
- Shell interface library
- USB (Host and Device) drivers
- MS-DOS File System Library (MFS)

CodeWarrior development studio is an integrated development environment (IDE) that provides a highly visual and automated framework to accelerate development of the most complex embedded applications. [10][11][12] CodeWarrior version 10.6 is used to program the MODBUS/TCP client server application onto the K-60 processor.

The Real-Time TCP/IP Communication Suite (RTCS) is an embedded Ethernet stack optimized to run on MQX RTOS which constitutes different protocols to support applications like HTTP, Telnet, FTP and DHCP. Figure below shows different layers and protocols employed in the RTCS.

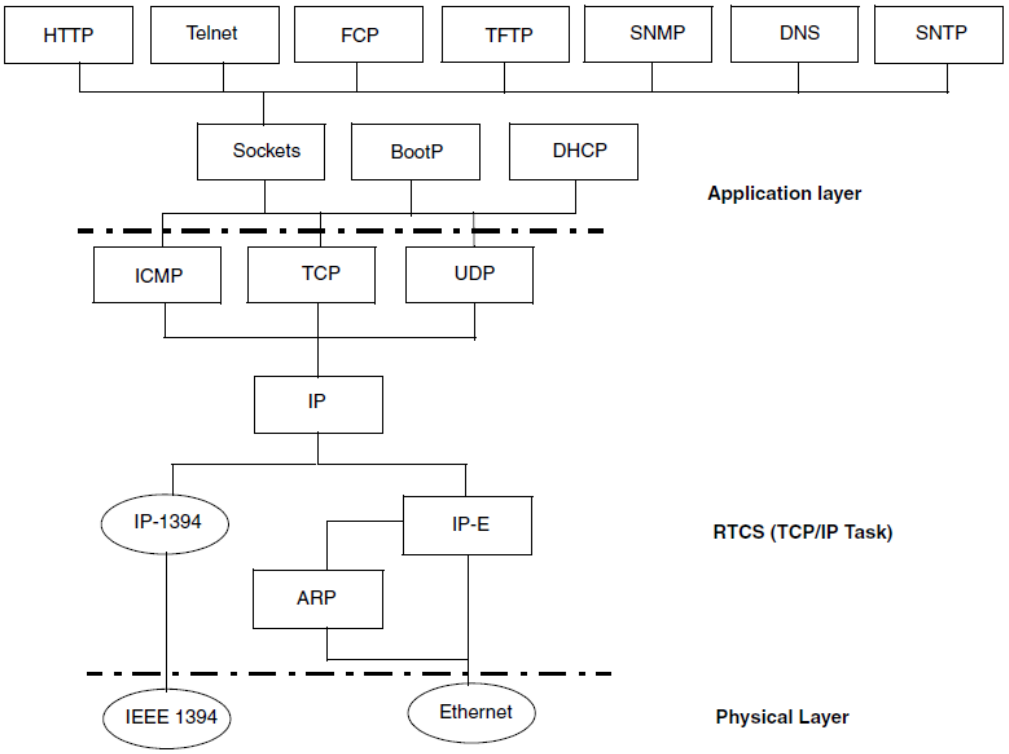

Figure 6: RTCS layers and protocols [6]

6. MODBUS/TCP Client Implementation on MQX

A basic MODBUS/ TCP client is implemented as follows [6][13][14]:

Step 1: Create an unbound socket using the socket() function.

Step 2: Assign a local socket address to a socket using the bind() function.

Step 3: Establish a TCP connection to a port (usually 502) at the desired server using connect()

Step 4: Prepare a MODBUS request including its 6-byte MODBUS/TCP prefix, as a single buffer to be transmitted using send().

Step 5: Wait for a response to appear on the same TCP connection. Run a timeout using select().

Step 6: Use recv() function to read the incoming bytes of the response.

Step 7: Shutdown the TCP connection if no further communication is expected to this particular target.

7. MODBUS/TCP Server Implementation on MQX

A MODBUS/TCP server application has to support multiple concurrent clients. A basic MODBUS/ TCP Server is implemented as follows [6][13]:

Step 1: Create an unbound socket using the socket() function.

Step 2: Assign a local socket address to a socket using the bind() function.

Step 3: Use listen() function to wait for incoming connections on a TCP port (usually 502).

Step 4: Use accept() function to handle the connection

Step 5: Do the following in an infinite loop:

Use a recv() function to read incoming bytes.

Generate the MODBUS/TCP prefix for the response.

Submit the response using send() including the MODBUS/TCP prefix, as a single buffer for transmission on the connection,

Wait for the next incoming message.

If the client terminates the connection, close the connection and cancel the current thread.

Either a multithreaded or single-threaded model could be employed to handle the multiple connections.

Figure 7 below illustrates the way data is exchanged between a client and server.

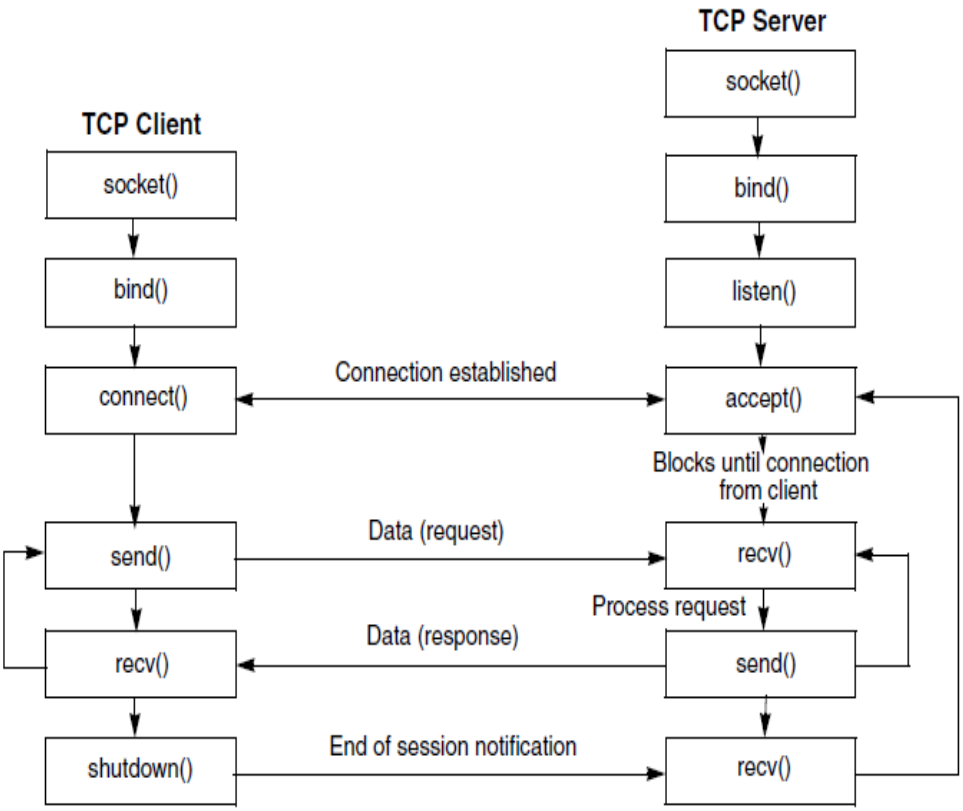

Figure 7: MODBUS/TCP Client Server Implementation [6]

8. CONCLUSION

Modbus TCP/IP is an industry standard communications protocol implemented over an industrial Ethernet-TCP/IP network. Paralleling of generators is achieved by synchronizing the electrical inputs by matching the output-voltage waveform of one system to another. We are able to remotely control and monitor the genset control panels via our program thus controlling the operation of diesel generators in real-time.

We have developed a genset driver card using the K-60 Freescale kinetis processor that utilizes the modbus TCP/IP protocol which independently controls and synchronizes the operation of diesel generators. CodeWarrior version 10.6 is used to implement the server/client applications. This genset controller operates as both MODBUS/TCP client and server. We can remotely monitor and obtain information regarding the status of generators from our genset controller driver card using the application software designed using Qt C++ software.

ACKNOWLEDGMENT

This work is supported in part by the Scientific Research Support Program Fund in Sakarya University with grant-number: 2014-50-01-041 (http://www.eee.sakarya.edu.tr/ tr/arastirma projeleri.)

REFERENCES

[1]. Kiran Daware (2012) http://www.electricaleasy.com/2015/10/diesel-power-generator-and-power-plant.html
[2]. www.modbus.org/ ,"MODBUS Messaging on TCP/IP Implementation Guide V1.0b", October 24, 2006.
[3]. Technical Reference, "Introduction to Modbus TCP/IP" , ACROMAG INCORPORATED, 2005.
[4]. http://www.aksapowergen.com/pdf/other/Parallel+Generators+Synchronization.pdf
[5]. Uzma Amin, Ghulam Ahmad, Sumbal Zahoor, Fariha Durrani, "Implementation of Parallel Synchronization Method of Generators for Power & Cost Saving in University of Gujrat", Energy and Power Engineering, 2014, 6, 317-332.
[6]. Antonio Ramos, Luis Garabito, "Using MQX Libraries", 2009.
[7]. Michal Princ, "Implementing an IEEE 1588 V2 Node on the Kinetis K60 Usingthe Freescale MQX IEEE 1588 Communication Library", 2011.
[8]. Carlos Musich, Alí Piña, and Carlos Casillas, Remote Monitoring Solution Using MQX and Kinetis", 2013.
[9]. Freescale MQX™ RTOS User's Guide, Rev. 14, 04/2015.
[10]. Freescale, "Processor Expert User Guide", 2014.
[11]. "CodeWarrior Development Studio for Microcontrollers V10.x Targeting Manual", 2014.
[12]. Freescale Semiconductor," K60 Sub-Family Data Sheet", 2011.
[13]. Andy Swales, "Open MODBUS /TCP Specification", Schneider Electric, March 1999.
[14]. Freescale Semiconductor,"Getting Started with Freescale MQX™ RTOS", 2011.

Effects of Topological Structure on the Synchronized Oscillatory Waves from Internal Dynamics in Thalamic Networks

Ramazan Tekin[1], Mehmet Emin Tagluk[2]

Abstract

Brain generates electrical waveforms, which characterizes different condition and behaviors. The structure and intra-harmony of simultaneously emergence of these characteristic waves in various regions of brain are entirely linked to brain functions. It has been reported that, in case of the characteristic structure and/or the harmony would detonate, it would lead to some abnormal conditions such as neurologic and neurophysiologic disorders. It is thought that, the source of various waves emerged in the brain mainly bases on the talamus and thalamocortical localities and the origination of rhythmic activities are depending upon the excitatory and inhibitory relationship between Thalamocortical Relay (TC) and thalamic reticular (RE) cells. In this study, an insulated thalamic network, which has internal rhythmicity, was developed using TC and RE cell models that appropriate to the electrophysiological reality. The main structure of this model bases on Small-World (SW) topology. The conversion of the rhythmicity that rely on the voltage-dependent calcium current into intra-thalamic synchronized waves and the impact of the topologic structure of SW on this phenomena was investigated. According to the obtained results, it was observed that the thalamic cells, which possess internal rhythmic activity in the shape of spikes without any external effects, are more synchronized at suitable SW rate values. In other words, a more phase synchronized rhythmic activities in the major parts of network were observed at suitable rate values of SW due to the mutual synaptic effect arising from inhibition and exhibition behavior of TC and RE cells. As a result of this phase synchronization, it is thought that comparatively more apparent and powerful waves are coming into view. According to this information, it may be considered that the various neurologic and neurophysiologic diseases may be linked to talamus and/or thalamocortical topologic structure depending to these abnormalities appeared in these waveforms.

Keywords: *Thalamus, rhythmicity, small-world networks, intra-thalamic waves*

1. INTRODUCTION

Depending on variety of sensorial excitations and internal processes involving some endogenous mechanisms, brain does generate spontaneous nonlinear complex spikes. This spontaneous spiking activity is not only due to a particular sensorial input, but also associated with synaptic interactions and electro-physiological properties of the neuron [1]. Generally, the high-frequency rhythmic oscillations are considered to occur in localized neuronal groups, while low-frequency rhythmic oscillations occur in comparatively large scale neural networks or zones [2,3]. However, the studies conducted in this direction have shown that the topological structure of the neuronal sector has a role in the generation of these oscillatory waves with various frequency components [4]. The interactions between these rhythmic activities and of course influence of many environmental factors lead to many vital biological functions to operate in a normal manner. Therefore the annihilation of such rhythmic events can cause to arise a range of pathologic conditions.

The cortex and thalamus EEG records show that rhythmic events or oscillations emerging during wakefulness or sleep are quite different. [1]. Depending on the condition and behavioral state of organism, this oscillations can involve various superimposed patterns, in the format of oscillatory waves in multiple frequency bands. The EEG recordings measured during sleep consists of spatiotemporal coherent waves with high amplitude and low frequencies. The EEG recordings measured during wakefulness, attention or REM sleep, show temporally and spatially less coherent waves with low-amplitude and high spatiotemporal complexity [5]. Therefore the same neuronal network may have different oscillatory patterns under different circumstances. The oscillation occurs due to interact with each other various types of endogenous currents, synaptic activity and external factors [6]. The slow-wave-sleep rhythms, which is known to have a an important role in memory consolidation, are explained with spindles, delta band and lower frequency rhythmic events [7].

This rhythms are considered to be due to the balance relationship between reciprocal excitatory-inhibitory thalamocortical relay (TC) cells and thalamic reticular (RE) cells as well as the endogenous characteristics of these cells in the thalamus. GABAergic RE cells, due to their relationships with each other and with TC cells operate as a pacemaker. On the contrary, TC cells do not have collateral axonal relationship. The rhythmic activity in these cells are considered to form through intrinsic

[1] *Corresponding author: Batman University, Department of Computer Engineering, 72060, Batman, Turkey. ramazan.tekin@batman.edu.tr*

[2]*Inonu University, Department of Electrical and Electronics Engineering, 44280, Malatya, Turkey. mehmet.tagluk@inonu.edu.tr*

characteristics of the cells and inhibitory post-synaptic potentials (IPSP) generated by GABAergic RE cells [8,9]. If the IPSP generated by RE cells can hyperpolarize TC cells sufficiently inactivation of low threshold Ca^{2+} spikes is eliminated and so cause these cells to fire rebound bursts [10]. This rebound burst activity transmitted to the cortex through thalamocortical projections of TC cells and reveal the spindle and similar rhythmic waves in the EEG signals [11].

Topological analysis of the mammalian cortex shows that, there are strong connections between neighboring regions, and fewer connections between distant regions [12,13]. This sort of anatomical connectivity based structure is appropriately modeled with small-world (SW) developed by Watts and Strogatz [14]. The analysis performed on magnetoencephalogrms (MEG), electroencephalograms (EEG) and magnetic resonance images (fMRI / MRI) showed that human brain exhibits patterns of connections between functional regions of the brain in the form of a shortcuts between different regions and clustered local connections similar to a small-world structure [15]. Accordingly, it can be said that aspects of the brain is to have complex functions developed with the lowest wiring cost. The emerged oscillatory waves are known to result from intrinsic characteristics and reciprocal interaction of the thalamic cells. It is important to understand the relationship between topological structure of neuronal system and this oscillatory waves, in terms of the normal brain functions. It is clear that experimentally investigation of such issues is very difficult. Therefore, usually computational methods are used to develop neuronal network models for revealing the relationship between the topological structure and mechanisms underlying these rhythmic oscillations. In this study a thalamic network model was developed. The model was designed to be close to biological reality and similar to anatomical structures as much as possible. In this network model, connections between neurons were restructured in accordance with the SW procedure. Thus, effects of SW topological structure on the spontaneously occurring rhythmic oscillations were investigated. According to the obtained results, it is understood that with appropriate SW rewiring probability (p) values, which is generated by intrinsic dynamics of thalamic cells, much more synchronized rhythmic activities and thereby stronger oscillations can occur.

2. MATERIALS AND METHODS

2.1 Computational models

Thalamus TC and RE cells are represented with single compartments holding Hodgkin-Huxley kinetics configured with voltage and calcium dependent channel currents [16]. Generally, cell models for TC an RE cells are represented as given in [17–20],

$$C_m \frac{dV_i}{dt} = g_L(V_i - E_L) - \sum_j I_{ji}^{ion} - \sum_k I_{ki}^{syn} \quad (1)$$

Where i is the neuron index, $C_m$is the membrane capacitance ($1\ \mu F/cm^2$ for each cell type), g_L is the leakage current conductivity ($g_L = 0.01\ mS/cm^2$ for TC cell, $g_L = 0.05\ mS/cm^2$for RE cell) and E_L is the leakage current reversal potential ($E_L = -70\ mV$ for TC cell and $E_L = -77\ mV$ for RE cell). I_{ji}^{ion} and I_{ki}^{syn} are internal ionic currents and the synaptic currents (between neuron k and neuron i), respectively. Ionic currents, synaptic currents and other parameters necessary for the model of TC and RE cells are selected based on studies carried out by Destexhe et al. [19,20] and Bazhenov et al. [17,18,21]. For the kinetic models of synaptic currents we used the models developed through a series of studies conducted by Destexhe et al. [20,22–24].

The sum of intrinsic and synaptic currents for a TC cell model are respectively given as,

$$\sum_j I_j^{ion} = I_{Na} + I_K + I_{KL} + I_T + I_h + I_A \quad (2)$$

and

$$\sum_k I_k^{syn} = I_{GABA_A}^{RE} + I_{GABA_B}^{RE} \quad (3)$$

$I_{GABA_A}^{RE}$ and $I_{GABA_B}^{RE}$ represent synaptic currents flowing between RE-TC $GABA_A$and RE-TC $GABA_B$synaptic current, respectively.

The sum of intrinsic and synaptic currents for RE cell model are respectively given as,

$$\sum_j I_j^{ion} = I_{Na} + I_K + I_{KL} + I_{Ts} \quad (4)$$

and

$$\sum_k I_k^{syn} = I_{AMPA}^{TC} + I_{GABA_A}^{RE} \quad (5)$$

$I_{GABA_A}^{RE}$ and I_{AMPA}^{TC} represent the synaptic currents flowing between RE-RE $GABA_A$ and TC-RE $AMPA$ synaptic current, respectively.

2.2 Application and Geometry

In order to be consistent with the anatomical and morphological fundamentals $N_{TC} = 50$ and $N_{RE} = 50$ cells were used to in the thalamic network structure [18]. The synaptic receptors in the model used in this study were configured similar to the ones used in the network models reported in the Bazhenov's studies [17,18,21]. Accordingly, the connection domain ratio in the direction of the projection target cell (K, radius ratio) is limited to 5% for each cell type. For any given cell type and synaptic connection type, the cell to cell synaptic projections have a same length and equal synaptic conductivity. For example, each TC and RE cells used in the models, have an equal number ($2 * N_{RE} * 5/100$) of $GABA_A$ projections from RE cells.

In this study, the impact of the topological structure, which configured according to the principles of SW model, on rhythmic oscillation activities, was investigated. The investigation was done as considering isolated thalamus. For this purpose, thalamic network model has been designed in the form of regular lattice (radius $K = 5\%$). Then, according to the SW restructuring probability (p) current connection was restructured. The probability p has the values ranging from 0 to 1 and increasing with steps of 0.1. Here, 0.1 represents 10% of the existing connections, while 1 represents 100%. For all p probability values the simulations were performed for 20 seconds (with 0.1 ms steps). By gradually changing the topological structure of the network from regular lattice to irregular network structure, the relationship between the thalamic rhythm and the topological structure of the SW was investigated.

2.2 Analysis Methods

To determine a measure of synchronization of the thalamic network two different methods were used which are based on the voltage traces and the spike times, respectively. The voltage-based synchronization measure used here, (population-averaged potential) is based on the time-dependent voltage fluctuation activity [25,26]. The other method is based on spike times, which is proposed by Wang and Buzsáki [27]. This method is considered the normalized cross-correlation (CC) of spike creation time of the neurons in the network. The coherence between the activity of any two neurons in the network (i and j) is measured by the normalized cross-correlation between spike firing times determined based on zero time-delay in a certain time window ($\Delta t = \tau$) [27].

3 RESULTS AND DISCUSSION

In order to model the slow wave activity primarily a simple thalamic network, which has the spindle activity and containing two TC and two RE cells is formed, as shown in Figure 1(a). The burst spiking activity of inhibitor RE neurons creates IPSPs in TC cells. With motivation of these IPSPs if TC cells hyperpolarized enough it discharges rebound burst spikes. Thereby, the RE cells are stimulated and a subsequent RE-TC rebounds burst cycle of spindle oscillation occurs. As the zoomed graphs shown in Figure 1(b), are observed, it is seen that the TC cells did not produced any EPSPs versus the first few IPSPs produced by RE cells. In this model, h-current and potassium leakage current conductivity values for TC cells are different from each other, a heterogeneous structure is considered (Figure 1 (c)). As can be seen in Figure 1(b), the oscillation first starts at the point marked by one (1) and then transferred to RE cells by AMPA synaptic connections. Then, as shown in Figure 1(b), the oscillation at the point marked by two (2) is transmitted to TC2 cells by GABAergic synapses. After several consecutive burst cycles with (Ca^{2+}induced) the rise of h-current TC cells are depolarizes (ADP) and so oscillations stop out (Figure 1 (c)).

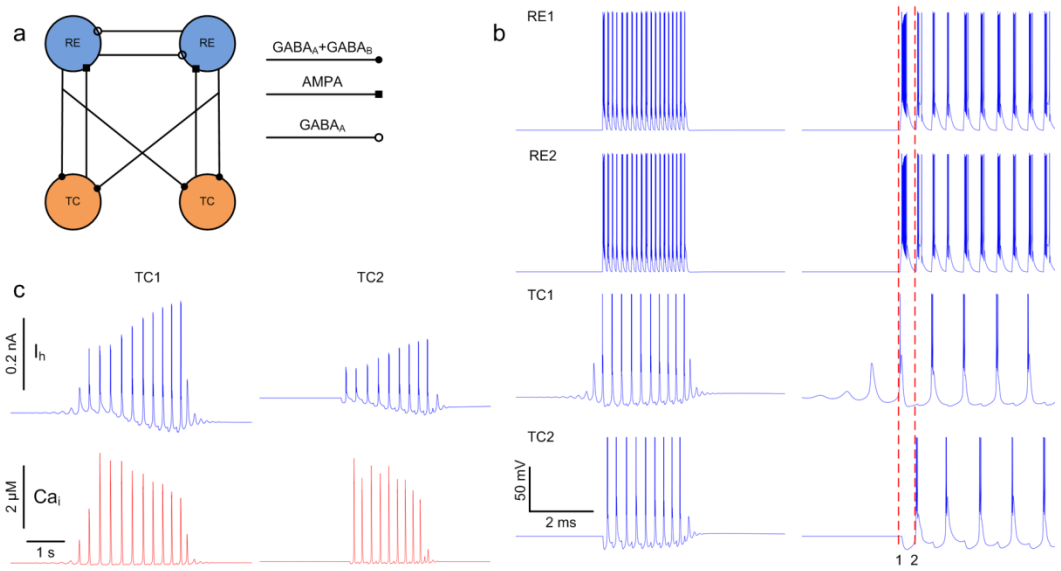

Figure 1. Close-up view of burst of rhythmic oscillations.

In a neuronal network the phase differences of independently emerged asynchronous rhythmic events can reduce and be more synchronized as the synaptic connections were harmonized [28]. This condition is in agreement with the high clustering characteristics of SW networks. In order to see the effect of small-world topological structure the isolated thalamic network model was expanded such that $N_{TC} = 50$ TC cells and $N_{RE} = 50$ RE cells. Because of that rhythmic oscillations in the isolated thalamic network arise spontaneously, we did not apply any external input to the TC and RE cells group. Thus, the effects of the topological structure of the SW on rhythmic spiking activity generated by the cells' intrinsic dynamics synchronization were identified. In order to have stable results, simulations were performed in the same initial conditions and analyzes were performed as excluding the first 5 seconds of simulations.

Figure 2 shows raster and voltages graphics of spiking activity of thalamic TC and RE cells in groups for different probability values of p (0.0, 0.3, 0.5 ve 0.9). In spite of using the same initial conditions, with different p values spiking activity of thalamic TC and RE cell groups became different. In addition, the spatial synchronization and temporal rhythmicity of these activities are also different from each other. As can be seen from the voltage traces shown in Figure 2(b) for a randomly selected TC and RE cells, all of cells have an intrinsic rhythmicity arising from rebounds bursts for all probability values of SW. However, as seen from raster graphics given in Figure 2(a) for $p = 0.0$ SW probability value there is not any synchronization between rhythmic activities of cells. With the increase of SW probability value, the independent intrinsic rhythmic activities begins to switch into a more synchronized and coherent activity. Thus, strong oscillations with significantly observable active-passive phases do occur.

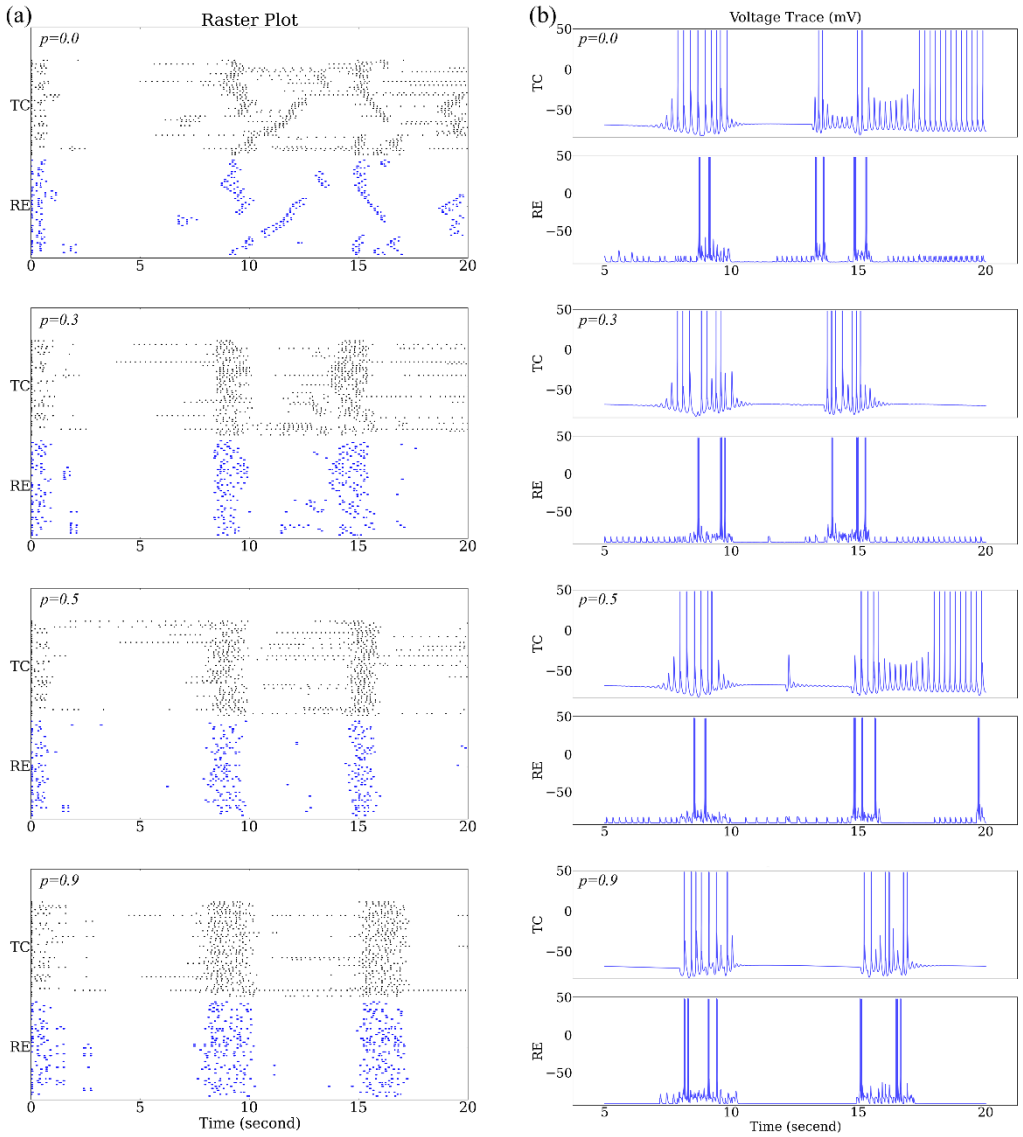

Figure 2. Raster graphics and voltage traces for different probability values SW.

In Figure 3, the variations in voltage dependent synchronization based on the variance of membrane potential and the spike coherence measured in compliance with spike times for different SW rewiring probabilities of thalamic network are illustrated. In order to gain robust results the data obtained through multiple experiments (10 experiments) were averaged. The changes in synchronization of TC and RE thalamic cells' groups are associated with changes of p. As p parameter has increased the degree of synchronization increased. . In the regular lattice structure of thalamic cells, both voltage dependent synchronization and spike coherence measures are quite low. Generally, the network synchronization can be said to be stable after $p = 0.4$. Through restructured connections according to the probability value of SW, it can be said that independent rhythmic activities generated by the internal dynamics becomes more synchronized.

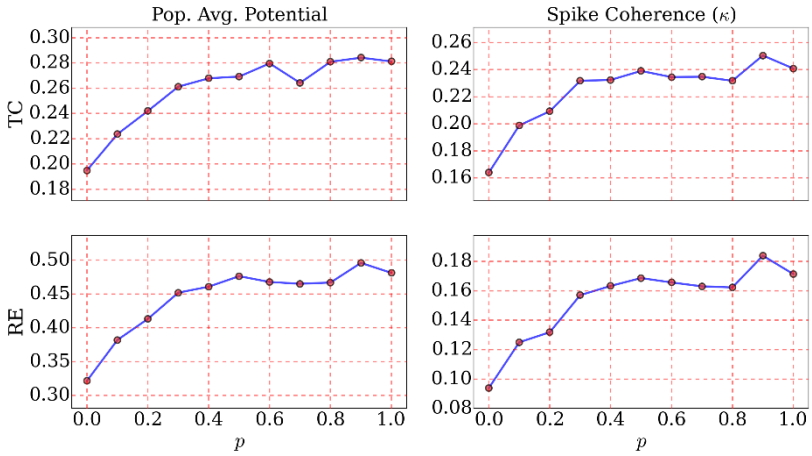

Figure 3. Voltage-dependent synchronization and spike coherence.

Thalamic TC and RE cells have the rebounds LTS spiking activities, caused by reciprocal EPSP and IPSP synaptic interaction between these cells groups. In the coherency of these endogenous rhythmic activities, subthreshold and/or suprathreshold PSP activities, or in other words, the balance of excitatory-inhibitory synaptic interactions have an important role. Accordingly, LTS spike activity, which is resulting from thalamic excitatory/inhibitory synaptic interactions between TC and RE cells, can be said to have a regulating role depending on the parameter p.

4 CONCLUSIONS

In this study, the relationship between SW topological structure and mechanism of formation of slow rhythmic oscillatory waves appearing during anesthesia and sleep in the thalamocortical system were investigated. With the transition to asleep state the arisen slow but strong synchronized oscillatory activities are believed to stabilize or make permanent the memory traces formed in the awake state [29]. It is known that the spindles and similar waves in the thalamus may occur spontaneously even without any external influence [30]. This oscillations produced by internal dynamics of thalamic cells (especially TC cells) are gradually spread to the entire network [20]. In the study, it was observed that without any external inputs to the isolated thalamic network model, spontaneous spike activities are generated by thalamic cells in the network with intrinsic properties. The result which may be deduced from this study is that SW topological structure has important role in the emergence of rhythmic activities triggered by endogenous characteristics and strong wave-shaped oscillations induced by the excitatory-inhibitory synaptic interaction between thalamic cells as well as their spread throughout the network.

REFERENCES

[1]. Destexhe A, Contreras D. Neuronal computations with stochastic network states. Science. 2006;314: 85–90. doi:10.1126/science.1127241
[2]. Contreras D, Llinás R. Voltage-sensitive dye imaging of neocortical spatiotemporal dynamics to afferent activation frequency. J Neurosci. Soc Neuroscience; 2001;21: 9403–9413. Available: http://www.jneurosci.org/content/21/23/9403.short
[3]. Penttonen M, Buzsáki G. Natural logarithmic relationship between brain oscillators. Thalamus Relat Syst. Cambridge Univ Press; 2003;2: 145–152.
[4]. Csicsvari J, Jamieson B, Wise KD, Buzsáki G. Mechanisms of gamma oscillations in the hippocampus of the behaving rat. Neuron. 2003;37: 311–322. doi:10.1016/S0896-6273(02)01169-8
[5]. Destexhe A, Sejnowski TJ. Interactions Between Membrane Conductances Underlying Thalamocortical Slow-Wave Oscillations. Physiol Rev. 2003;83: 1401–1453. doi:10.1152/physrev.00012.2003
[6]. Timofeev I, Bazhenov M. Mechanisms and biological role of thalamocortical oscillations. Trends Chronobiol Res. 2005; 1–47.
[7]. Steriade M. Grouping of brain rhythms in corticothalamic systems. Neuroscience. Elsevier; 2006;137: 1087–1106.
[8]. Steriade M, Deschenes M. The thalamus as a neuronal oscillator. Brain Res Rev. Elsevier; 1984;8: 1–63.
[9]. Steriade M, Deschenes M, Domich L, Mulle C. Abolition of spindle oscillations in thalamic neurons disconnected from nucleus reticularis thalami. J Neurophysiol. Am Physiological Soc; 1985;54: 1473–1497.
[10]. Jahnsen H, Llinás R. Ionic basis for the electro-responsiveness and oscillatory properties of guinea-pig thalamic neurones in vitro. J Physiol. 1984;349: 227–247. doi:10.1113/jphysiol.1984.sp015154
[11]. Contreras D, Destexhe A, Sejnowski TJ, Steriade M. Spatiotemporal patterns of spindle oscillations in cortex and thalamus. J Neurosci. 1997;17: 1179–1196.
[12]. Young MP. Objective analysis of the topological organization of the primate cortical visual system. Nature. 1992;358: 152–155.
[13]. Young MP. The organization of neural systems in the primate cerebral cortex. Proc R Soc London B Biol Sci. The Royal Society; 1993;252: 13–18.
[14]. Watts DJ, Strogatz SH. Collective dynamics of “small-world”networks. Nature. Nature Publishing Group; 1998;393: 440–442.
[15]. Bassett DS, Bullmore E. Small-World Brain Networks. Neurosci. 2006;12: 512–523. doi:10.1177/1073858406293182
[16]. Hodgkin AL, Huxley AF. A quantitative description of membrane current and its application to conduction and excitation in nerve. J Physiol. Wiley-Blackwell; 1952;117: 500.

[17]. Bazhenov M, Timofeev I, Steriade M, Sejnowski TJ. Computational models of thalamocortical augmenting responses. J Neurosci. 1998;18: 6444–6465.
[18]. Bazhenov M, Timofeev I, Steriade M, Sejnowski TJ. Model of thalamocortical slow-wave sleep oscillations and transitions to activated States. J Neurosci. 2002;22: 8691–8704. doi:22/19/8691 [pii]
[19]. Destexhe A, Contreras D, Steriade M. Mechanisms underlying the synchronizing action of corticothalamic feedback through inhibition of thalamic relay cells. J Neurophysiol. 1998;79: 999–1016. Available: http://www.ncbi.nlm.nih.gov/entrez/query.fcgi?cmd=Retrieve&db=PubMed&dopt=Citation&list_uids=9463458
[20]. Destexhe A, Bal T, McCormick DA, Sejnowski TJ. Ionic mechanisms underlying synchronized oscillations and propagating waves in a model of ferret thalamic slices. J Neurophysiol. 1996;76: 2049–70. Available: http://www.ncbi.nlm.nih.gov/pubmed/8890314
[21]. Bazhenov M, Timofeev I, Steriade M, Sejnowski TJ. Cellular and network models for intrathalamic augmenting responses during 10-Hz stimulation. J Neurophysiol. 1998;79: 2730–2748.
[22]. Destexhe A, Mainen ZF, Sejnowski TJ. An Efficient Method for Computing Synaptic Conductances Based on a Kinetic Model of Receptor Binding. Neural Comput. 1994;6: 14–18. doi:10.1162/neco.1994.6.1.14
[23]. Destexhe A, Mainen ZF, Sejnowski TJ. Synthesis of models for excitable membranes, synaptic transmission and neuromodulation using a common kinetic formalism. J Comput Neurosci. 1994;1: 195–230. doi:10.1007/BF00961734
[24]. Destexhe A, Mainen ZF, Sejnowski TJ. Kinetic models of synaptic transmission. Methods neuronal Model. Citeseer; 1998;2: 1–25.
[25]. Brunel N, Hansel D. How noise affects the synchronization properties of recurrent networks of inhibitory neurons. Neural Comput. 2006;18: 1066–1110. doi:10.1162/neco.2006.18.5.1066
[26]. Guo DQ, Wang QY, Perc M. Complex synchronous behavior in interneuronal networks with delayed inhibitory and fast electrical synapses. Phys Rev E. 2012;85: 1–8. doi:Artn 061905\rDoi 10.1103/Physreve.85.061905
[27]. Wang XJ, Buzsáki G. Gamma oscillation by synaptic inhibition in a hippocampal interneuronal network model. J Neurosci. 1996;16: 6402–6413. doi:citeulike-article-id:134404
[28]. Wang XJ. Neurophysiological and computational principles of cortical rhythms in cognition. Physiol Rev. 2010;90: 1195–1268. doi:10.1152/physrev.00035.2008.
[29]. Steriade M. Impact of network activities on neuronal properties in corticothalamic systems. J Neurophysiol. 2001;86: 1–39.
[30]. Morison RS, Bassett DL. Electrical activity of the thalamus and basal ganglia in decorticate cats. J Neurophysiol. 1945;8: 309–314.

ICENS
INTERNATIONAL CONFERENCE ON ENGINEERING AND NATURAL SCIENCES
24-28 May 2016 /Sarajevo

First Order Integral Sliding Mode Control Of The Magnetically Levitated 4-Pole Type Hybrid Electromagnet

H.Fatih Ertugru*[1], Kadir Erkan[1]

Abstract

In this study, 4-pole type yoke hybrid electromagnet is modeled with respect to motion dynamics of the system. The hybrid electromagnet inherently has a non-linear characteristic and from the point view of controllability, it is unstable. This paper concerns the design of robust controller using first order integral sliding mode control method. Thus, the system becomes stable and robust against parametric uncertainties, nonlinearity, unmodeled uncertainties and external disturbance.

Magnetic levitation system includes sensors that only measure the air gap. In order to estimate other states of the system, the full order disturbance observer is designed and integrated into the control loop. The estimated disturbance value is factored by the appropriate conversion gain and added to the input signal of the plant. The efficiency of control algorithm will be given in the paper by computer simulations.

Keywords: *Magnetic levitation, Integral Sliding mode control, Disturbance observer.*

1. INTRODUCTION

The non-contant magnetic levitation systems can operate without mechanical problem such as vibration, noise, abrasion, friction and so on. They also meet high accuracy and precision specifications. Because of these advantages, they are used in passenger transport vehicles, vibration isolation systems, biomedical devices, wind turbine, space studies and clean rooms as a key technology [1, 2].

The U and E-shaped electromagnets are often used in magnetic levitation systems, but they have only one degree of freedom control.4-Pole type hybrid electromagnet, which proposed by Koseki et al, has 3 degree of freedom. Each pole includes a coil (to control the field intensity) and a laminate permanent magnet leading to hybrid structure as shown in Fig.1.

The hybrid electromagnet inherently has a non-linear characteristic and from the point view of controllability it is unstable. In order to run such a system, it is required to actively control the hybrid electromagnet in multi axes. Several approaches have been proposed in the literature to control 4-pole type hybrid electromagnet [1-3]. In this paper, a sliding mode based control algorithm is proposed.[1]

Conventional sliding mode control method does not guarantee robustness throughout the entire system. The control system response is sensitive against uncertainty during the reaching phase. After sliding mode occurs, the system response remains insensitive to variations of system parameters and external disturbance. By adding the integral component to sliding mode control, which is named integral sliding mode control (ISMC),the system response is became robust in both the reaching and sliding phase. In addition, ISMC can be used to eliminate the control chattering, which is the high-frequency vibrations (oscillations) of the control signal [4].

The performance of feedback control algorithm is associated with the measurement of the state variables of the system model. However, in practice, all the state variables are not measurable or the measurements of the state variables can be costly because of the high price of the sensors [5]. In order to obtain all state variables, the observer can be designed.

This paper is organized as follows. First, the mathematical model of the system is briefly derived. Then, integral sliding mode control and disturbance observer are introduced and designed using pole placement method. Finally simulation results verify the effectiveness of controller.

[1]*Corresponding author: Yildiz Technical University, Department of Mechatronics Engineering,, fatiher@yildiz.edu.tr*

[2] *Yildiz Technical University, Department of Mechatronics Engineering,, Beşiktaş/İstanbul, Turkey.kerkan@yildiz.edu.tr*

2. 4-POLE TYPE HYBRID ELECTROMAGNET

4-pole type hybrid electromagnet has three degrees of freedom of movement (along Z plus rotation around X and Y).

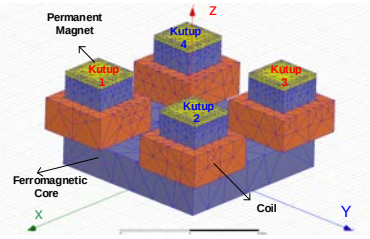

Figure 1. Basic structure of 4-pole hybrid electromagnet

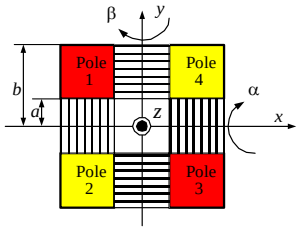

Figure 2. 4-pole hybrid electromagnet movement axis.

Independently control of each pole air gap is one of the way that can be followed to active control of the system. However, the implementation of this approach is difficult for controlling inclination axis motions and for compensating the unbalanced load. For this reason, system dynamics are developed independently using coordinate transformation. 4-Pole winding currents (i_1, i_2, i_3, i_4) are transformed virtual axis currents to provide control of each axis separately. Three virtual winding currents (i_z, i_α, i_β) are employed to control motion of vertical direction z, and inclinations α,β respectively.The relationships between virtual currents of the each degree of freedom and actual winding currents are represented by (Eq.1-2).

$$\begin{aligned} i_z &= \frac{1}{4}(i_1 + i_2 + i_3 + i_4) \\ i_\alpha &= \frac{1}{4}(-i_1 + i_2 + i_3 - i_4) \\ i_\beta &= \frac{1}{4}(-i_1 - i_2 + i_3 + i_4) \end{aligned} \qquad \begin{bmatrix} i_1 \\ i_2 \\ i_3 \\ i_4 \end{bmatrix} = \begin{bmatrix} 1 & -1 & -1 \\ 1 & 1 & -1 \\ 1 & 1 & 1 \\ 1 & -1 & 1 \end{bmatrix} * \begin{bmatrix} i_z \\ i_\alpha \\ i_\beta \end{bmatrix} \tag{1}$$

In considering figure-2, the axial displacements are subjected to the following conversion.

$$\begin{aligned} z &= \frac{1}{4}(z_1 + z_2 + z_3 + z_4) \\ \alpha &= \frac{1}{2b}\left(\frac{z_1 + z_4}{2} - \frac{z_2 + z_3}{2}\right) \\ \beta &= \frac{1}{2b}\left(\frac{z_1 + z_2}{2} - \frac{z_3 + z_4}{2}\right) \end{aligned} \qquad \begin{bmatrix} z \\ \alpha \\ \beta \end{bmatrix} = \frac{1}{4}\begin{bmatrix} 1 & 1 & 1 & 1 \\ 1/b & -1/b & -1/b & 1/b \\ 1/b & 1/b & -1/b & -1/b \end{bmatrix} * \begin{bmatrix} z_1 \\ z_2 \\ z_3 \\ z_4 \end{bmatrix} \tag{2}$$

Controller output signals are transformed to pole coil signals using H transformation matrix which is obtained from (Eq.1). Similarly, pole displacements are transformed to axial displacements using T transformation matrix which is obtained from (Eq.2). This axial transformation is shown in Fig. 3.

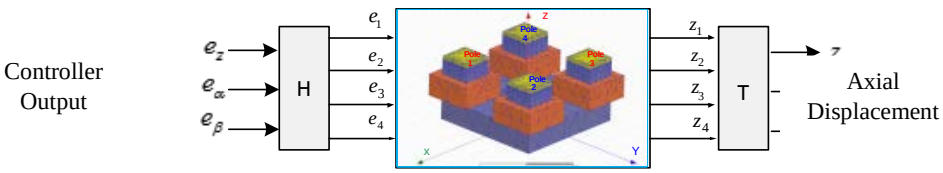

Figure 3. Axial transformation schematic.

The linearized mechanical system dynamics is given in below equation for z-axis motion [1-3].

$$Z(s) = \frac{K_B}{ms^2 - K_A} I_Z(s) - \frac{1}{ms^2 - K_A} F_d(s) \tag{3}$$

In the above equation, electrical input is the current form. In general, the voltage source is used to energize the coil of the magnetic levitation system.

$$I_Z(s) = \frac{1}{L_Z s - R_Z}\left[E_Z(s) - \frac{K_A L_Z}{K_B} sZ(s)\right] \tag{4}$$

The linearized system block diagram is shown in Figure 4(a) for z-axis motion. Changes are only encountered in the relevant parameters for inclination (α and β-axis) motion model (Figure 4(b)).

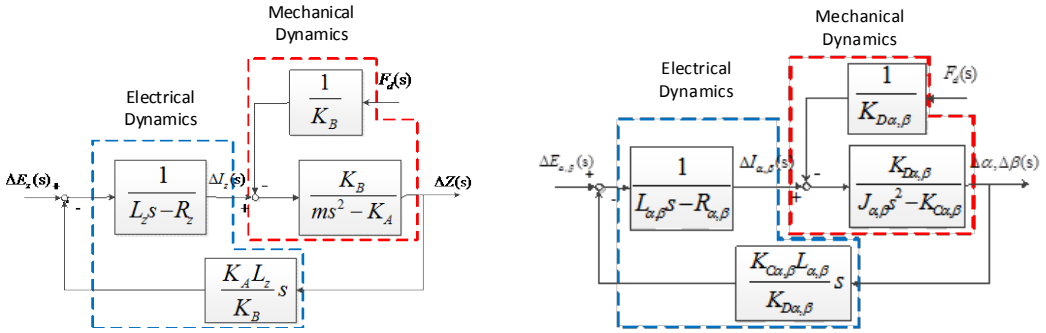

Figure 4. (a) System block diagram for z-axis motion. *(b) System block diagram for α, β axis motions.*

The state-space representation of the system is given in below.

$$\dot{x}(t) = Ax(t) + Bu(t) + EF_d(t) \tag{5}$$

$$\frac{d}{dt}\begin{bmatrix}\Delta z(t)\\ \Delta \dot{z}(t)\\ \Delta i_z(t)\end{bmatrix} = \begin{bmatrix}0 & 1 & 0\\ \frac{K_A}{m} & 0 & \frac{K_B}{m}\\ 0 & -\frac{K_A}{K_B} & -\frac{R_z}{L_z}\end{bmatrix}\begin{bmatrix}\Delta z(t)\\ \Delta \dot{z}(t)\\ \Delta i_z(t)\end{bmatrix} + \begin{bmatrix}0\\ 0\\ \frac{1}{L_z}\end{bmatrix}\Delta e_z(t) + \begin{bmatrix}0\\ -\frac{1}{m}\\ 0\end{bmatrix}F_d(t)$$

3. DISTURBANCE OBSERVER-BASED INTEGRAL SLIDING MODE CONTROL

5.1 Integral Sliding Mode Controller Design

Sliding mode control signal is separated two components to achieve asymptotic output tracking; one is linear component u_l, and the other is nonlinear component u_{nl}.

$$u = u_l + u_{nl} \tag{6}$$

u_l component of the control signal drive the sliding variable (σ) to zero in finite time. The sliding starts after the sliding variable reaches zero at time t_r. After that time point, $\sigma = \dot{\sigma} = 0$ is valid for all time [6].

The sliding surface can be defined as follows:

$$\sigma = Sx = \begin{bmatrix}S_1 & S_2\end{bmatrix}\begin{bmatrix}x_1\\ x_2\end{bmatrix} = 0 \qquad x_2 = \frac{-S_1}{S_2}x_1 \tag{7}$$

The sliding function is defined:

$$S = \begin{bmatrix}S_1\\ S_2\end{bmatrix} \qquad where\ k = S_2^{-1}S_1 \qquad S = \begin{bmatrix}S_2 k\\ S_2\end{bmatrix} = S_2\begin{bmatrix}k\\ 1\end{bmatrix} \tag{8}$$

The sliding function (S) is obtained with selecting (S_2) parameter and calculating k. The integral of the position error is added to eliminate the error at the steady-state. The extended steady-space equation decomposed as follows.

$$\frac{d}{dt}\begin{bmatrix}\int 0-\Delta z(t)dt\\ \Delta z(t)\\ \Delta \dot{z}(t)\\ \Delta i_z(t)\end{bmatrix}=\overset{A_{11}}{\overbrace{\begin{bmatrix}0 & -1 & 0\\ 0 & 0 & 1\\ 0 & \frac{K_A}{m} & 0\end{bmatrix}}}\ \overset{A_{12}}{\overbrace{\begin{bmatrix}0\\ 0\\ \frac{K_B}{m}\end{bmatrix}}}\ \overset{x_1}{\overbrace{\begin{bmatrix}\int 0-\Delta z(t)dt\\ \Delta z(t)\\ \Delta \dot{z}(t)\end{bmatrix}}}+\overset{B_1}{\overbrace{\begin{bmatrix}0\\ 0\\ 0\end{bmatrix}}}\Delta e_z(t)$$
$$\underset{A_{21}}{\underbrace{\begin{bmatrix}0 & 0 & -\frac{K_A}{K_B}\end{bmatrix}}}\ \underset{A_{22}}{\underbrace{\begin{bmatrix}-\frac{R_z}{L_z}\end{bmatrix}}}\ \underset{x_2}{\underbrace{\begin{bmatrix}\Delta i_z(t)\end{bmatrix}}}+\underset{B_2}{\underbrace{\begin{bmatrix}1\\ \frac{1}{L_z}\end{bmatrix}}} \qquad (9)$$

The (Eq.10) can be obtained from the (Eq.8) and (Eq.9) :

$$\begin{aligned}\dot{x}_1 &= A_{11}x_1 + A_{12}x_2 = (A_{11} - A_{12}S_2^{-1}S_1)x_1 \\ &= (A_{11} - A_{12}k)x_1 \qquad \text{where } k = S_2^{-1}S_1\end{aligned} \qquad (10)$$

Since (A_{11}, A_{12}) is controllable, pole placement method is used to select the gain k [7,8]. Kessler canonical form (KCF) approach is used to obtain the gain k . KCF is an effective method to find the coefficients of characteristics polynomial of the SISO system. The basic idea behind this approach is to determine proper and stable characteristic polynomial using stability index and equivalent time constant [10].The equivalent time constant specifies the output response speed while stability index determines robustness, stability and output response of the system against parameter changes.

The characteristic equation of the closed-loop control system is given as:

$$P(s) = a_3 s^3 + a_2 s^2 + a_1 s + a_0 \qquad (11)$$

Stability index (γ) and equivalent time constant (τ) can be described as follows:

$$\gamma_i = \frac{a_i^{\,2}}{a_{i+1}a_{i-1}} \quad (i = 1,2,3) \qquad \tau = \frac{a_1}{a_0} \qquad (12)$$

In 1960s, Kessler has proposed that values of the γi should be two. In 1980s, Manabe proposed small modification of making γ1=2.5 instead of 2 to obtain no overshoot condition.It is practically acceptable to take the equivalent time constant smaller than 0.1[s] in the magnetic levitation based system[1,2].

$$\frac{P_3(s)}{a_0} = \frac{a_3}{a_0}s^3 + \frac{a_2}{a_0}s^2 + \frac{a_1}{a_0}s + \frac{a_0}{a_0} = b_3 s^3 + b_2 s^2 + b_1 s + b_0$$

$$b_0 = 1 \qquad b_1 = \frac{a_1}{a_0} = \tau$$

$$\frac{b_1^2}{b_2 b_0} = \frac{\tau^2}{b_2} = \gamma_1 \qquad b_2 = \frac{\tau^2}{\gamma_1}$$

$$\frac{b_2^2}{b_3 b_1} = \gamma_2 \qquad b_3 = \frac{b_2^2}{b_1 \gamma_2} \qquad (13)$$

The characteristic equation is solved to obtain desired poles of the system. In this study, pole placement is performed with the following MATLAB command.

$$k = ac\ker(A_{11}, A_{12}, [\text{p1} \quad \text{p2} \quad \text{p3}]) \qquad (14)$$

Thus, the sliding function S is obtained from (Eq.14) and selecting S_2.

The linear component of control signal u_l can be calculated by:

$$\dot{\sigma} = S\dot{x} = S(Ax + Bu_l) = 0$$
$$u_l = -(SB)^{-1} SAx \tag{15}$$

The nonlinear component of control signal u_{nl} is selected as follows:

$$u_{nl} = -(SB)^{-1} \rho \operatorname{sgn}(\sigma) \text{ where } \rho \succ 0 \tag{16}$$

To show stability of system, a positive definite Lyapunov function is selected as [9]:

$$V = \frac{1}{2}\sigma^2 \tag{17}$$

The time derivative of Lyapunov function is negative definite:

$$\dot{V} = \sigma\dot{\sigma} = \sigma S(Ax + Bu)$$
$$= \sigma SAx + \sigma SB[-(SB)^{-1} SAx - (SB)^{-1} \rho \operatorname{sgn}(\sigma)] \quad \text{where } \sigma \neq 0 \tag{18}$$
$$= -\rho\sigma \operatorname{sgn}(\sigma) < 0$$

Hence, the system becomes asymptotically stable.

In nonlinear component of control signal u_{nl} contain signu*m* function which cause *chattering* problem *because of the discontinuity*. In practical case, the sigmoid function is used instead of signum function to eliminate chattering problem [6].

$$\operatorname{sgn}(\sigma) \approx \frac{\sigma}{|\sigma| + \varepsilon} \tag{19}$$

where ε is a small positive scalar. u_{nl} is commonly selected by:

$$u_{nl} = -\rho \operatorname{sgn}(\sigma) \approx -\rho \frac{\sigma}{|\sigma| + \varepsilon} \tag{20}$$

where ρ is a design parameter.

5.2 Disturbance Observer Based Design

Pole assignment is a basic design method for linear state feedback control system. In this method, it is assumed that all state variables are available for feedback. However, some state variables are not measurable directly or refrain from using of sensor because of noise occurring during the measurement. In order to estimate all state variables, the observer can be designed.

Disturbance force is added as a variable to obtain expanded system model (Eq.21). The disturbance force is generally step input in magnetic levitation system, so a zero line is added the system model. The expanded state equation is completely observable, thus observer can be designed. Figure 5 shows the block diagram of disturbance observer.

$$\frac{d}{dt}\begin{bmatrix} \Delta z(t) \\ \dot{\Delta z}(t) \\ \Delta i_z(t) \\ F_d \end{bmatrix} = \begin{bmatrix} 0 & 1 & 0 & 0 \\ \frac{K_A}{m} & 0 & \frac{K_B}{m} & -\frac{1}{m} \\ 0 & -\frac{K_A}{K_B} & -\frac{R_z}{L_z} & 0 \\ 0 & 0 & 0 & 0 \end{bmatrix} \begin{bmatrix} \Delta z(t) \\ \dot{\Delta z}(t) \\ \Delta i_z(t) \\ F_d \end{bmatrix} + \begin{bmatrix} 0 \\ 0 \\ \frac{1}{L_z} \\ 0 \end{bmatrix} \Delta e_z(t) \tag{21}$$

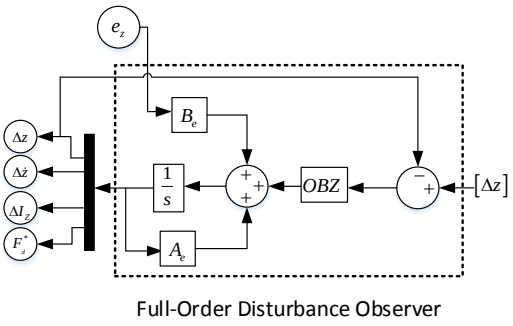

Figure 5. Full-Order Disturbance Observer Block Diagram.

Due to the separation principles, observer and controller can be designed independently of each other. The pole placement method is used to design full order disturbance observer similar to the controller design. Desired poles of the controllers and observers are decided by using Kessler's canonical form. However, the observer poles must be three to eight times faster than the controller poles to make sure the observation error converges to zero quickly [5].

Disturbance compensation gain is given as follows [2].

$$K_{Fd} = \frac{\Delta e_z(\infty)}{F_d} = \frac{R_z}{K_B} \tag{22}$$

Disturbance compensation gain is used to convert estimated force (N) into the control voltage (V). Figure 6 shows the Simulink model of the disturbance observer based integral sliding mode controller.

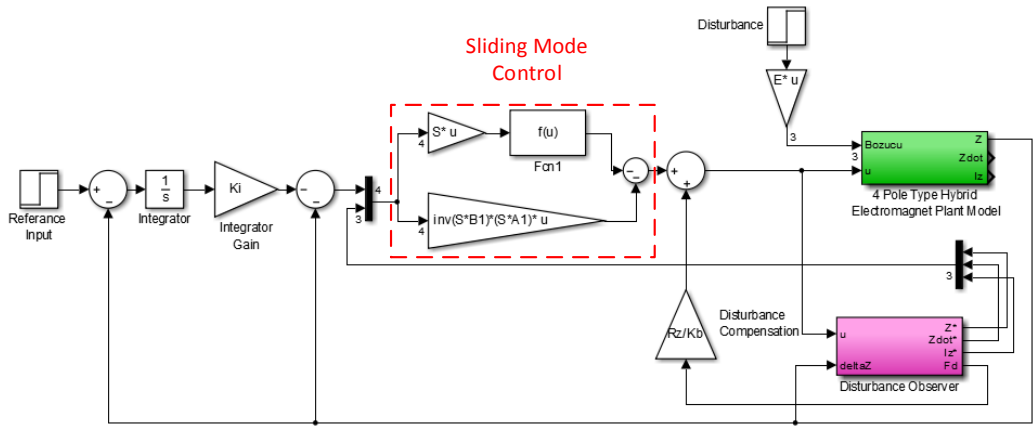

Figure 6. Simulink Model of the Control System

6. SIMULATION RESULTS AND EVALUATION

The effectiveness of integral sliding mode controller and disturbance observer, as discussed in the previous section, are shown using MATLAB environment. The simulation parameters for the 4-pole hybrid electromagnetic levitation system are shown in Table 1.

Table 11. System Parameters

Size / Unit	Value	Size / Unit	Value	Size / Unit	Value
m [kg]	10	z_0 [mm]	4.3	α_0, β_0[rad]	0.0
$J_{\alpha,\beta}$[kg.m^2]	0.3	i_{z0} [A]	0.0	$i_{\alpha 0}$, $i_{\beta 0}$ [A]	0.0
k [N^2/A^2]	6.84*10^{-6}	K_A[N/m]	20991	K_C[Nm/rad]	106.43
I_m [A]	13.44	K_B[N/m]	14.87	K_D [Nm/A]	3.13
$R_{z,\alpha,\beta}$ [Ω]	1.50	$L_{z,\alpha,\beta}$[H]	0.016	E_{pm} [AT]	2689

Figure 7-8 show z-axes position and control signal waveform when a reference input is applied at 0.5 sec. of simulation time and 1.5 kg mass loads to the 4 pole type hybrid electromagnet at 2 sec. In Figure 7, the system can track step reference input with zero steady-state error. The disturbance compensator does not have much effect on the system response. This result indicates that proposed controller is insensitive to disturbance input. In Figure 9-10, the results show that the sliding mode control approach is achieved not only for vertical axis but also for inclinations. The chattering occurs particularly as shown on the control signals when a reference input and disturbance are applied. ρ parameter in (Eq.20) is used to adjust chattering effect. The higher value of ρ causes the high frequency chattering. The actual and observed disturbance values are shown in Figure 11.

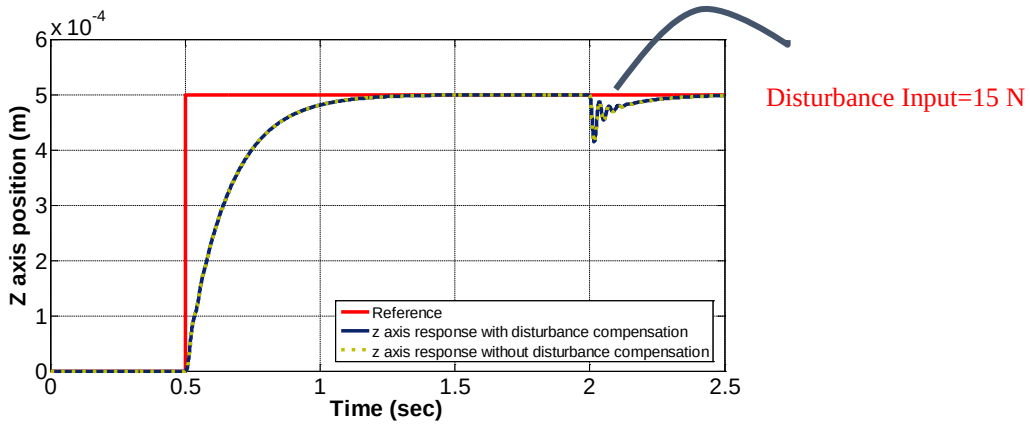

Figure 7. z-axis response for the step reference input and disturbance.

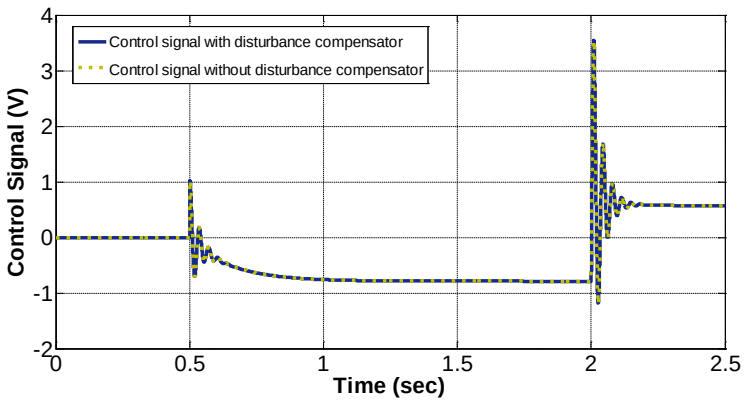

Figure 8. Control signal for z axes response.

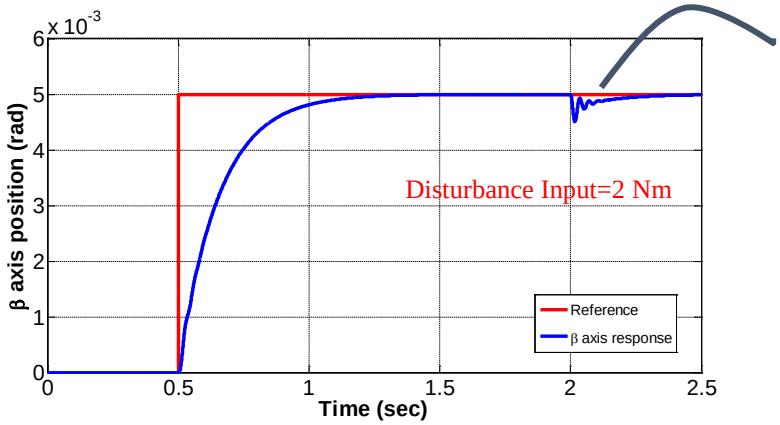

Figure 9: β-axes response for the step reference input and disturbance.

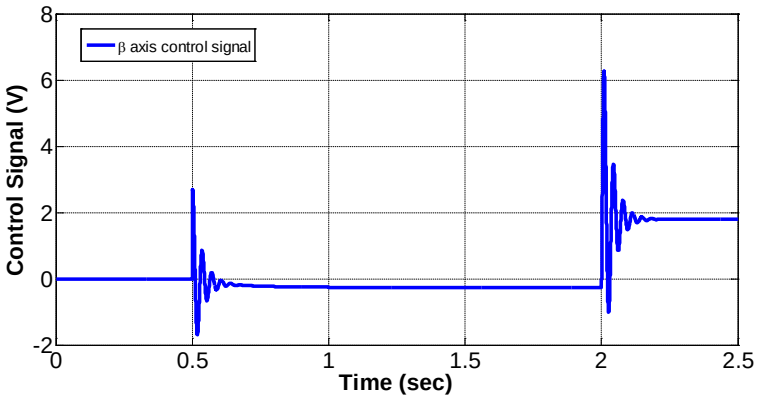

Figure 10. Control signal for β axes response.

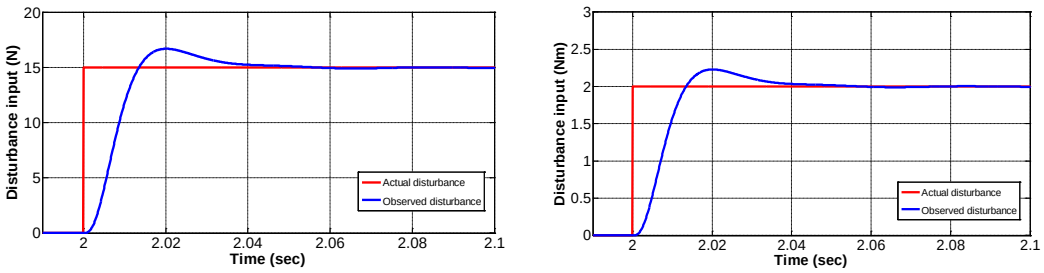

Figure 11. Actual and observed disturbance value for z and β axis.

7. CONCLUSION AND FUTURE WORK

In this paper, firstly, fundamentals of modeling of 4-pole hybrid electromagnet have been given and control methods of 4-pole hybrid electromagnet were explained by using virtual axis currents. Then, designing of a sliding mode controller and disturbance observer have been outlined. To clarify the effectiveness of the proposed design approach simulation studies was conducted in MATLAB environment. In the near future, we are planning to implement the controller on the experimental setup.

ACKNOWLEDGMENT

This study is supported by the Scientific and Technological Research Council of Turkey (TUBITAK) by project number 112M210.

REFERENCES

[1]. Y. Yakushi, T. Koseki and S. Sone, "3 degree-of-freedom zero power magnetic levitation control by a 4-pole type electromagnet", International Power Electronics Conference,vol.4, pp.2136-2141, April 3-7, 2000, Tokyo, Japan.
[2]. J. Liu, T. Koseki ,"Robust Control of a 4-Pole Electromagnet in Semi-Zero-Power Levitation Scheme with a Disturbance Observer" The Transactions of I.E.E. Japan, *A Publication of Industry Applications Society* Vol. 122-D, No. 1, pp. 7-15, January 2002
[3]. K. Erkan, B. Okur, T. Koseki, and F. Yigit, "Experimental evaluation of zero-power levitation control by transfer function approach for a 4-pole hybrid electromagnet," 2011 IEEE International Conference on Mechatronics, pp. 23–28, Apr. 2011.
[4]. Vadim Utkin, Juergen Guldner, Jingxin Shi, Sliding Mode Control in Electro-Mechanical Systems, Second Edition, CRC Press, 2009.
[5]. Katsuhiko Ogata, Modern Control Engineering, 5th Edition, Prentice Hall, 2009.
[6]. Shtessel, Y., Edwards, C., Fridman L., Levant A., "Sliding Mode Control and Observation (Control Engineering)",2013th Edition
[7]. J.-H. Lee, P. E. Allaire, G. Tao, and X. Zhang, "Integral sliding-mode control of a magnetically suspended balance beam: analysis, simulation, and experiment," IEEE/ASME Transactions on Mechatronics, vol. 6, no. 3, pp. 338–346, 2001.
[8]. Lee, J.-H., "A Design of Integral Sliding Mode Suspension Controller to Reject the Disturbance Force Acting on the Suspension System in the Magnetically Levitated Train System" , Transactions of the Korean Society for Noise and Vibration Engineering, Volume 17, Issue 12 2007, pp.1152-1160
[9]. Zhen Gang Sun; Cheung N.C; Shi Wei Zhao; Wai-Chuen Gan, Integral sliding mode control with integral switching gain for magnetic levitation apparatus, 2009. PESA 2009. 3rd International Conference on Power Electronics Systems and Applications, 2009.
[10]. Manabe, S."Coefficient diagram method", 14th IFAC Symposium on Automatic Control in Aerospace, Aug. 24-28, 1998, Seoul, Korea, 199- 210. (1998).

ICENS
INTERNATIONAL CONFERENCE ON ENGINEERING AND NATURAL SCIENCES
24-28 May 2016 /Sarajevo

Investigation of Membrane Fouling Characterization for the Microfiltration Membrane using Ballast Water Treatment

Huseyin Elcicek[1], Adnan Parlak[1], Mehmet Cakmakci[1], Omer Savas[1]

Abstract

Membrane fouling is one of the most undesirable effects on membrane surfaces and it is considered a major problem in most water treatment applications. In this study, the effect of turbidity, total suspended solid and dissolved organic carbon on the fouling characterization and flux decline of the microfiltration (MF) membrane operated with ballast water is investigated. The samples, containing various concentration of bacteria and pollution load, are collected from the various points of Marmara Sea Region. The fastest reduction in flux depending on time is found in the samples obtained from Tuzla shipyard and Kartal Region when all the samples are compared with the others. At these regions, the permeability of the microfiltration membrane was reduced by approximately 60% after a period of 100 minutes. The results showed that total suspended solid is the one of the most important parameter affecting the fouling of the MF membrane.

Keywords: *Ballast water, microfiltration membrane, fouling characterization, scanning electron microscopy*

1. INTRODUCTION

In the past few decades, marine and coastal ecosystem have become more significant due to increasing discharge untreated effluents from industry and shipping activities. Through the ships, ballast water which includes a variety of organisms such as bacteria, virus, microbes, plankton and the adult and larval stages of the many marine and coastal plants and animals discharged to marine and coastal environment [1,2]. With the discharge of ballast water, harmful aquatic organisms and pathogens introduced and spread to new environment. These species are now commonly recognized as one of the main threats to marine biodiversity. Furthermore, they have serious environmental risks and human health effect [3,4]. To overcome discharge of ballast water and reduce the risk of introducing pathogen bacteria from ships' ballast water, the International Convention for the Control and Management of Ships' Ballast Water and Sediments (the Ballast Water Management or BWM Convention) has come into forced by International Maritime Organization (IMO) in February 2004 [5].

After the Convention released, researchers have focused on ballast water treatment technologies. Today, membrane processes are one of the most widely used in water treatment. Compared to conventional treatment processes, membrane provides an absolute barrier to large particles and various microorganisms and bacteria due to its small pore size and properties [6]. The membrane processes produce consistently high quality permeates regardless of feed water quality. However, disadvantage of the membrane is that fouling is taking place its surface during the operation of treatment systems. Fouling is commonly defined as the accumulation and formation of unwanted particles on the surface of the membrane [7–9]. It also causes flux decline during the membrane filtration.

In recent years, there have been significant studies in the literature regarding the effects of operating parameters on flux decline. Among them, Buetehorn et al., investigated on the filtration efficiency of hollow-fibre membrane at constant trans-membrane pressure. The results showed that the permeate flux has increased with the increase of cross-flow velocity, the decreases of solid concentration, particle size and viscosity of the liquid [10]. Fersi et al., examined the flux decline of the MF, ultrafiltration (UF) and nanofiltration (NF) membrane used in the treatment of textile effluent. The researchers reported that concentration polarization is the main cause of flux decline for UF membrane. On the other hand, rapid cake formation of the membrane surface was observed during initial filtration and caused an initial sharp decrease in permeate flux for MF and UF processes. The cake formation on the NF membrane surface was occurred as progressively and increased in the second state of filtration [11].

Some studies have focused on fouling characterization of membrane surface (autopsy) [12–15]. Pontié et al., analysed the autopsies of hollow-fibre MF/UF membranes after treatment of raw surface water. In their studies emphasized that flux declines were significantly more important for MF membranes in comparison to the UF membranes. The researchers also studied flux declines on the effect of MF which produced from polysulfone (PS) and polyvinylidene fluoride (PVDF). The results revealed that MF PS has lower flux decline than that of MF PVDF membrane [13]. In the other study, Tung et al.,

[1] *Corresponding author: Yildiz Technical University, Department of Naval Architect and Marine Engineering, 34349, Beşiktaş/İstanbul, Turkey.* helcicek@yildiz.edu.tr

investigated the effect of antibacterial property of the PVDF hollow fibre membrane on the membrane fouling and surface morphologies and flux decline in the fresh water system. they observed that *E. coli* cells were removed in rate of 99.9% during the test and showed that the PVDF hollow fibre ultrafiltration membrane has good antibacterial property and fouling resistance [16]. Moreover, fouling characteristic of MF PVDF membrane have not been sufficiently studied especially in ballast water.

The present study investigates fouling characterization on the surface of MF PVDF membrane used in for various ballast water samples. The effect of turbidity, total suspended solid and dissolved organic carbon on the fouling characterization and flux decline of the microfiltration (MF) membrane is investigated. The elemental analyses of the foulants on the membrane surface were also determined.

2. MATERIALS AND METHOD

2.1 Sample Collection

Marmara Sea is particularly vulnerable to ship-originated pollution generated mainly by tankers and cargo vessels. Marine biodiversity in the Marmara Sea is threatened by intensive ship activities. The ports of the Marmara Sea have become important gateways for the export-import cargoes of Turkey since most of industrial plants are located in this region. In this context, ballast water samples were collected from four different region of the Marmara Sea: Kartal, Tuzla shipyard, coastal of Tuzla and Derince. All samples have various pollution load and bacterial load. Physicochemical parameters of the feed water are given in Table 1.

Table 12. Physicochemical parameters of the feed water.

Parameters	**Region**			
	Kartal	**Derince**	**Coastal of Tuzla**	**Tuzla Shipyard**
Salinity (PSU)	21.58	15.18	15.14	13.39
Conductivity (µS.cm^{-1})	38.9	35.9	34.8	35.1
Turbidity (NTU)	101	11.2	10.6	17.2
TSS (mg. L^{-1})	175	9.2	7.5	10.5
pH	8.00	8.34	8.52	7.07
DOC (ppm)	36.62	19.32	22.75	28.94

2.2 Experimental procedure

Experiments were performed in a dead end stirred cell filtration system (Sterlitech, HP4750). The active filtration area used in the module is 14.6 cm^2. Permeate was collected in sterile bottles. The schematic diagram of the experimental setup is shown in Fig. 1.

A virgin membrane is mounted up in the filtration cell and the feed reservoir is first filled with the ballast water. Then, system pressurized with nitrogen gas until desired pressure value is obtained. Permeate is collected in a beaker sitting on an electronic balance. The balance connected to a computer and the cumulative permeate mass is recorded as a function of time. The permeate flux (J) was calculated according to the following equations;

$$J = \frac{\Delta M}{\rho \times A \times \Delta t} \quad (1)$$

where ΔM (kg) is the mass of permeate collected during a time period of Δt, ρ (kg/m^3) is the density of water samples, A (m) is the effective membrane area and Δt (h) is the permeation time. MF PVDF membrane was used in filtration cell. Advantages of PVDF membrane include excellent chemical stability, thermal stability, resistance to radiation and good mechanical strength [16].

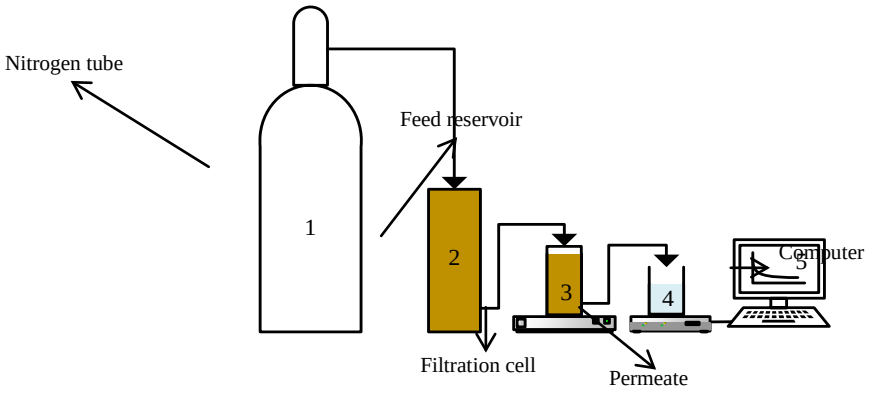

Figure 1 Schematic diagram of the experimental set-up.

2.3 Characterization of the membrane surface

Both scanning electron microscopy (SEM) and energy dispersive X-ray spectroscopy (EDS) measurements were performed to determine membrane surface characteristics. This is based on analysis of X-rays produced via electron beam excitation of a sample area. This technique allows analysis of a sample in specific areas. The scanning electron microscopic analysis (SEM) and the energy dispersive X-ray spectroscopy (EDX) of the virgin membrane are shown Fig. 2. The main elements which are Si, F, O and C was detected on the virgin membrane surface.

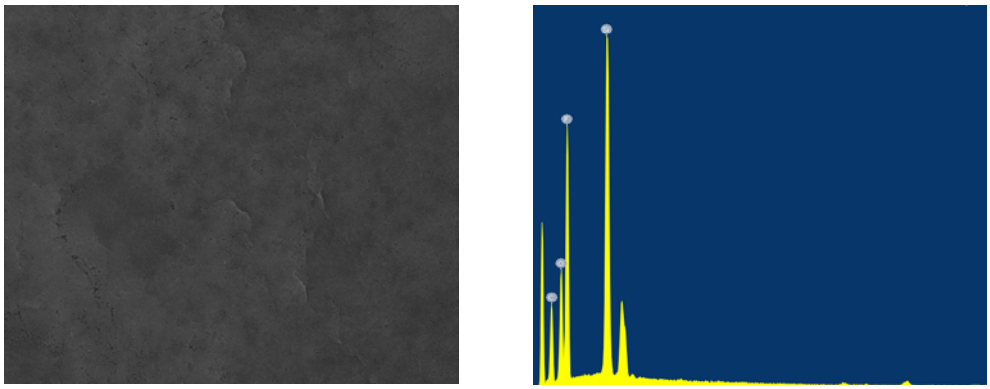

Figure 2 SEM images and EDS spectrum of the virgin membrane.

3 RESULTS AND DISCUSSION

3.1 Water quality

After filtration of the ballast water samples, TSS, and DOC significantly reduced as the MF membrane removed particulate and colloidal pollutants which higher diameter than the MF pore size. Change of pH, conductivity and salinity parameters depends on the ion exchange of membrane. Since there is no ion exchange as a characteristic of MF membrane, pH, conductivity, and salinity parameters have not changed as expected.

The percentages of removal efficiencies were found within the ranges from 55.81% to 95% for DOC and from 97.83 % to 99.89 % for TSS for all ballast water samples tested. High turbidity rejection rate of MV020 membrane was also observed as 85%.

3.2 SEM and EDS analysis

MV020 membrane surface characterization was investigated after treatment of the ballast water. Elemental analysis of the fouled membrane surface has done by using SEM analysis and EDS spectrum as can be seen from Figure 3-4.

From the EDS results, elemental composition on the membrane surfaces showed the changes depending on the area that the samples were collected. Main compositions on the membrane surface are found as Mg, Cl, and O elements (Fig. 3a) for

coastal of Tuzla; Fe, F, Ca, C, K and O elements (Fig. 3b) for Derince; Ca, C, K, Cl and O elements (Fig. 4a) for Tuzla shipyard and Fe, C, Cl and O (Fig. 4b) for Kartal. Trace amounts of Mg, Al, Zn, S and Cu were also detected.

As expected, high concentration of salt components (especially NaCl and CaCl) in seawater were accumulated at the membrane surface. It was observed that salt components have been accumulated randomly on the membrane surface. This is the main cause of permanent flux which affects the treated water quality. In addition to, Fe, Zn and Cu may be used as a source of nutrients that are required for various biochemical and physiological functions for the fish and shellfish [17]. However, potential toxicity is possible for fishes and their consumers in case of contamination of high level of Fe, Zn and Cu contents to the sea water. For this reason, a large proportion of these contaminants should be eliminated before discharge to the marine environment. In present study, these elements were rejected by the MV020 membrane and retained at the membrane surface. Removal rate of the elements was not investigated however the identified metals could be removed to a certain extent from the ballast water with the MV020 membrane.

It is considered that these contaminations come from anti-fouling paints and sediments collected in the ballast tanks and the industrial activities to the marine environment could be influenced their concentrations in ballast water.

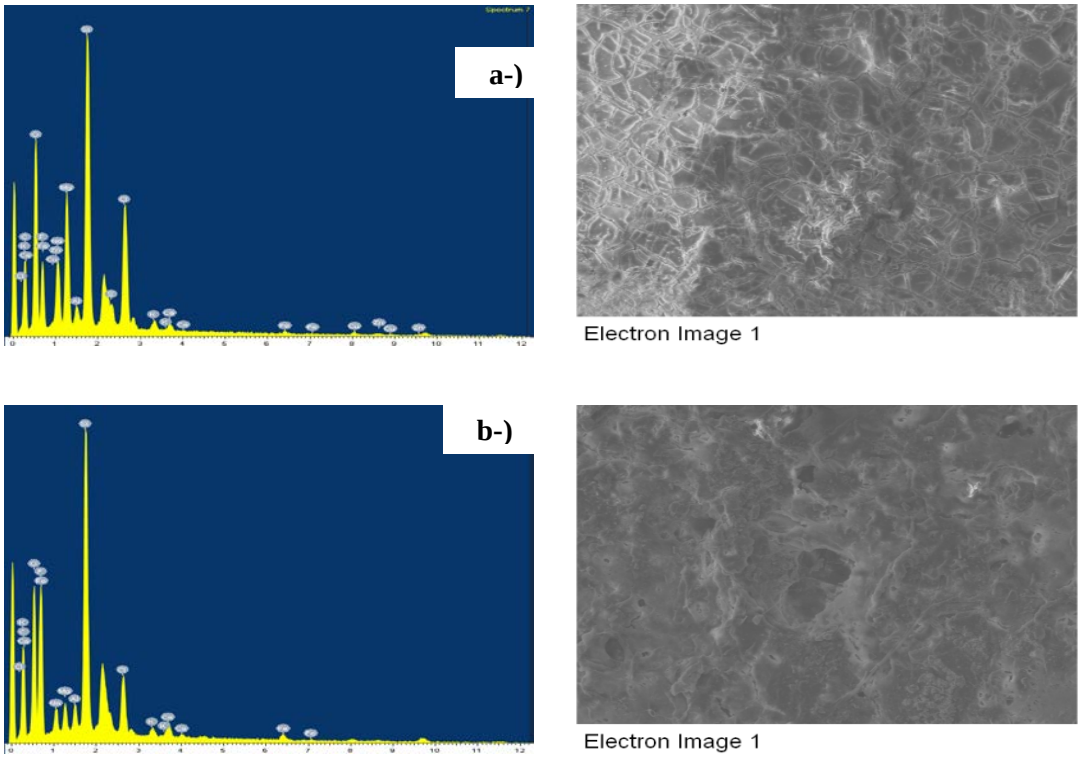

Figure 3 SEM images and EDS spectrum of the membrane used Tuzla (a) and Derince ballast water (b).

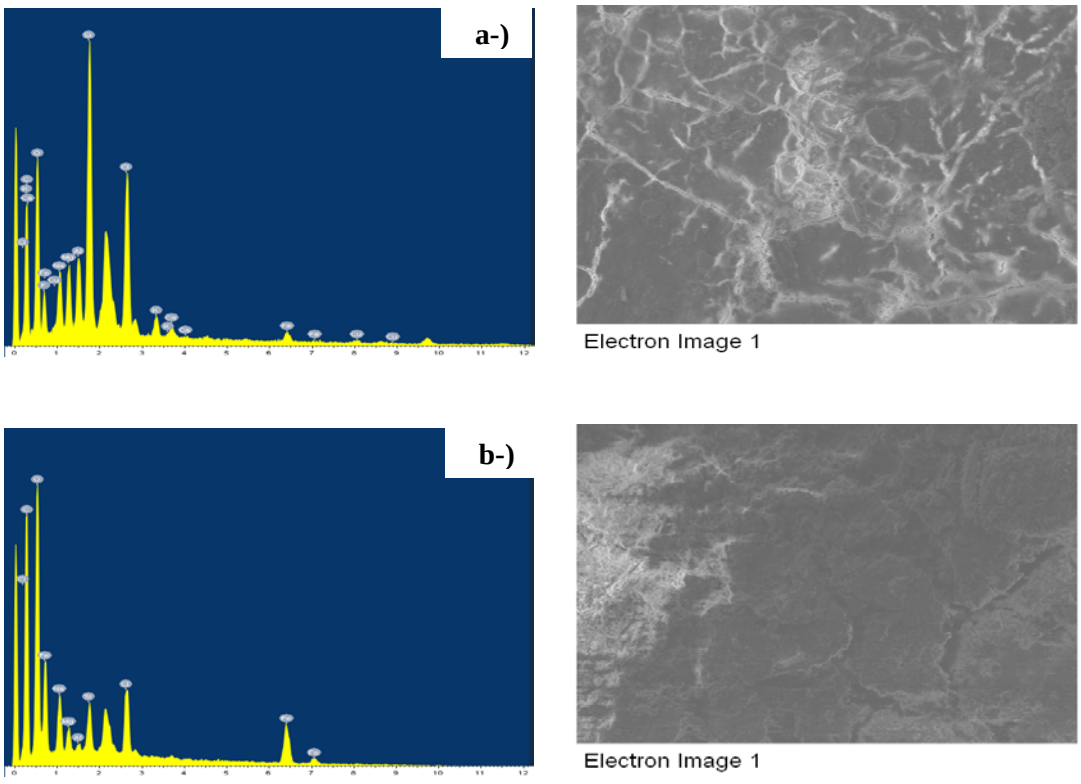

Figure 4 SEM images and EDS spectrum of the membrane used Tuzla shipyard (a) and Kartal (b) ballast water.

3.3 Flux decline

Permeate water flux during the filtration process is one of the most important parameter for evaluating membrane performance. Flux decline at the constant transmembrane pressure were performed to investigate fouling in MF membrane. The normalized flux versus filtration time during dead end microfiltration of the four ballast water samples is given in Figure 5. The flux decline curves exhibited qualitatively similar behavior as shown in Fig. 5. Also, each initial flux of the membrane with the all ballast water samples and percent flux decline are shown in Table 2.

As can be seen Figure 5, normalized flux (J/J_0) reduces significantly during the filtration process. The flux decays drastically at the beginning of each experiments due to significant blockage of pores within the membrane. The flux attenuation becomes slower after 60 min. This is because the filtration mode gradually changes from membrane internal blocking to cake filtration [18]. Accumulation of the salt components on the membrane surface contribute to the partly block of the membrane pores.

Table 2. Initial flux and percent flux decline for the all samples.

Region	Parameter	
	Initial flux [L/m^2.h]	Flux decline rate [%]
Kartal	1458.3	81.7
Derince	682.6	73.4
Coastal of Tuzla	651.2	70.9
Tuzla Shipyard	472.4	85.6

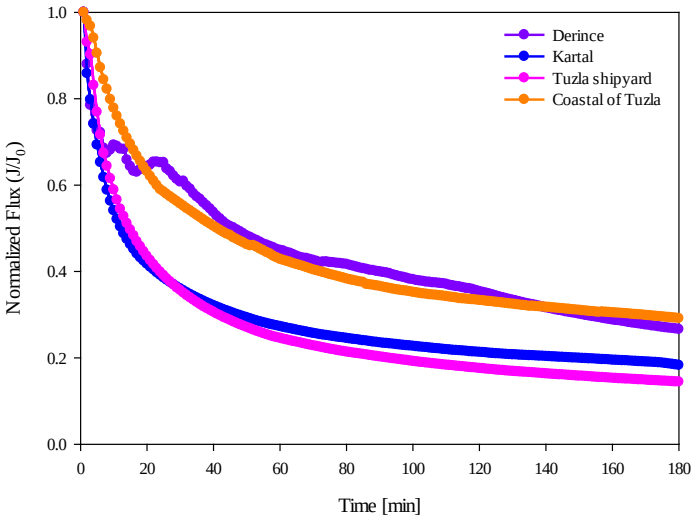

Figure 5 Normalized fluxes during the filtration for the all samples.

4 CONCLUSION

In the present study, characterization of the fouled membrane after filtration of ballast water collected from the various point of the Marmara Sea was investigated. Characterization of the fouled membrane using di fferent methods (S concluded that the fouling was mainly caused by a combination of colloidal particles, organic matter, and multivalent ions. The EDX results showed that Fe, Cu, Zn, Cl, Ca, Mg, K and Na as the major inorganic foulants include in ballast water as well as invasive aquatic species. In addition to, removing capability of the MV020 membrane for TSS, DOC and turbidity was found about 75%, 99% and 85%, respectively. Moreover flux decline versus filtration time was examined at the constant transmembrane pressure. The permeability of the microfiltration membrane was reduced by approximately 60% after a period of 100 minutes. In order to minimize and differentiate any kind of membrane fouling on the membrane surface an effective cleaning method should be considered for further studies.

This study demonstrated that membrane characterization is a valuable tool to develop the ballast water treatmeant systems, and based on the present results, pretreatment, periodic cleaning, etc. were also suggested to control fouling. The pretreatment is provided to improve the removal efficiency of the membrane and remove all potential membrane foulant matter from the ballast water.

ACKNOWLEDGMENT

This study was supported by Yildiz Technical University with the Project No. 2013-10-02-KAP01. Thanks to YTU BAPK for the financial support.

REFERENCES

[1]. Altug G, Gurun S, Cardak M, Ciftci PS, Kalkan S. The occurrence of pathogenic bacteria in some ships' ballast water incoming from various marine regions to the Sea of Marmara, Turkey. Mar Environ Res 2012;81:35–42. doi:10.1016/j.marenvres.2012.08.005.
[2]. Guilbaud J, Massé A, Wolff F-C, Jaouen P. Porous membranes for ballast water treatment from microalgae-rich seawater. Mar Pollut Bull 2015;101:612–7. doi:10.1016/j.marpolbul.2015.10.044.
[3]. Elçiçek H, Parlak A, Çakmakcı M. Effect of Ballast Water on Marine and Coastal Ecology. J Selcuk Univ Nat Appl Sci 2013;ICOEST Conf. 2013 (Part 1):454–63.
[4]. Hilliard R. Silent Invasion – The spread of marine invasive species via ships' ballast water. Switzerland: WWF International; 2009.
[5]. International Maritime Organization (IMO). International Convention for the Control and Management of Ships' Ballast Water and Sediments. London: 2004.
[6]. Marcano JGS, Tsotsis TT. Catalytic Membranes and Membrane Reactors, Weinheim,: Wiley-VCH; 2002, p. 150.
[7]. Peña N, Gallego S, Vigo F del, Chesters SP. Evaluating impact of fouling on reverse osmosis membranes performance. Desalination Water Treat 2013;51:958.
[8]. Sotto A, Rashed A, Zhang R-X, Martínez A, Braken L, Luis P, et al. Improved membrane structures for seawater desalination by studying the influence of sublayers. Desalination 2012;287:317–25. doi:10.1016/j.desal.2011.09.024.

[9]. Pangarkar BL, Sane MG, Guddad M, Pangarkar BL, Sane MG, Guddad M. Reverse Osmosis and Membrane Distillation for Desalination of Groundwater: A Review, Reverse Osmosis and Membrane Distillation for Desalination of Groundwater: A Review. Int Sch Res Not Int Sch Res Not 2011;2011, 2011:e523124. doi:10.5402/2011/523124, 10.5402/2011/523124.

[10]. Buetehorn S, Carstensen F, Wintgens T, Melin T, Volmering D, Vossenkaul K. Permeate flux decline in cross-flow microfiltration at constant pressure. Desalination 2010;250:985–90. doi:10.1016/j.desal.2009.09.087.

[11]. Fersi C, Gzara L, Dhahbi M. Flux decline study for textile wastewater treatment by membrane processes. Desalination 2009;244:321–32. doi:10.1016/j.desal.2008.04.046.

[12]. Al-Amoudi A, Lovitt RW. Fouling strategies and the cleaning system of NF membranes and factors affecting cleaning efficiency. J Membr Sci 2007;303:4–28. doi:10.1016/j.memsci.2007.06.002.

[13]. Pontié M, Thekkedath A, Kecili K, Habarou H, Suty H, Croué JP. Membrane autopsy as a sustainable management of fouling phenomena occurring in MF, UF and NF processes. Desalination 2007;204:155–69. doi:10.1016/j.desal.2006.03.538.

[14]. Tung K-L, Teoh H-C, Lee C-W, Chen C-H, Li Y-L, Lin Y-F, et al. Characterization of membrane fouling distribution in a spiral wound module using high-frequency ultrasound image analysis. J Membr Sci 2015;495:489–501. doi:10.1016/j.memsci.2015.08.035.

[15]. Blandin G, Vervoort H, Le-Clech P, Verliefde ARD. Fouling and cleaning of high permeability forward osmosis membranes. J Water Process Eng 2016;9:161–9. doi:10.1016/j.jwpe.2015.12.007.

[16]. Shi H, Liu F, Xue L. Fabrication and characterization of antibacterial PVDF hollow fibre membrane by doping Ag-loaded zeolites. J Membr Sci 2013;437:205–15. doi:10.1016/j.memsci.2013.03.009.

[17]. World Health Organization (WHO). Trace elements in human nutrition and health. Switzerland: Geneva: 1996.

[18]. Hwang K-J, Liao C-Y, Tung K-L. Analysis of particle fouling during microfiltration by use of blocking models. J Membr Sci 2007;287:287–93. doi:10.1016/j.memsci.2006.11.004.

Comparison of Magnetic Barkhausen Noise Method and Erichsen Cupping Test Method for Determination of The Formability of Sheet Material

Oguz Kocar[1], Osman Ozdamar[2]

Abstract

Erichsen cupping test is a technique, which is used to evaluate the formability of sheet metal materials. The test is performed by pressing a spherical punch on prepared samples until a crack appears. The height of the cup at the moment of crack determines Erichsen Number, which is used to compare the formability of materials. When variable magnetic field is applied on a ferromagnetic material, a signal is generated due to movement of domain walls indirection of the applied magnetic field. This signal is call as Magnetic Barkhausen Noise (MBN). MBN is one of the non-destructive testing methods and it is sensitive to the internal structure of materials. In this study, the characteristics of samples having different mechanical properties are compared in terms of the Erichsen numbers and MBN properties. Also, the relationship between the magnetic properties and formability of materials are investigated.

Keywords: *sheet metal materials, formability of materials, magnetic field*

1. INTRODUCTION

Parts produced with sheet metal forming method (parts of automobile, plane, etc.) have a wide range of applications in the industry [1]. The complexity of the forming process makes the desired manufacture difficult. Different methods are used in order to increase product quality. One of these methods is the optimization of forming conditions by developing numeric models by using mechanical properties of the material. [2]. Another method is to form a new material (trip steels, etc.) or improving mechanical features of the material used. Mechanical properties of materials should be known and their forming capacity (formability) should be compared in both methods. Uniaxial tensile test, hydraulic bulge test, Nakizma tests, etc. are used to determine mechanical features of the material, and Erichsen and Olsen tensile test, etc. are used to compare formability of the material.

Erichsen and Olsen tensile test is the most suitable test method for material behavior and closer to the actual production conditions [2]. Preliminary studies on behavior of sheet metal during tensile process are made in these tests. Erichsen IE is calculated through the distance from the moment the staples contacts with the metal sheet to the moment when rupture occurs. Higher Erichsen IE value means a higher material formability. [3]. Suni et all [4] used Erichsen buckling test in their study in order to compare formability of cold worked and tempered steel sheets. They stated that, if the hardness of the material decreases, Erichsen IE and formability capacity will increase. In another study, Ti-6A1-4V titanium material is heated with electrical current in different temperatures in order to increase formability of the material. In order to determine changes in mechanical features in heating process, Erichsen IE is measured. It is observed that mechanical features remain unchanged due to heating and cooling processes applied rapidly in samples [5].

Many samples is needed for the standard tests used for determining the mechanical properties, and comparison of the formability of materials. Tests are performed by damaging the samples and big machines are required to do this [6], which increases the cost and time loss.

Mechanical properties (hardness, strength, ductility etc.) are directly affected by the microstructure, chemical composition and production method. Similarly, the magnetic properties are sensitive to chemical composition, microstructure and process conditions, which enables using magnetic properties during the examination of the mechanical properties of material [7].

Ferromagnetic materials are magnetically neutral when no external magnetic field is applied onto them [8]. This is because the ferromagnetic materials are composed of small regions magnetized in direction opposite to each other called magnetic domain. These regions are separated from each other by domain walls. Magnetization is distributed homogenously inside the

[1]*Corresponding author: Bülent Ecevit University, Department of Engineering, 67100, İncivez/Zonguldakl, Turkey.* oguz.kocar@yahoo.com.tr
[2]*Bilecik Şeyh Edebali University, Osmaneli Vocational School, Bilecik/Turkey,* osman.ozdamar@bilecik.edu.tr

domain. When a magnetic field which changes through time is applied from outside, domain walls are moved through the magnetizing direction until a single region is formed. Sound waves produced by the movement and orientation of the magnetic domains are known as the Barkhausen noise [9]. The hysteresis curve in Figure 1 shows the movement of domain walls with increasing magnetic field and flux intensity [10].

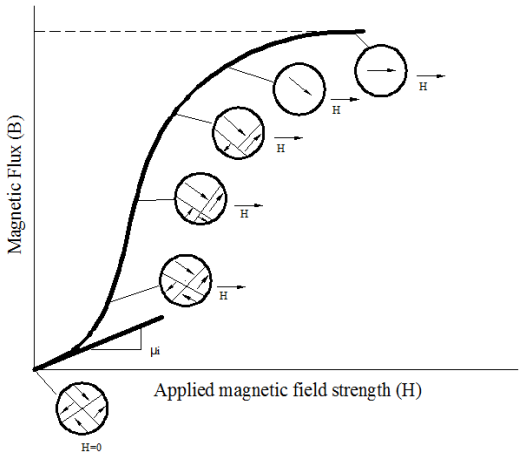

Figure 1. Domen movements in Histeresis loop[11]

Magnetic Barkhausen noise is used for determining the mechanical properties of a material since it is closely related to the microstructure, chemical composition and production method of the material. Trillon et al. determined a linear relationship between the hardness and MBG signals and argued that MBG method can be used as an alternative method in the evaluation of steel pipes [11]. In another study, it is argued that the phase ratio and tensile strength values of dual phased (DP) commercial steels with different qualities can be evaluated [12]. In another study, P91 steel was plastically deformed with different ratios. Then a uniaxial tensile test and MBG measurements were conducted and the relationship between the yield point/tensile strength and MBG parameters. It was determined that basic magnetic properties and mechanical properties can be estimated without using tensile test [13]. Besides, MBG analysis method is used for estimating the mean grain size [10-14], residual stress [9-10].

In this study, the formability of different quality steel sheet metal samples with 2 mm thickness is compared to each other using Erichsen cupping test by determining the force at Erichsen IE and shear. Besides, the relationship between MBG analysis parameters and Erichsen IE/Erichsen force is investigated.

2. MATERIAL

In this study, four different material type is studied among the ferromagnetic material types with 2mm thickness. The chemical compositions of these steels can be found in Table 1. Ck67 sheet metal gains spring property. It is suitable for cold forming and can be brought to desired hardness after heat treatment following the forming process. E3937 is low-to-medium hardness steel that is mainly used to produce rim pulley. E3955 is the steel that is used for producing rim based on customer specification. DC01 is a steel material that is preferred in general applications suitable for tensile processes.

Table 1. Composition of Ferromagnetic materials

Element	C	Mn	P	S	SI	AL	CU	NI	V	NB	Ti
E3955	0.059 0.024	0.816	0.015	0.005	0.056	0.028	0.015	0.037	0.008	0.058	--
E3937	0.080 0.002	0.0453	0.0075	0.028	0.032	0.015	0.018	0.039	0.002	0.163	--
Ck67	0.65 0.75	0.60 0.90	0.030	0.035	0.15 1035	--	--	--	--	--	--
DC01	0.12	0.60	0.045	0.045	0.030	0.020	--	--	--	--	--

3. EXPERIMENTATION AND RESULTS

3.1. Erichsen Cupping Test

Erichsen cupping test is a ductility test, which is employed to evaluate the ability of metallic sheets and strips to undergo plastic deformation in stretch forming [3,15]. To conduct this test, a coated sheet metal panel is clamped between blank holder and drawing die and then dented (cupped) with a hardened spherical punch. In this procedure the coating is subject to an increasing elongation and bending stress until first cracks appear. The forming of cracks during the ERICHSEN Cupping Test is observed visually with the eye or preferably with a microscope [16]. The design of the classical Erichsen test used in the Europe is defined by a hemispherical punch of steel (20 mm Ø), an active die (27 mm Ø), a blank holder (33 mm Ø) and a sheet metal (90 mm Ø) (see Figure 2). The radius of the die is 0.75 mm. In Erichsen cupping test, the cup height at fracture (or, preferably, maximum load or punch force) is taken as the measure of stretchability or formability index [17].

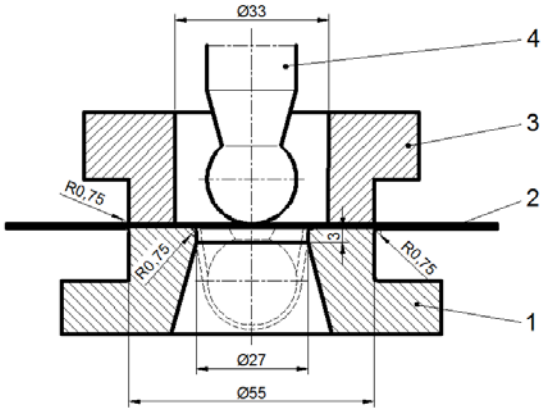

Figure 2. Experimental set-up of the Erichsen test (1- Die, 2- Sheet metal, 3- Blank Holder, 4- Punch)

Erichsen cupping tests are made in Yildiz Technical University, Plastic Forming Laboratory. Samples are prepared as 12x50 cm size and the tests are repeated three times (Figure 3). Test is paused when cracks are initiated on the sample, and the cup height and maximum load are recorded. Then the mean values of the tests are calculated.

Table 2. Cupping Test Results for Selected Samples

Sheet Metal	Max. Load (kN)	Erichsen ID
Ck 67	45.7	14.33
DC01	29.50	14.30
E3937	31.93	14.47
E3955	40,87	14.60

Table 2 shows the Erichsen ID and maximum values of the cupping test. Although the formability of the materials are close to each other, their strength values are found to be different. E3955 material can be preferred in complex forming processes.

Figure 3. Erichsen Cupping Test Results

3.2. Magnetic Barkhausen Noise Measurements

MBN measurements are made using Stress Tech Microscan 500-2 MBN measurement system. Magnetic noise signals formed are converted to numerical values. Table 3 gives the measurement adjustment parameters.

Tablo 3. Ölçüm ayar parametreleri

Device	Microscan 500-2
Frequency	5-125 Hz
Voltage	10 Volt
Filtering range	0.1-500 kHz
Sampling Frequency	2 MHz

Barkhausen Noise (BN) profile is drawn according to the measurement results. Peak position, peak width and Root Mean Square (RMS) values are obtained from this profile. Figure 4 shows the properties obtained from the BN profile [18]. Figure 5 shows the BN profiles for sheet materials, and Table 4 gives the properties obtained from the BN profile.

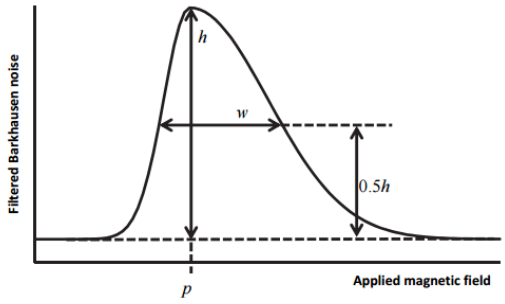

Figure 4. Calculation of peak width (h is peak height, p is peak position and w is peak width).

Tablo 4. BN profillinden türetilmiş özellikler

Sheet Metal	**Max. Load**	**Peak Poz.**	**Peak Height**	**RMS**
DC01	29.5	1.162	68.53	43.21
E3937	31.93333	7.325	78.6	46.88
E3955	40.86667	16.7	38.69	21.14
Ck67	45.7	27.91	45.52	23.3

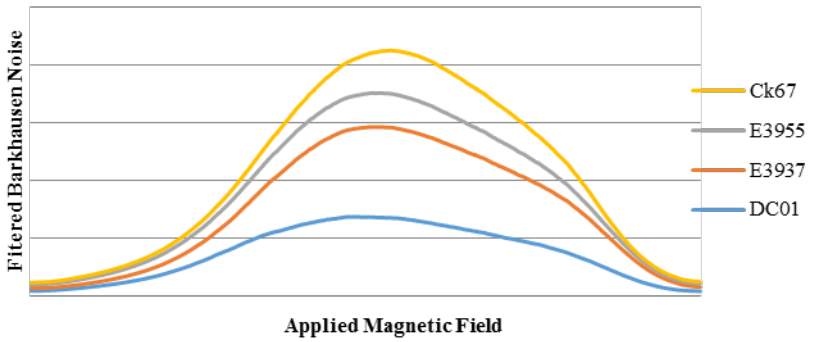

Figure 5. BN profiles for sheet material.

The relationship between the values obtained from BN profile and the maximum load obtained from cupping test is investigated. BN peak position is observed to increase as the maximum load value at the shear point of the material is increased (Figure 6). Literature survey shows that BN peak position is sensitive to hardness value of the material and there is a linear correlation between them. This study revealed that there is a relationship between the BN peak position and the strength of the material at shear point

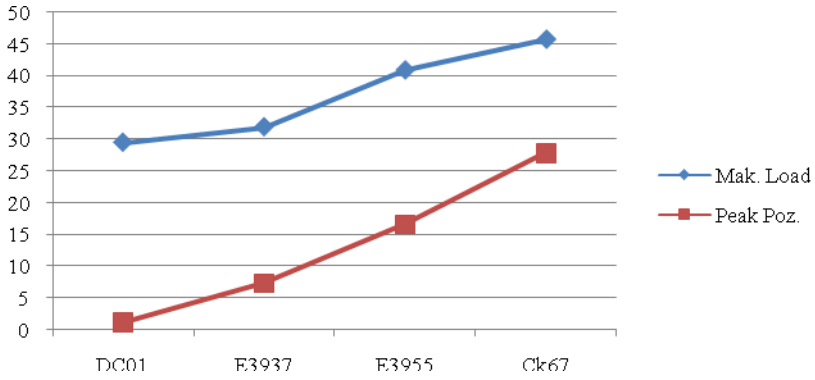

Figure 6. Maximum load and peak position drawing

4. CONCLUSIONS

It is observed that although the formability of sheet materials are close to each other, the forces at shear point are different. Ck 67 is the sheet material having the highest strength with a 45.7 kN punch force at the shear point. Therefore it can be argued that it can be more successful in complex forming processes compared to other materials.

Peak position, peak height and RMS values of the sheet materials are calculated from their obtained BN profiles. BN properties are compared to the punch force of Erichsen machine and it is determined that the peak position changes with increasing sheet material strength. Therefore, the magnetic properties of ferromagnetic materials can be used to evaluate the strength of materials. Further studies may include regression analyses between the material strength and magnetic properties.

REFERENCES

[1]. O. Koçar, D. Karayel, O. Eldoğan and S.S. Özkan, Tersine Mühendislik Yaklaşımı Kullanarak Sac Metalin Şekillendirme Sınır Diyagramının Belirlenmesi, 1st Internatıonal Symposıum On Innovatıve Technologıes in Engıneerıng and Science, Turkey, Sakarya, 7-10 May., 2013.
[2]. A. Gavrus, M. Banu, E. Ragneau and C. Mailer, An Inverse Analysis of the Erichsen Test Applied for the Automatic Identification of Sheet Materials Behavior, SciRes. Engineering, vol. 2, pp. 471-476, May. 2010.
[3]. O. Anket, t. koruvatan and İ. Ay, Sac Malzemelerin Şekillendirilmesinde Şekillendirme Sınır Diyagramının Kullanımı, Journal of Polytechnic, vol. 14-1, pp. 39-47, May. 2011.
[4]. S. U. Sunil, K. B. Pai, Investigation of Formability of CRCA Steel by Erichsen Cupiing test Analysis, ıOSR Journal of Mechanical and Civil Engineering, vol. 11, pp. 52-55, Apr. 2014.
[5]. R. E. ECE, F. Öztürk, Elektirik Akımı ile Isıtma Yönteminin Sıcak Sac Şekillendirme uygulamalarında Kullanımının İncelenmesi, 2. Ulusal Tasarım İmalat ve Analiz Kongresi, Turkey, Balıkesir, 11-12 Nov., 2010.
[6]. T. E. Garcia, C. Rodriguez, F. J. Belzunce and C. Suarez, Estimation of The Mechanical Properties of Metallic materials by Means of the Small Punch Test, Journal of Alloys and Compounds, vol. 582, pp. 708-717, August, 2013.

[7]. D. X. Yang, K. P. Kankolenski, S. Z. Hua, L. J. Swartzendruber, G. E. Hicho and H. D. Chopra, *Evaluation of Mechanical Properties of Magnetic Materials Using a Non-Destructive Method*, IEEE Transactions on Magnetic, vol. 37-4, pp. 2758-2760, 2001.
[8]. P. Wang, L. Zhu, Q. Zhu, X. Ji, H. Wang, G. Tian and E. Yao, *An Application of Back Propagation Neural Network for The Steel Stress Detection Based on Barkhausen Noşse Theory,* NTD&E International, vol. 55, pp. 9-14, 2013.
[9]. H. I. Yelbay, *Developments In Residual Stress Measurement by Nondestructive Methods*, 3rd International Non-Destructive Tetsting Symposium and Exhibition, Turkey, Istanbul, April, 2008.
[10]. K. Davut, C. H. Gür, *Nondestructive Charecterization of Steel Microstructures by Magnetic Barkhausen Noise Method*, 3rd International Non-Destructive Tetsting Symposium and Exhibition, Turkey, Istanbul, April, 2008.
[11]. A. Trillon, F. Deneuville and B. Bisiaux, *Magnetic Barkhausen Noise for Hardness Checking on Steel*, 18th World Conference on Nondestructive Testing, South Africa, Durban, 16-20 April, 2012.
[12]. X. Kleber, A. H. Amalric and J. Merlin, *Evaluation of The Proportion of Phases and Mechanical Strenght of Two-Phases Steels Using Barkhausen Noise Measurements: Application to Commersial Dual-Phase Steel*, Metallurgical and Metarials Transactions A, vol. 39A, pp. 1308-1318, 2008.
[13]. K. Makowska, Z. L. Kowalewski, B. Augustyniak nad L. Piotrowski, *Determination of Mechanical Properties of P91 Steel by Means of Magnetic Barkhausen Emission*, Journal of Theoretical and Applied Mechanics, vol. 52, pp. 181-188, 2014).
[14]. S. Ghanei, A. S. Alam, M. Kashefi, M. Mazinani, *Nondesructive Characterization of Microstructure and Mechanical Properties of Intercritically Annealed Dual-Phase Steel by Magnetic Barkhausen Noise Technique*, Materials Science & Engineering A, vol. 607, pp. 253-260, 2014.
[15]. A. Kocanda, C. Jasiski, *Extended Evaluation of Erichsen Cupping Test Results by Means of Laser Speckle*, Archives of Civil and Engineering, vol. 16, pp. 211-216, 2016.
[16]. (2007) The IEEE website. [Online]. Available: http://www.ieee.org/
[17]. S. M. Metev and V. P. Veiko, *Laser Assisted Microtechnology*, 2nd ed., R. M. Osgood, Jr., Ed. Berlin, Germany: Springer-Verlag, 1998.
[18]. Sorsa, Aki, (Ph.), Prediction of Material Properties Based on Nondestructive Barkhausen noise Measurement, University of Oulu, Faculty of Technology Depertment of Process and Environmental Environmental Engineering, 2013.

ICENS
INTERNATIONAL CONFERENCE ON ENGINEERING AND NATURAL SCIENCES
24-28 May 2016 /Sarajevo

Safety Measures on Tanker Ships and Analysis of Incidents on Board

Ersoy Kacmaz[1], E. Gul Emecen Kara[2], Murat Yildiz[3]

Abstract

Tanker ships carry liquid cargo. Liquid cargoes are produced from petroleum. As known, petroleum products are dangerous. This dangerous arises as fire, explosion, poisoning and marine pollution. Tanker ships' crews take precaution against risk of dangerous, while they carry at sea and on loading, unloading at terminals. Precautions are taken in two ways, namely structural and operational of ships. Structural precautions are defined by regulations and naval architecture technics. Operational precautions are only defined by regulations. However, human factor is very important on tanker ships operations. Ship captains considering this factor evaluate the risks to prevent accidents. All works are realized within a systematic for good work. Accidents have been observed despite of all precautions and systematic works. In this study, safety measures of tanker ships against incidents are examined and accidents on board are analyzed for a tanker management company.

Keywords: *Maritime, Tanker Ship, Operation, Accident, Safety on Board*

1. INTRODUCTION

Tanker shipping has an important share in the maritime transport. Tanker ships compose of %27 on world merchant fleet [1]. Liquid and gas cargoes are carried by tanker ships (simply-Tanker). Tankers are divided into four types: crude oil tankers, product oil tankers, chemical tankers and gas carriers.

Tankers carry cargoes from the rawest cargo crude oil to various type of final chemical products. Most of cargoes which are carried by tankers are dangerous cargoes. Therefore, safety is very important on tankers. There are international regulations such as International Code for the Construction and Equipment of Ships carrying Dangerous Chemicals in Bulk (IBC Code), International Safety Guide for Oil Tankers and Terminals(ISGOT) and International Maritime Dangerous Goods (IMDG Code) in order to carry dangerous cargoes safely. According to these regulations tankers apply precautions.

Tanker shipping has a potential risk because of its nature. Despite of taken precautions and applied regulations, various incidents and accidents occur on tankers. In this study precautions are examined and accidents and incidents on tankers are evaluated around a tanker management company.

2. TANKERS

Tankers are ships which are designed to transport liquid, usually hazardous or dangerous goods in bulk. Main types of tankers are the oil tanker, the chemical tanker and the liquefied gas carriers. A wide range of products are carried by tankers as hydrocarbon products, petroleum, chemical products, natural gases, wine, and molasses [3].

Oil tanker, also known as a petroleum tanker, is a merchant ship designed for the bulk transport of oil. There are two basic types of oil tankers: the crude tanker and the product tanker. Crude tankers move large quantities of unrefined crude oil from its point of extraction to refineries. Product tankers, generally much smaller, are designed to move refined products from refineries to points near consuming markets [4].

Figure 1. Example of an Oil Tanker [5].

Chemical tankers are based on a slightly different design than crude oil and product tankers for example, because the products they carry require special tanks and storage and transportation procedures. The different chemicals are labelled with different International Maritime Organization (IMO) classes according to the degree of hazard [6]. These Classes are 3 types and named IMO class 1, IMO Class 2 and IMO class 3. Gradation is from very dangerous chemical goods carriers to light dangerous chemical goods carriers [7].

Figure 2. Example of a Chemical Tanker [8].

Gas carrier ships are especially designed ocean-going vessels that are dedicated for transporting all types of liquefied natural gases (LNG) and liquefied petroleum gases (LPG) to their destinations. These ships are inbuilt with tankers of plain surface, spherical or cylindrical shape to carry the gas [9].

Figure 3. Example of a Chemical Tanker [10].

2.1 Hazardous and Safety Precautions on Tankers

Tankers carry oil, oil product and chemical goods. They have risks, those based hazardous of petroleum. Hazardous of Petroleum:

- Flammability and Property of explosive
- Toxicity
- Pollute of Environment [10].

Tanker operations are done with minimized risks. Cargo operations and handling are the most important in all operations. Cargoes are needed operations under control strictly. It's vital based on human health. At the same time a lot of cargoes, carried on tankers has got low flash point. Loading and discharging operations must have taken under control on board and at terminal. Otherwise, fire and explosion arise on boards and terminals together pollution, injury and losses of life [11].

Taking Precautions could be tackled two topics as structural and operational. Structural precautions ordered by International Maritime Organization (IMO) at several rule and publications. They are cargo following systems, fixed gas and vapor alert systems. All equipment must be approved by an independent class accordance to IMO instructions. Apart from these using equipment must be approved type for tankers from laid keel until end of Tanker's service life [7].

Operational precautions have been issued by relevant organizations and are being issued as circulars and alert guide regularly. These organizations are OCIMF (Oil Companies International Marine Forum), ITOPF (International Tanker Owner Pollution Federation), ICS (International Chamber of Shipping) and relevant Insurance companies, protected and indemnity clubs mainly.

Operational precautions could be evaluated general precautions and precautions at operations. They are shown at table 1, all works and operations are done on board forethoughtfully. At the same time a safety system is carried out on tankers mandatorily accordance to IMO's regulations [12].

The safety system is named International Safety Management (ISM). The objectives of the ISM Code are to ensure safety at sea, prevention of human injury or loss of life, and avoidance of damage to the environment, in particular, to the marine environment, and to property. The Code requires companies to establish safety objectives as described in rules [13].

Risk assessments are applied to describe of safety for vessels and maritime companies. Requirements of safety have been described and taken precautions against accidents and emergency situation on tankers, although they have been happened by reason of various elements as human factor, technical failure, major force effect.

Table 1. Precautions at Tanker Ships as Risks [10].

TOPICS	PRECAUTIONS
• FLAMMABILTY	• Naked light and unapproved electrical equipment must not be used anywhere.
• HEALTH HAZARD	• Crewmember must be avoid contact of cargo and cargo's vapor.
• CARGO INFORMATIONS	• Certain cargo information should be hold on board as material safety data sheet.
• MOORING	• Tankers must be all fast with significant and safe mooring area.
• FIRE ON BOARD	• Towing of wires should be ready to use in case of fire on board.
• ACCESS TO SHIP	• Entrance point should be designated as one way for safety and security.
• WEATHER CONDITION	• Crewmember must be check mooring line regularly due to bad weather condition, at the same time needed awareness against gas vapor on windy weather.
• ENGINE AND BOILER ROOM	• They source light. These area should be isolated from cargo area.
• GROUNDING	• Electrically continuous should be provided between shore and tanker with bonding cable against static electric.
• HOT WORK ON BOARD	• Hot work is forbidden without permit from authority.
• TOOL USING FOR SHIP'S MAINTENANCE	• All tools those are used on deck, approved type. They are made of non-spark material.
• ENCLOSED SPACE ON BOARD	• Enclosed space entry is done with permit from authorized officer and master.
• POLLUTION PREVENTION	• Crewmember should be trained for pollution. Pollution prevention equipment must be on board for emergency using.
• NAVIGATION	• Tankers should be navigated as per bridge resource standards with high safe.
• FIRE FIGHTING AND FIRE PROTECTION EQUIPMENT	• Crewmember should be trained about firefighting. All equipments must be ready on board.

3. INCIDENTS ON BOARD

Despite of taken precautions, various incidents and accidents occur on tankers. Precautions, accidents and incidents on tankers are evaluated around a tanker management company in this study.

3.1 Describe of Sampling Tanker Management Company

Sampling Tanker Management Company has established for years in Istanbul. They have 33 several type vessels. 11 vessels of them are tankers. Company owns various department as operation, financing, training, safety, quality and other departments those are needed for a shipping management company. They don't use out source for management and other critical services. They have certificates as safety and quality, those have given by recognized authority worldwide.

3.2 Company Evaluation of Incidents

Company evaluate incidents, accidents and near miss accidents periodical accordance to safety management system and safety culture requirements. Periods are 4 time in working year. It means each incident, accident and near miss accident reports are issued for 3 months as 1st, 2nd, 3rd and 4th quarterly reports.

Result of Incidents are categorized as Lost Workday Case (LWC), Medical Treatment Case (MTC), Permanent Partial Disability (PPD), Restricted Work Case (RWC) and First Aid Case (FAC). This categories are made as per the OCIMF Injury standards.

LWC is an injury which results in an individual being unable to carry out any of his duties or to return to work on a scheduled work shift on the day following the injury unless caused by delays in getting medical treatment ashore.

MTC means that is any work-related loss of consciousness, injury or illness requiring more than first aid treatment by a physician, dentist, surgeon or registered medical personnel under the standing orders of a physician or under the specific order of a physician or if at sea with no physician onboard could be considered as being in the province of a physician.

PPD is any work injury which results in the complete loss, or permanent loss of use, of any member or part of the body, or any impairment of functions of parts of the body, regardless of any pre-existing disability of the injured member or impaired body function, that partially restricts or limits an employees basis to work on a permanent basis at sea.

RWC is an injury which results in an individual being unable to perform all normally assigned work functions during a scheduled work shift or being assigned to another job on a temporary or permanent basis on the day following the injury.

FAC is any one-time treatment and subsequent observation or minor injuries such as bruises, scratches, cuts, burns, splinters. The first aid may or may not be administered by a physician or registered professional [14].

3.3 Analyses of Incidents on Boards

All Incidents, accidents and near miss accidents are analyzed by relevant department in Tanker Management Company. Results of analyses are given as below.

Table 2. Fleet as per cases in 2015

Vessels/Case	LWC	MTC	PPD	RWC	FAC
Tanker Ship 1st	0	0	0	1	2
Tanker Ship 2nd	0	0	0	0	1
Tanker Ship 3rd	0	0	0	0	1
Tanker Ship 4th	1	0	0	0	2
Tanker Ship 5th	1	0	0	0	0
Tanker Ship 6th	1	0	0	0	0
Tanker Ship 7th	1	0	0	0	0
Tanker Ship 8th	0	0	0	0	1
Tanker Ship 9th	0	0	0	0	1
Tanker Ship 10th	0	0	0	0	1
Tanker Ship 11th	0	0	0	0	1

Incidents are shown Table 3 from 2012 to 2014. There is ratio equally. However company own a target. This should be decreased gradually year by year.

Table 3. Incidents of Fleet as per cases yearly (2012-2014)

CASE/YEAR	2012	2013	2014
LWC	6	7	7
MTC	5	7	2
FATALITY	0	0	0
PTD	0	0	0
PPD	0	0	0
RWC	0	0	2

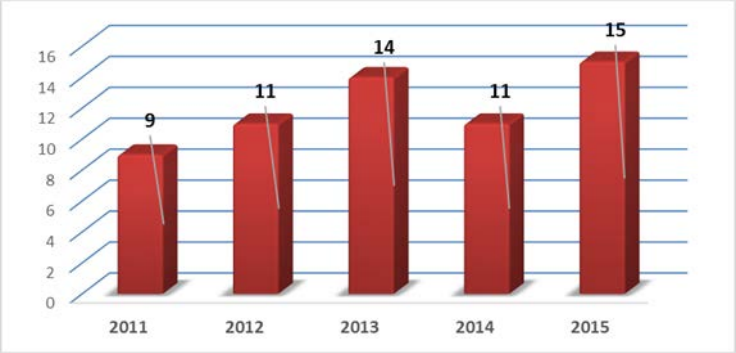

Figure 4. Compare of Incidents as per years (2011-2015)

This graphic at figure 4 shown that is equaled. However it's expected, incidents has been decreased slightly. When case of incidents are evaluated, deck department is the most accident occurred department comparing to other departments. Engine department follows as second effected department. Third is galleys.

Mainly the cases are attributed to lack of awareness, use of PPE which is not suitable for the matter job and action in rush. In addition to the human factors, other contributing factor was weather condition which leaded to some of the accident cases. Company has decided to goal for 2016, incidents will be decreased accordance to company annual report and key performance indicator.

4 CONCLUSION

Tankers carry dangerous goods generally. Relevant countries, various organization and authorities have been issued and applied many regulations and procedures. They content precaution against tanker operations and hazardous of tanker cargoes. They are applied on sail and at terminal seriously.

According to analysis of company data, incident, accident and near miss accident are occurred despite of taken precautions. These incidents own potential high risks on injury, dead, pollution and loose of ship. Shipping companies try to quality service on the sea. They analyses incidents on board for this reason. Incidents and accidents are equal by years. However, their goal is zero accident on their tanker. There is difference between years. Cause of incidents are unconsciousness, carelessness, hurriedness and inefficient crew. It is seen that main factor is human and training correlatively.

In order to ensure safety on tankers, rules and precautions should be clear technically. If crew have inadequate training or there are neglecter people on board, incidents may be happened. Main cause of unexpected status on tanker ships must be investigated. After that, in addition to formal precautions additional precautions are taken according to result. Tanker safety system and training program are suitable for this process to goal of zero incidents on tanker ships.

REFERENCES

[1]. Statista. [Online] Available: http://www.statista.com/statistics/264024/number-of-merchant-ships-worldwide-by-type
[2]. UNCTAD. [Online] Available: http://unctad.org/en/PublicationsLibrary/rmt2015_en.pdf
[3]. Rowbotham, M. *Introduction to marine cargo management*. CRC Press. (2014)
[4]. M. S. Vassiliou, *Historical Dictionaryof the Petroleum Industry*. Scarecrow Press, 2009.
[5]. Marine Connector. [Online] Available: http://maritime-connector.com/ship/saiq-9406166/
[6]. DSF. [Online] Available: http://www.shipfinance.dk/en/SHIPPING-RESEARCH/Tankskibe/Kemikalietankskibe
[7]. IBC, IMO. International Maritime Organization, *International Code for the Construction and Equipment of Ships carrying Dangerous Chemicals in Bulk*. IMO Press, London, United Kingdom, 2013.
[8]. Framo. [Online] Available: http://www.framo.com/default.aspx?pageId=104
[9]. Marine Sight. [Online] Available: http://www.marineinsight.com/types-of-ships/what-are-gas-carrier-ships/
[10]. ICS, O. IAPH. *ISGOTT– international safety guide for oil tankers and terminals* (2006)
[11]. [1] Emecen Kara E.G., Kaçmaz E., (2015), "Determining the Risk in Maritime Container Terminal Operations: Health and Safety Applications", International Conference on Engineering and Natural Sciences (ICENS 2015), Skopje, Macadonia, 15-19 May 2015, pp 15-20.
[12]. SOLAS, IMO. International Convention for the Safety of Life at Sea. London. *International Maritime Organization* (2003)
[13]. Diseselduck. [Online] Available: http://www.dieselduck.info/library/03%20regulatory/ism_info.htm
[14]. OCIMF. *Marine injury reporting guidelines.* London (1997)

Effects of High Temperature on Physical and Mechanical Properties of Polymer Modified Cement Mortars

Yusuf Kaya[1], Ahmet Cavdar[2], Sedat Sevin[2]

Abstract

Concrete is a composite material that may be deformed because of dynamic effects such as overloading and earthquake, as well as environmental and climatic conditions. In this study, it is aimed to increase high temperature resistance of cement mortars due to modified with various liquid polymer materials. Firstly, three different types of polymers are added to cement mortars in five different ratios (0.0%, 5%, 10%,15%, 20%) under dry cure condition. After that it is determined physical and mechanical properties of mortars. It is determined two addition ratios give the best results for each polymer and it is aimed to developed physical and mechanical properties of prepared mortars under high temperature. In this study, Stiren Butadien Rubber (SBR), styrene acrylic co-polymer (SAC), Modified Polycarboxylate-Stiren Butadien Rubber (PSBR) polymers are chosen as polymers. The samples which cured watering twice a day for 28 days, exposed four different temperatures (20 °C (control), 100 °C, 200 °C, 250 °C). It is observed the flexural strength, compressive strength, deflection and change of physical property of concrete under this conditions.

PSBR modified mortars shows the best performance on physical properties. When PSBR is used, depth of penetration of water under pressure and water absorption of mortars, decrease (90%) and (66%), respectively according to control sample. The mortars modified with SBR polymer show the best performance for the highest temperature (250 °C). For the highest temperature, when SBR is used, the flexural strengths of the samples increase (42%), deflections increase (15%) and compressive strength increase (21%)according to control sample.

Keywords: *Polymer Modified Cement Mortar, Physical Properties, High Temperature, Mechanical Properties*

1 INTRODUCTION

Concrete is a composite material that may be deformed because of dynamic effects such as overloading and earthquake, as well as environmental and climatic conditions. Concrete's durability has been studied and investigated during the last 50 years [1]. The studies on improving the durability of concrete by using polymeric material present a promising strategy [2–4].

Polymers could be added to concrete in solid form as fibers [5–7] or in liquid form as in this study. Polymer modified mortar is generally prepared by mixing either a polymer or monomer in liquid form or a dispersible powder with fresh cement mortar [8].

Previous studies have shown that the incorporation of polymers into cement mortar or concrete often improved impermeability such as lower chloride diffusivity [9], improved resistance to permeation of water [10] and eventual improvement in the durability [11,12] of the concrete structure [13].

Another factor that affects the durability of concrete is high temperature. High temperature that leads to durability problems in a structure by creating permanent damage to the structure may cause that structure to go out of service or cause loss of life and property [15].

In this study, the aim was to enhance the high temperature resistance of mortars by means of liquid polymer modification. SBR, PSBR and SCA polymers are chosen as liquid polymers and these are first added to mortars in five different ratios (0% (control), 5%, 10%, 15% and 20%) by mass of cement and the polymer modified mortars are cured over 28 days by watering twice a day in laboratory conditions. Then the physical and mechanical properties of the samples were observed. In the second stage, the high temperature resistance of samples was investigated. The produced samples with these ratios were cured in the same conditions over 28 days and they were exposed to four different temperatures (21 ºC, 100 ºC, 200 ºC and 250 ºC) during one hour. After that, the changes in the mechanical properties of cement mortars were investigated.

[1] *Corresponding author: Gumushane University, Department of Civil Engineering, Gumushane, Turkey.* yusufkaya@gumushane.edu.tr

[2] *Gumushane University, Department of Civil Engineering, Gumushane, Turkey.*

The upper limit of the high temperature was selected as 250 ºC, since most of these polymers melted or deteriorated above 80-110 ºC.

2 MATERIAL AND METHOD

2.1. Material

Three different types of polymer are used in the experimental process (Table 1). These are SBR, PU and MAD polymers.

Table 1. The properties of the polymer used in the experiments

Properties	Stiren Butadien Rubber (SBR)	Polycarboxylate-Stiren Butadien Rubber (PSBR)	Stiren Acrylic Co-Polymer (SAC)
Specific Mass (gr/cm^3)	1.01	1.01-1.04	1.02-1.04
pH Value	8	6	7.5-9
Colour	White	Light Bluish	Bluish White
Alkali Resistance	High	High	Normal

In the experiments, CEM I 42.5 R type cement is used. The experiments are conducted according to EN 196, so CEN-standard sand is used as aggregate in mortars (Table 2).

Table 2. Chemical, Physical and Mechanical Properties of the CEM I 42.5 R Type Cement

Chemical Analysis (%)		Blaine surface (cm^2/g)	4050
SiO_2	21.21	Initial Setting Time (min.)	140
Al_2O_3	3.23	Final Setting Time (min.)	195
Fe_2O_3	1.37	Specific Gravity (g/cm^3)	3.08
CaO	60.44	Le Chatelier Expansion (mm)	2
MgO	3.51	**Strength (MPa)**	
SO_3	2.90	1^{st} Day	17.8
LOI	3.34	2^{nd} Day	28.8
Total	96.00	28^{th} Day	60.5

2.2. Methods

In accordance with the objective of the study, firstly polymer modified cement mortars were prepared with 3 different polymer types (SBR, MAD, PU) and 5 different proportions (0%, 5%, 10%, 15%, 20%). The “reference mortar” consists of 450 g of the cement mixture, 1350 g of graded standard sand, and 225 g of water, and consequently the water/cement ratio is 0.50. While polymer modified mortar is being produced, water is reduced by half of the mass of polymer. After the mixing water is added to the cement-sand mixture, the selected polymer is added to fresh mortar and the mortar is mixed as long as obtained homogeneous mixture. After the molding process, the molds were placed in the moist room at 23±1°C for 24 h and removed at the end of this period, and the mortar prismatic specimens were cured under dry conditions until 28 days. After that the physical properties such as dry specific mass and water absorption are determined. The flexural and compression tests were conducted according to the suggested principles in EN 196. Thus, it is investigated the best performance of polymers ratios. Additionally to observe the depth of penetration of water into polymer additive samples to three difference ratio (0%, 10%, 20%) and 10 cm height, the cylindirical samples were prepared and specimens were cured under dry conditions until 28 days. After the depth of penetration of water of samples was determined according to TS EN12390-8.

In the main part of the study, reference samples and the samples containing polymer are produced for high temperature. These mortars are cured during 28 days by watering twice a day in laboratory condition and then, they are exposed to 4 different (21°C, 100°C, 200°C and 250 ºC) temperatures during 1 hour, and mechanical properties are investigated.

Table 3. Mix design of polymer modified mortars

Polymer Ratio by Mass of Cement	Cement (CEM-I/42.5R) (g)	Standard sand (g)	Polymer content by mass	Water (g)	Water/Cement
0%	450	1350	0	225	0.5
5%	450	1350	22.5	213.75	0.475
10%	450	1350	45	202.5	0.45
15%	450	1350	67.5	191.25	0.425
20%	450	1350	90	180	0.4

3 RESULT AND DISCUSSION

3.1. The Effects of Polymer Type and Content on Specific Mass of Mortars

Because the specific masses of polymers are lighter than those of cement mortars, it was expected that the addition of polymer would decrease the unit masses of the cement mortars. All types of polymer used in this study have closely similar unit masses (1.01-1.11 g/cm^3). Thus the unit masses of the mortars are expected to be similar. The unit mass of control samples is observed as 2.1 g/cm^3. It is seen from Figure 1 that polymer addition decreases the unit mass of mortar. The unit mass of all polymer modified mortars decreased by almost the same amount for 5% addition ratio. The minimum decrease is observed for SBR with a 20% ratio at about 10% as 1.885 g/cm^3 and the biggest decrease is observed for SAC with a 20% ratio at about 32% as 1.425 g/cm^3. PSBR showed the similar behavior with SAC at the same addition ratios, and the specific mass of the 20% addition samples is observed to be at about 30% as 1.486 g/cm^3.

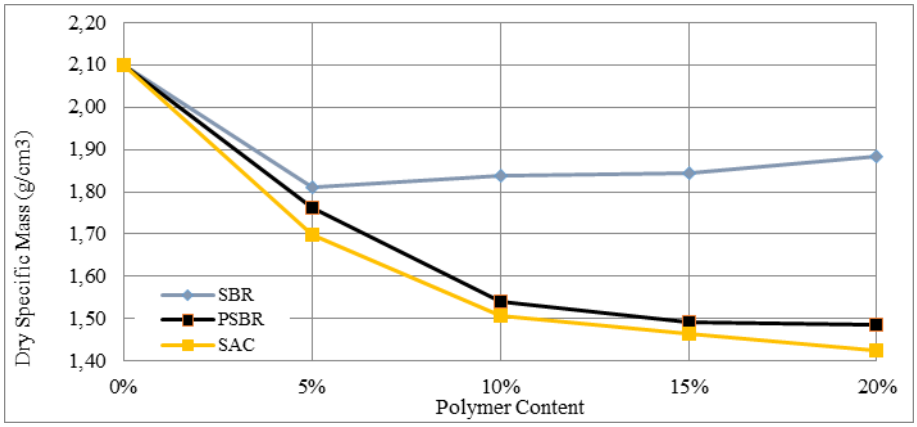

Figure 1. Relationship between polymer content and dry specific mass

3.2. The Effects of Polymer Type and Content on Water Absorption of Mortars

Due to polymers increased workability of the cement mortars, it was expected that the addition of polymer would decrease the water absorption of the samples. It is seen from Figure 2 that polymer addition decreases the water absorption of mortar. It is observed for control samples as 2.5%. For all ratios of SBR and PSBR, similar behaviors are observed. However, for SAC with 10%, 15%, and 20% a constant increase is observed. The biggest decrease is observed for PSBR with a 15% ratio at about 66% as %0.85 and the minimum decrease is observed for SAC and PSBR with a 5% ratio at about 28% as %1.8. The maximum increase is observed for SAC with a 20% ratio at about 72% as %4.3.

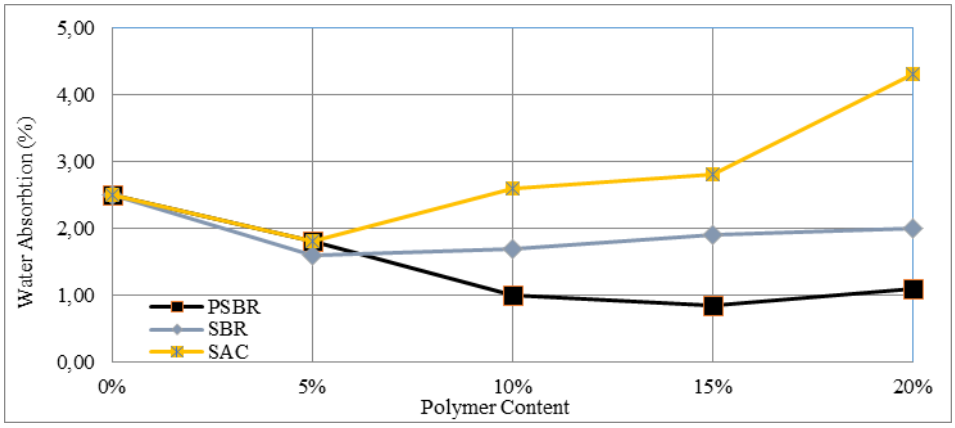

Figure 2. Relationship between polymer content and water absorption

3.3. The Effects of Polymer Type and Content on Depth of Penetration of Water of Mortars

Because polymers increased workability of the cement mortars, cracks in mortar was decreased, so it was expected that the addition of polymer would decrease the depth of penetration of water of the cement mortars. It is seen from Figure 3 that polymer addition decreases the depth of penetration of water of cement mortar. It is observed for control samples as 3.43 cm. The decrease is observed for SBR with a 10% and 20% ratios at about 17% as 2.82 cm and about %80 as 0.71 cm respectively. The biggest decrease is observed for PSBR with a 20% ratio at about 90% as 0.35 cm. When the test started, leaking water was observed from the surface of SAC additive cement mortar, so experimental period was not progress.

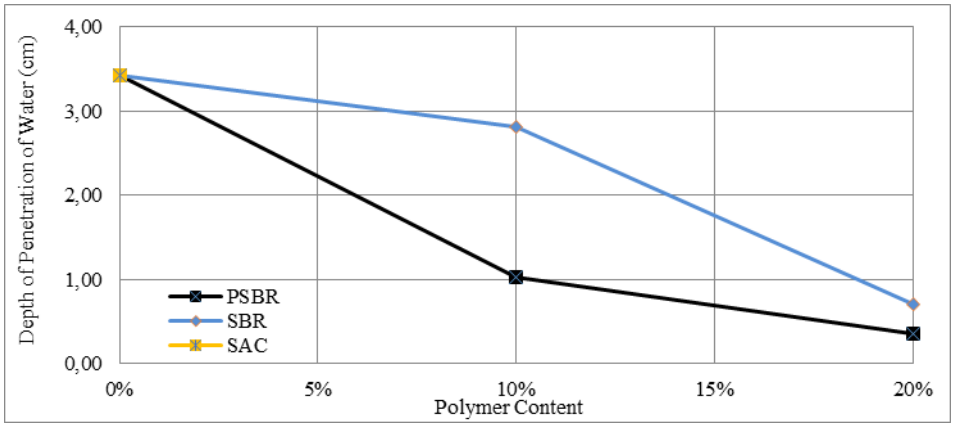

Figure 3. Relationship between polymer content and depth of penetration of water

3.4. Determining Optimum Polymer Content in Terms of both Flexural and Compressive Strengths under Normal Conditions

Generally, with polymer modification, as flexural strength improves, compressive strengths are negatively influenced with regard to the reference condition. It is understood from Figure 4 that each polymer shows the best performance at different addition ratios when flexural and compressive strength are simultaneously taken into consideration.

Figure 4 shows that the highest increase in flexural strength and the smallest decrease in compressive strength are obtained at 5% and 15% addition ratios for the sample with SBR added, although the samples containing PSBR present the best flexural strength of 10-20% by mass of polymer addition. On the other hand, the samples containing SAC show a marginal advantage in both flexural strength and compressive strength with all ratios.

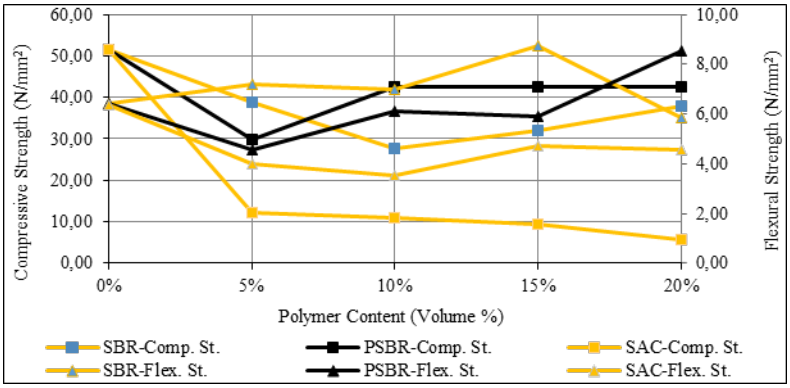

Figure 4. Relationship between compressive strength and flexural strength of polymer mortars for different polymer contents

3.4. The Effects of Polymer Type and Content on Flexural Strength of Mortars under High Temperature

It is seen from Figure 5 that as temperature rises, the flexural strength decreases for all polymer added mortars. For non-additive mortars (control samples), as the temperature increases, the flexural strength decreases. At 100 ºC and 250 ºC, the flexural strength of the control samples decreases by about 1% and 40%, respectively. However, at 200 ºC the flexural strength of control samples increases by about 5%. When SBR polymer additive is used at 15%, the flexural strength of mortar is shown to be 8.72 N/mm^2 under the reference condition and increases by about 35% compared to non-additive mortars. When exposed to different temperatures, the flexural strength of the mortars is observed as 6.31 N/mm^2 under 100 ºC, as 7.85 N/mm^2 under 200 ºC, and finally as 6.63 N/mm^2 under 250 ºC; meanwhile, the flexural strength of the mortars increases 15% under 200 ºC and 72% under 250 ºC compared to control samples. When PSBR polymer additive is used at the 20% ratio, the flexural strength of mortars is revealed to be 8.51 N/mm^2 under the reference condition and about 33% higher than non-additive mortars. When exposed to different temperatures, the flexural strength of the mortar is 5.56 N/mm^2 under 100 ºC, 7.35 N/mm^2 under 200 ºC, and finally 4.62 N/mm^2 under 250 ºC. This means that compared to the same temperatures of 200 ºC and 250 ºC, the properties of the samples with 20% PSBR are higher than those of non-additive samples by about 8% and 20%, respectively. When SAC polymer is used, the flexural strength shows a dramatic decrease. The flexural strength of the mortars with SAC decreases by on average 45% at the reference condition, by about 37% at 100 °C, by about 50% at 200 °C and by approximately 15% at 250 °C compared to the control samples.

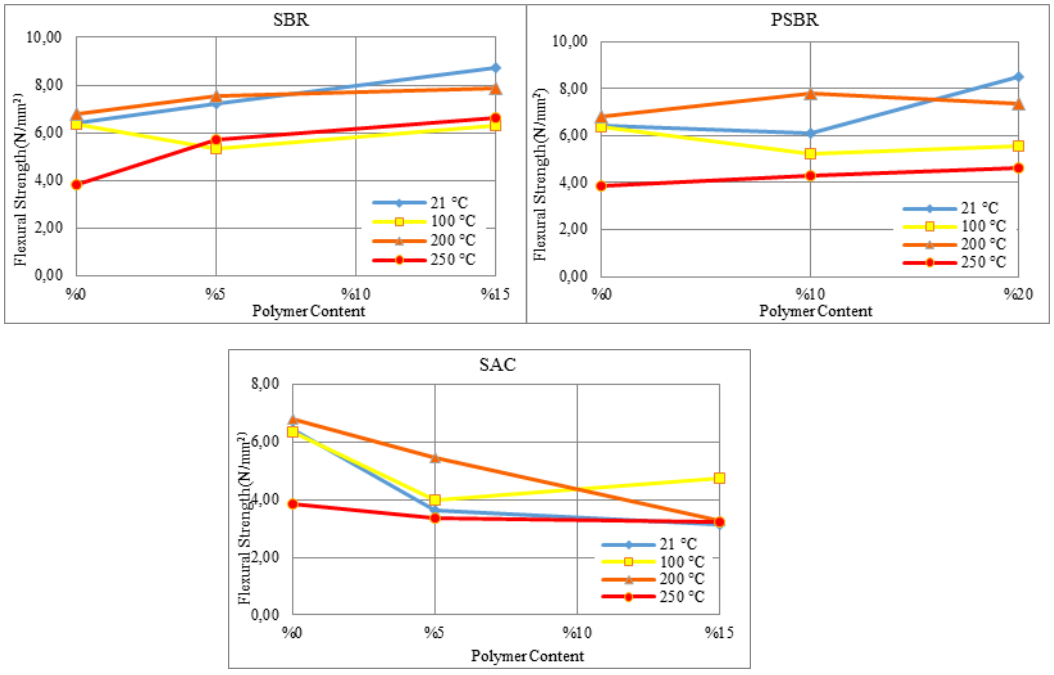

Figure 5. Relationship between polymer content and flexural strength under high temperature for each polymer type (SBR, PSBR, SAC)

3.5. The Effects of Polymer Type and Content on Deflection of Mortars under High Temperatures

While flexural strengths are being tested, the deflections of the beam samples are determined. One important reason for the addition of polymer to mortar is to increase the ductility of mortars so they do not crack under small tensile stress.

It is seen from Figure 6 that, as temperature rises, the deflections decrease for all polymer added mortars. For non-additive mortars, as the temperature increases, a slight decrease in deflections is obtained. The deflection of non-additive mortar decreases by about 6% at 100 °C, and by about 17% at 250 °C. However, almost equal deflections for non-additive mortar are observed at 200 °C compared to the reference condition. Deflections of the mortars with SBR added decrease by, on average, 15% at 100 °C, 10% at 200 °C and 13% at 250 °C compared to the same addition ratio at 21 ºC. However, deflections of the mortars with SBR added increase by about 17% at the reference condition (21 °C), by about 6% at 100 °C, by an average of 5% at 200 °C, and by about 22% at 250 °C compared to control samples at these temperatures. Deflections of the mortars with PSBR added increase by 6% on average at 21 °C and at 100 °C, by about 11% at 200 °C and by approximately 30% at 250 °C compared to non-additive samples at these temperatures. Besides this, deflections of the mortars with PSBR added increase by about 5% at 200 °C and by about 2% at 250 °C, but decrease by on average 6% at 100 °C compared to the same added ratio at 21 ºC. For SAC, the decreases are on average 8% at 200 °C, and about 10% at 250 °C.

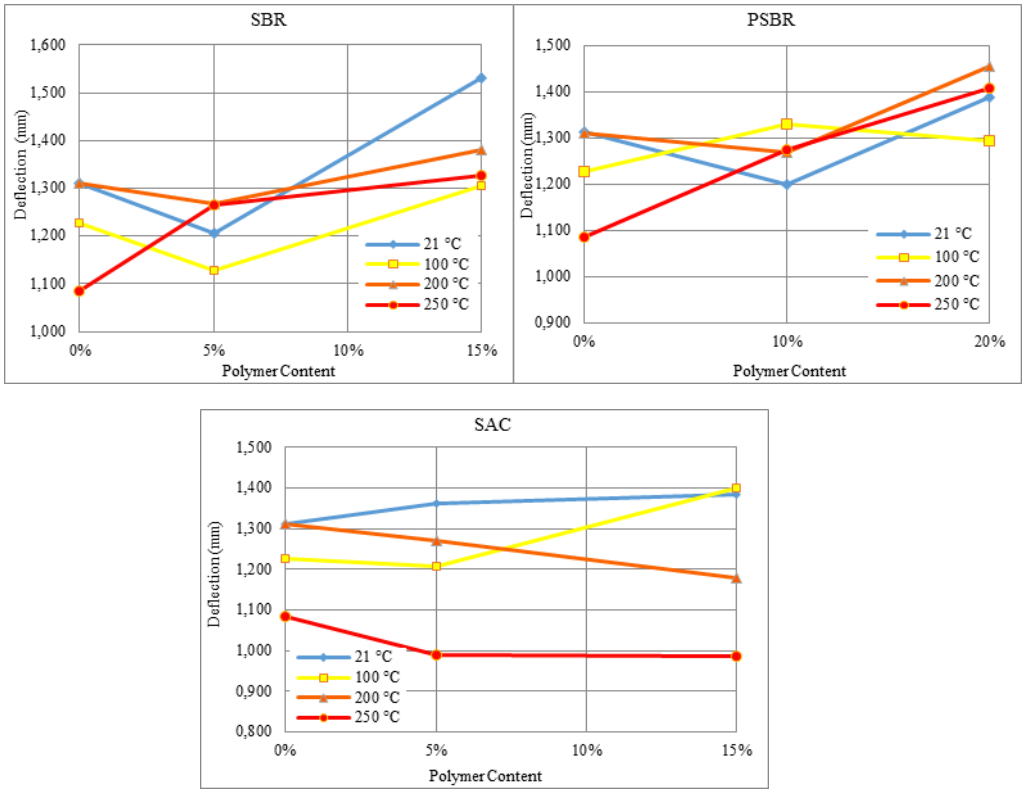

Figure 6. Relationship between polymer content and deflection under high temperature for each polymer type (SBR, PSBR, SAC)

3.6. The Effects of Polymer Type and Content on Compressive Strength of Mortars under High Temperature

Figure 7 show that as temperature rises, the compressive strengths decrease for all polymer added mortars. For non-additive mortars, as the temperature increases, the compressive strengths decrease dramatically, especially at 250 °C. The compressive strength of non-additive mortar decreases by about 12% at 100 °C, by about 1% at 200 °C, and by about 20% at 250 °C. When SBR polymer additive is used in the 5% ratio, compressive strength of mortars is recorded as 38.91 N/mm^2 under the reference condition and decreases by about 24% compared to non-additive mortars. When exposed to different temperatures, the compressive strength of mortars is observed as 35.86 N/mm^2 under 100 ºC, as 48.99 N/mm^2 under 200 ºC and finally as 49.97 N/mm^2 under 250 ºC. In brief, at 250 ºC an increase of approximately 26% is seen compared to the control samples. When PSBR polymer additive is used in the 10% ratio, the compressive strength of the mortars is shown to be about 42.60 N/mm^2 under reference conditions and decreases by about 17% compared to non-additive mortars. When exposed to different temperatures, the compressive strengths of the mortars decrease by about 26% under 100 ºC, and by about 22% under 200 ºC compared to control samples. However, a 3% increase is observed under 250 ºC compared to control samples. When SAC polymer is used, the compressive strength shows a dramatic decrease. The compressive strength of the mortars with SAC

decreases by on average 80% at the reference condition, about 70% at 100 °C, about 75% at 200 °C, and approximately 85% at 250 °C compared to control samples.

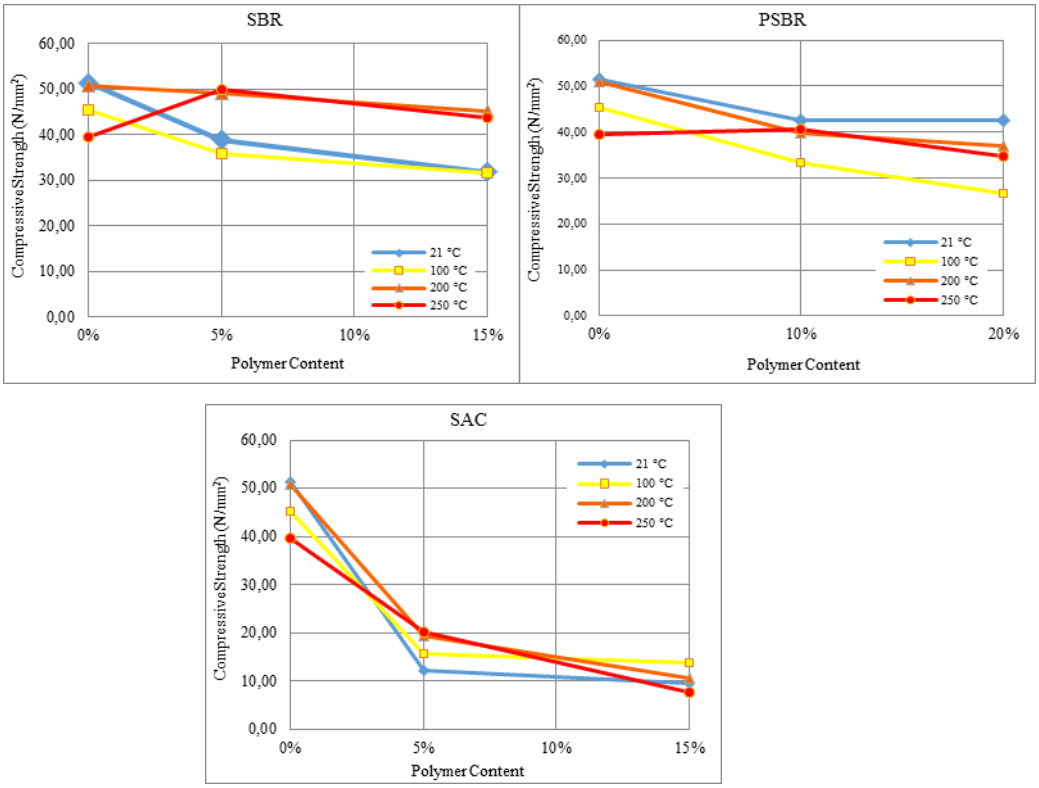

Figure 7. Relationship between polymer content and compressive strength under high temperature for each polymer type (SBR, PSBR, SAC)

4. CONCLUSIONS

This study investigates the effects of high temperatures on the physical and mechanical properties of polymer modified cement mortars. Conclusions drawn from this study are as follows.

- Because the specific masses of polymers are lighter than cement mortars, it the addition of polymer would decrease the unit masses of the cement mortars. Maximum decrease is observed for SAC with a 20% ratio at about 32% compared to control samples.
- Due to polymers increased workability of the cement mortars, the addition of polymer would decrease the water absorption of the samples. The biggest decrease is observed for PSBR with a 15% ratio at about 66% compared to non-additive samples.
- Because polymers increased workability of the cement mortars, cracks in mortar was decreased, so it was expected that the addition of polymer would decrease the depth of penetration of water of the cement mortars. The biggest decrease is observed for PSBR with a 20% ratio at about 90% compared to control samples.
- Polymer modified mortar exposed to high temperatures, an improvement in compressive strength was observed compared to conventional mortars. At 250 ºC heat according to reference samples, it is observed that compressive strength has increased about 21% and 10% by using %5 and %15 addition ratios of SBR, respectively.
- It is also seen that flexural strength of polymer modifies samples has generally increased when compared to the reference samples for the highest heat levels. Especially, flexural strength in the 15% addition ratio of SBR has increased 42% at 250 ºC.
- The study also shows that deflections decrease as heats increase for traditional mortars and polymer modified mortars. As compared to the reference sample at 250 ºC, 15% increase is observed for 5% and 15 % addition ratio of SBR.
- Consequently, High temperature has a negative effect on the mechanical properties of mortar. However, polymer addition improves high temperature resistance of mortars.

ACKNOWLEDGEMENT

This study is funded by Gumushane University (Project No. 13.F5110.02.1). Thanks to Gumushane Cement Factory for materials and laboratory possibilities.

REFERENCES

[1]. Shaker, F.A., El-Dieb, A.S. and Reda, M.M., (1997). Durability of Styren-Butadiene Latex Modified Concrete. Cem Concr Reserach. Vol.27, No.5,pp.711-720.
[2]. Yang, Z., Shi, X., Creighton, A.T., Peterson, M.M., (2009). Effect of styrene - butadiene rubber latex on the chloride permeability and microstructure of Portland cement mortar. Construction and Building Materials Vol. 23, pp. 2283–2290.
[3]. Van Gemert D, Czarnecki L, Maultzsch M, Schorn H, Beeldens A, Łukowski P, et al. (2004) Cement concrete and concrete-polymer composites: two merging worlds. A report from 11th ICPIC congress in Berlin, Cem Concr Compos 2005;27(9):926–33.
[4]. Fowler DW. (1999) Polymers in concrete: a vision for the 21st century. Cem Concr Compos;21(5):449–52.
[5]. Çavdar, A. (2014) Investigation of Freeze-Thaw Effects on Mechanical Properties of Fibre Reinforced Cement Mortars, Composites Part B: Engineering (ISI), Volume 58, Pages 463-472.
[6]. Çavdar, A. (2013) The Effects of High Temperature on Mechanical Properties of Cementitious Composites Reinforced with Polymeric Fibers, Composites Part B: Engineering (ISI),Volume 45, Issue 1, Pages 78-88.
[7]. Çavdar, A. (2012) A Study on the Effects of High Temperature on Mechanical Properties of Fiber Reinforced Cementitious Composites, Composites Part B: Engineering (ISI), Volume 43, Issue 5, Pages 2452-2463.
[8]. Ohama, Y., (1995). Hand book of polymer - modified concrete and mortars properties and process technology. Noyes Publications, New Jersey, USA.
[9]. Zhong, SY., Shi, ML., Chen, ZY., (2002). The AC response of polymer-coated mortar specimens. Cem Concr Res Vol.32, No.6, pp. 983–7.
[10]. ACI Commitee 548, (1997). Guide for the Use of Polymers in Concrete, ACI 548.1R-97, 26 pp.
[11]. Al-Zahrani, MM., Maslehuddin, M., Al-Dulaijan, SU., Ibrahim, M., (2003). Mechanical properties and durability characteristics of polymer and cement-based repair materials. Cem Concr Compos. Vol.25,No.4-5, pp.527-37.
[12]. Ohama, Y., (1996). Polymer-based materials for repair and improved durability: Japanese experience. Constr Build Mater Vol.10,No.1,pp.77–82.
[13]. Kong, XM., Wu, CC., Zhang, YR., Li, JL., (2013). Polymer-modified mortar with a gradient polymer distribution: Preparation, permeability, and mechanical behavior. Construct and Building Materials. Vol.38, pp. 195,203.
[14]. Aydın, S. ve Baradan, B., (2003). "Yüksek Sıcaklığa Dayanıklı Harç Geliştirilmesi", TMMOB İnşaat Mühendisleri Odası, 5. Ulusal Beton Kongresi, İstanbul.
[15]. Çavdar, A., Sevin, S., Kaya, Y., Bingöl, Ş., (2013).The Effects of Cure Conditions on Mechanical Properties of Polymer Modified Cement Mortars, The First International Symposium on Engineering, Artificial Intelligence and Applications (ISEAIA), Girne, North Cyprus.

The Physical Properties of Polymer Modified Mortars and Freeze-Thaw Effects

Sedat Sevin[1], Ahmet Cavdar*[2], Yusuf Kaya[1]

Abstract

In this study, it is aimed to increase physical and mechanical properties of cement mortars by means of polymer addition. In addition to, freeze-thaw resistance of cement mortars is observed depend on polymer addition ratios. In this study, Stiren Butadien Rubber (SBR), Stiren Butadien and modified polycarboksilat rubber (PSBR), Modified Acrylic Dispersion (MAD) polymers are chosen as polymers. Firstly, three different types of polymers are added to cement mortars in five different ratios (0.0%, 5%, 10%, 15%, 20%) and cured watering twice a day for 28 days. Then, physical properties of mortars are observed. Secondly, the samples which cured watering twice a day for 28 days, exposed three different freeze-thaw cycles (0, 100, 200). It is observed the flexural strength, compressive strength and deflection under this condition.

It is concluded that each polymer contributes physical properties of mortars. All polymer additions contribute to physical properties. Especially, permeability of mortars dramatically decreases about 90% thanks to polymer addition. The mortars modified with SBR polymer show the best performance for the highest freeze-thaw cycle (200).

Keywords: *Polymer Modified Concrete, Freeze-Thaw Effect, Stiren Butadien Rubber, Physical Properties*

1. INTRODUCTION

Concrete may be damaged because of various environmental effects throughout its service life. These effects may physical, chemical, physico-chemical or mechanical. The performance of the concrete reduces due to these environmental effects, its function and strength completely can lose prior to project life. Repeated freeze-thaw effect of concrete is one of the physical effects. The materials, environmental conditions, humidity can increase damage as a result of freeze-thaw (ACI 201-2R, 1992). Concrete is a heterogeneous material including aggregate, cement and water. All components of the concrete have a gapping structure. Therefore, under repetitive freeze-thaw effect concrete compressive strength can be reduced by freezing and expanding of the water filled gaps (Baradan et al., 2002; Baradan et al., 2010; Öztütüncü, 1992; Türkmen, 1997). The harmful effect of freeze-thaw can be reduced thanks to polymer additive materials (Akkaya Özden, 2010).

Recent years, polymers have widely used as additive materials in cement mortars thanks to developments in polymer technology. Polymer additives increase the physical and mechanical properties of the concrete. In addition, polymer additives contribute concrete for durability by increasing resistance of concrete against such as freeze-thaw cycles, acid attack and sulphate attacks (Fowler, 1999; Ohama, 1997)

In this study, it is aimed to increase physical and mechanical properties of cement mortars by means of polymer addition. In addition to, freeze-thaw resistance of cement mortars is observed depend on polymer addition ratios. In this study, Stiren Butadien Rubber (SBR), Polycarboxylate Modified Stiren Butadien Rubber (PSBR) and Modified Acrylic Dispersion (MAD) polymers are chosen as polymers. Firstly, three different types of polymers are added to cement mortars in five different ratios (0.0%, 5%, 10%, 15%, 20%) and cured watering twice a day for 28 days. Then, physical properties of mortars are observed. Secondly, the samples which cured watering twice a day for 28 days, exposed three different freeze-thaw cycles (0, 100, 200). It is observed the flexural strength, compressive strength and deflection under this condition.

Then, physical properties of mortars are observed. Secondly, the samples which cured watering twice a day for 28 days, exposed three different freeze-thaw cycles (0, 100, 200). It is observed the flexural strength, compressive strength and deflection under this condition.

It is concluded that each polymer contributes physical properties of mortars. All polymer additions contribute to physical properties. Especially, permeability of mortars dramatically decreases about 90% thanks to polymer addition. The mortars modified with SBR polymer show the best performance for the highest freeze-thaw cycle (200).

[1] *Gumushane University, Department of Civil Engineering, Gumushane, Turkey.*

[2]*Corresponding author: Gumushane University, Department of Civil Engineering, Gumushane, Turkey.*

2. MATERIALS AND METHODS

2.1. Material

Three different types of polymer are used in the experimental process. These are SBR, MAD and PSBR polymers. Some properties of these fibers presented in (Table 1).

Table 1. The properties of the polymer used in the experiments

Material	SBR	MAD	PSBR
Specific Mass (kg/l)	1,005-1,025	1,08	1,01-1,04
pH Value	8-12	7-10	6
Colour	White	White	Light Bluish
Alkali Resistance	High	High	High

In the experiments, CEM I 42.5 R type cement is used. The experiments are conducted according to EN 196, so CEN-standard sand is used as aggregate in mortars.

2.2 Methods

In accordance with the objective of the study, polymer modified cement mortars are prepared with three different polymer types and five different proportions (Table 2).

Table 2. Mix design of thirteen different fiber reinforced mortars

Fiber ratio by volume	Cement (g)	Sand (g)	SBR, PSBR and MAD (g)	Water (g)	W/C
0%	450	1350	0	225	0,5
5%	450	1350	22,5	213,75	0,475
10%	450	1350	45	202,5	0,45
15%	450	1350	67,5	191,25	0,425
20%	450	1350	90	180	0,4

The flexural and compression tests were conducted according to the suggested principles in EN 196. The “test mortar” consists of 450 g of the cement mixture, 1350 g of graded standard sand, and 225 g of water, and consequently the water/cement ratio is 0.50. While polymer modified mortar is being produced, water is reduced by half the amount of polymer. After the mixing water is added to the cement-sand mixture, the selected polymer is added to fresh mortar and the mortar is mixed as long as obtained homogeneous mixture. After the molding process, the molds (with the mortars in them) were placed in the moist room at 23±1°C for 24 h and removed at the end of this period, and the mortar prismatic specimens were cured under twice a day cure condition until 28 days. After that the physical properties such as dry specific mass and water absorption are determined. The flexural and compression tests were conducted according to the suggested principles in EN 196. Thus, it is investigated the best performance of polymers ratios. Additionally to observe the depth of penetration of water into polymer additive samples to three difference ratio (0%, 10%, 20%) and 10 cm height, the cylindrical samples were prepared and specimens were cured under dry conditions until 28 days. After the depth of penetration of water of samples was determined according to TS EN12390-8.

The freeze–thaw tests were conducted according to Turkish Standard TS 699. The samples were subjected to three different freeze–thaw cycles (zero, 100 and 200), and mechanical properties are investigated. As the maximum number of freeze–thaw cycles chosen was 200, visible deteriorations occurred in the samples.

3. RESULTS AND DISCUSSIONS

3.1. The Effects of Polymer Type and Content on Unit Mass of Mortars

When polymers which specific mass about 1.05 g/cm^3 is lower than mortar 2.1 g/cm^3 is added to mortar, it is expected that the mortar’s unit mass is decreases. It is seen that MAD and PSBR presents similar results to SBR with 5% ration. The unit mass

of mortar decreases down to roughly 1.80 g/cm^3 with the addition of 5% by volume of SBR, PSBR and MAD. All ratios of SBR and MAD similar behavior is observed. But, for PSBR with 5%, 10%, 15%, 20% constant decrease is observed. The biggest decline is observed with 29% for PSBR with 20% ration (Fig 1).

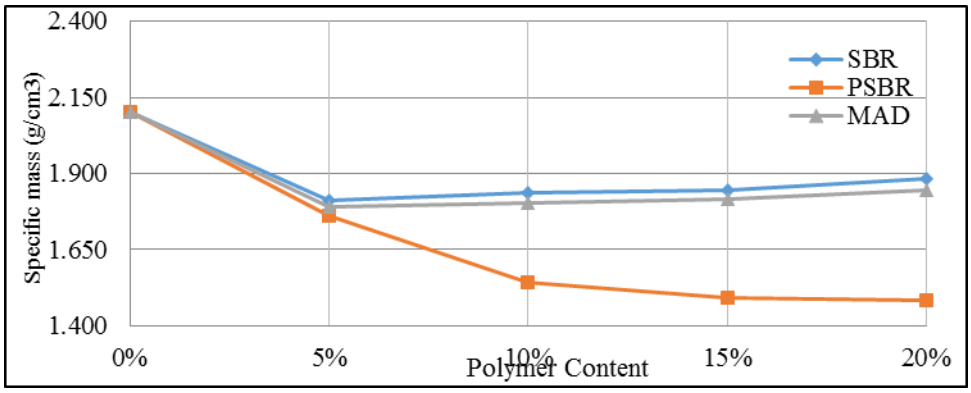

Figure 1. Relationship between polymer content and specific mass

3.2. The Effects of Polymer Type and Content on Depth of Penetration of Water of Mortars

It is seen from Figure 2 that polymer addition decreases the depth of penetration of water of cement mortar. It is observed for control samples as 3.43 cm. The decrease is observed for SBR with a 10% and 20% ratios at about 17% as 2.82 cm and about %80 as 0.71 cm respectively. The biggest decrease is observed for PSBR with a 20% ratio at about 90% as 0.35 cm. MAD polymer additive show same behavior with PSBR additive. While polymers increased workability of the cement mortars, cracks in mortar was decreased, so it was expected that the addition of polymer would decrease the depth of penetration of water of the cement mortars.

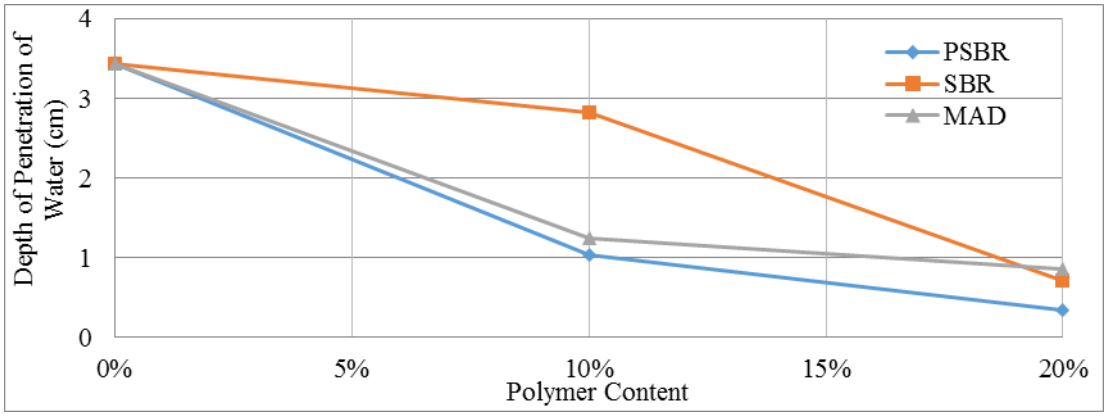

Figure 2. Relationship between polymer content and depth of penetration of water

3.3. The Effects of Polymer Type and Content on Water Absorption of Mortars

Due to polymers increased workability of the cement mortars, it was expected that the addition of polymer would decrease the water absorption of the samples. It is seen from Figure 3 that polymer addition decreases the water absorption of mortar. It is observed for control samples as 2.5%. For all ratios of SBR and PSBR, similar behaviors are observed. The biggest decrease is observed for PSBR with a 15% ratio at about 66%.

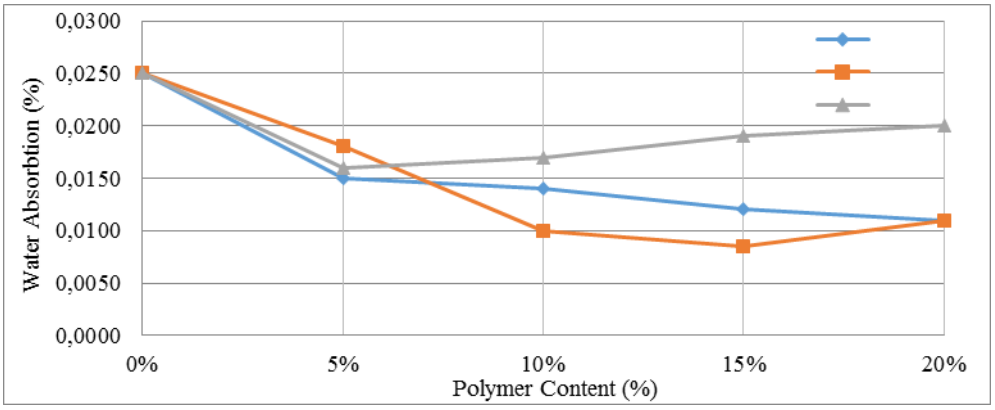

Figure 3. Relationship between polymer content and water absorption

3.4. The Mechanical Properties of the Polymer-Modified Mortars under Repetitive Freeze–Thaw Effects

3.4.1 The Effects of Polymer Addition on Deflections of Cement Mortars under Repetitive Freeze–Thaw Effect

The relationship between deflection and polymer ratio is presented in Figure 4. Deflections of the reference samples and after 100 and 200 cycles are measured as 1.200, 1.074 and 0.766 mm, respectively. All mortars with PSBR show almost the same deflection of about 1.200 mm for all cycles and about 57% higher than the reference for 200 cycles (0.766 mm). The deflection of all mortars modified with SBR increases for 100 cycles range from 5% to 13%. Similarly, an increase is noted at the end of 200 cycles, from 26% to 50%. Modified mortars with MAD show a positive effect for all three cycles.

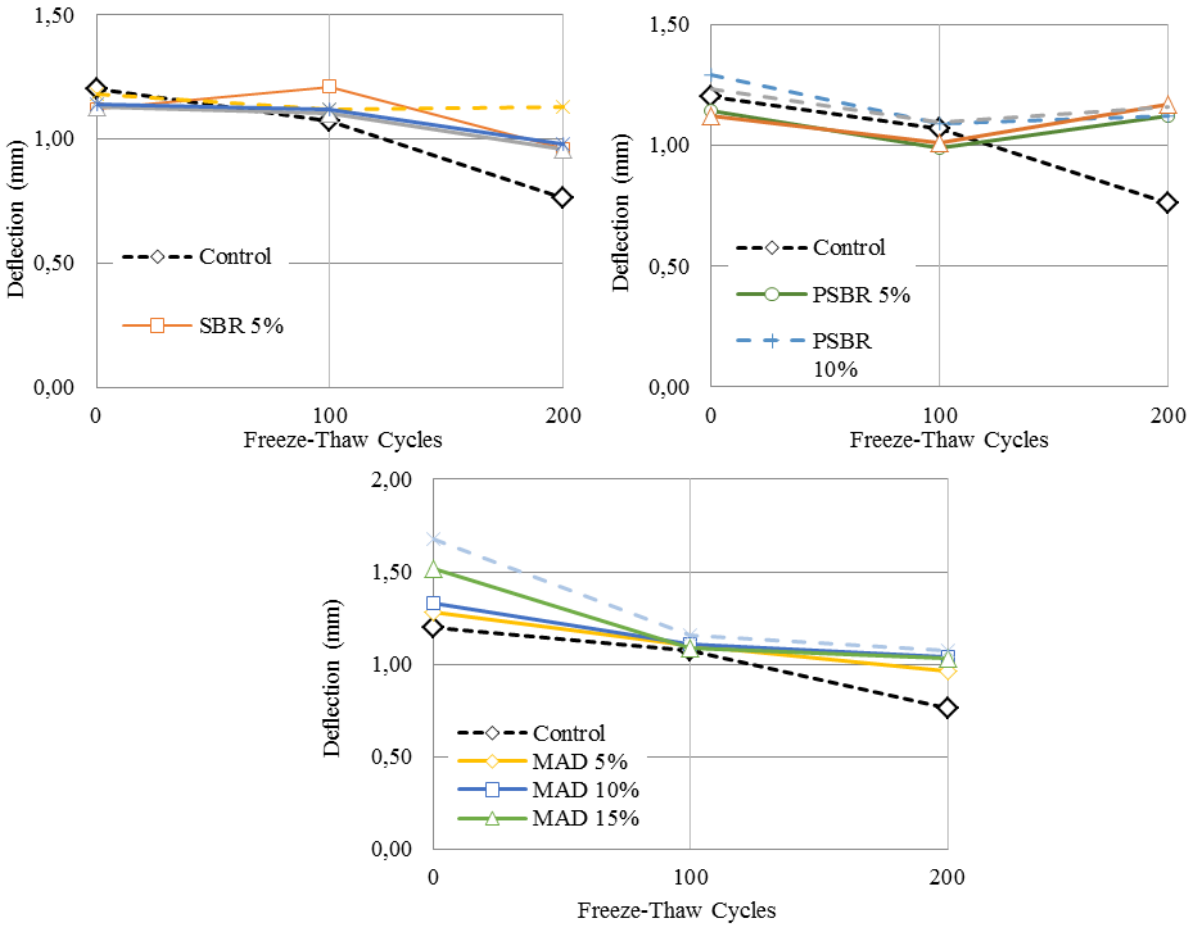

Figure 4. Relationship between polymer ratios and deflections of the mortars under freeze–thaw effects.

3.4.2. The Effects of Polymer Addition on Flexural Strengths of Cement Mortars under Repetitive Freeze–Thaw Effect

When the effects of freeze–thaw cycles on the flexural strength of the polymer-modified mortars were investigated, it was seen that, as the number of freeze–thaw cycles increased, the flexural strengths of the mortars decreased. However, the polymer-modified mortars showed better comparative performance than non-polymer ones (Fig. 5).
When SBR polymer additive is used at 15% ratio, the flexural strength of mortars is noted as 6.35 N/mm^2 for zero cycles, 5.74 N/mm^2 for 100 cycles and finally 5.77 N/mm^2 for 200 cycles. When MAD polymer additive is used at 20% ratio, the flexural strengths of mortars are observed as 7.28 N/mm^2 for 100 cycles and 5.44 N/mm^2 for 200 cycles. When all the ratios of PSBR additive are used at 100 cycles, the flexural strength of mortars is measured at nearly the same level, at about 4.48-4.78 N/mm^2.

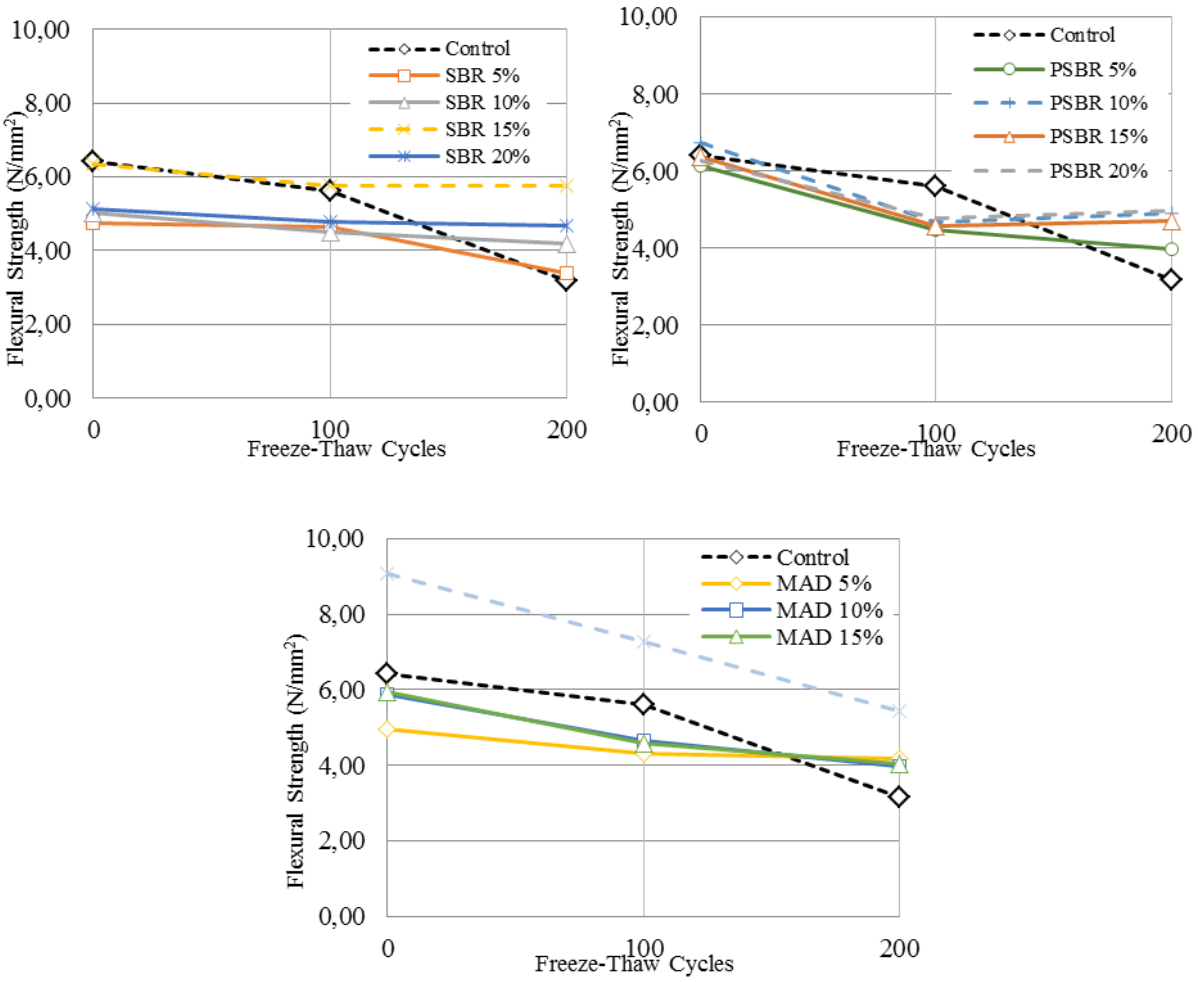

Figure 5. Relationship between polymer ratios and flexural strengths of the mortars under freeze–thaw effects

3.4.3. The Effects of Polymer Addition on Compressive Strength of Cement Mortars under Repetitive Freeze–Thaw Effect

The compressive strength dramatically decreases starting from the 100th freeze–thaw cycles for the samples that were non-modified (Fig. 6). However, the strength loss was less for polymer-modified mortars than for the control samples. Although the samples with SBR, PSBR and MAD generally had less compressive strength than the control samples, the strength loss percentages in the modified mortars were less than in the control samples. While the compressive strength of the reference samples is measured at about 50 N/mm^2 for both zero cycles and 100 cycles, it is measured about 30% lower than the reference of zero cycles, at 37.58 N/mm^2 for 200 cycles.

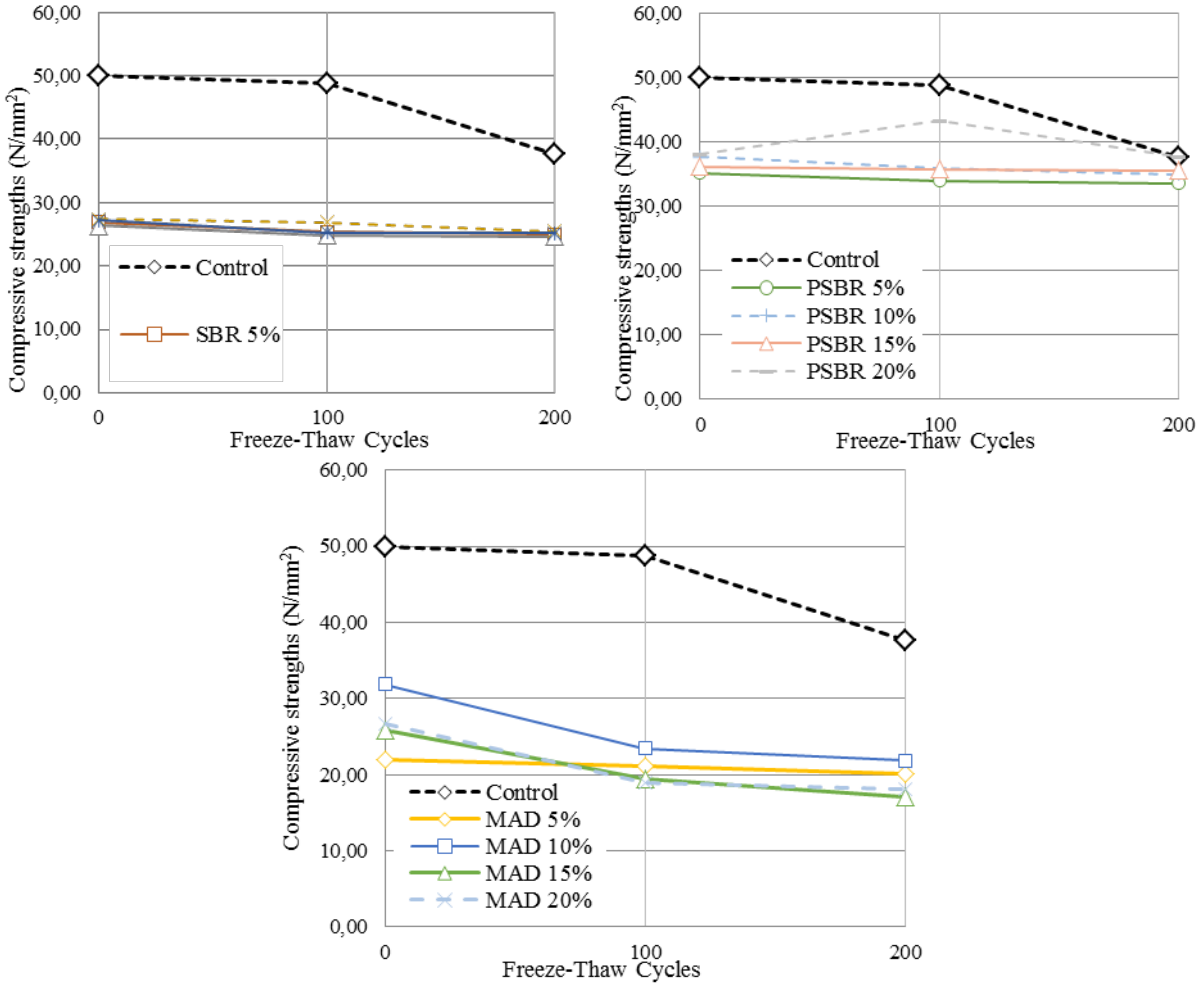

Figure 6. Relationship between polymer ratios and compressive strengths of the mortars under freeze–thaw effects.

4. CONCLUSIONS

This study investigates the effects of high temperatures on the physical and mechanical properties of polymer modified cement mortars. Conclusions drawn from this study are as follows.

- When polymer which specific masses are rather lower than mortar are added to mortar, the mortar's unit mass is decreases. SBR and PSBR show similar behavior in all ratios. It is seen that 20% SBR and MAD polymers addition decreases unit mass 10-15%, however PSBR decreases dramatically (29%).

- Due to polymers increased workability of the cement mortars, the addition of polymer would decrease the water absorption of the samples. The biggest decrease is observed for PSBR with a 15% ratio at about 66% compared to non-additive samples.

- Because polymers increased workability of the cement mortars, cracks in mortar was decreased, so it was expected that the addition of polymer would decrease the depth of penetration of water of the cement mortars. The biggest decrease is observed for PSBR with a 20% ratio at about 90% compared to control samples.

- All mechanical properties of the samples decline under repetitive freeze–thaw effects. However, the polymer-modified samples presented better performance than the non-modified ones.

- It was observed that, even though the flexural strengths of the polymer-modified mortars were less than that of the control samples prior to freeze–thaw cycles, the modified mortars were higher after 200 freeze–thaw cycles.

ACKNOWLEDGEMENT

This study is funded by Gumushane University (Project No. 13.F5110.02.1). Thanks to Gumushane Cement Factory for materials and laboratory possibilities.

REFERENCES

[1]. ACI Commitee 201, 1992. Guide to Durable Concret, ACI 201.2R-92, 39 pp.
[2]. Akkaya Özden, Ç., (2010). Durability of Polymer Concrete under Freeze-Thaw, University of Namık Kemal, Tekirdağ.
[3]. Baradan, B., Yazıcı, H., Ün, H., (2002). Durability of Reinforced Concrete Construction. D.E.Ü. Müh. Fak. Yayın No 298, İzmir.
[4]. Baradan, B., Yazıcı, H., Ün, H., (2010). Durability of Concrete and Reinforced Concrete Construction. Türkiye Hazır Beton Birliği, İstanbul
[5]. Fowler, D.W., "Polymers in Concrete: A Vision for the 21st Century", Cement and Concrete Composites, V.21, pp. 449-452, 1999.
[6]. Ohama, Y., "Recent Progress in Concrete – Polymer Composites", Advanced Cement Based Materials, V.5, pp. 31-40, 1997.
[7]. Öztütüncü, G.H., (1992) The Effect of light weight aggregate fraction on the freezing-thawing resistance of semi-light weight concretes İTÜ FBE İstanbul
[8]. Türkmen, İ., (1997). Investigation of Durability Freezing Thawing of Lightweight Concrete Manufactured with Van-Erciş Pumice, Van, Turkey.

ICENS
INTERNATIONAL CONFERENCE ON ENGINEERING AND NATURAL SCIENCES
24-28 May 2016 /Sarajevo

Effect of Heat Input on Microstructure of Fe-Cr-W-B-C Powder Coating Prepared by Plasma Transferred Arc Welding

Turan Gurgenc[1], *Cihan Ozel*[2]

Abstract

In present paper, FeB, FeW and FeCrC powders with about 38 µm size were blended in chemical composition of (wt.%) 80FeCrC -10FeW-10FeB. Surface of AISI 1020 was coated by using these powder composition with Plasma Transferred Arc (PTA) welding process To achieve different heat inputs, experimental samples were coated at two different currents (120A, 140A) and two different travel speeds (0.1 m/min, 0.15 m/min). The microstructure characterization of the coated samples were made by OM, SEM/EDS/WDX and XRD analysis. For determining the mechanical properties of coating microhardness tester was used. Results show that the coating layers consists of dendritic microstructure in high heat input. The maximum microhardness is 1668 HV and maximum coating depth is 2001 µm.

Keywords: *PTA Coating, Fe-Cr-W-B-C Powders, Microstructure, Microhardness, Heat Input.*

1. INTRODUCTION

Wear and corrosion causing undesirable deterioration and material losses reduces the life of the machine parts [1]-[3]. Coating of the materials surface with high wear and corrosion resistant materials, both economically and technologically, is the most efficient method used to increase moving metallic parts of the life and performance [4], [5].

Modifying the surfaces of the materials with melting of metallic powders to protect from harsh environment by using method such as plasma transferred arc welding (PTAW), tungsten inert gas welding (TIGW), gas tungsten arc welding (GTAW), laser welding and electric arc welding have been often used in the industry [6]-[9]. Coating with PTA welding process has advantages compared to other fusion welding methods such as high temperature (from 20000 to 30000 °C), high energy input, low thermal input and lower fabrication costs [3], [10], [11].

Iron-based alloys are frequently used for protection in components, which exposed to high wear and corrosion [10], [12], [13]. High chromium content of coatings have perfect wear and corrosion resistance. This is because of M_7C_3, $M_{23}C_6$ (M=Fe, Cr) carbides in the structure. M_7C_3 (M=Fe, Cr) carbides are kwon high hardness, wear and corrosion resistant structures [4], [14]-[16]. Microstructure of the coating made of Fe-Cr-C alloy shows hypereutectic, hypoeutectic and eutectic structures depending on the chemical composition and solidification speed [12], [17]-[19]. Coating the surface of materials with containing W and B alloys increase the hardness and wear resistance because of the borides, WC, $M_7(C,B)_3$ and $M_{23}(C,B)_6$ boride carbide structures formed on the surface [20]-[23]. In many studies it was investigated that changes in heat input effected microstructure [24], [25].

In this study, AISI 1020 steel surface was coated Fe-Cr-W-B-C alloy with different heat inputs by using PTA welding method and microstructure of the coating layers were analyzed by using OM, SEM/EDS/WDX and XRD techniques. Microhardness was determined for investigation of coating layers hardness.

2. MATERIAL AND METHOD

In present study, low carbon steel AISI 1020 was used as substrate and was prepared as seen Figure 1. For alloying materials about 38 µm size FeCrC, FeW and FeB powders were used. The substrate material and alloying powders chemical composition are listed in Table 1. Before PTA coating, substrates were cleaned with air spray and acetone. After that substrates were dried in laboratory owen at a temperature of 60 °C for 30 min. Alloying powders were dried in to furnace at 110 °C for 1h and blended chemical composition of (wt.%) 80FeCrC -10FeW-10FeB with mechanical blender at 150 rpm for 1h and were placed in to the substrate groove by alcohol. For each coating sample total weight of 3g alloy powders mixture were used. To resolve the moisture, experimental samples placed in to a furnace and were held at a temperature of 100 °C for

[1] *Firat University, Department of Automotive Engineering, 23119, Elazig, Turkey, tgurgenc@firat.edu.tr*

[2] *Firat University, Department of Mechanical Engineering, 23119, Elazig, Turkey, cozel@firat.edu.tr*

1h. Samples were cooled to room temperature. For coating method PTA welding is used and samples were coated at parameters seen in Table 2.

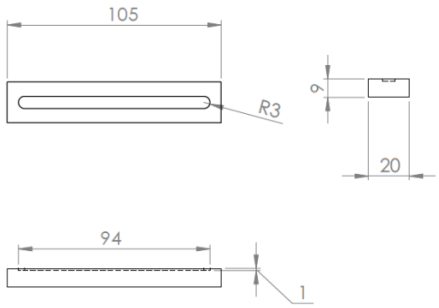

Figure 10. Dimensions of substrate material (all dimensions in mm).

Table 1 Chemical composition (wt.%) of the AISI 1020, FeCrC, FeB and FeW

Material	Cr	B	C	P	Si	W	Mn	Fe
AISI 1020	-	-	0,2	0,02	0,286	-	0.356	Bal.
FeCrC	66.77	-	7.95	0.007	0.55	-	-	Bal.
FeW	-	-	0.045	0.05	0.52	79.26	-	Bal.
FeB	-	18.22	0.3	0.05	0.5	-	-	Bal.

Table 2 PTA coating parameters

Sample	S1	S2	S3	S4
Current	120A	140A	120A	140A
Travelling speed	0.15 m/min.	0.15 m/min.	0.1 m/min.	0.1 m/min.
Voltage	18-19V			
Plasma gas flow (Ar)	0.5 lt/min.			
Shield gas flow (Ar)	8 lt/min.			
Diameter	2 mm			
Heat input	0,475 kj/mm	0,585 kj/mm	0,713 kj/mm	0,878 kj/mm

To analyzing the microstructure of coating layers, coated samples were cut from the center in perpendicular direction to the coating surface. Microstructural samples were polished 60, 120, 180, 240, 400, 600, 800, 100, 1200 mesh SiC sandpaper and diamond paste respectively. The polished microstructure samples surfaces were cleaned with alcohol and dried. After that they were etched for 1 min with 15g FeCl3, 15 ml HCl and 100 ml distilled water mixture. The microstructures of the surface coated samples were characterized by optical microscope (OM) and scanning electron microscope (SEM). Alloying elements compositions and forms of structure were determined by energy dispersive X-ray analysis (EDS), wavelength-dispersive X-ray analysis (WDX) and X-ray diffraction (XRD). For determining the microhardness of layers microhardness test machine was used.

3. RESULTS AND DISCUSSION

3.1 Microstructure

Effect of heat input and process parameters on coating thickness of samples coated by PTA method are given in Table 3. As seen in figure 2, the coated surface did not find any cracks or porosity. Also SEM photographs, given in figure 3, show that no crack were occurred in interface region and melted powders metallurgically bonded well to the substrate material in all samples. As seen in figure 3, due to rapid cooling martensitic structures are formed in the region just below the coating layer of all samples and in all samples the base material is dispersed into the coating layer by melt. The results show that the coating thickness and width increases with increasing heat input. These results are in agreement with the research studies in the literature [24].

Table 3 Coating layer dimensions

Sample	S1	S2	S3	S4
Coating layer width (µm)	5600	6185	6307	7641
Coating layer depth (µm)	1874	1913	2000	2001

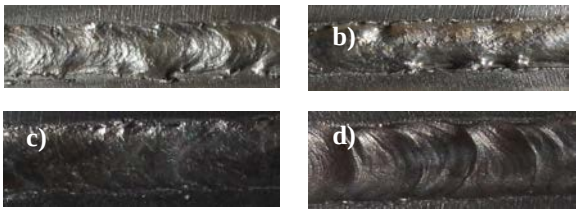

Figure 2. Macro image of coating surface a) S1, b) S2, c) S3 and d) S4.

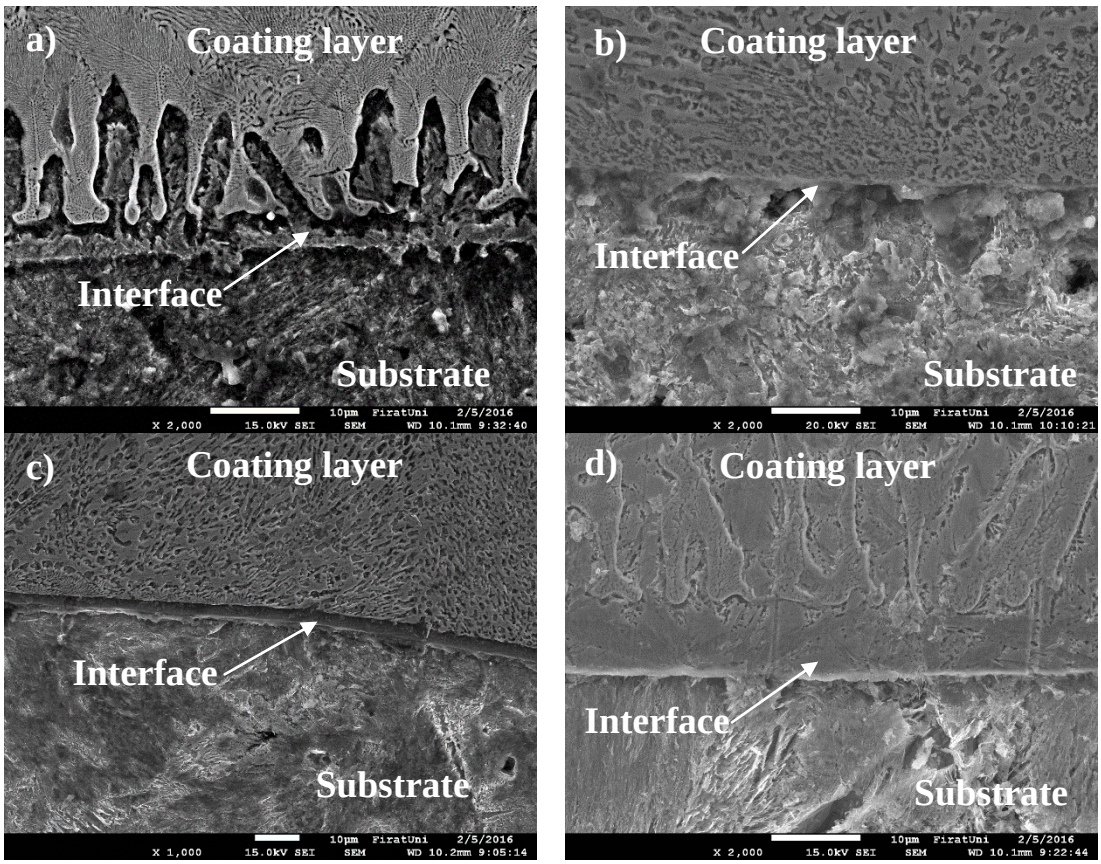

Figure 3. Coating interface layer SEM photographs of samples a) S1 (x2000), b) S2 (x2000), c) S3 (x1000) and d) S4 (x2000).

The effect of different heat inputs on microstructure of the coating layers are shown by OM in figure 4. and by SEM in figure 5. As seen in figure 4.d., S4, which coated with low travelling speed and high heat input microstructure is dendritic with the effect of rapid cooling and fast solidification. The other samples are consist of hexagonal and strip-shaped structures. When the XRD analysis examined, which is given in figure 6, hexagonal and strip-shaped structures was determined that M_7C_3 (M=Cr, Fe, W) carbides. These structures were seen in similar researches [6], [17], [26].

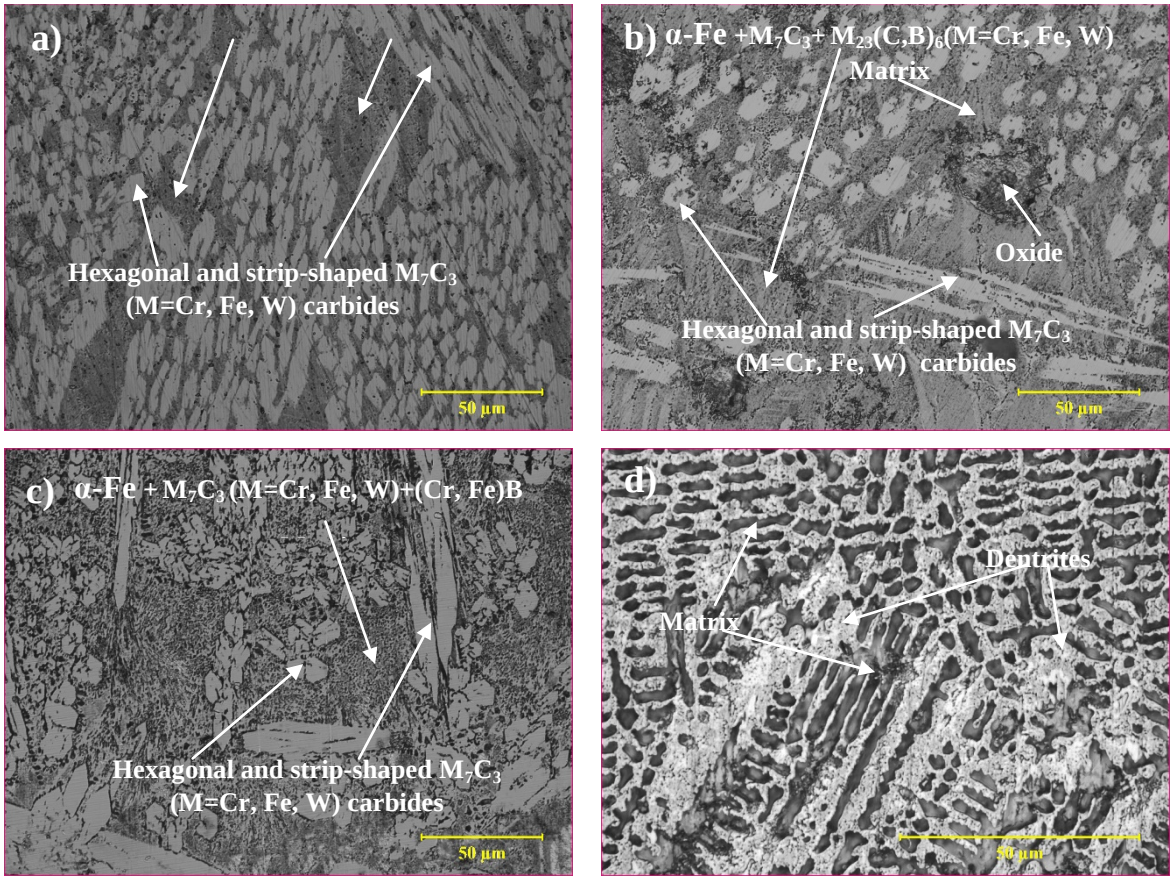

Figure 4. Coating layer OM photographs of samples a) S1 (x500), b) S2 (x500), c) S3 (x500) and d) S4 (x1000).

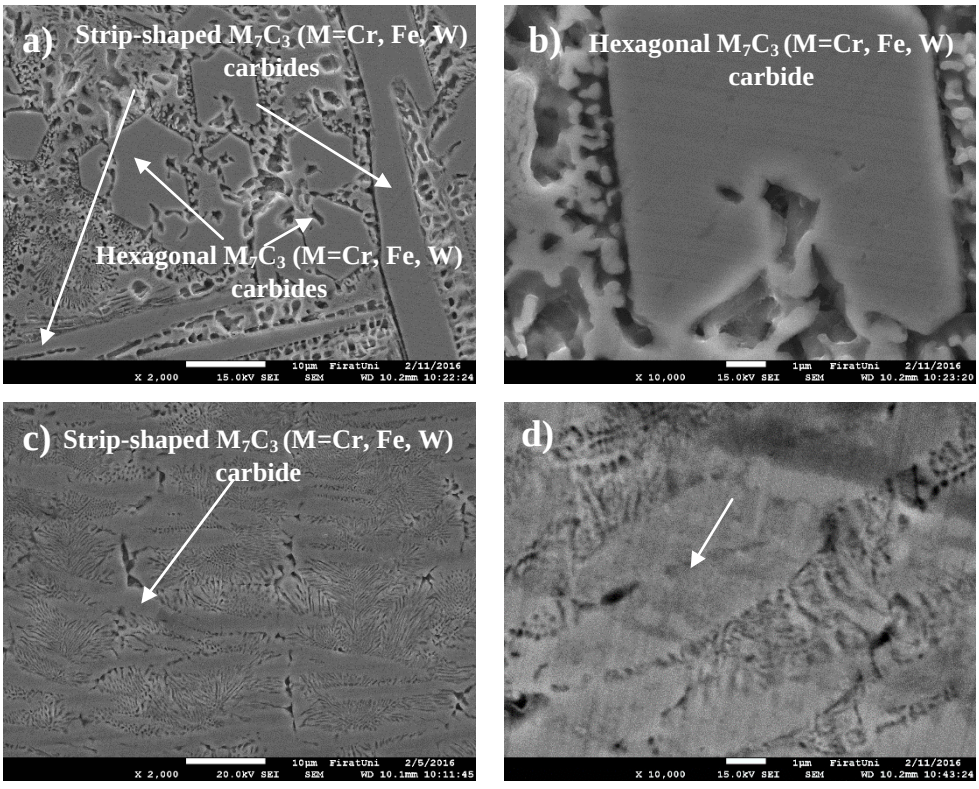

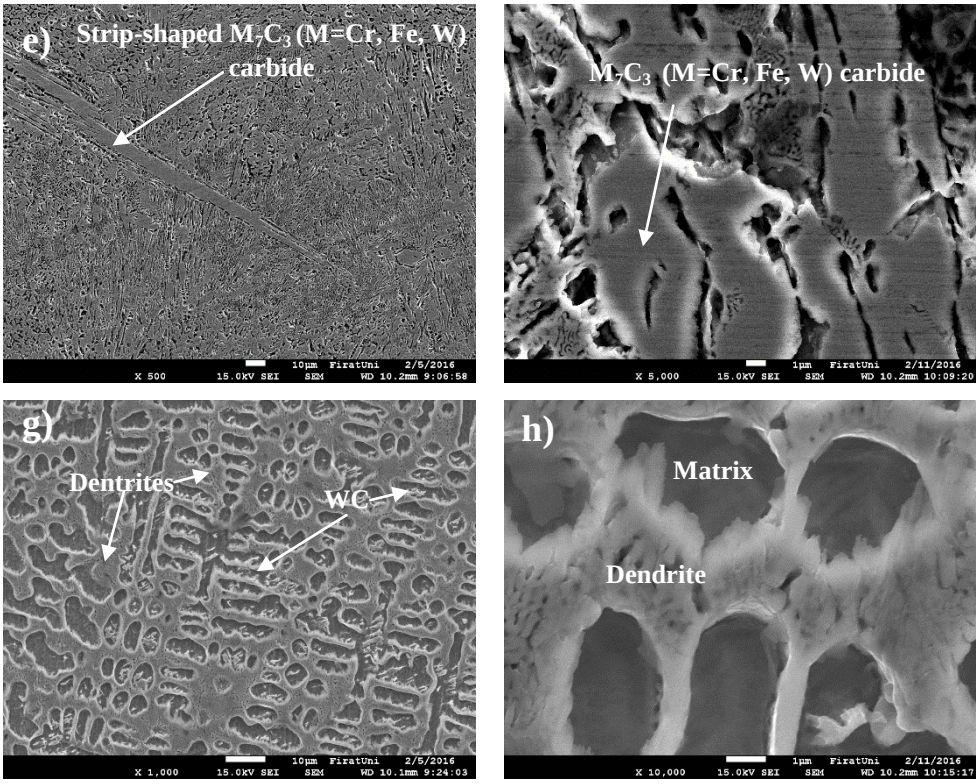

Figure 5. Coating layer SEM images of samples a) S1 (x2000), b) S1 (x10000), c) S2 (x2000), d) S2 (x10000), e) S3 (x500), f) S3 (x5000), g) S4 (x1000) and h) S4 (x10000).

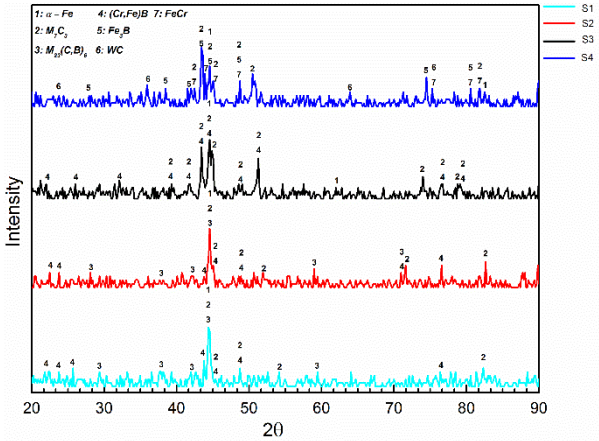

Figure 6. XRD analysis of Fe-Cr-W-B-C coating layer prepared by PTA welding.

According to the XRD analysis coating layers of S1 and S2 consists of mostly M_7C_3 (M=Cr, Fe, W) carbides and in an amount of $M_{23}(C, B)_6$ (M=Cr, Fe, W) boride carbides and (Cr, Fe)B boride. Also S1 and S2 matrix consists of α-Fe, M_7C_3 (M=Cr, Fe, W) and $M_{23}(C, B)_6$ (M=Cr, Fe, W) structure. WDX analysis also confirms these structures. According to the WDX data obtained from the cross-section of coating layers, S1 chemical composition is (wt.%) 26.4Fe-43.37Cr-19.43C-6.4W-4.4B and S2 chemical composition is (wt.%) 32.14Fe-38.48Cr-20.12C-5.29W-3.97. Due to the low atomic radius of boron atoms do not identify with EDS analysis, but boron-containing structures have been identified in XRD results. As seen in Figure 6, in S2 the amount of M_7C_3 (M=Cr, Fe, W) carbides, $M_{23}(C, B)_6$ (M=Cr, Fe, W) boride carbides and (Cr, Fe)B is more than the S1. This is thought to be due to the different solidification rates with increasing heat input and change of the chemical composition of coating layer due to intensive melting [16], [27], [28]. As seen in XRD results, the S3 coating microstructure consists of mostly M_7C_3 (M=Cr, Fe, W) carbide and in an amount of (Cr, Fe)B boride and it's matrix consists of α-Fe, M_7C_3 (M=Cr, Fe, W) and (Cr, Fe)B eutectic structure with the effect of increasing heat input and decreasing travelling speed. In S3 no $M_{23}(C, B)_6$ (M=Cr, Fe, W) carbide was observed unlike the S1 and S2. It is believed that due to the more intensive melting of the substrate material and thus increase of Fe content. It is known that, with the increasing of Fe content the cooling rate increases. In addition, transformation of M_7C_3 carbide to $M_{23}C_6$ carbide can be observed in high chromium content and the change of M:C ratio M_7C_3, M_3 C, $M_{23}C_6$ and M_6C carbides may occur in the structure [29], [30]. In high heat input and low travelling speed the base material is melted more, this changing the chemical composition of the

coating. For these reasons, the conversion of M_7C_3 (M=Cr, Fe, W) carbide to $M_{23}C_6$ (M=Cr, Fe, W) carbide may have not occurred as a result of rapid cooling and the change in M:C ratio [31], [32]. According to the XRD results, carbide ratio and (Cr, Fe)B ratio is maximum in this sample. EDS results show that the average composition of the hexagonal carbides are (wt.%) 18.9C-47.86Cr-46.55Fe-5.59W in S1, 21.93C-28.48Cr-41.67Fe-7.92W in S2 and 29.68C-33.83Cr-32.02Fe-4.45W in S3. Also the average chemical composition of the strip-shaped carbides are (wt.%) 20.40-40.50Cr-36.07Fe-3.03W, 21.05-44.03Cr-29.91Fe-5.01W and 39.49-31.70Cr-25.64Fe-3.16W in S1, S2 and S3 respectively. Matrix includes (wt.%) 20.94-29.83Cr-42.46Fe-6.77W, 21.86-22.42Cr-51.39Fe-4.33W and 21.68-24.85Cr-49.23Fe-4.24W for S1, S2 and S3 respectively. When the XRD and EDS results examined, the composition of α-Fe increases with increasing heat input. The XRD results, shown in figure 6 are analyzed, it is seen that coating layer of the S4 comprises different structures from other three samples. As seen from XRD results coating microstructure of S4 consists of mainly M_7C_3 (M=Cr, Fe, W) carbide, Fe_3B boride and a small amount of WC carbide and FeCr. Also matrix is formed α-Fe+ M_7C_3 (M=Cr, Fe, W)+FeCr eutectic structure. According to the EDS results dendritic structure contains 23.79C-20.40Cr-52.55Fe-3.26W and the matrix contains 19.87C-16.64Cr-60.57Fe-2.93W. Due to the high heat input and low forward speed increasing intensity of melting, the amount of α-Fe maximum in this sample. When the SEM image given in figure 5.g. is investigated, it is observed that, WC carbide, which is not occur in other samples, are formed that the regions between the matrix and dendritic structures. Similar study have also been identified this type structure [33]. It can be said that, WC is formed only in this sample due to the generation of WC at high temperature and different solidification rates with increasing heat input [33]. Again in contrast to other samples in S4 Fe_3B boride was determined. This is thought to be variation of solidification rate due to high heat input and due to more iron interference structure with increasing melting of base material. The EDS results are also confirm that there is more iron in the coating layer of S4.

3.1. Microhardness

The microhardness distribution of the coating layer is shown in figure 7.

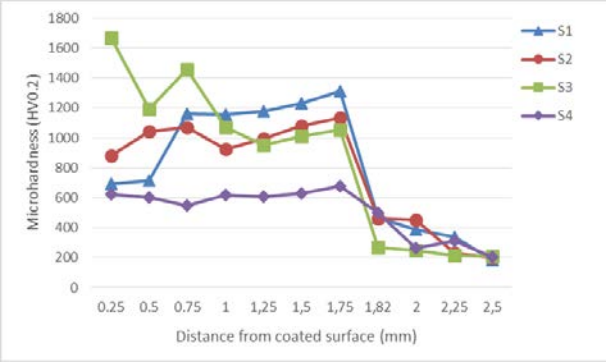

Figure 7. Microhardness profile of S1, S2, S3 and S4.

As seen in figure 7., maximum microhardness is 1668 $HV_{0.2}$ in the S3. This has caused excess of M_7C_3 (M=Cr, Fe, W) carbides and (Cr, Fe)B borides in the structure. Also the coating layers average microhardness are 990 $HV_{0.2}$, 950 $HV_{0.2}$, 1085 $HV_{0.2}$ and 601 $HV_{0.2}$ in S1, S2, S3 and S4 respectively. The average microhardness are much higher than the AISI 1020 low carbon steel, which microhardness value is about 160 HV. The microhardness value of the hexagonal phase were measured 1341 $HV_{0.2}$ in S1, 1250 $HV_{0.2}$ in S2 and 1584 $HV_{0.2}$ in S3. Strip-shaped phases microhardness are 1155 $HV_{0.2}$, 1122 $HV_{0.2}$, 1057 $HV_{0.2}$ in S1, S2 and S3 respectively.

4. CONCLUSIONS

In this study the Fe-Cr-W-B-C powder mixture was deposited in AISI 1020 steel substrate with different travelling speeds and different current by PTA welding. Microstructure of the coating, which is coated with low travelling speed and low heat input consists of mainly M_7C_3 (M=Cr, Fe, W) carbides and a little amount of $M_{23}(C, B)_6$ (M=Cr, Fe, W) boride carbides and (Cr, Fe)B borides. Microstructure with increased heat input is comprised of M_7C_3 (M=Cr, Fe, W) carbides and (Cr, Fe)B borides. Coating microstructure consists of dendritic microstructure in high heat input and low travelling speed. WC carbides and Fe_3B borides are formed only in the coating layer which is coated with low travelling speed and high heat input. The maximum average microhardness was 1085 $HV_{0,2}$

ACKNOWLEDGMENT

The authors thanks to the Firat University Research Fund (FUBAP-MF.15.09) for their financial contribution to this research.

REFERENCES

[1] amborenea, J., "Surface Modification of Metals by High Power Lasers," *Surface and Coatings Technology*, vol. 100, pp. 377-382, 1998.

[2] ɔurithis and G. D. Papadimitriou, "The Effect of Microstructure and Wear Conditions on the Wear Resistance of Steel Metal Matrix

Composites Fabricated with PTA Alloying Technique," *Wear*, vol.266, no.11, pp.1155-1164, 2009.

[3] Cheng, B. S. Xu, X. B. Liang and Y. X. Wu, ''Microstructure and Mechanical Characteristics of Iron-Based Coating Prepared by Plasma Transferred Arc Cladding Process,'' *Materials Science and Engineering: A*, vol.492, no.1, pp.407-412, 2008.

[4] uan and Z. Li, ''Effects of rod carbide size, content, loading and sliding distance on the friction and wear behaviors of (Cr, Fe)7C3-einforced α-Fe based composite coating produced via PTA welding process,'' *Surface and Coatings Technology*, vol.248, pp.9-22, 2014

[5] Liu, Z. Y. Xia, J. M. Han, G. L. Zhang and S. Z. Yang, ''Microstructure and wear behavior of (Cr, Fe)7C3 reinforced composite coating roduced by plasma transferred arc weld-surfacing process,'' *Surface and Coatings Technology*, vol.201, no.3, pp.863-867, 2006.

[6] . Hou, J. S. Gao and F. Zhou, ''Microstructure and wear characteristics of cobalt-based alloy deposited by plasma transferred arc weld urfacing,'' *Surface and Coatings Technology*, vol.194, no.2, pp. 238-243, 2005.

[7] kin, I. Hussainova, C. Katsich, E. Badisch, and C. Tomastik, ''Advanced chromium carbide-based hardfacings,'' *Surface and Coatings Technology*, vol.206, no.19, pp.4270-4278, 2012.

[8] Flores, A. Neville, N. Kapur and A. Gnanavelu, ''An experimental study of the erosion–corrosion behavior of plasma transferred arc MMCs,'' *Wear*, vol.267, no.1, pp.213-222, 2009.

[9] Deuis, J. M. Yellup and C. Subramanian, ''Metal-matrix composite coatings by PTA surfacing,''. *Composites science and technology*, ol.58, no.2, pp.299-309, 1998.

[10] einthal, F. Sergejev, A. Zikin, R. Tarbe and J. Hornung, ''Abrasive impact wear and surface fatigue wear behaviour of Fe–Cr–C PTA verlays,'' *Wear*, vol.301, no.1, pp.102-108, 2013.

[11] ourithis, S. Papaefthymiou and G. D. Papadimitriou, ''Plasma transferred arc boriding of a low carbon steel: microstructure and wear roperties,'' *Applied Surface Science*, vol.200, no.1, pp.203-218, 2002.

[12] Flores, A. Neville, N. Kapur and A. Gnanavelu, ''Erosion–corrosion degradation mechanisms of Fe–Cr–C and WC–Fe–Cr–C PTA verlays in concentrated slurries,'' *Wear*, vol.267, no.11, pp.1811-1820, 2009.

[13] irchgaßner, E. Badisch and F. Franek, ''Behaviour of iron-based hardfacing alloys under abrasion and impact,'' *Wear*, vol.265, no.5, p.772-779, 2008.

[14] uan, and Z. Li, ''Analysis of nucleation of carbide (Cr, Fe)7C3 in the Cr3C/Fe-CrNiBSi composite coating,'' *Surface and Coatings Technology*, vol.228, pp.41-47 ,2013

[15] . Chang, Y. C. Chen and W. Wu, ''Microstructural and abrasive characteristics of high carbon Fe–Cr–C hardfacing alloy,'' *Tribology nternational*, vol.43, no.5, pp.929-934, 2010.

[16] . Chang, C. C. Hsieh, C. M. Lin, J. H. Chen, C. M. Fan, and W. Wu, ''Effect of carbon content on microstructure and corrosion behavior f hypereutectic Fe–Cr–C claddings,'' *Materials Chemistry and Physics*, vol.123, no.1, pp.241-246, 2010.

[17] ytoz, A. Orhan, A. K. Gur and U. Caligulu ''Microstructural Development of Fe–Cr–C and B4C Powder Alloy Coating on Stainless teel by Plasma-Transferred Arc Weld Surfacing,'' *Arabian Journal for Science and Engineering*, vol.38, no.8, pp.2197-2204, 2013.

[18] ang, F. Han, X. Liu, S. Qu, and Z. Zou, ''Microstructure and wear properties of the Fe–Ti–V–Mo–C hardfacing alloy,'' *Wear*, vol.265, o.5, pp.583-589, 2008.

[19] n, M. C. Chen, C. M. Chang and W. Wu, ''Microstructure change caused by (Cr, Fe)23C6 carbides in high chromium Fe–Cr–C ardfacing alloys,'' *Surface and Coatings Technology*, vol.201, no.3, pp.908-912, 2006.

[20] Yilmaz, M. Özenbas and M. Yaz, ''FeCrC, FeW, and NiAl Modified Iron-Based Alloy Coating Deposited by Plasma Transferred Arc rocess,'' *Materials and Manufacturing Processes*, vol.26, no.5, pp.722-731, 2011.

[21] holzer, C. Cusano and J. Mazumder, ''Wear properties of laser alloyed and clad Fe-Cr-Mn-C alloys,'' *In Proc. ICALEO*, Vol. 84, pp. 59-167, 1985.

[22] agarathnam and K. Komvopoulo, ''Microstructural characterization,'' *Metallurgical and Materials Transactions A-physical Metallurgy nd Materials Science*, vol.24, no.7, pp.1621-1629, 1993.

[23] agarathnam and K. Komvopoulo, ''Processing and characterization of laser-cladded coating materials,'' *J. Eng. Mater. Technol.*, vol.112, o.2, pp.131-143, 1990.

[24] ytoz, M. M. Yildirim and H. Eren, ''Microstructural and microhardness characteristics of gas tungsten are synthesized Fe–Cr–C coating n AISI 4340,'' *Materials Letters*, vol.59, no.6, pp.607-614, 2005.

[25] Yılmaz, ''Wear behavior of gas tungsten arc deposited FeCr, FeCrC, and WC coatings on AISI 1018 steel,'' *Surface and Coatings Technology*, vol.201, no.3, pp.1568-1575, 2006.

[26] Lin, H. M. Chen and Y. C. Chen, ''Microstructures and wear properties of various clad layers of the Fe–W–C–B–Cr system,'' *urface and Coatings Technology*, 236, 410-419, 2013.

[27] C. M. d'Oliveira, R. Vilar and C. G. Feder, ''High temperature behaviour of plasma transferred arc and laser Co-based alloy coatings,'' *Applied Surface Science*, vol.201, no.1, pp.154-160, 2002.

[28] ytoz, M. Ulutan and M. M. Yildirim, ''Dry sliding wear behavior of TIG welding clad WC composite coatings,'' *Applied Surface cience*, vol.252, no.5, pp.1313-1323, 2005.

[29] iengmoon, T. Chairuangsri, N. Poolthong and J. T. Pearce, ''Electron microscopy and hardness study of a semi-solid processed 27wt% Cr cast iron,'' *Materials Science and Engineering: A*, vol.480, no.1, pp.333-341, 2008.

[30] iengmoon, ''Carbides in High Chromium Cast Irons,'' *Naresuan University Engineering Journal*, vol.6, no.1, pp.64, 2011.

[31] oue and T. Masumoto, ''Carbide reactions (M3C→ M7C3→ M23C6→ M6C) during tempering of rapidly solidified high carbon Cr-W nd Cr-Mo steels,'' *Metallurgical Transactions A*, vol.11, no.5, pp.739-747, 1980.

[32] ytoz, ''Microstructural properties of M 7 C 3 eutectic carbides in a Fe–Cr–C alloy,'' *Materials Letters*, vol.60, no.5, pp.605-608, 2006.

[33] ajihashemi, M. Shamanian and G. Azimi, ''Physical, Mechanical, and Dry Sliding Wear Properties of Fe-Cr-WC Hardfacing Alloys Under Different Tungsten Addition,'' *Metallurgical and Materials Transactions B*, vol.46, no.2, pp. 919-927, 2015.

BIOGRAPHY

Turan Gürgenç: He is a Research Assistant at Firat University Technology Faculty Department of Automotive Engineering. He completed his MSc at Erciyes University mechanical engineering department. His research interests are surface coating, alloying, wear, fatigue and welding**.**

Improving the Characteristics of A Rectangular Microstrip Patch Antenna By Using Various EBG Structures

Oguzhan Akgol[1]

Abstract

The work proposes a rectangular patch antenna working in WI-FI (2.4 GHz) frequency whose background plate is replaced with EBG structures having various shapes and variations. The resonance frequency is chosen so that it can be used for Wi-Fi systems. For the simulations, CST Microwave Studio software is used. In order to find the best dimensions, genetic algorithm included in CST is used and the optimized EBG dimensions is used to improve the parameters of the antenna and compared with the one originally designed with full coper rectangular background. The variation in the background structures improves the bandwidth and gain of the structure. It is also proven that the resonance frequency can be changed by adjusting the EBG structure. The model has simple geometries that can be easily manufactured and/or adjusted in any desired operation frequencies.

Keywords*: EBG, Antennas, EBG backgrounds, Microstrip antennas*

1. INTRODUCTION

After Victor Veselago's theoretical study on new type of materials [1], a new era in electromagnetic area was opened. These new type of materials are called metamaterials (MTMs) which are also known as left-handed materials (LHM). In a wide definition, MTMs are considered to be the materials having unusual electromagnetic properties that cannot be found in conventional materials in nature. In this type of materials it is possible to obtain negative permeability and permittivity simultaneously leading negative refractive index. Unfortunately, this theoretical work wasn't put into reality for almost thirty years. In 1996, Prof. J. B. Pendry achieved to obtain negative permittivity ε and permeability μ by using thin wires and Split Ring Resonator (SRR) which is one of the most commonly used structure in MTM designs [2-3]. Dr. Smith et. al. were able to produce first double negative materials (DNG) by combining these two structures which are SRRs and thin wires that is the first realization of obtaining negative ε and μ [4].

There are many application areas of MTMs including absorbers, sensors, perfect lenses, polarization rotator and etc. [5-10]. One of the most common type of metamaterials is Electronic Band Gap (EBG) structures which are composed of individual gaps placed in a periodic or sometimes in non-periodic order. Even though these structures find some interesting application areas, their most effectively usage area is on antennas. Antennas are well defined structures and for improving their characteristics many different and various techniques have been developed so far. With the realization of MTMs, the idea of using them with antennas has grown exponentially in the last few decades [11]. Using EBG materials in the antennas improve their characteristics by preventing or altering the wave propagation within the working frequency range or by preventing the surface waves of the microstrip antenna.

2. CONFIGURATION AND DESIGN OF THE MICROSTRIP PATCH ANTENNA

Design and calculation of a microstrip patch antenna is straight forward. The structure of the antenna is adjusted to have a working frequency of 2.4 GHz and the resulted design is shown in Fig.1 below. As is known, patch antenna consists of a ground plane, a dielectric layer and a patch layer on the top.

[1] *İskenderun Technical University, oguzhan.akgol@iste.edu.tr*

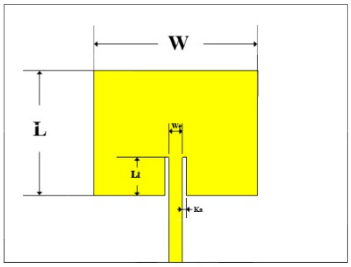

Figure 11. Geometrical Structure of the microstrip antenna

For the ground plane and the patch layer I have used copper having a conductivity of $5.8\times 10^7\ S/m$ with the thickness of $0.035\ mm$. For the dielectric layer, I have used FR4 since it has good electromagnetic response and a lot cheaper comparing to the other dielectrics. Substrate FR4 has the thickness of $1.6\,mm$ with $\varepsilon_r = 4.2$ relative permittivity, $\mu_r = 1$ relative permeability and $tan\delta = 0.02$ loss tangent values. The ground plane has the size of $80mm \times 60mm$ and the dimensions of the rest of the structure are given in Table 1.

Table 13. Dimensions of the Microstrip Patch Antenna

Parameters	Value (mm)
W	38
L	29
Li	8.85
We	3.13
Ka	1

3. SIMULATION RESULTS OF THE MICROSTRIP ANTENNA WITH VARIOUS EBG BACKGROUNDS

3.1 Circular Shape EBG Structure

For the simulations I have used CST Microwave Studio based on finite integration technique (FIT) commercial electromagnetic simulation software. The first structure consists of 7x5 EBG unit cells with circular shapes with vertical and horizontal lines on them. The detailed structure can be seen in Fig. 2.

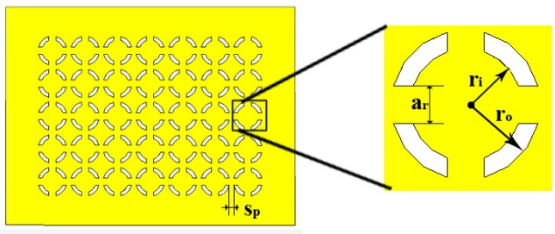

Figure 2. Geometrical Structure of the first EBG structure with circular shape

By using the genetic algorithm in CST Microwave Studio with entering the variables of a_r and the space between the cells, the best parameters for improving the return loss parameter of the microstrip antenna were obtained. They are $r_o = 4.95mm$, $a_r = 2mm$, $r_i = 2mm$ and the separation is found to be 0.5mm for the best performance. Obtained results and the comparison with the antenna with a solid copper background are shown in the following figures.

Farfield behavior of the antenna with the proposed EBG structure in polar coordinates for two principal cuts can be seen in Fig. 3 below. In the figure, top row shows two principal cuts for the antenna with the EBG structure (Fig. 3 (a) and (b)) while

the second row illustrates the farfield pattern of the antenna only. One can see from the figure that adding EBG structure not only gives a little higher directivity and thus more gain but it also offers an opportunity to change the beamwidth which changes from 92^0 to 88.5^0 degree without changing the antenna itself. In antenna industry, one of the most common ways to vary the beamwidth is to bend the extended ground plane which is both costly and hard to manufacture.

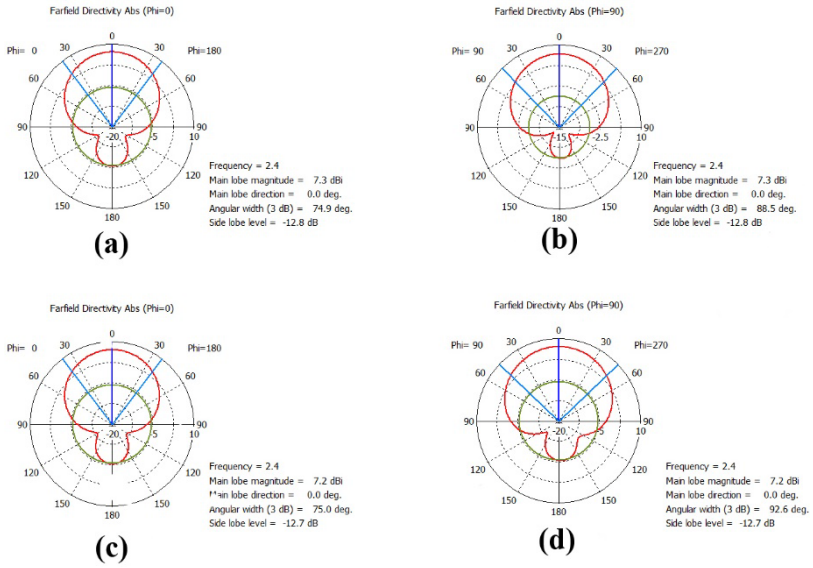

Figure 3. Polar plots of the antenna with the first EBG structure for a) $\varphi = 0$ and b) $\varphi = 90$ for the antenna with EBG-1 structure and c) $\varphi = 0$ and d) $\varphi = 90$ for the antenna without the EBG structure

By simply using the proposed EBG structure, we can easily change the beamwidth without requiring any extra physical space for additional parts. This can be considered as an added and original value of the proposed design. For a better understanding, 3D farfield radiation pattern of the antenna with and without the EBG structure is shown in Fig. 4. Left side of the figure shows the farfield pattern of the antenna with EBG structure and the right side is the farfield pattern of the antenna only. As expected, we obtained a little more gain at the frequency of $f = 2.4\ GHz$.

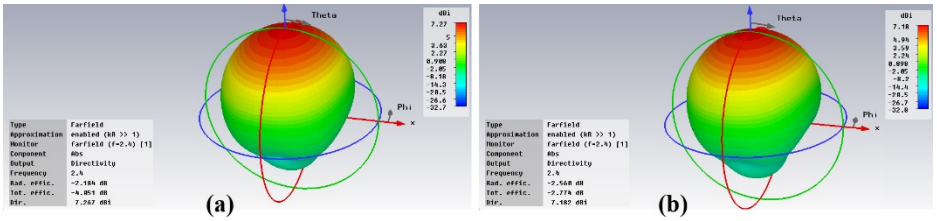

Figure 4. 3D Farfield radiation pattern (a) With EBG (b) without EBG structure

Another important advantage of the proposed design can be seen from the return loss graphs of the antenna with and without the first EBG structure (Fig. 5). As seen from the figure, return loss level goes below -15dB when EBG structure is added onto the back of the antenna which means that we can transmit more power than the conventional microstrip patch antenna. It should be noted that the dimensions are found by using genetic algorithm included in CST and it wasn't quite possible to run the algorithm by considering all the variables with a wide range. That is why only four variables are considered in the algorithm. As in the figure, even though the resonance frequency shifts right, it can also be considered another advantage of the system, by simple adjustments it can be used as a frequency shifter. With carefully chosen parameters, this technique can be used for antenna minimizations.

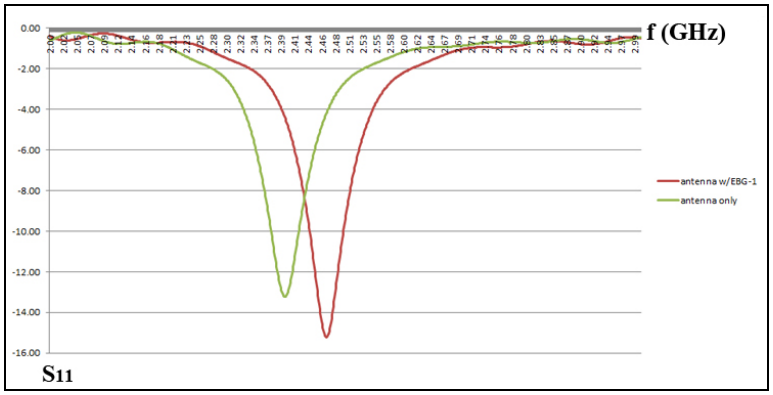

Figure 5. Simulation result for the Return Loss for microstrip patch antenna with and without the first EBG structure

3.2 Square Shape EBG Structure

A similar EBG structure is used in this part of the study. The unit cell and the overall structure can be seen in Fig. 6. In this configuration I have used square patches with vertical and horizontal lines having various thicknesses. I have used genetic algorithm in order to determine the best behavior of the microstrip patch antenna.

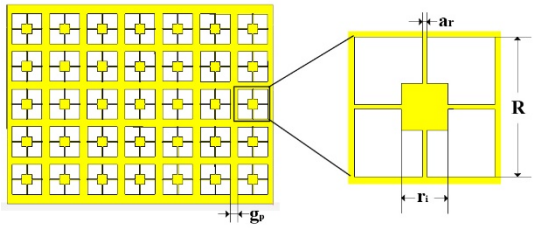

Figure 6. Geometrical Structure of the first EBG structure with square shape

Similar to the previous section, I have used four variables in the algorithm. As a result of the genetic algorithm from CST software, the following results are observed for the parameters of my second EBG structure. $R = 9mm$, $g_p = 2.33$, $a_r = 0.2845mm$ and the inner square has the size of $r_i = 3.083mm$. Farfield radiation pattern in polar plot can be seen in

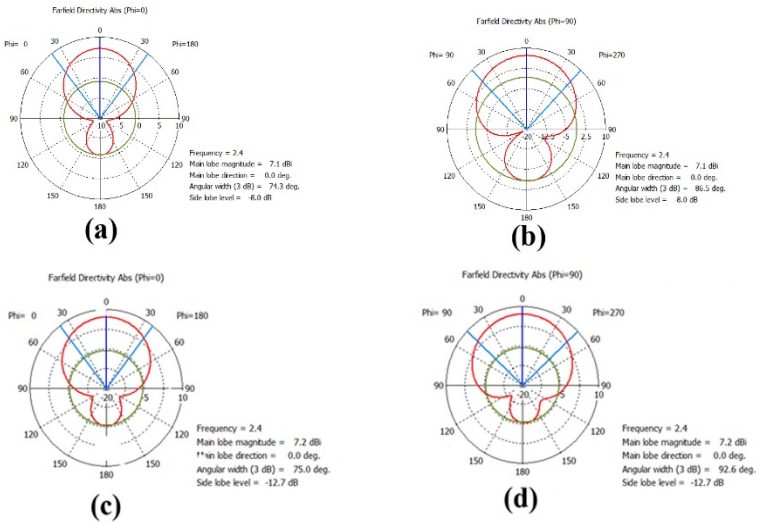

Fig. 7. One can see from the figure that even though the gain is decreased $0.1\ dB$, beamwidth of $\varphi = 90^0$ cut is reduced almost 6^0 . Therefore, the structure can be used to decrease the beamwidth of the antenna without touching the patch side of the structure.

Figure 7. Polar plots of the antenna with the first EBG structure for a) $\varphi = 0$ and b) $\varphi = 90$ for the antenna with square EBG structure and c) $\varphi = 0$ and d) $\varphi = 90$ for the antenna without the EBG structure

3D farfield pattern can be seen in Fig. 8 for $f = 2.4\ GHz$. Left side of the figure shows the antenna with EBG structure while the right side shows the antenna itself.

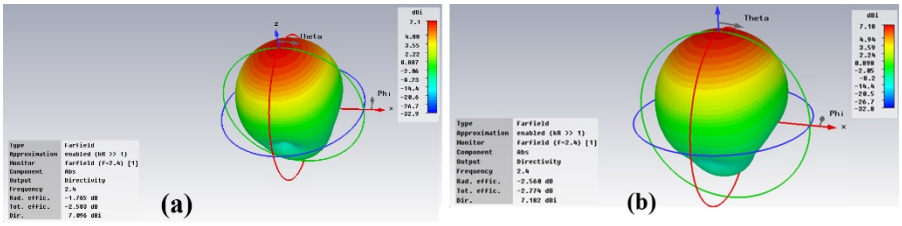

Figure 8. 3D Farfield radiation pattern (a) With EBG (b) without EBG structure

One of the other important parameter for an antenna is the return loss. Return loss graph with and without the second EBG structure can be seen in Fig. 9 below. The structure successfully provides an improved return loss parameter. As seen from the figure, the EBG structure does not only offer a 2dB improved S11 but it also provides a frequency shifting property. Therefore, this structure can also be used for frequency shifting applications without changing the structure or using any extra space.

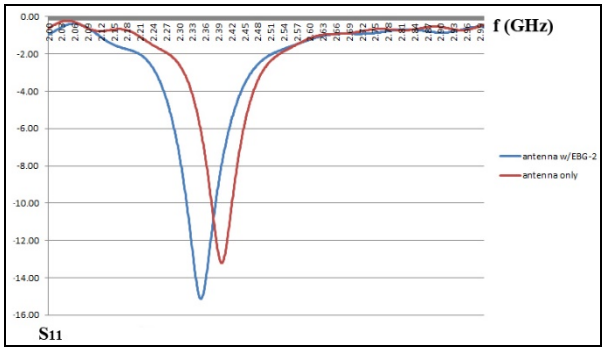

Figure 9. Simulation result for the Return Loss for microstrip patch antenna with and without the second EBG structure

As a special case, when we remove the horizontal and vertical lines, return loss gets better. On the other hand, the gain of the antenna becomes lower than the antenna itself. Resulting S_{11} graph can be seen in Fig. 10. This time, EBG structure draws the line down to approximately -32dB level which is a significant improvement.

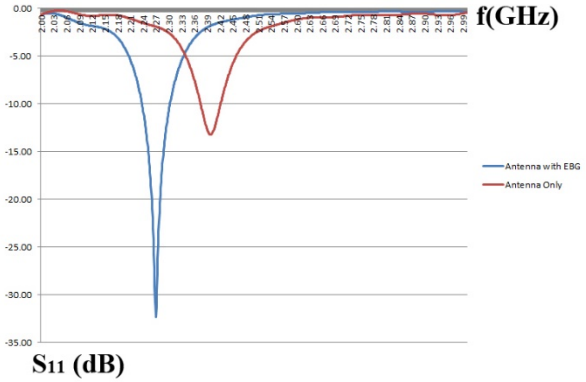

Figure 10. Simulation result for the Return Loss for microstrip patch antenna with and without the third EBG structure

For a better visualization 3D radiation pattern of the last EBG structure can be seen in Fig. 11.

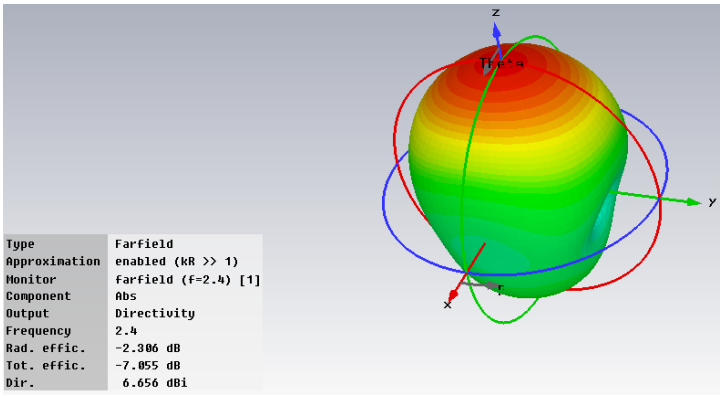

Figure 11. Simulation result for the Return Loss for microstrip patch antenna with and without the third EBG structure

4 CONCLUSION

In this study, a simple, easily manufactured EBG structures are presented. These structures improved some of the antenna parameters, including gain, return loss. In addition, it was shown that all structures have the ability to shift the working frequency depending on the structure type and dimensions, thus they can be used as a frequency shifter either. In order to find the best parameter for the dimensions of the EBG structures, genetic algorithm was used by processing four important parameters on the designs. For the future study, the comparison of the genetic algorithm included in CST will be compared with a customized version and with the other optimization algorithms that come with CST Microwave Studio.

REFERENCES

[1]. Veselago, V. G., The electrodynamics of substances with simultaneously negative values of and ," Sov. Phys. Usp., Vol. 10, No. 4, 509{514, 1968.
[2]. Pendry, J. B., Holden, A. J., Stewart, W. J.,Youngs, I., \Extremely low frequency plasmons in metallic mesostructures," Physical Review Letters, Vol. 76, 4773{4776, 1996.
[3]. Pendry, J. B., Holden, A. J., Robbins, D. J.,Stewart, W. J., \Magnetism from conductors and enhanced nonlinear phenomena," IEEE Transactions on Microwave Theory and Techniques, Vol. 47, 2075{2084, 1999.
[4]. Smith, D. R., Padilla, W. J., Vier, D. C., Nemat{Nasser, S. C., Schultz, S., \Composite medium with simultaneously negative permeability and permittivity," Physical Review Letters, Vol. 84, 4184{4187, 2000.
[5]. Karaaslan M, Bakir M., Chiral metamaterial based multifunctional sensor applications. Progress in Electromagnetics Research. 2014; 149: 55-67.
[6]. Sabah C, Dincer F, Karaaslan M, Unal E, Akgol O, Demirel E. Perfect metamaterial absorber with polarization and incident angle independencies based on ring and cross-wire resonators for shielding and a sensor application. Opt. Comm. 2014; 322: 137-142.
[7]. F. Dincer, M. Karaaslan, O. Akgol, E. Unal, C. Sabah, “Polarization-Insensitive FSS based Perfect Metamaterial Absorbers in GHz and THz Frequencies”, Radio Science, 49, 2014, pp. 306-314.
[8]. Y. Ye and S. He, “90° polarization rotator using a bilayered chiral metamaterial with giant optical activity”, Appl Phys Lett, vol. 96, 2010. pp. 203501.
[9]. F. Dincer, M. Karaaslan, E. Unal, and C. Sabah, “Dual-band polarization independent metamaterial absorber based on omega resoanator and octa-star strip configuration,” Prog. Electromagn. Res, vol. 141, pp. 219, 2013.
[10]. Ekmekci, E., Sayan, G. T., "Multi-functional metamaterial sensor based on a broad-side coupled SRR topology with a multi-layer substrate," Applied Physics A: Materials Science & Processing, vol. 110, no. 1, 189-197, 2013
[11]. R. G. P. De Maagt, J. C. Vardaxoglou, and J. M. Baracco, "Photonic Bandgap Antennas and Components for Microwave and (Sub)millimetre wave Applications," Special issue on Metamaterials, IEEE Trans. on Antennas and Propagation, vol. 51, pp. 2667-2677, 2003

Effect of Mg Addition on Thermal Conductivity of Al/B_4C Composites

H. Cug[1], E. Cevik[2], Y. Sun [2], Y. Turen [2], H. Ahlatci[2]

Abstract

In this study, the effects of matrix compounds on the thermal conductivity behaviour of AA1050-XMg matrix composites reinforced by 60 % B_4C particles were analyzed. The microstructure analysis of the composite materials showed that the porosities accumulated around B_4C reinforcement particles. By increasing Mg addition, there was considerable decrease in the thermal conductivities of composites. Thermal conductivity results there was a 37 % decrease with 4 % Mg addition in AA1050 matrix composites.

Keywords: *AA1050-XMg/B_4C, thermal conductivity.*

1. INTRODUCTION

Aluminum and copper are important due to the high conductivity metal matrix composite matrix material. Copper, although having a higher thermal conductivity than aluminum due to its high density is not preferred in applications where lightness. The low melting point, low density, a suitable thermal conductivity and thermal expansion coefficient, high corrosion resistance, low cost, adequate strength and ease of manufacture, of aluminum has the most commonly used matrix element for electronic packaging and thermal management applications [1].

Overall, the most commonly used reinforcing element is SiC. In recent years, many researchers of carbon compounds (Graphite, KNT, etc.) Is used as a reinforcing element made intensive studies and provide superior thermal properties [2,3].

Xue working as a matrix element in A356 aluminum alloy were used as a reinforcing element diamond and SiC together. With the increase in volume fraction of reinforcement of the diamond, the thermal conductivity of the composite material have recorded increases of up to 100% [4,5].

Wu and colleagues, made clear in his work Al-diamond composites with different proportions to determine the impact on the thermal properties of Cu element (0-3%) were found in addition Cu. Reported that increased thermal conductivity with the addition of C's arrival [6].

In this study, produced by high-pressure infiltration process particles (60% B4C) reinforced Al, Al-Mg matrix composites are designed to investigate the microstructural characterization and thermal properties.

2. MATERIALS AND METHODS

In this study, the commercially available AA1050 aluminum alloys by adding Mg to the weight % ratio of 1-2-4 matrix elements 4 having different chemical compositions were produced. 7 mm diameter stainless steel tubes B_4C prepared in preforms, the matrix alloy produced was infiltrated using a pressure infiltration technique. Microstructural characterization and thermal conductivity have been studied of the produced composite materials.

The microstructure analysis of the composite materials was carried out by light optical microscope (LOM) and scanning electron microscope (SEM). In determination of the matrix element and structural differences, X-Ray diffraction was used.

Thermal conductivity (κ) of the sample are determined by Anter FL-2000 device. Thermal conductivity coefficient at three different temperatures (100-200-300 °C) were measured.

3. RESULTS AND DISCUSSION

Figure 1 supplemented with B4C particles of average size 48 µm AA1050-XMg matrix shows the microstructure at low magnification of the composite material. The matrix in the absence of agglomeration problem, particle distribution is uniform, it is understood from microstructural investigations. However, the particles are focused around porosity. AA1050 composites in larger porosity are seen, after adding only around 4% Mg is observed that the reinforcing elements consist of small porosity.

[1]*Corresponding author: Karabük University, Department of Mechanical Engineering, 78150, Karabük, Turkey. hcug@karabuk.edu.tr*

[2]*Karabük University, Department of Metallurgical and Materials Engineering, 78150, Karabük, Turkey.*

Investigated AA1050 matrix and reinforcing the composite produced by the addition of Mg matrix and porosity volume ratios are given in Table 1. B_4C particle volume ratio is about 60% of the amount of porosity with the addition of 4% Mg had decreased 0.77% from 6.60%.

Table 1. AA1050 reinforcing composites materials containing Mg in different ratios, porosity, and matrix volume ratios.

Matrix	*Mg Content (%)*	*Volume Ratio (%)*		
		B_4C	*Matrix*	*Porosity*
AA1050	0	58,80	34,60	6,60
	1	59,30	36	4,70
	2	60,47	37,64	1,89
	4	57,36	41,87	0,77

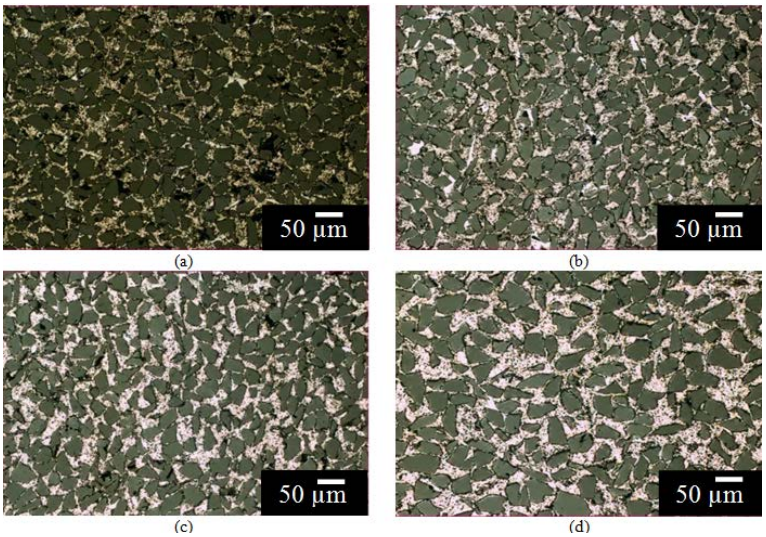

Figure 1.Optical light photograph at low magnification of the composite material containing Mg in different proportions, a) AA1050-B_4C, b) AA1050-1Mg-B_4C, c) AA1050-2Mg-B_4C and d) AA1050-4Mg-B_4C.

AA1050 aluminum alloy produced by the addition of 0-4% Mg is located XRD patterns of the composite at Figure 2. XRD analysis of the pure aluminum matrix composites with B_4C supplement, has been shown to consist of Al_3BC, AlB_2 and AlB_{10} phase. These phases have been found to occur in addition to the $Al_{37}Mg_3$ phase with the addition of Mg.

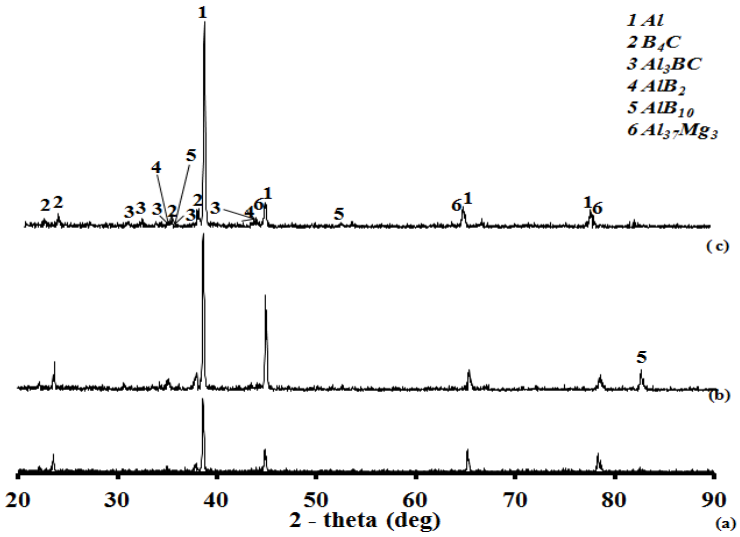

Figure 2. The XRD patterns of the composite material containing Mg in different proportions, a) AA1050-B_4C, b) AA1050-2Mg-B_4C and c) AA1050-4Mg-B_4C.

Thermal conductivity measurements were carried out for the examined composite material three different temperatures (100-200-300 °C). The effect of temperature and thermal conductivity of the matrix composition is given in Figure 3.

Addition of Mg matrix thermal conductivity and the measurement temperature has decreased. As expected due to the low thermal conductivity compared to aluminum of Mg, addition of Mg results in a decrease in thermal conductivity value of the produced composite was observed [7-9].

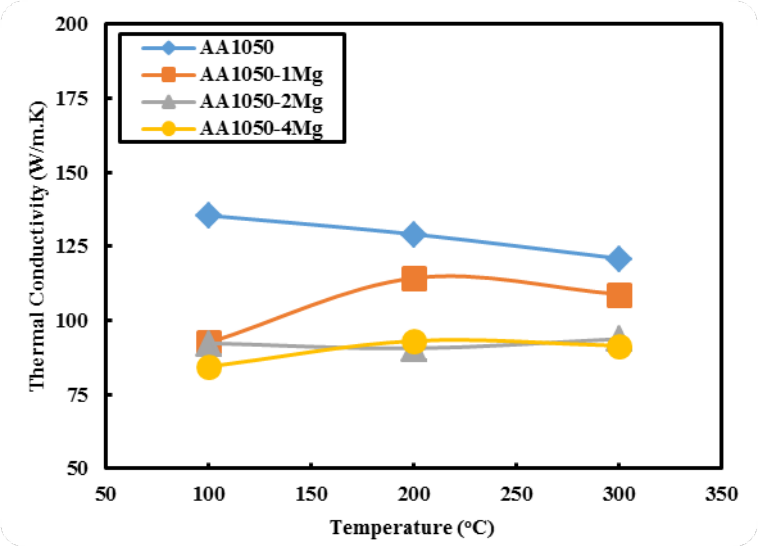

Figure 3. The thermal conductivity changes depending on temperature.

Figure 3 we see an increase in thermal conductivity of 200 ° C, while the value of composites produced with the addition of Mg, the decline is at 300 ° C again. These results are thought to be connected with the addition of Mg. Earlier studies on the thermal conductivity of the elements Mg also supports our argument is in the nature of a thermal conductivity of 148 W/m.K to 100 °C, which rises 163 W/m.K to 200 °C, 300 °C is reduced to the 145 W/m.K.

It is known that the thermal conductivity of B_4C drops with increasing temperature.[12]. Figure 3 we see that increasing the temperature of the decline in thermal conductivity measurement value was observed. Mg reduction in thermal conductivity with temperature in the composite is believed to be effective without adding substantially B_4C particles [10].

CONCLUSIONS

The following general results were obtained in this study.

- In the produced composite porosity it is generally realized in reinforced matrix interface. The amount of 4% as a result of the addition of Mg decreased from 6.60% to 0,77'y% porosity.
- XRD analysis of the pure aluminum matrix composites with B_4C supplement, has been shown to consist of Al_3BC, AlB_2 and AlB_{10} phase. These phases have been found to occur in addition to the $Al_{37}Mg_3$ phase with the addition of Mg.
- Thermal conductivity of 148 W/m.K to 100 °C, which rises 163 W/m.K to 200 °C, 300 °C is reduced to the 145 W/m.K.

ACKNOWLEDGMENT

This study is a part of project which has been supported by Karabük University.

REFERENCES

[1]. D. D. L. Chung and C. Zweben "Composites for electronic packaging and thermal management", *Comprehensive Composite Materials*, 6, 701-725, 2000.
[2]. J. M.Molina, M. Rheme, J. Carron and L. Weber "Thermal conductivity of aluminum matrix composites reinforced with mixtures of diamond and SiC particles" *Scripta Materialia*, 58, 393–396, 2008.
[3]. J. K. Chen and I. S. Huang, "Thermal properties of aluminum–graphite composites by powder metallurgy" *Composites, Part B*, 44, 698–703, 2013.
[4]. C. Xue, J. K. Yu and X. M. Zhu "Thermal properties of diamond/SiC/Al composites with high volume fractions" *Materials and Design*, 32, 4225–4229, 2011.
[5]. C. Zhou, G. Ji, Z. Chen, M. Wang, A. Addad, D. Schryvers, and H. Wanga, "Fabrication, interface characterization and modeling of oriented graphite flakes/Si/Al composites for thermal management applications" *Materials and Design*, 63, 719–728, 2014.
[6]. J.Wu, H. Zhang, Y. Zhang, J. Li and X. Wang"Effect of copper content on the thermal conductivity and thermal expansion of Al–Cu/diamond composites", *Materials and Design*, 39, 87–92, 2012.
[7]. T. Ying, H. Chi, M. Zheng, Z. Li and C.Uher"Low-temperature electrical resistivity and thermal conductivity of binary magnesium alloys", *Acta Materalia*, 80, 288-295, 2014.
[8]. Available:http://www.efunda.com/materials/elements/TC_Table.cfm?Element_ID=Mg ,2015.
[9]. T. Ashworth, and D. R. Smith "Thermal Conductivity", *Springer Science + Business Media, Inc.*, New York, 1983.
[10]. Available: International Magnesium Association, "Physical Properties of Magnesium"http://www.intlmag.org/magnesiumbasics/physical.cfm, 2015.
[11]. N. Tang, J. Chen and H. Hung, "The effect of silicon on the thermal conductivity of Al-Si alloys", *Materials Science and Technology Conference and Exhibition* , Quebec, 1339-1343, 2013.
[12]. I. Ursu "Physics and Technology of Nuclear Materials" *Pergamon Press Ltd.*, New York, 217, 1985.

Influence of Nano-clay on Properties of Cement Paste and Mortar

Riza Polat[1], Ramazan Demirboga[1,2], Fatma Karagöl[1,*]

Abstract

This study focused on the influence of the nano-clay, at an addition of 1.5, 3 and 4.5% by mass of binder, on the properties of cement paste and mortar. The water/binder ratio was 0.30 and kept constant throughout the study. Setting time and volumetric autogenous shrinkage testes were carried out on paste; at 7 and 28 days compressive strength, heat of hydration, ultrasonic pulse velocity (UPV) and 28 days linear autogenous shrinkage were determined on mortar samples. It was experimentally concluded that the lowest autogenous shrinkage was observed for1.5percent of nano-clay and it decreased the autogenous shrinkage by 43% when compared to that of the control sample and when the content of nano-clay increased, their effects on the autogenous shrinkage decreased. The compressive strength of the specimen containing nano-clay increased with the increasing of nano-clay content. The duration between the initial setting time and the final setting time and the heat of hydration increased when the content of nano-clay increased.

Keywords: *Nano-clay, autogenous shrinkage, compressive strength, setting time, heat of hydration*

1. INTRODUCTION

Nanotechnology touches on small structures or small-sized materials. Nanomaterials are very reactive because of the small particle size and large surface area and have large potential in developing cement properties in regards to compressive strength [1-3]. Scientists stated that nanoparticles can develop the smart materials which enhance properties such as durability, mechanical performance, thermal, electrical and conductivity insulation, etc… [4]. In addition, nano-particles fill pores to increase the strength as silica fume has done. However, when the nano-particles cannot be well dispersed, as the case of extensive nano-particles content, the aggregating nanoparticles create weak zone in the form of voids, consequently, the homogeneous hydrate microstructure cannot be formed, and low strength will be expected [5]. Recently, nanotechnology has been applied in the production of concrete to reduce permeability, which is essential in extending service life [6]. In addition, the nano modification can result in improvements in strength, shrinkage, ductility, and impact resistance [7]. The nanoparticles act as "nuclei" of hydration, possess pozzolanic behavior (pozzolans chemically react with calcium hydroxide liberated during hydration to form cementitious compounds [8]), and can fill the voids in the cement matrix [9-11].
Patel 2012 [11] stated that different forms of nano-silica and nano-clay in cement paste showed an increment in compressive strength, reduced permeability, and caused a denser microstructure. Brightson et al. 2013 [12] expressed that using nano-clay allows the reduction of the cement content and it acts as crack arrester, enhances post-crack tensile strength and fatigue strength of concrete structures.
The goal of this study was to determine the effect of nano-clay on the concrete properties like setting time, volumetric and linear autogenous shrinkage, compressive strength and heat of hydration. This study evaluated the use of nano-clay in cement paste and mortar compared with conventional cement paste and mortar.

2. EXPERIMENTAL WORK

2.1. Materials

Portland cement (CEM I 42.5R) according to ASTM C150 / C150M [13], 7% silica fume (SF), as cement replacement and nano-clay were used for all mixtures. The chemical properties of Portland cement, SF and nano-clay are shown in Table 1. The river sand was used according to ASTM C33 / C33M [14] for mortar and its maximum size was 4 mm. Table 2 shows the sieve analysis of aggregates. The water to binder ratio was 0.30 and constant throughout the study. Naphthalene sulfonate base superplasticizer (SP) was 0.5% and 2% for paste and mortar, respectively. The particle density and surface area of nano-clay are 2.96g/cm^3 and 2.09m^2/g, respectively. The water absorption value of nano-clay was 130% and for this reason nano-clay has become saturated with water for 24 hours before use.

* Corresponding author: Phone: +90 505 678 41 71
E-mail address: fkayaaydin@gmail.com
[1]*Department of Civil Engineering, Atatürk University, 25240, Erzurum, Turkey*
[2]*Engineering Faculty, Civil Engineering Department, King Abdulaziz University, Jeddah, Saudi Arabia*

Table 1. Properties of Portland cement, SF and nano-clay.

Component	Portland cement	SF	Nano-clay
CaO (%)	63.56	0.80	1.71
SiO_2 (%)	19.67	93.7	53.28
Al_2O_3 (%)	5.10	0.30	20.67
Fe_2O_3 (%)	3.12	0.35	6.13
MgO (%)	1.62	0.85	2.82
SO_3 (%)	2.84	0.30	-
K_2O (%)	0.77	-	0.82
TiO_2 (%)	-	-	0.63
Na_2O (%)	0.29	-	0.02
Cl^- (%)	0.0055	-	-
S^{-2}	-	0.1-0.03	-
Ignition loss (%)	1.86	0.5-0.1	14
Insoluble Residue (%)	0.27	-	-
% 40 µ	10.5	-	-
% 90 µ	1.0	-	-
Specific surface (cm^2/g)	3511	-	-
Setting time initial (min)	110	-	-
Setting time final (min)	250	-	-
Volume expansion (Le Chatelier, mm)	1.0	-	-
2 days Compressive strength (MPa)	29.2	-	-
28 days Compressive strength (MPa)	54.9	-	-
Particle density (g/cm^3)	3.15	2.2	2.72

Table 2. Sieve analysis of aggregates

Sieve size (mm)	Mixture (0-4 mm) Passing (%)
4.00	100
2.00	70
1.00	29
0.50	17
0.25	8
0.125	5
0.0063	2

2.2. Paste and Mortar Preparation

Cement pastes and mortars were mixed according to ASTM C305 [15] with a binder to water ratio of 1:0.30. The binder to sand ratio was 1:2.75 for mortars. Firstly, nano-clay, cement and SF was mixed together in the dry mixer for 7 minutes to disperse homogeneously in the cement pastes. After the completion of 7 minutes, water and SP were added and mixed for further 5 minutes. Mix proportions of cement pastes are given in Table 3.

For mortar mixtures, nano-clay, cement and SF were mixed during 7 minutes in the dry mixer and then the sand was added to the mixture for 5 minutes, and lastly the water and SP were added into the dry ingredients. Because the water absorption percentage of the clay is very high, nano-clay was kept in the water for 24 hours before mixing. Three groups of samples containing 1.5%, 3.0% and 4.5% nano-clay and control sample were cast into 5 cm x 5 cm × 5 cm cubes to test compressive strength and UPV and 10 cm × 10 cm× 40 cm rectangles to test linear autogenous shrinkage. Control sample did not include nano-clay, it includes only PC and 7% SF. Mixtures for heat of hydration were prepared according to TS EN 196-9 [16] and mix proportions of mortar are given in Table 4. After completion of mixing and casting, all specimens were stored in the molds for 24 hours at 60 ± 5% relative humidity and a room temperature of 20°C. After 24 hours, specimens were demolded and cured according to ASTM C511 [17] until a predetermined testing time for mechanical properties like compressive strength, UPV and autogenous shrinkage. Table 5 shows the mixture proportions for mortar used to test compressive strength, UPV and linear autogenous shrinkage.

Table 3. Mix proportions for paste mixtures

Mixture type	Water (g)	Binder (g)			SP (g)
		Cement	SF	Additives	
C	30	93.00	7	-	0.5
Nano-Clay15	30	91.50	7	1.50	0.5
Nano-Clay30	30	90.00	7	3.00	0.5
Nano-Clay45	30	88.50	7	4.50	0.5

Table 4. Mix compositions for mortar mixtures at w/b: 0.30 (heat of hydration)

Mixture type	Aggregates (g)	Water (g)	Binder (g)		
			Cement	SF	Additives (CaO. MgO)
C	1080	180	335.00	25	-
Nano-Clay15	1080	180	329.60	25	5.40
Nano-Clay30	1080	180	324.20	25	10.80
Nano-Clay45	1080	180	318.80	25	16.20

Table 5. Mix proportions for mortar mixtures w/b: 0.30 (compressive strength, UPV and linear autogenous shrinkage)

Mixture type	Water (g)	Cement (g)	SF (g)	Additive Nano-clay (g)	SP (g)	Quartz sand (%7) (g)	Aggregate (0-2 mm) (%63) (g)	Aggregate (2-4 mm) (%30) (g)
C	30	93.0	7	-	2	19	173	83
Nano-clay15	30	91.5	7	1.5	2	19	173	83
Nano-clay30	30	90.0	7	3.0	2	19	173	83
Nano-clay45	30	88.5	7	4.5	2	19	173	83

2.3. Testing

The initial and the final setting time were determined according to ASTM C191 [18]. The tests were repeated 3 times for each mixture. Early-age autogenous shrinkage was measured by volumetric methods. The cement paste sample was poured into an elastic membrane and sealed in a climate room at 20±0.2°C. It was assessed by measuring the weight change of the sample underwater , the detail of the specification is given elsewhere [19]. Volumetric autogenous shrinkage results were measured until 72 hours by recording every 5 minutes after casting.

The semi-adiabatic calorimetry method is based on the detection of the amount of heat generated during cement hydration into calorimetry [16]. While the temperature change is necessary to understand how real massive structures will perform [20]. Since the exterior conditions have a strong influence, the test is carried out in a perfectly climatized room at 20±2°C. The heat of hydration is expressed in joules per gram of cement. The experiments were completed over 2 days.

The compressive strength and UPV tests were applied at 7 and 28 days and determined according to ASTM C109 / C109M [21] and ASTM C597 [22], respectively.

Linear autogenous shrinkage measurements are done on the mortar sample that is cast in a slab mold. After the initial setting time, the autogenous shrinkage was determined until 28 days by recording every one hour with a strain gauge (with a length of 10 cm) and a thermocouple embedded in the sample. The measurements were corrected for thermal strain due to hydration, by assuming that the coefficient of linear thermal expansion is 10x10-6/°C [23-24].

3. RESULTS AND DISCUSSION

3.1. Paste

3.1.1. Setting time

The results showed that initial setting times reduced when the content of nano-clay increased. The final setting times of sample with nano-clay was lower than that of control sample, but it was observed that the increase in the amount of nano-clay induced to rise in the final setting time. However, setting (the duration between final and initial setting times) times of samples

containing nano-clay were higher than that of control sample and rose when the content of nano-clay increased. The nano-clay encircles around the cement grains and hence, the rate of hydration slows.

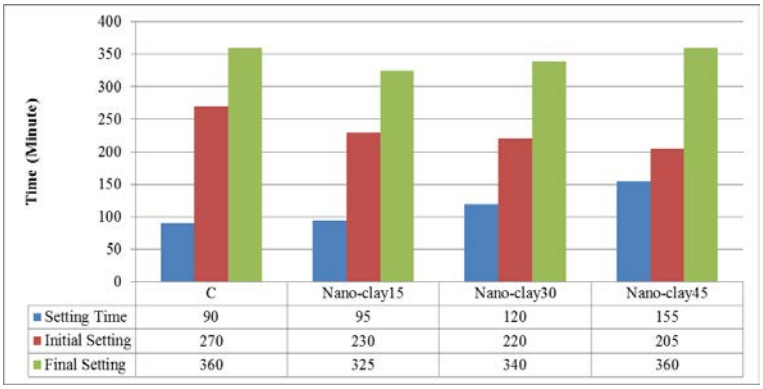

Figure 1. The setting times of C, nano-clay15, nano-clay30 and nano-clay 45

3.1.2. Volumetric autogenous shrinkage

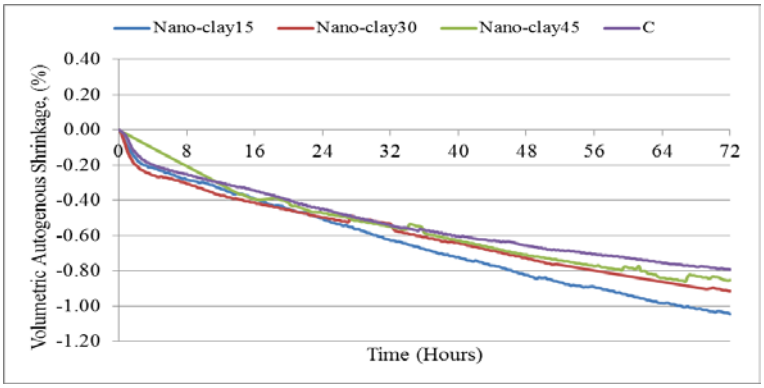

Figure 2. The volumetric autogenous shrinkages of C, nano-clay15, nano-clay30 and nano-clay 45

Volumetric autogenous shrinkages of all groups as functions of time were illustrated in Fig 2. As it can be seen from Figure 2, at the first 8 hours the volumetric autogenous shrinkage of the sample containing 4.5% nano-clay is lower than the other groups. But, this effect disappears after 72 hours and the volumetric autogenous shrinkage of the sample with nano-clay increases compared to the control sample. The volumetric autogenous shrinkage of mixtures containing nano-clay decreases with an increment in the amount of additives compared to each other. Nevertheless, the lowest value belongs to the control sample. Gao *et al.* (2012) [25] stated that the clay raises the autogenous shrinkage at early ages but at later ages it does not have the same effect.

3.2. Mortar

3.2.1. Compressive strength

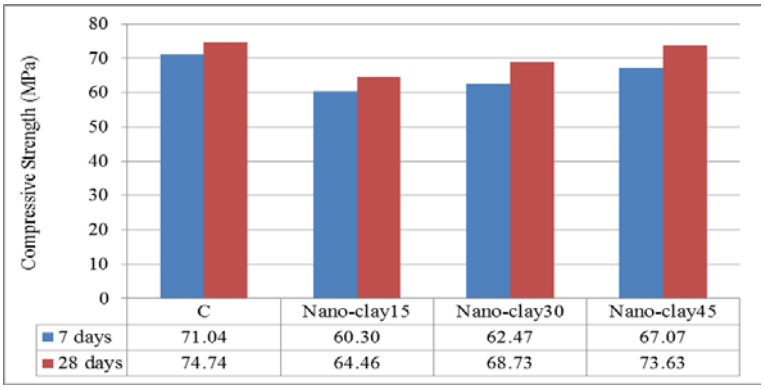

Figure 3. The compressive strengths of C, nano-clay15, nano-clay30 and nano-clay 45

The compressive strengths of the control and nano-clay-added mortars are shown in Fig. 3. The addition of nano-clay decreased the compressive strength compared to the control sample. These reductions for 1.5%, 3.0% and 4.5% nano-clay are %15, %12 and %5 at 7 days, respectively. In the same way, 18%, 8% and 1% reductions occur in the compressive strengths for 28 days. The addition of nano-clay decreased the strength, but the strength improved by increasing the amount of nano-clay. For instance, while the increment in compressive strength of sample with 1.5% nano-clay is 6.8% from 7 to 28 days, the increment in compressive strength of sample containing 4.5% nano-clay is 9.8%. This implies that nano-clay containing water significantly was improved by the hydration. Furthermore, the Ca^{+2} cations and $(OH)^{-}$ ions react with the active silica in SF and CSH that improves the strength [26]. Morsy et al. (2010) [5] studied the effects of nano- clay on the compressive strength and stated that the improvement in the compressive strength was 7% at 8% nano-metakaolin clay.

3.2.2. UPV

The changes of nano-clay on the UPV values are shown in the Figure 4. The UPV results are consistent with the compressive strengths. The UPV value of 28 days control specimen was accepted 100%. The increase in the UPV values of control sample is 1.70% from 7 to 28 days. The increments for nano-clay15, nano-clay30 and nano-clay45 are 1.5%, 3% and 1.75%, respectively. It was appeared from these increments that nano-clay improves the properties of concrete both in fresh and hardened phase and thus it can make a concrete more durable [12].

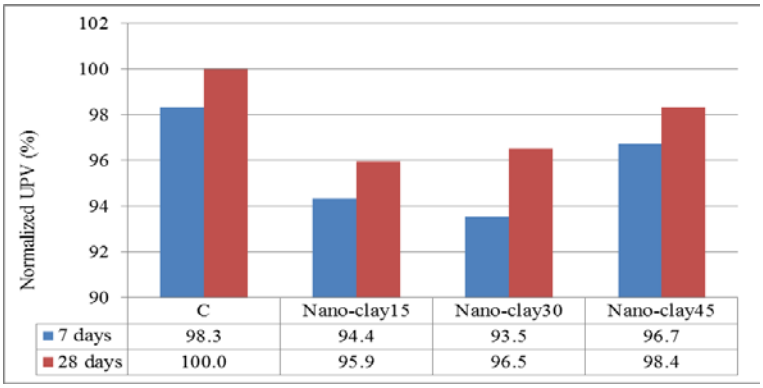

Figure 4. The UPV values of C, nano-clay15, nano-clay30 and nano-clay 45

3.2.3. Linear autogenous shrinkage

The linear autogenous deformations are given in Figure 5. They are recorded for 28 days as the average of three samples for each group. The autogenous shrinkage strains for C, nano-clay15, nano-clay30 and nano-clay45 mixes were about 300, 170,186 and 305 με for 28 days. During about the first 12 hour period the autogenous shrinkages of samples with nano-clay are lower than that of control samples. Although after 28 days, the autogenous strain of nano-clay45 is higher than that of control samples. The autogenous strains increased with an increment in amount of nano-clay. Gao et al. (2012) [25] studied the effects of different nano-clay on the shrinkage and cracking mechanism of self-consolidating concrete containing SF and stated that all mixtures with nano-clay increased at a very early age, however the increment on the final autogenous shrinkage can be neglected. Wang et al. (2011) [27] expressed that some nano-clay materials slightly increased shrinkage in self-consolidating concrete, while some nano-clay material (like quartz) decreased shrinkage. Polat et al. (2015) [24] implied that clays have different absorbed and chemical structure and hence, they reduce or increase the autogenous shrinkage according to their structure.

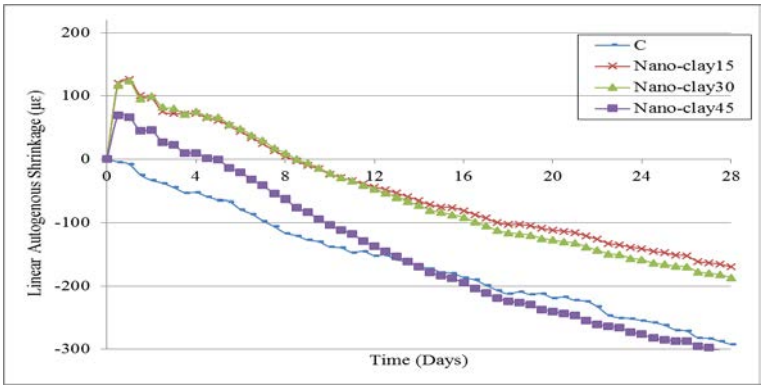

Figure 5. The Linear autogenous shrinkage of C, nano-clay15, nano-clay30 and nano-clay 45

3.2.4. Heat of hydration

The results in the Figure 6 showed that the addition of nano-clay enhanced the heat of hydration with respect to that of the control mixture. For instance, the increment in the percentage of heat of hydration for nano-clay15, nano-clay30 and nano-clay45 was 5%, 7% and 10% at 48 hours, respectively, compared to the control. The reason of this case was the continuing hydration reaction between cement and the absorbed water in the nano-clay (saturated with water for 24 hours before the experiment). As a result of this reaction heat was released. Furthermore, the addition of SF can increase the heat of hydration.

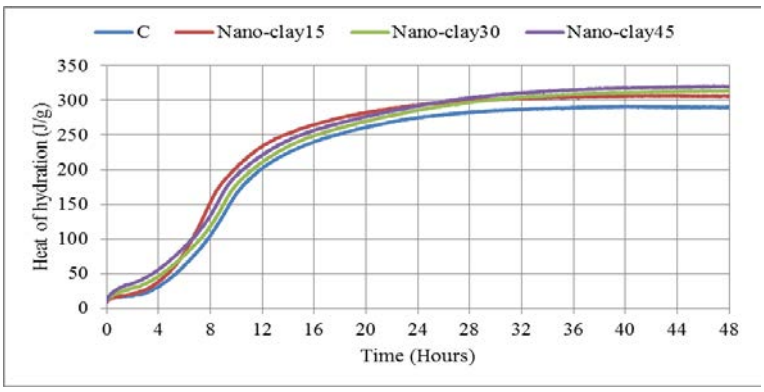

Figure 6. The heats of hydration of C, nano-clay15, nano-clay30 and nano-clay 45

4. CONCLUSIONS

The following conclusions can be drawn from this study:

- The setting times of sample containing nano-clay are higher than that control sample and increased with the addition of nano-clay. The nano-clay encircles the cement grains and hence, the rate of hydration slows.
- At 72 hours the volumetric autogenous shrinkage of the sample containing nano-clay increases compared to the control sample. The volumetric autogenous shrinkage of mixtures containing nano-clay decreases with an increment in the amount of additives compared to each other.
- The addition of nano-clay decreased the compressive strength when compared to the control sample. These reductions for 1.5%, 3.0% and 4.5% nano-clay are %15, %12 and %5 at 7 days and 18%, 8% and 1% at 28 days respectively.
- The UPV results are consistent with the compressive strengths.
- During about the first 12 hour period the linear autogenous shrinkages of samples with nano-clay are lower than that of the control sample. However, after 28 days, the autogenous strain of nano-clay45 is higher than the control samples. The autogenous strains increased with an increment in the amount of nano-clay.
- The addition of nano-clay enhanced the heat of hydration with respect to that of the control mixture. For instance, the increment in the percentage of heat of hydration for nano-clay15, nano-clay30 and nano-clay45 was 5%, 7% and 10% at 48 hours, respectively.

ACKNOWLEDGMENTS

This research was supported by the research project "Investigation shrinkage of HSC and modelling by neural network" (BAP Code: 2010/97) from the Atatürk University, Scientific Research Projects (BAP) Program in Erzurum, Turkey.

REFERENCES

[1]. Rashad, A.M. *A synopsis about the effect of nano-Al_2O_3, nano-Fe_2O_3, nano-Fe_3O_4 and nano-clay on some properties of cementitious materials – A short guide for Civil Engineer*, Materials and Design 52 (2013) 143–157
[2]. Farzadnia N, Ali AAA, Demirboğa R. *Characterization of high strength mortars with nano alumina at elevated temperatures*. Cement Concrete Res 2013;54:43–54.
[3]. Berra M, Carassiti F, Mangialardi T, Paolini AE, Sebastiani M. *Effects of nanosilica addition on workability and compressive strength of Portland cement pastes*. Constr Build Mater 2012; 35: 666–75.
[4]. Şahin R., Oltulu M., *New materials for concrete technology: nano powders*. In: 33rd Conference on "Our world in concrete & structures'', Singapore; 25–27 August 2008.
[5]. Morsy M.S, Alsayed S.H, Aqel M. *Effect of nano-clay on mechanical properties and microstructure of ordinary Portland cement mortar*. International Journal of Civil & Environmental Engineering IJCEE-IJENS 2010;10(01):23–7
[6]. He, X., and Shi, X. *Chloride Permeability and Microstructure of Portland Cement Mortars Incorporating Nanomaterials*. In *Transportation Research Record: Journal of the Transportation Research Board*, No. 2070. Transportation Research Board of the National Academies, Washington, DC, 2008, pp. 13-21.
[7]. Birgisson, B. *Nanomodification of Cement Paste to Improve Bulk Properties of Concrete*. Presented at the National Science Foundation Workshop on Nanomodification of Cementitious Materials, University of Florida, Gainesville, August 8-11, 2006.
[8]. Kosmatka, S.H, Kerkhoff, B., and Panarese, W.C. *Design and Control of Concrete Mixtures*. Portland Cement Association. Skokie, IL, 2002.
[9]. Li, H., Xiao, H., Yuan, J., and Ou, J. *Microstructure of Cement Mortar with Nano-Particles*. *Composites Part B: Engineering*, Vol. 35, No. 2, 2004, pp. 185-189.
[10]. Shih, J., Chang, T., and Hsiao, T. *Effect of Nanosilica on Characterization of Portland Cement Composite*. *Materials Science and Engineering A*, Vol. 424, Nos. 1-2, 2006, pp. 266-274.
[11]. Patel K., *The use of nano-clay as a Constructional Material*, International Journal of Engineering Research and Applications, 2, 4, July-August 2012, pp.1382-1386.
[12]. Brightson P. , Baskar G., Gnanappa S. B., *Strength & Durability Analysis of Nano Clay in Concrete*. Life Science Journal 2013; 10(7s).
[13]. ASTM C150 / C150M. Standard Specification for Portland Cement. ASTM International, West Conshohocken, PA, www.astm.org; 2015.
[14].ASTM C33 / C33M. Standard Specification for Concrete Aggregates. ASTM International, West Conshohocken, PA, www.astm.org; 2013.
[15].ASTM C305. Standard Practice for Mechanical Mixing of Hydraulic Cement Pastes and Mortars of Plastic Consistency. ASTM International, West Conshohocken, PA, www.astm.org; 2014.
[16].TS EN 196-9. Methods of testing cement - Part 9: Heat of hydration - Semi-adiabatic method. Ankara: Turkish Standard; 2011.
[17].ASTM C511. Standard Specification for Mixing Rooms, Moist Cabinets, Moist Rooms, and Water Storage Tanks Used in the Testing of Hydraulic Cements and Concretes. ASTM International, West Conshohocken, PA, www.astm.org; 2013.
[18].ASTM C191. Standard Test Methods for Time of Setting of Hydraulic Cement by Vicat Needle. ASTM International, West Conshohocken, PA, www.astm.org; 2013.
[19]. Barcelo L., Moranvill M., Clavaud B., *Autogenous shrinkage of concrete: a balance between autogenous swelling and self-desiccation*, Cement and Concrete Research 35 (2005) 177–183)
[20]. Berger S., Coumes CCD., Bescop PL., Damidot D., *Influence of a thermal cycle at early age on the hydration of calcium sulphoaluminate cements with variable gypsum contents*, Cement and Concrete Research 41 (2011) 149–160
[21].ASTM C109 / C109M. Standard Test Method for Compressive Strength of Hydraulic Cement Mortars (Using 2-in. or [50-mm] Cube Specimens). ASTM International, West Conshohocken, PA, www.astm.org; 2016.
[22].ASTM C597. Standard Test Method for Pulse Velocity Through Concrete. ASTM International, West Conshohocken, PA, www.astm.org; 2009.
[23].Kohno K, Okamoto T, Isikawa Y, Sibata T, Mori H. *Effects of artificial lightweight aggregate on autogenous shrinkage of concrete*. Cement Concrete Res. 1999; 29 (4):611-4.
[24].Polat R, Demirboga R, Khushefati WH. *Effects of nano and micro size of CaO and MgO, nano-clay and expanded perlite aggregate on the autogenous shrinkage of mortar*. Constr Build Mater. 2015; 81:268-75.
[25]. Gao X, Kawashima S, Liu X, Shah SP. *Influence of clays on the shrinkage and cracking tendency of SCC*. Cement Concrete Compos 2012; 34:478–85.
[26]. Kalkan E, Akbulut S. *The positive effects of silica fume on the permeability, swelling pressure and compressive strength of natural clay liners.* Eng Geol 2004; 73:145–56.
[27]. Wang K, Shah SP, Grove J, Taylor P, Wiegand P, Steffes B, Lomboy G, Quanji Z, Gang L, Tregger N. *Self-consolidating concrete-applications for slip-form paving: phase II.* National Concrete Pavement Technology Center Institute for Transportation Iowa State University. DTFH61-06-H-00011 Work Plan 6, Pooled Fund Program Study TPF-5(098). May 2011.

ICENS
INTERNATIONAL CONFERENCE ON ENGINEERING AND NATURAL SCIENCES
24-28 May 2016 /Sarajevo

Comparison of Nano and Micro Sizes of CaO and MgO on the Physical and Mechanical Properties of Cement Paste and Mortar

***Riza Polat*[1,*], *Ramazan Demirboga*[1,2], *Fatma Karagol*[1],**

Abstract

In this study, the effect of nano and micro sizes of CaO and MgO on the fresh and hardened properties of cement paste and mortar was experimentally investigated and compared. 2.5, 5.0 and 7.5% nano and micro sizes of CaO and MgO by weight of binder were used in mortar and paste. The water-to-binder ratio (w/b) was 0.30 and constant throughout the study. Setting time tests were carried out on paste. Compressive strength, heat of hydration, ultrasonic pulse velocity (UPV) at 7 and 28 days and 28 days linear autogenous shrinkage were determined on mortars. It was experimentally concluded that when MgO decreased the compressive strength of nano-CaO, CaO and nano-MgO samples increased. The autogenous shrinkage decreased with the increase of all the additives content. Although nano size materials have more effect than micro size in reducing autogenous shrinkage. The addition of nano-CaO, MgO and CaO additive significantly effects the initial and final setting times and postpones the initial setting time from about 20 to 120 minutes. The setting times of nano-MgO are longer than the other additives.

Keywords: *Nano-CaO, nano-MgO, CaO, MgO, autogenous shrinkage, compressive strength, setting time, heat of hydration*

1. INTRODUCTION

Nanoparticles, particles of less than 100 nm in diameter, generally show the properties of electrical, physical, mechanical or chemical that are entirely dissimilar from those showed by the same products with larger dimensions. Different nano-particles have been used in the production of cement-based composites and improved the mechanical properties and durability of cement-based materials [1-18].

MgO and CaO based expansive additives with micro size for shrinkage reduction were discovered and used for years. MgO reacts with water, and the hydration reaction produces $Mg(OH)_2$. In fact, the difference in density between MgO (3.58 g/cm^3) and $Mg(OH)_2$ (2.36 g/cm^3), when MgO converts to $Mg(OH)_2$, the volume more than the double volume of MgO [19-25]. As a result, micron sized MgO generally decreases the autogenous shrinkage but, on the other hand, also decreases the strength. The properties of mortars containing the nano-MgO were experimentally studied by Moradpour et al. (2013) [26], Polat et al. (2015) [27] and Ye et al. (2015) [28]. Moradpour et al. (2013) [26] stated that the strengths increased for samples containing nano-MgO particle, the reason may be due to the behaving of nano-MgO as a filler to improve composites microstructure. Ye et al. (2015) [28] expressed that nano-MgO can be used as the expansive agent for cement and concrete. Polat et al. (2015) [27] experimentally showed that reduction in autogenous shrinkage due to nano-MgO was higher than that of MgO for the same mix proportions. Moradpour et al. (2013) [26] and Ye et al. (2015) [28] studied the strength of mortars with a water/binder ratio of 0.50 and reported that the strength increased even due to the small amount addition of nano-MgO. On the other hand, CaO based expansive additives with micro size increase the compressive strength and reduce autogenous shrinkage [29-31]. CaO reacts with water, and the hydration reaction produces $Ca(OH)_2$ and the volume expands. For early strength gaining concretes, CaO-based expansive agent is more appropriate with respect to the ettringite based expansive agent for the shorter period of wet curing (1–7 days) [27,31]. Polat et al. (2015) [27] stated that replacement of 2.5%, 5.0% and 7.5% of Portland Cement by nano-CaO lead to a successive reduction of this autogenous deformation by 7, 10 and 20 percent, respectively, at 28 days.

In this study, the effects of nano and micro sizes of CaO and MgO on strength and other properties of pastes and mortars were investigated. For this aim, setting time tests were carried out on paste; at 7 and 28 days compressive strength, heat of hydration, ultrasonic pulse velocity (UPV) and 28 days linear autogenous shrinkage were determined on mortar samples. For

[*] Corresponding author: Phone.: +90 554 569 05 64; fax : +90 442 231 47 63
E-mail address: rizapolat@gmail.com; rizapolat@atauni.edu.tr
[1]*Department of Civil Engineering, Atatürk University, 25240, Erzurum, Turkey*
[2]*Engineering Faculty, Civil Engineering Department, King Abdulaziz University, Jeddah, Saudi Arabia*

these experiments, the effect of the particle size of CaO and MgO on the properties of fresh and hardened cementitious materials was compared.

2. EXPERIMENTAL WORK

2.1. Material

In this study, ordinary Portland cement (PC) (CEM I 42.5 R), according to ASTM C150 / C150M [32], 7% silica fume (SF) as cement replacement and river sand according to ASTM C33 / C33M [33] are used in all mixtures. The properties of PC and SF are given in Table 1. Naphthalene sulfonate based superplasticizer (SP) was used by 0.5% for cement paste and 2% for all mortar groups. Water –binder ratio was 0.30 for all mixtures throughout the study. Sieve size of aggregates is given Table 2. The CaO and MgO were used 2.5%, 5% and 7.5% by weight of binder as replacement for cement throughout the study for all mixtures. Properties of CaO - MgO and nano-CaO - nano-MgO are given in Tables 3-4, respectively.

The saturated surface dry particle densities of aggregate with two size fractions, 0-2 mm and 2-4 mm, were 2.56 g/cm^3 and 2.60 g/cm^3, respectively. The quartz sand was used as filler material with a specific gravity and particle diameter of 2.85 and 0-250µm, respectively.

Table 1. Properties of PC and SF

Component	PC	SF
CaO (%)	63.56	0.80
SiO_2 (%)	19.67	93.7
Al_2O_3 (%)	5.10	0.30
Fe_2O_3 (%)	3.12	0.35
MgO (%)	1.62	0.85
SO_3 (%)	2.84	0.30
K_2O (%)	0.77	-
TiO_2 (%)	-	-
Na_2O (%)	0.29	-
Cl^- (%)	0.0055	-
S^{-2}	-	0.1-0.03
Ignition loss (%)	1.86	0.5-0.1
Insoluble Residue (%)	0.27	-
% 40 µ	10.5	-
% 90 µ	1.0	-
Specific surface (cm^2/g)	3511	-
Setting time initial (min)	110	-
Setting time final (min)	250	-
Volume expansion (Le Chatelier, mm)	1.0	-
2 days Compressive strength (MPa)	29.2	-
28 days Compressive strength (MPa)	54.9	-
Specific gravity	3.15	2.2

Table 2. Sieve analysis of aggregates

Sieve size (mm)	Mixture (0-4 mm), Passing (%)
4.00	100
2.00	70
1.00	29
0.50	17
0.25	8
0.125	5
0.0063	2

Table 3. Properties of CaO and MgO

Properties of materials	CaO	MgO
Chemical component (mass %)	98.8	99
Particle density (g/cm$^{3)}$	3.35	3.58
Average particle size (µm)	3.314	4.185

Table 4. Properties of nano-CaO and nano-MgO

Formula	Nano-CaO	Nano-MgO
Molecular weight (g/mol)	56.08	40.31
Density (g/cm^3)	3.300	3.580
Melting point (°C)	2580	2800
Boiling point (°C)	2850	3600
Average particle diameter (nm)	100	100

2.2. Paste and Mortar Preparation

Cement pastes and mortars were mixed according to ASTM C305 [34] with water to binder ratio of 0.30. Mortars with a binder to sand ratio of 1:2.75 were prepared. Powder components like cement, SF, CaO, MgO, nano-CaO and nano-MgO were added to the dry mixer for 7 minutes for paste and mortar mixtures. And then SP and water were added for 5 minutes for paste mixtures. The sand was added into a drum mixer for 5 minutes and then water and SP was added for mortar mixtures. Table 5 shows mix proportions for paste mixture. For total 15 group specimens; control (with only PC and 7% SF), CaO (2.5%, 5%, 7.5%), MgO (2.5%, 5%, 7.5%), 2.5% CaO+2.5% MgO, nano-CaO (2.5%, 5%, 7.5%), nano-MgO (2.5%, 5%, 7.5%) and 2.5% nano-CaO+2.5% nano-MgO were prepared. 5 cm x 5 cm × 5 cm cube molds were produced for compressive strength and UPV tests and 10 cm × 10 cm× 40 cm rectangles for linear autogenous shrinkage. Table 6 shows proportions of specimens of mortar for compressive strength, UPV and linear autogenous shrinkage. Furthermore, for the control sample, 1080 g water, 360 g binder (335 g PC+ 25 g SF), 1080 g sand were used for heat of hydration experiment and other mixtures, the additives was used by weight of binder.

Table 5. Mix proportions for paste mixtures (water: 30 g, binder: 100 g, SP: 0.5 g)

Mixture Type*	Water (g)	Binder (g)			SP (g)
		PC	SF	Additive	
C	30	93.00	7	-	0.5
Nano-CaO25	30	90.50	7	2.5	0.5
Nano-CaO50	30	88.00	7	5.0	0.5
Nano-CaO75	30	85.50	7	7.5	0.5
Nano-MgO25	30	90.50	7	2.50	0.5
Nano-MgO50	30	88.00	7	5.00	0.5
Nano-MgO75	30	85.50	7	7.50	0.5
Nano-CM50	30	88.00	7	5.00	0.5
CaO25	30	90.50	7	2.50	0.5
CaO50	30	88.00	7	5.00	0.5
CaO75	30	85.50	7	7.50	0.5
MgO25	30	90.50	7	2.50	0.5
MgO50	30	88.00	7	5.00	0.5
MgO75	30	85.50	7	7.50	0.5
CM50	30	88.00	7	5.00	0.5

**C, Nano-CaO25, Nano-MgO25, Nano-MgO75 and Nano-CM50: denotes samples of control, 2.5% nano-CaO, 2.5% nano-MgO, 7.5% nano-MgO and 2.5% nano-CaO, respectively.*

2.3. Testing

The initial and the final setting time were determined according to ASTM C191 [35]. All specimens were stored at a room moisture of 60±5%, temperature of 20°C, after 24 hours specimens were demolded and cured in lime saturated water according to ASTM C511 for 7 and 28 days. Following that the compressive strength tests were completed according to ASTM C109/C109M [36]. Three specimens were produced for each group and UPV tests were applied before the compressive tests. After, the average of these values was taken. The UPV of mortars were conducted according to ASTM C597 [37]. According to TS EN 196-9 [38], mixtures were prepared for heat of hydration. The specimens for autogenous shrinkage were stored at a room temperature of 20°C and a relative humidity of 60±5% for 24 hour period. Afterwards, at the same moisture and temperature, the autogenous shrinkage of a demolded specimen was recorded for 28 days with a strain gauge and a thermocouple embedded in the specimen. The measurements were corrected by assuming that the coefficient of linear thermal expansion is $10x10^{-6}$/°C [27, 39].

Table 6. Mix proportions for mortar mixtures (binder;water;sand : 1/0.30/2.75)

Mixture Type	Water (g)	PC (g)	SF (g)	Additive (g)	SP (g)	Quartz Sand (%7) (g)	Aggregate (g)	
							(0-2) (%63)	(2-4) (%30)
C	30	93.0	7	-	2	19	173	83
Nano-CaO25	30	90.5	7	2.5	2	19	173	83
Nano-CaO50	30	88.0	7	5.0	2	19	173	83
Nano-CaO75	30	85.5	7	7.5	2	19	173	83
Nano-MgO25	30	90.50	7	2.5	2	19	173	83
Nano-MgO50	30	88.00	7	5.0	2	19	173	83
Nano-MgO75	30	85.50	7	7.5	2	19	173	83
Nano-CM50	30	88.00	7	5.0	2	19	173	83
CaO25	30	90.5	7	2.5	2	19	173	83
CaO50	30	88.0	7	5.0	2	19	173	83
CaO75	30	85.5	7	7.5	2	19	173	83
MgO25	30	90.5	7	2.5	2	19	173	83
MgO50	30	88.0	7	5.0	2	19	173	83
MgO75	30	85.5	7	7.5	2	19	173	83
CM50	30	88.0	7	5.0	2	19	173	83

3. RESULTS AND DISCUSSION

3.1. Paste

3.1.1. Setting times

The initial and final setting times (the duration between final and initial setting times) of nano and micro CaO mixtures are lower than that of C (Figure 1). For instance, while the initial setting time of C is 90 minutes, the initial setting times of micro CaO25, CaO50 and CaO75 are 85, 70 and 60 minutes, respectively. When the particle diameter of CaO decreases and surface area of CaO increases, the setting times of samples produced with CaO gradually reduced when compared to the C [27]. Hosseini et al. (2014) [40] stated that due to the high specific surface area and the high surface activity characteristics of nano-particles, they have a significant effect on the acceleration of cement hydration. Furthermore, the reduction of CaO with water is very fast. Throughout this reduction high amounts of heat are released and high amounts of water are used. In regards to these reasons, the setting time of samples with CaO is lower than that of C.

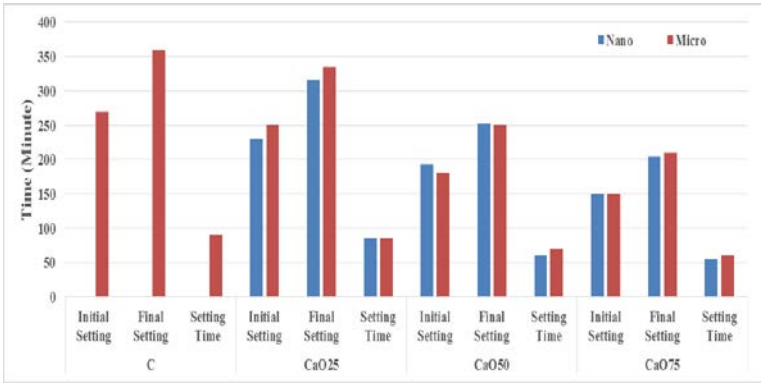

Figure 1. Comparison of initial, final and total setting times of C, CaO25, CaO50 and CaO75

Figure 2 shows that the setting times of samples with micro-MgO are higher than that of nano-MgO compared to each other. This is may be due to the smaller particle diameter and the higher surface area that allows a shorter setting time. The setting times of nano-MgO samples decrease with increasing of its content and their setting times are lower than that of the C. However, the setting times of micro-MgO samples are higher than that of the C.

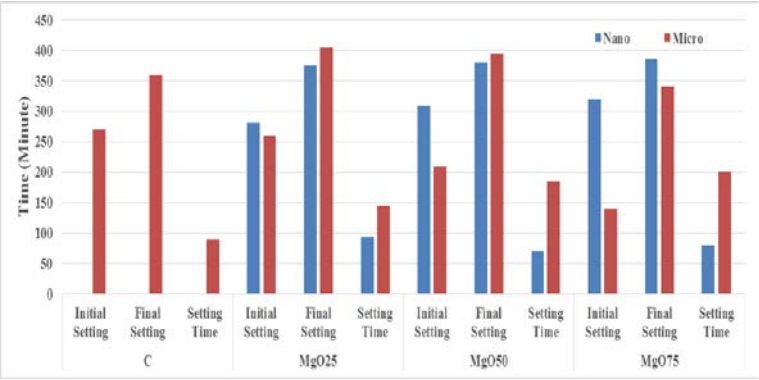

Figure 2. Comparison of initial, final and total setting times of C, MgO25, MgO50 and MgO75

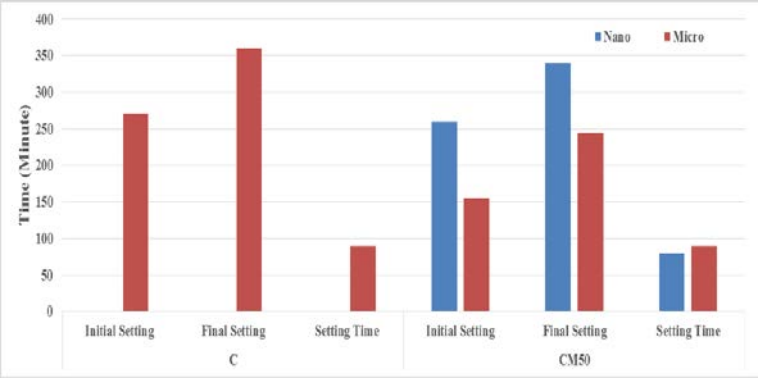

Figure 3. Comparison of initial, final and total setting times of C and CM50

The initial, final and setting times of CM50 sample are lower than the C's (Figure 3). Additionally, initial and final setting times of nano-MgO sample are higher than micro-MgO sample's. However the total setting time of nano-MgO is lower than the micro-MgO sample's. The solution constant of MgO is lower than the CaO's and it earlier precipitates. The formation of $Mg(OH)_2$ reduced the saturation of $Ca(OH)_2$ and thus the initial time of hydration is postponed. $Mg(OH)_2$ forms a protective layer surrounding the cement grains and thus the hydration is delayed [25].

3.2. Mortar

3.2.1. Compressive strength

Figure 4 shows that the compressive strengths of C, CaO, MgO and the combination of CaO and MgO for 7 and 28 days. The 7 and 28 days compressive strengths of the samples produced with nano-CaO are higher than that of the C. The difference between 7 days the compressive strengths of C and nano-CaO samples rises by increasing the admixture amount. The compressive strengths of the nano-CaO25, nano-CaO50 and nano-CaO75 improved about 12%, 11% and 14%, and 12%, 13% and 16% according to C for 7, and 28 days, respectively. The $Ca(OH)_2$, which formed by the reaction between CaO and water, precipitates in the pores of concrete and a denser paste was obtained. SF, $Ca(OH)_2$ reacts with water and may form C-S-H. In this way the gel amount rises and capillary void dimensions and quantities decreases. As a result of this phenomena, the compressive strength of the sample produced with nano-CaO increases [41-42].

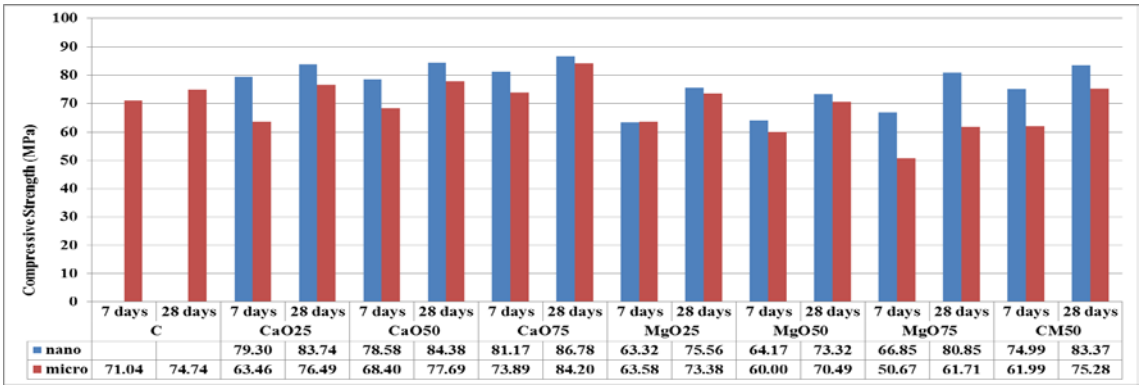

	7 days	28 days	7 days	28 days	7 days	28 days	7 days	28 days	7 days	28 days	7 days	28 days	7 days	28 days	7 days	28 days
	C		CaO25		CaO50		CaO75		MgO25		MgO50		MgO75		CM50	
nano			79.30	83.74	78.58	84.38	81.17	86.78	63.32	75.56	64.17	73.32	66.85	80.85	74.99	83.37
micro	71.04	74.74	63.46	76.49	68.40	77.69	73.89	84.20	63.58	73.38	60.00	70.49	50.67	61.71	61.99	75.28

Figure 4. The compressive strengths of C and CaO25, Ca50, Ca75, MgO25, MgO50, MgO75 and CM50 for 7 and 28 days

The compressive strengths of nano-CaO are higher than that of micro-CaO samples. The 7 days compressive strengths of the C are higher than that of micro-CaO. However, the 28 days compressive strengths of micro-CaO are higher than that of the C. The compressive strengths of micro-MgO samples are lower than that of the C. For example, the 7 days compressive strengths of C, MgO25, MgO50 and MgO75 are 71.04, 63.58, 60.00 and 50.67 MPa, respectively. The 7 days compressive strengths of samples with nano-MgO are lower than that of the C. But the 28 days compressive strengths of nano-MgO samples are higher than that of the C. The reason of this result is that MgO which initially slows hydrate; it has contributed to the continuation of hydration at a later age. The rate of increase in compressive strengths of nano and micro sizes CM50, which significantly effects of the concrete properties, are 11% and 21% from 7 to 28 days while the C's is 5%. The highest compressive strength is 86.78 MPa at 28 days curing duration and it belongs to CaO75.

3.2.2. UPV

UPV test is based on the measurement of the speed of electronic waves through materials [43]. Internal cracks, voids and micro structure of cement paste or mortar can be detected with this test [44-45]. UPV value of 28 days C was assumed that 100% and UPV values of the other mixtures were proportioned to the control UPV values. Figure 5 shows UPV values of all mixtures. The UPV values are correlative with compressive strengths. The highest UPV value belongs to CaO75. Compared to the C, it can be concluded that the groups containing CaO have a denser structure.

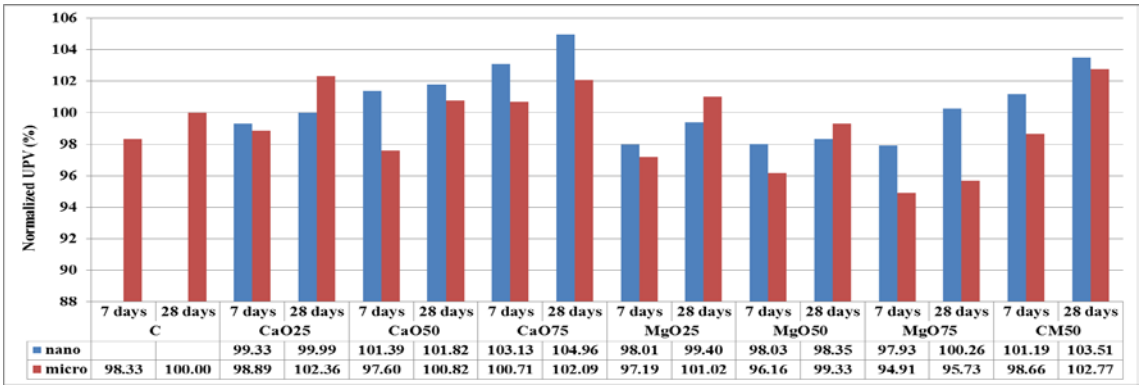

	7 days	28 days	7 days	28 days	7 days	28 days	7 days	28 days	7 days	28 days	7 days	28 days	7 days	28 days	7 days	28 days
	C		CaO25		CaO50		CaO75		MgO25		MgO50		MgO75		CM50	
nano			99.33	99.99	101.39	101.82	103.13	104.96	98.01	99.40	98.03	98.35	97.93	100.26	101.19	103.51
micro	98.33	100.00	98.89	102.36	97.60	100.82	100.71	102.09	97.19	101.02	96.16	99.33	94.91	95.73	98.66	102.77

Figure 5. The UPV values of C and CaO25, Ca50, Ca75, MgO25, MgO50, MgO75 and CM50 for 7 and 28 days

3.2.3. Heat of hydration

As shown in Table 7, the heat of hydration increased with time for all the mixtures and very fast during the first 16 hours. The heats of hydration of all samples are higher than that of the C. Especially, the samples containing nano-CaO have much the highest heat of hydration. There is a linear relationship between amount of CaO and heat of hydration. After 48 hours, the lowest value is 290.6j/g that belongs to C and the highest value is 338.1j/g that belongs to micro-CaO75. As a result of the study it can be conclude that the use of CaO and MgO have a positively effect on the heat of hydration.

Table 7. The heat of hydration for all mixtures (j/g)

Time (h)	C	CaO25		CaO50		CaO75		MgO25		MgO50		MgO75		CaO25-MgO25	
	-	nano	micro	nano	micro	nano	micro	nano	micro	nano	micro	nano	micro	nano	micro
	Heat (J/g)														
0	12.9	28.6	23.0	45.8	23.7	54.9	25.0	0.0	11.5	9.3	6.5	10.0	12.2	22.91	20.08
1	16.2	45.4	37.4	60.8	41.8	67.7	56.4	13.8	19.1	24.8	16.1	26.3	24.9	37.32	29.3
2	18.0	54.5	47.8	70.3	52.3	80.1	80.3	21.4	23.2	31.2	20.1	33.5	30.6	45.49	35.1
3	22.1	69.6	63.5	91.6	73.1	105.6	114.2	32.1	30.2	44.3	27.2	45.1	39.3	60.36	45.4
4	31.3	95.9	84.6	130.0	101.0	152.3	158.4	51.7	43.3	64.9	39.4	68.7	54.1	87.91	64.0
5	45.1	139.5	111.3	186.0	136.2	210.0	218.1	81.9	63.9	99.1	57.1	105.1	75.7	134.23	90.2
6	61.5	193.6	146.6	224.6	183.7	243.2	253.9	125.9	88.0	150.1	80.2	159.1	101.5	190.43	122.1
7	81.8	225.8	193.0	249.5	223.0	266.5	275.2	174.0	117.0	195.1	105.4	200.0	131.5	221.83	162.0
8	104.8	250.7	220.1	267.0	243.5	281.8	288.1	203.6	150.9	222.9	134.8	227.3	164.3	243.77	204.4
9	134.2	265.2	238.3	278.2	259.3	292.1	297.6	225.8	185.8	242.0	167.8	245.7	195.8	258.16	228.1
10	165.7	275.6	252.5	287.3	269.6	300.9	305.7	240.5	210.5	254.9	197.1	257.9	221.4	268.4	245.8
11	186.2	284.0	261.8	294.3	277.8	308.2	313.2	251.9	227.7	264.3	217.0	267.3	240.3	277.35	257.2
12	201.4	291.6	270.5	301.4	285.3	314.0	319.8	261.2	240.2	272.3	232.8	276.2	255.9	283.43	266.6
13	214.0	297.9	277.1	307.0	290.6	319.9	325.8	266.9	249.9	279.7	243.9	283.7	268.2	290.23	274.6
14	224.6	303.4	283.0	311.9	297.4	324.1	330.3	274.1	258.3	286.4	254.3	289.7	278.4	296.32	282.0
15	233.1	308.2	288.1	314.5	302.1	327.6	334.7	280.0	265.3	292.4	262.0	295.8	287.2	300.96	287.9
16	240.3	310.8	294.0	317.9	307.4	330.2	337.6	285.1	272.3	296.9	269.8	300.3	294.7	304.83	293.9
17	246.0	314.6	299.0	320.4	311.2	332.6	341.0	289.3	277.8	299.9	276.0	304.8	301.4	307.92	299.0
18	252.6	317.0	303.3	322.8	315.0	333.5	343.1	292.1	282.0	303.6	281.7	307.2	306.1	310.21	302.7
19	256.9	318.6	306.2	324.4	318.7	334.2	343.5	294.9	287.0	306.5	286.6	309.4	310.7	311.68	305.6
20	262.0	320.1	309.0	324.4	320.3	335.6	345.3	297.5	290.3	307.9	290.7	311.6	313.8	311.61	308.5
21	264.9	320.7	311.7	325.8	322.5	335.4	345.5	299.4	292.9	309.9	293.5	312.9	315.5	312.86	310.6
22	269.2	321.3	313.6	326.3	323.8	336.5	346.3	300.5	295.5	311.1	296.8	314.9	317.7	313.98	312.6
23	272.8	322.4	315.4	325.9	325.7	336.0	347.0	302.2	296.6	312.2	299.4	314.5	319.1	314.27	314.4
24	274.8	322.0	315.7	325.4	326.8	336.1	346.8	303.7	298.2	313.2	300.4	315.6	321.1	314.42	315.5
25	277.5	322.2	317.4	326.3	327.8	336.8	347.9	303.8	299.7	314.0	302.0	316.4	321.5	315.17	316.5
26	279.5	322.9	318.2	326.2	329.5	336.6	347.4	304.4	300.4	314.1	302.9	316.5	322.6	314.37	317.4
27	280.6	323.6	318.9	325.4	329.5	336.3	346.8	305.0	301.0	314.7	304.3	317.1	322.8	314.87	318.9
28	282.4	323.3	320.2	325.8	328.7	336.7	347.5	306.1	301.5	314.5	304.9	317.7	323.6	315.25	318.8
29	283.4	323.7	320.0	325.4	329.3	336.9	346.6	305.7	302.6	314.9	305.4	318.1	324.4	314.8	319.3
30	285.8	323.3	320.3	324.8	329.7	336.2	346.4	305.9	302.9	315.1	305.8	318.4	324.2	314.95	319.8
31	286.6	323.4	321.3	324.9	329.3	336.1	345.2	306.0	302.4	315.3	306.9	317.9	324.0	314.26	320.1
32	287.3	323.4	320.7	324.9	329.4	335.2	344.7	306.0	303.1	314.6	307.0	318.0	325.0	314.17	320.3
33	288.7	322.6	320.7	324.7	330.2	334.9	345.5	305.9	303.1	314.6	307.1	317.9	324.6	313.26	321.1
34	288.5	322.5	321.4	325.1	329.5	334.5	344.7	306.4	302.9	315.1	307.1	318.5	324.7	314.38	320.3
35	289.0	322.9	321.2	324.7	329.3	334.8	343.8	306.1	303.4	314.2	307.7	317.6	324.7	313.2	320.3
36	289.4	322.5	320.9	323.5	329.0	335.0	342.9	306.4	303.1	314.5	307.5	317.2	324.6	313.39	320.7
37	290.4	322.7	320.5	323.7	328.7	334.3	342.4	305.2	302.6	314.0	307.1	317.5	324.4	312.76	320.4
38	290.6	322.1	321.5	323.0	327.4	333.4	341.9	306.0	302.8	314.1	307.4	316.2	324.8	312.03	320.7
39	290.7	322.1	319.5	322.9	327.6	333.3	342.0	305.3	302.8	314.2	307.6	316.9	324.4	311.92	320.2
40	291.4	321.3	319.5	322.0	326.9	333.0	341.2	305.9	303.5	313.4	307.7	316.2	323.9	310.99	320.2
41	291.4	321.1	318.7	322.5	326.8	332.6	339.7	305.0	302.7	313.2	307.7	316.0	324.0	310.68	319.5
42	290.5	320.9	319.9	321.4	326.6	332.2	340.2	305.4	302.5	312.9	306.9	315.0	324.1	310.28	318.6
43	290.3	320.5	318.2	320.9	326.3	331.6	339.8	305.0	302.9	312.6	308.1	314.7	324.0	309.79	318.4
44	290.6	320.0	317.9	321.1	326.0	330.9	339.4	304.6	302.6	311.4	306.4	314.3	323.1	309.93	318.8
45	290.9	319.5	318.1	320.5	325.5	331.0	339.6	304.0	302.1	312.3	306.8	314.5	322.8	309.27	317.7
46	290.5	318.8	318.2	319.7	324.9	330.9	339.0	304.1	302.3	311.7	307.0	313.8	322.4	308.52	317.9
47	289.9	318.8	316.9	319.6	325.0	330.7	338.3	303.3	301.6	311.0	306.5	313.8	322.6	308.41	318.1
48	290.6	318.6	316.8	319.4	325.0	330.4	338.1	303.7	302.2	311.6	305.8	313.6	322.0	308.89	318.5

3.2.4. Linear autogenous shrinkage

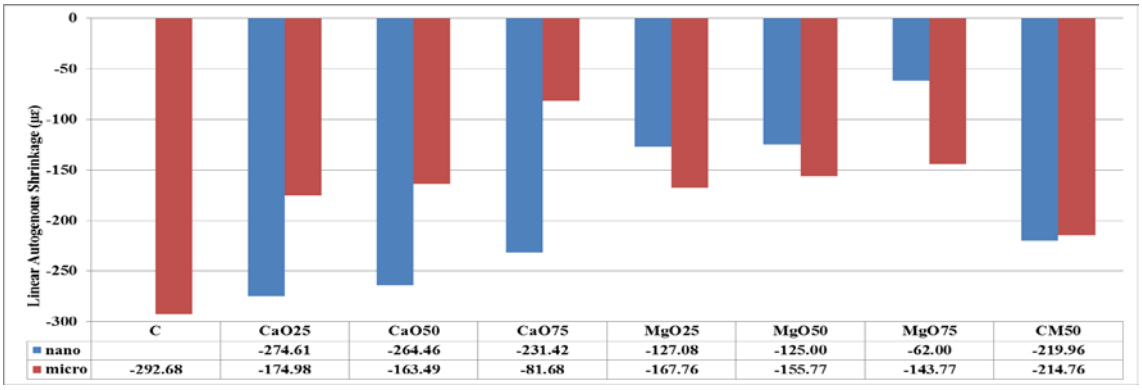

	C	CaO25	CaO50	CaO75	MgO25	MgO50	MgO75	CM50
nano		-274.61	-264.46	-231.42	-127.08	-125.00	-62.00	-219.96
micro	-292.68	-174.98	-163.49	-81.68	-167.76	-155.77	-143.77	-214.76

Figure 6. The linear autogenous shrinkage of C and CaO25, Ca50, Ca75, MgO25, MgO50, MgO75 and CM50

It can be seen from Figure 6 that the autogenous shrinkage of the C is higher than those of the other mixtures. In other words, the autogenous shrinkage was reduced by increasing the amount of additives for 28 days. The autogenous shrinkage of the nano-CaO sample is higher than that of the micro-CaO sample. This can be attributed to the rapid reaction of nano-CaO and water. During the reaction, too much water is used and a large amount of heat is released. Thus the autogenous shrinkage occurs. The particle size of nano material is lower than that of micro material and the specific surface area of nano material is greater than that of micro material and thus nano-MgO expands at early ages, which results in higher amount of the autogenous shrinkage [46]. The autogenous shrinkage of nano-CM50 was lower than C due to CaO and MgO. In addition, the autogenous shrinkages of both size of CM50 are higher than that of the sample with both size of MgO.

4. CONCLUSIONS

The following conclusions can be drawn from this study:

- The addition of nano-CaO and nano-MgO substantially affects the initial, final and total setting time and the total setting time of the nano-CaO sample is shorter than that of the C. The formation of Mg $(OH)_2$ reduced the saturation of Ca $(OH)_2$ and thus the initial time of hydration is postponed. The initial, final and setting times of CM50 sample are lower than that of the C.
- The compressive strengths of nano-CaO25, nano-CaO50 and nano-CaO75 improved about 12%, 13% and 16% for 28 days according to C, respectively. The 28 days compressive strengths of nano-MgO samples are higher than that of the C. The highest 28 days compressive strength is 86.78 MPa and belongs to CaO75 group.
- The UPV values are correlative with compressive strengths. The highest UPV value belongs to samples of CaO75. Compared to the C, it can be said that the groups containing CaO have a denser structure.
- The heat of hydration increased for all the mixtures at an early age (in particular, for the first 16 hours) and very rapid between 4-16 hours.
- In the sample with MgO, the autogenous shrinkage of the sample in the nano size is lower than that of the micro size samples. Both of CaO and MgO provide a significant positive effect on the autogenous deformation, when compared to the C.

ACKNOWLEDGMENTS

This research was supported by the research project “Effects of nano materials on the autogenous shrinkage of high strength concretes” (BAP Code: 2012/441) by Atatürk University, Scientific Research Projects (BAP) Program, Erzurum, Turkey.

REFERENCES

[1]. Hou, P.K., Kawashima, S., Wang, K.J., Corr, D.J., Qian, J.S. and Shah, S.P., 2013. *Effects of colloidal nanosilica on rheological and mechanical properties of fly ash-cement mortar*. Cement & Concrete Composites, 35(1): 12-22.
[2]. Li, H., Xiao, H.G., Yuan, J. and Ou, J.P., 2004. *Microstructure of cement mortar with nano-particles*. Composites Part B-Engineering, 35(2): 185-189.
[3]. Noorvand, H., Ali, A.A.A., Demirboga, R., Noorvand, H. and Farzadnia, N., 2013b. *Physical and chemical characteristics of unground palm oil fuel ash cement mortars with nanosilica*. Construction and Building Materials, 48: 1104-1113.
[4]. Leon, N., Massana, J., Alonso, F., Moragues, A. and Sanchez-Espinos, E., 2014. *Effect of nano-Si_2O and nano-Al_2O_3 on cement mortars for use in agriculture and livestock production*. Biosystems Engineering, 123: 1-11.
[5]. Senff, L., Tobaldi, D.M., Lucas, S., Hotza, D., Ferreira, V.M. and Labrincha, J.A., 2013. *Formulation of mortars with nano-SiO_2 and nano-TiO_2 for degradation of pollutants in buildings*. Composites Part B-Engineering, 44(1): 40-47.
[6]. Morsy, M.S., Alsayed, S.H. and Aqel, M., 2011. *Hybrid effect of carbon nanotube and nano-clay on physico-mechanical properties of cement mortar*. Construction and Building Materials, 25(1): 145-149.

[7]. Farzadnia, N., Ali, A.A.A., Demirboga, R. and Anwar, M.P., 2013. *Effect of halloysite nanoclay on mechanical properties, thermal behavior and microstructure of cement mortars*. Cement and Concrete Research, 48: 97-104.
[8]. Aly, M., Hashmi, M.S.J., Olabi, A.G., Messeiry, M. and Hussain, A.I., 2011. *Effect of nano clay particles on mechanical, thermal and physical behaviours of waste-glass cement mortars.* Materials Science and Engineering a-Structural Materials Properties Microstructure and Processing, 528(27): 7991-7998.
[9]. Hakamy, A., Shaikh, F.U.A. and Low, I.M., 2013. *Microstructures and mechanical properties of hemp fabric reinforced organoclay-cement nanocomposites.* Construction and Building Materials, 49: 298-307.
[10]. Noorvand, H., Ali, A.A.A., Demirboga, R., Farzadnia, N. and Noorvand, H., 2013a. *Incorporation of nano TiO_2 in black rice husk ash mortars*. Construction and Building Materials, 47: 1350-1361.
[11]. Nazari, A. and Riahi, S., 2011. *TiO_2 nanoparticles effects on physical, thermal and mechanical properties of self compacting concrete with ground granulated blast furnace slag as binder*. Energy and Buildings, 43(4): 995-1002.
[12]. Farzadnia, N., Ali, A.A.A. and Demirboga, R., 2013. *Characterization of high strength mortars with nano alumina at elevated temperatures*. Cement and Concrete Research, 54: 43-54.
[13]. Farzadnia, N., Ali, A.A.A., Demirboga, R. and Anwar, M.P., 2013. *Characterization of high strength mortars with nano Titania at elevated temperatures*. Construction and Building Materials, 43: 469-479.
[14]. Liu, X.Y., Chen, L., Liu, A.H. and Wang, X.R., 2012. *Effect of Nano-CaCO3 on Properties of Cement Paste*. 2012 International Conference on Future Energy, Environment, and Materials, Pt B, 16: 991-996.
[15]. Sato, T. and Diallo, F., 2010. *Seeding Effect of Nano-$CaCO_3$ on the Hydration of Tricalcium Silicate*. Transportation Research Record(2141): 61-67.
[16]. Oltulu, M. and Sahin, R., 2013. *Effect of nano-SiO_2, nano-Al_2O_3 and nano-Fe_2O_3 powders on compressive strengths and capillary water absorption of cement mortar containing fly ash: A comparative study*. Energy and Buildings, 58: 292-301.
[17]. Nazari, A. and Riahi, S., 2011. *The effects of TiO_2 nanoparticles on physical, thermal and mechanical properties of concrete using ground granulated blast furnace slag as binder*. Materials Science and Engineering a-Structural Materials Properties Microstructure and Processing, 528(4-5): 2085-2092.
[18]. Nazari, A. and Riahi, S., 2011. *The effects of zinc dioxide nanoparticles on flexural strength of self-compacting concrete.* Composites Part B-Engineering, 42(2): 167-175.
[19]. Choi, S.W., Jang, B.S., Kim, J.H. and Lee, K.M., 2014. *Durability characteristics of fly ash concrete containing lightly-burnt MgO*. Construction and Building Materials, 58: 77-84.
[20]. Gao, P.W., Lu, X.L., Jin, S.C., Hui, Z. and Guo, C.X., 2008. *Using a new composite expansive material to decrease deformation and fracture of concrete*. Materials Letters, 62(1): 106-108.
[21]. Gao, P.W., Xu, S.Y., Chen, X., Li, J. and Lu, X.L., 2013. *Research on autogenous volume deformation of concrete with MgO*. Construction and Building Materials, 40: 998-1001.
[22]. Liu, Z., Cui, X.H. and Tang, M.H., 1992. *Hydration and Setting Time of Mgo-Type Expansive Cement*. Cement and Concrete Research, 22(1): 1-5.
[23]. Mo, L., Deng, M. and Wang, A., 2012. *Effects of MgO-based expansive additive on compensating the shrinkage of cement paste under non-wet curing conditions.* Cement & Concrete Composites, 34(3): 377-383.
[24]. Xu, L.L. and Deng, M., 2005. *Dolomite used as raw material to produce MgO-based expansive agent.* Cement and Concrete Research, 35(8): 1480-1485.
[25]. Zheng, L., Cui, X.H. and Tang, M.S., 1991. *MgO-Type Delayed Expansive Cement*. Cement and Concrete Research, 21(6): 1049-1057.
[26]. Moradpour, R., Taheri-Nassaj, E., Parhizkar, T. and Ghodsian, M., 2013. *The effects of nanoscale expansive agents on the mechanical properties of non-shrink cement-based composites: The influence of nano-MgO addition.* Composites Part B-Engineering, 55: 193-202.
[27]. Polat, R., Demirboga, R. and Khushefati, W.H., 2015. *Effects of nano and micro size of CaO and MgO, nano-clay and expanded perlite aggregate on the autogenous shrinkage of mortar.* Construction and Building Materials, 81: 268-275.
[28]. Ye, Q., Yu, K.K. and Zhang, Z.A., 2015. *Expansion of ordinary Portland cement paste varied with nano-MgO.* Construction and Building Materials, 78: 189-193.
[29]. Maltese C, Pistolesi C, Lolli A, Bravo A, Cerulli T, Salvioni D. *Combined effect of expansive and shrinkage reducing admixtures to obtain stable and durable mortars.* Cement Concrete Res. 2005;35(12):2244-51.
[30]. Corinaldesi V. *Combined effect of expansive, shrinkage reducing and hydrophobic admixtures for durable self compacting concrete*. Constr Build Mater. 2012;36:758-64.
[31]. Collepardi M, Borsoi A, Collepardi S, Olagot JJO, Troli R. *Effects of shrinkage reducing admixture in shrinkage compensating concrete under non-wet curing conditions*. Cement Concrete Comp. 2005;27(6):704-8.
[32]. ASTM C150 / C150M. Standard Specification for Portland Cement. ASTM International, West Conshohocken, PA,www.astm.org; 2015.
[33]. ASTM C33 / C33M. Standard Specification for Concrete Aggregates. ASTM International, West Conshohocken, PA, www.astm.org; 2013.
[34]. ASTM C305. Standard Practice for Mechanical Mixing of Hydraulic Cement Pastes and Mortars of Plastic Consistency. ASTM International, West Conshohocken, PA, www.astm.org; 2014.
[35]. ASTM C191. Standard Test Methods for Time of Setting of Hydraulic Cement by Vicat Needle. ASTM International, West Conshohocken, PA, www.astm.org; 2013.
[36]. ASTM C109 / C109M. Standard Test Method for Compressive Strength of Hydraulic Cement Mortars (Using 2-in. or [50-mm] Cube Specimens). ASTM International, West Conshohocken, PA, www.astm.org; 2016.

[37]. ASTM C597. Standard Test Method for Pulse Velocity Through Concrete. ASTM International, West Conshohocken, PA, www.astm.org; 2009.
[38]. TS EN 196-9. Methods of testing cement - Part 9: Heat of hydration - Semi-adiabatic method. Ankara: Turkish Standard; 2011.
[39]. Kohno K, Okamoto T, Isikawa Y, Sibata T, Mori H. *Effects of artificial lightweight aggregate on autogenous shrinkage of concrete*. Cement Concrete Res. 1999;29(4):611-4.
[40]. Hosseini P, Hosseinpourpia R, Pajum A, Khodavirdi MM, Izadi H, Vaezi A. *Effect of nano-particles and aminosilane interaction on the performances of cement-based composites: An experimental study*. Constr Build Mater. 2014; 66:113-24.
[41]. Siddique R., 2011. *Utilization of silica fume in concrete: Review of hardened properties,* Resources, Conservation and Recycling, 55, 923– 932.
[42]. Erdoğan, T.Y., 2003. Beton. Orta Doğu Teknik Üniversitesi Yayını, Ankara
[43]. Marfisi E, Burgoyne CJ, Amin MHG, Hall LD. *The use of MRI to observe the structure of concrete*. Mag Concrete Res. 2005;57(2):101-9.
[44]. Domingo R, Hirose S. *Correlation between Concrete Strength and Combined Nondestructive Tests for Concrete Using High-Early Strength Cement*. Tokyo Institute of Technology. 2009(3):1-8.
[45]. Karagol F, Demirboga R, Kaygusuz MA, Yadollahi MM, Polat R. *The influence of calcium nitrate as antifreeze admixture on the compressive strength of concrete exposed to low temperatures.* Cold Reg Sci Technol. 2013;89:30-5.
[46]. Li, F.X., Chen, Y.Z. and Long, S.Z., 2010. *Influence of MgO Expansive Agent on Behavior of Cement Pastes and Concrete*. The Arabian Journal for Science and Engineering, 35, 125-139.